

LEGO : linear embedding via Green's operators

Citation for published version (APA):

Water, van de, A. M. (2007). *LEGO : linear embedding via Green's operators*. [Phd Thesis 1 (Research TU/e / Graduation TU/e), Electrical Engineering]. Technische Universiteit Eindhoven. <https://doi.org/10.6100/IR630251>

DOI:

[10.6100/IR630251](https://doi.org/10.6100/IR630251)

Document status and date:

Published: 01/01/2007

Document Version:

Publisher's PDF, also known as Version of Record (includes final page, issue and volume numbers)

Please check the document version of this publication:

- A submitted manuscript is the version of the article upon submission and before peer-review. There can be important differences between the submitted version and the official published version of record. People interested in the research are advised to contact the author for the final version of the publication, or visit the DOI to the publisher's website.
- The final author version and the galley proof are versions of the publication after peer review.
- The final published version features the final layout of the paper including the volume, issue and page numbers.

[Link to publication](#)

General rights

Copyright and moral rights for the publications made accessible in the public portal are retained by the authors and/or other copyright owners and it is a condition of accessing publications that users recognise and abide by the legal requirements associated with these rights.

- Users may download and print one copy of any publication from the public portal for the purpose of private study or research.
- You may not further distribute the material or use it for any profit-making activity or commercial gain
- You may freely distribute the URL identifying the publication in the public portal.

If the publication is distributed under the terms of Article 25fa of the Dutch Copyright Act, indicated by the "Taverne" license above, please follow below link for the End User Agreement:

www.tue.nl/taverne

Take down policy

If you believe that this document breaches copyright please contact us at:

openaccess@tue.nl

providing details and we will investigate your claim.

LEGO
Linear Embedding via Green's Operators

LEGO
Linear Embedding via Green's Operators

PROEFSCHRIFT

ter verkrijging van de graad van doctor aan de
Technische Universiteit Eindhoven, op gezag van de
Rector Magnificus, prof.dr.ir. C.J. van Duijn, voor een
commissie aangewezen door het College voor
Promoties in het openbaar te verdedigen
op woensdag 31 oktober 2007 om 16.00 uur

door

Albertus Maria van de Water

geboren te Wijchen

Dit proefschrift is goedgekeurd door de promotor:

prof.dr. A.G. Tijhuis

Copromotoren:

dr.ir. B.P. de Hon

en

dr.ir. P.J.I. de Maagt

CIP-DATA LIBRARY TECHNISCHE UNIVERSITEIT EINDHOVEN

Water, Albertus M. van de

LEGO: Linear Embedding via Green's Operators / by Albertus M. van de Water. – Eindhoven : Technische Universiteit Eindhoven, 2007.

Proefschrift. – ISBN 978-90-386-1634-6

NUR 959

Trefw.: elektromagnetisme ; numerieke methoden / integraalvergelijkingen / elektromagnetische verstrooiing / fotonische kristallen.

Subject headings: computational electromagnetics / integral equations / electromagnetic wave scattering / photonic crystals.

Copyright ©2007 by A.M. van de Water

The work in this thesis has been financially supported by the Inter-University Research Institute COBRA and the European Space Agency ESA/ESTEC.

“Science does not know its debt to imagination.”

R.W. Emerson

Contents

1	Introduction	1
1.1	Towards a modular design approach	1
1.2	Historical context	5
1.3	General idea and features of LEGO	6
1.4	Example of a design application	9
1.5	Outline of the thesis	12
2	General Field Representations	15
2.1	Introduction	15
2.2	Maxwell's equations	16
2.3	Duality principle	18
2.4	Boundary conditions	19
2.5	The Lorentz reciprocity theorem	22
2.6	Electromagnetic dyadic Green's functions	24

2.7	Huygens' principle and extinction theorem	27
2.8	Love's and Schelkunoff's equivalence principles	32
3	Boundary integral equations	39
3.1	Introduction	39
3.2	General boundary integral formulations	40
3.3	Integral equations for perfectly conducting objects	46
3.4	Interior resonances	47
3.5	Boundary integral equations for dielectric objects	49
3.6	Method of moments and projection methods	50
3.7	Mapping properties of the boundary integral operators	55
4	Linear embedding via Green's operators	59
4.1	Introduction	59
4.2	The scattering operator	61
4.3	Embedding in operator form	68
4.4	Discretization	73
4.5	Composition of scattering operators	77
4.6	Memory requirements and computational costs	89
4.7	Local structure optimization and modification	98
4.8	Embedding versus direct approach	100

4.9	Extension to hybrid methods	104
5	2D scattering objects	107
5.1	Introduction	107
5.2	TE/TM decomposition	108
5.3	Discretization	111
5.4	Integration of the singular integrand parts	125
5.5	Perfect electric conductors	132
5.6	Regularization	146
5.7	Perfect magnetic conductors	148
5.8	Dielectric objects	152
6	Demonstration of LEGO with EBG structures	173
6.1	Introduction	174
6.2	Numerical validation	175
6.3	The construction of large scattering operators	177
6.4	Local structure optimization	184
6.4.1	EBG power splitter	185
6.4.2	EBG mode splitter	190
6.5	Numerical Comparison	194
6.5.1	Love's versus Schelkunoff's equivalence principle	194

6.5.2	Interior resonances	204
6.5.3	Building sequence and accumulation error	208
6.6	Continuity of objects across adjacent domains	211
6.7	Band-gap diagrams	215
7	3D scattering objects	225
7.1	Introduction	225
7.2	Discretization	226
7.3	Integration of the singular integrand parts	239
7.4	Perfect electric conductors	241
7.5	Dielectric objects	252
7.6	Embedding of 3D structures	260
8	Conclusions and recommendations	265
8.1	Recommendations	269
A	Analytical parts of 2D integrals	271
A.1	Evaluation of the singular integrals	271
A.2	The avoidance of branch cuts	274
A.3	Self term	276
B	Scattering from canonical objects	279

B.1	Scattering by circular cylinders	279
B.2	Scattering by spheres	283
C	Far field integrals in closed form	289
C.1	3D far-field integral	289
C.2	2D radiation pattern	291
	References	293
	Summary	304
	Curriculum Vitae	308
	Acknowledgements	310

Chapter 1

Introduction

As a general introduction, this chapter describes the relevance of the work, the connection with existing work, and its potential with respect to future applications. First, we discuss what properties simulation software for device design should ideally have. By indicating the opportunities for further improvement in present electromagnetic design techniques, we substantiate how the modeling technique that we demonstrate may contribute in this matter. Subsequently, we provide a historical context that describes the underlying techniques. Next, the scope of our method is illustrated through a list of features. Finally, we outline the organization of the thesis.

1.1 Towards a modular design approach

Nowadays, businesses are facing an ever stronger competition in an expanding global market. Consequently, products have to be developed and improved more rapidly to meet the demand of the consumers. On the other hand, products become more complex and involve more sophisticated and expensive production processes. The incentive to reduce lead time and product costs calls for ongoing improvements in product development time. Before the introduction of the computer, product specifications were attained through an iterative process in product manufacturing. Each subsequent iteration involved further product optimization and tuning through feedback from measurements on prototypes. Because this often required several prototypes to be made before specifications were satisfied, product development tended to be slow. The prototype was preceded by a design stage, which usually amounted to making predictions based on

extracted models, possibly supported by small but indicative experiments. Such an approach is at present considered as too costly and time-consuming for product development.

The advance of computers has led to a shift of product optimization from the production stage to the preceding design stage. Via numerical methods, the behavior of the final product can be predicted in a real-life environment. As a result, less prototypes have to be constructed before the final product can be manufactured. To minimize product variation, the fault tolerances of the manufacturing process may be accounted for in the design stage through a sensitivity analysis. The optimization and sensitivity analysis call for repeated simulation steps, which in case of stringent product specifications or large complex products can be time-consuming. Consequently, the design stage has become a decisive factor in the overall product development time.

According to Moore's law [1], the number of transistors on integrated circuits doubles every 18 months. Ever since the introduction of the computer, Moore's law represented a rough measure of computer processing power. Present developments in integrated circuits tend to focus on parallel processing, e.g., grid computing and multi-core processors, or on Hyper-Threading technologyTM, rather than the increase of CPU speed. Most single-computer applications for electromagnetic simulations are not fully taking advantage of parallel-processing technologies. In particular, large complex products often need to be simulated in one go to account for the interaction between all its parts. Such common simulation approaches are thus not necessarily well suited for parallel processing. Although parallel processing can often be introduced in the implementation, it may come at the cost of efficiency. In electromagnetics, a new modeling technique that inherently lends itself to parallel processing would be a most welcome asset.

Device design involves tuning of certain product properties, referred to as the design parameters. The design parameters that require tuning are first identified from the product specifications and the design draft. Depending on the complexity and size of the product, there may be a large number of design parameters. Commercial simulation software packages that are available nowadays, at best come with a straightforward optimization shell, i.e., optimum parameter values are determined through parameter sweeps. Intuitively, more parameter evaluations lead to a better analysis of the design. Each set of parameter values that is considered usually requires a full recomputation of the entire device, which may be time-consuming. Clearly, the overall computation burden to consider all parameter variations with such brute-force optimization methods will soon become an obstacle in view of the stringent constraints on the development time of products. Hence, either the simulation time for each parameter value or the optimization strategy has to be improved to prevent the product design from becoming too costly.

One should also consider that the composition of an initial design draft is normally realized via a top-down approach, whereas the device constituents are mostly developed via a bottom-up approach. The design draft is then systematically subdivided into definite blocks of a tree diagram. This systematic design approach is preferably followed in the actual device design as well, such that blocks may be designed and optimized separately. At each stage, the performance of the composite device is then evaluated by combining the known properties of its already optimized constituents rather than by a full recomputation of the complete structure. Unfortunately, present simulation software is not in line with this desired systematic design approach, since a minor structure modification often requires repeating a full simulation of the entire product. Intuitively, the re-evaluation of the entire structure for a minor local modification seems excessive.

In network theory, simulation methods exist that are consistent with the preferred systematic design approach described above. In particular, in electrical networks the physical properties of a circuit element that contribute to its electric behavior are captured in terms of the relation between voltages and currents at input and output ports. A network is readily extended by combining the corresponding circuit(s), i.e., by accounting for the electric interaction at the ports. This is referred to as diakoptics [2]. As regards optimization in network theory, the linked circuit elements are first converted into a simple equivalent network defined at the ports of the element that is optimized, thereby attaining maximum efficiency for repeated component modifications. Accordingly, via the modular approach associated with network theory, circuit elements are reusable and can be tuned efficiently.

In a full electromagnetic device design, there are at present no tools available that are in line with the desired systematic design approach. Most electromagnetic simulation methods are still brute-force solvers, for which each minor structure modification requires a full recomputation. Moreover, in commercial software packages, optimization is based on straightforward parameter sweeps, if available at all. The only way in which structure parts are reused in software to date is in structures that are fully periodic along a predefined direction. Large finite arrays are then initially treated as infinite arrays to exploit reusability, while effective finiteness is reintroduced through analytic approximations [3,4].

The schematic design approach in network theory could be applied in an electromagnetic sense through the introduction of a modular electromagnetic modeling technique. The challenge is to define appropriate input and output ports in combination with a method that determines the field interaction between different elements. We have developed a new electromagnetic modeling procedure that allows a modular design approach, called linear embedding via Green's opera-

tors (LEGO). The definition of the ports is based on equivalence principles. In particular, the electromagnetic field response of scattering objects that are enclosed by a scattering domain is described in terms of equivalent boundary current distributions. Through an extension of a diakoptics method, referred to as embedding [5, 6], we account for the electromagnetic interaction between separate domains to arrive at a full electromagnetic characterization of the combined domain. In turn, the composite domain can be repeatedly reused to form larger composite domains, which illustrates the modular building approach.

Via our modular approach, the electromagnetic structure design process could be made to mimic present circuit design. Ideally, structure modifications then amount to combining appropriate electromagnetic building blocks in a design diagram. Such electromagnetic blocks are predefined at an earlier stage and are provided through large databases, similar to circuit and component libraries in network theory. These databases contain the elementary structure constituents. The design stage is then limited to the proper combination of blocks, thereby attaining maximum efficiency. The results of each intermediate combination step may be appended to existing databases and reused at will. Attention can thus be focussed on the critical design parameters in localized blocks. This approach facilitates an interactive design process and provides insight into the behavior of the separate structure parts, as the field responses may be visualized at any stage within a building sequence. Since the memory size and data transfer rate of data storage devices such as hard disks have improved significantly over the last decade, managing large databases that are stored on disk has become feasible. Clearly, the modular approach is inherently suitable for parallel processing. This modular electromagnetic technique corresponds with the desired schematic design approach, since products can be conveniently subdivided into elementary blocks that are designed separately and combined at a later stage.

The modular electromagnetic approach that we propose also facilitates structure optimization. Owing to the modular concept, a full recomputation of the entire structure is already avoided since only the block that encloses the structure modifications is to be recomputed, while the electromagnetic interaction with the unchanged blocks is determined through embedding. Electromagnetic optimization often implies local structure variations within a small designated domain. Analogous to network theory, the field response of the fixed large structure can be described in terms of an equivalent surrounding environment defined at the boundary (ports) of the designated domain. Because the boundary of the designated domain is significantly smaller than that of the large structure, subsequent structure modifications within the designated domain can be carried out with great efficiency.

Other techniques are available to speed up optimization. For instance, “reduced-order-modeling” [7], amounts to a simplified model using a decomposition into dominant and subdominant eigenstates. In “marching on in anything” [8, 9], the results of simulations for previous parameter values are combined to generate an initial estimate so as to accelerate iterative solution methods. With these techniques, either the accuracy of the model is compromised, or the full complexity of the entire structure has still to be accounted for. Because repeated simulations of the entire structure for each new parameter value dominate the overall computation time, most improvement can be attained there. This is provided by our modular approach.

1.2 Historical context

In this section, we provide a historical overview of electromagnetic methods that form a basis for the modular electromagnetic procedure that we propose. Here, we follow the introduction of [10], except that we leave out the review of electromagnetic bandgap structures.

The field scattered in an inhomogeneous region with electromagnetic contrast may be considered as being generated by secondary contrast sources inside, or on the boundary of that region. Invoking Huygens’ principle [11], we may consider the scattered field outside a contour (or surface in the 3-D case) surrounding the inhomogeneous region, as having been generated by an equivalent source distribution on that contour (surface). Mathematically, this is referred to as an equivalence principle. The equivalent source distribution is not unique. Love’s equivalence principle [12] is based on both electric and magnetic equivalent current sources, whereas Schelkunoff’s equivalence principle [13] involves either electric or magnetic equivalent current sources. From the perspective of an observer outside the contour surrounding the inhomogeneous region, that region may be fully characterized electromagnetically through the scattering response via the equivalent source distributions that effectively constitute a multi-port system (albeit a continuous one).

The decomposition of large systems into interacting multi-port subsystems is called diakoptics [2]. Having been used in early days for problems in structural mechanics and electric networks, diakoptics has later been combined with the method of moments for the analysis of wire antennas [14, 15], and for planar microwave circuits [16]. For these problems, the definition of the ports comes naturally. Diakoptics has been applied to field problems in quantum mechanics and electromagnetics through the introduction of a non-local admittance operator that provides the

boundary conditions for a variational field problem in a confined region of space [17–20]. This method is referred to by the generic term embedding. More recently, diakoptics has been used for supplying boundary conditions for the Finite-Difference Time-Domain technique, which resulted in the so-called Green’s Function Method [21,22]. Embedding has been proposed in inverse scattering [5, 6] as an alternative to de-embedding, which, like deconvolution, is not stable *per se*. We have developed a specific variety of the Huygens-Schelkunoff principle based diakoptics, referred to as linear embedding via Green’s operators (LEGO). A first 2D theoretical derivation of the embedding stage of LEGO using Schelkunoff’s equivalence principle has been given in [23], which presents an extension of embedding applied to surrounding scattering domains used in inverse profiling [8] towards adjacent domains. This extension has provided a starting point for the work that is presented in this thesis. In addition, for the full 3D implementation of LEGO, we have continued the work of [24].

Several domain decomposition methods similar to diakoptics have been presented in the last decade to reduce the computational burden associated with electromagnetically large scattering configurations, e.g., a network representation of the domains by means of an equivalent circuit extraction procedure [25]. Further, by using entire domain functions via synthetic basis functions (SBF) that sample the solution space [26], a strong reduction of memory usage can be attained. Alternatively, via the characteristic basis function method (CBFM) [27] the scattering object can be partitioned into distinct domains which can be described by a set of basis functions that are characteristic for the individual domains. Most recently, a domain decomposition method has been presented that applies a domain characterization that is similar to that of LEGO [28].

1.3 General idea and features of LEGO

As illustrated in Figure 1.1, we start by sketching the general idea of linear embedding via Green’s operators (LEGO). The abbreviation “LEGO” reflects the modular building principle of the method that is common to the well-known LEGOTM bricks. In the first step we identify and construct the elementary building blocks. A building block involves a scattering domain that encloses one or more scattering objects. In Figure 1.1, a hexagonal shape has been selected for the scattering domain of an elementary building block. To combine a block with other ones or itself in an electromagnetic sense, a full electromagnetic characterization of its scattering properties is required. A conventional scattering operator relates the scattered fields to fields that are incident on the boundary. Our scattering operator is a Green’s operator, since it relates equivalent

sources that would produce the scattered field exterior to the domain to the equivalent sources that would produce the incident field inside the domain.

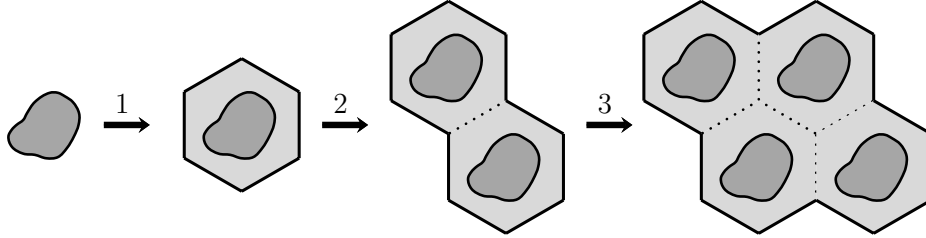


Figure 1.1: Building large structures through a sequence of domain combinations. Dotted lines indicate removed common boundary parts.

In the second step in Figure 1.1, we combine two elementary blocks. Via embedding, we first determine the electromagnetic interaction between the adjacent elementary building blocks in terms of their scattering operators. Embedding is regarded as a linear process since the medium properties of the environment and hence the associated scattering operators are considered linear. The LEGO approach is completed upon composing the scattering operator of the combined domain. To this end, the scattering operators of the individual blocks are merged via their known electromagnetic interaction. Common boundary parts are removed in this process. In turn, the composite block can be combined with itself, indicated by the third step in Figure 1.1, or with a different block.

To provide an impression of the potential applications of the LEGO procedure, we list the features of LEGO below.

- The scattering domain of a LEGO building block may be of arbitrary shape.
- The scatterer(s) that are enclosed by the scattering domain may be of arbitrary shape.
- The scattering operator that electromagnetically characterizes a scattering domain encompasses the scattered field for all possible excitations.
- Scattering operators of separate building blocks can be merged to create larger ones.
- Owing to the modular approach of LEGO, it is in line with the preferred systematic approach of a design process.
- With LEGO it is not required to identify all elementary blocks *a priori*, i.e., new blocks can be constructed on the fly through an interactive design process.

- Common boundary parts are removed when scattering domains are combined. In this way, subsequent LEGO steps become more efficient.
- Via repeated application of the LEGO approach, it is possible to handle large finite structures, e.g., antenna arrays, frequency selective surfaces or meta-materials. Especially for blocks that enclose scattering objects with high refractive indices.
- Databases can be constructed and managed which provide libraries of electromagnetic blocks that have been predefined at an earlier stage. The design stage is then limited to the proper combination of blocks in a schematic approach. Each combination of blocks may be appended to existing databases.
- LEGO blocks are reusable. Hence, we can take full advantage of the reusability of structure parts, no matter how insignificant the scale of repetition is. In Figure 1.1 is visible how the reusability of the elementary block is used in the building sequence of LEGO.
- Since various LEGO blocks can be constructed via independent building sequences, LEGO is inherently suitable for parallel processing technologies of modern computers.
- Owing to the modular approach of LEGO, design modifications can be performed without the need for repeated full simulations of the entire structure. Instead, only those blocks that are modified have to be recombined with the other one(s).
- Since device design often involves tuning local structure properties, the optimization stage of LEGO can be accelerated considerably. Namely, restricting the embedding steps in the design stage to a designated domain that is small compared to the large structure that requires tuning, subsequent embedding steps for parameter sweeps become very efficient.
- Scattering objects may continue beyond domain boundaries. Because of this, the shape of the scattering object(s) pose no restrictions on the choice of the enclosing domain shape.
- LEGO is a flexible method. On the one hand, any fundamental solution to Maxwells equations for the enclosed interior domain may be employed to construct the scattering operators of the elementary building blocks. On the other hand, the LEGO approach can be integrated within existing software design packages. In particular the optimization step of LEGO.
- Within the LEGO procedure, the band diagram of EBG structures can be determined via the scattering operator of a unit cell. The unit cell may contain inhomogeneous or perfectly conducting objects that may be continuous across the cell boundary.

- Since the frequency is kept fixed in the LEGO procedure, it automatically applies to dispersive and lossy media.

1.4 Example of a design application

Below, we present an example of a design application involving electromagnetic bandgap structures (EBG). The design has been realized via a commercial full 3D general purpose finite-element method, viz., Ansoft HFSSTM. Afterwards, we review the design approach and indicate how the design process could have benefited from the LEGO approach. As an example, we design a transition between a standard-size rectangular waveguide with perfectly conducting walls, and a linear-defect dielectric EBG-waveguide with a full 3D bandgap, centered at about 250GHz in the mm-wave regime. In addition, bends and power splitters connected to this transition have been tuned.¹ We expect that these are to be basic components for devices in future integrated technologies based on EBG's. The woodpile EBG structure [29], which yields a full 3D bandgap, is employed as a basis. An illustration of the woodpile structure is given in Figure 1.2a. It consists of stacked layers of rectangular silicon bars with a relative permittivity of $\epsilon_r = 11.7$.

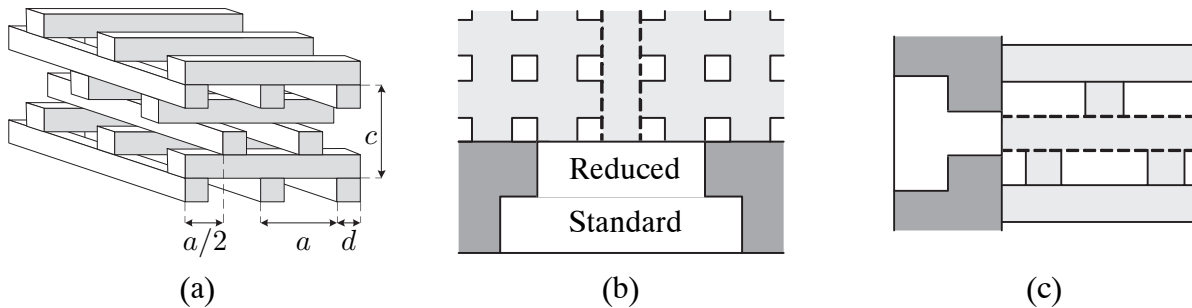


Figure 1.2: The woodpile structure (a) with $a = 471 \mu\text{m}$, $d = 146 \mu\text{m}$ and $c = 576 \mu\text{m}$ for a bandgap of 20% and a center frequency of 250 GHz. The top (b) and side-view (c) of the two-step transition of standard-size metallic waveguide into EBG-waveguide. The removed bar is the dashed one. The dark and light gray regions indicate metal and silicon, respectively.

An EBG waveguide inside a woodpile structure can be realized by removing a single bar in the desired direction of propagation. To interface a waveguide in EBG technology with one implemented in conventional waveguide technology, an efficient tapered transition is necessary to avoid large insertion loss at the junction due to a mode mismatch between both waveguides.

¹This work has been carried out for the European Space Agency StarTiger initiative (<http://www.startiger.org>).

Integration of a dielectric waveguide in the EBG via tapering is a commonly used approach in the optical regime to avoid unwanted radiation into the surroundings [30, 31]. The design of a practical connection between a metallic and an EBG waveguide is more challenging.

In Figure 1.2, we show the final two-step transition by which a TE_{01} mode of a standard-size metallic waveguide can be coupled to an EBG waveguide. By trial and error, we have determined the position at which the EBG must be terminated so as to provide the best mode-match between the EBG-waveguide mode and the TE_{01} mode. In Figure 1.3, the electric field is depicted for a standard-size rectangular waveguide that couples, using the two-step transition of Figure 1.2, at both ends of an EBG waveguide that is 7.5 periods long. The transmission efficiency is 97.9% with an insertion loss of the transitions that is less than 1%. The remaining losses are due to radiation emanating from the woodpile.

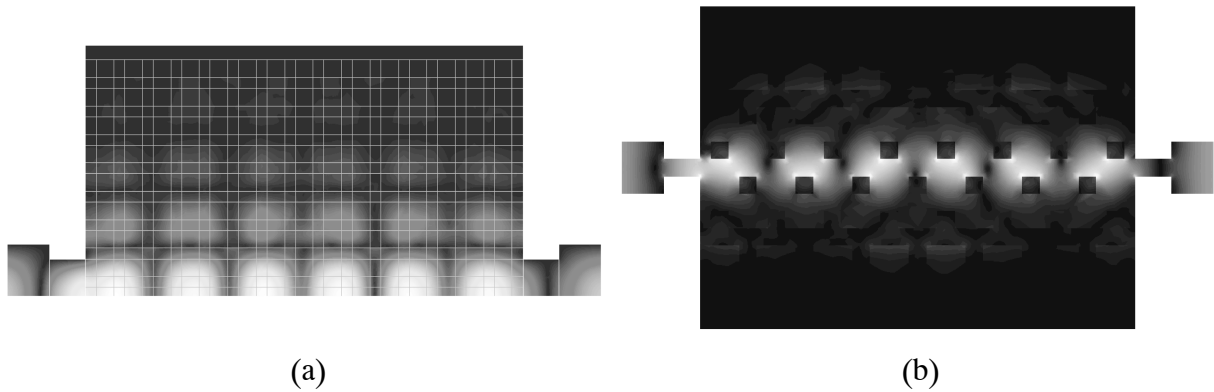


Figure 1.3: The electric field for a cross section at the center of the EBG-waveguide parallel to the top (a) and side (b) view of Figure 1.2b and Figure 1.2c, respectively. The transition into standard-size metallic waveguide are employed at both EBG-waveguide ends. White regions indicate a high field amplitude.

Bends and splitters can be created in the woodpile structure by partial removal of bars at right angles, allocated one layer above or below each other, as illustrated in Figure 1.4a. The overshoot distances, (Δ_b and Δ_s) of the two removed crossing bars are utilized to create a localized cavity that provides the necessary coupling between both layers [32]. In Figure 1.4, we have shown the electric field for an EBG bend and a power splitter-branch. The use of the two-step transition yields 96.6% transmission.

The design of the EBG-technology components has been successful. However, the design process has been very slow because at every step in the brute-force optimization stage based on parameter sweeps, the field simulation had to be repeated for the entire 3D structure. With a mesh

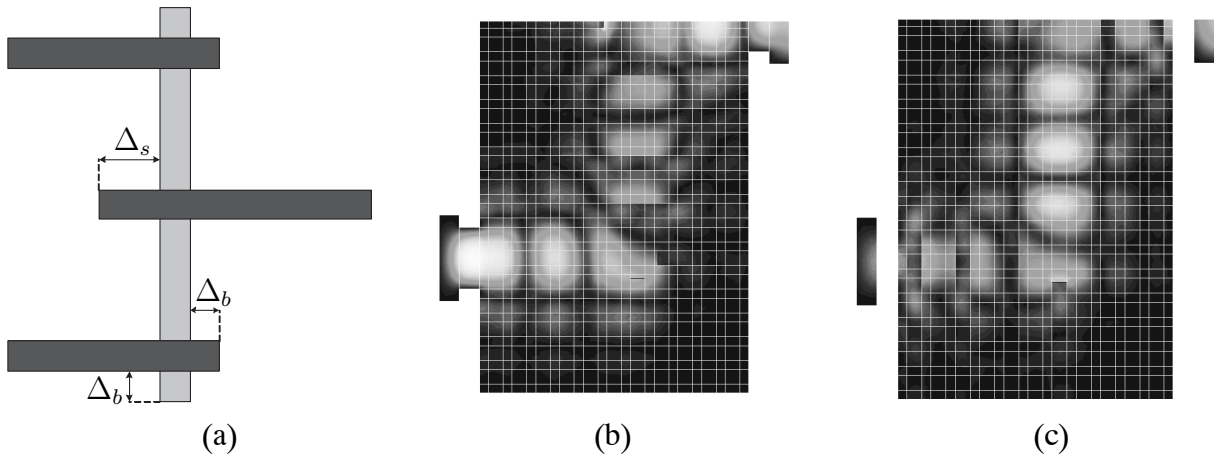


Figure 1.4: An overview of the removed bars for a power splitter and two bends in an EBG-waveguide (a). The grey-colored bar represents a layer up or down. The electric field is shown for a cross section at the black- (b) and grey-colored (c) bar(s), with transitions into metallic waveguides. White regions indicate a high field amplitude.

consisting of about $2 \cdot 10^5$ tetrahedra, which is modest by today's standards, such an optimization approach required several hours for each set of parameter values.

If the LEGO approach had been applied, the first step in the design would be the construction of the elementary building block(s). A convenient choice would be a single unit cell of the wood-pile EBG. Next, we would compose the large basis EBG structure through repeated embedding steps. LEGO would take advantage of the reusability of the elementary blocks. By building a large database, each block combination can be conveniently reused at a later point. Common boundaries are removed when blocks are merged. In this way, consecutive combinations become more efficient. In combination with the reusability of blocks, the computational complexity of LEGO may be competitive with that of the direct solver. Further, each block is defined in terms of scattering operators, which encompasses the field response for all possible excitation. In particular, if we select a small designated domain in which we allow for structural variations, its boundary and hence the associated scattering operator that describes the response of the fixed environment would be small as well. Thus, the fine tuning of the bend, splitter and two-step transition would become very efficient in the optimization stage of the LEGO procedure. At present, the LEGO software is a research code, which lacks a user-friendly I/O interface and a versatile mesh generator, which is why we have not attempted to process the structures described above using the LEGO approach.

1.5 Outline of the thesis

In the LEGO approach, equivalence principles are used to formulate scattering problems in terms of equivalent source distributions, which, when used in source-type integral representations, produce the incident or scattered field in certain subdomains in space. In Chapter 2, we present the basic theory in which those integral representations are formulated. In particular, after deriving the general field integral representation in terms of the well-known Stratton-Chu formulas, we discuss Love's and Schelkunoff's equivalence principles (LEP and SEP), and define the equivalent boundary current distributions associated with the equivalent field states. In Chapter 3, these equivalent states are applied to formulate boundary integral equations by which the scattered field response of perfectly conducting and dielectric objects may be determined. These integral equations may also be employed to construct the elementary LEGO building blocks. Since the tangential scattered field on the object boundary is unknown, the method of moments procedure is employed to determine the equivalent currents. This solution strategy may also be used to compute the unknown equivalent currents on the scattering domain boundary for LEGO.

In Chapter 4, the principle of LEGO is introduced in terms of a transparent operator formalism. The general definition of the pertaining operators applies to both LEP and SEP. The LEGO approach is extended to optimize large structures efficiently within small designated domains. After the discretization of the operators, we assess the computational complexity of the LEGO approach, which is compared with direct solution methods. Further, a hybrid variety of LEGO is discussed by which other electromagnetic solution methods may be incorporated.

In Chapters 5 and 7, we discretize and investigate the integral equations for the scattering from perfectly conducting and dielectric objects for the 2D and 3D cases, respectively. The solvability and the order of convergence of the numerical approximation for the scattered fields are investigated. Several ideas are proposed to improve the results. The insight that is gained may be utilized in the LEGO approach to attain maximum performance through an optimal choice of the equivalence principle, the domain shape, the mesh density, the quadrature rule and the test and expansion functions.

In Chapter 6, we illustrate the LEGO approach numerically for examples involving electromagnetic bandgap structures. The wide applicability as a design tool for large finite structures is demonstrated and the optimization stage of LEGO is used to design EBG power and mode splitters. The accuracy of LEGO based on SEP and LEP is investigated, in combination with the

suppression of interior resonances. More general aspects are treated as well, e.g., the dependence on the building sequence, the choice of domain shape and the loss of accuracy due to the accumulation of errors associated with a sequence of embedding steps. Further, we consider scattering objects that are continuous beyond domain boundaries. As an additional application of LEGO specific to EBG structures, we determine the band structure of EBG materials. The LEGO approach is demonstrated for a full 3D scattering configuration at the end of Chapter 7. Finally, in Chapter 8, the main conclusions are drawn of the work that is reported in this thesis and recommendations are given for further development and applications of the LEGO method.

Chapter 2

General Field Representations

In the LEGO approach, equivalence principles are used to formulate scattering problems in terms of equivalent source distributions, which, when used in source-type integral representations, produce the incident or scattered field in certain subdomains in space. In this chapter, we present the basic theory by which those integral representations may be formulated. In particular, after deriving the general field integral representation in terms of the well-known Stratton-Chu formulas, we discuss Love's and Schelkunoff's equivalence principle and define the equivalent boundary current distributions associated with the equivalent field states.

2.1 Introduction

In Section 2.2, the Maxwell's equations, which describe the electromagnetic field, are introduced in the time domain. By enforcing causality of the field, appropriate boundary conditions ensure uniqueness of the field. The general medium properties are set out and, subsequently, Maxwell's equations are considered in the Laplace-transform domain. For the construction of the LEGO scheme it is convenient to introduce notional magnetic sources and currents in Maxwell's equations, which is described in Section 2.3. Boundary conditions for the tangential and normal field components across an interface between two media are presented in Section 2.4. The boundary conditions account for the presence of surface currents. Although Sections 2.2- 2.4 describe basic electromagnetics that can be found in most textbooks and may be skipped, we prefer to include these sections for the sake of completeness and the organization of the thesis.

Next, in Section 2.5 we introduce the Lorentz reciprocity theorem which lays the foundation for the mathematical formulation of Huygens' principle and reciprocal systems. The dyadic Green's function of a homogeneous medium is defined in Section 2.6 to formulate an integral representation for the field that is generated by a point source. In Section 2.7, we derive general field representations for a bounded domain, leading to Huygens' principle and Oseen's extinction theorem. The corresponding integral representation are expressed in terms of the familiar Stratton-Chu formulas. Subsequently, the pertaining equivalent currents are defined in Section 2.8. Further, we present the particular equivalent states by which the field may be partitioned. Finally, we explore the differences between the equivalence principles.

2.2 Maxwell's equations

The electromagnetic field is governed by Maxwell's equations. Together with the constitutive relations these equations describe the coupled behavior of the electric and magnetic field strengths in space and time. Assuming that appropriate boundary conditions are provided for domains with a boundary, uniqueness is guaranteed by enforcing causality conditions. The macroscopic Maxwell equations in the time-domain constitute a hyperbolic system of partial differential equations, given by [33],

$$\nabla \times \mathcal{H} = \partial_t \mathcal{D} + \mathcal{J}, \quad (2.1a)$$

$$-\nabla \times \mathcal{E} = \partial_t \mathcal{B}, \quad (2.1b)$$

where ∇ is the gradient operator and ∂_t denotes differentiation with respect to t . Here, Eq. (2.1a) is referred to as the Ampère-Maxwell law, and Eq. (2.1b) as the Faraday-Henri law. The script font indicates a time-domain representation. The field quantities in Maxwell's equations are set in boldface to emphasize their vectorial nature and represent,

- $\mathcal{E}(\mathbf{r}, t)$ electric field strength [Vm^{-1}],
- $\mathcal{H}(\mathbf{r}, t)$ magnetic field strength [Am^{-1}],
- $\mathcal{D}(\mathbf{r}, t)$ electric flux density [Asm^{-2}],
- $\mathcal{B}(\mathbf{r}, t)$ magnetic flux density [Vsm^{-2}],
- $\mathcal{J}(\mathbf{r}, t)$ volume source density of electric current [Am^{-2}].

Note that \mathcal{J} includes the impressed and induced electric current distributions. Although Maxwell's equations are independent of the applied coordinate system, right-handed orthogonal coordinate systems are applied. In case of a Cartesian reference frame, the position vector reads

$\mathbf{r} = x\hat{\mathbf{x}} + y\hat{\mathbf{y}} + z\hat{\mathbf{z}}$, where the hat denotes a unit-length vector. Maxwell's equations are supplemented with the continuity equation, also referred to as the local form of the charge conservation law,

$$\nabla \cdot \mathcal{J} + \partial_t \rho_e = 0, \quad (2.2)$$

which relates electric charge and current densities with ρ_e being an electric-charge density [Asm⁻³]. Upon taking the divergence of Maxwell's equations and using the continuity equation, we arrive at the so-called compatibility relations,

$$\nabla \cdot \partial_t \mathcal{B} = 0, \quad (2.3a)$$

$$\nabla \cdot \partial_t \mathcal{D} = \partial_t \rho_e. \quad (2.3b)$$

To meet the requirements for uniqueness, the causality condition has to be satisfied, which states that the electromagnetic field is causally related to the action of sources and hence should vanish prior to the instant, say, $t = t_0 = 0$, at which the sources are switched on. Furthermore, the media considered in this thesis are assumed to be linear, passive and time-invariant. To exploit these properties a Laplace transformation with respect to time is performed. The one-sided Laplace transformation is defined as

$$\mathbf{F}(\mathbf{r}, s) = \int_0^{\infty} \mathcal{F}(\mathbf{r}, t) e^{-st} dt, \quad (2.4)$$

with $s = \beta + j\omega$, where $\omega \geq 0$ is the angular frequency. Further, j is the imaginary unit, $j^2 = -1$. An italic font indicates the Laplace-transform vectors. Causality of the field is taken into account by requiring that all causal field quantities are analytic functions of s in the right half ($0 \leq \beta < \infty$) of the complex s -plane. The corresponding inverse Laplace transformation is given by the Bromwich inversion integral,

$$\mathcal{F}(\mathbf{r}, t) = \frac{1}{2\pi j} \int_{\beta-j\infty}^{\beta+j\infty} \mathbf{F}(\mathbf{r}, s) e^{st} ds. \quad (2.5)$$

Usually we select $\beta = 0$, and define the frequency f [Hz] as $f = \omega/2\pi$. From Eq. (2.5) we infer that time-harmonic fields have an $e^{j\omega t}$ time dependence. The continuity equation in the Laplace-transform domain is given by

$$\nabla \cdot \mathbf{J} + s\rho_e = 0, \quad (2.6)$$

and the compatibility relations read

$$\nabla \cdot \mathbf{B} = 0, \quad (2.7a)$$

$$\nabla \cdot (s\mathbf{D} + \mathbf{J}) = 0. \quad (2.7b)$$

Thus far, the system of partial differential equations is incomplete since the constitutive relations describing the field-matter interaction have not yet been specified. We assume that the media are isotropic, locally reacting, and non-chiral, i.e., linear, such that we have the constitutive relations

$$\mathbf{B} = \mu \mathbf{H}, \quad (2.8a)$$

$$\mathbf{D} = \varepsilon \mathbf{E}. \quad (2.8b)$$

The scalars ε and μ represent the complex permittivity [$\text{AsV}^{-1}\text{m}^{-2}$] and permeability [$\text{VsA}^{-1}\text{m}^{-2}$] of the medium. These scalars depend on \mathbf{r} in case of inhomogeneous media and may be cast in the following form

$$\varepsilon = \varepsilon_0 \varepsilon_r + \frac{\sigma_e}{s}, \quad (2.9a)$$

$$\mu = \mu_0 \mu_r, \quad (2.9b)$$

in which σ_e is the scalar electric conductivity [$\text{AV}^{-1}\text{m}^{-1}$], with ε_r , μ_r and σ_e real and positive. Note that \mathbf{D} now incorporates the electric conducting current. Accordingly, henceforth all currents are assumed to be primary sources. The quantities μ_0 and ε_0 represent the free space permeability and permittivity. By definition, $\mu_0 = 4\pi 10^{-7} \text{VsA}^{-1}\text{m}^{-2}$, while ε_0 follows from the speed of light in free space, $c_0[\text{m/s}]$, according to $\sqrt{\mu_0 \varepsilon_0} = c_0^{-1}$. Furthermore, ε_r and μ_r are dimensionless and represent the relative permittivity and permeability of the corresponding medium. Hence, for a dielectric, possibly conducting medium, Maxwell's equations in the Laplace-transform domain reduce to,

$$\nabla \times \mathbf{H} = s\varepsilon \mathbf{E} + \mathbf{J}, \quad (2.10a)$$

$$-\nabla \times \mathbf{E} = s\mu \mathbf{H}. \quad (2.10b)$$

2.3 Duality principle

At present, no magnetic sources have been found in nature. For this reason Maxwell's equations contain only electric sources and currents. However, in the construction of computational schemes it is often convenient to use the concept of fictitious magnetic currents and charges. In the extended formulation, Maxwell's equations take the more symmetric form

$$\nabla \times \mathbf{H} = s\varepsilon \mathbf{E} + \mathbf{J}, \quad (2.11a)$$

$$-\nabla \times \mathbf{E} = s\mu \mathbf{H} + \mathbf{M}. \quad (2.11b)$$

where $\mathbf{M}[\text{Vm}^{-2}]$ represents a magnetic volume source which now may incorporate the magnetic conduction current, through the permeability of the medium, i.e., $\mu = \mu_0\mu_r + \sigma_m/s$, where $\sigma_m[\text{VA}^{-1}\text{m}^{-1}]$ represents the fictitious magnetic conductivity of the medium. The corresponding compatibility relations read

$$\nabla \cdot (s\mathbf{D} + \mathbf{J}) = 0, \quad (2.12a)$$

$$\nabla \cdot (s\mathbf{B} + \mathbf{M}) = 0. \quad (2.12b)$$

Note that these currents are now primary sources.

According to the *duality principle* the electric and magnetic fields are interrelated for linear isotropic media via the following set of formal substitutions:

$$\begin{aligned} \mathbf{D}' &= -\mathbf{B}, & \mathbf{B}' &= \mathbf{D}, & \varepsilon' &= \mu, \\ \mathbf{E}' &= -\mathbf{H}, & \mathbf{H}' &= \mathbf{E}, & \mu' &= \varepsilon. \\ \mathbf{J}' &= -\mathbf{M}, & \mathbf{M}' &= \mathbf{J}, & & \end{aligned} \quad (2.13)$$

The primed field $\{\mathbf{E}', \mathbf{H}'\}$ also satisfies Maxwell's equations and is referred to as the *dual* of the original field $\{\mathbf{E}, \mathbf{H}\}$. The same word is also used for sources and media. Save for a change in sign, the dual of the dual of a field corresponds to the field itself. Although other dual relations are possible, we prefer the dual sets above, since the medium parameters have the same sign. The introduced fictitious magnetic charges and currents will be useful not only when duality is invoked to generate new classes of solutions to Maxwell's equations, but also for computational applications, and especially for those involving equivalence principles.

2.4 Boundary conditions

In Section 2.2 uniqueness was achieved by imposing the condition that the electromagnetic field must be causally related to the action of sources. In addition to imposing causality, we must also specify the behavior of the electromagnetic fields across a smooth interface $\partial\mathcal{D}$ between two media with different electromagnetic properties. Across an interface the field is not continuously differentiable in the sense of ordinary functions, which implies that the partial differential equations (2.11) cease to hold. Across such an interface certain field components are related via boundary conditions, while others are left free to jump. These boundary conditions are derived from the (global) integral form of Maxwell's equations via Gauss' theorem.

For a surface $\partial\mathcal{D}$ of a closed bounded medium (volume) \mathcal{D} , with a unique tangent plane that is piecewise smooth in every point and a vector \mathbf{A} which is continuously differentiable, *Gauss' theorem* states that

$$\int_{\mathcal{D}} (\nabla \cdot \mathbf{A}) \, dV = \oint_{\partial\mathcal{D}} \hat{\mathbf{n}} \cdot \mathbf{A} \, dA, \quad (2.14)$$

while for a scalar f , the generalized Gauss' theorem reads

$$\int_{\mathcal{D}} (\nabla f) \, dV = \oint_{\partial\mathcal{D}} \hat{\mathbf{n}} f \, dA, \quad (2.15)$$

where dA denotes the differential area element, and $\hat{\mathbf{n}}$ represents the unit-length normal vector on the surface $\partial\mathcal{D}$ oriented outwards. Upon substituting $\mathbf{B} \times \mathbf{A}$ for \mathbf{A} in Eq. (2.14), where \mathbf{B} is independent of position, we obtain with the relation $\nabla \cdot (\mathbf{B} \times \mathbf{A}) = -\mathbf{B} \cdot \nabla \times \mathbf{A}$ and cyclic rotation,

$$\int_{\mathcal{D}} (\nabla \times \mathbf{A}) \, dV = \oint_{\partial\mathcal{D}} \hat{\mathbf{n}} \times \mathbf{A} \, dA \quad (2.16)$$

where the dot-multiplication by \mathbf{B} on both sides is left out as \mathbf{B} is an arbitrary vector that is independent of position.

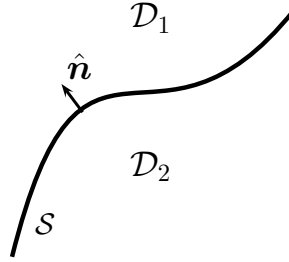


Figure 2.1: Stationary boundary surface $\partial\mathcal{D}$ between two adjacent domains.

Now consider a piecewise smooth stationary interface $\partial\mathcal{D}$ that separates two electromagnetically penetrable regions 1 and 2, as depicted in Figure 2.1, where the normal $\hat{\mathbf{n}}$ points into region 1. At this interface, a primary impressed distribution of surface currents \mathbf{J}_S , \mathbf{M}_S is taken into account. By assuming a pillbox volume across $\partial\mathcal{D}$, integration of the macroscopic Maxwell's equations (2.11) over the volume, application of Eq. (2.16), and subsequent shrinking the pillbox volume in the limit towards the boundary interface yields the boundary conditions for the tangential field across the interface

$$\hat{\mathbf{n}} \times (\mathbf{H}_1 - \mathbf{H}_2) = \mathbf{J}_S, \quad (2.17a)$$

$$-\hat{\mathbf{n}} \times (\mathbf{E}_1 - \mathbf{E}_2) = \mathbf{M}_S. \quad (2.17b)$$

Application of a similar approach to the compatibility equations (2.12), in combination with Gauss' theorem, leads to the boundary conditions for the field components normal to the interface [33, 34],

$$s\hat{\mathbf{n}} \cdot (\mu_1 \mathbf{H}_1 - \mu_2 \mathbf{H}_2) = -\nabla_S \cdot \mathbf{M}_S, \quad (2.18a)$$

$$s\hat{\mathbf{n}} \cdot (\varepsilon_1 \mathbf{E}_1 - \varepsilon_2 \mathbf{E}_2) = -\nabla_S \cdot \mathbf{J}_S. \quad (2.18b)$$

Here, the subscript S implies that only the components tangential to the the interface $\partial\mathcal{D}$ are taken into account (surface divergence). Observe that the duality principle holds for both sets of boundary conditions. A dual field configuration should therefore be supplemented with the dual boundary conditions. Because the compatibility relations in Eq. (2.12) follow from the Maxwell's equations, the necessary and sufficient boundary conditions are the jump conditions (continuity for source free interfaces) for the tangential field, Eq. (2.17).

In case medium 2 is a perfect electric conductor, the conductivity, and thereby also the (complex) permittivity becomes infinite. Because the field must always remain finite, medium 2 cannot sustain a non-identically vanishing electric field in its interior while the boundary condition for the tangential electric field is maintained. Therefore, the necessary and sufficient boundary condition is that the tangential electric field is zero on the boundary,

$$\hat{\mathbf{n}} \times \mathbf{E}_1 = \mathbf{0}, \quad (2.19)$$

while the induced surface current is then given by

$$\hat{\mathbf{n}} \times \mathbf{H}_1 = \mathbf{J}_S. \quad (2.20)$$

The dual counterparts constitute the boundary conditions for a (fictitious) perfect magnetic conductor,

$$\hat{\mathbf{n}} \times \mathbf{H}_1 = \mathbf{0} \quad \text{and} \quad \mathbf{E}_1 \times \hat{\mathbf{n}} = \mathbf{M}_S. \quad (2.21)$$

When the medium extends to infinity, i.e., free-space, uniqueness is preserved by imposing causality conditions on Maxwell's equations such that the field generated by a source is radiating or decaying towards infinity. Suppose that the source of excitation is positioned at the origin, the Silver-Müller *radiation conditions* [35] read

$$\begin{aligned} \lim_{r \rightarrow \infty} r [\hat{\mathbf{r}} \times \mathbf{H} + Z\mathbf{E}] &= \mathbf{0}, \\ \lim_{r \rightarrow \infty} r [Z\hat{\mathbf{r}} \times \mathbf{E} - \mathbf{H}] &= \mathbf{0}, \end{aligned} \quad (2.22)$$

where $\hat{\mathbf{r}}$ is the unit-length vector in the radial direction, and $Z = \sqrt{\mu/\varepsilon}$ the impedance of the medium.

2.5 The Lorentz reciprocity theorem

With the aid of the reciprocity theorem we can establish the correlation between the field and source distributions of two initially unrelated states “a” and “b” within a closed domain \mathcal{D} , i.e., it relates the field response at one source due to a second source to the field response at the second source due to the first source. We shall restrict our treatment of reciprocity to cases in which we have one and the same isotropic material medium occupying the domain \mathcal{D} for both states. We will follow the treatment of [36]. Reciprocity will be used to obtain field representations that describe the field within a domain in terms of the field components tangential to its outer boundary. This lays the foundation of Huygens’ principle which enables the construction of scattering operators of separate scattering domains via the equivalence principle which encompasses the underlying idea of the embedding approach. For applications involving non-reciprocal media, a hybrid form of LEGO will be presented in Section 4.9.

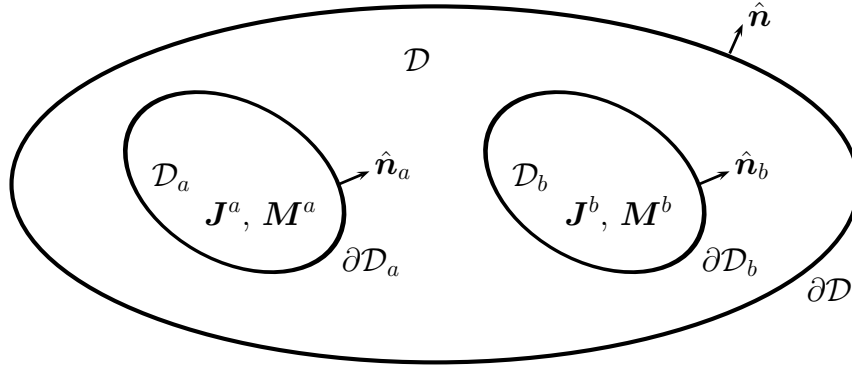


Figure 2.2: The Lorentz reciprocity theorem applied to a domain \mathcal{D} with boundary $\partial\mathcal{D}$. The source distributions that generate the fields for two possible states “a” and “b” are inside the source domains \mathcal{D}_a and \mathcal{D}_b , respectively.

Let us introduce the reciprocity theorem by means of the configuration illustrated in Figure 2.2. Consider a set of sources \mathbf{J}^a and \mathbf{M}^a distributed in some manner inside a linear isotropic medium \mathcal{D} with constitutive parameters ε and μ . The fields \mathbf{E}^a , \mathbf{H}^a produced by the currents \mathbf{J}^a , \mathbf{M}^a constitute state “a” of the system under consideration. If these sources are replaced with a different set of sources \mathbf{J}^b and \mathbf{M}^b that are in general unrelated to \mathbf{J}^a , \mathbf{M}^a , but placed in the same medium and boundary geometry, we have the fields \mathbf{E}^b , \mathbf{H}^b that constitute a state “b”. Note that both source domains \mathcal{D}_a and \mathcal{D}_b may (partially) coincide. Obviously, both states are

governed by Maxwell's equations,

$$\nabla \times \mathbf{H}^{a,b} = s\varepsilon \mathbf{E}^{a,b} + \mathbf{J}^{a,b}, \quad (2.23a)$$

$$-\nabla \times \mathbf{E}^{a,b} = s\mu \mathbf{H}^{a,b} + \mathbf{M}^{a,b}. \quad (2.23b)$$

Further, $\mathbf{E}^{a,b}$ and $\mathbf{H}^{a,b}$ must satisfy (the same) appropriate boundary and radiation conditions relevant to the domain \mathcal{D} . Although both states do not exist simultaneously in the domain being considered, their field and source distributions will be interrelated in a mathematical sense. To this end, we take the dot product of \mathbf{H}^b with Eq. (2.23b) for state “a” and of \mathbf{E}^a with Eq. (2.23a) for state “b”, and we subtract the resulting equations,

$$\begin{aligned} \mathbf{H}^b \cdot \nabla \times \mathbf{E}^a - \mathbf{E}^a \cdot \nabla \times \mathbf{H}^b &= \nabla \cdot (\mathbf{E}^a \times \mathbf{H}^b) \\ &= -s\mu \mathbf{H}^a \cdot \mathbf{H}^b - s\varepsilon \mathbf{E}^a \cdot \mathbf{E}^b - \mathbf{M}^a \cdot \mathbf{H}^b - \mathbf{J}^b \cdot \mathbf{E}^a, \end{aligned} \quad (2.24)$$

where the vector identity $\nabla \cdot (\mathbf{A} \times \mathbf{B}) = \mathbf{B} \cdot \nabla \times \mathbf{A} - \mathbf{A} \cdot \nabla \times \mathbf{B}$ has been used. A second, dual, relation is readily obtained by interchanging the subscripts a and b ,

$$\nabla \cdot (\mathbf{E}^b \times \mathbf{H}^a) = -s\mu \mathbf{H}^b \cdot \mathbf{H}^a - s\varepsilon \mathbf{E}^b \cdot \mathbf{E}^a - \mathbf{M}^b \cdot \mathbf{H}^a - \mathbf{J}^a \cdot \mathbf{E}^b, \quad (2.25)$$

By subtracting Eq. (2.25) from (2.24) the local (differential) form of *Lorentz reciprocity theorem* is obtained. Upon integrating over the domain \mathcal{D} bounded by the closed surface $\partial\mathcal{D}$, we arrive at

$$\int_{\mathcal{D}} \nabla \cdot [\mathbf{E}^a \times \mathbf{H}^b - \mathbf{E}^b \times \mathbf{H}^a] dV = \int_{\mathcal{D}} \mathbf{E}^b \cdot \mathbf{J}^a - \mathbf{H}^b \cdot \mathbf{M}^a dV - \int_{\mathcal{D}} \mathbf{E}^a \cdot \mathbf{J}^b - \mathbf{H}^a \cdot \mathbf{M}^b dV. \quad (2.26)$$

Finally, after applying Gauss' divergence theorem, Eq. (2.14), we arrive at the global form of Lorentz reciprocity theorem,

$$\oint_{\partial\mathcal{D}} [\mathbf{E}^a \times \mathbf{H}^b - \mathbf{E}^b \times \mathbf{H}^a] \cdot \hat{\mathbf{n}} dA = \langle b, a \rangle - \langle a, b \rangle \quad (2.27)$$

where the two terms on the right-hand side of the equation are defined as

$$\begin{aligned} \langle a, b \rangle &\equiv \int_{\mathcal{D}_b} \mathbf{E}^a \cdot \mathbf{J}^b - \mathbf{H}^a \cdot \mathbf{M}^b dV, \\ \langle b, a \rangle &\equiv \int_{\mathcal{D}_a} \mathbf{E}^b \cdot \mathbf{J}^a - \mathbf{H}^b \cdot \mathbf{M}^a dV. \end{aligned} \quad (2.28)$$

The quantity $\langle a, b \rangle$ is called the *reaction* introduced by Rumsey [37] and may roughly be interpreted as a measure of how well the fields of state “a” are correlated with the sources of state “b”.

In Eq. (2.28) we have replaced the domain of integration \mathcal{D} by \mathcal{D}_b and \mathcal{D}_a respectively, which is allowed since both source domains \mathcal{D}_b and \mathcal{D}_a are completely enclosed by \mathcal{D} . It is important to point out that the global form of the reciprocity theorem holds for domains involving piecewise smooth surfaces only, due to the application of Gauss' theorem.

As a final remark, we will highlight *reciprocal systems* [34, Section 4.10.2]. This concept is frequently called upon throughout the remainder of this thesis. A “system” within $\partial\mathcal{D}$ is said to be reciprocal if the closed surface integral becomes zero, i.e.,

$$\oint_{\partial\mathcal{D}} [\mathbf{E}^a \times \mathbf{H}^b - \mathbf{E}^b \times \mathbf{H}^a] \cdot \hat{\mathbf{n}} \, dA = 0. \quad (2.29)$$

In that case both states impose equal reaction on each another, i.e.,

$$\langle a, b \rangle = \langle b, a \rangle. \quad (2.30)$$

This condition for reciprocity is called the *reaction theorem*.

When the domain exterior to \mathcal{D} is a perfect electric conductor, the tangential electric field $\hat{\mathbf{n}} \times \mathbf{E}$ is zero on $\partial\mathcal{D}$. Via cyclic rotation of the inner and outer product in the integrand in Eq. (2.29), it is clear that the boundary integral vanishes and that the system is reciprocal. A similar remark holds for a perfect magnetic conductor. Otherwise, when the domain \mathcal{D} covers all sources, its boundary $\partial\mathcal{D}$ can be extended to infinity without loss of generality. In that case the radiation conditions in Eq. (2.22) hold. Since $\hat{\mathbf{r}} \rightarrow \hat{\mathbf{n}}$ on $\partial\mathcal{D}$, the system that results upon letting $\partial\mathcal{D}$ expand to infinity is also reciprocal. Both type of reciprocal systems are relevant for the equivalence principles that will be introduced in Section 2.8.

2.6 Electromagnetic dyadic Green's functions

Since electromagnetic fields are vector fields, the corresponding general wave equation is a vector wave equation. Hence, we will consider the general, time harmonic form of the vector wave equation first for an electric current distribution only. The field response from a magnetic current distribution is readily obtained by duality afterwards. The corresponding medium is considered homogeneous, i.e., we shall assume that both ε and μ are independent of position. Upon taking the curl of Eq. (2.10b) and eliminating \mathbf{H} using Eq. (2.10a) of Maxwell's equations, we obtain

$$\nabla \times \nabla \times \mathbf{E} + \gamma^2 \mathbf{E} = -s\mu\mathbf{J}, \quad (2.31)$$

for an impressed source distribution \mathbf{J} . The introduced propagation coefficient γ [m^{-1}] reads

$$\gamma \equiv s\sqrt{\mu\epsilon}. \quad (2.32)$$

With the vector identity, $\nabla \times \nabla \times \mathbf{A} = \nabla[\nabla \cdot \mathbf{A}] - \nabla^2 \mathbf{A}$ for the electric field, we have

$$[\nabla^2 - \gamma^2] \mathbf{E} = \nabla[\nabla \cdot \mathbf{E}] + s\mu\mathbf{J}. \quad (2.33)$$

where the operator ∇^2 is the Laplacian, such that ∇f of a scalar function $f(\mathbf{r})$ stands for $\nabla \cdot (\nabla f)$. From the compatibility equation (2.12a), and the constitutive relation, Eq. (2.8b), the equation for the electric field reduces to

$$[\nabla^2 - \gamma^2] \mathbf{E} = s\mu \left[\bar{\bar{\mathbf{I}}} - \frac{1}{\gamma^2} \nabla \nabla \right] \cdot \mathbf{J} = -\mathbf{f}_S \quad (2.34)$$

with $\bar{\bar{\mathbf{I}}}$ being the dyad identity operator, where the double bar indicates a dyadic operator. The dyads that we consider may be represented by 3×3 matrices which map vectors on to other vectors. In index notation, the i -th cartesian component of the dot product of a dyad and a vector, $\bar{\bar{\mathbf{A}}} \cdot \mathbf{B}$, is $\sum_{j=1}^3 \bar{\bar{\mathbf{A}}}_{ij} B_j$. Equation (2.34) yields a modified vector Helmholtz equation with a source function \mathbf{f}_S . Actually, a modified Helmholtz equation is the Laplace-transform of a scalar wave equation. Nevertheless, henceforth we shall loosely refer to it as the scalar wave equation. In a cartesian coordinate system, Eq. (2.34) can be decomposed into three scalar wave equations. Because of this, the well-known Green's function for the scalar wave equation can be used to derive the dyadic Green's function for the vector wave equation. The scalar Green's function for an unbounded homogeneous medium, given by

$$G(\mathbf{r}, \mathbf{r}') = \frac{e^{-\gamma|\mathbf{r}-\mathbf{r}'|}}{4\pi|\mathbf{r}-\mathbf{r}'|} \quad (2.35)$$

is the point source solution of the scalar wave equation,

$$[\nabla^2 - \gamma^2]G(\mathbf{r}, \mathbf{r}') = -\delta(\mathbf{r} - \mathbf{r}'), \quad (2.36)$$

In turn, the solution due to an arbitrary source distribution follows from the superposition principle, which states that a general source may be described as a linear superposition of point sources. Accordingly, the source distribution \mathbf{f}_S in Eq. (2.34) may be cast in the following form

$$\mathbf{f}_S(\mathbf{r}) = \int_{\mathcal{D}} \mathbf{f}_S(\mathbf{r}') \delta(\mathbf{r} - \mathbf{r}') dV'. \quad (2.37)$$

Because $G(\mathbf{r}, \mathbf{r}')$ is the point source solution of Eq. (2.36), the solution for the electric field in a cartesian reference system follows the superposition

$$\mathbf{E} = -s\mu \int_{\mathcal{D}} G(\mathbf{r}, \mathbf{r}') \left[\bar{\bar{\mathbf{I}}} - \frac{1}{\gamma^2} \nabla' \nabla' \right] \cdot \mathbf{J}(\mathbf{r}') dV', \quad (2.38)$$

where the source domain \mathcal{D} encloses the support of the current source distribution \mathbf{J} such that $\mathbf{J} = \mathbf{0}$ on $\partial\mathcal{D}$. Now, let us assume that \mathbf{r} is located outside the source domain. Using the vector identity $f\nabla g = \nabla(gf) - g\nabla f$, the generalized Gauss' theorem, Eq. (2.15), and the fact that the current vanishes on the boundary $\partial\mathcal{D}$ of \mathcal{D} , we infer

$$\int_{\mathcal{D}} G(\mathbf{r}, \mathbf{r}') \nabla' [\nabla' \cdot \mathbf{J}(\mathbf{r}')] dV' = - \int_{\mathcal{D}} [\nabla' \cdot \mathbf{J}(\mathbf{r}')] \nabla' G(\mathbf{r}, \mathbf{r}') dV'. \quad (2.39)$$

Application of the identity $f\nabla \cdot \mathbf{A} = \nabla \cdot (f\mathbf{A}) - \mathbf{A} \cdot \nabla f$ to the Cartesian components of the right-hand side of Eq. (2.39), and Gauss' theorem, Eq. (2.14), leads to

$$- \int_{\mathcal{D}} [\nabla' \cdot \mathbf{J}(\mathbf{r}')] \nabla' G(\mathbf{r}, \mathbf{r}') dV' = \int_{\mathcal{D}} \nabla' \nabla' G(\mathbf{r}, \mathbf{r}') \cdot \mathbf{J}(\mathbf{r}') dV'. \quad (2.40)$$

Thus, we have diverted the $\nabla' \nabla'$ term to the scalar Green's function. Accordingly, the electric field may be cast in the following form

$$\mathbf{E} = -s\mu \int_{\mathcal{D}} \bar{\bar{\mathbf{G}}}(\mathbf{r}, \mathbf{r}') \cdot \mathbf{J}(\mathbf{r}') dV', \quad (2.41)$$

where we have introduced the dyadic Green's function $\bar{\bar{\mathbf{G}}}$. Upon applying the symmetry of the Green's function, $\nabla G(\mathbf{r}, \mathbf{r}') = -\nabla' G(\mathbf{r}, \mathbf{r}')$, the dyadic Green's function is found to be

$$\bar{\bar{\mathbf{G}}}(\mathbf{r}, \mathbf{r}') = \left[\bar{\bar{\mathbf{I}}} - \frac{1}{\gamma^2} \nabla \nabla \right] G(\mathbf{r}, \mathbf{r}'). \quad (2.42)$$

For example, the matrix element G_{xy} of the dyadic Green's function represents the x -component of the dyadic Green's function at \mathbf{r} due to a point source located at \mathbf{r}' and oriented in the $\hat{\mathbf{y}}$ -direction. Upon substituting the expression for the electric field, Eq. (2.41), back in Maxwell's equations, the magnetic field due to an electric current distribution is found in terms of the dyadic Green's function as well. In turn, the field response due to a magnetic current distribution is obtained through the duality principle. Finally, by superposition, the field at some point \mathbf{r} outside the source domain as a result of an arbitrary composite source distribution inside a domain \mathcal{D} follows from

$$\begin{aligned} \mathbf{E} &= -s\mu \int_{\mathcal{D}} \bar{\bar{\mathbf{G}}}(\mathbf{r}, \mathbf{r}') \cdot \mathbf{J}(\mathbf{r}') dV' - \int_{\mathcal{D}} \nabla \times \bar{\bar{\mathbf{G}}}(\mathbf{r}, \mathbf{r}') \cdot \mathbf{M}(\mathbf{r}') dV', \\ \mathbf{H} &= -s\varepsilon \int_{\mathcal{D}} \bar{\bar{\mathbf{G}}}(\mathbf{r}, \mathbf{r}') \cdot \mathbf{M}(\mathbf{r}') dV' + \int_{\mathcal{D}} \nabla \times \bar{\bar{\mathbf{G}}}(\mathbf{r}, \mathbf{r}') \cdot \mathbf{J}(\mathbf{r}') dV'. \end{aligned} \quad (2.43)$$

Now, let us consider the case in which the point \mathbf{r} where the fields \mathbf{E} , \mathbf{H} are observed, lies inside the source region \mathcal{D} . Then, the distance between source and observation $|\mathbf{r} - \mathbf{r}'|$ can become

zero. If this happens, the scalar $G(\mathbf{r}, \mathbf{r}')$ becomes singular, and with the $\nabla\nabla$ term operating on $G(\mathbf{r}, \mathbf{r}')$ in the dyadic Green's function, the integral over the source region is divergent as the kernel becomes hypersingular. As a remedy, the integral should be treated as a principal value integral integrated over a specific exclusion domain. To avoid otherwise non-existing surface-charges on the surface of the excluded domain, the dyadic Green's function, Eq. (2.42) is then augmented with a second term which depends only on the shape of the excluded domain [38]. If modified accordingly, the dyadic Green's function is valid throughout for the determination of the field due to volume sources. Since the remainder of this thesis only deals with surface sources, source-free domains, or observation points outside the source region, we shall omit further details regarding this matter.

2.7 Huygens' principle and extinction theorem

In the previous section the dyadic Green's function has been introduced, and a field representation has been formulated for the fields at any point in an unbounded domain generated by a volume source distribution. If we are only interested in the field within a certain source-free subdomain, the field incident on that subdomain would suffice to separate that domain from its surrounding environment. Similar to the treatment in [34], we will start from the reciprocity theorem, from which we derive the more general field representations for a closed domain inside a configuration where the exterior impressed tangential field on the boundary will account for the interior field contribution.

The reciprocity theorem applied to the domain \mathcal{D} depicted in Figure 2.2 is used as a starting point. For state "a" some arbitrary volume source distribution \mathbf{J}^a , \mathbf{M}^a is chosen which is entirely contained inside \mathcal{D} and not on its boundary $\partial\mathcal{D}$. From now on, the superscript of the fields in state "a" will be dropped as well. For the source distribution of state "b", only an electric point source is selected which is located at \mathbf{r}_b and directed in $\hat{\mathbf{b}}$. Accordingly, we have

$$\text{State "a"} \left\{ \begin{array}{l} \mathbf{J}^a = \mathbf{J} \\ \mathbf{M}^a = \mathbf{M} \end{array} \right. , \quad \text{State "b"} \left\{ \begin{array}{l} \mathbf{J}^b = \hat{\mathbf{b}}\delta(\mathbf{r} - \mathbf{r}_b) \\ \mathbf{M}^b = \mathbf{0} \end{array} \right. , \quad (2.44)$$

where $\delta(\mathbf{r} - \mathbf{r}_b)$ represents the three-dimensional unit impulse at the point $\mathbf{r} = \mathbf{r}_b$. Upon substituting the source distribution of these states in the general global form of Lorentz reciprocity

theorem, Eq. (2.27), we have

$$\chi_{\mathcal{D}}(\mathbf{r}_b)\hat{\mathbf{b}} \cdot \mathbf{E}(\mathbf{r}_b) = \int_{\mathcal{D}} \mathbf{E}^b \cdot \mathbf{J} - \mathbf{H}^b \cdot \mathbf{M} \, dV - \oint_{\partial\mathcal{D}} [\mathbf{E} \times \mathbf{H}^b - \mathbf{E}^b \times \mathbf{H}] \cdot \hat{\mathbf{n}} \, dA, \quad (2.45)$$

where the function $\chi_{\mathcal{D}}$ is the characteristic function associated with a domain \mathcal{D} with a smooth boundary $\partial\mathcal{D}$, i.e.,

$$\chi_{\mathcal{D}}(\mathbf{r}) = \begin{cases} 1, & \text{for } \mathbf{r} \in \mathcal{D}, \\ 1/2, & \text{for } \mathbf{r} \in \partial\mathcal{D}, \\ 0, & \text{otherwise.} \end{cases} \quad (2.46)$$

The characteristic function originates from the integration of a delta function over \mathcal{D} where the domain $\bar{\mathcal{D}}$ denotes the complementary domain of \mathcal{D} . If the electric point source is located exactly on $\partial\mathcal{D}$, a semispherical surface is excluded and integrated separately in the limit where the radius approaches zero. For piecewise smooth boundaries, we indeed obtain $\chi_{\mathcal{D}}(\mathbf{r}) = \frac{1}{2}$ for $\mathbf{r} \in \partial\mathcal{D}$. For a general boundary shape, $\chi_{\mathcal{D}}(\mathbf{r}) = (1 - \Omega/2\pi)$ for $\mathbf{r} \in \partial\mathcal{D}$ with Ω being the subtended solid angle as explained in [39].

After cyclic rotation of the dot and cross products in the integrand of the boundary integral in Eq. (2.45), we obtain

$$\chi_{\mathcal{D}}(\mathbf{r}_b)\hat{\mathbf{b}} \cdot \mathbf{E}(\mathbf{r}_b) = \int_{\mathcal{D}} \mathbf{E}^b \cdot \mathbf{J} - \mathbf{H}^b \cdot \mathbf{M} \, dV - \oint_{\partial\mathcal{D}} \mathbf{E}^b \cdot (\hat{\mathbf{n}} \times \mathbf{H}) - \mathbf{H}^b \cdot (\mathbf{E} \times \hat{\mathbf{n}}) \, dA. \quad (2.47)$$

Note that the electric field of state “a”, observed at the source point \mathbf{r}_b of the electric point source excitation of state “b”, is related to the magnetic and electric field response of that point source. Observe that the orientation of the point source $\hat{\mathbf{b}}$ is yet undefined and may be arbitrary. To extract the observation, we employ the dyadic Green’s functions of which the cartesian components describe the field solutions of a point source oriented along the three axes $\{\hat{\mathbf{x}}, \hat{\mathbf{y}}, \hat{\mathbf{z}}\}$ of the cartesian coordinate system. Owing to the superposition principle, the radiated field of the point source in the $\hat{\mathbf{b}}$ direction follows from the dot product of the dyadic Green’s function with $\hat{\mathbf{b}}$, i.e.,

$$\begin{aligned} \mathbf{E}^b &= \bar{\bar{\mathbf{G}}}^{EJ}(\mathbf{r}, \mathbf{r}_b) \cdot \hat{\mathbf{b}} \\ \mathbf{H}^b &= \bar{\bar{\mathbf{G}}}^{HJ}(\mathbf{r}, \mathbf{r}_b) \cdot \hat{\mathbf{b}} \end{aligned} \quad (2.48)$$

These two Green’s functions provide the electric and magnetic field response due to an electric point source at \mathbf{r}_b . Likewise, for a magnetic point source, $\mathbf{M}_b = \hat{\mathbf{b}}\delta(\mathbf{r} - \mathbf{r}_b)$, we obtain similar expressions, though the dyadic’s, $\bar{\bar{\mathbf{G}}}^{EM}$ and $\bar{\bar{\mathbf{G}}}^{HM}$, are used for the electric, respectively, magnetic field. Note that superscripts respectively indicate what type of field is produced by what type of point source.

Next, let us consider the states associated with two electric-current point sources $\mathbf{J}^a = \hat{\mathbf{a}}\delta(\mathbf{r}-\mathbf{r}_a)$ and $\mathbf{J}^b = \hat{\mathbf{b}}\delta(\mathbf{r}-\mathbf{r}_b)$ with $\mathbf{M}^a = \mathbf{M}^b = \mathbf{0}$, and let $\partial\mathcal{D} \rightarrow \infty$ in a homogeneous domain. The corresponding system is reciprocal and the reaction theorem, Eq. (2.30), leads to the so-called source reciprocity,

$$\hat{\mathbf{b}} \cdot \bar{\bar{\mathbf{G}}}^{EJ}(\mathbf{r}_b, \mathbf{r}_a) \cdot \hat{\mathbf{a}} = \hat{\mathbf{a}} \cdot \bar{\bar{\mathbf{G}}}^{EJ}(\mathbf{r}_a, \mathbf{r}_b) \cdot \hat{\mathbf{b}}. \quad (2.49)$$

Upon employing the identity, $\hat{\mathbf{a}} \cdot \bar{\bar{\mathbf{G}}} \cdot \hat{\mathbf{b}} = \hat{\mathbf{b}} \cdot \bar{\bar{\mathbf{G}}}^T \cdot \hat{\mathbf{a}}$, where the superscript T denotes transposition, we arrive at

$$\bar{\bar{\mathbf{G}}}^{EJ}(\mathbf{r}, \mathbf{r}_b) = \left[\bar{\bar{\mathbf{G}}}^{EJ}(\mathbf{r}_b, \mathbf{r}) \right]^T. \quad (2.50)$$

Via a similar procedure with a magnetic instead of an electric current source for one of the two states, we obtain

$$\bar{\bar{\mathbf{G}}}^{HJ}(\mathbf{r}, \mathbf{r}_b) = - \left[\bar{\bar{\mathbf{G}}}^{EM}(\mathbf{r}_b, \mathbf{r}) \right]^T. \quad (2.51)$$

Now, let us return to the original states “a” and “b”, defined in Eq. (2.44). The expressions in Eq. (2.48) for the field response from an electric point source may be rewritten using the relations obtained above, which results in

$$\begin{aligned} \mathbf{E}^b &= \hat{\mathbf{b}} \cdot \bar{\bar{\mathbf{G}}}^{EJ}(\mathbf{r}_b, \mathbf{r}), \\ \mathbf{H}^b &= -\hat{\mathbf{b}} \cdot \bar{\bar{\mathbf{G}}}^{EM}(\mathbf{r}_b, \mathbf{r}). \end{aligned} \quad (2.52)$$

Upon substituting Eq. (2.52) in Eq. (2.47), and replacing $\{\mathbf{r}_b, \mathbf{r}\}$ by $\{\mathbf{r}, \mathbf{r}'\}$, we obtain the following general expression for the electric field,

$$\begin{aligned} \chi_{\mathcal{D}}(\mathbf{r})\mathbf{E}(\mathbf{r}) &= \int_{\mathcal{D}} \bar{\bar{\mathbf{G}}}^{EJ}(\mathbf{r}, \mathbf{r}') \cdot \mathbf{J}(\mathbf{r}') + \bar{\bar{\mathbf{G}}}^{EM}(\mathbf{r}, \mathbf{r}') \cdot \mathbf{M}(\mathbf{r}') dV' \\ &\quad - \oint_{\partial\mathcal{D}} \bar{\bar{\mathbf{G}}}^{EJ}(\mathbf{r}, \mathbf{r}') \cdot [\hat{\mathbf{n}} \times \mathbf{H}(\mathbf{r}')] + \bar{\bar{\mathbf{G}}}^{EM}(\mathbf{r}, \mathbf{r}') \cdot [\mathbf{E}(\mathbf{r}') \times \hat{\mathbf{n}}] dA'. \end{aligned} \quad (2.53)$$

Note that the original dot product with $\hat{\mathbf{b}}$ has been left out, which is allowed as it occurred every term and $\hat{\mathbf{b}}$ is independent of position and arbitrary. By taking a magnetic instead of an electric point source for state “b”, the magnetic field counterpart follows from a similar procedure as

$$\begin{aligned} \chi_{\mathcal{D}}(\mathbf{r})\mathbf{H}(\mathbf{r}) &= \int_{\mathcal{D}} \bar{\bar{\mathbf{G}}}^{HJ}(\mathbf{r}, \mathbf{r}') \cdot \mathbf{J}(\mathbf{r}') + \bar{\bar{\mathbf{G}}}^{HM}(\mathbf{r}, \mathbf{r}') \cdot \mathbf{M}(\mathbf{r}') dV' \\ &\quad - \oint_{\partial\mathcal{D}} \bar{\bar{\mathbf{G}}}^{HJ}(\mathbf{r}, \mathbf{r}') \cdot [\hat{\mathbf{n}} \times \mathbf{H}(\mathbf{r}')] + \bar{\bar{\mathbf{G}}}^{HM}(\mathbf{r}, \mathbf{r}') \cdot [\mathbf{E}(\mathbf{r}') \times \hat{\mathbf{n}}] dA. \end{aligned} \quad (2.54)$$

If no sources are present in the complementary domain $\bar{\mathcal{D}}$, the surface $\partial\mathcal{D}$ may be extended to infinity without loss of generality, and the contribution from the resulting boundary integral at

infinity vanishes owing to the radiation conditions. Upon comparing Eqs. (2.53) and (2.54) with the formulated field expressions in Eq. (2.43) it is clear that

$$\left\{ \begin{array}{l} \bar{\bar{\mathbf{G}}}^{EJ} = -s\mu\bar{\bar{\mathbf{G}}}, \\ \bar{\bar{\mathbf{G}}}^{HJ} = \nabla \times \bar{\bar{\mathbf{G}}}, \end{array} \right. \quad \text{and} \quad \left\{ \begin{array}{l} \bar{\bar{\mathbf{G}}}^{EM} = -\nabla \times \bar{\bar{\mathbf{G}}}, \\ \bar{\bar{\mathbf{G}}}^{HM} = -s\varepsilon\bar{\bar{\mathbf{G}}}. \end{array} \right. \quad (2.55)$$

These representations can be generalized to be valid everywhere if the volume integrals are evaluated in the sense of principle value integrals in the source region, as discussed at the end of Section 2.6.

Another interesting property of the obtained general field representations is *Oseen's extinction theorem* [40], which provides the foundation for the so-called *null-field method*. It states that in the complementary domain $\bar{\mathcal{D}}$ the fields generated by the volume sources \mathbf{J} , \mathbf{M} and the contribution from the tangential fields at the boundary $\partial\mathcal{D}$ combine to produce a null field. In other words, the field generated by the volume sources is canceled out by the contribution from the boundary.

Equations (2.53) and (2.54) also provide for $\mathbf{r} \in \bar{\mathcal{D}}$ the mathematical formulation of *Huygens' principle*, which states that the field at a point of observation generated by some source distribution is equal to the field generated by equivalent surface sources defined in terms of the tangential field components on the boundary of a domain that encloses this source distribution in some arbitrary fashion. This volume vis-a-vis boundary source field representation equivalence paves the way towards the partitioning of field configurations into separate domains that are interconnected by their tangential field distributions on the boundaries.

Because the field calculations in the remainder of this thesis mainly rely on boundary integral equations and representations via Huygens' principle, we should elaborate on the corresponding boundary integral further. The curl of the dyadic Green's function defined in Eq. (2.42), can be simplified according to

$$\nabla \times \bar{\bar{\mathbf{G}}}(\mathbf{r}, \mathbf{r}') = \nabla \times \left[\bar{\bar{\mathbf{I}}}G(\mathbf{r}, \mathbf{r}') \right] = \nabla G(\mathbf{r}, \mathbf{r}') \times \bar{\bar{\mathbf{I}}}, \quad (2.56)$$

because the curl of a gradient is zero. Using Eqs. (2.42), (2.55) and (2.56) in the general field

representation associated with a source-free interior domain \mathcal{D} , we obtain

$$\begin{aligned}\chi_{\mathcal{D}}\mathbf{E} &= \oint_{\partial\mathcal{D}} s\mu \left[\bar{\bar{\mathbf{I}}} - \frac{1}{\gamma^2} \nabla\nabla \right] G(\mathbf{r}, \mathbf{r}') \cdot [\hat{\mathbf{n}} \times \mathbf{H}(\mathbf{r}')] + \nabla G(\mathbf{r}, \mathbf{r}') \times [\mathbf{E}(\mathbf{r}') \times \hat{\mathbf{n}}] \, dA', \\ \chi_{\mathcal{D}}\mathbf{H} &= \oint_{\partial\mathcal{D}} s\varepsilon \left[\bar{\bar{\mathbf{I}}} - \frac{1}{\gamma^2} \nabla\nabla \right] G(\mathbf{r}, \mathbf{r}') \cdot [\mathbf{E}(\mathbf{r}') \times \hat{\mathbf{n}}] - \nabla G(\mathbf{r}, \mathbf{r}') \times [\hat{\mathbf{n}} \times \mathbf{H}(\mathbf{r}')] \, dA'.\end{aligned}\tag{2.57}$$

One of the gradients in the field components involving the $\nabla\nabla$ term operating on $G(\mathbf{r}, \mathbf{r}')$ can be avoided by considering the normal field components instead of the tangential ones, viz., via the symmetry property $\nabla G(\mathbf{r}, \mathbf{r}') = -\nabla' G(\mathbf{r}, \mathbf{r}')$ and the cyclic rotation of the dot and cross product, we obtain

$$\begin{aligned}\oint_{\partial\mathcal{D}} \nabla\nabla G(\mathbf{r}, \mathbf{r}') \cdot [\hat{\mathbf{n}} \times \mathbf{H}(\mathbf{r}')] \, dA' &= -\nabla \oint_{\partial\mathcal{D}} \hat{\mathbf{n}} \cdot [\mathbf{H}(\mathbf{r}') \times \nabla' G(\mathbf{r}, \mathbf{r}')] \, dA' \\ &= -\nabla \oint_{\partial\mathcal{D}} G(\mathbf{r}, \mathbf{r}') \hat{\mathbf{n}} \cdot [\nabla' \times \mathbf{H}(\mathbf{r}')] \, dA'\end{aligned}\tag{2.58}$$

after applying the vector identity $\mathbf{A} \times \nabla f = f \nabla \times \mathbf{A} - \nabla \times (f \mathbf{A})$, where the term that results from the last term on the right-hand side of the vector identity vanished under the surface integration because according to Gauss' theorem (2.14), it is equivalent to the volume integral of the divergence of a curl. The subsequent substitution of the source-free Maxwell equation (2.10b), together with $\nabla \times \nabla \times \mathbf{E} = -\gamma^2 \mathbf{E}$ for $\mathbf{J} = \mathbf{0}$ from Eq. (4.10), leads to the observation that the relation

$$\begin{aligned}\oint_{\partial\mathcal{D}} \nabla\nabla G(\mathbf{r}, \mathbf{r}') \cdot [\hat{\mathbf{n}} \times \mathbf{H}(\mathbf{r}')] \, dA' &= \frac{1}{s\mu} \nabla \oint_{\partial\mathcal{D}} \hat{\mathbf{n}} \cdot [\nabla' \times \nabla' \times \mathbf{E}(\mathbf{r}')] \, dA' \\ &= \frac{\gamma^2}{s\mu} \oint_{\partial\mathcal{D}} [\hat{\mathbf{n}} \cdot \mathbf{E}(\mathbf{r}')] \nabla' G(\mathbf{r}, \mathbf{r}') \, dA',\end{aligned}\tag{2.59}$$

holds on $\partial\mathcal{D}$. With this simplification, we arrive at

$$\begin{aligned}\chi_{\mathcal{D}}\mathbf{E} &= s\mu \oint_{\partial\mathcal{D}} [\hat{\mathbf{n}} \times \mathbf{H}(\mathbf{r}')] G(\mathbf{r}, \mathbf{r}') \, dA' - \oint_{\partial\mathcal{D}} [\hat{\mathbf{n}} \cdot \mathbf{E}(\mathbf{r}')] \nabla' G(\mathbf{r}, \mathbf{r}') \, dA' \\ &\quad + \oint_{\partial\mathcal{D}} [\mathbf{E}(\mathbf{r}') \times \hat{\mathbf{n}}] \times \nabla' G(\mathbf{r}, \mathbf{r}') \, dA',\end{aligned}\tag{2.60}$$

and, again by duality,

$$\begin{aligned} \chi_{\mathcal{D}} \mathbf{H} = & s\varepsilon \oint_{\partial\mathcal{D}} [\mathbf{E}(\mathbf{r}') \times \hat{\mathbf{n}}] G(\mathbf{r}, \mathbf{r}') dA' - \oint_{\partial\mathcal{D}} [\hat{\mathbf{n}} \cdot \mathbf{H}(\mathbf{r}')] \nabla' G(\mathbf{r}, \mathbf{r}') dA' \\ & - \oint_{\partial\mathcal{D}} [\hat{\mathbf{n}} \times \mathbf{H}(\mathbf{r}')] \times \nabla' G(\mathbf{r}, \mathbf{r}') dA', \end{aligned} \quad (2.61)$$

which are the familiar Stratton-Chu formulas [41] for the electric and magnetic fields. Because we assumed a source-free domain \mathcal{D} , the domain integrals that account for the volume sources in Eqs. (2.53) and (2.54), have been omitted. Therefore, the Stratton-Chu formulas provide a mathematical implementation of Huygens' principle as they reproduce the field in \mathcal{D} due to some externally impressed source distribution. Following the line of argument in [36, Section 4.2], and the proof in [42, p. 471-2], we infer that it is not necessary to consider the boundary integrals in the principle value sense when $\partial\mathcal{D}$ is a smooth boundary. Therefore, the occurring surface integrals are merely ones with removable singularities. Note that, apart from the tangential components of the fields, also the normal field components are involved. It is shown below that from the boundary conditions it turns out that we only require the tangential field components. For the application to scattering problems we refer to Chapter 3.

2.8 Love's and Schelkunoff's equivalence principles

Above, general field integral representations have been formulated in terms of dyadic Green's functions, and the boundary integrals have been recognized as the well-known Stratton-Chu formulas. Invoking Huygens' principle, the field inside a boundary $\partial\mathcal{D}$ enclosing a domain \mathcal{D} , may be considered as being generated by an equivalent source distribution on that boundary, thereby separating that domain from its environment in an electromagnetic sense. This is referred to as an *equivalence principle*. The associated equivalent source distribution is not unique. To this end, we introduce two distinct equivalence principles, viz. *Love's equivalence principle* (LEP), and *Schelkunoff's equivalence principle* (SEP). Below, we aim to represent a field distribution within a domain due to the action of some external sources in terms of such equivalent boundary sources. We will follow the treatment of [43]. Further, we shall investigate the differences between both concepts, especially concerning multiply connected domains.

Before we can introduce an equivalent state, we should first define the corresponding *original* state. For LEP, we have the original state depicted in Figure 2.3a. A certain domain \mathcal{D} is chosen,

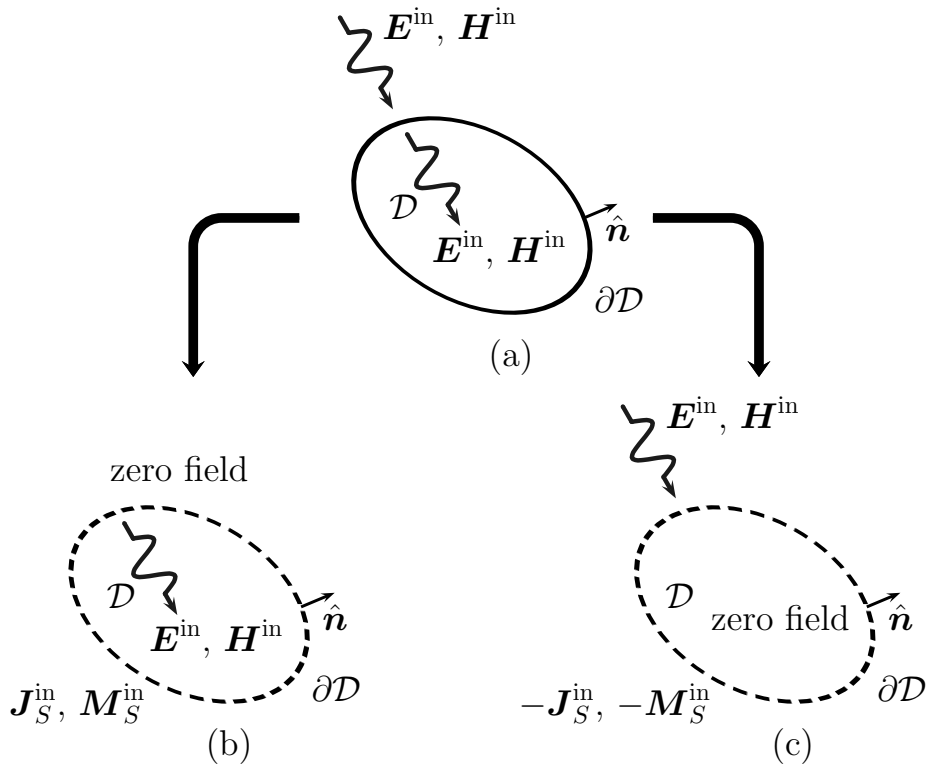


Figure 2.3: The field inside a domain \mathcal{D} , due to external sources (a). Love's equivalence principle applied to the so-called *interior equivalent* state (b), and Oseen's extinction principle for the *exterior equivalent* state (c).

with on its outer boundary $\partial\mathcal{D}$ a unit-normal vector \hat{n} oriented outwards. The boundary shape may be arbitrary, as long as it is smooth. The surrounding complementary domain $\bar{\mathcal{D}}$ may involve a complicated (inhomogeneous) scattering environment and source distribution. Domain \mathcal{D} , is considered to be source-free and homogeneous for the moment. In the LEGO concept however, \mathcal{D} may also hold arbitrary scattering objects. The electric and magnetic field distributions under consideration $E^{\text{in}}, H^{\text{in}}$ denote the fields generated in the surrounding environment. Accordingly, the superscript "in" indicates that this field signifies an incident field with respect to \mathcal{D} . For now, we assume that the tangential field components along the boundary $\partial\mathcal{D}$ are known. These tangential fields are associated with an impressed source distribution in the equivalent states. The corresponding boundary current distributions, also called *equivalent currents*, are J_S^{in} and M_S^{in} . The subscript "S" is added to emphasize that we deal with surface sources.

Huygens' principle states that the equivalent boundary currents reproduce the field within the domain \mathcal{D} , generated by all the sources (primary or scattering) in $\bar{\mathcal{D}}$, i.e., the incident field. Also,

in $\bar{\mathcal{D}}$ these currents yield no field contribution on account of Oseen's extinction theorem, which also indicates that the exterior medium properties may be changed without affecting the fields in \mathcal{D} . Because the original *interior* fields are maintained, we define this field distribution as the *interior equivalent* state of LEP, illustrated in Figure 2.3b.

Due to the linearity of Maxwell's equations, the *opposite* equivalent currents produce the negative incident fields in \mathcal{D} . In the presence of the original impressed incident fields \mathbf{E}^{in} , \mathbf{H}^{in} from the surrounding environment, these fields combine to produce a zero field in \mathcal{D} . This is referred to as the *exterior equivalent* state of LEP since the original exterior fields are maintained, which is shown in Figure 2.3c, where the minus sign then originates from the fixed outward orientation of the normal $\hat{\mathbf{n}}$. This state is covered by Oseen's theorem applied to $\bar{\mathcal{D}}$. Consequently, with the same currents \mathbf{J}_S^{in} , \mathbf{M}_S^{in} , we can in \mathcal{D} either reproduce a field or cancel that same field. Note that the composite state by superposition of the interior and exterior equivalent state again provides the source-free original state.

The equivalent currents \mathbf{J}_S^{in} , \mathbf{M}_S^{in} follow directly from the incident fields \mathbf{E}^{in} , \mathbf{H}^{in} on $\partial\mathcal{D}$ upon applying appropriate boundary conditions. In particular, the boundary conditions for the tangential field, Eq. (2.17), applied to the interface $\partial\mathcal{D}$ in Figure 2.3b, imply that [41, p. 464-8],

$$\mathbf{J}_S^{\text{in}} = -\hat{\mathbf{n}} \times \mathbf{H}^{\text{in}}, \quad (2.62a)$$

$$\mathbf{M}_S^{\text{in}} = -\mathbf{E}^{\text{in}} \times \hat{\mathbf{n}}, \quad (2.62b)$$

for a zero field in $\bar{\mathcal{D}}$. Note that the sign convention for the currents has been chosen such that it facilitates the formulation of LEGO. Likewise, from the boundary conditions for the field component normal to the surface, Eq. (2.18), with a zero field in $\bar{\mathcal{D}}$, we have

$$\begin{aligned} \hat{\mathbf{n}} \cdot \mathbf{E}^{\text{in}} &= \frac{1}{s\epsilon} \nabla_S \cdot \mathbf{J}_S^{\text{in}}, \\ \hat{\mathbf{n}} \cdot \mathbf{H}^{\text{in}} &= \frac{1}{s\mu} \nabla_S \cdot \mathbf{M}_S^{\text{in}}. \end{aligned} \quad (2.63)$$

For Eq. (2.63) to be valid, the boundary currents must be continuously differentiable everywhere on $\partial\mathcal{D}$. Nevertheless, its use has the advantage that the double gradient on the scalar Green's function is avoided by means of Eq. (2.59). On that account, the boundary integral in the Stratton-Chu formulation may be regarded in the sense of ordinary functions with removable singularities. Upon substituting Eq. (2.63), together with the definitions of the surface currents, Eq. (2.62), in

the Stratton-Chu formulas, Eqs. (2.60) and (2.61), we have

$$\begin{aligned} \chi_{\mathcal{D}} \mathbf{E}^{\text{in}} = & -s\mu \oint_{\partial\mathcal{D}} \mathbf{J}_S^{\text{in}}(\mathbf{r}') G(\mathbf{r}, \mathbf{r}') dA' + \frac{1}{s\varepsilon} \nabla \oint_{\partial\mathcal{D}} [\nabla'_S \cdot \mathbf{J}_S^{\text{in}}(\mathbf{r}')] G(\mathbf{r}, \mathbf{r}') dA' \\ & - \oint_{\partial\mathcal{D}} \mathbf{M}_S^{\text{in}}(\mathbf{r}') \times \nabla' G(\mathbf{r}, \mathbf{r}') dA', \end{aligned} \quad (2.64)$$

and by duality for the magnetic field,

$$\begin{aligned} \chi_{\mathcal{D}} \mathbf{H}^{\text{in}} = & -s\varepsilon \oint_{\partial\mathcal{D}} \mathbf{M}_S^{\text{in}}(\mathbf{r}') G(\mathbf{r}, \mathbf{r}') dA' + \frac{1}{s\mu} \nabla \oint_{\partial\mathcal{D}} [\nabla'_S \cdot \mathbf{M}_S^{\text{in}}(\mathbf{r}')] G(\mathbf{r}, \mathbf{r}') dA' \\ & + \oint_{\partial\mathcal{D}} \mathbf{J}_S^{\text{in}}(\mathbf{r}') \times \nabla' G(\mathbf{r}, \mathbf{r}') dA', \end{aligned} \quad (2.65)$$

with the function $\chi_{\mathcal{D}}(\mathbf{r})$ as defined in Eq. (2.46). Recall that the currents \mathbf{J}_S^{in} , \mathbf{M}_S^{in} are considered to be known source quantities, as the fields \mathbf{E}^{in} , \mathbf{H}^{in} are known. Addition of the incident field to the opposite of Eqs. (2.64) and (2.65) gives the exterior equivalent state depicted in Figure 2.3c. Note that \mathbf{J}_S^{in} , \mathbf{M}_S^{in} depend on the tangential field components only.

In contrast with LEP, which principle is based on both electric and magnetic equivalent currents, Schelkunoff [13] showed that it suffices to use *either* electric or magnetic currents. This is referred to as Schelkunoff's equivalence principle (SEP). The use of only one type of equivalent current may lead to strong computational advantages in a numerical implementation. In [44, p. 35-36] it is proven that a single prescribed tangential field component already yields a unique solution, except for lossless media at (physical) resonant mode solutions of the domain which may occur at discrete frequencies. This matter will be addressed later on in Section 3.4. However, note that LEP does not suffer from spurious interior resonances and as such is more robust than SEP, at the costs of both electric and magnetic currents.

Schelkunoff's equivalence principle can be deduced in a manner similar to LEP. However, suppose we would like to represent the incident electromagnetic fields \mathbf{E}^{in} , \mathbf{H}^{in} in the same domain \mathcal{D} by only one equivalent current distribution, say \mathbf{J}_S , we must perform an intermediate step. Let us start by regarding the fields in the interior of \mathcal{D} in Figure 2.4a, as the desired interior equivalent state of SEP. As stated above, we would like the fields to be generated by an electric current distribution \mathbf{J}_S only. As the intermediate step, we replace the medium in \mathcal{D} of the original state in Figure 2.3a, with a perfect electric conductor (PEC), or at least a perfectly conducting sheet at its boundary $\partial\mathcal{D}$ to arrive at the original state of SEP shown in Figure 2.4b.

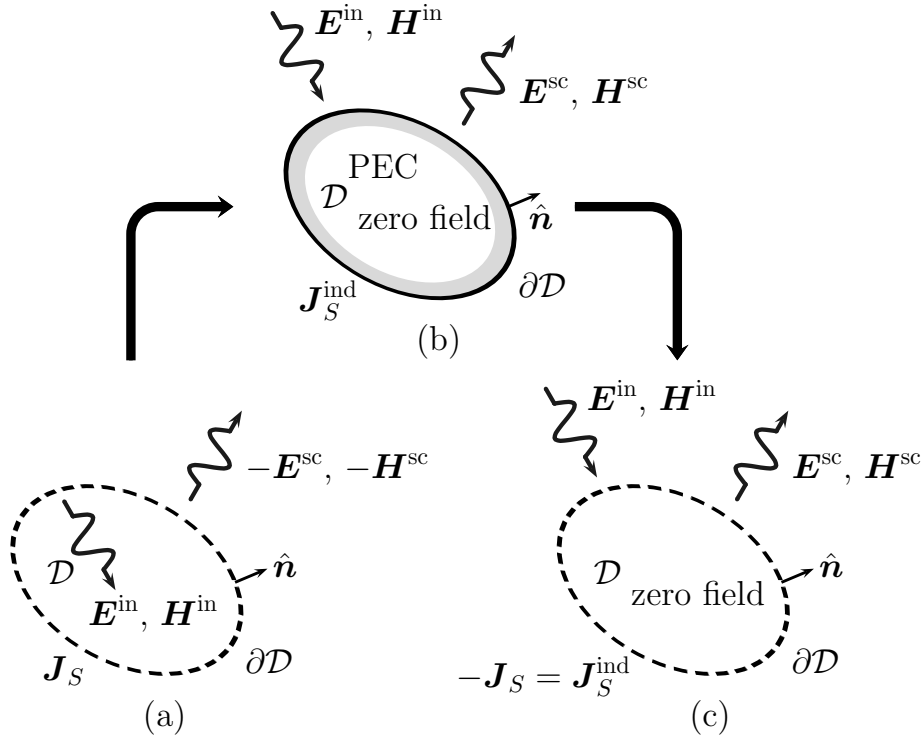


Figure 2.4: Schelkunoff's equivalence principle applied to the *interior equivalent* state (a). The *original* (intermediate) state with a PEC (b), and the *exterior equivalent* state of SEP (c).

Inside a PEC the electromagnetic field must vanish identically. If a field is incident on a PEC, an electric surface current will be induced $\mathbf{J}_S^{\text{ind}}$ on the boundary of that conductor, such that the joint field contribution of the incident field and the field generated by the induced current (scattered field) will cancel inside the domain occupied by the PEC in the absence of the PEC. This covers the exterior equivalent state associated with SEP as depicted in Figure 2.4c. Hence, the opposite of $\mathbf{J}_S^{\text{ind}}$ is the desired equivalent electric boundary current distribution \mathbf{J}_S . The presence of a PEC in the original state of SEP gives rise to the scattered fields $\mathbf{E}^{\text{sc}}, \mathbf{H}^{\text{sc}}$ in $\bar{\mathcal{D}}$, which is *also* generated by $\mathbf{J}_S^{\text{ind}}$. The field in $\bar{\mathcal{D}}$ for the interior equivalent state, Figure 2.4a, is therefore not zero as with LEP, since \mathbf{J}_S produces in addition to the desired incident field in \mathcal{D} , also the negative scattered field from the PEC in $\bar{\mathcal{D}}$. A similar (dual) approach is also possible with only a magnetic equivalent current \mathbf{M}_S , via a perfect magnetic conductor (PMC). Note that we have omitted the subscript “in” to avoid confusion with the equivalent surface currents for LEP defined in Eq. (2.62).

However, an important difference between both equivalence principles should be emphasized as it poses a significant implication for the LEGO approach. As we mentioned, a side effect

emerges from the restriction to either electric or magnetic equivalent currents in Schelkunoff's approach, i.e., the remaining equivalent current produces a non-zero field in the complementary domain. Although this seems insignificant at a first glance, since we are mainly interested in the interior domain, where the single equivalent current does indeed produce the proper desired field, it bears a consequence when multiply connected domains are considered. The underlying reasons and associated implications will be addressed in Section 4.5.

Chapter 3

Boundary integral equations

The partitioning of fields through equivalent states involving either Love's or Schelkunoff's equivalence principle has been explained in Chapter 2. These are the fundamental principles in the construction of the elementary LEGO building blocks. In this chapter, the equivalent states are applied to formulate boundary integral equations, by which the scattered field response of perfectly conducting and dielectric objects may be determined. Since the tangential scattered field on the domain boundary is unknown, the method of moments (MoM) procedure is employed to determine the equivalent currents. This solution strategy may also be used to compute the unknown equivalent currents for LEGO. In addition, the boundary integral equations that are formulated in this chapter can also be employed to construct the elementary scattering operators for LEGO.

3.1 Introduction

In Section 3.2, general boundary integrals equations are formulated for the scattering from a dielectric object via a proper combination of equivalent states of the interior and exterior field problems. In Section 3.3, we consider the scattering from perfectly conducting objects, which results in the electric and magnetic field integral equations on which Schelkunoff's equivalence principle is based. We demonstrate in Section 3.4 that these integral equations suffer from interior resonances that are not associated with physical modes. We will discuss several methods to ensure uniqueness, among which the formulation of a combined field integral equation. In the

formulation of boundary integral equations, there are many linear combinations possible to reduce the interior and exterior integral equations into a coupled pair of equations. In Section 3.5, we discuss the well-known PMCHW formulation and the less familiar Müller formulation. To solve the unknown equivalent currents from an integral equation, the method of moments (MoM) procedure is employed in Section 3.6. The solvability of the integral equations as regards their well-posedness is discussed in Section 3.7. There, we also derive general constraints for the test and expansion function used in the MoM procedure. To this end, we provide a brief overview of the mapping properties of the pertaining integral operators. A more detailed account for 2D and 3D configurations are given in Chapters 5 and 7, respectively.

3.2 General boundary integral formulations

With the aid of equivalence principles, integral representations have been formulated in Chapter 2 that express the field distribution within a source-free homogeneous domain in terms of equivalent current sources on its boundary. So far, these currents followed directly from tangential incident field components that are assumed to be known on the boundary of that domain. In this chapter, we assume that the domain contains scattering objects with homogeneous medium properties. The same methodology will be applied to describe the corresponding scattered field in the exterior of the domain. However, unlike the incident field, the tangential scattered field on the boundary of the domain is not known *a priori*. As such, the associated equivalent currents are left to be determined. To this end, we employ boundary integral equations. Below, general boundary integrals equations are formulated via a proper combination of equivalent states that are related to the respective interior and exterior field problems.

To describe the electromagnetic scattering from an arbitrarily shaped smooth object due to a certain incident field generated by an externally impressed source distribution, let us consider the general scattering configuration depicted in Figure 3.1a. For simplicity we shall discuss a single scatterer. The generalization to a collection of scatterers of different shape and medium properties is straightforward. The medium interior and exterior to the scattering object that occupies the domain \mathcal{D} enclosed by the boundary $\partial\mathcal{D}$ are both considered to be homogeneous and isotropic, albeit that any of the constitutive parameters may be discontinuous across $\partial\mathcal{D}$. Accordingly, we consider $\{\varepsilon_v, \mu_v\}$, with $v = 1, 2$, where the subscript $v = 1$ indicates the exterior medium, and $v = 2$ the interior medium. The fields that are present in the respective media, and also the equivalent currents that radiate into the respective media carry the same subscript. Lossy media

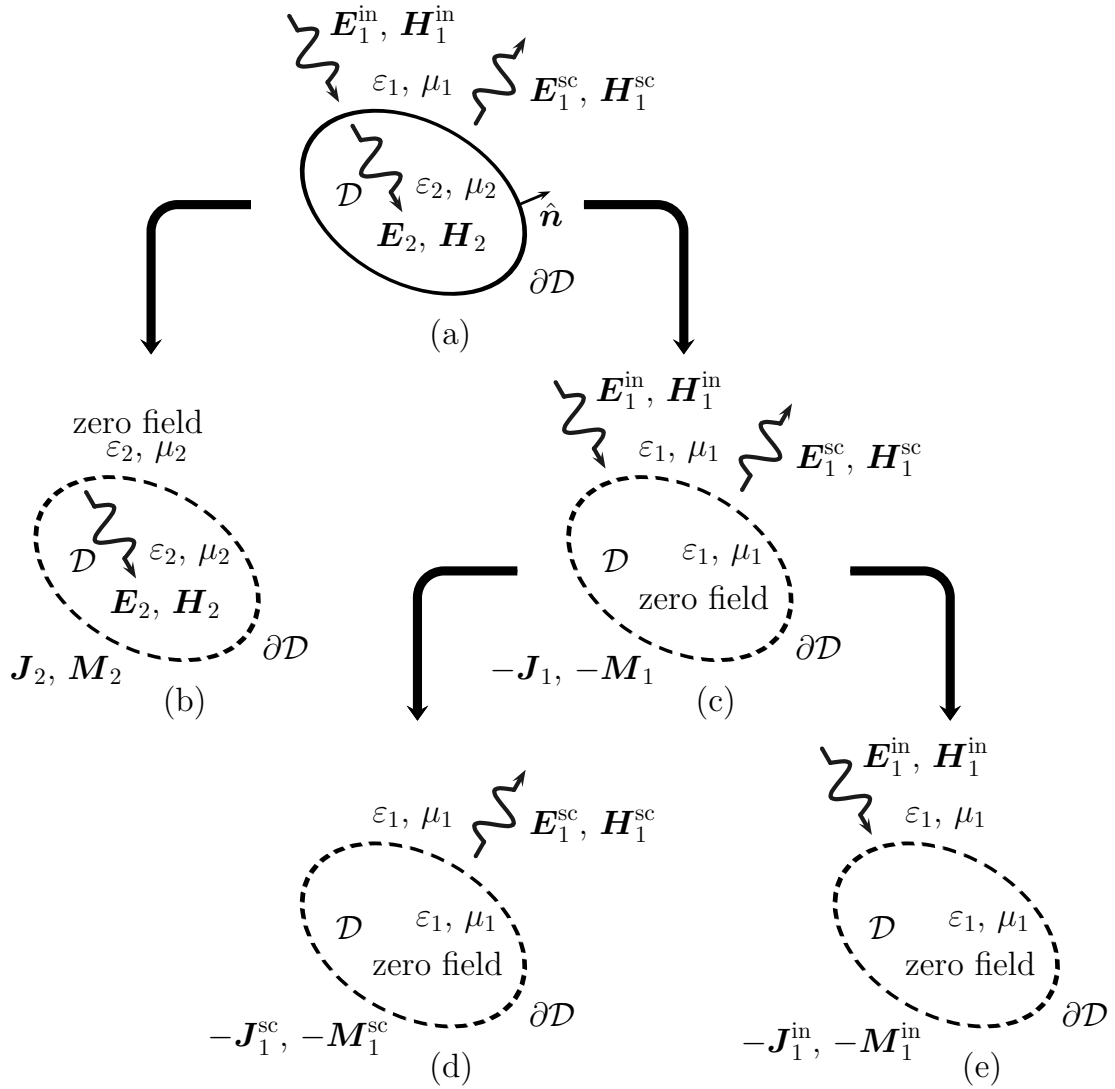


Figure 3.1: The subdivision of a general electromagnetic scattering phenomenon for a penetrable dielectric object (a) into two auxiliary equivalent configurations. The equivalent currents in the interior equivalent state (b) account for the field penetrated in \mathcal{D} . The currents in the exterior equivalent state (c) generate the field that annihilates the impressed incident field in \mathcal{D} and also reproduces the corresponding exterior scattered field in $\bar{\mathcal{D}}$. The exterior equivalent state can be decomposed into two states in which only the scattered (d) and incident (e) fields are present.

are readily accounted for, by allowing ε_v and μ_v to be complex. The presence of an externally impressed source distribution is captured in terms of the field $\{\mathbf{E}_1^{\text{in}}, \mathbf{H}_1^{\text{in}}\}$, which is incident on \mathcal{D} , i.e., this would be the field in the absence of the scattering object.

With the aid of Love's equivalence principle (LEP), the general scattering problem depicted in Figure 3.1a can be subdivided into two simplified auxiliary field problems, describing *interior* and *exterior* equivalent states. In the interior equivalent state indicated in Figure 3.1b, the interior fields $\{\mathbf{E}_2, \mathbf{H}_2\}$ in \mathcal{D} are generated in a homogeneous medium with $\{\varepsilon, \mu\} = \{\varepsilon_2, \mu_2\}$ by the equivalent current distribution $\{\mathbf{J}_2, \mathbf{M}_2\}$ in the absence of the incident field. Note that the sources $\{\mathbf{J}_2, \mathbf{M}_2\}$ generate no field in $\bar{\mathcal{D}}$. On the other hand, in the *exterior* equivalent state shown in Figure 3.1c, a homogeneous medium with $\{\varepsilon, \mu\} = \{\varepsilon_1, \mu_1\}$ is considered. The opposite of the equivalent currents $\{\mathbf{J}_1, \mathbf{M}_1\}$ annihilate the incident field, $\{\mathbf{E}_1^{\text{in}}, \mathbf{H}_1^{\text{in}}\}$ within \mathcal{D} , and also generate the scattered fields \mathbf{E}_1^{sc} and \mathbf{H}_1^{sc} within $\bar{\mathcal{D}}$. On account of the equivalence and superposition principles, this exterior equivalent state may be further subdivided into a part that cancels the incident fields through $\{\mathbf{J}_1^{\text{in}}, \mathbf{M}_1^{\text{in}}\}$, depicted in Figure 3.1e, and a part that generates the scattered field through $\{\mathbf{J}_1^{\text{sc}}, \mathbf{M}_1^{\text{sc}}\}$, shown in Figure 3.1d. Throughout this chapter we deal with surface current distributions only, therefore the subscript S has been omitted to maintain a concise notation.

The simplified interior and exterior equivalent states are ideally suited to determine the appropriate fields in the respective media by means of integral representations, since the associated equivalent current distribution are considered in an unbounded homogeneous medium. That is, because the equivalent currents $\{\mathbf{J}_2, \mathbf{M}_2\}$ of the interior equivalent state in Figure 3.1b generate a zero field in $\bar{\mathcal{D}}$, the exterior medium properties may be changed into $\{\varepsilon_1, \mu_1\}$, without any consequences to the fields in \mathcal{D} . Likewise, for the exterior equivalent state in Figure 3.1c, the interior medium properties may be changed into $\{\varepsilon_2, \mu_2\}$, as the equivalent currents $\{\mathbf{J}_1, \mathbf{M}_1\}$ yield a zero field in \mathcal{D} . Hence, the states in Figure 3.1a and Figure 3.1b are indeed equivalent to the original field state in Figure 3.1 with regard to the domains \mathcal{D} and $\bar{\mathcal{D}}$, respectively.

The interior and exterior equivalent states described here, are similar to those in Figure 2.3, where LEP was introduced. Thus, the same definitions, Eq. (2.62), hold for the equivalent currents in terms of the tangential fields along the boundary $\partial\mathcal{D}$, albeit that different sub- and superscripts are used, depending on the medium and field of interest. Further, upon crossing $\partial\mathcal{D}$, the tangential electric and magnetic field are both continuous in the original scattering problem shown in Figure 3.1a, as there are no genuine boundary sources involved. Hence, boundary conditions of the continuity type for the tangential field components, Eq. (2.17), apply, and they relate the

interior and the exterior equivalent states. Together with the definition of the equivalent currents in terms of the tangential field, as in Eq. (2.62), it directly follows that

$$\mathbf{J}_1 = \mathbf{J}_2, \quad \text{and} \quad \mathbf{M}_1 = \mathbf{M}_2. \quad (3.1)$$

Given this, the composite configuration of Figure 3.1b, combined with Figure 3.1c, indeed yields the source-free original configuration in Figure 3.1a.

Now that the general scattering problem has been decomposed into equivalent states by means of LEP, the integral representations for the respective media are formulated. Let us start with the subproblem shown in Figure 3.1e, where $\{\mathbf{J}_1^{\text{in}}, \mathbf{M}_1^{\text{in}}\}$ annihilate the incident field. These currents have also been introduced in the description of LEP, as depicted in Figure 2.3b. The associated integral representations are thus governed by the Stratton -Chu expressions given in Eqs. (2.64-2.65).

Since \mathbf{J}_1^{sc} and \mathbf{M}_1^{sc} in Figure 3.1d reproduce an exterior field, the corresponding integral representations follow from the application of the reciprocity theorem on the complementary domain $\bar{\mathcal{D}}$. Further, in view of the observation that the contribution of the boundary $\partial\mathcal{D}_\infty$ at infinity vanishes on account of the radiation condition, Eq. (2.22), only the boundary integral on $\partial\mathcal{D}$ with $\{\mathbf{J}_1^{\text{sc}}, \mathbf{M}_1^{\text{sc}}\}$ remains. Although the boundary integral should actually be supplemented with a volume integral over the impressed volume sources in $\bar{\mathcal{D}}$, their contribution is captured in terms of the known tangential incident field components $\{\mathbf{E}^{\text{in}}, \mathbf{H}^{\text{in}}\}$ on $\partial\mathcal{D}$. Hence, only the boundary integral on $\partial\mathcal{D}$ with $\{\mathbf{J}_1^{\text{sc}}, \mathbf{M}_1^{\text{sc}}\}$ remains. Therefore, the equivalent exterior state is dual to the interior equivalent state in Figure 2.3b, except that the outward normal $\hat{\mathbf{n}}$, should actually be pointing inwards here. However, for the sake of consistency, we only consider normals that point outwards. Accordingly, the negative of $\{\mathbf{J}_1^{\text{sc}}, \mathbf{M}_1^{\text{sc}}\}$ generate the scattered fields \mathbf{E}_1^{sc} and \mathbf{H}_1^{sc} . In view of the integral representations in Eqs. (2.64-2.65), the scattered electric field thus follows from

$$\begin{aligned} \chi_{\bar{\mathcal{D}}} \mathbf{E}_1^{\text{sc}} = & s\mu_1 \oint_{\partial\mathcal{D}} \mathbf{J}_1^{\text{sc}}(\mathbf{r}') G_1(\mathbf{r}, \mathbf{r}') dA' - \frac{1}{s\varepsilon_1} \nabla \oint_{\partial\mathcal{D}} [\nabla'_S \cdot \mathbf{J}_1^{\text{sc}}(\mathbf{r}')] G_1(\mathbf{r}, \mathbf{r}') dA' \\ & + \oint_{\partial\mathcal{D}} \mathbf{M}_1^{\text{sc}}(\mathbf{r}') \times \nabla' G_1(\mathbf{r}, \mathbf{r}') dA', \end{aligned} \quad (3.2)$$

and the magnetic field reads

$$\begin{aligned} \chi_{\bar{\mathcal{D}}}\mathbf{H}_1^{\text{sc}} = & s\varepsilon_1 \oint_{\partial\mathcal{D}} \mathbf{M}_1^{\text{sc}}(\mathbf{r}') G_1(\mathbf{r}, \mathbf{r}') dA' - \frac{1}{s\mu_1} \nabla \oint_{\partial\mathcal{D}} [\nabla'_S \cdot \mathbf{M}_1^{\text{sc}}(\mathbf{r}')] G_1(\mathbf{r}, \mathbf{r}') dA' \\ & - \oint_{\partial\mathcal{D}} \mathbf{J}_1^{\text{sc}}(\mathbf{r}') \times \nabla' G_1(\mathbf{r}, \mathbf{r}') dA'. \end{aligned} \quad (3.3)$$

With reference to Eq. (2.46), the characteristic function of the complementary domain is given by $\chi_{\bar{\mathcal{D}}}(\mathbf{r}) = \{1, 1/2, 0\}$ for $\mathbf{r} \in \{\bar{\mathcal{D}}, \partial\mathcal{D}, \mathcal{D}\}$. As mentioned above, the exterior equivalent state in Figure 3.1c follows from a superposition of the equivalent state associated with the exterior scattered field in Figure 3.1d, and the incident field in Figure 3.1e. Hence, $\{\mathbf{E}_1, \mathbf{H}_1\}$ and $\{\mathbf{J}_1, \mathbf{M}_1\}$ represent total fields, and total equivalent currents, i.e.,

$$\begin{cases} \mathbf{E}_1 = \mathbf{E}_1^{\text{in}} + \mathbf{E}_1^{\text{sc}}, \\ \mathbf{H}_1 = \mathbf{H}_1^{\text{in}} + \mathbf{H}_1^{\text{sc}}, \end{cases} \quad \begin{cases} \mathbf{M}_1 = \mathbf{M}_1^{\text{in}} + \mathbf{M}_1^{\text{sc}}, \\ \mathbf{J}_1 = \mathbf{J}_1^{\text{in}} + \mathbf{J}_1^{\text{sc}}. \end{cases} \quad (3.4)$$

By subtracting the integral representations in Eqs. (2.64-2.65) for the incident field from the ones for the scattered field, Eqs. (3.2-3.3), both field distributions are expressed in terms of the same total equivalent currents $\{\mathbf{J}_1, \mathbf{M}_1\}$, associated with the exterior state in Figure 3.1c. For the electric field, we obtain

$$\begin{aligned} \left\{ \mathbf{E}_1^{\text{sc}}, \frac{1}{2} [\mathbf{E}_1^{\text{sc}} - \mathbf{E}_1^{\text{in}}], -\mathbf{E}_1^{\text{in}} \right\} = & s\mu_1 \oint_{\partial\mathcal{D}} \mathbf{J}_1(\mathbf{r}') G_1(\mathbf{r}, \mathbf{r}') dA' \\ & - \frac{1}{s\varepsilon_1} \nabla \oint_{\partial\mathcal{D}} [\nabla'_S \cdot \mathbf{J}_1(\mathbf{r}')] G_1(\mathbf{r}, \mathbf{r}') dA' + \oint_{\partial\mathcal{D}} \mathbf{M}_1(\mathbf{r}') \times \nabla' G_1(\mathbf{r}, \mathbf{r}') dA', \end{aligned} \quad (3.5)$$

for $\mathbf{r} \in \{\bar{\mathcal{D}}, \partial\mathcal{D}, \mathcal{D}\}$, and for the magnetic field,

$$\begin{aligned} \left\{ \mathbf{H}_1^{\text{sc}}, \frac{1}{2} [\mathbf{H}_1^{\text{sc}} - \mathbf{H}_1^{\text{in}}], -\mathbf{H}_1^{\text{in}} \right\} = & s\varepsilon_1 \oint_{\partial\mathcal{D}} \mathbf{M}_1(\mathbf{r}') G_1(\mathbf{r}, \mathbf{r}') dA' \\ & - \frac{1}{s\mu_1} \nabla \oint_{\partial\mathcal{D}} [\nabla'_S \cdot \mathbf{M}_1(\mathbf{r}')] G_1(\mathbf{r}, \mathbf{r}') dA' - \oint_{\partial\mathcal{D}} \mathbf{J}_1(\mathbf{r}') \times \nabla' G_1(\mathbf{r}, \mathbf{r}') dA', \end{aligned} \quad (3.6)$$

for $\mathbf{r} \in \{\bar{\mathcal{D}}, \partial\mathcal{D}, \mathcal{D}\}$. These equations describe the field generated by the equivalent sources only, i.e., in the absence of the incident field. Referring to Section 2.8, it is clear that the equivalent current \mathbf{J}_S in Schelkunoff's equivalence principle (SEP) which gives rise to $\{\mathbf{E}^{\text{in}}, \mathbf{H}^{\text{in}}\}$ inside \mathcal{D} is, unlike the \mathbf{J}_S^{in} of LEP, indeed related to a *total* field.

Next, we define the linear boundary integral operators,

$$\mathbf{L}_v(\mathbf{r})\mathbf{X}_S \equiv \gamma_v \oint_{\partial\mathcal{D}} \mathbf{X}_S(\mathbf{r}') G_v(\mathbf{r}, \mathbf{r}') dA' - \frac{1}{\gamma_v} \nabla \oint_{\partial\mathcal{D}} [\nabla'_S \cdot \mathbf{X}_S(\mathbf{r}')] G_v(\mathbf{r}, \mathbf{r}') dA', \quad (3.7a)$$

$$\mathbf{K}_v(\mathbf{r})\mathbf{X}_S \equiv \oint_{\partial\mathcal{D}} \mathbf{X}_S(\mathbf{r}') \times \nabla' G_v(\mathbf{r}, \mathbf{r}') dA', \quad (3.7b)$$

which act on a boundary current \mathbf{X}_S defined on $\partial\mathcal{D}$. The subscript $v \in \{1, 2\}$ refers to the index of the constitutive parameters ε_v, μ_v . The first integral on the left-hand side of Eq. (3.7a) is commonly known as a *vector potential*, and the second integral as a *scalar potential*. More specifically, they are magnetic vector- and electric scalar potentials if \mathbf{X}_S is an electric current, and electric vector- and magnetic scalar potentials if \mathbf{X}_S is a magnetic current. It should be kept in mind though, that the derivation of the scalar potential in Chapter 2 was subject to the continuous differentiability of \mathbf{X}_S on $\partial\mathcal{D}$.

To arrive at concise expressions that describe the total fields anywhere in the exterior equivalent configuration of Figure 3.1c, we add the incident field to both sides of Eqs. (3.5-3.6) and use the introduced L and K operators, which results in

$$\chi_{\bar{\mathcal{D}}} \mathbf{E}_1 = \mathbf{E}_1^{\text{in}} + Z_1 \mathbf{L}_1 \mathbf{J}_1 + \mathbf{K}_1 \mathbf{M}_1, \quad (3.8a)$$

$$\chi_{\bar{\mathcal{D}}} \mathbf{H}_1 = \mathbf{H}_1^{\text{in}} + Y_1 \mathbf{L}_1 \mathbf{M}_1 - \mathbf{K}_1 \mathbf{J}_1, \quad (3.8b)$$

where $Y_1 = \sqrt{\varepsilon_1/\mu_1}$ represents the admittance of medium 1, and $\chi_{\bar{\mathcal{D}}}$ has been defined below Eq. (3.3). Similar integral representations can be obtained for the interior equivalent state depicted in Figure 3.1b, where $\{\mathbf{J}_2, \mathbf{M}_2\}$ are considered in an empty homogeneous medium, 2, and reproduce the penetrated fields, \mathbf{E}_2 and \mathbf{H}_2 in \mathcal{D} , which are total fields, since \mathcal{D} is presumed source-free. This equivalent state is consistent with the interior equivalent state in Figure 2.3b. Therefore, the integral representations in Eqs. (2.64-2.65) are also applicable here, albeit with fields $\{\mathbf{E}_2, \mathbf{H}_2\}$ and currents $\{\mathbf{J}_2, \mathbf{M}_2\}$. In terms of the operators L and K, we have

$$-\chi_{\mathcal{D}} \mathbf{E}_2 = Z_2 \mathbf{L}_2 \mathbf{J}_2 + \mathbf{K}_2 \mathbf{M}_2, \quad (3.9a)$$

$$-\chi_{\mathcal{D}} \mathbf{H}_2 = Y_2 \mathbf{L}_2 \mathbf{M}_2 - \mathbf{K}_2 \mathbf{J}_2. \quad (3.9b)$$

Upon comparing Eqs. (3.8) and (3.9), we observe that an impressed source distribution in \mathcal{D} is readily accounted for, by appending its field contribution to the right-hand side of the equation. Once the related equivalent currents are obtained, the fields in the original scattering problem depicted in Figure 3.1a are described by the above two sets of integral representations.

To determine the yet unknown equivalent currents, the integral representations are evaluated on the boundary $\partial\mathcal{D}$. Upon applying the counterpart of Eq. (2.62) for the equivalent currents \mathbf{J}_1 and \mathbf{M}_1 , to the total fields \mathbf{E}_1 and \mathbf{H}_1 in Eq. (3.8), we obtain the integral equations associated with the exterior equivalent state,

$$-\hat{\mathbf{n}} \times \mathbf{E}_1^{\text{in}} = \hat{\mathbf{n}} \times [Z_1 L_1 \mathbf{J}_1 + K_1 \mathbf{M}_1] - \frac{\mathbf{M}_1}{2}, \quad (3.10a)$$

$$-\hat{\mathbf{n}} \times \mathbf{H}_1^{\text{in}} = \hat{\mathbf{n}} \times [Y_1 L_1 \mathbf{M}_1 - K_1 \mathbf{J}_1] + \frac{\mathbf{J}_1}{2}, \quad (3.10b)$$

with $\mathbf{r} \in \partial\mathcal{D}$. In a similar manner, from Eq. (3.9) we arrive at the integral equations,

$$\mathbf{0} = \hat{\mathbf{n}} \times [Z_2 L_2 \mathbf{J}_2 + K_2 \mathbf{M}_2] + \frac{\mathbf{M}_2}{2}, \quad (3.11a)$$

$$\mathbf{0} = \hat{\mathbf{n}} \times [Y_2 L_2 \mathbf{M}_2 - K_2 \mathbf{J}_2] - \frac{\mathbf{J}_2}{2}, \quad (3.11b)$$

for $\mathbf{r} \in \partial\mathcal{D}$, associated with the interior equivalent state. Observe that the signs of the last term on the right-hand side of Eqs. (3.10-3.11), which we henceforth denote as an identity operator, $l_v \equiv \mathbf{X}_v/2$ for $i = \{1, 2\}$, are opposite with respect to K . This originates from the fact that Eq. (3.10) describes an exterior, and Eq. (3.11) an interior field formulation, while at the same time, the outward pointing normal is unchanged. In general, the same sign is used for $\hat{\mathbf{n}} \times K$ and l when $\hat{\mathbf{n}}$ points outwards. Note that, without imposing the equality of the currents, Eq. (3.1), the integral equations associated with the exterior Eq. (3.10) and the interior fields, Eq. (3.11), would not be coupled. Hence, considered separately, any solution will not uniquely describe the fields in the composite scattering configuration, until appropriate boundary conditions for the interface $\partial\mathcal{D}$ have been imposed that relate the interior to the exterior fields. For dielectric objects the equations can be combined in several ways; this will be described in Section 3.5.

3.3 Integral equations for perfectly conducting objects

In the limiting case of the electric conductivity $\sigma_{e;2}$, and the complex permittivity ε_2 for the general scattering problem depicted in Figure 3.1a going to infinity, \mathcal{D} becomes electrically impenetrable, i.e., a perfect electric conductor (PEC), in which $\{\mathbf{E}_2, \mathbf{H}_2\}$ are both zero. Therefore, only the exterior equivalent configuration in Figure 3.1c needs to be considered. From the boundary condition for a PEC, Eq. (2.19), and the definition of the equivalent magnetic current, Eq. (2.62b), we readily obtain

$$\hat{\mathbf{n}} \times \mathbf{E}_1 = \mathbf{M}_1 = \mathbf{0}. \quad (3.12)$$

Now, LEP has reduced to SEP as only \mathbf{J}_1 remains. Also for a PEC, the subdivision of the general scattering problem into separate equivalent states, as depicted in Figure 3.1 for dielectric objects, is no longer required. Instead, for a PEC the situation reduces to the original and exterior equivalent state illustrated in Figure 2.4b, respectively, Figure 2.4c, of SEP upon defining $\mathbf{J} \equiv \mathbf{J}_1$. From the definition of equivalent currents, Eq. (2.62), we thus infer that

$$\hat{\mathbf{n}} \times \mathbf{H}_1 = \mathbf{J}_S^{\text{ind}} = -\mathbf{J}. \quad (3.13)$$

Although the PEC is absent in the exterior equivalent state depicted in Figure 2.4c, its response is accounted for by the induced current $\mathbf{J}_S^{\text{ind}}$. As such, the corresponding total electric and magnetic fields are determined from \mathbf{J} through the integral representations in Eq. (3.8) upon substituting $\mathbf{J}_1 = \mathbf{J}$ and $\mathbf{M}_1 = \mathbf{0}$. In turn, via the integral equations (3.10) on $\partial\mathcal{D}$, \mathbf{J} can be solved. Accordingly, with Eq. (3.10a) we arrive at the *Electric Field Integral Equation* (EFIE),

$$-\hat{\mathbf{n}} \times \mathbf{E}_1^{\text{in}} = Z_1 \hat{\mathbf{n}} \times [\mathbf{L}_1 \mathbf{J}], \quad (3.14)$$

while with Eq. (3.10b), we have the *Magnetic Field Integral Equation* (MFIE),

$$\hat{\mathbf{n}} \times \mathbf{H}_1^{\text{in}} = \hat{\mathbf{n}} \times [\mathbf{K}_1 \mathbf{J}] - \frac{\mathbf{J}}{2}. \quad (3.15)$$

Equation (3.14) is a Fredholm integral equation of the first kind, as the unknown current \mathbf{J} appears only under the integral sign, whereas Eq. (3.15) is a Fredholm integral equation of the second kind as \mathbf{J} also appears outside the integral. Note that an integral equation of the second kind is generally less sensitive to the type of discretization, as will be discussed in 3.7. Observe also that the integral equation associated with the scattering from a *Perfect Magnetic Conductor* (PMC), which is magnetically impenetrable, readily follows from the above via the duality principle discussed in Section 2.3.

3.4 Interior resonances

Despite the fact that appropriate boundary conditions have been applied, the EFIE and MFIE (and thus also SEP) may not always yield unique solutions. If, for example, there is a nonzero solution ($\mathbf{E} \neq \mathbf{0}$) to the homogeneous modified vector Helmholtz equation

$$\nabla \times \nabla \times \mathbf{E}_1 = -\gamma^2 \mathbf{E}_1, \quad (3.16)$$

while at the same time the boundary condition in Eq. (3.12) is satisfied for $\mathbf{r} \in \partial\mathcal{D}$, the solution of the EFIE is not unique, and a spurious resonance associated with a corresponding surface

current $\mathbf{J}_S^{\text{res}}$ exists. Unlike the exterior problem, with a PEC in \mathcal{D} and a homogeneous lossless medium in $\bar{\mathcal{D}}$, the interior problem, with a PEC in $\bar{\mathcal{D}}$ and a homogeneous lossless medium in \mathcal{D} does possess such nontrivial solutions at discrete values of ω . These are just the resonant cavity modes of \mathcal{D} . Although there is no direct physical relationship between the exterior and interior problems, they are mathematically related by sharing a common integral equation. In [44, p. 35-36] it is proven that non-uniqueness only occurs at such resonant (cavity) modes for lossless media.

A similar non-uniqueness is associated with the MFIE, i.e., the source-free Helmholtz equation for the magnetic field is given by

$$\nabla \times \nabla \times \mathbf{H}_1 = -\gamma^2 \mathbf{H}_1. \quad (3.17)$$

Because the fields inside a perfect conductor vanishes, we have just inside \mathcal{D} ,

$$\hat{\mathbf{n}} \times \mathbf{H}_1 = \mathbf{0}. \quad (3.18)$$

Observe that Eqs. (3.16) and (3.12) are mathematically of the same form as Eqs. 3.17 and 3.18 and therefore share the same resonant conditions. Thus, the resonance conditions where the MFIE is not unique correspond with those of the EFIE [24, 45]. Note that is not the case for 2D configurations where fields are separated into different polarizations, i.e., the EFIE and MFIE represent a Dirichlet and Neuman problem.

In contrast with the MFIE, a resonant current $\mathbf{J}_S^{\text{res}}$ of the EFIE for a PEC theoretically yields no contribution to the field in $\bar{\mathcal{D}}$. This readily follows from the reciprocity theorem, i.e., according to Section 2.5, only the EFIE yields a reciprocal system in \mathcal{D} for the interior resonant mode, because the MFIE satisfies Eq. (3.18) instead of (3.12). Only for a reciprocal system we have, in the absence of magnetic sources,

$$\int_{\mathcal{D}} \mathbf{E}^a \cdot \mathbf{J}^b \, dV = \int_{\mathcal{D}} \mathbf{E}^b \cdot \mathbf{J}^a \, dV, \quad (3.19)$$

which follows from the reaction theorem. If \mathbf{J}^a is chosen to be a surface current tangential to $\partial\mathcal{D}$, the right-hand side is zero as for the EFIE the tangential components of \mathbf{E}^b must be zero on $\partial\mathcal{D}$, independent of \mathbf{J}^b . This can only be true if \mathbf{E}^a , and thus also \mathbf{H}^a is zero everywhere. Accordingly, the field produced by $\mathbf{J}_S^{\text{res}}$ is indeed equal to zero in $\bar{\mathcal{D}}$ for the EFIE.

Unless losses are introduced, additional constraints on the field are required [46] to ensure unique solutions. For instance, via a dual (parallel) boundary [47], or the boundary condition for the field

component normal to $\partial\mathcal{D}$ [45], or by forcing consistency on the boundary of a relative small domain inside \mathcal{D} [48] via the null-field method [49], or by identifying the associated eigencurrent via a *Singular Value Decomposition* (SVD) and subsequently remove its contribution from the numerical solution [50]. However, the most commonly used remedy to avoid interior resonances is the *Combined Field Integral Equation* (CFIE) [51], which represents a scaled linear combination of the MFIE and EFIE method,

$$\text{CFIE} = Y_1\alpha\text{EFIE} + (1 - \alpha)\text{MFIE} \quad (3.20)$$

The admittance Y_1 is included to give the EFIE, like the MFIE, the dimension of the electric current. The parameter α can be varied between 0 and 1 to have a pure MFIE or EFIE, or a combination of both. In [51] it is proven that the CFIE is free of interior resonances if $0 < \alpha < 1$, even at frequencies where the EFIE and MFIE both fail to produce a unique solution.

3.5 Boundary integral equations for dielectric objects

For a (lossy) dielectric object the incident field penetrates the scattering object, as ε_2, μ_2 have finite values. Hence, both the interior and the exterior equivalent states depicted in Figure 3.1 must be taken into account. Upon crossing $\partial\mathcal{D}$, the tangential electric and magnetic field are both continuous as there are no genuine boundary sources involved in the original scattering problem shown in Figure 3.1a. Hence, boundary conditions of the continuity type for the tangential field components, Eq. (2.17), apply, and they relate the interior to the exterior equivalent state. Together with the definition of the equivalent currents in terms of the tangential field, as in Eq. (2.62), it directly follows that

$$\mathbf{J}_1 = \mathbf{J}_2, \quad \text{and} \quad \mathbf{M}_1 = \mathbf{M}_2. \quad (3.21)$$

Henceforth, the subscript of the current is omitted. Given this, the composite configuration of Figure 3.1b combined with Figure 3.1c, indeed yields the source-free original configuration in Figure 3.1a. Equations (3.10) and (3.11) now form a set of four integral equations in the two unknowns \mathbf{J} and \mathbf{M} . Usually one would like to have the same number of equations as the number of unknowns. The original four equations can be reduced to a coupled pair of equations by taking linear combinations. Because many pairs of linear combinations are possible, there are also many boundary integral equation formulations for the scattering problem. For instance, the addition of the electric field equations (3.10a) and (3.11a), respectively, the magnetic field

equations (3.10b) and (3.11b), gives

$$\begin{aligned} -\hat{\mathbf{n}} \times \mathbf{E}_1^{\text{in}} &= \hat{\mathbf{n}} \times [(Z_1 \mathbf{L}_1 + Z_2 \mathbf{L}_2) \mathbf{J} + (\mathbf{K}_1 + \mathbf{K}_2) \mathbf{M}], \\ -\hat{\mathbf{n}} \times \mathbf{H}_1^{\text{in}} &= \hat{\mathbf{n}} \times [(Y_1 \mathbf{L}_1 + Y_2 \mathbf{L}_2) \mathbf{M} - (\mathbf{K}_1 + \mathbf{K}_2) \mathbf{J}]. \end{aligned} \quad (3.22)$$

This set of integral equations is widely used for the scattering by dielectric bodies and is called the *Poggio, Miller, Chang, Harrington, Wu* formulation (PMCHW) [39, Chapter 4]. Observe that Eq. (3.22) has reduced to a coupled pair of integral equations of the *first kind* as the last terms on the right side in Eqs. (3.10) and (3.11) cancel.

Another, but less popular choice of combination constants gives rise to the formulation proposed by *Müller* [52]. That is, upon subtracting $\varepsilon_2/\varepsilon_1$ times Eq. (3.11a) from Eq. (3.10a) for the electric, and μ_2/μ_1 times Eq. (3.11b) from Eq. (3.10b) for the magnetic field integral equation, we obtain

$$\begin{aligned} -\hat{\mathbf{n}} \times \mathbf{E}_1^{\text{in}} &= \hat{\mathbf{n}} \times \left[\left(Z_1 \mathbf{L}_1 - \frac{\varepsilon_2}{\varepsilon_1} Z_2 \mathbf{L}_2 \right) \mathbf{J} + \left(\mathbf{K}_1 - \frac{\varepsilon_2}{\varepsilon_1} \mathbf{K}_2 \right) \mathbf{M} \right] - \frac{\varepsilon_1 + \varepsilon_2}{2\varepsilon_1} \mathbf{M}, \\ -\hat{\mathbf{n}} \times \mathbf{H}_1^{\text{in}} &= \hat{\mathbf{n}} \times \left[\left(Y_1 \mathbf{L}_1 - \frac{\mu_2}{\mu_1} Y_2 \mathbf{L}_2 \right) \mathbf{M} - \left(\mathbf{K}_1 - \frac{\mu_2}{\mu_1} \mathbf{K}_2 \right) \mathbf{J} \right] + \frac{\mu_1 + \mu_2}{2\mu_1} \mathbf{J}. \end{aligned} \quad (3.23)$$

In [53] it is proven that the PMCHW, as well as the Müller formulation, yield unique solutions. Unlike the PMCHW equations, this choice of combination yields a coupled set of integral equations of the second kind. Further, if the dielectric contrast of the interior and exterior medium vanishes, the Müller formulation reduces to the trivial solution. Regarding the terms within the square brackets in Eq. (3.23), the singularity is known to be less dominant than the corresponding singularity in Eq. (3.22) due to cancellations. Finally, the low-frequency breakdown problem is naturally avoided without the need for loop-tree or loop-star basis functions [54, 55]. Despite these advantages, the main reason why the Müller formulation has not become popular is that, when the equations are solved using a similar testing procedure as has been known to yield accurate solutions with the PMCHW formulation, the solution is unstable [56]. However, as we will demonstrate in Section 7.5, this can be attributed to a poor choice of testing functions.

3.6 Method of moments and projection methods

Now that the boundary conditions have been discussed, the integral equations can be applied to a scattering problem. The corresponding equivalent boundary currents uniquely describe the scattered field. With respect to the numerical implementation, a general framework is given by

the *Method of Moments* (MoM) procedure [57, p. 5-9] for the reduction of the integral equations into a linear system of algebraic equations. The MoM procedure is based on projection methods. This section describes the basic idea of the MoM and its application to determine the equivalent surface currents numerically.

The integral equations under consideration can all be cast in the form,

$$Ax = b \quad (3.24)$$

with a linear operator A , the equivalent electric and/or magnetic currents as the unknown solution x , and an excitation or forcing function b , that accounts for the incident field on $\partial\mathcal{D}$. The operator A performs a mapping from a normed space, say, X to a normed space Y . Here X is the domain of A . The range of A , $\mathcal{R}(A)$, is contained in Y .

In the MoM approach two successive projections are applied, viz., the projection \mathcal{Q}_N which projects X onto the subspace X_N , spanned by an N -dimensional set of expansion functions, and the projection \mathcal{P}_N which projects $\mathcal{R}(A)$ onto the subspace Y_N . These subspaces represent an approximation and should become dense in the original spaces in the limit $N \rightarrow \infty$. The projection \mathcal{P}_N is constructed by using a normed space W_N dual to Y_N , such that both normed spaces are equipped with a nondegenerate bilinear form denoted by the duality product $\langle W_N, Y_N \rangle$. The projection operator \mathcal{P}_N is then defined by

$$\mathcal{P}_N y = \sum_{k=1}^N \langle w_k, y \rangle y_k. \quad (3.25)$$

where $\{w_1, \dots, w_N\}$ is the set of test functions that form a basis in W_N dual to $\{y_1, \dots, y_N\}$. As a basic property of projection operators, \mathcal{P}_N must be idempotent, i.e., a projection of a projection is the projection itself. Thus, the property $\mathcal{P}_N(\mathcal{P}_N y) = \mathcal{P}_N y$ should be satisfied. This follows immediately if the the dual system W_N is chosen such that

$$\langle w_k, y_\ell \rangle = \delta_{k,\ell} \quad (3.26)$$

holds, where $\delta_{k,\ell}$ is the Kronecker symbol. The projection operator \mathcal{Q}_N for the unknown equivalent currents u , is expressed in a similar way

$$\mathcal{Q}_N x = \sum_{\ell=1}^N \alpha_\ell x_\ell, \quad (3.27)$$

although here we have used the fact that the duality product of x with its dual space represents the set of unknown current amplitudes $\{\alpha_\ell\}$ of the expansion functions $\{x_\ell\}$ which form a basis

of the subspace X_N . Accordingly, the strong form of the integral equation, Eq. (3.24), for which the equality sign holds at each point on $\partial\mathcal{D}$, is replaced with the approximate system

$$\mathcal{P}_N \mathbf{A} \mathcal{Q}_N x = \mathcal{P}_N b. \quad (3.28)$$

Thus, the integral equation, Eq. (3.24), has been reduced to an equation in a (weighted) average sense. The subsequent substitution of the representations of \mathcal{Q}_N and \mathcal{P}_N yields

$$\sum_{k=1}^N \left(\sum_{\ell=1}^N \langle w_k, \mathbf{A} x_\ell \rangle \alpha_\ell \right) y_k = \sum_{k=1}^N \langle w_k, b \rangle y_k, \quad (3.29)$$

Hence, the current amplitudes α_ℓ can be determined from the linear system of equations

$$\sum_{\ell=1}^N \langle w_k, \mathbf{A} x_\ell \rangle \alpha_\ell = \langle w_k, b \rangle, \quad k = 1, \dots, N, \quad (3.30)$$

provided that the square matrix $\langle w_k, \mathbf{A} x_\ell \rangle$, often referred to as the MoM or impedance matrix, has full rank, which essentially imposes a first restriction on the choice of test functions w_k and expansion functions x_ℓ , i.e., the expansion functions should be linearly independent. Otherwise, the above matrix would not be invertible and yields, as we will see later on, a non-unique system, even though the original equation (3.24) may be well-posed. A poor choice for w_k and x_ℓ could thus destroy the uniqueness of the integral equation, by allowing a non-trivial solution to the homogeneous system of equation to exist, which is commonly referred to as a spurious mode.

Upon refining the discretization, we expect that the approximation being made converges to the exact solution. This is guaranteed if the projection converges, such that apart from invertibility, point-wise convergence ensues, i.e., $\mathbf{A}_N^{-1} \mathcal{P}_N \mathbf{A} x \rightarrow x$ when $N \rightarrow \infty$, holds for all $x \in X$ [58, p. 185]. In general, the convergence of a projection \mathcal{P}_N is expected *only if* its subspace X_N is ultimately dense in X , i.e., if for all $x \in X$,

$$\inf_{x_N \in X_N} \|x - x_N\| \rightarrow 0 \quad \text{for } N \rightarrow \infty. \quad (3.31)$$

Consequently, if the chosen type of expansion function x_ℓ is ultimately dense in X , then a further increase of the dimension of X_N and W_N would lead to a more accurate approximation.

The first step in the MoM is the expansion of the unknown equivalent boundary currents into a truncated series of expansion functions via the projection \mathcal{Q}_N ,

$$\mathcal{Q}_N^J \mathbf{J}_S(\mathbf{r}) = \sum_{n=1}^N J_n \mathbf{f}_n^J(\mathbf{r}), \quad (3.32a)$$

$$\mathcal{Q}_N^M \mathbf{M}_S(\mathbf{r}) = Z_1 \sum_{n=1}^N M_n \mathbf{f}_n^M(\mathbf{r}), \quad (3.32b)$$

where J_n and M_n are the unknown current amplitudes that are determined by the MoM approach. The superscript of \mathbf{f}_n indicates whether the expansion function of the electric or magnetic current is concerned. Further, $\mathbf{f}_n^{J,M}$ are tangential to $\partial\mathcal{D}$, since we deal with boundary currents. Note that the expansion of \mathbf{M}_S has been scaled with the wave impedance Z_1 , such that the discretized currents \mathbf{f}_n^J and \mathbf{f}_n^M have the same dimension, and are of the same order of magnitude, which reduces the condition number of the MoM-matrix.

To arrive at a set of linear algebraic equations, the integral equations are tested via the projection \mathcal{P}_N , as defined in Eq. (3.30). Yet, an cross product with $\hat{\mathbf{n}}$ is involved with the fields (and integral operators). To avoid this, and instead apply a test function \mathbf{f}_m directly on these fields, the property, $\hat{\mathbf{n}} \times (\hat{\mathbf{n}} \times \mathbf{A}) = -\mathbf{A}_{\text{tan}}$ is utilized, where \mathbf{A} represents a field vector and the subscript in $\mathbf{A}|_{\text{tan}}$ indicates the components tangential to $\partial\mathcal{D}$ only. Accordingly, since the duality product $\langle \cdot, \cdot \rangle$ on $\partial\mathcal{D}$ reads

$$\langle \mathbf{A}, \mathbf{B} \rangle = \int_{\partial\mathcal{D}} \mathbf{A} \cdot \mathbf{B} \, dA, \quad (3.33)$$

testing with $\hat{\mathbf{n}} \times \mathbf{f}_m$ gives,

$$\langle \hat{\mathbf{n}} \times \mathbf{f}_m, \hat{\mathbf{n}} \times \mathbf{A} \rangle = \langle \mathbf{f}_m, \mathbf{A} \rangle, \quad (3.34)$$

under the assumption that \mathbf{f}_m is tangential to $\partial\mathcal{D}$. Following the line of argument in the expansion of \mathbf{M}_S , either the electric or magnetic field equation should be scaled such that both equations carry the same dimension. Although the usual approach is to multiply the magnetic field with Z_1 , we prefer to scale the electric field with Y_1 instead, as it leads to a more symmetric concise form for both the Müller and PMCHW formulations. Therefore, $Y_1 \hat{\mathbf{n}} \times \mathbf{f}_m^E$ and $\hat{\mathbf{n}} \times \mathbf{f}_m^H$ are used as testing functions for the electric and magnetic field integral equations, respectively. From the expansion in Eq. (3.32), together with Eq. (3.34), the discrete counterparts of the integral equations (3.22) associated with the PMCHW formulation read

$$\sum_{n=1}^N \langle \mathbf{f}_m^E, J_n (\mathbf{L}_1 + Y_1 Z_2 \mathbf{L}_2) \mathbf{f}_n^J + M_n (\mathbf{K}_1 + \mathbf{K}_2) \mathbf{f}_n^M + Y_1 \mathbf{E}_1^{\text{in}} \rangle = 0, \quad (3.35a)$$

$$\sum_{n=1}^N \langle \mathbf{f}_m^H, M_n (\mathbf{L}_1 + Z_1 Y_2 \mathbf{L}_2) \mathbf{f}_n^M - J_n (\mathbf{K}_1 + \mathbf{K}_2) \mathbf{f}_n^J + \mathbf{H}_1^{\text{in}} \rangle = 0, \quad (3.35b)$$

for $m = 1, \dots, N$. Likewise, for the Müller formulation, Eq. (3.23), we obtain

$$\sum_{n=1}^N \left\langle \mathbf{f}_m^E, J_n \left(\mathbf{L}_1 - \frac{\gamma_2}{\gamma_1} \mathbf{L}_2 \right) \mathbf{f}_n^J + M_n \left(\mathbf{K}_1 - \frac{\varepsilon_2}{\varepsilon_1} \mathbf{K}_2 \right) \mathbf{f}_n^M + M_n \frac{\varepsilon_1 + \varepsilon_2}{2\varepsilon_1} \hat{\mathbf{n}} \times \mathbf{f}_n^M + Y_1 \mathbf{E}_1^{\text{in}} \right\rangle = 0, \quad (3.36a)$$

$$\sum_{n=1}^N \left\langle \mathbf{f}_m^H, M_n \left(\mathbf{L}_1 - \frac{\gamma_2}{\gamma_1} \mathbf{L}_2 \right) \mathbf{f}_n^M - J_n \left(\mathbf{K}_1 - \frac{\mu_2}{\mu_1} \mathbf{K}_2 \right) \mathbf{f}_n^J - J_n \frac{\mu_1 + \mu_2}{2\mu_1} \hat{\mathbf{n}} \times \mathbf{f}_n^J + \mathbf{H}_1^{\text{in}} \right\rangle = 0, \quad (3.36b)$$

for $m = 1, \dots, N$. The two resulting coupled systems of equations may also be understood as residuals that are weighted to zero at all points on the boundary of the scatterer with respect to the testing functions, $\mathbf{f}_m^{\text{E,H}}$.

If the applied test and expansion functions originate from the same set of functions, this procedure is in electromagnetic literature widely known as *Galerkin's method* [59, p. 212] and [60]. This approach is beneficial in the discretization of a symmetric operator like \mathbf{L} , because it may preserve the symmetry in the discretized version as well, which saves the numerical determination of (nearly) half of the operator. On that account, expanding with \mathbf{f}_n , while testing with $\hat{\mathbf{n}} \times \mathbf{f}_m$ given that $\{\mathbf{f}_m\} = \{\mathbf{f}_n\}$ also complies with the Galerkin approach.

Considering arbitrarily shaped domains poses severe demands on the flexibility of the test and expansion functions. Due to a lack of flexibility and ease of implementation of entire-domain basis functions, they are not very well suited for our application, and local expansion functions are selected instead. Thereby, we accept the disadvantage that their use requires considerably more computational effort than properly chosen entire-domain functions, as more test and expansion functions are required for a good approximation.

In the formulation of the integral representations it was assumed that, for the scalar potential, the boundary currents are continuously differentiable on $\partial\mathcal{D}$, Eq. (2.63). However, this requirement is too stringent in the construction of a numerical scheme. Yet, through the definition of the solution space of the associated current, it is possible to weaken the constraint of continuous differentiability for the surface divergence to a reduced differentiability of a generalized function. In particular, this procedure involves Cauchy sequences generated by functions that are continuously differentiable in the solution space of the boundary current. In this manner, piecewise differentiable functions are permitted for the expansion of the boundary current that is subject to the surface divergence.

3.7 Mapping properties of the boundary integral operators

In this section the solvability of the integral equations is discussed in terms of the well-posedness of the integral equations, which depends on the mapping properties of the operators L and K . The aim is to present a brief overview of the mapping properties, and to deduce general constraints for the associated test and expansion functions. More specialized restrictions for 2D and 3D configurations follow in Chapters 5 and 7, respectively. Further, the analysis of the MFIE is somewhat different from that of the EFIE, because the MFIE also contains an additive multiple of the identity operator I .

On physical grounds, the stored and dissipated power must remain finite within a bounded domain with sufficiently smooth boundary. From the complex power balance it can then be shown that the vector space \mathcal{L}^2 on this bounded domain of square integrable functions in \mathbb{C}^3 is therefore an appropriate function space for the description of the electromagnetic field. Upon defining the inner product,

$$(f, g) = \int_{\mathcal{D}} f \cdot g^* dA, \quad (3.37)$$

where g^* is the adjoint of g , the vector space \mathcal{L}^2 is complete under the norm $\|f\| = \sqrt{(f, f)}$ and hence represents a Hilbert space. This includes the cases involving infinitely thin sheets, such as a PEC thin plate, where the finite-energy holds on the volume surrounding the sharp edge.

The solvability of an integral equation like Eq. (3.24), is subject to the well-posedness of the problem. The problem is well-posed if the inverse operator A^{-1} exists and is bounded. Boundedness of A^{-1} implies that there exists a positive number C such that $\|A^{-1}y\|_X \leq C\|y\|_Y$ for all $y \in Y$. If existence and uniqueness of the solution is proven, then A^{-1} exists. In addition, if A^{-1} is a bounded operator, it can be shown that A^{-1} is also continuous. Continuity of A^{-1} ensures that the solution x depends continuously on the excitation function f , i.e., small errors in b only cause limited errors in x . Otherwise, the solution could become unstable. If either existence, uniqueness or continuity is not achieved, the problem is ill-posed. In that case, it becomes extremely difficult to obtain an approximate solution. Yet, notice that these three properties are not inherently independent.

The mapping properties of the MFIE, symbolically written as $I+K$, on a smooth boundary can be derived from the Riesz and Fredholm theory [61, Chapter 1]. The underlying observation is that

$\mathcal{R}(K)$ is a compact subset¹, as long as the boundary is smooth. Then, the Riesz theory states that the existence and boundedness of the inverse operator is guaranteed if uniqueness can be proven. In case uniqueness fails to hold, an additional condition on the excitation is required to ensure existence of the solution. As K is compact², and therefore bounded, it has an adjoint operator K^* , such that $\langle Kx, b \rangle = \langle x, K^*b \rangle$. Given this, the additional condition in case uniqueness fails to hold amounts to an orthogonality relation between the null space of K^* , indicated by $\mathcal{N}(K^*)$, and the excitation function b . Further, if b is smooth on the boundary $\partial\mathcal{D}$, then the solution of the integral equation is also smooth on $\partial\mathcal{D}$. In that case, a numerical scheme with smooth basis functions will exhibit more rapid convergence compared to schemes with non-smooth basis functions.

If $\partial\mathcal{D}$ is not smooth, e.g., it contains corners or edges, then the mapping properties of the MFIE change drastically. In that case, the operator K loses its compactness property in the neighborhood of the corners or edges. Several techniques have been proposed to analyze such cases, e.g., a Banach contraction argument [58, p. 76-79], and an alternative way of showing that the range is closed [63]. In most cases, the invertibility of this operator is considered on $\mathcal{L}^2(\partial\mathcal{D})$, which allows for the elegance of the Hilbert-space framework and the natural way of computing inner products to be exploited. In that case, the Galerkin method gives rise to a converging and stable numerical solution, provided that the set of expansion functions is ultimately dense in $\mathcal{L}^2(\partial\mathcal{D})$. Consequently, in the $\mathcal{L}^2(\partial\mathcal{D})$ framework, continuity of the testing and expansion functions is not required in any direction. For example, expansion by piecewise-constant functions is allowed.

In all cases of the EFIE, for both smooth and non-smooth boundaries, the general idea is to split the operator L in a bounded coercive³ part, denoted by B , and a compact part C . Then, the Lax-Milgram theorem [58, p. 201] is invoked to show that B has a bounded inverse. Consequently, the operator can be written as $L = B(I + B^{-1}C)$, where the operator combination $B^{-1}C$ is again compact. Hence, the bounded invertibility of L is established if $(I + B^{-1}C)$ has a bounded inverse. However, the latter operator falls within the framework of the Riesz theory, in which uniqueness automatically implies existence and boundedness of the solution. The main difficulty of this approach is the introduction of a framework in which the coerciveness of B holds. At present, the most complete results have been obtained on the so-called fractional-order Sobolev spaces [64, p. 96-99], denoted by $H^\ell(\partial\mathcal{D})$ for $-1 < \ell < 1$. Further deduction of the well-posedness for the

¹A subset M of X is compact if every sequence in M has a convergent subsequence whose limit is in M [62, p. 77].

²A linear operator A with domain X and range Y is called compact if and only if for each bounded subsequence x_n in X the sequence Ax_n contains a convergent subsequence in Y [58, p. 18].

³A linear operator A is coercive if there exists a positive constant C such that $\Re\{(Ax, x)\} \geq C\|x\|^2$ for all $x \in X$ [58, p. 201].

EFIE is treated separately with respect to 2D (Section 5.3) and 3D (Section 7.2) configurations.

In the construction of a numerical scheme, mainly two properties of the scheme are of interest: order of convergence of the numerical approximation and the conditioning of the linear system. In general, the order of convergence of the numerical approximation (equivalent current) is determined by two issues: the smoothness of the exact solution and the smoothness of the expansion functions, which includes the smoothness of the parametrization of the (approximated) boundary. The second issue is also known as the interpolation error. Combined, this is known as Cea's lemma [58, p. 186]. Further, the smoothness of the exact solution is determined by the smoothness of the exact boundary, the smoothness of the excitation function and the mapping properties of the integral operator. It should be noted that smooth expansion functions do not improve the convergence compared to non-smooth expansion functions if the exact solution or the approximated boundary is non-smooth. The testing functions only play a marginal role at this point. Their impact is limited to the stability of the numerical scheme, which determines whether or not the scheme will converge, but they do not influence the order of the convergence. However, Cea's lemma does imply that the testing functions could have an impact on the magnitude of the error in the approximation. On the other hand, the testing function does play a role with respect to the field that the approximate equivalent current generates. For instance, in [60], it is demonstrated that, for a smooth exact boundary, the error in the far field is equally dependent on the test and expansion functions, i.e., similar accuracy was obtained if the combined order of the basis and testing functions are comparable.

Chapter 4

Linear embedding via Green's operators

In the following, we have develop a specific variety of the Huygens-principle based diakoptics, referred to as linear embedding via Green's operators (LEGO). The Green's operators part indicates that these operators lead to integral representations with kernels that contain the Green's function of a background medium. Further, embedding via Green's operators is considered linear since the medium properties of the environment and hence the associated integral operators are considered linear. In addition, the resulting abbreviation "LEGO" reflects the modular building principle of the electromagnetic method that is common to the well-known LEGOTM bricks. Via embedding, we determine the electromagnetic interaction between elementary building blocks that is required to merge these blocks in an electromagnetic sense. In the introduction, Section 1.3, we have emphasized the LEGO approach as a modular electromagnetic design tool. In this chapter we present the theoretical background, the discretization, and an assessment of the computational complexity of the LEGO approach.

4.1 Introduction

The construction of the elementary building blocks for LEGO is described in Section 4.2. This is realized through a so-called scattering operator that is associated with equivalent states for the incident and scattered fields. The corresponding field representations are described in terms of propagator operators. In Section 4.3, we describe the embedding part of LEGO in its most general form via a compact operator formalism. Through embedding, the electromagnetic in-

teraction between two adjacent scattering domains is determined in terms of equivalent-current scattering operators of the individual domains. Green's operators are introduced and are discretized in Section 4.4. The resulting matrix form is expressed in terms of the discretized integral operators that are used to determine the scattered field for conducting and dielectric objects in Sections 5.3 and 7.2 for 2D and 3D implementations, respectively. In addition, an alternative discretization inherent to Love's equivalence principle (LEP) is proposed, which avoids the use of inverse propagator (MoM) matrices and amounts to a scheme that is more efficient than the ordinary implementation of LEP. The LEGO approach is completed in Section 4.5, where a combined scattering matrix is composed. Common boundary parts are removed in the combined scattering matrix. Repeated application of the embedding procedure allows for the construction of scattering matrices for large composite domains. Further, we specialize to either SEP or LEP, and eliminate computational redundancies in the corresponding computational schemes.

In Section 4.6 we determine the memory requirements and computational costs of the LEGO approach for both SEP and LEP. Special attention is given to domains that are closely packed. After a discussion of the associated computational schemes, the computational costs of a single embedding step of SEP and LEP are compared.

Although the modular building principle of LEGO already improves the efficiency of structure optimization in comparison with direct solvers, since a full recomputation of the entire structure is avoided, further improvement can be attained. Namely, since structure optimization usually amounts to local structure modifications, we restrict future embedding steps to a designated domain, which become fast. This optimization stage of LEGO is described in Section 4.7, and an indication of the additional gain in efficiency is provided. Furthermore, the reusability of previously treated composite scattering domains is a unique feature of LEGO. This matter is investigated in Section 4.8, where we perform a comparative assessment between LEGO and a direct solver.

Finally, the LEGO approach is extended towards a hybrid variety in Section 4.9. The hybridization of LEGO applies in two ways. First, alternative electromagnetic solution methods can be used for the construction of the elementary scattering domains. Second, the LEGO approach can be incorporated into existing software design packages. In particular, the optimization stage in LEGO, presented in Section 4.7, can be employed as an additional design tool.

4.2 The scattering operator

This section describes the construction of the elementary building blocks for LEGO. To assemble such blocks in an electromagnetic sense, a full electromagnetic characterization of the individual building blocks is required in advance. This is realized through so-called scattering operators. The scattering operator produces the scattered field pertaining to an incident field in terms of equivalent currents. The equivalent currents are associated with either an interior or exterior equivalent state. Below, we formulate the scattering operator via these equivalent states. For transparency, the associated integral representations are generalized to an operator formalism that applies to both SEP and LEP.

We prefer to treat the LEGO concept in the most general form possible. To this end, we do not restrict ourselves to a particular equivalence principle, because the general idea behind LEGO largely applies in a similar fashion to both Love's equivalence principle (LEP) and Schelkunoff's equivalence principle (SEP). Therefore, where possible, a generalized form of the fields and equivalent currents is used. The fields and currents are henceforth represented by

$$\mathbf{F}(\mathbf{r}) = \begin{bmatrix} \mathbf{E}(\mathbf{r}) \\ \mathbf{H}(\mathbf{r}) \end{bmatrix} \quad \text{and} \quad \mathbf{Q}(\mathbf{r}) = \begin{bmatrix} \mathbf{M}(\mathbf{r}) \\ \mathbf{J}(\mathbf{r}) \end{bmatrix}, \quad (4.1)$$

respectively. The boundary currents are considered in a 3D imbedding, i.e., \mathbf{J} and \mathbf{M} are spanned by three vector components, albeit that the component normal to the boundary is zero. If SEP is employed instead of LEP, \mathbf{Q} comprises either an electric or a magnetic equivalent current, and consequently only has three components.

Let us begin with the construction of an elementary LEGO building block. Such a building block has a simply connected bounded domain, containing one or more objects with electromagnetic contrast in a homogeneous background. We want to determine the scattered fields for all possible excitations, on or outside the boundary of the domain. Thus, we capture the complete electromagnetic characterization of the scattering domain in a scattering operator. Inside the scattering domain, any field incident on it may be considered as excited by an equivalent current source distribution on the boundary of the domain. In turn, the scattering operator produces an equivalent current distribution that represents the corresponding scattered field in the exterior domain. The scattering operator thus relates the incident to the scattered equivalent electric current sources. Hence, the interaction between adjacent scattering domains will be established by relating equivalent currents on the boundaries of the domains that generate incident and scattered fields.

To illustrate the scattering operator, we consider the scattering problem depicted in Figure 4.1, involving a scattering domain \mathcal{D}_1 bounded by the boundary $\partial\mathcal{D}_1$. The scattering object and observation boundary may be chosen arbitrarily, as long as the scatterers are enclosed by the boundary. The domain exterior to \mathcal{D}_1 , denoted by $\bar{\mathcal{D}}_1$, contains the source distribution that produces an arbitrary incident field. Incident plane waves are included implicitly, as being generated by sources at infinity. Throughout, we reserve the symbol F^{in} for the impressed incident field in the background medium.

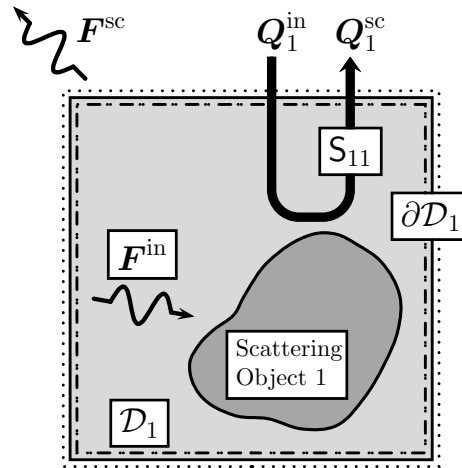


Figure 4.1: Scattering by an object in a homogeneous environment using the scattering operator.

To compose the scattering operator of \mathcal{D}_1 , the *interior* and *exterior* field problems are partitioned by application of an equivalence principle along $\partial\mathcal{D}_1$ for both domains. In this approach, equivalent current distributions, $Q_1^{\text{in}} = Q^{\text{in}}(\mathbf{r})$ and $Q_1^{\text{sc}} = Q^{\text{sc}}(\mathbf{r})$ for \mathbf{r} on $\partial\mathcal{D}_1$, are defined that reproduce the original *interior* incident and *exterior* scattered fields, respectively. Note that the superscripts for the sources only indicate what type of field they generate. By coincidence for LEP the currents Q_1^{in} and Q_1^{sc} happen to follow directly from the incident and scattered fields. For SEP this is not the case (see Section 2.8).

The partitioning of fields depicted in Figure 4.2 is the key step in the construction of the elementary LEGO building blocks. The field is partitioned into associated interior and exterior equivalent states illustrated in Figure 4.2b and Figure 4.2c, respectively. Combined, these equivalent states describe the scattering problem depicted in Figure 4.1. The medium properties in the hatched regions are those of the background medium. In these regions the fields generated by the equivalent currents are of no importance and hence they have been omitted. The equivalent states shown in Figure 4.2 describe both LEP and SEP, since Love's and Schelkunoff's equivalence principle differ only in the hatched regions, i.e., LEP yields a zero field, whereas

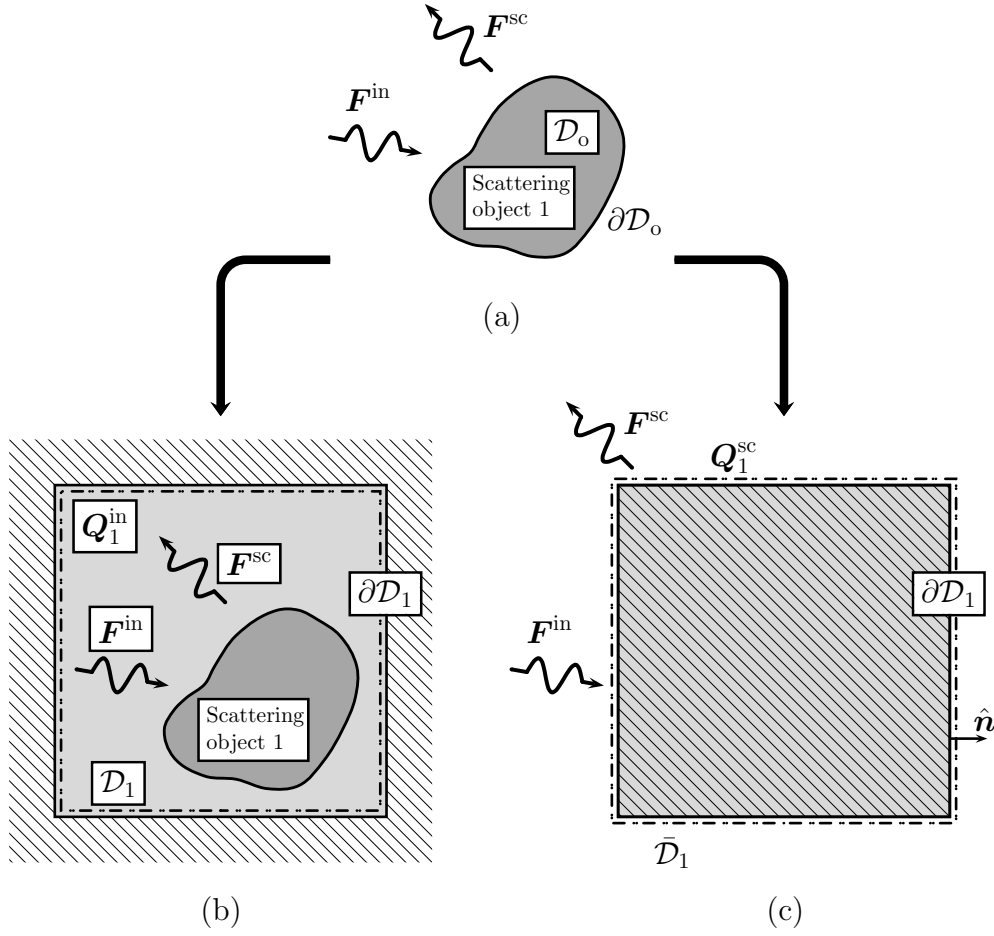


Figure 4.2: The partitioning of the field (a) into two equivalent states via a repeated application of an equivalence principle. The equivalent current Q_1^{in} produces F^{in} in \mathcal{D}_1 (b), while Q_1^{sc} produces F^{sc} in $\bar{\mathcal{D}}_1$ (c).

SEP yields a nonzero field, as explained in Section 2.8. Although this difference is irrelevant at present, it is important in the composition of scattering operators, treated in Section 4.5.

Because Q_1^{in} generates F^{in} in \mathcal{D}_1 , it is indicated by the dash-dotted lines just inside $\partial\mathcal{D}_1$. Likewise, since Q_1^{sc} produces the scattered field in $\bar{\mathcal{D}}_1$, it is indicated by the dash-dotted line just outside \mathcal{D}_1 . The field constituents generated by the equivalent currents are depicted in Figure 4.1. The incident field for $r \in \bar{\mathcal{D}}_1$ and the scattered field response of the enclosed object(s) for $r \in \mathcal{D}_1$ are considered known. The current Q_1^{in} directly follows from the applied incident field. Because the incident field may be arbitrary, we are interested in the scattering operator that relates Q_1^{sc} to Q_1^{in} . The current Q_1^{sc} in Figure 4.1 is indicated by a dotted line since it follows from the field generated by Q_1^{in} .

Next, we introduce a field propagator that operates on the equivalent currents, and is valid to both LEP and SEP. This leads to a general field representation in the entire configuration. Let us start with the representations for the scattered and incident fields in the LEP framework. Subsequently, we shall generalize to the field propagator in operator form. In terms of the integral operators L_v and K_v with medium index v as defined in Eq. (3.7), the representation for the incident field reads

$$\chi_{\mathcal{D}_1} \mathbf{E}^{\text{in}} = -Z_v L_{v;1} \mathbf{J}_1^{\text{in}} - K_{v;1} \mathbf{M}_1^{\text{in}}, \quad (4.2a)$$

$$\chi_{\mathcal{D}_1} \mathbf{H}^{\text{in}} = -Y_v L_{v;1} \mathbf{M}_1^{\text{in}} + K_{v;1} \mathbf{J}_1^{\text{in}}, \quad (4.2b)$$

with the characteristic function defined as $\chi_{\mathcal{D}}(\mathbf{r}) = \{1, 1/2, 0\}$ for $\mathbf{r} \in \{\mathcal{D}, \partial\mathcal{D}, \bar{\mathcal{D}}\}$. An additional subscript has been added to L and K to indicate the boundary on which the associated equivalent current is defined. Since the properties of the background medium are the same throughout, the medium index v is omitted in the subscript of the fields and currents. Appropriate boundary conditions have been discussed in Section 2.8, yielding the definitions of the equivalent currents as in Eq. (2.62). To arrive at an expression for the incident field in \mathcal{D} and on its boundary, we add $\chi_{\bar{\mathcal{D}}_1} \mathbf{E}^{\text{in}}$ and $\chi_{\bar{\mathcal{D}}_1} \mathbf{H}^{\text{in}}$ to the left and right-hand side of Eqs. (4.2a) and (4.2b), respectively. By restricting to a representation that is valid in $\mathcal{D}_1 \cup \partial\mathcal{D}_1$, we have

$$\mathbf{E}^{\text{in}} = -Z_v L_{v;1} \mathbf{J}_1^{\text{in}} - K_{v;1} \mathbf{M}_1^{\text{in}} + \chi_{\bar{\mathcal{D}}_1} \mathbf{E}^{\text{in}}, \quad (4.3a)$$

$$\mathbf{H}^{\text{in}} = -Y_v L_{v;1} \mathbf{M}_1^{\text{in}} + K_{v;1} \mathbf{J}_1^{\text{in}} + \chi_{\bar{\mathcal{D}}_1} \mathbf{H}^{\text{in}}. \quad (4.3b)$$

The field representation for the exterior scattered field is dual to that of the interior incident field. Instead, we shall assume that the normal $\hat{\mathbf{n}}_i$ to any domain \mathcal{D}_i points outwards. Accordingly, the equivalent state of LEP as depicted in Figure 3.1d corresponds to the one involving \mathbf{Q}_1^{sc} in Figure 4.2.

Next, for $\mathbf{r} \in \partial\mathcal{D}_i$ we express the incident field on the right-hand side of Eq. (4.3) in equivalent currents. For that reason, the field is split up in its normal and tangential components via $\mathbf{F} = \hat{\mathbf{n}}(\hat{\mathbf{n}} \cdot \mathbf{F}) - \hat{\mathbf{n}} \times (\hat{\mathbf{n}} \times \mathbf{F})$. In turn, with the relations in Eqs. (2.62) and (2.63) obtained through appropriate boundary conditions applied to the equivalent states of LEP, the incident field, $\mathbf{F}_1^{\text{in}} = \mathbf{F}^{\text{in}}(\mathbf{r})$ for $\mathbf{r} \in \partial\mathcal{D}_1$, is expressed in terms of equivalent currents,

$$\mathbf{E}_1^{\text{in}} = \hat{\mathbf{n}}_1 \frac{\nabla_S \cdot \mathbf{J}_1^{\text{in}}}{s\epsilon_v} - \hat{\mathbf{n}}_1 \times \mathbf{M}_1^{\text{in}}, \quad (4.4a)$$

$$\mathbf{H}_1^{\text{in}} = \hat{\mathbf{n}}_1 \frac{\nabla_S \cdot \mathbf{M}_1^{\text{in}}}{s\mu_v} + \hat{\mathbf{n}}_1 \times \mathbf{J}_1^{\text{in}}, \quad (4.4b)$$

Likewise, from the equivalent state for the exterior scattered field, Figure 3.1d, and corresponding boundary conditions, it follows that Eq. (4.4) also applies to the scattered field and currents for $\mathbf{r} \in \partial\mathcal{D}_1$.

To keep the principle of LEGO lucid, we define a propagation operator, \mathbf{P} , which relates the field quantities to the action of the sources via $\mathbf{F} = \mathbf{P}\mathbf{Q}$. The definition of \mathbf{P} follows from Eqs. (4.3) and (4.4), and reads

$$\mathbf{P} = \begin{cases} \mathbf{P}_i(\mathbf{r}) = \sigma_{\mathcal{D}_i} \begin{bmatrix} Z_v L_{v;i}(\mathbf{r}) & K_{v;i}(\mathbf{r}) \\ -K_{v;i}(\mathbf{r}) & Y_v L_{v;i}(\mathbf{r}) \end{bmatrix}, & \text{for } \mathbf{r} \in \mathcal{D}_i, \\ \mathbf{P}_{ii} = \begin{bmatrix} \sigma_{\mathcal{D}_i} Z_v L_{v;ii} + \frac{1}{2s\varepsilon_v} \hat{\mathbf{n}}_i \nabla_{S^\cdot} & \sigma_{\mathcal{D}_i} K_{v;ii} - \frac{1}{2} \hat{\mathbf{n}}_i \times \\ -\sigma_{\mathcal{D}_i} K_{v;ii} + \frac{1}{2} \hat{\mathbf{n}}_i \times & \sigma_{\mathcal{D}_i} Y_v L_{v;ii} + \frac{1}{2s\mu_v} \hat{\mathbf{n}}_i \nabla_{S^\cdot} \end{bmatrix}, & \text{for } \mathbf{r} \in \partial\mathcal{D}_i. \end{cases} \quad (4.5)$$

The subscript of the propagator refers to the boundary, $\partial\mathcal{D}_i$, on which \mathbf{Q}_i is defined. An extra subscript has been added to $\mathbf{P}_i(\mathbf{r})$ for points of observation on $\partial\mathcal{D}_i$, i.e., $\mathbf{P}_{ii} = \mathbf{P}_i(\mathbf{r})$ for $\mathbf{r} \in \partial\mathcal{D}_i$. The same comment applies to the integral operators L and K . The symbol $\sigma_{\mathcal{D}_i} = \pm 1$ selects the interior or exterior field representation. The positive sign applies to an exterior field representation, and the negative sign to an interior field representation. For the equivalent states depicted in Figure 4.2, $\sigma_{\mathcal{D}_1} = 1$ for \mathbf{Q}_1^{sc} and $\sigma_{\mathcal{D}_1} = -1$ for \mathbf{Q}_1^{in} . For embedding purposes, we shall use \mathbf{P}_i to produce the field for $\mathbf{r} \in \mathcal{D}_i$. In case we want to determine the equivalent currents due to an incident field, we apply \mathbf{P}_{ii} . Hence, the field in \mathcal{D}_i and on $\partial\mathcal{D}_i$ follows from

$$\begin{cases} \mathbf{F}(\mathbf{r}) = \mathbf{P}_i(\mathbf{r})\mathbf{Q}_i, & \text{for } \mathbf{r} \in \mathcal{D}_i, \\ \mathbf{F}_i = \mathbf{P}_{ii}\mathbf{Q}_i, & \text{for } \mathbf{r} \in \partial\mathcal{D}_i. \end{cases} \quad (4.6)$$

The introduced notation is used for transparency. Note that in case of LEP, \mathbf{P}_i in principle suffices since the equivalent currents directly follow from the field components tangential to $\partial\mathcal{D}_i$. Via a similar derivation of the propagation operator for the SEP framework, it is found that, depending on whether SEP is based on the magnetic or electric equivalent currents, Eq. (4.6) holds, by setting either the electric or the magnetic equivalent currents to zero in Eq. (4.5).

With the introduction of the propagation operator in Eq. (4.5), the total field, $\mathbf{F}(\mathbf{r})$, in the entire scattering configuration depicted in Figure 4.1 follows from the equivalent current distributions

on $\partial\mathcal{D}_1$ and the incident field via

$$\mathbf{F}(\mathbf{r}) = \begin{cases} \mathbf{P}_1 \mathbf{Q}_1^{\text{in}} + \int_{\partial\mathcal{D}_1} \mathbf{F}^{\text{sc}}(\mathbf{r}, \mathbf{r}') \mathbf{Q}^{\text{in}}(\mathbf{r}') \, dA', & \mathbf{r} \in \mathcal{D}_1, \\ \mathbf{F}^{\text{in}} + \mathbf{P}_1 \mathbf{Q}_1^{\text{sc}}, & \mathbf{r} \in \bar{\mathcal{D}}_1. \end{cases} \quad (4.7)$$

Note that the initial equivalent state in Figure 4.2b, where \mathbf{Q}_1^{in} generates in a *homogeneous* background medium the appropriate interior incident field, remains applicable to a *complete* incident field, i.e., with the inclusion of multiple scattering effects with other domains. Likewise, in Figure 4.2c, \mathbf{Q}^{sc} will generate the *complete* exterior scattered field of several combined scattering domains in a homogeneous background medium.

Now that we have arrived at a concise representation of the field in the entire configuration, we shall demonstrate how to obtain \mathbf{Q}_1^{in} , and the scattering operator that gives the corresponding \mathbf{Q}_1^{sc} . The current \mathbf{Q}_1^{in} follows from the field evaluated at $\mathbf{r} \in \partial\mathcal{D}_1$. The representation for the incident field in Eq. (4.2) poses an integral equation for $\mathbf{r} \in \partial\mathcal{D}_1$, which is written as

$$\mathbf{P}_{11} \mathbf{Q}_1^{\text{in}} = \mathbf{F}_1^{\text{in}}. \quad (4.8)$$

Because this equation describes a linear problem, we may formally introduce the inverse propagator of Eq. (4.5) such that

$$\mathbf{Q}_1^{\text{in}} = \mathbf{P}_{11}^{-1} \mathbf{F}_1^{\text{in}}, \quad (4.9)$$

provided that the corresponding homogeneous equation has only the trivial solution. Although the equivalent current distribution \mathbf{Q}_1^{sc} that reproduces the *exterior* scattered field may be obtained directly from the scattered field for a specific incident field via a single integral equation, we prefer using the scattering operator, \mathbf{S}_{11} , instead to encompass the scattered field for all possible excitations. The scattering operator is defined through

$$\mathbf{Q}_1^{\text{sc}} = \mathbf{S}_{11} \mathbf{Q}_1^{\text{in}} = \int_{\partial\mathcal{D}_1} \mathbf{S}_{11}(\mathbf{r}, \mathbf{r}') \mathbf{Q}^{\text{in}}(\mathbf{r}') \, dA'. \quad (4.10)$$

In contrast with \mathbf{P}_{11} , the kernel of the scattering operator involves $\mathbf{S}_{11}(\mathbf{r}, \mathbf{r}')$ instead of the free-space Green's function. To determine the kernel $\mathbf{S}_{11}(\mathbf{r}, \mathbf{r}')$, let us consider a source at \mathbf{r}' , which generates a field that impinges upon the scattering object(s) in \mathcal{D}_1 , giving rise to a scattered field \mathbf{F}^{sc} . We regard \mathbf{F}^{sc} in $\bar{\mathcal{D}}_1$ as if it were generated by secondary contrast sources in a homogeneous background medium. The kernel of the scattering operator follows from a similar integral equation as in Eq. (4.9),

$$\mathbf{S}_{11}(\mathbf{r}, \mathbf{r}') = \mathbf{P}_{11}^{-1} \mathbf{F}_{11}^{\text{sc}}, \quad (4.11)$$

where the field $\mathbf{F}_{11}^{\text{sc}} = \mathbf{F}^{\text{sc}}(\mathbf{r}, \mathbf{r}')$ in the kernel of the inverse propagator is the scattered field at \mathbf{r} on $\partial\mathcal{D}_1$ for a source at \mathbf{r}' on $\partial\mathcal{D}_1$. The field $\mathbf{F}_{11}^{\text{sc}}$ can be determined using conventional methods, e.g., a domain integral equation with second order accuracy [65], or a boundary integral equation (BIE) for dielectric objects [66].

In this thesis arbitrarily shaped scattering objects are considered with homogeneous, possibly lossy or perfectly conducting medium properties. Boundary integral equations are therefore ideally suited to determine the corresponding scattered field. Chapter 3 contains a survey on the choice of integral formulation with corresponding discretization. Let $X_o(\mathbf{r})$ represent an appropriate integral operator for the scattering object in question. Because X_o is a linear operator, the scattered field $\mathbf{F}_{11}^{\text{sc}}$ in the kernel of the scattering operator may formally be written as

$$\mathbf{F}_{11}^{\text{sc}} = P_{1o} X_{oo}^{-1} P_{o1}. \quad (4.12)$$

The propagator P_{o1} produces on $\partial\mathcal{D}_o$ the field due to a source distribution on $\partial\mathcal{D}_1$. From the incident field on $\partial\mathcal{D}_o$, X_{oo}^{-1} produces an equivalent current, \mathbf{Q}_o^{sc} , which generates the scattered field outside \mathcal{D}_o due to sources on $\partial\mathcal{D}_1$. In turn, the propagation operator P_{1o} generates the scattered field on $\partial\mathcal{D}_1$. To solve the scattered field numerically for all source positions on $\partial\mathcal{D}_1$, a ‘‘marching on in source position’’ scheme [9] may be utilized as a predictor-corrector method to reduce computation times considerably. Such computational considerations of LEGO are discussed in more detail in Section 4.6. Note that the combination $X_{oo}^{-1}P_{o1}$ can be reused in the determination of the total field in the entire configuration via Eq. (4.7).

Finally, a comment should be made regarding the choice of boundary shape in a design process using LEGO. Because of the freedom regarding the choice of the shape of \mathcal{D}_1 , an appropriate choice requires some foresight with respect to the eventual scattering configuration being constructed. The choice of a suitable domain shape mainly involves the ease of evaluating the scattered field of the enclosed scattering object(s) and the possibility of reusing the scattering domain at a later stage in a sequence of LEGO steps. For instance, in a 2D configuration involving several circular cylinders, starting domains enclosing only a single cylinder poses an ideal choice as there is a high degree of reusability, while analytical solutions are available for the field scattered by a single cylinder.

4.3 Embedding in operator form

In this section we describe the embedding part of the LEGO concept in its most general form. In addition to the scatter(s) in \mathcal{D}_1 , a second scattering domain \mathcal{D}_2 with boundary $\partial\mathcal{D}_2$ is introduced, close enough that the multiple scattering effects between both scattering domains may not be neglected. The embedding procedure accounts for this interaction. It provides the multiple scattering in terms of the scattering operators of the individual domains that have been characterized at an earlier stage. To accomplish this, the domain \mathcal{D}_2 is considered as a part of the environment of \mathcal{D}_1 and vice versa.

In principle, the equivalent currents that generate the scattered fields exterior to the respective domains are still valid. However, the field scattered by one object is part of the incident field of the other. We will describe the resulting multiple scattering in terms of a feedback loop involving a modified, “complete” current \mathbf{Q}^{cp} . By replacing \mathbf{Q}^{in} with \mathbf{Q}^{cp} , the complete field in domain \mathcal{D}_1 follows immediately from Eq. (4.7). The combined exterior scattered fields are obtained by application of the scattering operators of both domains via Eq. (4.10). To convert the incident-field currents \mathbf{Q}^{in} , associated with the single scattering domains in absence of the others, into the desired complete current distributions \mathbf{Q}^{cp} , four Q operators are introduced,

$$\begin{bmatrix} \mathbf{Q}_1^{\text{cp}} \\ \mathbf{Q}_2^{\text{cp}} \end{bmatrix} = \begin{bmatrix} \mathbf{Q}_{11} & \mathbf{Q}_{12} \\ \mathbf{Q}_{21} & \mathbf{Q}_{22} \end{bmatrix} \begin{bmatrix} \mathbf{Q}_1^{\text{in}} \\ \mathbf{Q}_2^{\text{in}} \end{bmatrix}. \quad (4.13)$$

Again, from left to right, the subscripts in the operator Q respectively denote the boundaries on which the observation and source distributions are located. For example, \mathbf{Q}_{12} yields an equivalent current distribution on $\partial\mathcal{D}_1$ for the complete field in \mathcal{D}_1 due to the field incident on \mathcal{D}_2 , in the absence of scattering objects in \mathcal{D}_1 . Once the four Q operators have been determined, the entire field problem has effectively been solved.

To find expressions for the Q operators, we introduce two current-transfer operators. In Figure 4.3, the action of the transfer operator \mathbf{T}_{21} is depicted. It produces an equivalent current distribution on $\partial\mathcal{D}_2$ for the field in \mathcal{D}_2 for each possible current distribution on $\partial\mathcal{D}_1$. The construction of the transfer operator \mathbf{T}_{21} involves two steps. First, the current on $\partial\mathcal{D}_1$ generates a field that is propagated to $\partial\mathcal{D}_2$, via the propagation operator \mathbf{P}_{21} . Second, the equivalent current distribution that would produce the corresponding field in \mathcal{D}_2 is obtained by applying the inverse propagator \mathbf{P}_{22}^{-1} on $\partial\mathcal{D}_2$. This results in

$$\begin{aligned} \mathbf{T}_{21} &= \mathbf{P}_{22}^{-1} \mathbf{P}_{21}, \\ \mathbf{T}_{12} &= \mathbf{P}_{11}^{-1} \mathbf{P}_{12}. \end{aligned} \quad (4.14)$$

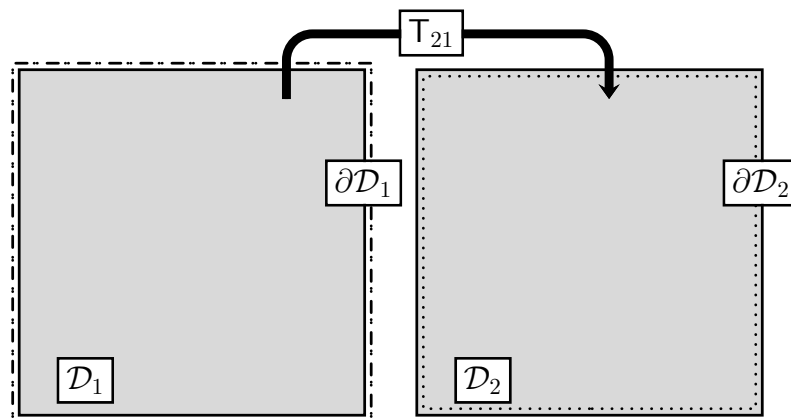


Figure 4.3: The current-transfer operator T_{21} transfers current distributions that radiate into \bar{D}_1 from the first onto the second boundary and subsequently produce the same field in D_2 .

Note that $P_{22}^{-1} = P_{11}^{-1}$ for boundaries with identical shape and corresponding field representation (interior or exterior), while P_{21} follows from P_{12} by exchanging source and observation boundary (reciprocity). Also, when both boundaries coincide, the transfer operators reduce to identity operators.

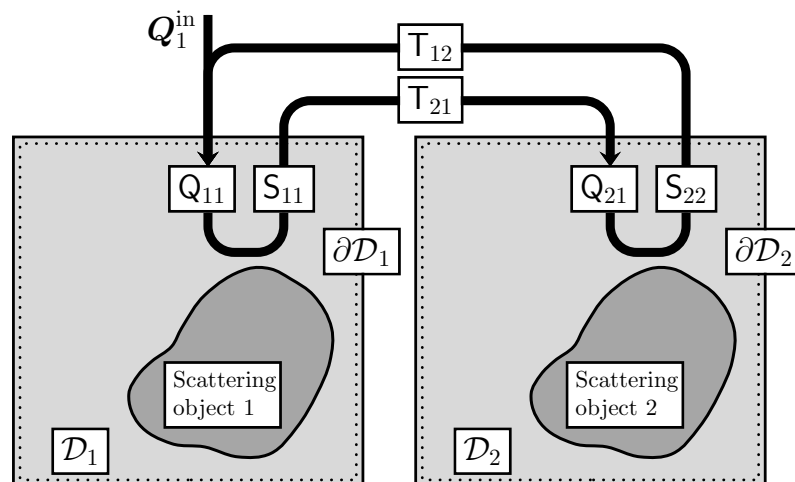


Figure 4.4: The Q_{11} and Q_{21} operators for an incident current Q_1^{in} that include the direct incident field and the occurring multiple scattering represented by the loop.

In Figure 4.4, we have sketched the part of the multiple-scattering process that corresponds to an incident field on ∂D_1 , *only*. In this case, D_2 is considered as the environment of D_1 . As illustrated in Figure 4.4, Q_{11} is obtained from Q_{21} through scattering in domain D_2 , with scattering operator S_{22} , and a subsequent transfer of the resulting equivalent current distributions

to the first boundary via T_{12} . However, this does not represent the complete field incident on \mathcal{D}_1 as the current distribution Q_1^{in} also produces a direct contribution in \mathcal{D}_1 , which is accounted for by an additional unit-amplitude identity operator I_{11} . The resulting expression for Q_{11} thus becomes,

$$Q_{11} = I_{11} + T_{12} S_{22} Q_{21}. \quad (4.15)$$

Similarly, Q_{21} is obtained from Q_{11} through scattering via S_{11} , and a transfer of the corresponding equivalent currents to $\partial\mathcal{D}_2$ via T_{21} . Hence, we obtain

$$Q_{21} = T_{21} S_{11} Q_{11}. \quad (4.16)$$

For the incident current Q_2^{in} , \mathcal{D}_1 is considered as the environment of \mathcal{D}_2 . By duality, the Q_{22} and Q_{12} operators are readily obtained by swapping the indices 1 and 2, thereby exchanging source and observation boundary. Combining Eqs. (4.15) and (4.16), together with their dual counterparts, yields the following matrix equation

$$\begin{bmatrix} Q_{11} & Q_{12} \\ Q_{21} & Q_{22} \end{bmatrix} = \begin{bmatrix} 0 & T_{12} S_{22} \\ T_{21} S_{11} & 0 \end{bmatrix} \begin{bmatrix} Q_{11} & Q_{12} \\ Q_{21} & Q_{22} \end{bmatrix} + \begin{bmatrix} I_{11} & 0 \\ 0 & I_{22} \end{bmatrix}, \quad (4.17)$$

where the last matrix on the right-hand side accounts for the contribution of the incident field in the absence of scatterers in \mathcal{D}_1 and \mathcal{D}_2 . Next, let us define the reflection operators R_{11} and R_{22} . For \mathcal{D}_1 ,

$$R_{11} = T_{12} S_{22} T_{21}, \quad (4.18)$$

produces equivalent currents on $\partial\mathcal{D}_1$ that represent the scattered field from \mathcal{D}_2 in \mathcal{D}_1 due to currents on $\partial\mathcal{D}_1$. For clarity, the action of the reflection operator R_{11} is visualized in Figure 4.5. Note that R_{11} constitutes the Green's operator that characterizes the environment of \mathcal{D}_1 in terms of equivalent currents. Likewise, we have

$$R_{22} = T_{21} S_{11} T_{12}. \quad (4.19)$$

Now, we may express the solution of Eq. (4.17) in terms of scattering and reflection operators according to

$$\begin{bmatrix} Q_{11} & Q_{12} \\ Q_{21} & Q_{22} \end{bmatrix} = \begin{bmatrix} (I_{11} - R_{11} S_{11})^{-1} & 0 \\ 0 & (I_{22} - R_{22} S_{22})^{-1} \end{bmatrix} \begin{bmatrix} I_{11} & T_{12} S_{22} \\ T_{21} S_{11} & I_{22} \end{bmatrix}. \quad (4.20)$$

The two terms $R_{11} S_{11}$ and $R_{22} S_{22}$ both describe the closed loop as depicted in Figure 4.4. The last matrix on the right-hand side contains the incident field contribution of Eq. (4.17). In particular, $T_{12} S_{22}$ provides the contribution of the incident field on \mathcal{D}_1 in the absence of scatterers

in \mathcal{D}_1 , whereas $T_{21} S_{11}$ provides the contribution of the incident field on \mathcal{D}_2 in the absence of scatterers in \mathcal{D}_2 . Further, we may expand $(I - RS)^{-1}$ in terms of a Neumann series according to

$$(I - RS)^{-1} = \sum_{n=0}^{\infty} (RS)^n, \quad (4.21)$$

from which the multiple scattering behavior is apparent.

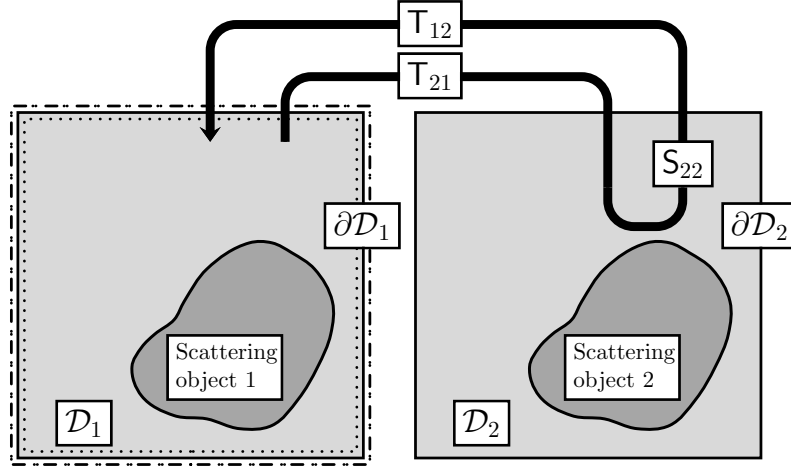


Figure 4.5: The reflection operator R_{11} characterizes the electromagnetic environment of \mathcal{D}_1 .

Upon reviewing Eq. (4.20), one might think that both embedding operators, $(I_{11} - R_{11} S_{11})$ and $(I_{22} - R_{22} S_{22})$ have to be evaluated to obtain the four Q operators. This is not the case, since the complete incident field in \mathcal{D}_1 , provided by Q_{11} and Q_{12} , is obtained via the embedding operator, $(I_{11} - R_{11} S_{11})$, in Eq. (4.20). Subsequently, the complete incident field in \mathcal{D}_2 , provided by Q_{22} and Q_{21} , follows from Q_{11} and Q_{12} upon applying Eq. (4.17). This may be illustrated through the relation,

$$T_{21} S_{11} (I_{11} - R_{11} S_{11}) = (I_{22} - R_{22} S_{22}) T_{21} S_{11}, \quad (4.22)$$

which follows from

$$T_{21} S_{11} R_{11} = R_{22} S_{22} T_{21}, \quad (4.23)$$

and is a direct consequence of the definitions for the reflection operators in Eqs. (4.18) and (4.19).

Now that the four Q operators have been determined, the equivalent currents that account for the complete field incident on the scattering domains, Q_1^{cp} and Q_2^{cp} , follow from Eq. (4.13). Upon replacing Q_i^{in} with Q_i^{cp} , the complete total field in domain \mathcal{D}_i follows immediately from

Eq. (4.7). The total field in the entire configuration then reads

$$\mathbf{F} = \begin{cases} P_i \mathbf{Q}_i^{\text{cp}} + \int_{\partial \mathcal{D}_i} \mathbf{F}^{\text{sc}}(\mathbf{r}, \mathbf{r}') \mathbf{Q}^{\text{cp}}(\mathbf{r}') \, dA', & \mathbf{r} \in \mathcal{D}_i, \\ \mathbf{F}^{\text{in}} + P_1 \mathbf{Q}_1^{\text{sc}} + P_2 \mathbf{Q}_2^{\text{sc}}, & \mathbf{r} \in \bar{\mathcal{D}}_1 \cap \bar{\mathcal{D}}_2. \end{cases} \quad (4.24)$$

Notice that at present the complete exterior scattered field still requires the scattering operators of the individual domains as

$$\mathbf{Q}_i^{\text{sc}} = S_{ii} \mathbf{Q}_i^{\text{cp}}, \quad \text{for } i = 1, 2, \quad (4.25)$$

analogous to Eq. (4.10).

Up to this point, the source distribution that generates the arbitrary incident field is initially considered to be outside the scattering domains. Let us briefly elaborate how a source inside a scattering domain may be included in the embedding process. As an example, let domain \mathcal{D}_1 enclose both a scattering object and a source positioned at $\mathbf{r}_S \in \mathcal{D}_1$. This merely gives rise to an additional field, represented by the equivalent current \mathbf{Q}_1^{ad} on $\partial \mathcal{D}_1$. This additional field, $\mathbf{F}(\mathbf{r}, \mathbf{r}_S)$, is the linear combination of the field generated by the point source and the associated scattered field of the object(s) contained in \mathcal{D}_1 . Unlike \mathbf{Q}_1^{in} , \mathbf{Q}_1^{ad} comprises a field representation in the *exterior* domain, $\bar{\mathcal{D}}_1$. Therefore, regarding the multiple scattering represented by a closed loop in Figure 4.4, the contribution of \mathbf{Q}_1^{ad} enters into the loop at a different point, viz., just after S_{11} . The LEGO procedure applies to exterior incident fields only, and thus to equivalent currents involving an *interior* incident field representation. However, because the additional field $\mathbf{F}(\mathbf{r}, \mathbf{r}_S)$ remains an exterior incident field with respect to \mathcal{D}_2 , \mathbf{Q}_1^{ad} is transferred to $\partial \mathcal{D}_2$. Hence, $T_{21} \mathbf{Q}_1^{\text{ad}}$ should be added to the existing \mathbf{Q}_2^{in} .

Upon completing the embedding process, the corresponding additional multiple scattering caused by the point source is accounted for by the complete currents \mathbf{Q}_1^{cp} and \mathbf{Q}_2^{cp} . The representation for the total complete field in \mathcal{D}_2 , Eq. (4.24) remains unchanged, whereas for \mathcal{D}_1 the additional incident field $\mathbf{F}(\mathbf{r}, \mathbf{r}_S)$ is to be included. Exterior to \mathcal{D}_1 and \mathcal{D}_2 , this additional field is included via $P_1 \mathbf{Q}_1^{\text{ad}}(\mathbf{r})$. Because a source distribution within a scattering domain simply adds to the \mathbf{Q}^{in} of the other scattering domain(s), its contribution can be included *after* the embedding process, thus allowing for arbitrary source distributions within the scattering domains. Finally, the general definition of the propagation operator enables an arbitrary mutual orientation of the source and observation boundaries involving the transfer operators, e.g., one domain may enclose the other domain. Thus, the LEGO procedure readily applies to configurations with multiple scattering between a scattering domain and an arbitrary *surrounding* scattering environment.

4.4 Discretization

This section describes the discretization of the general embedding procedure, so far presented in operator form. Because the operators involved in the embedding process rely on propagation and scattering operators only, we restrict ourselves to the discretization of these propagators. We discuss a discretization based on LEP only. The discretization regarding SEP is treated by analogy afterwards. The discretized propagation operators are composed from the discretized integral operators in the MoM matrices for the scattering of conducting and dielectric objects to be discussed in Sections 5.3 and 7.2 for 2D and 3D implementations, respectively. Finally, a different definition of the transfer operators will be introduced that is applicable to LEP only. With this alternative definition, the use of an inverse propagator may be omitted which leads to computational advantages.

At first glance, it may seem adequate to evaluate the integral operators at discrete points on the boundaries of scattering domains. However, such a direct approach is problematic when source and observation boundaries (partially) overlap, as the kernel of the integral operators is singular for source and observation points that coincide. Moreover, overlapping source and observation boundaries occur intrinsically in the embedding procedure via the use of the propagators P_{11} and P_{22} in the definition of the transfer operators, given by Eq. (4.14).

To mitigate the singular field behavior on the boundary, the field propagators are considered in a weighted average sense similar to the MoM method discussed in Section 3.6. Therefore, the fields are tested and the currents are expanded through appropriate test and expansion functions, respectively. Throughout, we apply a Galerkin weak formulation. The expansion of an equivalent boundary current implies an approximation of that current by a finite set of fixed known expansion functions in combination with appropriate *current amplitudes*. In view of Eq. (4.1), the discretization of a boundary current, say \mathbf{Q}_1 , leads to a vector \mathbf{Q}_1 , with elements that are magnetic and electric current amplitudes. Likewise, upon testing a field \mathbf{F}_1 on $\partial\mathcal{D}_1$, we obtain a vector \mathbf{F}_1 , the elements of which are the duality product of the test functions with the electric and magnetic fields, henceforth referred to as *field amplitudes*. Accordingly, after discretization we have the vectors

$$\mathbf{F}_1 = \begin{bmatrix} \mathbf{E}_1 \\ \mathbf{H}_1 \end{bmatrix} \quad \text{and} \quad \mathbf{Q}_1 = \begin{bmatrix} \mathbf{M}_1 \\ \mathbf{J}_1 \end{bmatrix}. \quad (4.26)$$

The typewriter font indicates a matrix form representation. Likewise, the field produced by a propagation operator with a double boundary index is tested on the boundary of a domain. After

discretization, the propagator, say P_{21} , has become a MoM matrix, P_{21} . The matrix representation of a propagator P_{21} that operates on a current Q_1 , amounts to the matrix-vector product, $P_{21}Q_1$. Likewise, a transfer operator T_{21} leads to the transfer matrix T_{21} , and follows from the matrix product $P_{22}^{-1}P_{21}$. For clarity, an interpretation of the discretized operators is given by

$$P_{21} = \begin{bmatrix} E_{21}^M & E_{21}^J \\ H_{21}^M & H_{21}^J \end{bmatrix} \quad \text{and} \quad T_{21} = \begin{bmatrix} M_{21}^M & M_{21}^J \\ J_{21}^M & J_{21}^J \end{bmatrix}. \quad (4.27)$$

Both matrices operate on current amplitudes related to $\partial\mathcal{D}_1$, such as Q_1 in Eq. (4.26). The superscript indicates whether the field or equivalent current on $\partial\mathcal{D}_2$ is generated by an electric or magnetic current on $\partial\mathcal{D}_1$. The size of the vectors and matrices follows implicitly from the number of unknowns on the boundaries indicated by the corresponding subscripts.

The discretization of the propagator operator only is sufficient to perform the embedding numerically, since the transfer matrix, say T_{21} , follows from the matrix product $P_{22}^{-1}P_{21}$. By expanding and testing the propagator P_1 for $r \in \partial\mathcal{D}_2$, defined in Eq. (4.5), the propagation matrix P_{21} reads

$$P_{21} = \begin{bmatrix} \sigma_{\mathcal{D}_1} K_{v;21}^{EM} - \mathbb{I}_{21}^{EM} & \sigma_{\mathcal{D}_1} Z_v \mathbb{L}_{v;21}^{EJ} \\ \sigma_{\mathcal{D}_1} Y_v \mathbb{L}_{v;21}^{HM} & -\sigma_{\mathcal{D}_1} K_{v;21}^{HJ} + \mathbb{I}_{21}^{HJ} \end{bmatrix} \quad (4.28)$$

For identical source and observation boundaries, the submatrices on the upper and lower right correspond with the conventional EFIE and MFIE MoM matrices for the scattering from a PEC. For 2D configurations, the four submatrices of P_{21} follow from the discretized integral operators to be discussed in Section 5.3, with piecewise constant, $\square(\rho)$, or piecewise linear, $\wedge(\rho)$, test and expansion functions to be defined in Eq. 5.15. For 3D configurations, we consider expansion by RWG-functions, $\wedge_n(\mathbf{r})$. The testing function comprises a linear combination of \wedge_m and $\vee_m = \hat{\mathbf{n}} \times \wedge_m$ as will be explained in Chapter 7. The resulting propagation matrix is composed in accordance with the discretization process in Section 7.2. For instance, testing with \wedge_m leads to constituents $\{\mathbb{L}_v, K_v, \mathbb{I}_v\}$ that in Chapter 7 are defined as $\{\mathbb{L}_v^\wedge, K_v^\wedge, \mathbb{I}_v^\vee\}$. Observe that the impedance scaling introduced in Section 3.6, applied to the field and currents to improve the condition number, has been omitted for brevity.

Next, let us consider the cases where the propagation operator is applied as a field representation to reproduce a field. This is the case for propagation operators P with a single boundary index, as in Eq. (4.5). Because the definition of the operator P_i ceases to hold for observation points on the boundary $\partial\mathcal{D}_i$ where the equivalent current is defined, the field representation may not be used exactly on the boundary. In principle, the resulting field should show no singular behavior as the actual sources that generate this field in the original configuration are located elsewhere.

For the evaluation of the field on $\partial\mathcal{D}_i$ it suffices to slightly move the observation point $\mathbf{r} \in \partial\mathcal{D}_i$ away from the boundary into the domain where \mathbf{Q}_i represents its associated field. Once the current amplitudes are determined, the pertaining field for $\mathbf{r} \notin \partial\mathcal{D}_i$ follows by the substitution of the current expansion into the field representation in Eq. (4.5),

$$\mathbf{F} = \mathbf{P}_i \mathbf{Q}_i = \sigma_{\mathcal{D}_i} \sum_{n=1}^{N_i} \begin{bmatrix} \mathbf{K}_{v;i}^{EM} & \mathbf{Z}_v \mathbf{L}_{v;i}^{EJ} \\ \mathbf{Y}_v \mathbf{L}_{v;i}^{HM} & -\mathbf{K}_{v;i}^{HJ} \end{bmatrix} \begin{bmatrix} \mathbf{M}_{n;i} \mathbf{f}_{n;i}^M \\ \mathbf{J}_{n;i} \mathbf{f}_{n;i}^J \end{bmatrix}. \quad (4.29)$$

The current expansion functions of the electric and magnetic current on $\partial\mathcal{D}_i$ are denoted as $\mathbf{f}_{n;i}^J$ and $\mathbf{f}_{n;i}^M$, respectively. The field representation in Eq. (4.29) is defined in accordance with the 2D and 3D ones to be discussed in Eqs. (5.53) and (7.32), respectively. Although an observation point may be very close to the boundary, proper handling of the singular integrand parts by analytical means avoids large quadrature errors in the evaluation of the expansion integrals.

An implementation based on SEP readily follows from that of LEP by setting either the electric or the magnetic current to zero. The submatrices which have vanishing currents in their superscripts are omitted. By further omitting the submatrices related to an electric or magnetic field in Eq. (4.28), one obtains an MFIE or EFIE, respectively. Conversely, via a linear combination as in Eq. (3.20), both integral equations may be combined to form a CFIE. The remaining matrices are four times smaller than with LEP in case the same number of unknowns is applied to the single equivalent current with SEP and the two individual equivalent currents of LEP. This observation appears to indicate that LEGO based on LEP is less memory efficient and more time-consuming as with SEP. However, this observation is not certain *a priori* as the use of two equivalent currents with LEP may lead to better results than the use of a single current in SEP. A more appropriate computational comparison between both equivalence principles should therefore be related to the accuracy of the obtained fields. Such a comparison is performed in Section 6.5.

Next, let us consider Eqs. (4.10–4.12) which describe the scattering operator S_{11} of domain \mathcal{D}_1 that contains a homogeneous scatterer with boundary $\partial\mathcal{D}_o$. After substituting the transfer operator $\mathbf{T}_{1o} = \mathbf{P}_{11}^{-1} \mathbf{P}_{1o}$, and discretization by appropriate test and expansion functions, the construction of the scattering matrix S_{11} involves the matrix multiplications

$$\mathbf{S}_{11} = \mathbf{T}_{1o} \mathbf{X}_{oo}^{-1} \mathbf{P}_{o1}. \quad (4.30)$$

The matrix \mathbf{X}_{oo} represents the MoM matrix of the enclosed scattering objects. The propagator matrix \mathbf{P}_{o1} produces the tested field amplitudes on $\partial\mathcal{D}_o$ due to current distributions on $\partial\mathcal{D}_1$. In turn, the combination $\mathbf{X}_{oo}^{-1} \mathbf{P}_{o1}$, produces the current amplitudes of the equivalent current on $\partial\mathcal{D}_o$ that reproduces the scattered field of \mathcal{D}_o . These current amplitudes are transferred to the

boundary of the scattering domain by the matrix multiplication with \mathbb{T}_{10} . Hence, similar to a transfer matrix, the elements of our scattering matrix are current amplitudes, i.e., we consider the scattering operator in the bases spanned by the current expansion and test functions. The elements of a vector column of \mathbb{S}_{11} are thus the current amplitudes of an equivalent current on $\partial\mathcal{D}_1$ that reproduces the exterior scattered field response from the objects in \mathcal{D}_1 due to a *single* current expansion function on $\partial\mathcal{D}_1$. Although the MoM matrix X_{00} may be related to dielectric and/or perfectly conducting scattering objects, both LEP and SEP are suitable for the construction of the scattering matrix. Of course, the test function used in \mathbb{P}_{01} and the expansion function used in \mathbb{P}_{10} (concealed in \mathbb{T}_{10}) should be in accordance with the discretization of X_{00} .

The formulation and discretization of the transfer operator given above generally applies to both LEP and SEP. A different way of discretization is possible for LEP, in which an inverse propagator matrix becomes superfluous. To explain this, let us recapitulate the definition of the equivalent electric and magnetic boundary currents given by Eq. (2.62),

$$\mathbf{M} = \hat{\mathbf{n}} \times \mathbf{E}, \quad (4.31a)$$

$$\mathbf{J} = -\hat{\mathbf{n}} \times \mathbf{H}. \quad (4.31b)$$

Whether this definition applies to an incident or scattered field will be indicated through the superscript of the fields and currents. These relations are only true for LEP. With SEP, the fields in Eq. (4.31) are not directly related to the fields represented by the currents. This discrepancy between SEP and LEP has been explained explained in Sections 2.8 and 3.2. Superscripts assigned to the equivalent currents of SEP, merely imply that they produce the relevant field in the domain of interest. The difficulty in the determination of the current amplitudes from the field amplitudes required for SEP is thus avoided with LEP.

To elucidate the approach of the alternative discretization of LEP, test and expansion functions should be applied in Eq. (4.31). In Section 5.3, functions \mathbf{f}_m^E and \mathbf{f}_m^H will be introduced to test the electric and magnetic fields, respectively. In particular, we employ

$$\langle \hat{\mathbf{n}} \times \mathbf{f}_m^E, \mathbf{M} \rangle = \langle \mathbf{f}_m^E, \mathbf{E} \rangle, \quad (4.32a)$$

$$-\langle \hat{\mathbf{n}} \times \mathbf{f}_m^H, \mathbf{J} \rangle = \langle \mathbf{f}_m^H, \mathbf{H} \rangle. \quad (4.32b)$$

Thus, testing the field with \mathbf{f}_m implies testing of the currents with $\hat{\mathbf{n}} \times \mathbf{f}_m$. By substitution of the expansion of the currents without impedance scaling in Eq. (4.32), we have

$$-\langle \mathbf{f}_m^E, \hat{\mathbf{n}} \times \mathbf{f}_n^M \rangle M_n = \langle \mathbf{f}_m^E, \mathbf{E} \rangle, \quad (4.33a)$$

$$\langle \mathbf{f}_m^H, \hat{\mathbf{n}} \times \mathbf{f}_n^J \rangle J_n = \langle \mathbf{f}_m^H, \mathbf{H} \rangle. \quad (4.33b)$$

where \mathbf{f}_n^M and \mathbf{f}_n^J are the expansion functions for the magnetic and electric equivalents, respectively. The current amplitudes J_n and M_n have been extracted from the duality products. With reference to our general definition of current and field amplitudes in Eq. (4.26), they are related through the use of an inverse *Gram matrix* via

$$\mathbf{Q}_1 = \mathbf{G}_{11}^{-1} \mathbf{F}_1 \quad \Leftrightarrow \quad \begin{bmatrix} \mathbf{M}_1 \\ \mathbf{J}_1 \end{bmatrix} = \begin{bmatrix} \mathbf{G}_{11}^{EM} & 0 \\ 0 & \mathbf{G}_{11}^{HJ} \end{bmatrix}^{-1} \begin{bmatrix} \mathbf{E}_1 \\ \mathbf{H}_1 \end{bmatrix}. \quad (4.34)$$

Again, the superscripts in Eq. (4.34) indicate the index of the boundary under consideration. The matrix size implicitly follows from the number of unknowns used for the indicated boundaries. By comparing Eqs. (4.10) and (4.34), the use of Gram matrices for embedding via LEP amounts to the substitution of an inverse propagator by an inverse Gram matrix. The elements of the two submatrices of \mathbf{G}_{11} are given by

$$\mathbf{G}_{11;mn}^{EM} = \langle \mathbf{f}_m^E, \hat{\mathbf{n}} \times \mathbf{f}_n^M \rangle, \quad (4.35a)$$

$$\mathbf{G}_{11;mn}^{HJ} = -\langle \mathbf{f}_m^H, \hat{\mathbf{n}} \times \mathbf{f}_n^J \rangle. \quad (4.35b)$$

Hence, the Gram matrix readily follows from the discretized counterpart of the identity operator in $\hat{\mathbf{n}} \times \mathbf{l}$. Invertibility of the Gram matrix is required to obtain the current amplitudes from the field amplitudes. The Gram matrix is invertible if it has full rank, i.e., the duality product must be non-degenerate, and the elements of each of the sets of test and expansion functions must be independent. Note that the condition number of the Gram matrix poses a measure of the well-posedness of the problem and therefore the stability of the solution.

Throughout, the same type of expansion function is applied for the electric and magnetic currents. A similar remark can be made regarding the test function of the electric and magnetic fields. Therefore, \mathbf{G}_{11}^{EM} follows directly from \mathbf{G}_{11}^{HJ} and vice versa. In fact, for 2D implementations, $\mathbf{G}_{11}^{EM} = \mathbf{G}_{11}^{HJ} = 2\mathbf{I}^{EM}$, as can be observed from Eq. (5.41). For 3D implementations with RWG test and expansion functions, we have $\mathbf{G}_{11}^{EM} = -\mathbf{G}_{11}^{HJ} = 2\mathbf{I}^\vee$, with $\vee = \hat{\mathbf{n}} \times \wedge$, and \mathbf{I}^\vee to be given in Eq. (7.27). Note that \mathbf{f}_m itself may consist of a linear combination of \wedge_m and \vee_m . As outlined in Section 4.6, the use of the inverse Gram matrix instead of the inverse propagator matrix has some appealing advantages regarding memory requirements and computational costs.

4.5 Composition of scattering operators

With the embedding concept presented in Section 4.3, the interaction between two scattering objects is accounted for. Although the complete *interior* and *exterior* total field can be constructed

with the Q-operators, the procedure still relies on the availability of the incident field currents Q_1^{in} and Q_2^{in} and the scattering operators S_{11} and S_{22} of the individual subdomains. To compose a new scattering operator of the combined domain, which may in turn interact with other domains, the LEGO procedure will be completed below. Common domain boundaries, if present, are removed in this process. Further, the complete interior fields of an arbitrary selection of previously combined domains can be updated and reconstructed for successive embedding steps. Finally, we investigate what computational redundancies occur, upon specializing to either LEP or SEP.

To combine separate scattering operators, we first consider the ultimate composite scattering problem in Figure 4.6, in relation to the one in Figure 4.7 that is obtained after the embedding step in Section 4.3. Clearly, Figure 4.6 illustrates an overview of the final configuration. The two starting scattering domains \mathcal{D}_1 and \mathcal{D}_2 considered in the embedding step may be connected, i.e., they may have a common boundary, $\partial\mathcal{D}_C = \partial\mathcal{D}_1 \cap \partial\mathcal{D}_2$. The composite scattering operator of the combined domain $\mathcal{D}_3 = \mathcal{D}_1 \cup \mathcal{D}_2$, given by S_{33} , is defined only on the outer boundary, $\partial\mathcal{D}_3 = \partial\mathcal{D}_1 \cup \partial\mathcal{D}_2 \setminus \partial\mathcal{D}_C$. The current Q_3^{in} on $\partial\mathcal{D}_3$ produces the impressed incident field in \mathcal{D}_3 . The pertaining current Q_3^{sc} that reproduces the scattered field of the composite configuration is obtained via S_{33} , i.e., including the electromagnetic interaction of the enclosed scattering objects. Hence, the common contour $\partial\mathcal{D}_C$, indicated by a dashed line has been removed, in the sense that currents are only defined on the outer boundary $\partial\mathcal{D}_3$. The ultimate scattering problem in Figure 4.6 is in principle identical to the elementary one described in Figure 4.1, (except for the particular scattering objects of course). In turn, \mathcal{D}_3 may be embedded with other domains in the same way.

The scattering configuration depicted in Figure 4.7 is obtained upon completing the embedding steps described in Section 4.3. Although the electromagnetic interaction between both domains is accounted for, the fields are still represented by equivalent currents Q_i^{in} and Q_i^{sc} defined on the individual boundaries. Namely, the exterior scattered field follows from the combined contribution of the currents Q_1^{sc} and Q_2^{sc} which are obtained via the scattering operators of the individual domains. Likewise, the complete incident fields produced by Q_1^{cp} and Q_2^{cp} are related to the Q_1^{in} and Q_2^{in} of the separate domains. In other words, the embedding steps do not yet distinguish between configurations with or without connected domains. Therefore, current constituents on possible common boundaries remain to be removed.

To arrive at the composite scattering configuration depicted in Figure 4.6, we start from the situation depicted in Figure 4.7. The four Q operators that account for the electromagnetic interaction between \mathcal{D}_1 and \mathcal{D}_2 are associated with the currents Q_1^{in} and Q_2^{in} for the incident field in the

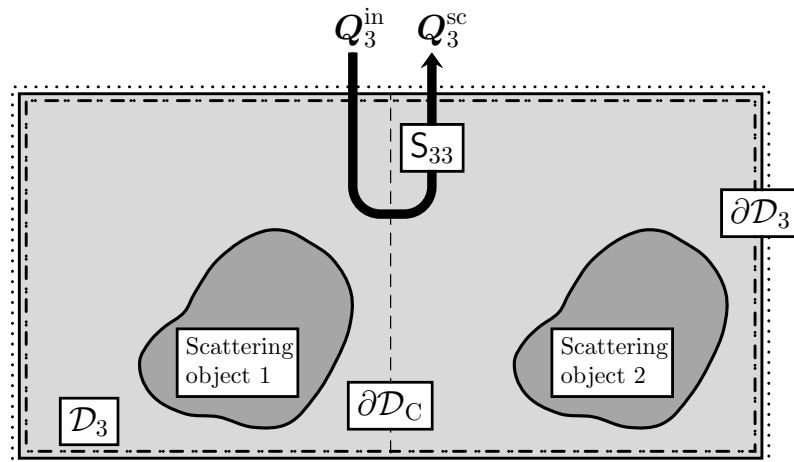


Figure 4.6: The ultimate composite configuration where separate domains have been combined into a single scattering domain. The combined operator S_{33} is defined only on the outer contour $\partial\mathcal{D}_3$ of $\mathcal{D}_3 = \mathcal{D}_1 \cup \mathcal{D}_2$. The dashed line indicates the removed common contour $\partial\mathcal{D}_C$.

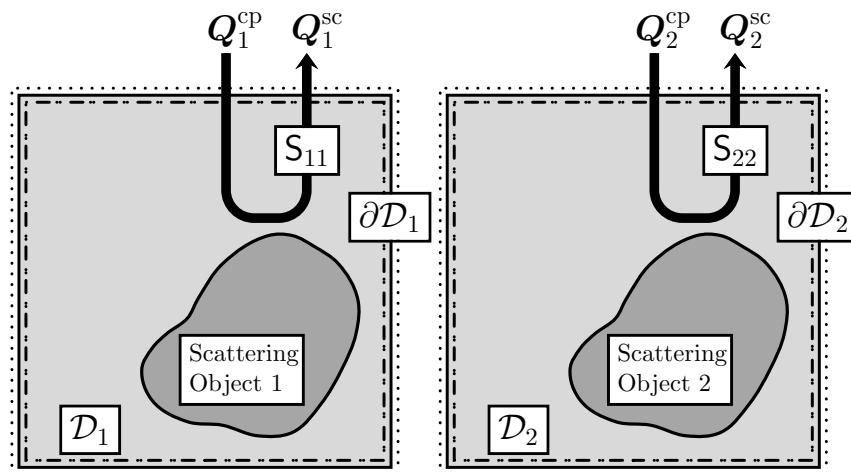


Figure 4.7: The scattering configuration after the embedding step. The currents Q_1^{cp} and Q_2^{cp} reproduce the complete incident field in \mathcal{D}_1 and \mathcal{D}_2 , respectively. Combined, the currents Q_1^{sc} and Q_2^{sc} produce the complete exterior scattered field.

individual domains. Therefore, the next step involves the transfer of Q_3^{in} from the boundary $\partial\mathcal{D}_3$ to the separate boundaries $\partial\mathcal{D}_1$ and $\partial\mathcal{D}_2$. These current transfers are realized via the transfer operators T_{13} and T_{23} , which follow from a similar definition as Eq. (4.14). Accordingly, we have

$$\begin{bmatrix} Q_{13} \\ Q_{23} \end{bmatrix} = \begin{bmatrix} Q_{11} & Q_{12} \\ Q_{21} & Q_{22} \end{bmatrix} \begin{bmatrix} T_{13} \\ T_{23} \end{bmatrix}. \quad (4.36)$$

The operators Q_{13} and Q_{23} act on the current Q_3^{in} of the combined domain.

With these intermediate results it remains possible to describe the complete interior fields of a subdomain of interest, say \mathcal{D}_i , in terms of an current on the outer boundary only, i.e.,

$$Q_i^{\text{cp}} = Q_{i3} Q_3^{\text{in}}, \quad (4.37)$$

in conformity with Eq. (4.13). The operator Q_{i3} , henceforth referred to as *interior field operator*, transforms Q_3^{in} on the outer boundary *directly* into a Q_i^{cp} on the boundary of subdomain \mathcal{D}_i . In a subsequent embedding step, each Q_{i3} can be updated independently to account for the presence of additional domains. By recursion, the embedding of a previously combined domain \mathcal{D}_3 with another domain, which changes the outer boundary into, say $\partial\mathcal{D}_4$, yields

$$Q_{i4} = Q_{i3} Q_{34}, \quad (4.38)$$

which replaces Q_{i3} for the new composite structure, i.e., the boundary index $\partial\mathcal{D}_3$ changes into $\partial\mathcal{D}_4$ in Eq. (4.37). Via Q_{i4} and the known initial scattered field response of the objects contained in an initial subdomain \mathcal{D}_i , the complete interior field in \mathcal{D}_i follows. With a following embedding step, Q_{i4} may in turn be updated in the same way. The freedom to choose for which of the subdomains \mathcal{D}_i the complete interior field is preserved (and updated) or not, is an additional appealing feature of the LEGO procedure.

The following step towards a composite scattering operator is the determination of the scattering response to Q_1^{cp} and Q_2^{cp} via the scattering operators of the individual domains, as illustrated in Figure 4.7. Finally, the resulting Q_1^{sc} and Q_2^{sc} are transferred to the outer boundary $\partial\mathcal{D}_3$ via similar transfer operators as applied in Eq. (4.36). As such, the scattering operator of the composite configuration follows from the superposition

$$S_{33} = T_{31} S_{11} Q_{13} + T_{32} S_{22} Q_{23} \quad (4.39)$$

Substitution of Eq. (4.36) into Eq. (4.39) yields the full definition of S_{33} in terms of S_{11} , S_{22} and the Q operators obtained in the embedding step. This definition applies to both LEP and SEP,

and accounts for both connected and unconnected (multiply connected) domains. With reference to Eq. (4.24), the resulting total field in the entire configuration is given by

$$\mathbf{F} = \begin{cases} P_i \mathbf{Q}_i^{\text{cp}} + \int_{\partial \mathcal{D}_i} \mathbf{F}^{\text{sc}}(\mathbf{r}, \mathbf{r}') \mathbf{Q}^{\text{cp}}(\mathbf{r}') \, dA', & \mathbf{r} \in \mathcal{D}_i, \\ \mathbf{F}^{\text{in}} + P_3 \mathbf{Q}_3^{\text{sc}}, & \mathbf{r} \in \bar{\mathcal{D}}_3. \end{cases} \quad (4.40)$$

The operator combinations in Eqs. (4.36) and (4.39) become matrix multiplications after discretization. The composition of a combined scattering operator may therefore appear as a time-consuming process. In addition, the steps above are in principle also required if a combined scattering operator is composed from domains that are not connected although this is not necessarily the case. In particular for LEP, \mathbf{Q}_3^{in} follows from a mere superposition of \mathbf{Q}_1^{in} and \mathbf{Q}_2^{in} , whereas for SEP the situation is more complicated. Nonetheless, there are many computational redundancies concealed in the construction of the transfer operator that has been applied. The redundancies regarding LEP differ from those of SEP. By eliminating the redundancies as explained below, much computational effort can be saved.

Let us start by considering scattering domains that are not connected. In that case there is no common boundary, and the outer boundary is given by $\partial \mathcal{D}_3 = \partial \mathcal{D}_1 \cup \partial \mathcal{D}_2$. A transfer operator which involves $\partial \mathcal{D}_3$ may then be subdivided into parts on $\partial \mathcal{D}_1$ and $\partial \mathcal{D}_2$. After discretization, the transfer matrix \mathbb{T}_{13} that transfers \mathbf{Q}_3^{in} on $\partial \mathcal{D}_3$ into \mathbf{Q}_1^{in} on $\partial \mathcal{D}_1$ may be written as

$$\mathbb{T}_{13} = \begin{bmatrix} \mathbb{T}_{11} & \mathbb{T}_{12} \end{bmatrix} = \begin{bmatrix} \mathbb{I}_{11} & \mathbb{T}_{12} \end{bmatrix}, \quad (4.41)$$

where \mathbb{I}_{11} represents the identity matrix. Hence, the current amplitudes of \mathbf{Q}_3^{in} located on $\partial \mathcal{D}_1$ directly add to \mathbf{Q}_1^{in} . We emphasize that \mathbb{T}_{12} in Eq. (4.41) transfers only currents that generate a field in the exterior of \mathcal{D}_2 , and contribute to the field in \mathcal{D}_1 .

At this point, we need to make a distinction between LEP and SEP. Recall that in the complement of the domain where the equivalent currents of LEP reproduce a field, the same currents produce a zero field owing to Oseen's extinction theorem. Hence, \mathbb{T}_{12} vanishes, which implies that for LEP $[\mathbb{T}_{13}^{\text{T}} \ \mathbb{T}_{23}^{\text{T}}]^{\text{T}}$ in Eq. (4.36) reduces to the identity matrix in the absence of common boundaries. In other words, there is a one-to-one relation between the current amplitudes of \mathbf{Q}_3^{in} and those of \mathbf{Q}_1^{in} and \mathbf{Q}_2^{in} . In contrast with LEP, we have already demonstrated that an equivalent current of SEP generates a nonzero field in its complementary domain. Therefore, the part of \mathbf{Q}_3^{in} located on $\partial \mathcal{D}_2$ does contribute to the incident field in \mathcal{D}_1 via \mathbb{T}_{12} . Hence, we may not simply omit \mathbb{T}_{13} and \mathbb{T}_{23} with SEP.

In the next step towards the description of the composite configuration in Figure 4.6, Q_1^{sc} and Q_2^{sc} are transferred to $\partial\mathcal{D}_3$ via T_{31} and T_{32} , respectively. In the absence of common boundaries T_{31} and T_{32} reduce to the corresponding parts of identity matrices on account of the superposition principle. Note that this is the case for both LEP and SEP. Accordingly, if $\partial\mathcal{D}_3 = \partial\mathcal{D}_1 \cup \partial\mathcal{D}_2$,

$$S_{33} = \begin{bmatrix} S_{11} & 0 \\ 0 & S_{22} \end{bmatrix} \begin{bmatrix} Q_{11} & Q_{12} \\ Q_{21} & Q_{22} \end{bmatrix}, \quad (4.42)$$

for LEP.

The transfer matrices, T_{13} and T_{23} in Eq. (4.36) may be applied alternatively in case of SEP such that Eq. (4.42) is valid for both equivalence principles in the absence of common boundaries. To achieve this, the general embedding process is completed to accommodate for SEP by adding the transfer operator T_{21} that follows from Eq. (4.41) to the expression for Q_{21} in Eq. (4.16). By duality, the expression of the four Q operators in Eq. (4.17) becomes

$$\begin{bmatrix} Q_{11} & Q_{12} \\ Q_{21} & Q_{22} \end{bmatrix} = \begin{bmatrix} 0 & T_{12} S_{22} \\ T_{21} S_{11} & 0 \end{bmatrix} \begin{bmatrix} Q_{11} & Q_{12} \\ Q_{21} & Q_{22} \end{bmatrix} + \begin{bmatrix} I_{11} & T_{12} \\ T_{21} & I_{22} \end{bmatrix}. \quad (4.43)$$

The solution is expressed in terms of scattering and reflection operators

$$\begin{bmatrix} Q_{11} & Q_{12} \\ Q_{21} & Q_{22} \end{bmatrix} = \begin{bmatrix} (I_{11} - R_{11} S_{11})^{-1} & 0 \\ 0 & (I_{22} - R_{22} S_{22})^{-1} \end{bmatrix} \begin{bmatrix} I_{11} + R_{11} & T_{12} (I_{22} + S_{22}) \\ T_{21} (I_{11} + S_{11}) & I_{22} + R_{22} \end{bmatrix}, \quad (4.44)$$

similar to Eq. (4.20). With this completed definition of the four Q operators, Eq. (4.42) also holds for SEP. Although the completed Q operators in Eq. (4.44) apply only in the absence of common boundaries, they may result in a more efficient embedding scheme with SEP. Note that LEP is impervious to the changes made.

In case \mathcal{D}_1 and \mathcal{D}_2 have common boundary parts, none of the transfer operators may be omitted. Nevertheless, there are still redundancies concealed in transfer matrices for both LEP and SEP. Some caution would be required near the junction of the common boundary $\partial\mathcal{D}_C$ and the outer boundary $\partial\mathcal{D}_3$, if the support of certain test and expansion functions crosses the junction. This is the case for the piecewise linear functions. A junction amounts to the start and end points of a common contour in a 2D configuration, or the boundary of a common surface in a 3D configuration. In Figure 4.8, we have illustrated the discretization of the composite configuration introduced in Figure 4.6. The boundaries \mathcal{D}_1 , \mathcal{D}_2 and \mathcal{D}_3 are subdivided with respect to test or expansion functions on the junction and the common boundary through a lowered subscript. For instance, the lowered subscript of $\partial\mathcal{D}_{3_1}$ indicates test or expansion functions on $\partial\mathcal{D}_3$ that are also

entirely on $\partial\mathcal{D}_1$. As such, $\partial\mathcal{D}_{3_1} = \partial\mathcal{D}_{1_3}$. The test and expansion functions on \mathcal{D}_1 , \mathcal{D}_2 and \mathcal{D}_3 whose support crosses the junction(s) are denoted as the junction test and expansion functions, $\partial\mathcal{D}_{1_\perp}$, $\partial\mathcal{D}_{2_\perp}$ and $\partial\mathcal{D}_{3_\perp}$, respectively. The junction test and expansion functions are indicated with black triangles in Figure 4.8.

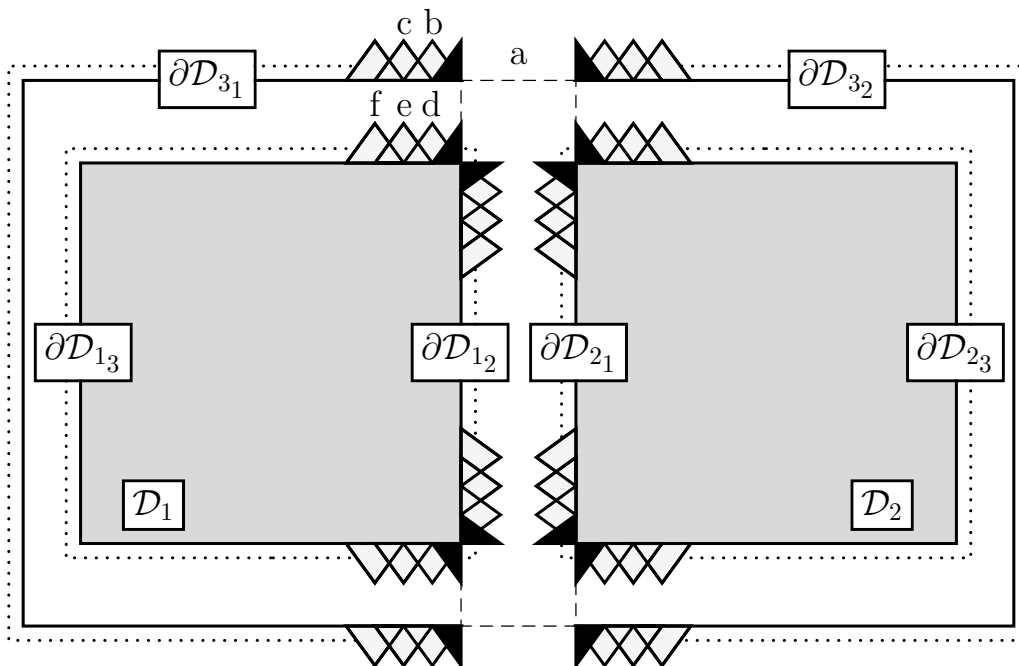


Figure 4.8: Discretization by means of piecewise linear test and expansion functions. The junction test and expansion functions $\partial\mathcal{D}_{1_\perp}$, $\partial\mathcal{D}_{2_\perp}$ and $\partial\mathcal{D}_{3_\perp}$, are indicated by black triangles on $\partial\mathcal{D}_1$, $\partial\mathcal{D}_2$ and $\partial\mathcal{D}_3$, respectively.

There are two methods (I and II) to remove computational redundancies in the transfer operator. Both methods provide efficiency improvements to *all* transfer operators in the presence of a common boundary, and thus also to T_{12} and T_{21} used in the general embedding step in Section 4.3. The redundancies occur for part of identity matrices concealed in the transfer matrix. Identifying these matrices not only reduces the computational complexity of associated matrix multiplications, but also leads to a reduction of the number of elements of the propagator matrices that would still have to be determined. Depending on the size of the source and observation boundaries of a transfer operator in relation to their common boundary part(s), either method I or II is favorable. This will be explained later on. Further, method I applies to both LEP and SEP, whereas method II applies to LEP only.

To elucidate both methods, let us first consider the case of a multiply connected domain in the absence of a common boundary, i.e., $\partial\mathcal{D}_3 = \partial\mathcal{D}_1 \cup \partial\mathcal{D}_2$, and restrict ourselves to LEP. The transfer of the current amplitudes from $\partial\mathcal{D}_3 = \partial\mathcal{D}_1 \cup \partial\mathcal{D}_2$ to $\partial\mathcal{D}_1$ and $\partial\mathcal{D}_2$ is described by the transfer matrix \mathbb{T}_{i3} for $i = 1, 2$. An overview of the action of the transfer matrices, \mathbb{T}_{13} and \mathbb{T}_{23} for the multiply connected domain $\partial\mathcal{D}_3$ is illustrated in Figure 4.9. We can apply one of three alternative approaches to realize the transfer of currents via \mathbb{T}_{i3} .

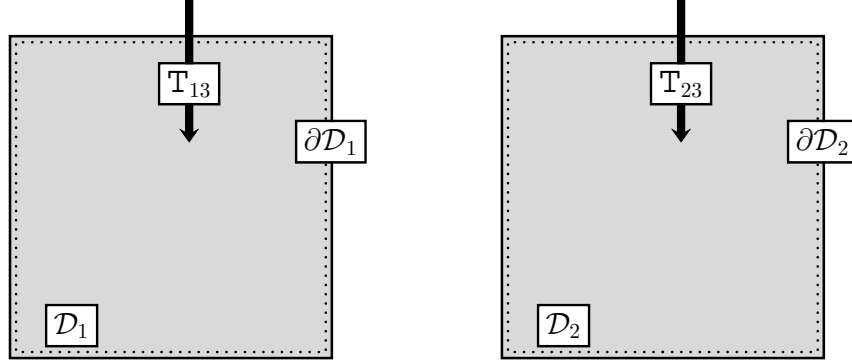


Figure 4.9: The matrices, \mathbb{T}_{13} and \mathbb{T}_{23} for the multiply connected domain $\partial\mathcal{D}_3 = \partial\mathcal{D}_1 \cup \partial\mathcal{D}_2$.

Firstly, one may compute the fields on $\partial\mathcal{D}_1$ and $\partial\mathcal{D}_2$ as generated by the equivalent sources on $\partial\mathcal{D}_3$. Owing to Oseen's extinction theorem, the equivalent boundary currents on the closed boundary parts $\partial\mathcal{D}_i$ for $i = 1, 2$ of the boundary $\partial\mathcal{D}_3$ produce a vanishing field exterior to \mathcal{D}_i . The field on $\partial\mathcal{D}_i$ may subsequently be converted into equivalent currents by applying an inverse propagator matrix \mathbb{P}_{ii}^{-1} , i.e.,

$$\mathbb{Q}_i = \mathbb{P}_{ii}^{-1} \mathbb{P}_{i3} \mathbb{Q}_3, \quad \text{for } i = 1, 2. \quad (4.45)$$

Alternatively, one may employ the definition of the equivalent currents in terms of the fields, given by Eq. (4.31), to extract the current amplitudes from the field amplitudes. Accounting for the testing procedure in the weak formulation, this amounts to applying an inverse Gram matrix, \mathbb{G}_{ii}^{-1} , i.e.,

$$\mathbb{Q}_i = \mathbb{G}_{ii}^{-1} \mathbb{P}_{i3} \mathbb{Q}_3, \quad \text{for } i = 1, 2. \quad (4.46)$$

Note that \mathbb{G}_{ii} is a local operator, whereas \mathbb{P}_{ii} and \mathbb{P}_{i3} are global ones. Nevertheless, for physical incident fields, \mathbb{G}_{ii} and \mathbb{P}_{ii} have the same effect. If no discretization errors were incurred, these approaches would be equivalent. Moreover, it would amount to a simple act of copying \mathbb{Q}_3 onto its constituents parts, i.e.,

$$\mathbb{Q}_i = \mathbb{I}_{i3} \mathbb{Q}_3, \quad \text{for } i = 1, 2. \quad (4.47)$$

Hence, we have

$$\mathbf{T}_{i3} = \mathbf{P}_{ii}^{-1} \mathbf{P}_{i3}, \quad \text{or} \quad \mathbf{T}_{i3} = \mathbf{G}_{ii}^{-1} \mathbf{P}_{i3}, \quad \text{or} \quad \mathbf{T}_{i3} = \mathbf{I}_{i3}, \quad \text{for } i = 1, 2. \quad (4.48)$$

Clearly, the simple act of copying source amplitudes not only saves computing time, it is an exact procedure, which can be repeated indefinitely. However, it is only feasible if $\partial\mathcal{D}_1$ and $\partial\mathcal{D}_2$ are not connected. Observe that $\mathbf{P}_{ii}^{-1} \mathbf{P}_{i3} = \mathbf{I}_{i3}$, whereas $\mathbf{G}_{ii}^{-1} \mathbf{P}_{i3} \neq \mathbf{I}_{i3}$. Hence, if one uses $\mathbf{P}_{ii}^{-1} \mathbf{P}_{i3} = \mathbf{I}_{i3}$, further discretization errors are avoided.

Next, let us investigate what happens if $\partial\mathcal{D}_1$ and $\partial\mathcal{D}_2$ have a common boundary. In this case, the currents on the open $\partial\mathcal{D}_1$ part of $\partial\mathcal{D}_3$ do produce a field on $\partial\mathcal{D}_2$ and vice versa. As an example of method I, let us consider the transfer matrix \mathbf{T}_{13} . Firstly, we use an inverse propagator matrix, Eq. (4.48). By subdivision of the source boundary $\partial\mathcal{D}_3$ into the boundary constituents indicated in Figure 4.8, we obtain

$$\mathbf{T}_{13} = \mathbf{P}_{11}^{-1} \mathbf{P}_{13} = \mathbf{P}_{11}^{-1} \begin{bmatrix} \mathbf{P}_{13_1} & \mathbf{P}_{13_{2,\perp}} \end{bmatrix} = \begin{bmatrix} \mathbf{I}_{13_1} & \mathbf{P}_{11}^{-1} \mathbf{P}_{13_{2,\perp}} \end{bmatrix}, \quad (4.49)$$

where we have used the property $\mathbf{P}_{13_1} = \mathbf{P}_{11_3}$. Note that here the identity matrix directly follows from the propagator matrix multiplications. An element of \mathbf{I}_{13_1} does not vanish only if an expansion function on $\partial\mathcal{D}_1$ coincides with one on $\partial\mathcal{D}_3$, which implies that,

$$\mathbf{I}_{13_1} = \begin{bmatrix} \mathbf{I}_{13_3_1} \\ \mathbf{I}_{1_{2,\perp}3_1} \end{bmatrix} = \begin{bmatrix} \mathbf{I}_{13_3_1} \\ 0 \end{bmatrix}. \quad (4.50)$$

As a result, the current amplitudes on $\partial\mathcal{D}_{3_1}$ are directly copied to the ones on $\partial\mathcal{D}_{1_3}$. In method I, we only have to determine the field on $\partial\mathcal{D}_1$ that is generated by the sources on $\partial\mathcal{D}_{3_{2,\perp}}$, viz., $\mathbf{P}_{13_{2,\perp}}$ in Eq. (4.49). The action of \mathbf{T}_{13} via method I is illustrated in the top-left figure of Figure 4.10. The dashed line indicates the boundary part where current amplitudes are directly copied from $\partial\mathcal{D}_3$ to $\partial\mathcal{D}_1$, while the source and observation boundary parts of $\mathbf{P}_{13_{2,\perp}}$ are denoted by the dash-dotted and dotted lines, respectively. Hence, via Huygens' principle, we have transferred (removed) sources by applying the equivalence principle for the fields due to individual sources. Other transfer matrices are treated in the same way.

Secondly, we consider method I in case an inverse Gram matrix is employed for \mathbf{T}_{i3} , as in Eq. (4.48), which applies to LEP only. Again, Huygens' principle is employed in the same way to transfer sources, while the current amplitudes on $\partial\mathcal{D}_{3_1}$ are copied to $\partial\mathcal{D}_{1_3}$,

$$\mathbf{T}_{13} = \mathbf{G}_{11}^{-1} \mathbf{P}_{13} = \mathbf{G}_{11}^{-1} \begin{bmatrix} \mathbf{P}_{13_1} & \mathbf{P}_{13_{2,\perp}} \end{bmatrix} \xrightarrow{\text{Huygens}} \mathbf{T}_{13} = \begin{bmatrix} \mathbf{I}_{13_1} & \mathbf{G}_{11}^{-1} \mathbf{P}_{13_{2,\perp}} \end{bmatrix}. \quad (4.51)$$

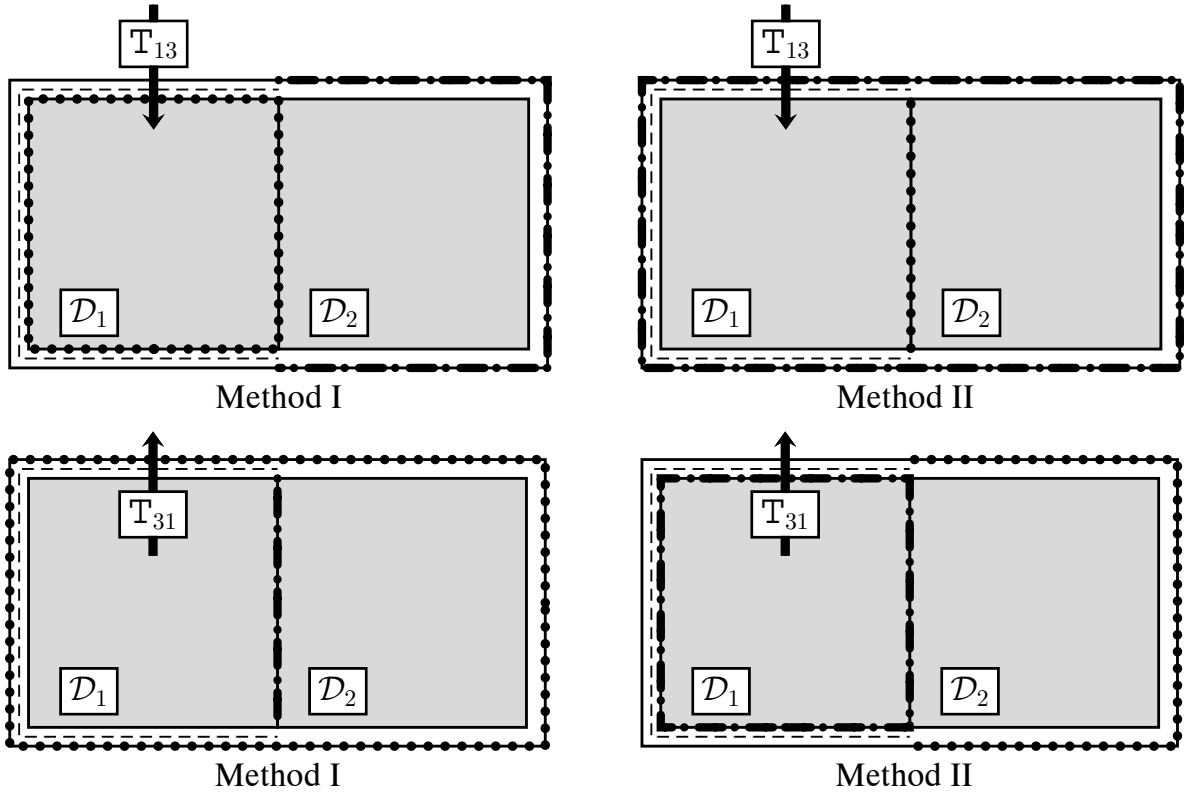


Figure 4.10: The difference between method I and II for the transfer matrices T_{13} and T_{31} in the top and bottom figures, respectively. The dashed line denotes the current amplitudes of the source boundary that are directly copied to the ones on the observation boundary. The dash-dotted and dotted lines represent the source and observation boundary parts, respectively, of the field propagator matrices P_{13} (top) and P_{31} (bottom) that remain to be determined. Method I is based on Huygens' principle, whereas method II is based on Oseen's extinction principle.

By copying sources directly via I_{131} , we have avoided an unnecessary discretization step. With reference to Eq. (4.49), we note that this is only the case if an inverse Gram matrix is applied.

Next, method II relies on the definition of the equivalent currents in Eq. (4.31), and therefore applies only to LEP based on Gram matrices. In contrast with method I, we now subdivide the observation boundary $\partial\mathcal{D}_1$ for T_{13} according to

$$T_{13} = G_{11}^{-1} P_{13} = G_{11}^{-1} \begin{bmatrix} P_{133} \\ P_{12,\perp 3} \end{bmatrix}. \quad (4.52)$$

The field amplitudes that P_{133} produces on $\partial\mathcal{D}_{13}$ can be extracted directly from the current amplitudes Q_3 on which T_{13} operates. The extraction of these field amplitudes is based on

Oseen's extinction theorem. Namely, although the current \mathbf{Q}_3 may contribute to the field in \mathcal{D}_1 , it yields a zero field exterior to \mathcal{D}_3 . Through $\mathbf{Q}_1 = \mathbf{T}_{13} \mathbf{Q}_3$, the current \mathbf{Q}_1 shall produce that same field in \mathcal{D}_1 , but also yields a zero field exterior to \mathcal{D}_3 . From the definition of the equivalent currents in Eq. (4.31), which is based on the zero field assumption in the complementary domain, in principle, the currents \mathbf{Q}_1 and \mathbf{Q}_3 are the same for $\partial\mathcal{D}_1 \cap \partial\mathcal{D}_3$. However, the pertaining current amplitudes \mathbf{Q}_3 and \mathbf{Q}_1 differ for $\partial\mathcal{D}_1 \cap \partial\mathcal{D}_3$, since \mathbf{G}_{33}^{-1} and \mathbf{G}_{11}^{-1} differ (see also Eq. (4.34)). Nonetheless, the field amplitudes \mathbf{F}_3 and \mathbf{F}_1 remain the same for the boundary part $\partial\mathcal{D}_{13}$, i.e., $\mathbf{F}_{13} = \mathbf{F}_{31}$. Thus, instead of obtaining these field amplitudes via $\mathbf{F}_{13} = \mathbf{P}_{133} \mathbf{Q}_3$, we may alternatively extract the field amplitudes, $\mathbf{F}_{13} = \mathbf{G}_{133} \mathbf{Q}_3$. In this way, we avoid an unnecessary discretization step. Accordingly, upon applying this relation to Eq. (4.52), we have

$$\xrightarrow{\text{Oseen}} \mathbf{T}_{13} = \mathbf{G}_{11}^{-1} \begin{bmatrix} \mathbf{G}_{313} \\ \mathbf{P}_{12,\perp 3} \end{bmatrix} = \mathbf{G}_{113}^{-1} \mathbf{G}_{313} + \mathbf{G}_{112,\perp}^{-1} \mathbf{P}_{12,\perp 3}. \quad (4.53)$$

The matrix product $\mathbf{G}_{113}^{-1} \mathbf{G}_{313}$ contains the block identity matrix in which we are interested. Thus, we also directly copy the current amplitudes from $\partial\mathcal{D}_{31}$ to $\partial\mathcal{D}_{13}$, albeit that the remaining part, $\mathbf{Q}_{12,\perp}$, is obtained by reproducing $\mathbf{F}_{12,\perp}$ through the propagator matrix $\mathbf{P}_{12,\perp 3}$. Hence, in method II, we transfer a current by first determining the pertaining field on the observation boundary from which the transferred current follows, similar to Eq. (4.46). In the top right figure of Figure 4.10, the direct transfer of current amplitudes, in combination with the action of $\mathbf{P}_{12,\perp 3}$ is visualized.

To extract the identity matrix from Eq. (4.53), via $\partial\mathcal{D}_{31} = \partial\mathcal{D}_{13}$, we decompose the source boundary of \mathbf{G}_{313} into its constituents,

$$\mathbf{G}_{113}^{-1} \mathbf{G}_{313} = \mathbf{G}_{113}^{-1} \begin{bmatrix} \mathbf{G}_{133_1} & \mathbf{G}_{133_\perp} & 0 \end{bmatrix}, \quad (4.54)$$

in which we have used $\mathbf{G}_{133_2} = 0$. Let us continue the analysis by comparing the column vectors of \mathbf{G}_{133_1} with those of \mathbf{G}_{13_1} , since $\mathbf{G}_{11}^{-1} \mathbf{G}_{13_1} = \mathbf{I}_{13_1}$. For the 2D case with the $\wedge\wedge$ discretization illustrated in Figure 4.8, each expansion function $\wedge_\beta \in \partial\mathcal{D}_{31}$, indicated by $\partial\mathcal{D}_{3_\beta}$, corresponds to a column vector \mathbf{G}_{13_β} . For $\wedge_\beta \in \partial\mathcal{D}_{31}$, the column vector \mathbf{G}_{13_β} contains three nonzero elements such that $\mathbf{G}_{11}^{-1} \mathbf{G}_{13_\beta}$ is a column vector \mathbf{I}_{13_β} of the identity matrix \mathbf{I}_{13_1} . For instance, with reference to Figure 4.8, \wedge_c yields a nonzero duality product with $\{\wedge_d, \wedge_e, \wedge_f\}$. In case all three nonzero elements of \mathbf{G}_{13_β} for $\wedge_\beta \in \partial\mathcal{D}_{31}$ are also element of the vector column part \mathbf{G}_{133_β} , then $\mathbf{G}_{113}^{-1} \mathbf{G}_{133_\beta} = \mathbf{I}_{13_\beta}$, otherwise $\mathbf{G}_{113}^{-1} \mathbf{G}_{133_\beta}$ yields a dense vector. In view of Figure 4.8, this is the case for $\wedge_\beta = \wedge_b$, since \wedge_b only yields a nonzero duality product with $\{\wedge_d, \wedge_e\} \in \partial\mathcal{D}_{31}$. Generalizing this observation, we infer

$$\mathbf{G}_{113}^{-1} \mathbf{G}_{133_\beta} = \mathbf{I}_{13_\beta}, \quad \text{for } \langle \wedge_\beta, \wedge_\perp \rangle = 0 \quad \forall \wedge_\beta \in \partial\mathcal{D}_{31}, \wedge_\perp \in \partial\mathcal{D}_{3_\perp}. \quad (4.55)$$

Accordingly, besides an identity matrix, $G_{113}^{-1} G_{133}$ in Eq. (4.54) also produces two dense matrix columns, per junction, i.e., for $G_{133\perp}$ and $G_{133\beta}$ with $\langle \wedge_\beta, \wedge_\perp \rangle \neq 0$. Both vectors $G_{133\perp}$ and $G_{133\beta}$ have altogether three nonzero elements. For the junction on the top in Figure 4.8, these are the duality products $\langle \wedge_a, \wedge_d \rangle$, $\langle \wedge_b, \wedge_d \rangle$ and $\langle \wedge_b, \wedge_e \rangle$.

A fundamental difference between methods I and II is that in method I the observation boundary remains a closed boundary throughout, whereas in method II the source boundary remains a closed boundary throughout. Recall that for SEP only method I applies, whereas for LEP we may choose between methods I and II. Because the computational efficiency is subject to the size of the source and observation boundary of a transfer operator in relation to their common boundary part, either method I or II is more efficient. To gain insight into the appropriate choice of method, the distinctions and similarities between method I and II are illustrated in Figure 4.10. The dashed line denotes the current amplitudes of the source boundary that directly add to the ones on the observation boundary. The respective dotted and dash-dotted lines represent the source and observation boundary parts of the field propagator that remains to be determined.

Observe that the propagator parts in methods I and II are reciprocal, i.e., upon exchanging the source and observation boundary parts, method I for T_{13} corresponds to method II for T_{31} and vice versa. Hence, if method I is more efficient with $P_{12,\perp 3}$ for T_{13} , method II is more efficient with $P_{312,\perp}$ for T_{31} . As a consequence of mixing methods I and II as indicated, the propagator matrices $P_{12,\perp 3}$ and $P_{312,\perp}$ are interrelated through source reciprocity. The computational cost in the construction of the transfer matrix is primarily determined by the remaining matrix product, and thereby the size of the propagator matrix. For instance, let us neglect the junction elements for simplicity, and set N_1 , N_2 and N_C as the unknowns on ∂D_1 , ∂D_2 and ∂D_C , respectively. If $N_1 < N_2$, we deduce from Figure 4.10 that method II is more efficient for T_{13} if $N_C < N_2/2$, and method I is more efficient for T_{23} if $N_C < N_1/2$. However, this may differ depending on the matrices that are multiplied by the transfer matrix, especially since the transfer matrix becomes a full matrix in method II, whereas it becomes partially an identity matrix in method I. These considerations are taken into account in Section 4.6, where we give an assessment of the computational costs of LEGO.

It is much easier to handle a common boundary if the support of the applied test and expansion functions does not cross junctions, e.g., discretization with piecewise constant functions. We have applied this approach in [10]. In that case there are no junction elements because of which there is a one-to-one relation between *all* current amplitudes of expansion functions on a shared boundary for both methods. Since the interaction between neighboring functions disappears, the

Gram matrix is diagonal, and hence its inverse is also diagonal. The transfer matrix T_{13} still follows from the constituents I_{11} and T_{12} as in Eq. (4.41) by simply omitting the source contributions on $\partial\mathcal{D}_C$ as $\partial\mathcal{D}_C = \partial\mathcal{D}_{12} = \partial\mathcal{D}_{21}$. Via the alternative definition of the four Q operators in Eqs. (4.43) and (4.44), T_{13} and T_{23} are accounted for implicitly. The interior field operators Q_{13} and Q_{23} thus readily follow from these four Q operators. However, there remain equivalent currents on $\partial\mathcal{D}_C$ that contribute to the scattered field in $\bar{\mathcal{D}}_3$ and should still be transferred to the outer boundary via T_{31} and T_{32} . Via method I, T_{31} is decomposed into the nonzero constituents I_{3113} and T_{3C} . With a similar decomposition of T_{32} , Eq. (4.39) reduces to

$$S_{33} = \begin{bmatrix} S_{131} Q_{13} \\ S_{232} Q_{23} \end{bmatrix} + T_{3C} \begin{bmatrix} S_{C1} Q_{13} & S_{C2} Q_{23} \end{bmatrix}. \quad (4.56)$$

Hence, only the currents amplitudes on the common boundary have to be transferred to the outer boundary, if the discretization involves piecewise constant functions only.

4.6 Memory requirements and computational costs

There are two aspects related to the memory requirements of LEGO. On the one hand we have the storage demand of the scattering and (if required) interior field matrices. Conversely, we have the memory required as a workspace for the LEGO process. Both aspects will be treated separately. Most importantly, the computational costs of a single LEGO step will be determined. As such, the starting scattering matrices S_{11} and S_{22} are considered known *a priori*. These matrices have either been constructed in advance or followed from a previous embedding step. Since there are many schemes possible as regards the various matrix multiplications involved with embedding, the schemes that are suggested in this section represent in our view the most efficient ones as regards the computational costs and the workspace that is involved. For a comparison between embedding based on SEP and LEP, a computational scheme that is specialized to either equivalence principle will be considered. Via these schemes, this section explicitly describes the difference in computational costs of LEP versus SEP with embedding. However, a true measure should incorporate the corresponding accuracy of the resulting fields. To complete the comparison, we refer to Section 6.5. Finally, we will comment on the possible use of iterative solvers.

First, we discuss some general issues regarding memory and computational efficiency of the LEGO procedure. The overall computational costs and memory requirements of embedding are

primarily determined by the associated matrix operations and matrix sizes, respectively. For the optimum performance with respect to accuracy, field propagators should therefore reproduce the pertaining fields as accurately as possible given the number of unknowns. However, the accuracy that is achieved depends on the chosen set of test and expansion functions in relation to the mapping properties of the integral operators L and $K + \hat{n} \times l$ that are linked to the propagator matrix P . Hence, the quadrature error may play an important role in this matter. These considerations are to be addressed in Chapters 5 and 7.

Further, it may appear that various propagator matrices have to be determined in an embedding step, and the filling process of the propagator matrices may become a substantial part of the overall computational effort. This is particularly relevant since we aim for maximum accuracy, and hence a small quadrature error. Fortunately, these propagators are reusable. In fact, for LEGO based on LEP with Gram matrices, the construction of P_{12} suffices since P_{21} follows from P_{12} by exchanging source and observation boundary (source reciprocity). The remaining propagator matrices, which are related to the outer boundary $\partial\mathcal{D}_3$, follow implicitly. Clearly, these relations rely on the applied discretization, e.g., source reciprocity is not exact for schemes that are not based on Galerkin test and expansion functions. Source reciprocity also applies to SEP if the propagators are based on the EFIE. This is no longer the case if the propagators are based on the MFIE (or the CFIE for that matter). Further, P_{11} and P_{22} are required as well. Although the propagator matrices of LEP are four times larger than those of SEP, the associated filling process may be as efficient. This will be demonstrated in Section 5.3.

The LEGO procedure based on LEP is most efficient via inverse Gram matrices than via inverse propagator matrices. The computational complexity of, say, G_{11} is one fourth that of P_{11} . Moreover, the Gram matrix is a real symmetric matrix and therefore two times smaller than a complex one. Hence, in comparison with P_{11} , G_{11} saves a factor of 8 in storage costs, and a factor of 64 in computational costs for the inverse. Even in relation to SEP, the use of a Gram matrix saves a factor of two in storage costs, and a factor of eight in computational costs of the inverse. Moreover, since the inverse Gram matrix contains only two submatrices, a subsequent matrix multiplication saves half the computational costs in comparison with a full inverse propagator matrix. Further, the Gram matrix is a circulant system in 2D configurations, which reduces the complexity of the inverse Gram matrix to $(N^2/8) \log N$ [67, Section 10.1.1]. For 3D configurations the Gram matrix is symmetric and sparse. For simplicity, in determining the inverse, we shall assume a real symmetric Gram matrix for the evaluation of the computational costs of the scheme. Note that if the chosen set of test and expansion functions satisfies the duality product $\langle \mathbf{f}_m, \mathbf{f}_n \rangle = 0$ for $m \neq n$, the Gram matrix is diagonal, and the only inverse that is left in the embedding scheme

with LEP is that of the embedding matrix. As regards the filling process, P_{11} is $\mathcal{O}(N^2)$, while G_{11} is $\mathcal{O}(N)$. Besides that, G_{11} is computed analytically, whereas P_{11} involves quadrature rules which increases the overall filling time. Accordingly, we infer that LEP is favorable with regard to the construction of the propagator matrices.

To assess the overall storage demand, we consider a large domain \mathcal{D}_L with N_L unknowns (source positions) on its outer boundary $\partial\mathcal{D}_L$. \mathcal{D}_L contains N_T previously combined subdomains \mathcal{D}_i with an average number of unknowns N_i on $\partial\mathcal{D}_i$. Let us assume here that the interior field operators of all subdomains are stored. The associated required amount of storage is N_L^2 for the S_{LL} operator, and $N_i N_T N_L$ for the Q_{iL} operators. Note that the size of the combined structure varies substantially with respect to the shape of the outer boundary.

As we would like to relate the memory requirements to the size of the obtained structure, we will provide upper and lower limits for N_L in terms of the number of previously combined domains N_T and the corresponding average number of unknowns N_i on \mathcal{D}_i . In the worst case, when none of the subdomains have boundaries in common, i.e., $N_L = N_i N_T$, the size of the operators, S_{LL} and Q_{iL} , are proportional to $N_i^2 N_T$. In the best case, when all subdomains are closely packed together, we have $N_L = N_i N_T^{(\nu-1)/\nu}$ where ν denotes the dimension of the scattering problem, and the storage size of the operators reduces to $N_i^2 N_T^{2(\nu-1)/\nu}$ for S_{LL} and $N_i^2 N_T^{1+(\nu-1)/\nu}$ for Q_{iL} . Of course, the size of Q_{iL} reduces if only the complete interior field of specific subdomains is retained. Note that the memory requirements with embedding based on LEP are in general four times larger.

In case the interior field operators are preserved for a large number of previously combined domains, these operators yield a more substantial demand to the memory requirements. However, the interior field operators are addressed only once in an embedding step. As such, in the construction of large scattering domains, these operators are best stored on disk.

To gain more insight into the computational costs of the overall LEGO concept, we examine the matrix operations associated with a single embedding step and evaluate the computational cost of each operation. For a comparison between embedding based on SEP and LEP, both computational schemes are considered. Junction elements are neglected in the analysis for simplicity. Accordingly, N_1 , N_2 and N_C are set as the unknowns on $\partial\mathcal{D}_1$, $\partial\mathcal{D}_2$ and $\partial\mathcal{D}_C$, respectively. As such, for the outer boundary we have $N_3 = N_1 + N_2 - 2N_C$. Accordingly, in Tables 4.1 and 4.2 the operational costs of the computational schemes of LEGO are presented for SEP and LEP, respectively. We have introduced the (partial) reflection matrices R_{12} and R_{21} to minimize the

number of matrix multiplications. Checkmarks indicate if a matrix operation is required for the case with common boundary ($N_C \neq 0$) or without ($N_C = 0$), or both. Throughout we assume for simplicity that the complexity of the inverse of a $N \times N$ matrix is N^3 . Further, we have restricted to the computational costs of the matrix operations as these dominate the overall computational costs. Because LEP involves both electric and magnetic currents, a discretization as fine as the one for the single equivalent current in SEP generally implies double matrix sizes and matrix multiplications that are eight times less efficient.

In Section 4.3 we have demonstrated that it suffices to determine the embedding matrix $[\mathbf{I} - \mathbf{R}\mathbf{S}]$ for either \mathcal{D}_1 or \mathcal{D}_2 . When $N_1 < N_2$, it is more efficient to use the embedding matrix associated with domain \mathcal{D}_1 . In both computational schemes we assume that $N_1 \leq N_2$. Otherwise, the boundary indices are simply swapped. Further, the computational scheme based on LEP involves Gram matrices, which saves a factor of 64 in determining the inverse in comparison with a propagator matrix, and a factor of two in the pertaining matrix multiplications. Despite that, most matrix multiplication of LEP are eight times less efficient as with SEP, because LEP has both electric and magnetic equivalent currents and therefore twice the number of unknowns of SEP. As regards the memory requirements for the workspace of the embedding process, a total of $3(N_1 + N_2)^2$ proves to be adequate for the proposed scheme with SEP. For the scheme with LEP, the workspace is four times larger. Note that the workspace includes the storage demand of the starting scattering matrices \mathbf{S}_{11} and \mathbf{S}_{22} , but also that of the resulting composite scattering matrix \mathbf{S}_{33} .

In the absence of a common boundary the differences in matrix operations for LEP and SEP have been discussed in Section 4.5. The general embedding procedure as presented in Section 4.3. is then sufficient with LEP, in the sense that the transfer matrices involving $\partial\mathcal{D}_3$ may be omitted. Conversely, \mathbf{T}_{13} and \mathbf{T}_{23} have to be taken into account with SEP. In principle, the matrix operations starting from \mathbf{T}_{13} through \mathbf{S}_{23} in Table 4.1 thus apply if there are no common boundaries. As an alternative, the embedding step has been extended in Eqs. (4.43) and (4.44) to accommodate SEP. These definitions have been used in the embedding with SEP, since that turns out to be more efficient than via \mathbf{T}_{13} and \mathbf{T}_{23} . Notice that the procedure for a single embedding step is more complex in case of a common boundary. However, as has been explained above, subsequent combinations involving the composite domain require the removal of the common boundary.

The matrix multiplications related to the transfer matrices contain redundancies if the source and observation boundary of the transfer matrix have common parts. In Section 4.5, two meth-

N_C			
$= 0$	$\neq 0$	<i>matrix operation</i>	$\mathcal{O}(\dots)$
✓	✓	$\mathbf{P}_{11}^{-1}, \mathbf{P}_{22}^{-1}$	N_1^3, N_2^3
✓	✓	$\mathbf{R}_{12} = \mathbf{T}_{12}\mathbf{S}_{22} = \mathbf{P}_{11}^{-1}\mathbf{P}_{12}\mathbf{S}_{22}$	$N_1(N_2 - N_C)(N_1 + N_2)$
✓	✓	$\mathbf{R}_{21} = \mathbf{T}_{21}\mathbf{S}_{11} = \mathbf{P}_{22}^{-1}\mathbf{P}_{21}\mathbf{S}_{11}$	$N_2(N_1 - N_C)(N_1 + N_2)$
✓	✓	$[\mathbf{I}_{11} - \mathbf{R}_{11}\mathbf{S}_{11}]^{-1} = [\mathbf{I}_{11} - \mathbf{R}_{12}\mathbf{R}_{21}]^{-1}$	$N_1^2(N_1 + N_2)$
✓		$\mathbf{R}_{11} = \mathbf{R}_{12}\mathbf{T}_{21}$	$N_1^2N_2$
✓		$\mathbf{Q}_{11} = [\mathbf{I}_{11} - \mathbf{R}_{11}\mathbf{S}_{11}]^{-1}[\mathbf{I}_{11} + \mathbf{R}_{11}]$	N_1^3
✓		$\mathbf{Q}_{12} = [\mathbf{I}_{11} - \mathbf{R}_{11}\mathbf{S}_{11}]^{-1}[\mathbf{T}_{12} + \mathbf{R}_{12}]$	$N_1^2N_2$
✓		$\mathbf{Q}_{21} = \mathbf{T}_{21} + \mathbf{R}_{21}\mathbf{Q}_{11}$	$N_1^2N_2$
✓		$\mathbf{Q}_{22} = \mathbf{I}_{22} + \mathbf{R}_{21}\mathbf{Q}_{12}$	$N_1N_2^2$
✓		$\mathbf{S}_{33} = \begin{bmatrix} \mathbf{S}_{11} & 0 \\ 0 & \mathbf{S}_{22} \end{bmatrix} \begin{bmatrix} \mathbf{Q}_{11} & \mathbf{Q}_{12} \\ \mathbf{Q}_{21} & \mathbf{Q}_{22} \end{bmatrix}$	$(N_1^2 + N_2^2)(N_1 + N_2)$
	✓	$\mathbf{T}_{13} = \mathbf{P}_{11}^{-1}\mathbf{P}_{13}$	$N_1^2(N_2 - N_C)$
	✓	$\mathbf{T}_{23} = \mathbf{P}_{22}^{-1}\mathbf{P}_{23}$	$N_2^2(N_1 - N_C)$
	✓	$\mathbf{R}_{12}\mathbf{T}_{23}$	$N_1N_2(N_1 - N_C)$
	✓	$\mathbf{Q}_{13} = [\mathbf{I}_{11} - \mathbf{R}_{11}\mathbf{S}_{11}]^{-1}[\mathbf{T}_{13} + \mathbf{R}_{12}\mathbf{T}_{23}]$	$N_1^2N_3$
	✓	$\mathbf{Q}_{23} = \mathbf{R}_{21}\mathbf{Q}_{13} + \mathbf{T}_{13}$	$N_1N_2N_3$
	✓	$\mathbf{S}_{13} = \mathbf{S}_{11}\mathbf{Q}_{13}$	$N_1^2N_3$
	✓	$\mathbf{S}_{23} = \mathbf{S}_{22}\mathbf{Q}_{13}$	$N_2^2N_3$
	✓	\mathbf{P}_{33}^{-1}	N_3^3
	✓	$\mathbf{T}_{31}\mathbf{S}_{13} = \mathbf{P}_{33}^{-1}\mathbf{P}_{31}\mathbf{S}_{13}$	$2N_3^2N_C$
	✓	$\mathbf{T}_{32}\mathbf{S}_{23} = \mathbf{P}_{33}^{-1}\mathbf{P}_{32}\mathbf{S}_{23}$	$2N_3^2N_C$
	✓	$\mathbf{S}_{33} = \mathbf{T}_{31}\mathbf{S}_{13} + \mathbf{T}_{32}\mathbf{S}_{23}$	—

Table 4.1: The computational scheme of LEGO based on SEP with the complexity of each matrix operation for $N_1 \leq N_2$. The checkmarks indicate whether a matrix operation is required for the case with ($N_C \neq 0$) or without ($N_C = 0$) common boundary (or both). All transfer matrices are constructed via method I.

N_C				
= 0	$\neq 0$	<i>matrix operation</i>	$\mathcal{O}(\dots)$	Meth.
✓	✓	G_{11}^{-1}, G_{22}^{-1}	$N_1^3/8, N_2^3/8$	
✓	✓	$R_{12} = T_{12}S_{22} = G_{11}^{-1}P_{12}S_{22}$	$4N_2(N_1 - N_C)(N_1 + 2N_2)$	II
✓	✓	$R_{21} = T_{21}S_{11} = G_{22}^{-1}P_{21}S_{11}$	$4N_2(N_1 - N_C)(2N_1 + N_2)$	I
✓	✓	$[I_{11} - R_{11}S_{11}]^{-1} = [I_{11} - R_{12}R_{21}]^{-1}$	$8N_1^2(N_1 + N_2)$	
✓		$Q_{11} = [I_{11} - R_{11}S_{11}]^{-1}$	–	
✓		$Q_{12} = Q_{11}R_{12}$	$8N_1^2N_2$	
✓		$Q_{21} = R_{21}Q_{11}$	$8N_1^2N_2$	
✓		$Q_{22} = I_{22} + R_{21}Q_{12}$	$8N_1N_2^2$	
✓		$S_{33} = \begin{bmatrix} S_{11} & 0 \\ 0 & S_{22} \end{bmatrix} \begin{bmatrix} Q_{11} & Q_{12} \\ Q_{21} & Q_{22} \end{bmatrix}$	$8(N_1^2 + N_2^2)(N_1 + N_2)$	
	✓	$T_{13} = G_{11}^{-1}P_{13}$	$4N_1N_3N_C$	II
	✓	$T_{23} = G_{22}^{-1}P_{23}$	$4N_2^2(N_1 - N_C)$	I
	✓	$R_{12}T_{23}$	$8N_1N_2(N_1 - N_C)$	
	✓	$Q_{13} = [I_{11} - R_{11}S_{11}]^{-1}[T_{13} + R_{12}T_{23}]$	$8N_1^2N_3$	
	✓	$Q_{23} = R_{21}Q_{13} + T_{13}$	$8N_1N_2N_3$	
	✓	$S_{13} = S_{11}Q_{13}$	$8N_1^2N_3$	
	✓	$S_{23} = S_{22}Q_{13}$	$8N_2^2N_3$	
	✓	G_{33}^{-1}	$N_3^3/8$	
	✓	$T_{31}S_{13} = G_{33}^{-1}P_{31}S_{13}$	$12N_3^2N_C$	I
	✓	$T_{32}S_{23} = G_{33}^{-1}P_{32}S_{23}$	$12N_3^2N_C$	I
	✓	$S_{33} = T_{31}S_{13} + T_{32}S_{23}$	–	

Table 4.2: The computational scheme of LEGO based on LEP with the complexity of each matrix operation for $N_1 \leq N_2$. The checkmarks indicate whether a matrix operation is required for the case with ($N_C \neq 0$) or without ($N_C = 0$) common boundary (or both). The method used to construct the transfer matrices are indicated.

ods (I and II) have been presented to avoid these redundancies. The improvement in computational efficiency of each method varies, depending on the boundary sizes and the matrices that are multiplied with the transfer matrix. The most efficient methods for LEP are indicated in Table 4.2. With SEP, only method I can be used. The same considerations apply as in the case of Figure 4.10. The methods that are indicated in Table 4.2 for $N_1 < N_2$ are the most efficient ones if $N_C \leq N_1$, i.e., if $\partial\mathcal{D}_2$ does not enclose $\partial\mathcal{D}_1$ or vice versa. For \mathbb{T}_{23} , method I is most efficient, because \mathbb{T}_{23} contains a part of an identity matrix, which reduces the costs in evaluating $\mathbb{R}_{12}\mathbb{T}_{23}$. Notice that the computational costs of the other transfer matrices involving $\partial\mathcal{D}_3$ vanish naturally in case $N_C = 0$. Likewise, if $\partial\mathcal{D}_1 \subset \partial\mathcal{D}_2$ such that $N_C = N_1$, the transfer matrices \mathbb{T}_{12} and \mathbb{T}_{21} become trivial with LEP.

Further improvement of the presented computational schemes may be achieved. For instance, upon examining the embedding matrix $[\mathbb{I} - \mathbb{R}\mathbb{S}]$, we have $\|\mathbb{R}\mathbb{S}\| < 1$ and $\lim_{p \rightarrow \infty} (\mathbb{R}\mathbb{S})^p = 0$. With these conditions the inverse of the embedding matrix may also be obtained through a Neumann Series (special form of Jacobi iterations [67, Section 4.7]). This reduces the computational cost of the inverse embedding matrix to order pN^2 . Or alternatively, via successive overrelaxation [68].

The presented schemes only describe the construction of the composite scattering matrix that produces the exterior field. The interior field directly follows through the interior field matrices \mathbb{Q}_{13} and \mathbb{Q}_{23} via Eqs. (4.37) and (4.40) with \mathcal{D}_1 and \mathcal{D}_2 as elementary domains. Otherwise, if \mathcal{D}_1 and \mathcal{D}_2 contain $N_{T;1}$ and $N_{T;2}$ previously combined subdomains, respectively, with an average number of unknowns N_i on $\partial\mathcal{D}_i$, then the interior field matrices \mathbb{Q}_{i1} and \mathbb{Q}_{i2} have to be updated according to Eq. (4.38) to obtain \mathbb{Q}_{i3} for the subdomains of interest. The computational costs for updating the interior field matrices of all subdomains are $N_3 N_i (N_1 N_{T;1} + N_2 N_{T;2})$. From the assessment of the overall storage demand we may deduce that for closely packed subdomains, $N_i N_T^{(\nu-1)/\nu} \approx N_3$ with $N_T = N_{T;1} + N_{T;2}$. Accordingly, if $N_{T;1} \approx N_{T;2}$, the computational costs to update all interior field matrices are approximately $N_3^3 (N_1 + N_2) / 2N_i$ and $N_3^{5/2} (N_1 + N_2) / 2\sqrt{N_i}$ for $\nu = 2$ (2D) and $\nu = 3$ (3D), respectively. In that case, the update process will eventually dominate the embedding step if $(N_1 + N_2) \gg 2N_i$. In the worst case, when none of the subdomains share boundaries, $N_i N_T = N_3$, and the update process takes about $N_3^2 (N_1 + N_2) / 2$ evaluations. In the selection of domain boundaries one aims for closely packed subdomains. Nonetheless, in most practical design applications, one is usually primarily interested in the scattering matrix and possibly also the field in *some* previously combined subdomains of interest. The approximate computational costs of the update process for small values of N_T then becomes $N_3 (N_1 + N_2) N_i / 2$. In a sequence of embedding steps, $N_i \ll \min[N_1, N_2]$, so that the contribution

of the update process to the overall computational costs remains small.

Let us now perform an explicit comparison between the overall computational cost of the embedding scheme of SEP and LEP in Tables 4.1 and 4.2, respectively. Due to the use of both electric and magnetic currents, LEP initially may seem eight times less efficient than SEP. However, LEP becomes more efficient through the use of Gram matrices. Moreover, two methods to avoid computational redundancies apply to LEP, while only one applies to SEP. The difference in computational costs may vary depending on the common boundary size $\partial\mathcal{D}_C$ and the ratio N_2/N_1 . Accordingly, in Figure 4.11 we have compared the total computational cost of the embedding scheme of LEP in relation to that of SEP as a function of the common boundary size for various domain sizes. As remarked above, we restrict ourselves to the case $N_1 \leq N_2$. For $N_1 > N_2$, the boundary indices $\partial\mathcal{D}_1$ and $\partial\mathcal{D}_2$ may be swapped in the embedding schemes. The discontinuous derivatives at $N_C/N_1 = 0.5$ are caused by the transition from method I to method II for \mathbb{T}_{31} and \mathbb{T}_{32} in LEP. The largest difference in computational costs is a factor of five, which occurs if $N_1 = N_2 = 2N_C$. With an increasing imbalance between the number of unknowns N_1 and N_2 , the computational costs of LEP decrease compared to SEP, irrespective of the common boundary size. In the limit $N_2 \gg N_1$, we have $\#\text{LEP}/\#\text{SEP} = 2.75$. The common boundary case, $N_C \neq 0$, of the embedding scheme has been applied, otherwise, we have $\#\text{LEP}/\#\text{SEP} = 5.2$ for the non-common boundary case. Hence, instead of a factor of eight, the embedding scheme based on LEP with Gram matrices is at most about five times less efficient than SEP. By contrast, if the transfer matrices in LEP are also determined with inverse propagator matrices rather than inverse Gram matrices, the computational difference between SEP and LEP is exactly a factor eight for $N_C \neq 0$. Note that there then remains a factor of four difference in memory requirements of both schemes.

Iterative solvers may yield an improvement in the computational costs regarding the construction of the transfer and elementary scattering matrices if there is a significant imbalance between the number of unknowns of the source and observation boundaries. As an example, let us consider the transfer matrix $\mathbb{T}_{21} = \mathbb{P}_{22}^{-1}\mathbb{P}_{21}$ with N_1 and N_2 unknowns on the source and observation boundaries, respectively. In the absence of common boundary parts, the corresponding computational costs for an implementation based on SEP are $N_2^3 + N_1N_2^2$, with N_2^3 from the inverse of the propagator and $N_1N_2^2$ from the subsequent matrix product. Alternatively, by means of iterative solvers the computational costs for \mathbb{T}_{21} are $N_2^2N_1N_{\text{av}}$, with N_{av} the required average number of matrix-vector products (N_2^2) for N_1 current sources. With this, iterative solvers are more efficient than a direct inverse if $N_{\text{av}} < 1 + N_2/N_1$. A ‘‘marching on in source position’’ scheme [9] may be utilized as a predictor-corrector method to reduce N_{av} considerably.

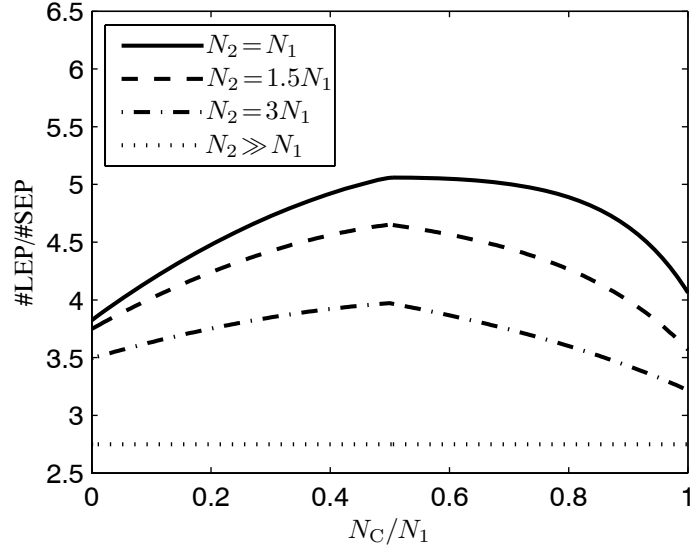


Figure 4.11: The difference in computational costs of the embedding scheme based on LEP (Gram matrices) and SEP as a function of the common boundary size for various domain sizes.

In case the boundaries have a segment in common, the balance may shift towards iterative solvers. For instance, T_{21} becomes $\begin{bmatrix} I_{21_2} & P_{22}^{-1} P_{21_3,\perp} \end{bmatrix}$ upon applying method I to the common boundary parts. Since the number of unknowns on $\partial D_{1_3,\perp}$ is approximately $N_1 - N_C$, the use of iterative solvers becomes more beneficial for T_{21} with increasing common boundary part N_C , i.e., if $N_{av} < 1 + N_2/(N_1 - N_C)$. For large values of N_C , iterative methods may also be preferred for T_{13} ($N_{av} < 1 + N_1/(N_2 - N_C)$) and T_{23} ($N_{av} < 1 + N_2/(N_1 - N_C)$). Note that a decreasing N_C favors iterative methods for T_{31} and T_{32} ($N_{av} < 1 + N_3/N_C$). The use of iterative solvers may also lead to a reduction of the computational costs for the construction of the elementary scattering matrices. For instance, in case the scattered field of the objects \mathcal{D}_o contained inside the scattering domain \mathcal{D}_1 is constructed via boundary integral equations, iterative solvers may be applied to T_{1o} and $X_{oo}^{-1} P_{o1}$ for S_{11} in Eq. (4.30).

However, it remains very difficult to estimate the break-even point in advance, as it varies with N_{av} , which in turn depends on the well-posedness of the system and thereby on the shape of the source and observation boundary, on their mutual orientation, and also on the discretization. Further, upon examining the computational schemes of the embedding process in Tables 4.1 and 4.2, it turns out that iterative solvers cannot compete with a direct inverse regarding the inverse embedding matrix $[I - RS]^{-1}$. Finally, upon comparing methods I and II, it is clear that the removal of computational redundancies in the transfer matrix may only be beneficial for iterative solvers through method I.

4.7 Local structure optimization and modification

The theory presented above can be used repeatedly to obtain operators that describe the complete *interior* and *exterior* field behavior for large finite structures. Local structure variations can be studied for optimization purposes by repeated embedding of such a large structure with a sequence of feasible inhomogeneous local domains.

Because the environment operators encompass all possible excitations, the computation time and the required storage demand will grow considerably for large structures, especially if the interior field of all subdomains is retained. However, both computation time and storage demands can be reduced significantly if the embedding of subsequent domains is restricted to a designated domain, \mathcal{D}_D , of interest. Let us elaborate on this via an example illustrated in Figure 4.12. Here, a large scattering domain \mathcal{D}_L obtained by repeated application of the embedding procedure is shown. The dotted lines indicate the common boundaries of the subdomains $\mathcal{D}_{i;L}$ that have been removed at preceding embedding stages. Let us select a designated domain, \mathcal{D}_D , which is relatively small compared to \mathcal{D}_L , and may even be multiply connected. Further, let us stipulate that the outer boundary $\partial\mathcal{D}_D$ of \mathcal{D}_D encloses both the source that excites the incident field, and the domains \mathcal{D}_E that are yet to be embedded. This restriction allows us to convert the large scattering operator S_{LL} into a reduced scattering operator S_{DD} on $\partial\mathcal{D}_D$, where S_{DD} reproduces the scattered field of \mathcal{D}_L in \mathcal{D}_D due to equivalent current distributions on $\partial\mathcal{D}_D$. Thus we would avoid the time-consuming direct embedding of \mathcal{D}_E with \mathcal{D}_L , which has a large outer boundary $\partial\mathcal{D}_L$, by considering the interaction between $\partial\mathcal{D}_D$ and $\partial\mathcal{D}_L$ across $\partial\mathcal{D}_D$ instead, thus significantly reducing computational costs. The initial composition of \mathcal{D}_L through repeated embedding is the most expensive step, while the subsequent embedding with a designated domain is very cheap, thus facilitating local structure optimization.

To obtain S_{DD} , we invoke the transfer operators, T_{DL} and T_{LD} ,

$$S_{DD} = T_{DL} S_{LL} T_{LD}, \quad (4.57)$$

which transfers the interaction from the large outer boundary $\partial\mathcal{D}_L$ to the significantly smaller boundary $\partial\mathcal{D}_D$. If N_D denotes the number of unknowns on $\partial\mathcal{D}_D$, the complexity of further embedding in \mathcal{D}_D reduces by a factor $(N_D/N_L)^2$. Because \mathcal{D}_D covers an *interior* embedding approach with respect to \mathcal{D}_E , S_{DD} corresponds to the reflection operator for the *exterior* configuration in Eq. (4.18). The embedding procedure presented in the previous sections remains valid throughout. After the embedding of \mathcal{D}_E with $\bar{\mathcal{D}}_D$, the complete currents, \mathbf{Q}_E^{cp} for \mathcal{D}_E and \mathbf{Q}_D^{cp} for $\bar{\mathcal{D}}_D$, include the interaction between \mathcal{D}_E and \mathcal{D}_L . They are readily obtained through Eq. (4.37),

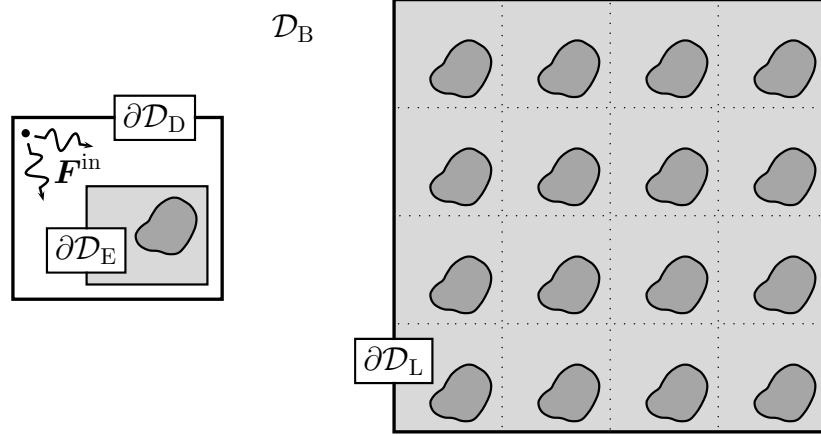


Figure 4.12: The designated domain \mathcal{D}_D for subsequent excitation variation and frequent embedding of a domain \mathcal{D}_E with a large scattering domain \mathcal{D}_L .

from the incident currents \mathbf{Q}_D^{in} and \mathbf{Q}_E^{in} due to a source distribution in $\mathcal{D}_D \cap \bar{\mathcal{D}}_E$ that generates an incident field \mathbf{F}^{in} . Introducing $\partial\mathcal{D}_3 = \partial\mathcal{D}_D \cup \partial\mathcal{D}_E$, we find that the total field in \mathcal{D}_D follows from (cf. Eq. (B.10))

$$\mathbf{F} = \begin{cases} \mathbf{P}_E \mathbf{Q}_E^{\text{cp}} + \int_{\partial\mathcal{D}_E} \mathbf{F}^{\text{sc}}(\mathbf{r}, \mathbf{r}') \mathbf{Q}^{\text{cp}}(\mathbf{r}') \, dA', & \mathbf{r} \in \mathcal{D}_E, \\ \mathbf{F}^{\text{in}} + \mathbf{P}_3 \mathbf{Q}_3^{\text{sc}}, & \mathbf{r} \in \mathcal{D}_D \setminus \mathcal{D}_E. \end{cases} \quad (4.58)$$

Note that \mathbf{S}_{DD} is only required for the embedding and the reconstruction of the complete field in \mathcal{D}_D .

The exterior field in \mathcal{D}_B and the interior field of \mathcal{D}_L can be obtained with relatively low additional costs once the ideal structure is obtained. Because incident currents \mathbf{Q}_D^{in} are only present on $\partial\mathcal{D}_D$, the (large) interior field operator \mathbf{Q}_{iL} , and the scattering operator \mathbf{S}_{LL} of \mathcal{D}_L can be reduced by a factor of N_D/N_L through application of the transfer operator, \mathbf{T}_{LD} , according to

$$\begin{aligned} \mathbf{Q}_{\text{iD}} &= \mathbf{Q}_{\text{iL}} \mathbf{T}_{\text{LD}}, \\ \mathbf{S}_{\text{LD}} &= \mathbf{S}_{\text{LL}} \mathbf{T}_{\text{LD}}, \end{aligned} \quad (4.59)$$

in which \mathbf{Q}_{iD} and \mathbf{S}_{LD} produce the respective complete *interior* and *exterior* fields in \mathcal{D}_L and $\bar{\mathcal{D}}_D \cup \bar{\mathcal{D}}_L$ due to an incident current \mathbf{Q}_D^{in} . Note that, if \mathcal{D}_D is completely enclosed by \mathcal{D}_L , i.e., $\partial\mathcal{D}_D$ is a subboundary of $\partial\mathcal{D}_L$, then the transfer operators \mathbf{T}_{LD} and \mathbf{T}_{DL} reduce to identity operators. The complete incident current \mathbf{Q}_i^{cp} for each subdomain $\mathcal{D}_{i;\text{L}}$ (e.g. the sixteen cells within $\partial\mathcal{D}_L$ in

Figure 4.12) and the scattered current \mathbf{Q}_L^{sc} are constructed from the complete current \mathbf{Q}_D^{cp} ,

$$\begin{aligned}\mathbf{Q}_i^{\text{cp}} &= \mathbf{Q}_{iD} \mathbf{Q}_D^{\text{cp}}, \\ \mathbf{Q}_L^{\text{sc}} &= \mathbf{S}_{LD} \mathbf{Q}_D^{\text{cp}}.\end{aligned}\tag{4.60}$$

The corresponding total field in $\bar{\mathcal{D}}_D$ is subsequently obtained from a relation similar to Eq. (4.58),

$$\mathbf{F} = \begin{cases} \mathbf{P}_i \mathbf{Q}_i^{\text{cp}} + \int_{\partial\mathcal{D}_{i;L}} \mathbf{F}^{\text{sc}}(\mathbf{r}, \mathbf{r}') \mathbf{Q}^{\text{cp}}(\mathbf{r}') \, dA', & \mathbf{r} \in \mathcal{D}_{i;L}, \\ \mathbf{P}_D \mathbf{Q}_D^{\text{cp}} + \mathbf{P}_L \mathbf{Q}_L^{\text{sc}}, & \mathbf{r} \in \mathcal{D}_B. \end{cases}\tag{4.61}$$

If a subdomain is frequently reused, which is very common for EBG-structures, \mathbf{F}^{sc} and \mathbf{P}_i can be reused, which accelerates the final field computations considerably.

4.8 Embedding versus direct approach

At a first glance, the performance of LEGO may seem inferior to a direct solution method due to the various matrix operations involved in the embedding process. However, an honest comparison should be based on the actual result that is obtained. We shall focus on the construction of the scattering matrix \mathbf{S}_{LL} of a large composite domain. For other types of problems, a hybrid scheme as discussed in the next section may be more appropriate. In case scattering domains are closely packed, a sequence of embedding steps may be more efficient as common boundary parts are removed in each stage. In this section, we perform a comparative assessment between embedding and a direct solution method.

As a direct solution method, we consider boundary integral equations. In principle, the choice between a boundary integral equation and embedding primarily depends on the ratio between the number of unknowns N_o for the boundary $\partial\mathcal{D}_o$ of the scattering objects \mathcal{D}_o , and the number of unknowns N_i for the enclosing boundary $\partial\mathcal{D}_i$ of the scattering domain \mathcal{D}_i . Let us assume that N_o and N_i are chosen such that the associated integral representations reproduce the pertaining field with roughly the same accuracy. Despite that the boundary $\partial\mathcal{D}_i$ of the scattering domain \mathcal{D}_i encloses the scattering objects \mathcal{D}_o , N_o may be larger than N_i , even if the boundary $\partial\mathcal{D}_o$ is smaller than $\partial\mathcal{D}_i$. This may be the case if the refractive index of \mathcal{D}_o is substantially larger than that of the background medium used in the embedding process, or if the boundary geometry of $\partial\mathcal{D}_o$ is less smooth in comparison with $\partial\mathcal{D}_i$. Note that in problems that do not involve close

packing the boundary $\partial\mathcal{D}_i$ may conveniently be chosen to be smooth. Moreover, if \mathcal{D}_o involves dielectric objects in boundary integral equations, both electric and magnetic equivalent currents are used, while either one of them suffices with embedding based on SEP.

For now, let us assume $N_o = N_i$ with a square domain shape \mathcal{D}_i , and consider the best case regarding embedding, i.e., all N_T subdomains are closely packed. If one wants to compute the full scattering matrix \mathbf{S}_{LL} by means of a direct solution method, the computational complexity of determining the associated inverse MoM matrix is $(N_T N_i)^3$. Suppose we like to construct a large finite array of scattering domains with identical elements. In embedding, we first electromagnetically characterize a single element as the elementary scattering domain and repeatedly combine that domain with itself. Thus, after n successive embedding steps, the obtained structure contains $N_T = 2^n$ elements. Common boundaries are removed in each embedding step. In this way, with each following embedding step the outer domain boundaries of the successive composite scattering matrices become smaller in relation to the corresponding structure size $N_T N_i$ in the direct solution method, which may favor the embedding approach.

In Figure 4.13, we have illustrated the total computational costs of successive embedding steps versus those of the direct boundary integral solver as a function of the number of elements N_T of the complete structure with SEP for 2D and 3D closely packed structures. Square elementary scattering domains have been employed. For the computational costs of each embedding step, the complexity of the matrix operations in Tables 4.1 has been used. The total costs of embedding at each stage include that of prior embedding steps. The difference in convergence rate is due to fact that N_C/N_1 for each embedding step is smaller for the 3D case. The complexity of the direct solver varies as $\mathcal{O}(N^3)$ with respect to the number of array elements N_T , whereas for both embedding based on SEP we have $\mathcal{O}(N^{1.5})$ and $\mathcal{O}(N^2)$ for the 2D and 3D case, respectively. Hence, if $N_o = N_i$, embedding based on SEP may be more efficient than a direct solver after two and three embedding steps for the 2D and 3D case, respectively.

The LEGO approach may also be more efficient than a direct boundary integral solver in conjunction with ordinary iterative methods, viz., although the corresponding complexity of the direct solver will reduce to $\mathcal{O}((N_i N_T)^2 N_{av})$ with N_{av} the number of matrix vector products, it remains an $\mathcal{O}(N^2)$ process. The multi-level fast-multipole methods are faster as they only require about $\mathcal{O}(N_{av} N_i N_T \log(N_i N_T))$ operations for problems involving a single source and $\mathcal{O}(N_{av} N_i^2 N_T^2 \log(N_i N_T))$ for the scattering matrix \mathbf{S}_{LL} . However, the intermediate results in the LEGO procedure may be very useful if stored in a library. Further it is possible to incorporate the multi-level fast-multipole ideas into the LEGO procedure for additional acceleration. Fur-

ther, as discussed in Section 4.6, iterative solvers may also accelerate the embedding process. For an elementary domain with a square boundary, the common boundary size alternates between $N_C = N_1/4$ and $N_C = N_1/3$ in the 2D case for successive embedding steps due to the square boundary shape. For the 3D case, the common boundary size changes as, $N_C = N_1/6$, $N_C = N_1/5$ and $N_C = N_1/4$. These variations resulted in small ripples in the embedding curves that become weaker as the number of subdomains increases. With reference to Section 4.6, instead of a factor of 5, LEP is only a factor of 4.7 and 4.4 less efficient than SEP because for the 2D and 3D case, respectively, $N_C < N_i/2$.

If $N_o \neq N_i$, the curve of the direct solver shifts upwards due to the multiplication by the constant factor of $(N_o/N_i)^3$. For instance, with $N_C = N_1/4$ in the 2D case, one embedding step with SEP or LEP is more efficient than a direct approach if $(N_o/N_i) > 2.6$ or $(N_o/N_i) > 12$, respectively. For the non-common boundary case, these factors are 2.1 and 11 for SEP and LEP, respectively.

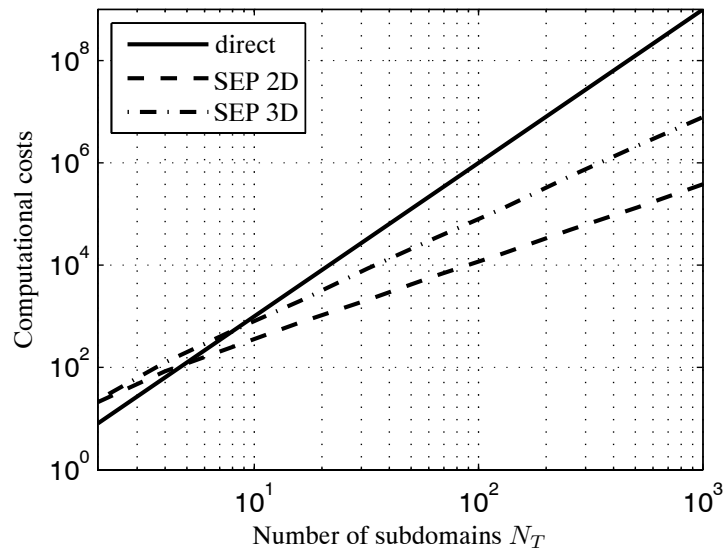


Figure 4.13: The computational costs (normalized with N_i^3) of the direct boundary integral solver and of the embedding based on SEP 2D and SEP 3D versus the number elements N_T .

Next, let us compare the required memory costs of the embedding and direct approach. Since an embedding step involves several matrix multiplications, we consider the complete workspace that is required. In accordance with Section 4.6, the size of the workspace for SEP is $3(N_1 + N_2)^2$. For LEP the size is four times larger. The workspace includes the starting and composite scattering operator(s). Although this is considerably larger than the storage demand of a MoM matrix of the scattering objects \mathcal{D}_o enclosed by \mathcal{D}_1 and \mathcal{D}_2 , the removal of common boundaries in

an embedding step reduces the memory requirement for following steps. In Figure 4.14 the memory costs of successive embedding steps versus those of the direct boundary integral solver are illustrated as a function of the number of elements N_T of the complete structure. The memory costs of embedding increase with $\mathcal{O}(N)$, and $\mathcal{O}(N^{1.3})$ for the 2D and 3D case, respectively, whereas those of the direct solver increase with $\mathcal{O}(N^2)$. Similar to Figure 4.13, the curve of the direct solver shifts upwards if $N_o \neq N_i$, due to multiplication by the constant factor $(N_o/N_i)^3$. However, because the complete workspace of the embedding process is considered rather than for the composite scattering only, the break-even point shifts slightly in favor of the direct approach.

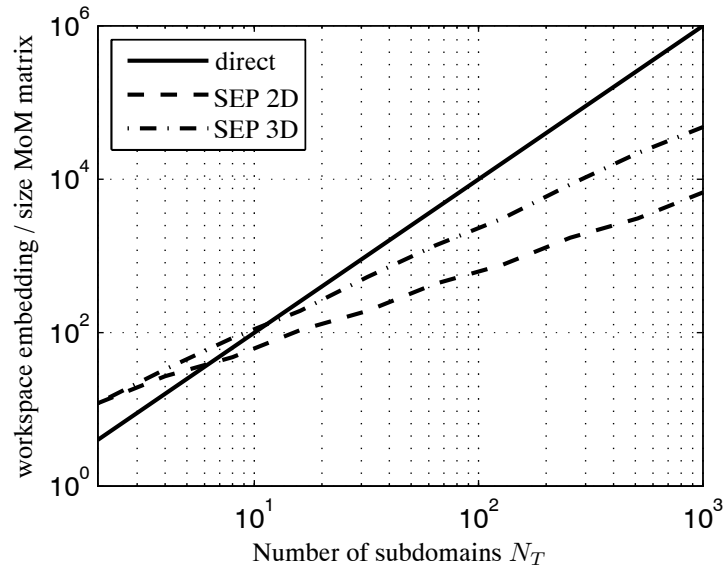


Figure 4.14: The memory requirements (normalized with N_i^2) of the direct boundary integral solver and of the embedding based on SEP 2D and SEP 3D versus the number elements N_T .

As a final remark we comment on the additional memory and computational costs in case the interior field operators of all previously combined subdomains are updated and stored. Since we consider a closely packed structure, this update process becomes dominant, as has been argued in Section 4.6. By taking the update process into account, the computational and memory costs for the 2D case increase to $\mathcal{O}(N^{1.8})$ and $\mathcal{O}(N^{1.4})$, respectively. For the 3D the computational and memory costs increase to $\mathcal{O}(N^{2.2})$ and $\mathcal{O}(N^{1.6})$. Compared with Figure 4.13 and Figure 4.14, the magnitude of the costs with two subdomains remains unchanged, as there is no update process involved with the first embedding step.

4.9 Extension to hybrid methods

So far, all field calculations are based on boundary integral equations. This includes the construction of the scattering matrices for the elementary building blocks. In this section, we discuss the extension of LEGO towards a hybrid variety. The hybridization of LEGO applies in two ways. First, various electromagnetic solution methods may be incorporated in the LEGO approach. In particular, the scattering matrix of an elementary scattering domain will be constructed via the dyadic Green's function of the enclosed medium that can be obtained by various techniques, e.g., a finite-element method, or a domain integro-differential equation, and it allows for acceleration techniques employed in the multi-level fast-multipole algorithm. The availability of alternative electromagnetic solution methods entails that inhomogeneous scatters may be considered as well. Further, owing to the freedom to choose the electromagnetic solver that is best suited for the computation of the pertaining scattered field, the flexibility of the LEGO method increases.

Second, the LEGO approach can be integrated with existing software design packages. In particular, the optimization step of LEGO presented in Section 4.7, which is ideal for rapid structure optimization for design purposes, can be employed as an additional design tool.

Let us discuss a hybrid method for the determination of the elementary scattering matrices. In general, the scattering matrix follows from the discretization of the scattering operator in Eq. (4.10) after the substitution of Eq. (4.11),

$$\mathbf{S}_{11} = \mathbf{P}_{11}^{-1} \mathbf{F}_{11}^{\text{sc}}. \quad (4.62)$$

With reference to the discretization step in Section 4.4, the field matrix $\mathbf{F}_{11}^{\text{sc}}$ describes the scattered field response of the objects in \mathcal{D}_1 in terms of field and current amplitudes, obtained using test and expansion functions on $\partial\mathcal{D}_1$, respectively. In accordance with Eq. (4.27), $\mathbf{F}_{11}^{\text{sc}}$ follows from the constituents

$$\mathbf{F}_{11}^{\text{sc}} = \begin{bmatrix} \mathbf{E}_{11}^{\text{M}} & \mathbf{E}_{11}^{\text{J}} \\ \mathbf{H}_{11}^{\text{M}} & \mathbf{H}_{11}^{\text{J}} \end{bmatrix}^{\text{sc}}. \quad (4.63)$$

In Section 4.2, Eq. (4.12) has been applied to obtain $\mathbf{F}_{11}^{\text{sc}}$ via boundary integral equations, which led to Eq. (4.30) for the scattering matrix \mathbf{S}_{11} . The elements of the submatrices of $\mathbf{F}_{11}^{\text{sc}}$, may be obtained alternatively through a more general approach. Via a test and expansion procedure, the electric field submatrices in Eq. (4.63) may be written as

$$\begin{bmatrix} \mathbf{E}_{11}^{\text{M}} \\ \mathbf{E}_{11}^{\text{J}} \end{bmatrix}_{mn} = \left\langle \mathbf{f}_m^E(\mathbf{r}), \int_{\partial\mathcal{D}_1} \begin{bmatrix} \bar{\mathbf{G}}_1^{EM}(\mathbf{r}, \mathbf{r}') \cdot \mathbf{f}_n^M(\mathbf{r}') \\ \bar{\mathbf{G}}_1^{EJ}(\mathbf{r}, \mathbf{r}') \cdot \mathbf{f}_n^J(\mathbf{r}') \end{bmatrix} dA' \right\rangle_{\partial\mathcal{D}_1}. \quad (4.64)$$

The dyadic Green's functions $\bar{\bar{\mathbf{G}}}_1$ provide the scattered field response of the medium enclosed by $\partial\mathcal{D}_1$ and are defined according to the definitions in Section 2.7. The magnetic field amplitudes follow by duality. The unknown dyadic Green's functions for $\{\mathbf{r}, \mathbf{r}'\} \in \partial\mathcal{D}_1$ may be determined by other electromagnetic solvers. More specifically, for each electric and magnetic surface current expansion function, the electric and magnetic field has to be determined for all test functions. Recall that to obtain the complete field in \mathcal{D}_1 after a sequence of embedding steps, the initial scattered field $\mathbf{F}_1^{\text{sc}}(\mathbf{r})$ for $\mathbf{r} \in \mathcal{D}_1$ is required. This field readily follows from the right-hand side of Eq. (4.64) upon omitting the test procedure.

Next, a hybrid variety is presented for the local structure optimization and modification of large domains as introduced in Section 4.7. In principle, the construction of a scattering matrix \mathbf{S}_{LL} of a large domain \mathcal{D}_L prior to the optimization step can alternatively be obtained through Eqs. (4.62–4.64). However, the subsequent reduction of \mathbf{S}_{LL} to a \mathbf{S}_{DD} for optimization purposes in a relatively small designated domain \mathcal{D}_D can be performed in a more direct and efficient approach. Namely, \mathbf{S}_{DD} may be constructed directly. This principle is illustrated in Figure 4.15. The configuration corresponds with that of Figure 4.4 in the general embedding step where \mathcal{D}_2 is adjacent to \mathcal{D}_1 , even though \mathcal{D}_1 completely encloses \mathcal{D}_2 here. Hence, the embedding process applies throughout, albeit that the incident field is generated by sources in $\bar{\mathcal{D}}_1 \cap \bar{\mathcal{D}}_2$.

With reference to the original optimization step presented in Figure 4.7, the designated domain \mathcal{D}_D corresponds with $\bar{\mathcal{D}}_1$, while the domain \mathcal{D}_E used for repeated embedding steps is associated with \mathcal{D}_2 . The reduced scattering matrix \mathbf{S}_{DD} that produces in \mathcal{D}_D the scattered field of the large scattering domain \mathcal{D}_L thus corresponds with \mathbf{S}_{11} . Hence, the construction of \mathbf{S}_{DD} can be determined directly in combination with alternative electromagnetic solvers. In fact, the optimization step may be included as an additional tool into existing simulation packages.

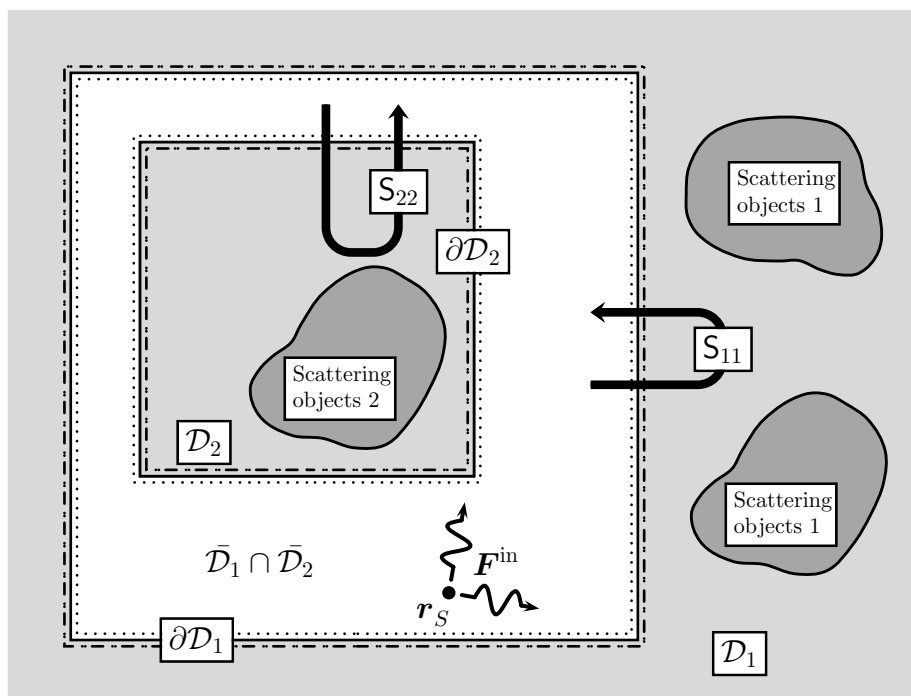


Figure 4.15: The domain \mathcal{D}_1 completely encloses \mathcal{D}_2 . The source distribution that generates the impressed incident field is located in $\bar{\mathcal{D}}_1 \cap \bar{\mathcal{D}}_2$.

Chapter 5

2D scattering objects

In this chapter, the integral equations for the scattering from two-dimensional (2D) objects are investigated. In Section 4.4, the fundamental propagator operator of the LEGO approach has been discretized. This was based on the discretized integral operators discussed in detail below. The insight that is gained through the investigation of the integral equations for perfectly conducting and dielectric objects has been used in the LEGO approach to attain maximum performance, through an optimal choice of the equivalence principle, the domain shape, the mesh density, the quadrature rule and the test and expansion functions. Furthermore, the integral equations can also be employed to construct the elementary scattering operators in the LEGO approach.

5.1 Introduction

For 2D configurations, the distribution of matter and sources is uniform in a certain direction. In Section 5.2, this invariance is exploited to simplify a 2D scattering problem by subdividing Maxwell's equations into transverse electric (TE) and transverse magnetic (TM) subsystems. Next, we specialize the mapping properties of the integral operators to the 2D case and derive the restrictions on the choice of test and expansion function in Section 5.3. Subsequently, by discretizing the electric and magnetic field equations on a flat-faceted mesh we model the scattering from electric and magnetic perfect conductors for the TM case. The pertaining discretized integral operators are then used to discretize the PMCHW and the Müller boundary integral formulations. Besides the well-known impedance scaling for the fields and currents, we propose an

additional scaling for Müller's equation to reduce the condition number of the associated MoM matrix. To minimize computational costs, we aim at maximum efficiency in the computation of the MoM-matrix elements. The parts of the test and/or expansion integrals that become singular when the source and observation points coincide are integrated analytically in Section 5.4. This amounts to double integrals for the MoM-matrix elements. For the self term, we apply analytic solutions for the double integrals in terms of Bessel function series constituents.

In Section 5.5, we investigate the solvability and the order of convergence of the numerical approximation for the special case of scattering from perfect electric conductors. In particular, we consider the dependence on the object shape, the applied mesh density and the interior resonance effect in combination with a CFIE formulation. Furthermore, we consider the impact of domain scaling for smooth object boundaries that have been approximated with a flat-faceted mesh. In Section 5.6, we introduce regularization of the identity operator in the MFIE to improve the effective smoothness of the test and expansion functions. The EFIE and MFIE for the TE case are discussed in Section 5.7, by considering the dual problem of the scattering from a perfect magnetic conductor for the TM case. Finally, we extend the analysis to dielectric scatterers in Section 5.8. In addition to the PMCHW and Müller formulations, an alternative boundary integral equation is proposed that has unique mapping properties regarding the order of convergence. Further, we investigate the dependence on the refractive index and the improvement of the solvability of Müller's formulation owing to the proposed additional scaling.

5.2 TE/TM decomposition

In a homogeneous, isotropic medium the electromagnetic fields can be expressed in terms of two scalar functions, weighted by the sources. This follows immediately from a decomposition of the fields, i.e., each field vector can be decomposed into a component along a certain predefined constant direction, and a component transverse to this direction. Depending on the spatial distribution of sources, it is possible that only one of these components remains, while the other one is zero everywhere.

A configuration is regarded as a two-dimensional (2D) configuration, if the distribution of matter and sources is uniform (invariant) in a certain direction, referred to as the longitudinal direction. A 2D scattering object is therefore automatically cylindrical in this direction. The derivation of the corresponding scattered-field distribution can be made much simpler by taking this particular

geometrical property into consideration from the outset. For 2D configurations, it is common to let the z -axis point in the longitudinal direction. In turn, normal to this direction, we define the so-called transverse plane, as a plane for which z is arbitrary but fixed. Accordingly, we decompose the vector quantities into their transverse and longitudinal components as

$$\begin{cases} \mathbf{E} = \mathbf{E}_t + E_z \hat{\mathbf{z}}, \\ \mathbf{H} = \mathbf{H}_t + H_z \hat{\mathbf{z}}, \end{cases} \quad \text{and} \quad \begin{cases} \mathbf{M} = \mathbf{M}_t + M_z \hat{\mathbf{z}}, \\ \mathbf{J} = \mathbf{J}_t + J_z \hat{\mathbf{z}}, \end{cases} \quad (5.1)$$

for the fields and sources, respectively. The vector-subscript, t , is used to indicate that the orientation is parallel to the transverse plane. The associated position vector is also decomposed, viz., $\mathbf{r} = \boldsymbol{\rho} + z\hat{\mathbf{z}}$, with $\boldsymbol{\rho} = x\hat{\mathbf{x}} + y\hat{\mathbf{y}}$ being the position vector in the transverse plane. The corresponding decomposition of the ∇ -operator reads, $\nabla = \nabla_t + \partial_z \hat{\mathbf{z}}$, where $\nabla_t = \partial_x \hat{\mathbf{x}} + \partial_y \hat{\mathbf{y}}$. A subsequent restriction to fields that are invariant in the z -direction is accounted for by setting $\partial_z \equiv 0$, and hence $\nabla \rightarrow \nabla_t$.

An important consequence of Maxwell's equations is that the transverse fields and sources may then be written entirely in terms of the longitudinal fields and sources, and vice versa. Namely, with the simplifications above, Maxwell's equations (2.11), may be subdivided into the parts

$$\nabla_t \times \mathbf{H}_t = s\epsilon E_z \hat{\mathbf{z}} + J_z \hat{\mathbf{z}}, \quad (5.2a)$$

$$-\nabla_t \times (E_z \hat{\mathbf{z}}) = s\mu \mathbf{H}_t + \mathbf{M}_t, \quad (5.2b)$$

and,

$$\nabla_t \times (H_z \hat{\mathbf{z}}) = s\epsilon \mathbf{E}_t + \mathbf{J}_t, \quad (5.3a)$$

$$-\nabla_t \times \mathbf{E}_t = s\mu H_z \hat{\mathbf{z}} + M_z \hat{\mathbf{z}}. \quad (5.3b)$$

Eqs. (5.2) and (5.3) constitute independent coupled systems of partial differential equations that may be solved separately. The first system, Eq. (5.2), describes the *Transverse Magnetic* (TM) case, since the magnetic field contains only transverse components, whereas the latter system, Eq. (5.3), describes the *Transverse Electric* (TE) case, since the electric field contains only transverse components. The composite case readily follows from a linear combination of the two. Note that with the inclusion of magnetic sources, by duality, the TE case readily follows from the TM case and vice versa.

The 3D integral representation, Eq. (2.43), which describes the fields in space generated by a volume source density is also applicable for the 2D case, although the volume integrals reduce to surface integrals with line, instead of point source distributions. The corresponding dyadic

Green's function, Eq. (2.42), becomes

$$\bar{\bar{\mathbf{G}}}_v(\boldsymbol{\rho}, \boldsymbol{\rho}') \equiv \left[\bar{\bar{\mathbf{I}}} - \frac{1}{\gamma_v^2} \nabla_t \nabla_t \right] G_v(\boldsymbol{\rho}, \boldsymbol{\rho}'), \quad (5.4)$$

with medium index v , and $G_v(\boldsymbol{\rho}, \boldsymbol{\rho}')$ being the scalar 2D Green's function which is the line source solution of the modified scalar Helmholtz equation,

$$[\nabla_t^2 - \gamma_v^2] G_v(\boldsymbol{\rho}, \boldsymbol{\rho}') = -\delta(\boldsymbol{\rho} - \boldsymbol{\rho}'). \quad (5.5)$$

and satisfies the radiation conditions (2.22). The scalar Green's function is given by

$$G_v(\boldsymbol{\rho}, \boldsymbol{\rho}') = \frac{1}{2\pi} K_0(\gamma_v |\boldsymbol{\rho} - \boldsymbol{\rho}'|). \quad (5.6)$$

Here, $K_0(z)$ represents the zeroth-order modified bessel function of the second kind with complex argument z (see also Appendix B.1).

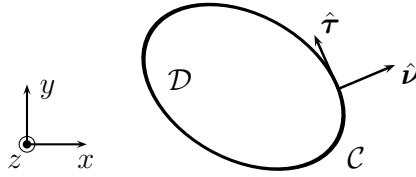


Figure 5.1: The vector orientation of a 2D configuration uniform in the \hat{z} -direction. The unit vectors $\hat{\nu}$ and $\hat{\tau}$ are respectively, directed, normally and tangentially in a counter-clockwise fashion to the boundary contour \mathcal{C} of \mathcal{D} .

The initially three-dimensional integral operators L and K, Eq. (3.7), are easily transformed into their 2D counterparts. Regarding the arbitrarily shaped scattering object depicted in Figure 3.1, the 2D versions of L and K involve a cylinder with an arbitrary cross-section. The boundary $\partial\mathcal{D}$ restricted to the transverse plane collapses into a boundary contour \mathcal{C} with an outward unit normal vector $\hat{\nu}$. Further, we introduce the unit vector, $\hat{\tau}$, also situated in the transverse plane, but tangential to \mathcal{C} and oriented CCW such that $\hat{z} = \hat{\nu} \times \hat{\tau}$, for $\boldsymbol{\rho} \in \mathcal{C}$. Similar definitions as in Eq. (2.62) are utilized for the equivalent boundary currents tangential to \mathcal{C} . After carrying out the outer products with $\hat{\nu}$, the definition of the equivalent currents, Eq. (2.62), for the TM case are

$$J_z = -H_\tau, \quad (5.7a)$$

$$M_\tau = -E_z, \quad (5.7b)$$

for $\boldsymbol{\rho} \in \mathcal{C}$. Hence, the boundary integral operators, Eq. (3.7), operating on an electric equivalent current read

$$\mathbf{L}_v(\boldsymbol{\rho})\mathbf{J} = \gamma_v \hat{\mathbf{z}} \int_{\mathcal{C}} J_z(\boldsymbol{\rho}') G_v(\boldsymbol{\rho}, \boldsymbol{\rho}') d\ell', \quad (5.8a)$$

$$\mathbf{K}_v(\boldsymbol{\rho})\mathbf{J} = \int_{\mathcal{C}} [J_z(\boldsymbol{\rho}') \hat{\mathbf{z}}] \times \nabla'_t G_v(\boldsymbol{\rho}, \boldsymbol{\rho}') d\ell', \quad (5.8b)$$

where γ_v represents the propagation coefficient for medium index v defined in Eq. (4.11). The operator \mathbf{L} consists of a vector potential constituent only, because the (transverse) divergence of $J_z \hat{\mathbf{z}}$ in the scalar potential is zero. For the magnetic equivalent current, we have

$$\mathbf{L}_v(\boldsymbol{\rho})\mathbf{M} = \gamma_v \int_{\mathcal{C}} M_\tau(\boldsymbol{\rho}') \hat{\boldsymbol{\tau}}' G_v(\boldsymbol{\rho}, \boldsymbol{\rho}') d\ell' - \frac{1}{\gamma_v} \nabla'_t \int_{\mathcal{C}} [\partial_{\tau'} M_\tau(\boldsymbol{\rho}')] G_v(\boldsymbol{\rho}, \boldsymbol{\rho}') d\ell', \quad (5.9a)$$

$$\mathbf{K}_v(\boldsymbol{\rho})\mathbf{M} = \int_{\mathcal{C}} [M_\tau(\boldsymbol{\rho}') \hat{\boldsymbol{\tau}}'] \times \nabla'_t G_v(\boldsymbol{\rho}, \boldsymbol{\rho}') d\ell', \quad (5.9b)$$

where the divergence of $M_\tau \hat{\boldsymbol{\tau}}$ in the scalar potential has reduced to a spatial derivative ∂_τ . Upon recalling that magnetic sources are fictitious and are only introduced for the construction of computational schemes, the *original* TM and TE case involve only J_z and J_τ sources, respectively. Since their magnetic source counterparts follow by duality, we point out that the mapping properties of the integral operators involving M_τ (TM case) thus fully correspond with J_τ of the original TE case.

5.3 Discretization

In the original TM case, the operator \mathbf{L} contains only the vector potential because the divergence of $J_z \hat{\mathbf{z}}$ in the scalar potential is zero. Regarding the mapping properties of \mathbf{L} , the general case has been handled by Costabel [69]. It was shown that if \mathbf{L} is considered as a mapping from $H^{-1/2}(\partial\mathcal{D})$ to $H^{1/2}(\partial\mathcal{D})$, then the general strategy for the EFIE, outlined in Section 3.7, holds, and the coercive part \mathbf{B} can be associated with Green's function in the static case. The advantage of this framework is twofold. First, $H^{-1/2}(\partial\mathcal{D})$ can be associated with the trace of functions that represent locally finite energy on a domain and therefore the finite-energy assumption that is required for uniqueness [70, Chapter 9] is automatically satisfied. By the trace of a function or distribution, defined on a domain, we mean the restriction of the function to the boundary of that

domain. Second, $H^{1/2}(\partial\mathcal{D})$ can be identified as the dual space of $H^{-1/2}(\partial\mathcal{D})$ if the $\mathcal{L}^2(\partial\mathcal{D})$ -inner product is extended to $\langle H^{-1/2}(\partial\mathcal{D}), H^{1/2}(\partial\mathcal{D}) \rangle$. As a result, the Galerkin method, with testing and expansion functions that belong to $H^{-1/2}(\partial\mathcal{D})$, can be applied on the computationally straightforward $\mathcal{L}^2(\partial\mathcal{D})$ -inner product. Since $\mathcal{L}^2(\partial\mathcal{D})$ is a subspace of $H^{-1/2}(\partial\mathcal{D})$, there are, in analogy with the MFIE case, no continuity restrictions for the testing and expansion functions.

With respect to the original TE case, the situation is somewhat more complex, as spatial derivatives act on the vector potential, which amount to a nonzero scalar potential. The most elegant framework is obtained by considering the mixed-potential formulation. In that case, all differential operators are tangential with respect to the boundary and a symmetric form between expansion and testing space is obtained. Since the part with the scalar potential contains a tangential derivative that acts on the current density and a tangential derivative that acts on the scalar potential, the function space for the current density, that corresponds to an electromagnetic field with locally finite energy on a domain, corresponds to $H^{1/2}(\partial\mathcal{D})$. The function space $H^{1/2}(\partial\mathcal{D})$ is extremely close to the space of continuous functions [71, p. 45]. Therefore, the testing and expansion functions could just be considered continuous in any practical case. The coercive part is also slightly more involved compared to the TM case. For all functions in $H^{1/2}(\partial\mathcal{D})$ that are orthogonal to the constant-current distribution, the singular static Green's function part of the scalar potential acts as the coercive part of the operator, while the remaining terms are compact. This indicates that the case of a constant-current distribution should be considered separately, to show that the integral operator is invertible. For the constant-current distribution, the part of the scalar potential is absent and only the vector potential remains. The invertibility of this part now follows directly from the TM case. This constant-current distribution amounts to instabilities in the time-domain [72, Sec. 3.2.3].

Before suitable test and expansion functions are introduced, we first discretize the boundary. In Figure 5.2, a fragment of a discretized boundary is shown with a piecewise flat faceted discretization consisting of connecting edge elements, Γ_n . The edge number n ascends in the direction $\hat{\tau}$, oriented counter clockwise (CCW) along the contour \mathcal{C} , which describes the boundary $\partial\mathcal{D}$ in the transverse plane. Let the coordinate vector of the first node associated with element n be denoted as ρ_n^1 , and the second as ρ_n^2 . For the corresponding edge length, L_n , we have $L_n = |\rho_n^2 - \rho_n^1|$. Further, ρ_n^c represents the position vector of the center of the edge, such that, $\rho_n^c = (\rho_n^1 + \rho_n^2)/2$. The orientation of each edge element Γ_n is specified by the unit-amplitude vectors, $\hat{\tau}_n$, and $\hat{\nu}_n$, that are tangential and normal to Γ_n , respectively. Note that these vectors are fixed for $\rho \in \Gamma_n$, and that $\hat{z} = \hat{\nu}_n \times \hat{\tau}_n$.

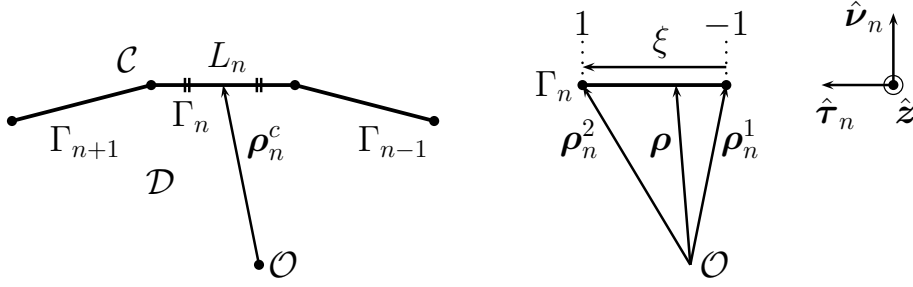


Figure 5.2: The discretization of a contour \mathcal{C} with a flat faceted mesh in terms of connecting edge elements, Γ_n (expansion), ascending in a CCW fashion with $\xi \in [-1, 1]$. For the edges related to the test functions (subscript m), η is used instead of ξ .

As asserted in Section 3.6, if the original boundary is smooth, our discretized flat faceted boundary, referred to as the mesh, will pose a mere approximation. In that case, we choose to let the start and end points of the edges, $\rho_n^{1,2}$, coincide with the smooth boundary. Although the mesh will converge to the actual boundary upon subsequent refinement, this discrepancy may affect, especially for a coarse mesh, the approximation of the equivalent currents and thereby also the associated scattered fields.

In 2D, an edge element can be directly associated with a specific test or expansion function. Therefore, to distinguish between the edges associated with the test and expansion function, we apply the same subscript $\{m, n\}$ to the edge elements. Henceforth, Γ_m and Γ_n are referred to as the observation and the source edge, respectively. The position vector $\rho \in \mathcal{C}$ is parameterized in terms of a position vector $\rho_{m,n}$ on the edge $\Gamma_{m,n}$ as illustrated on the right in Figure 5.2. Accordingly, the observation ρ_m and source ρ_n positions on the respective, test and expansion edges are decomposed in terms of the fixed vectors ρ^c and $\hat{\tau}$,

$$\rho_n = \rho_n^c + \xi d_n \hat{\tau}_n, \quad (5.10a)$$

$$\rho_m = \rho_m^c + \eta d_m \hat{\tau}_m, \quad (5.10b)$$

with the normalized local coordinates $\{\eta, \xi\} \in [-1, 1]$, and the length d_i defined as half the edge length, $d_i \equiv L_i/2$ for $i = \{m, n\}$. Keep in mind that although $\{\eta, \xi\}$ are associated with the test and expansion function, respectively, they each involve a *single* edge element. For the transformation of the corresponding test and expansion integrals to this local coordinate system,

we have,

$$\int_{\Gamma_m} \int_{\Gamma_n} g(\boldsymbol{\rho}, \boldsymbol{\rho}') d\ell' d\ell = d_m d_n \int_{-1}^1 \int_{-1}^1 g(\boldsymbol{\rho}_m, \boldsymbol{\rho}_n) d\xi d\eta. \quad (5.11)$$

Note that, although a range $[0, 1]$ is commonly used for normalized coordinates, our choice is more suitable for the general analysis presented in Section 5.4 and Appendix A, in view of the fact that ξ and η are symmetric functions with respect to the center of an edge element.

We discuss the discretization process for the TM case only, since the TE case readily follows by duality, as both electric and magnetic equivalent currents are considered. The first discretization step involves the expansion of the equivalent currents. For this purpose, we employ the 2D-version of the general expansion given by Eq. (3.32), with \mathbf{f}_n^J and $Z_1 \mathbf{f}_n^M$. Since $\mathbf{J} = J_z \hat{\mathbf{z}}$ and $\mathbf{M} = M_\tau \hat{\boldsymbol{\tau}}$ for the TM case, the expansion functions are scalars,

$$\mathbf{f}_n^J(\boldsymbol{\rho}) = f_n^J(\boldsymbol{\rho}) \hat{\mathbf{z}}, \quad (5.12a)$$

$$\mathbf{f}_n^M(\boldsymbol{\rho}) = f_n^M(\boldsymbol{\rho}) \hat{\boldsymbol{\tau}}. \quad (5.12b)$$

In view of Eqs. (5.8) and (5.9), we have, $f_n^J \sim J_z$, and $f_n^M \sim M_\tau$.

Since the second discretization step implies a testing procedure, we take, similar to Eq. (3.35), $Y_1 \hat{\boldsymbol{\nu}} \times \mathbf{f}_m^E$ and $\hat{\boldsymbol{\nu}} \times \mathbf{f}_m^H$ for the respective electric and magnetic integral equations. Under the assumption that \mathbf{f}_m contains components tangential to $\partial\mathcal{D}$ only, we may write

$$\langle \hat{\boldsymbol{\nu}} \times \mathbf{f}_m, \hat{\boldsymbol{\nu}} \times \mathbf{A} \rangle = \langle \mathbf{f}_m, \mathbf{A} \rangle. \quad (5.13)$$

Thus, \mathbf{f}_m acts directly on the components of the associated field vector \mathbf{A} tangential to $\partial\mathcal{D}$. Since the electric field is oriented in the $\hat{\mathbf{z}}$ direction, and the magnetic field is parallel to the transverse plane, proper testing demands that the direction of the corresponding test function is consistent with the single non-vanishing TM field component tangential to $\partial\mathcal{D}$. Accordingly, we have,

$$\mathbf{f}_m^E(\boldsymbol{\rho}) = f_m^E(\boldsymbol{\rho}) \hat{\mathbf{z}}, \quad (5.14a)$$

$$\mathbf{f}_m^H(\boldsymbol{\rho}) = f_m^H(\boldsymbol{\rho}) \hat{\boldsymbol{\tau}}. \quad (5.14b)$$

Hence, in 2D both the test and expansion functions reduce to scalar functions.

Subsequently, for the scalar expansion functions, $f_n^{J,M}$, we consider, $f_n(\boldsymbol{\rho}) = \{\wedge_n, \square_n\}(\boldsymbol{\rho})$, where \wedge_n is a piecewise linear function and \square_n is a piecewise constant one, referred to as triangle

and pulse expansion functions, respectively. An illustration of both expansion functions is given in Figure 5.3. The same functions also apply for the scalar test functions $f_m^{E,H}$ upon replacing the subscript “ n ” with “ m ”. It is clear that \square_n is directly associated with the edge Γ_n . However, \wedge_n stretches out over two edges. In our approach, we choose $\Gamma_n^+ \equiv \Gamma_n$, such that \wedge_n and \wedge_{n+1} are both nonzero on Γ_n . In this manner, the triangles lag behind with respect to the edge elements, i.e., \wedge_n has next to Γ_n also a contribution on Γ_{n-1} . Accordingly, the pulse and triangle expansion functions on a source edge are in local coordinates defined as

$$\square_n = \begin{cases} 1, & \text{for } \boldsymbol{\rho} \in \Gamma_n, \\ 0, & \text{elsewhere,} \end{cases} \quad \wedge_n = \begin{cases} \frac{1}{2}(1 \mp \xi), & \text{for } \boldsymbol{\rho} \in \Gamma_n^\pm, \\ 0, & \text{elsewhere,} \end{cases} \quad (5.15)$$

with $\xi \in [-1, 1]$.



Figure 5.3: The expansion function, f_n (solid), on the boundary \mathcal{C} , with on the left the pulse, \square_n , and on the right the triangle, \wedge_n . The neighboring expansion functions are dotted.

To obtain expressions for the various combinations of operators and test/expansion functions, we start with the EFIE concerning the scattering from a PEC, as described in Section 3.3. Accordingly, upon testing the EFIE, Eq. (3.14), with $Y_1 \hat{\boldsymbol{\nu}} \times \mathbf{f}_m^E$, expanding \mathbf{J} with \mathbf{f}_n^J , and subsequently applying Eq. (5.13), we arrive at

$$\sum_{n=1}^N \langle \mathbf{f}_m^E, \mathbb{L}_1 \mathbf{f}_n^J \rangle J_n = -Y_1 \langle \mathbf{f}_m^E, \mathbf{E}_1^{\text{in}} \rangle, \quad (5.16)$$

for $\boldsymbol{\rho} \in \mathcal{C}$, and $m = 1, \dots, N$. This system of linear algebraic equations can also be conveniently written in matrix form as

$$\mathbb{L}_1^{EJ} \mathbf{J} = -Y_1 \mathbf{E}_1^{\text{in}}. \quad (5.17)$$

We have obtained an approximation for \mathbb{L} , in the sense that \mathbb{L} follows from a projection of \mathbb{L} onto a subspace of $\mathcal{R}(\mathbb{L})$ spanned by the testing functions \mathbf{f}_m via the duality product. Since \mathbb{L} also operates on an expanded current distribution, \mathbb{L}_1^{EJ} , represents a matrix, called the MoM-matrix.

The typewriter font indicates the matrix form representation. A matrix element, $\mathbb{L}_{1;mn}^{EJ}$, represents the combination of substituting the m^{th} test and n^{th} expansion functions in Eq. (5.17). The superscript “ EJ ” indicates that \mathbb{L}_1 is tested in an electric field integral equation with an equivalent electric current. Similarly, the excitation vector, \mathbb{E}_1^{in} , follows from testing the incident electric field component that is tangential to $\partial\mathcal{D}$. In addition, \mathbb{J} is a column vector, whose components \mathbb{J}_n , are the unknown electric current coefficients J_n , which follow from a duality product, albeit with expansion functions. Finally, the remaining subscript “1” in Eq. (5.17) signifies the used medium index.

In view of Eq. (5.8a), \mathbb{L} involves only the vector potential as the divergence involved with the scalar potential is zero. Upon substituting Eqs. (5.12a) and (5.14a), for the respective expansion and test functions, the following expression is obtained for

$$\mathbb{L}_{v;mn}^{EJ} = \langle \mathbf{f}_m^E, \mathbb{L}_v \mathbf{f}_n^J \rangle = \gamma_v \int_{\mathcal{C}_m} f_m^E(\boldsymbol{\rho}) \int_{\mathcal{C}_n} f_n^J(\boldsymbol{\rho}') G_v(\boldsymbol{\rho}, \boldsymbol{\rho}') d\ell' d\ell \quad (5.18)$$

for a general medium index v . If triangle test and expansion is applied, we obtain

$$\mathbb{L}_{v;mn}^{EJ} = \gamma_v \int_{\Gamma_m^\pm} \wedge_m(\boldsymbol{\rho}) \int_{\Gamma_n^\pm} \wedge_n(\boldsymbol{\rho}') G_v(\boldsymbol{\rho}, \boldsymbol{\rho}') d\ell' d\ell \quad (5.19)$$

Since the triangle functions stretch out over two edges, four separate integrals have to be evaluated for each combination of test and expansion function. Since the 2D Green’s function involves a Bessel function, the computation time required for the evaluation of the double integral, is mainly dominated by the successive determination of the Green’s function. However, for a given edge pair, four test and expansion triangle combinations yield a contribution to the MoM-matrix, implying that for fixed quadrature rules source and observation points can be reused for the evaluation of the Green’s function. Therefore, these contributions are best determined *simultaneously*. Hence, the filling of the MoM-matrix is more efficient if we focus on pairs of edges, rather than pairs of triangles. In particular, each triangle is subdivided into two parts that correspond with a single edge element, as shown in Figure 5.4. Accordingly, \wedge_n^+ and \wedge_n^- signify the respective portions of \wedge_{n+1} and \wedge_n on edge Γ_n , such that

$$\wedge_m^\pm = \frac{1}{2}(1 \pm \eta), \quad \text{and} \quad \wedge_n^\pm = \frac{1}{2}(1 \pm \xi), \quad (5.20)$$

for $\boldsymbol{\rho} \in \Gamma_{m,n}$ and $\xi \in [-1, 1]$. Note that the subscript of \wedge_n^\pm refers to an edge element, while the subscript of \wedge_n refers to the expansion function f_n^J . As such, the MoM-matrix may be constructed out of the following constituents

$$\mathbb{L}_{v;mn}^{EJ;pq} = \gamma_v \int_{\Gamma_m} \wedge_m^p(\boldsymbol{\rho}) \int_{\Gamma_n} \wedge_n^q(\boldsymbol{\rho}') G_v(\boldsymbol{\rho}, \boldsymbol{\rho}') d\ell' d\ell, \quad (5.21)$$

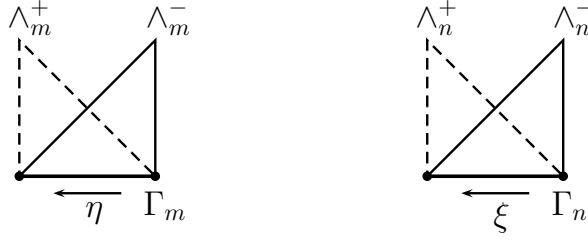


Figure 5.4: To accelerate the filling of the MoM-matrix, the test (left) and expansion (right) triangles are subdivided into the parts associated with a single edge element.

for $\{p, q\} = \{\pm, \pm\}$. Accordingly, each triangle test and expansion pair is decomposed into four separate contributions, viz.,

$$\{\wedge_m, \wedge_n\} = \{\wedge_m^-, \wedge_n^-\} + \{\wedge_m^-, \wedge_{n-1}^+\} + \{\wedge_{m-1}^+, \wedge_n^-\} + \{\wedge_{m-1}^+, \wedge_{n-1}^+\}. \quad (5.22)$$

With the definition of the 2D Green's function, Eq (5.6), each element is conveniently written in local coordinates by means of Eq. (5.11),

$$\mathbb{L}_{v;mn}^{EJ;pq} = \gamma_v \frac{d_m d_n}{2\pi} \int_{-1}^1 \int_{-1}^1 \wedge_m^p \wedge_n^q K_0(\gamma_v D) d\xi d\eta, \quad (5.23)$$

with the length $D = |\boldsymbol{\rho}_m - \boldsymbol{\rho}_n|$. Recall that for an efficient numerical evaluation of the double integral in Eq. (5.23), the four different integrands with respect to, $\{p, q\}$, are determined simultaneously. Further, observe that due to the application of Galerkin test and expansion, i.e., $f_m^E = f_n^J$, the MoM-matrix is symmetric, i.e.,

$$\mathbb{L}_{v;mn}^{EJ;pq} = \mathbb{L}_{v;nm}^{EJ;qp}. \quad (5.24)$$

As a consequence, the computation of the upper (or lower) part of the MoM-matrix (including the diagonal) is sufficient.

For the case with $\Gamma_m = \Gamma_n$ henceforth referred to as the self term, the modified Bessel function K_0 is replaced by its series expansion. In Appendix A.3, analytical solutions are provided for the entire double integral of Eq. (5.24) in terms of its series constituents. The presented results are applicable for all test and expansion combinations involving piecewise continuous and linear parts. It is also demonstrated that no more than 15 terms are required for any practical case. Hence, the numerical evaluation of Eq. (5.24) is only necessary for the lower or upper part of the MoM-matrix. Note that usually integration rules are utilized that are applicable to integrands

involving a singular behavior at the endpoint [73]. Since our method avoids time-consuming evaluation of the Bessel functions, it is more efficient.

The MFIE associated with a PEC, Eq. (3.15), involves the same electric equivalent current, \mathbf{J} , and thus also the expansion, \mathbf{f}_n^J , while the testing of the magnetic field involves, $\hat{\nu} \times \mathbf{f}_m^H$. We thus need to evaluate

$$\sum_{n=1}^N \left\langle \mathbf{f}_m^H, \mathbf{K}_1 \mathbf{f}_n^J + \frac{\hat{\nu} \times \mathbf{f}_n^J}{2} \right\rangle J_n = \langle \mathbf{f}_m^H, \mathbf{H}_1^{\text{in}} \rangle, \quad (5.25)$$

for $\rho \in \mathcal{C}$, and $m = 1, \dots, N$. The corresponding MoM-matrix equation for the MFIE reads

$$[\mathbf{K}_1^{HJ} + \mathbf{I}^{HJ}] \mathbf{J} = \mathbf{H}_1^{\text{in}}. \quad (5.26)$$

The matrix contains two parts, viz., the tested \mathbf{K} and $\hat{\nu} \times \mathbf{I}$ operators. The superscript “ HJ ” indicates an equivalent electric current in a magnetic-field integral equation. The excitation vector, \mathbf{H}_1^{in} , follows from testing the incident magnetic field that are tangential to $\partial\mathcal{D}$. Via Eqs. (5.12a) and (5.14b), the contribution of \mathbf{K} for each combination of test and expansion function, follows from

$$\begin{aligned} \mathbf{K}_{v;mn}^{HJ} &= \langle \mathbf{f}_m^H, \mathbf{K}_v \mathbf{f}_n^J \rangle = \int_{\mathcal{C}_m} f_m^H(\rho) \hat{\tau} \cdot \int_{\mathcal{C}_n} [f_n^J(\rho') \hat{\mathbf{z}}] \times \nabla'_t G_v(\rho, \rho') d\ell' d\ell \\ &= \int_{\mathcal{C}_m} f_m^H(\rho) \int_{\mathcal{C}_n} f_n^J(\rho') [\hat{\nu} \cdot \nabla'_t G_v(\rho, \rho')] d\ell' d\ell. \end{aligned} \quad (5.27)$$

With $\partial_z K_0(z) = -K_1(z)$, the gradient of the 2D Green's function, Eq. (5.6), can be written as

$$\nabla'_t G_v(\rho, \rho') = -\frac{\gamma_v}{2\pi} \frac{\rho - \rho'}{|\rho - \rho'|} K_1(\gamma_v |\rho - \rho'|). \quad (5.28)$$

Further, we introduce the unit-amplitude direction vector, $\hat{\mathbf{D}} = (\rho_m - \rho_n)/D$, with $D = |\rho_m - \rho_n|$, to maintain a concise notation for Eq. (5.27) in local coordinates. Again, upon considering pairs of edges instead of pairs of test and expansion functions, we may conveniently construct the MoM-matrix via the elements

$$\mathbf{K}_{v;mn}^{HJ;pq} = -\gamma_v \frac{d_m d_n}{2\pi} \int_{-1}^1 \int_{-1}^1 \wedge_m^p \wedge_n^q \hat{\nu}_m \cdot \hat{\mathbf{D}} K_1(\gamma_v D) d\xi d\eta. \quad (5.29)$$

Notice that, due to the inner product involving $\hat{\nu}_m$, the symmetry with respect to test and expansion is lost. Although this implies that we have to evaluate Eq. (5.29) for all matrix elements, the

same reduction as in the case of Eq. (5.23) can be achieved as regards the computational costs. We will elaborate this further where the operator \mathbf{K} involved with a PMC is treated. Further, Eq. (5.29) yields no contribution, if the test and expansion edge are each other's extension, as in that case, $\hat{\boldsymbol{\nu}}_m \cdot \hat{\boldsymbol{D}} = 0$. Hence, the self term for \mathbf{K} is zero.

As regards the tested identity operator, $\hat{\boldsymbol{\nu}} \times \mathbf{l}$, we have

$$\mathbb{I}_{mn}^{HJ} = \frac{1}{2} \langle \mathbf{f}_m^H, \hat{\boldsymbol{\nu}} \times \mathbf{f}_n^J \rangle = - \int_{\mathcal{C}_m} \frac{f_m^H(\boldsymbol{\rho}) f_n^J(\boldsymbol{\rho})}{2} d\ell. \quad (5.30)$$

Since f_n^J and f_m^H are both functions of bounded support, their product only differs from zero for identical edges, $\Gamma_m^\pm = \Gamma_n^\pm$. Triangle test and expansion reads

$$\mathbb{I}_{mn}^{HJ;pq} = -\frac{d_m}{2} \int_{-1}^1 \wedge_m^p \wedge_n^q d\eta = -d_m \begin{cases} \frac{1}{3}, & \text{for } m = n, p = q, \\ \frac{1}{6}, & \text{for } m = n, p \neq q, \\ 0, & \text{for } m \neq n. \end{cases} \quad (5.31)$$

Note that \mathbb{I} is apart from the exclusion of the two matrix elements \mathbb{I}_{1N} and \mathbb{I}_{N1} , a diagonally dominant tri-diagonal matrix, which is circulant for uniform edge elements. With respect to pulse test and expansion, the integral in Eq. (5.31) yields a nonzero contribution for the diagonal only, viz., $-d_m$ for $\Gamma_m = \Gamma_n$.

Based on the discussed mapping properties applicable to the above EFIE and MFIE, there are no continuity restrictions for the test and expansion functions, since the electromagnetic scattering from a PEC satisfies the TM description (J_z only). On that account, the triangle functions in the resulting expressions for the matrix elements, Eqs. (5.23) and (5.30), may simply be replaced by pulse functions.

The scattering from a PMC involves only a tangential equivalent magnetic current component M_τ , as H_τ is zero on \mathcal{C} . Therefore we apply the expansion $Z_1 \mathbf{f}_n^M$ and use Eq. (5.14b). In turn, the associated MFIE is obtained by duality from the EFIE, Eq. (3.14). Testing with $\hat{\boldsymbol{\nu}} \times \mathbf{f}_m^H$, gives via Eq. (5.13),

$$\sum_{n=1}^N \langle \mathbf{f}_m^H, \mathbb{L}_1 \mathbf{f}_n^M \rangle M_n = - \langle \mathbf{f}_m^H, \mathbf{H}_1^{\text{in}} \rangle. \quad (5.32)$$

In matrix notation, this is written as

$$\mathbb{L}_1^{HM} \mathbf{M} = -\mathbf{H}_1^{\text{in}}, \quad (5.33)$$

similar to Eq. (5.11). Nevertheless, \mathbb{L}_1^{HM} involves a magnetic field and current. In addition, \mathbf{M} consists of the amplitudes M_n of the equivalent magnetic current. Next, the test and expansion

functions are expressed in terms of their scalar counterparts, Eq. (5.14b) and Eq. (5.12b), respectively. In conjunction with Eq. (5.8a), the divergence in the scalar potential is nonzero for M_τ . Because the mapping properties of Eq. (5.33) satisfy the TE description, only piecewise-linear test and expansion function are applicable. With triangle test and expansion, the matrix elements are obtained from

$$\begin{aligned} \mathbb{L}_{v;mn}^{HM} = \langle \mathbf{f}_m^H, \mathbb{L}_v \mathbf{f}_n^M \rangle &= \gamma_v \int_{\Gamma_m^\pm} \Lambda_m(\boldsymbol{\rho}) \int_{\Gamma_n^\pm} [\hat{\boldsymbol{\tau}} \cdot \hat{\boldsymbol{\tau}}'] \Lambda_n(\boldsymbol{\rho}') G_v(\boldsymbol{\rho}, \boldsymbol{\rho}') d\ell' d\ell \\ &\quad - \frac{1}{\gamma_v} \int_{\Gamma_m^\pm} \Lambda_m(\boldsymbol{\rho}) \partial_\tau \int_{\Gamma_n^\pm} [\partial_{\tau'} \Lambda_n(\boldsymbol{\rho}')] G_v(\boldsymbol{\rho}, \boldsymbol{\rho}') d\ell' d\ell. \end{aligned} \quad (5.34)$$

The gradient of the scalar potential has been reduced to a partial derivative ∂_τ , which in turn can be diverted to the test function, i.e., via integration by parts for the test integral involving the scalar potential, the boundary terms do not contribute since Λ_m is piecewise continuous and vanishes at its endpoints. For a scalar function $\Phi(\boldsymbol{\rho})$, this implies the property,

$$\int_{\Gamma_m^\pm} \Lambda_m(\boldsymbol{\rho}) \partial_\tau \Phi(\boldsymbol{\rho}) d\ell = - \int_{\Gamma_m^\pm} [\partial_\tau \Lambda_m(\boldsymbol{\rho})] \Phi(\boldsymbol{\rho}) d\ell. \quad (5.35)$$

Furthermore, the partial derivative of Λ_n in local coordinates reads

$$d_n \partial_\tau \Lambda_n^\pm(\boldsymbol{\rho}) = \partial_\xi \Lambda_n^\pm = \pm \frac{1}{2} \Gamma_n. \quad (5.36)$$

When we consider edges rather than triangles, we have, analogously to Eq. (5.23)

$$\mathbb{L}_{v;mn}^{HM;pq} = [\hat{\boldsymbol{\tau}}_m \cdot \hat{\boldsymbol{\tau}}_n] \gamma_v \frac{d_m d_n}{2\pi} \int_{-1}^1 \int_{-1}^1 \Lambda_m^p \Lambda_n^q K_0(\gamma_v D) d\xi d\eta + \frac{pq}{\gamma_v 8\pi} \int_{-1}^1 \int_{-1}^1 K_0(\gamma_v D) d\xi d\eta \quad (5.37)$$

for $\{p, q\} \in \{\pm, \pm\}$. Observe that the first double integral on the right-hand side is the same as the one in Eq. (5.23) for $\mathbb{L}_{v;mn}^{EJ;pq}$. In addition, from the definition of the triangle function in Eq. (5.20), we recall that, $\Lambda_n^+ + \Lambda_n^- = \Lambda_m^+ + \Lambda_m^- = \frac{1}{2}$. Accordingly, the second double integral in Eq. (5.38) can be written in terms of $\mathbb{L}_{v;mn}^{EJ;pq}$ as well. Hence, we obtain

$$\mathbb{L}_{v;mn}^{HM;pq} = [\hat{\boldsymbol{\tau}}_m \cdot \hat{\boldsymbol{\tau}}_n] \mathbb{L}_{v;mn}^{EJ;pq} + \frac{pq}{\gamma_v^2 d_m d_n} \sum_{k,\ell=\pm} \mathbb{L}_{v;mn}^{EJ;k\ell}. \quad (5.38)$$

It should be noted that $\mathbb{L}_{v;mn}^{HM;pq} = \mathbb{L}_{v;mn}^{HM;qp}$.

By duality, the EFIE for a PMC follows from the MFIE for a PEC, Eq. (3.15). Upon expanding with $Z_1 \mathbf{f}_n^M$ and testing with $Y_1 \hat{\boldsymbol{\nu}} \times \mathbf{f}_m^E$, and using Eq. (5.13), we arrive at

$$\sum_{n=1}^N \left\langle \mathbf{f}_m^E, \mathbb{K}_1 \mathbf{f}_n^M + \frac{\hat{\boldsymbol{\nu}} \times \mathbf{f}_n^M}{2} \right\rangle M_n = -Y_1 \langle \mathbf{f}_m^E, \mathbf{E}_1^{\text{in}} \rangle, \quad (5.39)$$

for $\boldsymbol{\rho} \in \mathcal{C}$, and $m = 1, \dots, N$. In matrix notation, this is written as,

$$[\mathbf{K}_1^{EM} + \mathbf{\Gamma}^{EM}] \mathbf{M} = -Y_1 \mathbf{E}_1^{\text{in}}, \quad (5.40)$$

which is similar to Eq. (5.26), albeit that \mathbf{K}_1^{EM} involves an electric-field integral equation with a magnetic current. The tested identity operator has, apart from a minus sign, the same matrix elements as in Eq. (5.30), i.e.,

$$\mathbf{\Gamma}_{mn}^{EM} = \frac{1}{2} \langle \mathbf{f}_m^E, \hat{\boldsymbol{\nu}} \times \mathbf{f}_n^M \rangle = -\mathbf{\Gamma}_{mn}^{HJ}. \quad (5.41)$$

Via Eqs. (5.12b) and (5.14a), the matrix elements of \mathbf{K}_v^{EM} are given by

$$\mathbf{K}_{v;mn}^{EM} = \langle \mathbf{f}_m^E, \mathbf{K}_v \mathbf{f}_n^M \rangle = - \int_{\mathcal{C}_m} f_m^E(\boldsymbol{\rho}) \int_{\mathcal{C}_n} f_n^M(\boldsymbol{\rho}') \hat{\boldsymbol{\nu}}' \cdot \nabla'_t G_v(\boldsymbol{\rho}, \boldsymbol{\rho}') d\ell' d\ell, \quad (5.42)$$

which is analogous to Eq. (5.29). In local coordinates we have

$$\mathbf{K}_{v;mn}^{EM;pq} = \gamma_v \frac{d_m d_n}{2\pi} \int_{-1}^1 \int_{-1}^1 \wedge_m^p \wedge_n^q \hat{\boldsymbol{\nu}}_n \cdot \hat{\mathbf{D}} K_1(\gamma_v D) d\xi d\eta. \quad (5.43)$$

Upon comparing Eq. (5.43) with Eq. (5.29), we establish the relation,

$$\mathbf{K}_{v;mn}^{EM;pq} = \mathbf{K}_{v;nm}^{HJ;qp} \quad \Rightarrow \quad \mathbf{K}_v^{EM} = [\mathbf{K}_v^{HJ}]^T. \quad (5.44)$$

In conclusion, we mention that upon using Galerkin test and expansion, it is sufficient and also efficient to only evaluate the upper (or lower) part of the matrices, \mathbf{L}_v^{EJ} , \mathbf{K}_v^{HJ} , and \mathbf{K}_v^{EM} simultaneously by numerical integration rules based on pairs of edges. The remaining MoM-matrix parts immediately follow from the relations, Eqs. (5.38) and (5.44), derived above. No impedance scaling has been required to match the dimensions regarding the one-to-one relations between the MoM-matrices, since the equivalent magnetic current and the EFIE have been scaled with Z_1 and Y_1 , respectively. By duality, the resulting matrices are readily applicable for the TE case.

Let us now consider the excitation vector. Observe that the integral equations with the magnetic and electric equivalent currents involve the same two excitation vectors. The corresponding vector components read

$$\mathbf{E}_{1;m}^{\text{in}} = \langle \mathbf{f}_m^E, \mathbf{E}_1^{\text{in}} \rangle = \int_{\mathcal{C}_m} f_m^E(\boldsymbol{\rho}) E_{z;1}^{\text{in}}(\boldsymbol{\rho}) d\ell, \quad (5.45a)$$

$$\mathbf{H}_{1;m}^{\text{in}} = \langle \mathbf{f}_m^H, \mathbf{H}_1^{\text{in}} \rangle = \int_{\mathcal{C}_m} f_m^H(\boldsymbol{\rho}) H_{\tau;1}^{\text{in}}(\boldsymbol{\rho}) d\ell. \quad (5.45b)$$

For the TM case, the tested incident field may be considered as being generated by a superposition of electric line sources in the longitudinal direction and magnetic line sources in the transverse plane. This includes plane waves, which may be treated as being generated by a properly normalized source at infinity. We separately handle the field generated by a single electric and magnetic line source, respectively.

In turn, the field due to an arbitrary source distribution readily follows from an appropriate weighted combination of multiple line sources. In particular, the 2D version of the field integral representation, Eq. (2.43), with the 2D dyadic Green's function, Eq. (5.4) applies. Upon considering the electric line source, $\mathbf{J}(\boldsymbol{\rho}') = \hat{\mathbf{z}}\delta(\boldsymbol{\rho}' - \boldsymbol{\rho}_S)$, we obtain for the remaining electric and magnetic field component tangential to $\partial\mathcal{D}$,

$$E_{z;1}^{\text{in}} = -s\mu_1 G_1(\boldsymbol{\rho}, \boldsymbol{\rho}_S), \quad (5.46a)$$

$$H_{\tau;1}^{\text{in}} = \hat{\boldsymbol{\tau}} \cdot \nabla_t \times [G_1(\boldsymbol{\rho}, \boldsymbol{\rho}_S)\hat{\mathbf{z}}] = -\hat{\boldsymbol{\nu}} \cdot \nabla_t G_1(\boldsymbol{\rho}, \boldsymbol{\rho}_S). \quad (5.46b)$$

Likewise, for a magnetic line source, $\mathbf{M}(\boldsymbol{\rho}') = \hat{\boldsymbol{\alpha}}\delta(\boldsymbol{\rho}' - \boldsymbol{\rho}_S)$, pointing in the direction, $\hat{\boldsymbol{\alpha}}$, parallel to the transverse plane, we obtain,

$$E_{z;1}^{\text{in}} = -\hat{\mathbf{z}} \cdot \nabla_t \times [G_1(\boldsymbol{\rho}, \boldsymbol{\rho}_S)\hat{\boldsymbol{\alpha}}] = (\hat{\mathbf{z}} \times \hat{\boldsymbol{\alpha}}) \cdot \nabla_t G_1(\boldsymbol{\rho}, \boldsymbol{\rho}_S), \quad (5.47a)$$

$$H_{\tau;1}^{\text{in}} = -s\varepsilon_1 \left[(\hat{\boldsymbol{\tau}} \cdot \hat{\boldsymbol{\alpha}}) - \frac{1}{\gamma_1^2} \partial_\tau \partial_\alpha \right] G_1(\boldsymbol{\rho}, \boldsymbol{\rho}_S). \quad (5.47b)$$

By means of Eq. (5.35), the partial derivative ∂_τ may be diverted to the triangle testing function. If tested with a pulse function \square_m instead of \wedge_m , integration by parts involves the edge endpoints only. Below, it will be made clear that this poses a problem for source positions near \mathcal{C} . Further elaboration of the test integrals in Eq. (5.45), carried out by means of Eqs. (5.11) and (5.28), is straightforward and will be omitted.

The MoM matrices and excitation vectors for the electric and magnetic perfect conductor determined above can also be used for the composition of the MoM-matrix equations associated with the scattering from a dielectric object. Upon identifying these terms in the PMCHW formulation, Eq. (3.35), the corresponding matrix equation is found to be

$$\begin{bmatrix} \mathbf{L}_1^{EJ} + Y_1 Z_2 \mathbf{L}_2^{EJ} & \mathbf{K}_1^{EM} + \mathbf{K}_2^{EM} \\ -\mathbf{K}_1^{HJ} - \mathbf{K}_2^{HJ} & \mathbf{L}_1^{HM} + Z_1 Y_2 \mathbf{L}_2^{HM} \end{bmatrix} \begin{bmatrix} \mathbf{J} \\ \mathbf{M} \end{bmatrix} = - \begin{bmatrix} Y_1 \mathbf{E}_1^{\text{in}} \\ \mathbf{H}_1^{\text{in}} \end{bmatrix}. \quad (5.48)$$

In turn, the matrix equation in Müller's formulation, Eq. (3.36), is given by

$$\begin{bmatrix} \mathbb{L}_1^{EJ} - \frac{\gamma_2}{\gamma_1} \mathbb{L}_2^{EJ} & \mathbb{K}_1^{EM} - \frac{\varepsilon_2}{\varepsilon_1} \mathbb{K}_2^{EM} + \frac{\varepsilon_1 + \varepsilon_2}{\varepsilon_1} \mathbb{I}^{EM} \\ -\mathbb{K}_1^{HJ} + \frac{\mu_2}{\mu_1} \mathbb{K}_2^{HJ} - \frac{\mu_1 + \mu_2}{\mu_1} \mathbb{I}^{HJ} & \mathbb{L}_1^{HM} - \frac{\gamma_2}{\gamma_1} \mathbb{L}_2^{HM} \end{bmatrix} \begin{bmatrix} \mathbf{J} \\ \mathbf{M} \end{bmatrix} = - \begin{bmatrix} Y_1 \mathbf{E}_1^{\text{in}} \\ \mathbf{H}_1^{\text{in}} \end{bmatrix}. \quad (5.49)$$

In view of the remarks made above regarding efficiency, the computational costs involved in the construction of the PMCHW and Müller MoM-matrix is twice that of constructing a CFIE (or an EFIE) for a perfect conductor since. This is due to the fact that both interior and exterior medium indices are required.

Observe that, for the integral equations presented so far, the scaling of the magnetic current expansion and the testing function for the electric field equation has led to MoM matrices in which all elements have the same dimension. The elements are also in the same range of magnitude, which is beneficial for the condition number of the resulting MoM-matrix. However, further improvement may be achieved with respect to the Müller MoM-matrix in Eq. (5.49). In particular, the constituents of the upper-right and lower-right submatrices of the MoM-matrix in Eq. (5.49) that contain \mathbb{I}^{EM} and $\mathbb{I}^{HJ} = -\mathbb{I}^{EM}$, respectively, are the diagonally dominant parts of those submatrices. As the difference between $\varepsilon_{r;2}$ and $\mu_{r;2}$ increases, the imbalance between the pertaining elements grows. Therefore, these matrix parts do not seem to match ver well. Obviously, this not the case with the PMCHW MoM-matrix, as the identity operators of the interior and exterior medium cancel each other.

To mitigate the imbalance we propose an *additional scaling*, with the aim to improve the condition number of Müller's MoM-matrix. Since the submatrices with L seem to match, the scaling should only affect the submatrices with K. Accordingly, we introduce the scaling factors

$$\varsigma_\varepsilon \equiv \sqrt{\frac{\varepsilon_1 + \varepsilon_2}{\varepsilon_1}}, \quad \text{and} \quad \varsigma_\mu \equiv \sqrt{\frac{\mu_1 + \mu_2}{\mu_1}}. \quad (5.50)$$

Multiplying the electric and magnetic field equation by ς_μ and ς_ε , respectively, and substituting the relations

$$\mathbf{J}'_n = \varsigma_\mu \mathbf{J}_n, \quad \text{and} \quad \mathbf{M}'_n = \varsigma_\varepsilon \mathbf{M}_n, \quad (5.51)$$

into the current expansion, Eq. (3.32), the additional scaling leads to the scaled equation

$$\begin{bmatrix} \mathbb{L}_1^{EJ} - \frac{\gamma_2}{\gamma_1} \mathbb{L}_2^{EJ} & \frac{\varsigma_\mu}{\varsigma_\varepsilon} \left(\mathbb{K}_1^{EM} - \frac{\varepsilon_2}{\varepsilon_1} \mathbb{K}_2^{EM} \right) + \varsigma_\mu \varsigma_\varepsilon \mathbb{I}^{EM} \\ -\frac{\varsigma_\varepsilon}{\varsigma_\mu} \left(\mathbb{K}_1^{HJ} - \frac{\mu_2}{\mu_1} \mathbb{K}_2^{HJ} \right) - \varsigma_\mu \varsigma_\varepsilon \mathbb{I}^{HJ} & \mathbb{L}_1^{HM} - \frac{\gamma_2}{\gamma_1} \mathbb{L}_2^{HM} \end{bmatrix} \begin{bmatrix} \mathbf{J}' \\ \mathbf{M}' \end{bmatrix} = - \begin{bmatrix} \varsigma_\mu Y_1 \mathbf{E}_1^{\text{in}} \\ \varsigma_\varepsilon \mathbf{H}_1^{\text{in}} \end{bmatrix}. \quad (5.52)$$

In this equation, the diagonally dominant matrices have the same amplitude.

Once the current amplitudes J_n and/or M_n have been determined, the corresponding electric and magnetic field distributions follow from the integral representations presented in Section 3.2. For instance, the exterior scattered fields for the dielectric object follow from Eqs. (3.5) and (3.6). Substituting the applied current expansion, Eq. (3.32), back in the integral representations, results in expressions for the scattered TM fields

$$\hat{\mathbf{z}}E_z^{\text{sc}} = \sum_{n=1}^N [J_n \mathbf{L}_1 \mathbf{f}_n^J + M_n \mathbf{K}_1 \mathbf{f}_n^M] Z_1, \quad (5.53a)$$

$$\mathbf{H}_t^{\text{sc}} = \sum_{n=1}^N [M_n \mathbf{L}_1 \mathbf{f}_n^M - J_n \mathbf{K}_1 \mathbf{f}_n^J], \quad (5.53b)$$

for $\boldsymbol{\rho} \in \bar{\mathcal{D}}$. In view of the interior field representation, Eq. (3.9), changing the medium index of \mathbf{L}_v and \mathbf{K}_v into $v = 2$ in Eq. (5.53), and adding a minus sign as we deal with an interior equivalent state, produces the total interior fields, $\boldsymbol{\rho} \in \mathcal{D}$. Further, omitting either the magnetic or electric equivalent current parts readily reduces Eq. (5.53) to the representations associated with the scattered field from the PEC, respectively, PMC.

The application of Eq. (5.12) with triangle expansion for both the electric and magnetic equivalent currents gives

$$E_z^{\text{sc}} = \sum_{n=1}^N \left[J_n \gamma_1 \int_{\Gamma_n^\pm} \wedge_n(\boldsymbol{\rho}') G_1(\boldsymbol{\rho}, \boldsymbol{\rho}') d\ell' - M_n \int_{\Gamma_n^\pm} \wedge_n(\boldsymbol{\rho}') \hat{\boldsymbol{\nu}}' \cdot \nabla_t' G_1(\boldsymbol{\rho}, \boldsymbol{\rho}') d\ell' \right] Z_1, \quad (5.54a)$$

$$\mathbf{H}_t^{\text{sc}} = \sum_{n=1}^N \left[M_n \left\{ \gamma_1 \int_{\Gamma_n^\pm} \hat{\boldsymbol{\tau}}' \wedge_n(\boldsymbol{\rho}') G_1(\boldsymbol{\rho}, \boldsymbol{\rho}') d\ell' + \frac{1}{\gamma_1} \int_{\Gamma_n^\pm} [\partial_{\tau'} \wedge_n(\boldsymbol{\rho}')] \nabla_t' G_1(\boldsymbol{\rho}, \boldsymbol{\rho}') d\ell' \right\} - J_n \int_{\Gamma_n^\pm} \wedge_n(\boldsymbol{\rho}') \hat{\mathbf{z}} \times \nabla_t' G_1(\boldsymbol{\rho}, \boldsymbol{\rho}') d\ell' \right], \quad (5.54b)$$

for $\boldsymbol{\rho} \in \bar{\mathcal{D}}$. Again, by considering pairs of edges rather than triangles, the resulting equations in local coordinates are obtained via a similar analysis as applied in the construction of the various

MoM matrices:

$$E_z^{\text{sc}} = \frac{s\mu_1}{2\pi} \sum_{n=1}^N d_n \int_{-1}^1 \sum_{q=\pm} \wedge_n^q \left[J_n^q K_0(\gamma_1 D) + M_n^q \hat{\boldsymbol{\nu}}_n \cdot \hat{\mathbf{D}} K_1(\gamma_1 D) \right] d\xi, \quad (5.55a)$$

$$\mathbf{H}_t^{\text{sc}} = \frac{\gamma_1}{2\pi} \sum_{n=1}^N d_n \int_{-1}^1 \sum_{q=\pm} \left[M_n^q \left\{ \wedge_n^q K_0(\gamma_1 D) \hat{\boldsymbol{\tau}}_n - \frac{q}{2\gamma_1 d_n} \hat{\mathbf{D}} K_1(\gamma_1 D) \right\} + J_n^q \wedge_n^q \hat{\mathbf{z}} \times \hat{\mathbf{D}} K_1(\gamma_1 D) \right] d\xi, \quad (5.55b)$$

where J_n^q and M_n^q are the current amplitudes associated with the triangle (part) \wedge_n^q . Note that the substitution of Eq. (5.51) in Eq. (5.55) would be required for the proposed additional scaling of Müller's equations.

5.4 Integration of the singular integrand parts

In the formulation of the MoM-matrix equation, the integrand of the test and expansion integrals become singular when the source and observation points coincide. This is due to the singularity entrenched in the Green's function. Such singularities need to be treated analytically while the remaining regularized integrals involving non-singular integrands are treated numerically. This section mainly describes how the pertaining analytical solutions are obtained. For the MoM-matrix elements this involves the evaluation of double integrals. Single integrals also occur: the incident field in the (tested) excitation function generated by an electric or a magnetic line source becomes singular when the source position approaches the boundary where this field is tested. Also, the integral representations that reproduce the fields represented by an (expanded) equivalent current distribution involve integrands that become singular when the field is determined on the boundary on which these currents are defined. Below, we mainly focus on the underlying idea of our approach, while the resulting solutions for the (double) integrals are presented in Appendix A.1. Only the singularities related to the TM case are handled. By duality, our approach also applies to the TE case since we consider both electric and magnetic contrast sources and fields.

Let us first explain how the integrals are decomposed into a regular and a singular integrand part. Suppose we have a function $\Psi(\boldsymbol{\rho}, \boldsymbol{\rho}')$ that represents a (scalar) integrand which is singular at $\boldsymbol{\rho} = \boldsymbol{\rho}'$. Even if $\boldsymbol{\rho}$ does not lie on the integration contour but merely in its vicinity, straightforward integration remains problematic. For this reason, a singular integrand part, $\Psi_{\text{sing}}(\boldsymbol{\rho}, \boldsymbol{\rho}')$,

is subtracted first, such that we are left with an integral involving an integrand with a regular (non-singular) behavior only, and a separate integral involving $\Psi_{\text{sing}}(\boldsymbol{\rho}, \boldsymbol{\rho}')$ only. Accordingly, we have

$$\int_c \Psi(\boldsymbol{\rho}, \boldsymbol{\rho}') d\ell' = \int_c [\Psi(\boldsymbol{\rho}, \boldsymbol{\rho}') - \Psi_{\text{sing}}(\boldsymbol{\rho}, \boldsymbol{\rho}')] d\ell' + \int_c \Psi_{\text{sing}}(\boldsymbol{\rho}, \boldsymbol{\rho}') d\ell'. \quad (5.56)$$

The first integral on the right-hand side is regular, and thus amenable to numerical integration. The integral of the remaining singular integrand part is treated analytically below. An integral that involves only a singular integrand like Ψ_{sing} , is henceforth referred to as a *singular integral*.

The singular behavior of the integrals involved in the MoM originate from the scalar Green's function, Eq. (5.6), and its spatial derivatives, Eq. (5.28). The associated singularity thus follows from the small-argument behavior of the zeroth and first-order modified Bessel function of the second kind

$$K_0(z) = -\ln\left(\frac{z}{2}\right) - \gamma_E + \mathcal{O}(z), \quad \text{and} \quad K_1(z) = \frac{1}{z} + \mathcal{O}(z), \quad (5.57)$$

with γ_E being Euler's constant. Accordingly, in the analysis of 2D structures, the integrands of the various integrals are of the following types

$$\Psi(\boldsymbol{\rho}, \boldsymbol{\rho}') \propto \begin{cases} K_0(\gamma|\boldsymbol{\rho} - \boldsymbol{\rho}'|), \\ \hat{\boldsymbol{\alpha}} \cdot \nabla'_t K_0(\gamma|\boldsymbol{\rho} - \boldsymbol{\rho}'|), \end{cases} \quad \Rightarrow \quad \Psi_{\text{sing}}(\boldsymbol{\rho}, \boldsymbol{\rho}') \propto \begin{cases} -\ln(|\boldsymbol{\rho} - \boldsymbol{\rho}'|), \\ -\frac{\hat{\boldsymbol{\alpha}} \cdot (\boldsymbol{\rho} - \boldsymbol{\rho}')}{|\boldsymbol{\rho} - \boldsymbol{\rho}'|^2}, \end{cases} \quad (5.58)$$

with $\hat{\boldsymbol{\alpha}}$ oriented tangential or normal to the test or expansion edge. Notice that the term $\gamma/2$ is omitted from the argument of the logarithm, as it can be absorbed into the regular integral. To arrive at the complete integrand of the singular integrals the test and expansion function have to be included.

In the present analysis it is assumed that the edges, on which the test and expansion functions are evaluated, have no points in common, except for the start and end points. With respect to the self term, i.e., when both edges coincide ($\Gamma_m = \Gamma_n$), an exact solution is provided in Appendix A.3 for the integration of the singular, as well as the regular part up to a desired order of accuracy. In the singular integrands, we use the property

$$\ln(|\boldsymbol{\rho}_m - \boldsymbol{\rho}_n|) = \frac{1}{2} \ln(|\boldsymbol{\rho}_m - \boldsymbol{\rho}_n|^2). \quad (5.59)$$

As a consequence, the distance $|\boldsymbol{\rho}_m - \boldsymbol{\rho}_n|$ appears only in the form $|\boldsymbol{\rho}_m - \boldsymbol{\rho}_n|^2$, i.e., we have eliminated any square roots. The distance vector from the observation point $\boldsymbol{\rho}_m$ to the source

point $\boldsymbol{\rho}_n$ for a test and expansion edge pair may be written in terms of the local area coordinates $\{\eta, \xi\} \in [-1, 1]$ (cf. Eq. (5.10)) as

$$\boldsymbol{\rho}_m - \boldsymbol{\rho}_n = \boldsymbol{\rho}_m^c - \boldsymbol{\rho}_n^c + \eta d_m \hat{\boldsymbol{\tau}}_m - \xi d_n \hat{\boldsymbol{\tau}}_n. \quad (5.60)$$

with the length d_i defined as half the edge length, $d_i \equiv L_i/2$ for $i = \{m, n\}$. Accordingly, $|\boldsymbol{\rho}_m - \boldsymbol{\rho}_n|^2$ may be expressed in terms of inner products of vectors normal and tangential to the edges Γ_m and Γ_n , i.e.,

$$\begin{aligned} |\boldsymbol{\rho}_m - \boldsymbol{\rho}_n|^2 = & d_R^2 + 2\eta d_m (\boldsymbol{\rho}_m^c - \boldsymbol{\rho}_n^c) \cdot \hat{\boldsymbol{\tau}}_m - 2\xi d_n (\boldsymbol{\rho}_m^c - \boldsymbol{\rho}_n^c) \cdot \hat{\boldsymbol{\tau}}_n \\ & + (\eta d_m)^2 + (\xi d_n)^2 - 2\eta\xi d_m d_n (\hat{\boldsymbol{\tau}}_m \cdot \hat{\boldsymbol{\tau}}_n), \end{aligned} \quad (5.61)$$

with $d_R \equiv |\boldsymbol{\rho}_m^c - \boldsymbol{\rho}_n^c|$ and η and ξ as the only two varying parameters. Further simplification is achieved upon considering Figure 5.5, where the mutual orientation of a certain test and expansion edge pair for the non-self term is accounted for by the fixed angles ψ_m, ψ_n and ϕ .

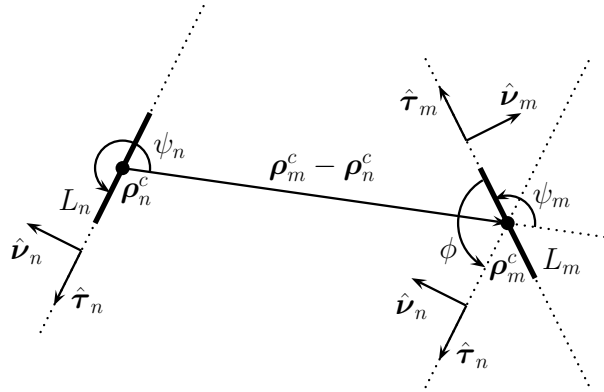


Figure 5.5: A pair of edges on which the test and expansion are evaluated, indicated by the subscripts m and n , respectively. The orientation of the unit-vectors, $\hat{\boldsymbol{\nu}}$ and $\hat{\boldsymbol{\tau}}$, is defined in Figure 5.2, and is accounted for by the angles ψ_m, ψ_n , and ϕ .

These angles are introduced to replace the remaining inner products by trigonometric functions. Note that, since we deal with arbitrarily shaped scattering objects, the mutual orientation of the edge pair is assumed arbitrary. The angles ψ_i are defined such that the inner products

$$\begin{aligned} \hat{\boldsymbol{\tau}}_i \cdot (\boldsymbol{\rho}_m^c - \boldsymbol{\rho}_n^c) &= d_R \cos(\psi_i), \\ \hat{\boldsymbol{\nu}}_i \cdot (\boldsymbol{\rho}_m^c - \boldsymbol{\rho}_n^c) &= d_R \sin(\psi_i), \end{aligned} \quad (5.62)$$

hold for $\psi_i \in [0, 2\pi]$ with $i = \{m, n\}$. Thus, ψ_i is the angle between edge i and the vector between the edge centers. The angle ϕ ,

$$\phi = \psi_n - \psi_m, \quad (5.63)$$

is defined through

$$\begin{aligned} \hat{\boldsymbol{\nu}}_m \cdot \hat{\boldsymbol{\nu}}_n &= \hat{\boldsymbol{\tau}}_m \cdot \hat{\boldsymbol{\tau}}_n = \cos(\phi), \\ \hat{\boldsymbol{\nu}}_m \cdot \hat{\boldsymbol{\tau}}_n &= \hat{\boldsymbol{\nu}}_n \cdot \hat{\boldsymbol{\tau}}_m = \sin(\phi). \end{aligned} \quad (5.64)$$

Thus, ϕ is the angle between edge m and n . From Eqs. (5.62) and (5.64), we observe that Eq. (5.61) reduces to

$$\begin{aligned} |\boldsymbol{\rho}_m - \boldsymbol{\rho}_n|^2 &= d_R^2 + 2\eta d_R d_m \cos(\psi_m) - 2\xi d_R d_n \cos(\psi_n) \\ &\quad + (\eta d_m)^2 + (\xi d_n)^2 - 2\eta\xi d_m d_n \cos(\phi). \end{aligned} \quad (5.65)$$

In this way, $|\boldsymbol{\rho}_m - \boldsymbol{\rho}_n|^2$ is completely expressed in the two varying parameters, η and ξ , involving constant angles as the orientation of each edge pair is fixed. This is further simplified upon introducing the complex constants,

$$q_0 \equiv \frac{d_R}{d_n} e^{j\psi_n} \quad \text{and} \quad q_1 \equiv \frac{d_m}{d_n} e^{j\phi}. \quad (5.66)$$

Expansion of the trigonometric functions in terms of exponential ones, and subsequent identification of q_0 and q_1 , leads to

$$|\boldsymbol{\rho}_m - \boldsymbol{\rho}_n|^2 = d_n^2 (\xi - \eta q_1 - q_0) (\xi - \eta q_1^* - q_0^*). \quad (5.67)$$

Because Eq. (5.67) is a product of a function and its complex conjugate, the logarithmic term becomes real-valued:

$$\begin{aligned} \ln(|\boldsymbol{\rho}_m - \boldsymbol{\rho}_n|) &= \frac{1}{2} \ln [d_n^2 (\xi - \eta q_1 - q_0) (\xi - \eta q_1^* - q_0^*)] \\ &= \Re \{ \ln [d_n (\xi - \eta q_1 - q_0)] \}, \end{aligned} \quad (5.68)$$

where \Re indicates the real part of the expression. Let $f(\eta, \xi)$ denote the product of the test and expansion function in local coordinates. For the test and expansion functions considered in this thesis, we have a linear combination of the terms

$$f(\eta, \xi) \sim \{1, \xi, \eta, \eta\xi\}. \quad (5.69)$$

The singular integrals will be treated for each term separately. The solution for a specific choice of test and expansion function follows directly from a proper linear combination. The logarithmic singularity in the operator L may via the transformation, Eq. (5.11), be written as

$$\int_{-1}^1 \int_{-1}^1 f(\eta, \xi) \ln(|\boldsymbol{\rho}_m - \boldsymbol{\rho}_n|) d\xi d\eta = \Re \left\{ \int_{-1}^1 \int_{-1}^1 f(\eta, \xi) \ln [d_n (\xi - \eta q_1 - q_0)] d\xi d\eta \right\}, \quad (5.70)$$

and is required for both L^{EJ} , Eq. (5.23), and L^{HM} , Eq. (5.38). Solving the singular integrals within the braces is a straightforward procedure. The resulting expressions are given in Appendix A.1 for the four cases in Eq. (5.69). The logarithm is a multiply-valued function: we consider the standard branch with a branch cut in the complex plane, placed at $(-\infty, 0]$. The integration area may cross the branch cut, but will not contain the branch point. In Appendix A.2, the conditions for integration across the branch cut are determined, and a simple remedy is presented, which amounts to a rotation of the branch cut in the complex plane. It is shown that this comes down to taking the opposite of q_0 and q_1 . As a consequence some terms in $f(\eta, \xi)$ will change in sign as well.

With respect to the singular parts related to K^{EM} , Eq. (5.43), the distance appears in the denominator. The remaining inner product in the numerator may be expressed in terms of q_0 and q_1 as well, according to

$$\begin{aligned} \hat{\boldsymbol{v}}_n \cdot (\boldsymbol{\rho}_m - \boldsymbol{\rho}_n) &= \hat{\boldsymbol{v}}_n \cdot (\boldsymbol{\rho}_m^c - \boldsymbol{\rho}_n^c) + \eta d_m (\hat{\boldsymbol{v}}_n \cdot \hat{\boldsymbol{\tau}}_m) = d_R \sin(\psi_n) + \eta d_m \sin(\phi) \\ &= -\frac{j d_n}{2} [\eta q_1 + q_0 - (\eta q_1^* + q_0^*)]. \end{aligned} \quad (5.71)$$

The singular integral can be further simplified,

$$\begin{aligned} \int_{-1}^1 \int_{-1}^1 f(\eta, \xi) \frac{\hat{\boldsymbol{v}}_n \cdot (\boldsymbol{\rho}_m - \boldsymbol{\rho}_n)}{|\boldsymbol{\rho}_m - \boldsymbol{\rho}_n|^2} d\xi d\eta &= -\frac{j}{2 d_n} \int_{-1}^1 \int_{-1}^1 f(\eta, \xi) \frac{\eta q_1 + q_0 - (\eta q_1^* + q_0^*)}{(\xi - \eta q_1 - q_0)(\xi - \eta q_1^* - q_0^*)} d\xi d\eta \\ &= \frac{1}{d_n} \Im \left\{ \int_{-1}^1 \int_{-1}^1 f(\eta, \xi) \frac{1}{\xi - \eta q_1 - q_0} d\xi d\eta \right\}, \end{aligned} \quad (5.72)$$

where \Im indicates the imaginary part of the expression. An analytic expression for the integral inside the braces is presented in Appendix A.1. The integrand of the outer integral involving η contains a logarithm which, like Eq. (5.70), may result into integration across its branch cut. The singular integrand of Eq. (5.72) is also encountered in the representation for K^{HJ} , Eq. (5.29), but

with $\hat{\boldsymbol{\nu}}_m$ instead of $\hat{\boldsymbol{\nu}}_n$. For the numerator, we have (cf. Figure 5.5)

$$\begin{aligned}\hat{\boldsymbol{\nu}}_m \cdot (\boldsymbol{\rho}_m - \boldsymbol{\rho}_n) &= \hat{\boldsymbol{\nu}}_m \cdot (\boldsymbol{\rho}_m^c - \boldsymbol{\rho}_n^c) - \xi d_n (\hat{\boldsymbol{\nu}}_m \cdot \hat{\boldsymbol{\tau}}_n) = d_R \sin(\psi_m) + \xi d_n \sin(\phi) \\ &= -\frac{j d_n^2}{2 d_m} [q_1 (\xi - q_0^*) - q_1^* (\xi - q_0)].\end{aligned}\quad (5.73)$$

Accordingly, the corresponding singular integral reads,

$$\begin{aligned}\int_{-1}^1 \int_{-1}^1 f(\eta, \xi) \frac{\hat{\boldsymbol{\nu}}_m \cdot (\boldsymbol{\rho}_m - \boldsymbol{\rho}_n)}{|\boldsymbol{\rho}_m - \boldsymbol{\rho}_n|^2} d\xi d\eta &= -\frac{j}{2 d_m} \int_{-1}^1 \int_{-1}^1 f(\eta, \xi) \frac{q_1 (\xi - q_0^*) - q_1^* (\xi - q_0)}{(\xi - \eta q_1 - q_0) (\xi - \eta q_1^* - q_0^*)} d\xi d\eta \\ &= \frac{1}{d_m} \Im \left\{ \int_{-1}^1 \int_{-1}^1 f(\eta, \xi) \frac{q_1}{\xi - \eta q_1 - q_0} d\xi d\eta \right\}.\end{aligned}\quad (5.74)$$

Apart from a factor q_1 , the integral inside the braces directly follows from the one in Eq. (5.72). If the singular integrals, Eqs. (5.72) and (5.74) involved an inner product with $\hat{\boldsymbol{\tau}}$ instead of $\hat{\boldsymbol{\nu}}$, a careful analysis indicates that the resulting expressions are the same, but instead of the imaginary, the real part is taken. This gives the equivalence relation

$$\{\hat{\boldsymbol{\nu}}_i, \Re, \Im\} \leftrightarrow \{\hat{\boldsymbol{\tau}}_i, \Im, \Re\}, \quad (5.75)$$

for $i = \{m, n\}$. The above relation will be used in the evaluation of the singular single integrals required in the field representation and the forcing function later on.

The integral representations that produce the field generated by the equivalent currents, Eq. (5.55), comprise single integrals. The kernels of the integrals exhibit a singular behavior when the observation point is located close to the boundary on which these currents are defined. We may still refer to Figure 5.5 for the definition of the parameters, as the analytical solutions of the singular integrals can be expressed in terms of the ones in Eqs. (5.70) and (5.72), upon applying the midpoint rule to the test integral. In that case, the test integral reduces to a single evaluation at the edge center, $\boldsymbol{\rho}_m^c$. In local coordinates, this amounts to the multiplication of $f(\eta, \xi)$ by $\delta(\eta)$. Accordingly, Eqs. (5.70) and (5.72), would reduce to the so-called midpoint solutions

$$\int_{-1}^1 f(\xi) \ln(|\boldsymbol{\rho}_m^c - \boldsymbol{\rho}_n|) d\xi = \Re \left\{ \int_{-1}^1 f(\xi) \ln[d_n (\xi - q_0)] d\xi \right\}, \quad (5.76a)$$

$$\int_{-1}^1 f(\xi) \frac{\hat{\boldsymbol{\nu}}_n \cdot (\boldsymbol{\rho}_m^c - \boldsymbol{\rho}_n)}{|\boldsymbol{\rho}_m^c - \boldsymbol{\rho}_n|^2} d\xi = \frac{1}{d_n} \Im \left\{ \int_{-1}^1 f(\xi) \frac{1}{\xi - q_0} d\xi \right\}. \quad (5.76b)$$

Expressions for the integrals inside the braces are given by Eq. (A.9) in Appendix A.1.

The midpoint solutions cover the singular integrals that occur in the field representation Eq. (5.55), by setting the observation point $\boldsymbol{\rho}$ to $\boldsymbol{\rho} = \boldsymbol{\rho}_m^c$. In that case, the singular integrals of Eq. (5.76) directly apply to the electric field representation, Eq. (5.55a). The magnetic field is first decomposed into its components along $\hat{\boldsymbol{\nu}}_n$ and $\hat{\boldsymbol{\tau}}_n$. In view of the magnetic field representation, Eq. (5.55a), the singular integral Eq. (5.76a) then applies to the vector potential. As regards the scalar potential and the integral operator K, Eq. (5.76b) is required, together with its counterpart, viz., $\hat{\boldsymbol{\tau}}_n$ instead of $\hat{\boldsymbol{\nu}}_n$, which readily follows by using the equivalence in Eq. (5.75). Hence, for each edge Γ_n , a single evaluation of the two singular integrals inside the braces in Eq. (5.76) is sufficient for the field representation of both the electric and magnetic field.

As regards the excitation function, the kernel of the test integral becomes singular for a line source that approaches the boundary contour. Again, consider Figure 5.5. The position of the line source, $\boldsymbol{\rho}_S$, is set here to $\boldsymbol{\rho}_S = \boldsymbol{\rho}_n^c$. Since there is no expansion function, the constants q_0 and q_1 are superfluous as ψ_n and ϕ are obsolete. Only the angle ψ_m remains, for which we introduce the constant q_3 ,

$$q_3 \equiv \frac{d_R}{d_m} e^{j\psi_m}. \quad (5.77)$$

In the singular integrand occurring in the excitation function, the following terms occur

$$|\boldsymbol{\rho}_m - \boldsymbol{\rho}_S|^2 = d_R^2 + 2\eta d_R d_m \cos(\psi_m) + (\eta d_m)^2 = d_m^2 (\eta + q_3) (\eta + q_3^*), \quad (5.78a)$$

$$\hat{\boldsymbol{\nu}}_m \cdot (\boldsymbol{\rho}_m - \boldsymbol{\rho}_S) = d_R \sin(\psi_m) = -\frac{j d_m}{2} [q_3 - q_3^*]. \quad (5.78b)$$

The corresponding singular integrals read

$$\int_{-1}^1 f(\eta) \ln (|\boldsymbol{\rho}_m - \boldsymbol{\rho}_S|) d\eta = \Re \left\{ \int_{-1}^1 f(\eta) \ln [d_m (\eta + q_3)] d\eta \right\}, \quad (5.79a)$$

$$\int_{-1}^1 f(\eta) \frac{\hat{\boldsymbol{\nu}}_m \cdot (\boldsymbol{\rho}_m - \boldsymbol{\rho}_S)}{|\boldsymbol{\rho}_m - \boldsymbol{\rho}_S|^2} d\eta = -\frac{1}{d_m} \Im \left\{ \int_{-1}^1 f(\eta) \frac{1}{\eta + q_3} d\eta \right\}. \quad (5.79b)$$

Upon comparing Eq. (5.79) with Eq. (5.76), it is clear that the integrals inside the braces are equal when q_0 is replaced with $-q_3$ and ξ with η . This relation may also be deduced using the reciprocity theorem.

For an electric line source, the singular integrals in Eq. (5.79) both apply to the electric and magnetic field parts in the excitation function, Eq. (5.46). Regarding the excitation function given

by Eq. (5.47), i.e., an incident field generated by a magnetic line source oriented in a direction $\hat{\alpha}$, the analytic solutions to the associated singular integrals are related to those of Eq. (5.79) by setting $\hat{\alpha} = \hat{\nu}_m$. By doing so, both singular integrals in Eq. (5.79) apply to the magnetic field part in Eq. (5.47b). For the electric field part, Eq. (5.47a), the counterpart of Eq. (5.79b) is required, i.e., with $\hat{\tau}_m$ instead of $\hat{\nu}_m$, which readily follows from the equivalence Eq. (5.75).

5.5 Perfect electric conductors

In the remaining sections, the solvability and the order of convergence of the numerical approximation obtained with the MoM approach is investigated. Initially, this involves the unknown equivalent current. Ultimately, we are interested in the accuracy of the corresponding (scattered) field that is generated by this approximate equivalent current. The accuracy that can be achieved depends on the applied discretization and the mapping properties of the involved integral operator. Based on the findings that follow, we will be able to make proper choices in the 2D numerical implementation of the LEGO approach later on.

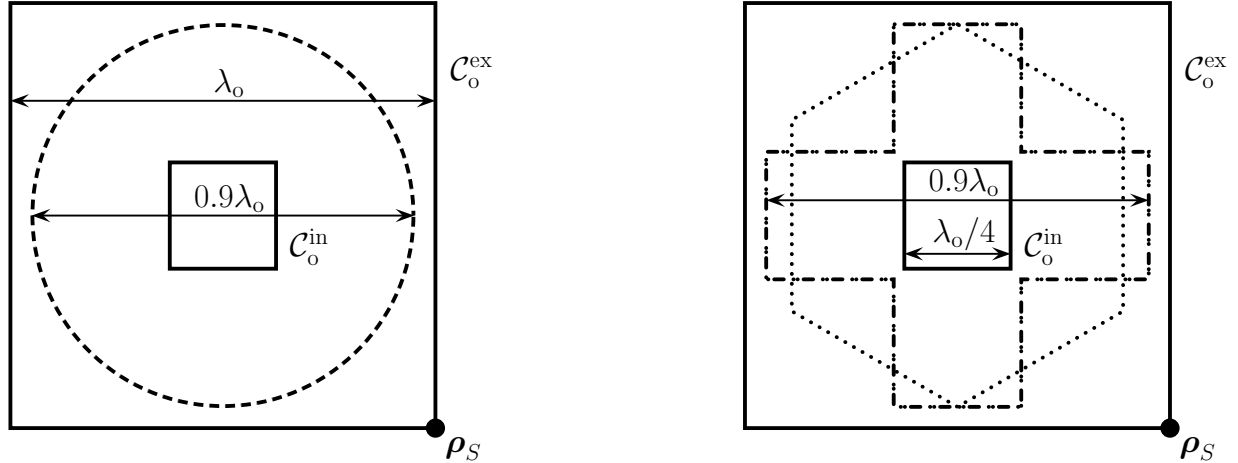


Figure 5.6: The three cylindrical scattering object shapes, viz., a circular one (left, dashed), a hexagonal one (right, dotted) and a cross shaped one (right, dash-dotted). The contours of observation are C_o^{in} and C_o^{ex} , and the position of the impressed line source excitation is ρ_S .

Before we start with the actual analysis of the discretized integral equations, let us first elucidate the framework in which the analysis is carried out by means of the basis configuration depicted in Figure 5.6. The dependence on the smoothness of the exact boundary of the scattering object

is investigated by considering three different cross-sectional shapes of the cylinder, viz., a circle (dashed), a hexagon (dotted) and a cross (dash-dotted). Their maximum electromagnetic size is chosen in the order of a wavelength, viz., $0.9\lambda_0$. For this particular choice, none of the three shapes gives rise to interior resonances. Note that their electromagnetic size is also comparable with the operating frequency range in the EBG applications discussed in Chapter 6.

Since we are primarily interested in the fields generated by the equivalent currents, rather than the currents itself, the accuracy of the associated scattered fields is the decisive measure, despite that the error in the currents remains the underlying cause. Therefore, an observation contour, \mathcal{C}_o , is employed, on which the scattered fields are evaluated, as illustrated in Figure 5.6. For a perfect electric conductor (PEC) this amounts to the rectangular exterior contour, $\mathcal{C}_o^{\text{ex}}$, with dimensions $\lambda_0 \times \lambda_0$, and positioned centered around the scattering object. The interior contour, $\mathcal{C}_o^{\text{in}}$, with dimensions, $\lambda_0/4 \times \lambda_0/4$, is not relevant for a PEC. For dielectric objects both $\mathcal{C}_o^{\text{in}}$ and $\mathcal{C}_o^{\text{ex}}$ are considered in Section 5.8. As an error criterion for the numerically obtained scattered field components, E_z^{num} and H_τ^{num} , tangential to \mathcal{C}_o , we employ a *normalized error*, defined as,

$$\text{norm. err.} = \sqrt{\frac{\int_{\mathcal{C}_o} |E_z^{\text{ref}} - E_z^{\text{num}}|^2 + Z_0^2 |H_\tau^{\text{ref}} - H_\tau^{\text{num}}|^2 d\ell}{\int_{\mathcal{C}_o} |E_z^{\text{ref}}|^2 + Z_0^2 |H_\tau^{\text{ref}}|^2 d\ell}} \quad (5.80)$$

based on a reference solution, $\{E_z^{\text{ref}}, H_\tau^{\text{ref}}\}$. For the circle, the reference solution for the scattered fields follows from the analytical expressions determined in Appendix B.1. In this section we shall discuss the mapping properties of the integral operators L and K. The chosen set of expansion functions turn out to be ultimately dense in the domain of L and K, which implies that the convergence of the method for successive refinement of the discretization. The reference solutions for the hexagon and cross shape have been calculated using $N = 6000$. The integral along the observation contour \mathcal{C}_o in Eq. (5.80) is evaluated at discrete points with 100 points per side. Further, for an assessment of the accuracy of the resulting equivalent currents, the same error criterion is applied, upon substituting $\{H_\tau, E_z\}$ by $\{J_z, M_\tau\}$ with $\mathcal{C}_o = \mathcal{C}$. As excitation, a unit-amplitude electric line source J_z is placed at $\boldsymbol{\rho}_S$, the bottom right corner of $\mathcal{C}_o^{\text{ex}}$. It generates the known incident fields, E_z^{in} and H_τ^{in} used in the excitation vector. Because the observation contour and the line source are situated 0.1λ to 0.3λ away from the scattering object, near-field effects are included in the error.

The accuracy by which the test and expansion integrals in the MoM method are determined plays a vital role in the overall performance. This so-called quadrature error will be considered

separately. The double integrals that remain after subtracting the singular parts are determined by adaptive quadrature rules, where the required relative accuracy is set to 10^{-2} . The analytical solutions provided in Section 5.4 are used for the extracted singular double integrals. For the self term, we refer to Appendix A.3.

A similar approach is applied to the single test integral as regards the excitation vector, since we are mainly interested in the error in the scattered field in relation with the MoM approach, and not in the error in the field generated by the approximate equivalent current, given by Eq. (5.53). Hence, the single expansion integral in the field representation is determined very accurately. Therefore, to guarantee a certain minimum error, the single expansion integrals are evaluated with adaptive quadrature rules (10^{-2}). For observation contours positioned close to the boundary of the scattering object, the singular behavior of the field is again accounted for by analytical solutions. In this way, the error attributed to the numerical evaluation of all the involved test and expansion integrals is negligible. The remaining error in the equivalent current, and thereby the scattered field, may thus be attributed to the mapping properties of the integral operators L or K, the applied discretization, and the smoothness of the exact boundary.

Discretization of the EFIE and MFIE results in the MoM-matrix equations (5.17) and (5.26). In view of Sections 3.7 and 5.3, triangle or pulse functions are suited for the expansion of J_z for the TM case. Accordingly, as Galerkin test and expansion functions, we take the pulse $\square\square$ and the triangle $\wedge\wedge$ combinations. As a non-Galerkin example, we consider a delta-pulse test and expansion combination, $\uparrow\square$, with delta testing at the edge center, i.e., $f_m(\boldsymbol{\rho}) = \uparrow_m = \delta(\boldsymbol{\rho} - \boldsymbol{\rho}_m^c)$. Throughout, we employ a uniform mesh.

The resulting matrix equation is, in most cases, solved for one or only a few excitation vectors. In such a case, an iterative solver like the *Conjugate Gradient* (CG) method is an efficient tool [74]. As these are approximate solvers, the required accuracy is expressed in terms of the remaining residual and is set in advance. Here, we shall employ an LU factorization or SVD decomposition for the MoM-matrix, because we want to avoid additional errors due to the CG procedure in our investigation of the discretization errors.

First we consider the convergence rate of the equivalent current J_z associated with the circle in the basis scattering configuration depicted in Figure 5.6. In Figure 5.7, the normalized error in J_z is shown as a function of the mesh density in terms of the number of points per wavelength. The approximate current improves upon continuous refinement of the discretization. This is an indication that the expansion functions are indeed ultimately dense in the domain of the L and

K operators. Since the exact boundary of the circle is smooth, the convergence rate is subject to the smoothness of the parametrization and the expansion function. For the EFIE and MFIE, the order of convergence is linear and quadratic for pulse and triangle expansions, respectively. According to Cea's lemma [58, p. 186], the convergence rate is independent of the smoothness of the testing function (Section 3.7). This is confirmed by the fact that the errors associated with $\square\square$ and $\uparrow\square$ test and expansion are commensurate. Nevertheless, the testing function may influence the overall magnitude of the error in the approximation, as observed with pulse expansion for the MFIE. Note also that the results for the operators L (EFIE) and K (MFIE) are comparable for corresponding expansion functions. Further, we remark that with \square expansion, the error in the current at the edge centers also converges quadratically as opposed to the weighted error over the pulse (which converges linearly).

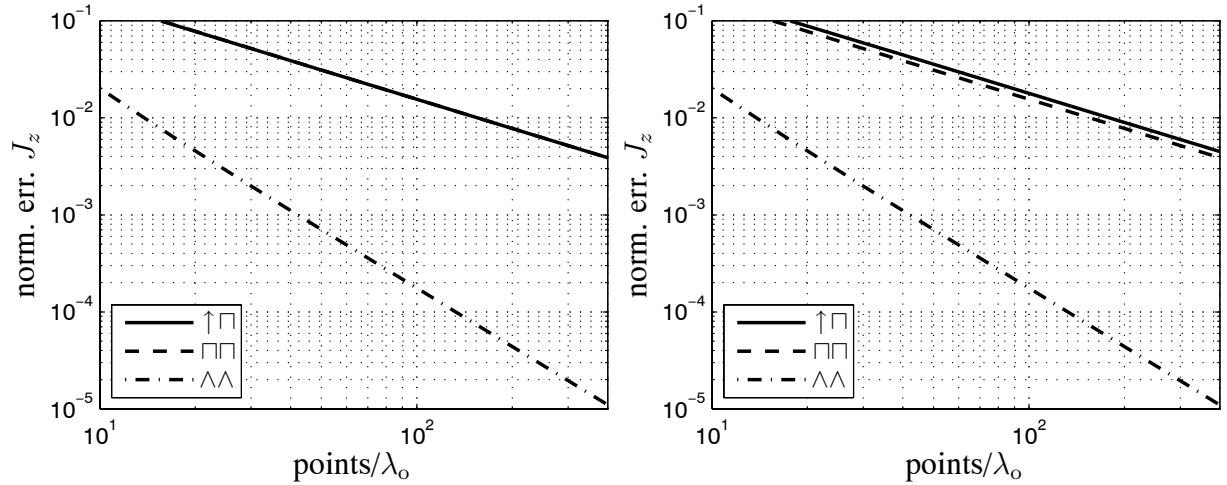


Figure 5.7: The error in the equivalent current, J_z , versus the mesh density, points/λ_0 , for the circle. On the left the EFIE, and on the right the MFIE results.

Next, in Figure 5.8, the amplitude of the equivalent current $|J_z|$ along the contour, \mathcal{C} , of the PEC is depicted for the circle (dashed) and the cross (solid). For compactness, the currents of the circle and cross are shown in the same figures. The direction of the source position with respect to the center of the scattering object, ϕ_S , is indicated explicitly. The current behaves smoothly for the circle. Therefore, piecewise linear and piecewise constant expansion functions provide a convenient approximation of the current. However, $|J_z|$ exhibits a singular behavior with respect to the cross due to the non-smoothness arising at the corners of the boundary. The vertical lines indicate the positions of the outward (dotted) and inward (dash-dotted) oriented corners of the cross. The behavior of the current near the corners is described by the *edge condition* [36, Section 3.8.2], which is based on the fact that the stored energy in any finite

volume of space must remain finite. Accordingly, for a wedge with an exterior angle ψ , the current behaves as $J_z(\rho) \sim \rho^{\frac{\pi}{\psi}-1}$, for the TM case, where ρ is the distance away from the wedge [34, Section 4.11.7]. For the inward and outward corners, we have, $J_z \sim \rho$ and $J_z \sim \rho^{-\frac{1}{3}}$, respectively. For a uniform mesh, the overall error in the approximation is primarily dominated by the error contribution from the corners. This may affect the apparent order of convergence, both for the current and the resulting scattered field [75].

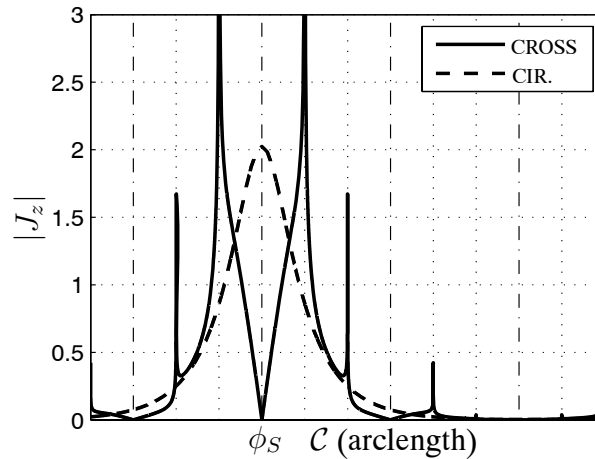


Figure 5.8: The equivalent current, $|J_z|$, along the boundary \mathcal{C} . The position that corresponds with the direction of the line source, ϕ_S , is highlighted. The vertical lines indicate the location of the outward (dotted) and inward (dash-dotted) corners.

Let us now focus on the order of convergence with respect to the scattered fields generated by the approximate equivalent current J_z via the integral representations in Eq. (5.55). In Figure 5.9, the normalized error in the scattered field at the observation contour $\mathcal{C}_o^{\text{ex}}$, as depicted in Figure 5.6, is shown as a function of the mesh density, with from top to bottom, the circle, the hexagon, and the cross, respectively. The figures on the left and the right are obtained via EFIE and an MFIE, respectively. For the circle with $\wedge\wedge$ test and expansion functions, the scattered field has similar to the current quadratic convergence. For the EFIE, the same performance for the circle is obtained with the $\uparrow\square$ and $\square\square$ combinations. Despite the smoother behavior of a triangle, the order of convergence for $\wedge\wedge$ is limited by the non-smoothness of the approximate boundary, i.e., the application of a flat-faceted mesh instead of a curved mesh [75]. For the MFIE, the scattered field for both $\wedge\wedge$ and $\square\square$ discretizations, yields quadratic convergence. The magnitude of the error for $\square\square$ discretization is four times larger as that for the $\wedge\wedge$ discretization. The convergence for $\uparrow\square$ discretization is of the same magnitude and linear order as the error observed in the current J_z .

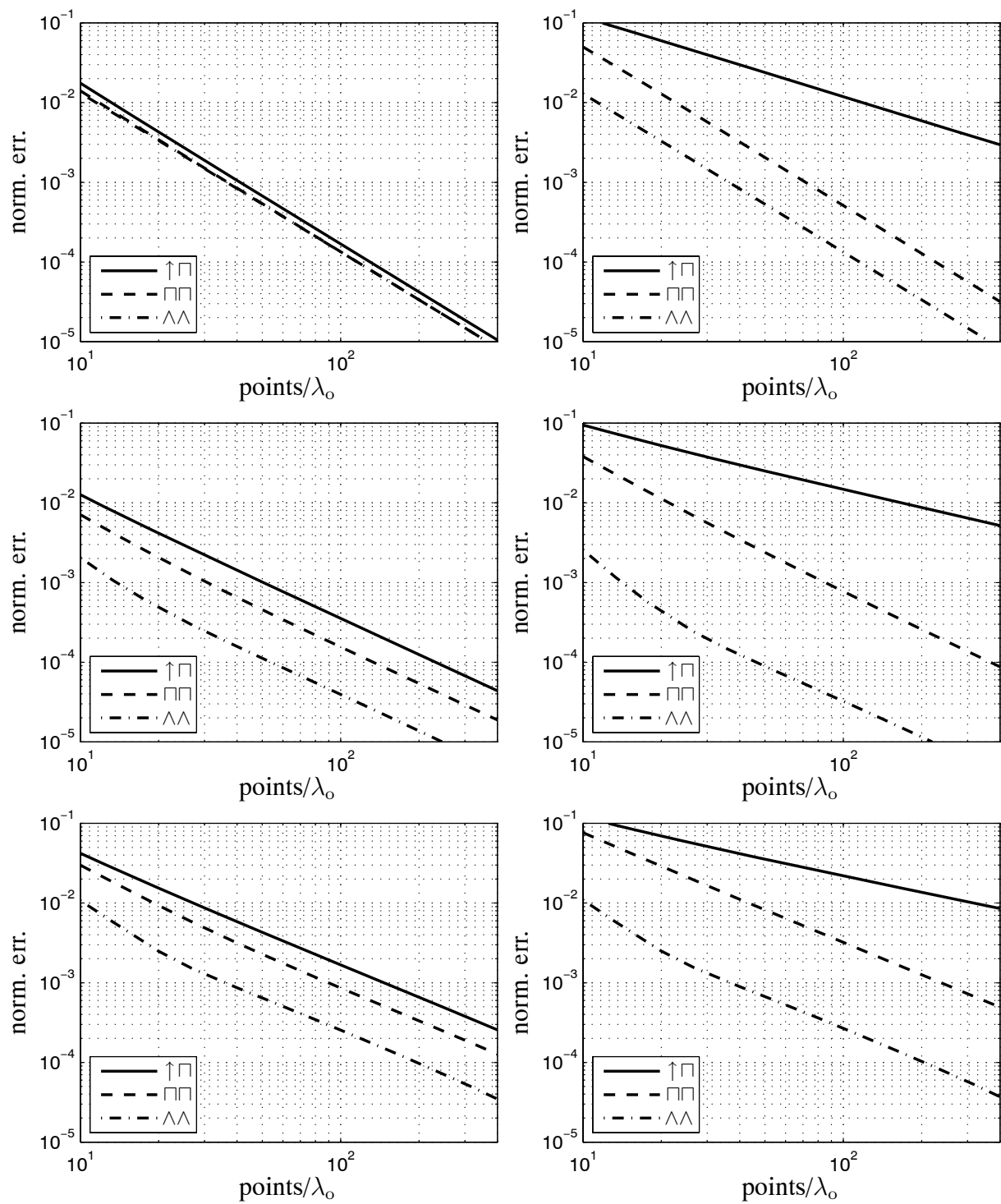


Figure 5.9: The error in the field versus the mesh density, points/λ_0 , for the EFIE (left) and MFIE (right). In the top, middle and bottom figures, we have the circle, the hexagon and the cross, respectively.

For the hexagon and cross, the order of convergence is somewhat less in comparison with the circle. This reduction is caused by the non-smoothness of the exact boundary. A possible explanation is the error at the corners determines the overall error due to the singular behavior in the equivalent current, as observed in Figure 5.8. For the stable part (above 50 points/ λ_o), the EFIE reaches for all three test and expansion combinations a convergence of about $\mathcal{O}(N^{-1.5})$ for the hexagon, and $\mathcal{O}(N^{-1.4})$ for the cross. The same rates are obtained with $\square\square$ and $\wedge\wedge$ for the MFIE, yet, $\uparrow\square$, leads to $\mathcal{O}(N^{-0.75})$ for the hexagon and $\mathcal{O}(N^{-0.7})$ for the cross. Hence, in comparison with the circle, we infer that the reduction in the order of convergence may be attributed to the degree of non-smoothness arising in the exact boundary. Moreover, this reduction is largely insensitive to the choice of test and expansion functions. Besides the order of convergence, also the magnitude of the error increases with an increasing non-smoothness, e.g., at 30 points/ λ_o the magnitude of the error with the hexagon is approximately 4 to 5 times less than with the cross for all three test and expansion combinations. Note that this loss of performance may be recovered through the application of *graded meshes* [76, Section 8.3.1], instead of uniform ones, i.e., by letting the mesh become more dense near the corners, with a gradation that is subject to the degree of non-smoothness.

Notice that, despite the better order of convergence for the circle, the magnitude of the error involving $\wedge\wedge$ starts at a much smaller value for the hexagon. At a first glance, this may seem contradictory, since the exact boundary of the hexagon is not smooth. However, unlike the circle, the approximate and exact boundary do coincide for the hexagon. This is also the underlying reason why the order of convergence of the hexagon and cross exceed that of the circle in the range from 10 to 20 points/ λ_o , i.e., where the overall error is not yet dominated by the contribution from the corners.

For applications where LEGO will be used, the domains are often electromagnetically large. To avoid unwanted interior resonances inherent to the EFIE and the MFIE, as described in Section 3.4, the CFIE may be employed. From Figure 5.9 it follows that *only* for the $\wedge\wedge$ combination, the magnitude of the error in the field calculated using the EFIE and MFIE are commensurate for all three object shapes. For $\square\square$, this observation is based on a comparison of the magnitude of the error, as the EFIE solution is always a factor of about 4 better than the MFIE solution, while for $\uparrow\square$ the order of convergence is different for the EFIE and MFIE. These observations have immediate consequences for the choice of the combination constant α in the application of the CFIE, given by Eq. (3.20). That is, the combination constant α in Eq. (3.20) is usually set around $\alpha = 0.2$, such that the CFIE has roughly the same condition number as the MFIE. For $\square\square$ this leads to a reduced accuracy compared with the EFIE, and for $\uparrow\square$ also a reduced convergence.

The choice of $\wedge\wedge$ test and expansion yields the best performance for all cases if integrals are computed with sufficient accuracy, i.e., with an error less than one percent.

Finally, we point out that upon gradually increasing the size of the observation contour $\mathcal{C}_0^{\text{ex}}$, from λ_0 to $10\lambda_0$, the magnitude of the error in the scattered field from the circle varies no more than 12%. This includes the dependence on the position of the line source, which remained at the bottom right corner of the varying observation contour. This relative independence of the error on the source and observation point is primarily due to the application of adaptive quadrature rules in the excitation vector and the field representations.

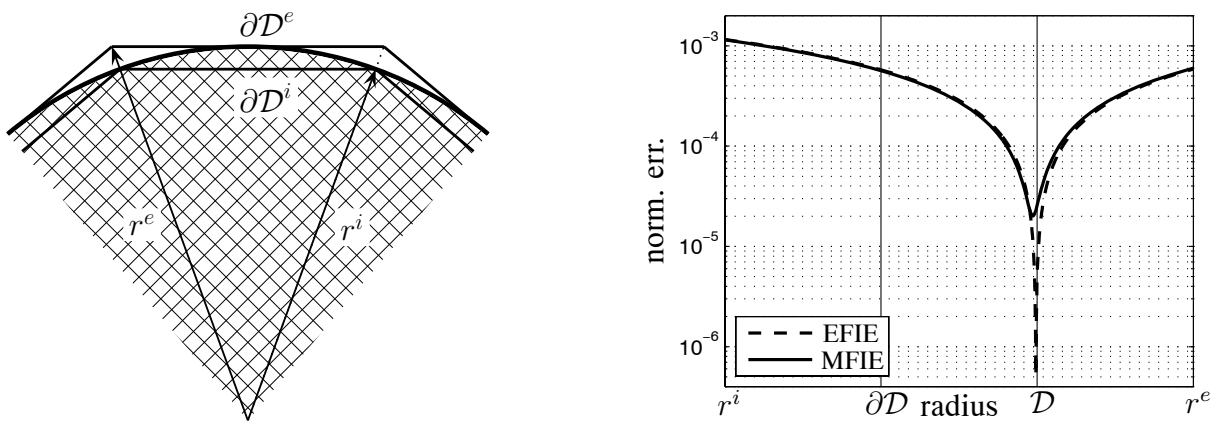


Figure 5.10: On the left the flat-faceted mesh of the circle for the inner, r^i , and outer closure, r^e . On the right the normalized error in the scattered field as a function of the radius for the EFIE and MFIE involving $\wedge\wedge$. The scaling radii with matching boundary length $\partial\mathcal{D}$ and matching area of the domain \mathcal{D} are indicated.

In the discretization of a smooth boundary via a flat-faceted mesh, the discretized approximate boundary only coincides with the exact smooth boundary at discrete points. In that case, the start and end node of each elementary edge are usually chosen to coincide with the exact smooth boundary. This methodology generally leads to a discretized boundary that is shorter than the actual boundary $\partial\mathcal{D}$. As illustrated for a single edge segment in Figure 5.10, application of this common discretization process to the circle (hatched), the boundary of the resulting mesh describes an inner closure $\partial\mathcal{D}^i$ of $\partial\mathcal{D}$. This mesh probably provides the worst results when the midpoint rule is applied to evaluate the test and expansion integrals, i.e., all sample points are taken furthest away from the exact boundary. In that case, the outer closure $\partial\mathcal{D}^e$ with the radius r^e at the edge nodes seems to be a more suitable discretization, since all edge centers would coincide with $\partial\mathcal{D}$. However, the analytically determined singular-integral contributions take the entire edge into account, as will higher order quadrature rules.

Hence, the question arises whether the use of a different mesh size could lead to a reduction of the error. Intuitively, the optimal choice of the radius r at the edge nodes is most likely situated somewhere between the inner and outer closure, i.e., $r^i < r < r^e$. To determine the optimal radius of the circle, the normalized error in the scattered field at $\mathcal{C}_o^{\text{ex}}$ as a function of the radius for the EFIE and MFIE formulation, involving $\wedge\wedge$ test and expansion, is illustrated on the right in Figure 5.10. We have indicated the radius at which the area of the approximate domain is equal to the actual area of the circle by \mathcal{D} and the radius at which the length of the boundary is equal to the actual circumference of the circle by $\partial\mathcal{D}$. It appears that scaling the radius, and thus the mesh size, such that the areas of the meshed and exact circle correspond (domain scaling), significantly reduces the error in the scattered field. Regarding the equivalent current J_z , which is not shown here, only a marginal reduction of the error was obtained, yet the optimum also occurred with domain scaling. Note that with pulse expansion, the impact of scaling on the error in the current proved to be negligible.

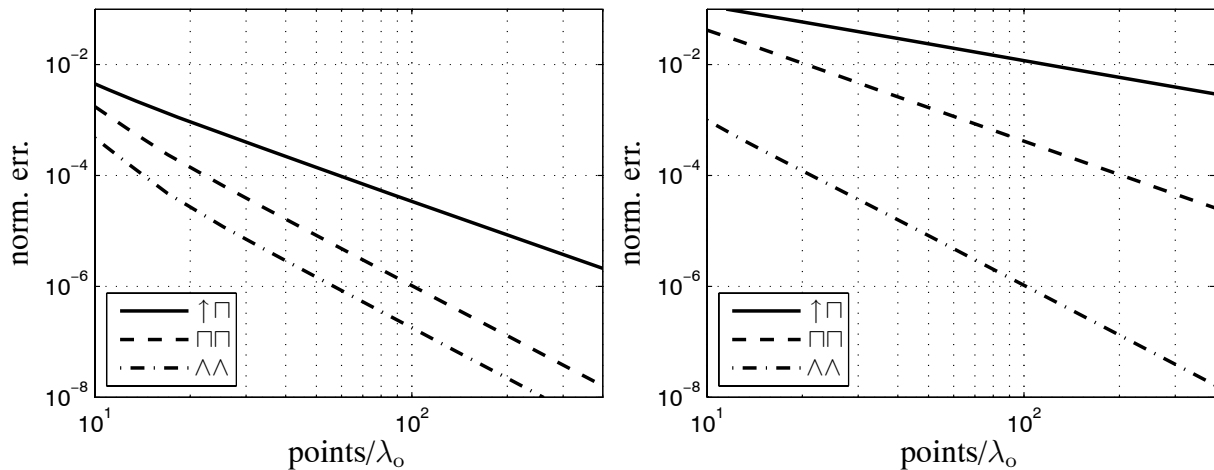


Figure 5.11: The normalized error in the field versus the mesh density in points/λ_o , for the domain-scaled circle with on the left the EFIE and on the right the MFIE results.

The convergence behavior of the normalized error in the scattered field for scattering by a circle with domain scaling is depicted in Figure 5.11 for the EFIE and the MFIE. In comparison with the results for the unscaled circle, as presented in the top row of Figure 5.9, the order of convergence involving $\wedge\wedge$ has increased one order, yielding, cubic convergence, for both, the EFIE and the MFIE. In the $\square\square$ case, the EFIE order of convergence increases, whereas the MFIE results are virtually the same for the scaled and unscaled circle. Regarding $\uparrow\square$, there is no improvement in the convergence rates, only the magnitude of the error has reduced with a factor 5 for the EFIE. It may seem peculiar that in comparison with $\wedge\wedge$, $\square\square$ leads to an increase in the order of

convergence for the EFIE *only*. The underlying reason for this is elucidated in Section 5.6, where we propose a regularization for the MFIE kernel.

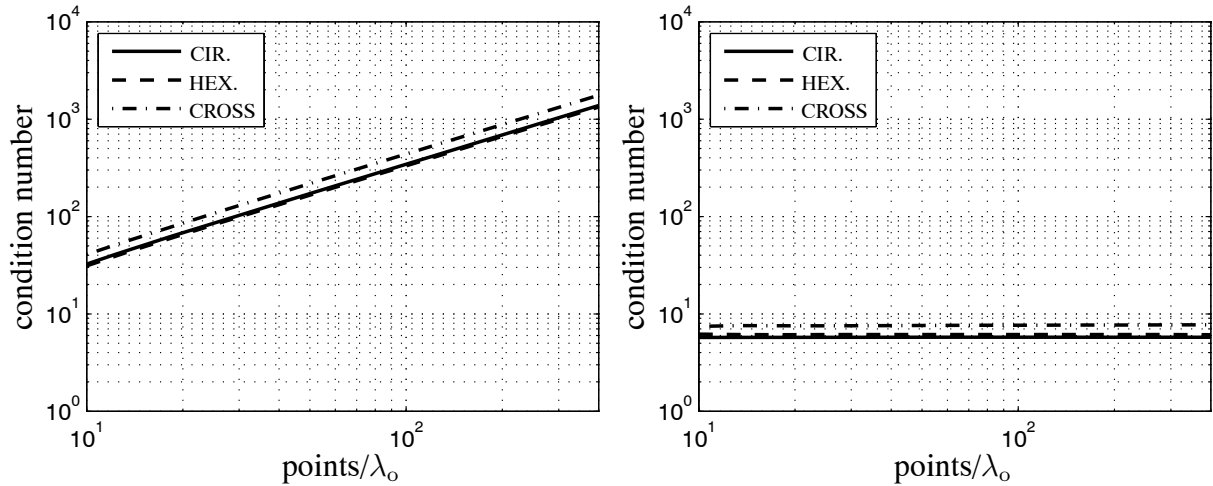


Figure 5.12: The condition number versus the number of unknowns, points/λ_0 , for the circle, hexagon, and cross with $\wedge\wedge$ discretization. On the left the EFIE and on the right the MFIE.

Next, we investigate the sensitivity of the MoM-matrix equations to small errors in relation to the condition number of the MoM-matrix. In Figure 5.12, the condition number is shown as a function of the mesh density for the circle, the hexagon, and the cross, with $\wedge\wedge$ test and expansion. For the EFIE, the condition number increases linearly, while for the MFIE the condition number is constant. The reason for the well-conditioned MoM-matrix of the MFIE, is that the MFIE is an integral equation of the second kind, while the EFIE is an integral equation of the first kind, as has been explained in Section 3.3. Despite the corners in the boundary of the cross and hexagon, no significant increase in the condition number with respect to the circle is observed for both, the MFIE and the EFIE.

Further, Figure 5.13 shows the dependence of the condition number on the test and expansion function combination. In particular we have considered the condition number with the $\uparrow\square$, $\square\square$, and $\wedge\wedge$ combinations for the cross. With reference to $\wedge\wedge$, the magnitude of the condition number for the EFIE is a factor of 2.5 for $\square\square$, and 3.5 for $\uparrow\square$. Comparing the EFIE results with those of the hexagon and the circle (not shown here) shows approximately the same factors occur. In conclusion, looking at both Figure 5.12 and Figure 5.13, we infer that the order of the condition number depends only on the mapping properties of the operator under consideration. Further application of a different combination of test and expansion functions has a negligible impact on the condition number for the MFIE, while magnitudes differ for the EFIE. Moreover, the

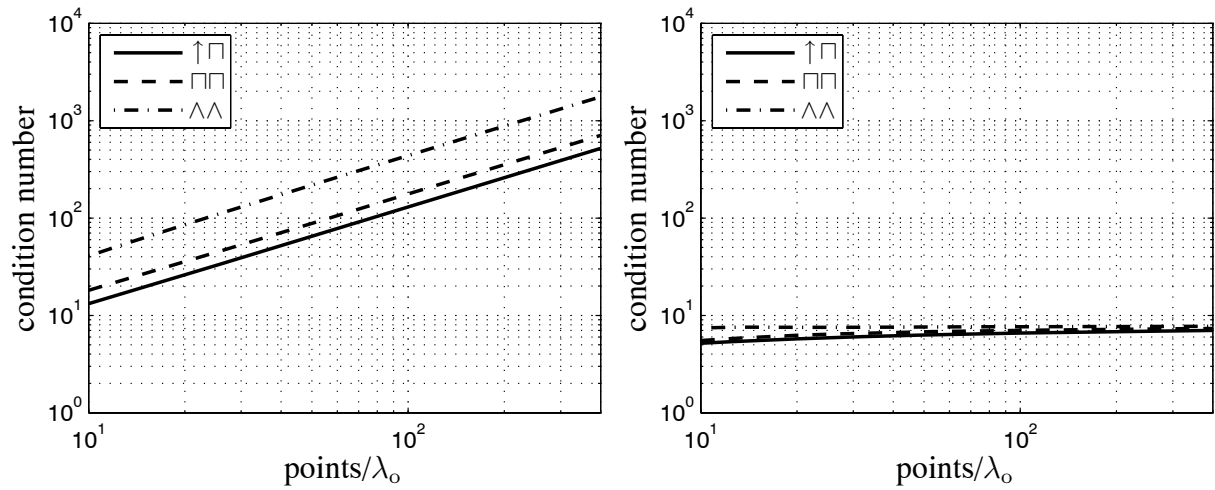


Figure 5.13: The condition number versus the number of unknowns, points/λ_0 , for the cross with $\uparrow\sqcap$, $\square\square$, and $\wedge\wedge$ test and expansion. On the left the EFIE and on the right the MFIE.

condition number seems to be largely insensitive to the corners of the exact boundary. Finally, the condition number of the EFIE MoM-matrix is primarily determined by the singular part, when the regular part was omitted the same behavior of the condition number was observed.

For the cases considered so far, all test and expansion integrals for the MoM-matrix, the excitation vector, and the field representation, have been determined with adaptive quadrature rules, to a maximum error of one percent in the evaluation of these integrals. Next, let us investigate the loss in accuracy due to more elementary quadrature rules. We aim at obtaining an estimate for the optimum balance between the efficiency of filling the MoM-matrix, versus the obtained accuracy. Accordingly, to assess the worst loss of accuracy, we consider the lowest order quadrature, i.e., the midpoint rule, as it involves only a single sampling point per edge. Beware though, that this affects the regular integrand contributions only, i.e., the singular integrand contributions of the various test and expansion integrals are accounted for analytically. Further, the self terms (overlapping edges) for both, the EFIE and MFIE are still calculated accurately.

In Figure 5.14, the results of the $\wedge\wedge$ discretization for the three object shapes in Figure 5.9 are repeated with the midpoint rule. The order of convergence of the error for the circle remains quadratic, while the magnitude increased by a factor of two to three. Yet, due to the high symmetry of the circle, error cancellation may occur [77], which makes this result inconclusive. However, we point out that the additional order of convergence gained with domain scaling is lost with the application of the midpoint rule. With respect to the hexagon and the cross, the

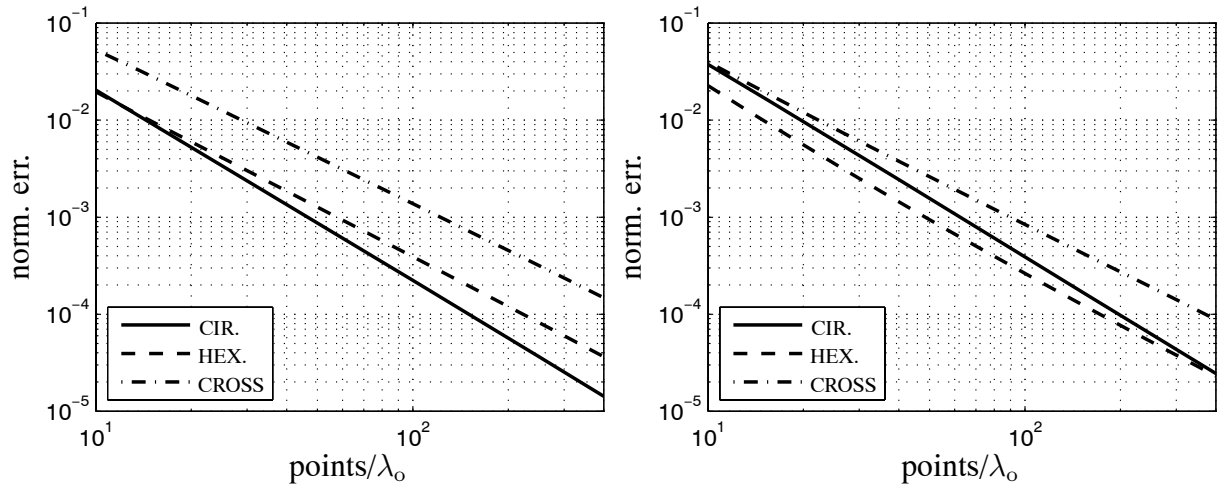


Figure 5.14: The normalized error versus the number of unknowns, points/λ_0 , for the circle, hexagon, and cross with $\wedge\wedge$ discretization involving the midpoint rule. On the left the EFIE and on the right the MFIE.

order of convergence has even improved, i.e., $\mathcal{O}(N^{-1.7})$ for the hexagon and $\mathcal{O}(N^{-1.6})$ for the cross. This improvement is attributed to the decreasing error in the evaluation of the integrals by the midpoint rule, as the integrand becomes more smooth when the mesh is refined. It is clear that with further mesh refinements, the convergence rates will gradually decrease towards the ones obtained with the adaptive quadrature rules, depicted in Figure 5.9. Despite that, in the shown mesh range the magnitude of the errors are larger than the corresponding errors for the adaptive quadrature. For example, to arrive at the accuracy obtained with 25 points/λ_0 via adaptive integrals, the mesh of the hexagon and cross should be about three to four times denser for the case with the midpoint rule. Further, applying adaptive quadrature rules to the excitation vector and scattered field representation only did not lead to significant changes in the results. If instead only the MoM is applied with adaptive quadrature rules, similar results follow. This observation indicates that the overall accuracy is bounded by the integrals determined with the most elementary quadrature rule.

We also employed the midpoint rule to the test and expansion integrals of the $\uparrow\sqcap$ and $\sqcap\sqcap$ discretizations for the EFIE and MFIE (not shown here). In comparison with the results in Figure 5.9, obtained via adaptive quadratures, the additional error in the scattered field proved to be negligible for all three object shapes. As such, the performance involving \uparrow and \sqcap functions is primarily determined by the contributions from the singular integral part and the self term, which are obtained by analytical means, i.e., a single sample point per edge suffices for the reg-

ular integral part. In fact, apart from the analytical contributions, $\uparrow\uparrow$ and $\uparrow\uparrow$ test and expansion functions are effectively equivalent for the midpoint rule on a uniform mesh. Hence, the superior performance of $\uparrow\uparrow$ over $\uparrow\uparrow$ may be solely attributed to the analytical evaluation of the singular (double) integral parts. This observation applies to the test integral in the MoM-matrix only. Applying the midpoint rule to the regular part of the test integral in the excitation function only leads to a minor increase in the magnitude of the error for about ten points per wavelength.

Let us now consider the frequency dependence of the integral equations and the suppression of the interior resonance modes by means of the CFIE. For the combination constant of the CFIE, we set $\alpha = 0.5$. The position of the line source and the dimensions of the scattering object, as assumed in the configuration depicted in Figure 5.6, are unchanged, i.e., λ_0 is fixed, and only the operating frequency λ of the line source is varied. As the construction of a reference solution for the hexagon and the cross for each successive frequency is rather time-consuming, only the circle is considered for which analytical solutions are available. The frequency dependence will be expressed in terms of the electromagnetic size of the circle, kr . Here, r denotes the radius of the (unscaled) circle, and k the wavenumber, with $k = 2\pi/\lambda$. Note that kr is the length of the circular contour relative to the wavelength λ . For the initial configuration we have $kr = k_0 r = 0.9\pi$, for which we take 34 points/ λ_0 (96 unknowns).

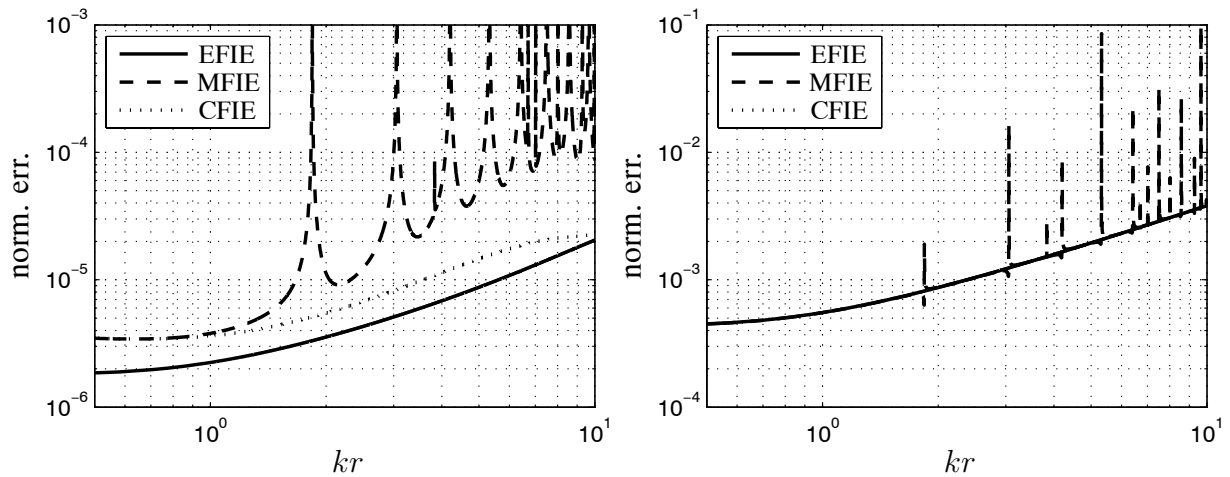


Figure 5.15: The normalized error in the scattered field from the circle as a function of the frequency in terms of kr with $\wedge\wedge$ discretization. On the left the domain scaled circle and on the right the unscaled circle. The number of unknown is fixed to 96.

The normalized error in the scattered field of a circle is depicted in Figure 5.15, as a function of kr . As observed in Figure 5.9, the EFIE and MFIE results for the unscaled circle are commen-

surate for $\wedge\wedge$ test and expansion functions. It is clear that the MFIE results show relatively large error spikes at discrete frequencies. At these frequencies, the MFIE suffers from the interior resonance effect. For a circle the EFIE and MFIE interior resonances occur at zeros of the Bessel function $J_n(kr)$ and its derivative $J'_n(kr)$, respectively, for $n \in N$. Despite that this may also imply that an EFIE and MFIE resonance may occur at the same frequency, e.g., at $kr = 3.8317$, the CFIE remains free of interior resonances. Apart from the CFIE, the EFIE results tend to be free of resonances as well, because an interior resonant electric boundary current yields a zero field contribution outside the circle, as has been elucidated in Section 3.4 with the aid of the reciprocity theorem and the boundary conditions of the PEC.

Because kr is inversely proportional to the number of points per wavelength, intuitively, the error for the EFIE and MFIE in Figure 5.15, should decrease cubic and quadratic for the scaled and unscaled circle, respectively. However, these convergence rates are not achieved here, as the approximate boundary does not converge towards the exact boundary as kr decreases because the same mesh size is applied. As such, the deviation between the approximate and exact boundary is constant, gradually becoming the limiting factor for the order of convergence. This is also the reason why the error eventually saturates.

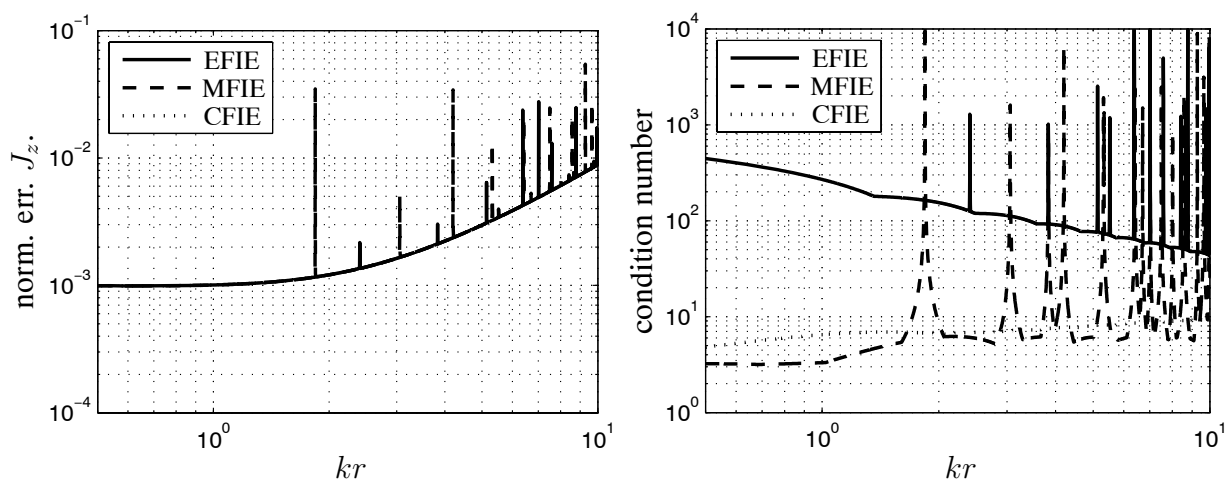


Figure 5.16: As a function of kr , the normalized error in J_z (left), and the condition number of the MoM-matrix (right), for the unscaled circle with $\wedge\wedge$ discretization.

On the left in Figure 5.16, the normalized error in the equivalent current J_z as a function of kr is presented. The saturation observed in the field error also occurs for the current. The EFIE and MFIE both suffer from resonant spikes in J_z , which are indeed suppressed by using the CFIE. On the right in Figure 5.16, the corresponding behavior of the condition number of the

MoM-matrix is illustrated. The MoM-matrices of the EFIE and MFIE are ill-conditioned at the interior resonances as the solution to both integral equations are not uniquely determined at these discrete frequencies. Near these frequencies, it becomes increasingly difficult to solve the MoM-matrix equation. Unlike the current and field convergence, no saturation occurs for the condition number, as it only depends on the relative mesh size, viz., points/λ_0 . Apart from the resonant spikes, the condition number of the CFIE involves a similar stable behavior as the MFIE and does not increase the EFIE linear line. Note that upon applying the midpoint rule to the unscaled circle, the narrow resonant spikes in the current will broaden for both the EFIE and MFIE.

Finally, enlarging the electromagnetic size of the scattering object, kr , raises the density of resonant frequencies, so that it becomes increasingly difficult to avoid them by shifting the operating frequency. Moreover, the exact resonance frequencies slightly deviate from the theoretical ones depending upon the applied mesh density. This comment is also valid for the cross and hexagon, where the exact and approximate boundaries do coincide. Hence for electromagnetically large objects, the application of the CFIE becomes essential. Although this implies the construction of both the EFIE and MFIE matrix elements, the additional computational costs are relatively small, as has been demonstrated in Section 5.3. On the other hand, since the CFIE is better conditioned at and near a resonance frequency, computing the equivalent current with an iterative solver is most efficient with the CFIE, as less iterations are required.

5.6 Regularization

Despite the fact that the scattered field improves upon increasing the smoothness of the test and expansion functions, one would expect a better order of convergence from the MFIE, especially since the MFIE kernel is continuous, whereas the EFIE kernel is singular. In [78] it is claimed that the reason for this poor convergence is that, although the identity operator associated with the MFIE is trivial to discretize, it behaves as an integral operator with a highly singular kernel in determination of the solution error, which causes the unexpected low convergence rates. Davis and Warnick proposed a regularization for the identity operator resulting in high-order convergence with a low-order discretization. Improvements in the convergence rate up to three orders were achieved even with $\uparrow \square$ discretization. Despite the fact that these results were obtained for scatterers involving smooth boundaries that were discretized via a curved mesh, the proposed regularization may also yield improvements with our flat-faceted mesh.

Let us first explain the numerical implementation and the properties of the reported regularization. The error in the scattered field can be expressed as a spectral error [79]. The discretization of the identity operator leads to a sinc function as regards the spectral error [78]. The proposed regularization of the identity operator, \mathbb{I} , implies the application of a filter, \mathcal{F} . As regards the spectral error, if the filter \mathcal{F} comprises a sinc function, it filters out the high-frequency content that is associated with the test and expansion functions, to improve their effective smoothness. Smoother test and expansion functions yield a stronger convergence of the scattered field error. The filter \mathcal{F} is given by

$$\mathcal{F}(\boldsymbol{\rho}, \boldsymbol{\rho}') = \frac{1}{C} \frac{\sin \frac{\pi}{L}(\tau - \tau')}{\sin \frac{\pi}{C}(\tau - \tau')} e^{j \frac{\pi}{C}(\tau - \tau')}, \quad (5.81)$$

irrespective of the applied test and expansion combinations. Here, C indicates the total perimeter length of the contour \mathcal{C} of the scattering object, and τ is the arc length measured from an arbitrary point on \mathcal{C} . With L being the edge length, the filter involves a sinc function with height $1/L$, and width $2L$, which is made periodic with respect to the contour \mathcal{C} . In the case of a nonuniform mesh, L is taken as the mean element width. For the MFIE involving a PEC, Eq. (5.25), this filter implies the following modification to the identity operator,

$$\mathbb{I}_{mn}^{HJ} = \frac{1}{2} \left\langle \mathbf{f}_m^H(\boldsymbol{\rho}), \hat{\boldsymbol{\nu}} \times \int_{\mathcal{C}_n} \mathbf{f}_n^J(\boldsymbol{\rho}') \mathcal{F}(\boldsymbol{\rho}, \boldsymbol{\rho}') d\ell' \right\rangle, \quad (5.82)$$

in the corresponding matrix equation (5.26). As an implementation note we mention that the smallest error is achieved if the test and expansion integrals of \mathbb{I}^{HJ} and \mathbb{K}^{HJ} are evaluated using the same quadrature rule in which case the leading error term of the quadrature errors cancel in the final solution.

The normalized error in the scattered field resulting from applying this regularization to the MFIE involving $\square\square$ test and expansion functions is shown in Figure 5.17 for the circle and the cross. For convenience, the results of the nonregularized version have been repeated. With regularization, the order of convergence improves from quadratic to cubic for the domain-scaled circle only. In the case of the cross and the unscaled circle, the improvement still leads to a significant reduction in error magnitude. Hence, if the exact boundary is not smooth, the error is primarily determined by the inaccuracy in the approximation of the singular behavior of the current at the corners, irrespective of the smoothness of the applied test and expansion functions. It is noted that in all cases that we have considered, the regularization did not affect the condition number.

Furthermore, saturation of the error occurs for the unscaled circle above 100 points/ λ_0 . This effect is less pronounced for the scaled circle. Upon increasing the required accuracy of the

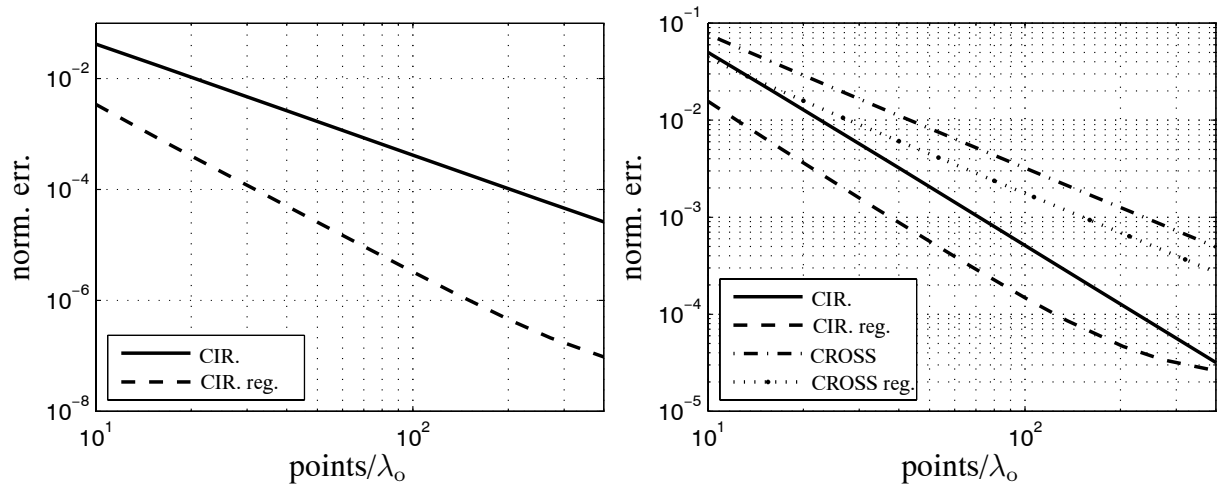


Figure 5.17: Regularization (reg.) of the MFIE with $\square\square$ discretization. The normalized error in the field versus the number of unknowns, points/λ_0 . On the left the domain scaled circle and on the right the unscaled circle and the cross.

adaptive integrals from 10^{-2} to 10^{-4} , the saturation disappears and the slope of the convergence rate becomes constant again. The underlying reason is that, with an increasing mesh density, the contribution of \mathcal{K}^{HJ} is relatively small compared to that of the regularized \mathcal{I}^{HJ} , Eq. (5.82). Note also that, with the inclusion of the filter \mathcal{F} , the integrand behaves more erratically, which implies that more sampling points have to be taken to achieve the same accuracy as without the filter. Low-order quadrature rules like the midpoint rule should in that case be avoided for the expansion integral; otherwise the filtering function is lost due to an insufficient number of sampling points. With regularization, the performance of the MFIE with $\square\square$ discretization improved for the domain-scaled circle towards that of $\wedge\wedge$ discretization. It is noted that the regularization does not improve the results for the hexagon and cross shape. Finally, with regularization applied to the $\wedge\wedge$ combination, no improvement was observed. Hence, $\wedge\wedge$ without regularization remains the preferred choice for discretizations involving a flat-facetted mesh.

5.7 Perfect magnetic conductors

In this section we investigate the accuracy of the error in the scattered field as a function of the applied discretization, for the solution of the integral equations that satisfy the TE-description (Section 5.2). To this end, let us consider the electromagnetic scattering from a PMC involving

a magnetic current distribution, M_τ . In the TE case related to the PMC, the same incident field can be employed for the excitation vector as has been applied before, i.e., the incident field generated by an electric line source at the bottom right corner of the observation contour $\mathcal{C}_o^{\text{ex}}$. Thus, deviations attributed to a different incident field distribution are avoided. Furthermore, when considering problems involving a dielectric object in the TM case, the MoM matrices related to the PMC (and PEC) may directly be employed. Again, the basis configuration of Figure 5.6 is considered, with the same object shapes. The EFIE and MFIE matrix equations for a PMC are given by Eqs. (5.40) and (5.33), respectively. In contrast with the PEC, the MFIE now involves L , while the EFIE involves K . Also, the scalar potential yields a nonvanishing contribution for the TE case. In our mixed-potential formulation, the differential operators are diverted to the test and expansion functions. Hence, only (piecewise) continuous functions are allowed. Accordingly, we restrict the analysis to the $\wedge\wedge$ test and expansion function combination.

Before we proceed with the error in the scattered field, we first consider the behavior of the magnetic equivalent current, M_τ , in its dependence on the smoothness of the boundary. In Figure 5.18, the amplitude of the equivalent current $|M_\tau|$ along the contour \mathcal{C} of the circle (dashed) and the cross (solid) is depicted. For compactness, the currents of the circle and cross are shown in the same figures. The vertical lines indicate the positions of the outward (dotted) and inward (dash-dotted) oriented corners of the cross. The direction of the source position with respect to the center of the scattering object, ϕ_S , is indicated. The current behaves smoothly for the circle. Therefore, $\wedge\wedge$ discretization provides a convenient approximation of the current.

In contrast with the electric equivalent current J_z associated with a PEC, $|M_\tau|$ remains finite for the cross as well. From the edge conditions for a wedge with an exterior angle ψ , we have that the current behaves as $M_\tau(\rho) \sim b_0 + b_1\rho^{\frac{\pi}{\psi}}$ for the TE case, where ρ is the distance away from the wedge with b_0 and b_1 being constants that depend on the form of the incident field [34, Section 4.11.7]. Hence, for the behavior of M_τ at the inward and outward corners, we have, $M_\tau \sim b_0 + b_1\rho^2$ and $M_\tau \sim b_0 + b_1\rho^{\frac{2}{3}}$, respectively, as can be observed in Figure 5.18. Accordingly, for the TE case, expansion by piecewise linear functions provides an appropriate approximation of the current for non-smooth object shapes as well.

Let us now focus on the order of convergence of the scattered fields generated by the approximate equivalent current M_τ , via the integral representations, Eq. (5.55). In Figure 5.19 the normalized error in the field as a function of the sampling density is shown for the unscaled circle, the hexagon and the cross. The magnitude and the order of convergence of the EFIE and MFIE are comparable. Likewise, in view of the scattering from a PEC with $\wedge\wedge$ discretization in Figure 5.9,

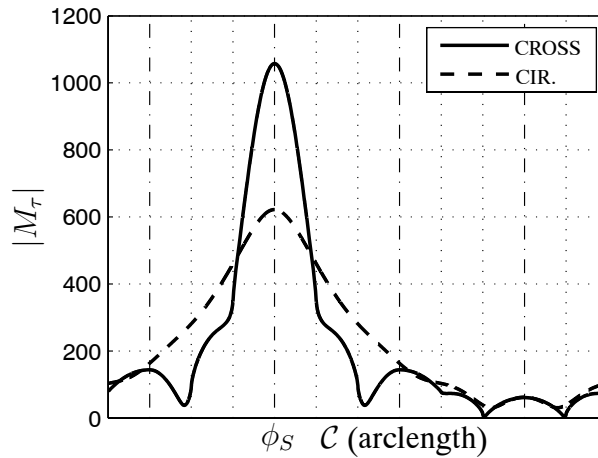


Figure 5.18: The equivalent current, $|M_\tau|$, along the boundary \mathcal{C} . The position that corresponds with the direction of the line source, ϕ_S , is highlighted. The vertical lines indicate the location of the outward (dotted) and inward (dash-dotted) corners.

we observe that approximately the same convergence rates are obtained for the PEC and PMC. The more smooth behavior of the M_τ (PMC) in comparison with J_z (PEC), for the hexagon and cross, does not lead to an improvement in the error. Hence, the order of convergence is bounded by the non-smoothness of the geometry only. This statement is corroborated by the observation made in Section 5.5 that the order of convergence is largely insensitive to the chosen set of test and expansion functions. Finally, applying domain scaling to the circle leads to an improvement of the convergence rate of the error for both the EFIE and MFIE by one order, as with the PEC.

Because $|M_\tau|$ remains finite for scatterers involving non-smooth contours, a well-converged reference solution can be constructed for the hexagon and cross to investigate the order of convergence of the error in M_τ . In this manner we may relate the reduction in convergence observed in the scattered field with the hexagon and cross to a similar reduction in the generating equivalent current. In Figure 5.20, the normalized error in M_τ is shown as a function of the sampling density for a circle, hexagon, and cross. With respect to the circle, the same convergence rate, quadratic, and magnitude is obtained as with the scattering from a PEC, depicted in Figure 5.7. On the other hand, for both the EFIE and MFIE, the order of convergence concerning the hexagon and cross has reduced to, respectively, $\mathcal{O}(N^{-1.25})$ and $\mathcal{O}(N^{-1.19})$. These convergence rates are roughly the square root of those associated with the corresponding field behavior. This minor deviation in the field convergence may be assigned to the subsequent application of the integral representation that produces the fields generated by the equivalent current M_τ .

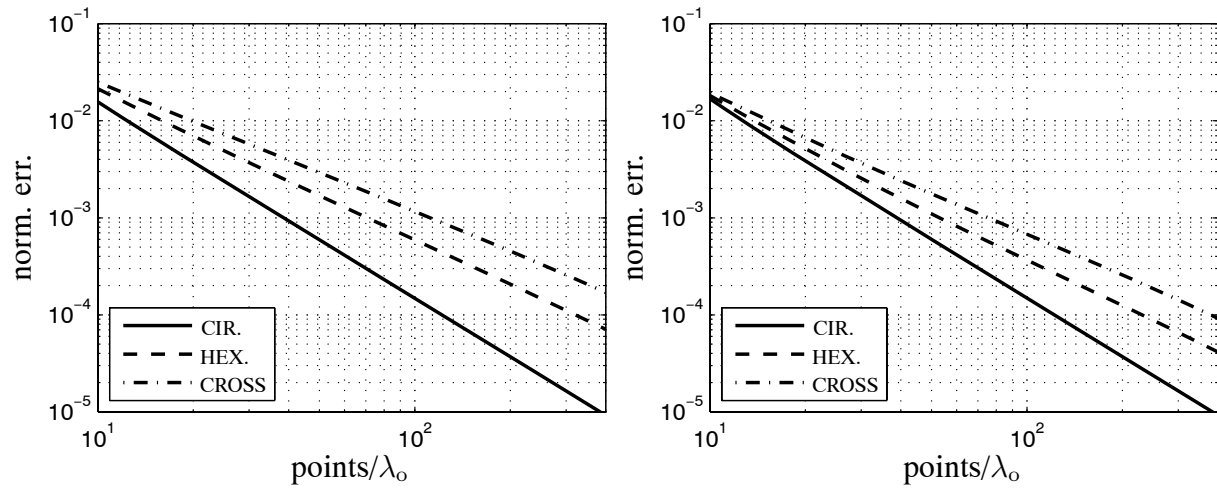


Figure 5.19: The normalized error in the field versus the sampling density for a circle, hexagon, and cross. On the left the EFIE (K^{EM}), and on the right the MFIE (L^{HM}) results.

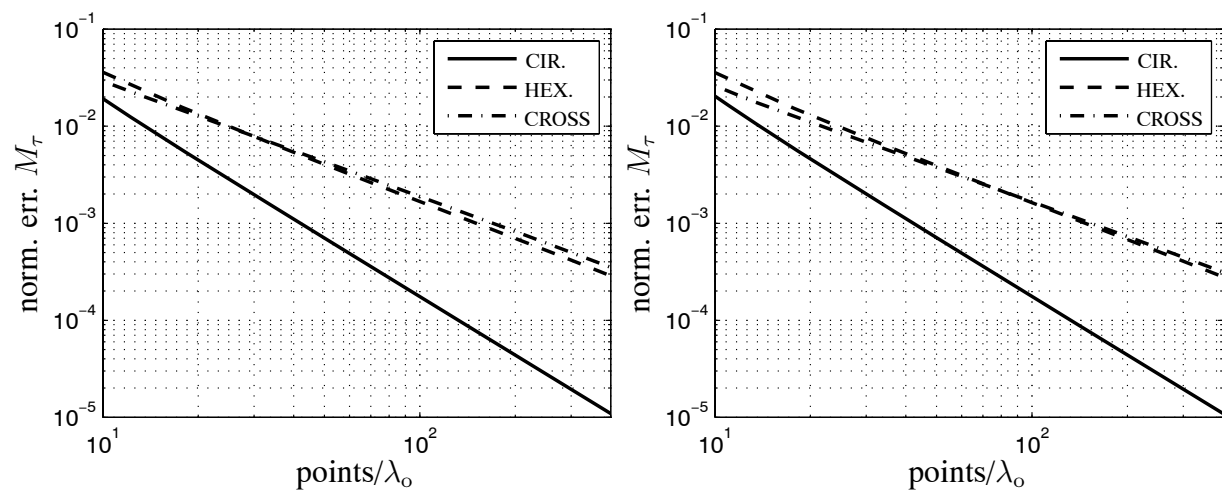


Figure 5.20: The normalized error in M_τ versus the number sampling density for a circle, hexagon, and cross. On the left the EFIE (K^{EM}), and on the right the MFIE (L^{HM}) results.

Next, we investigate the sensitivity of the EFIE and MFIE matrix equations related to small errors by considering the condition number versus the mesh density in Figure 5.21. As the EFIE now represents an integral equation of the second kind, while the MFIE represents an integral of the first kind, the condition number of the EFIE is constant, while for the MFIE it increases linearly. In comparison with the PEC, the magnitude of the condition number for the MFIE (\mathbb{L}^{HM}) is about five times lower than for the EFIE (\mathbb{L}^{EJ}), while for the hexagon and cross this is a factor of eight. This improvement may be attributed to the fact that the scalar potential does not vanish for the TE case. Finally, the dependence of \mathbb{K}^{EM} (EFIE, PMC) on the non-smoothness of the boundary seems stronger than for \mathbb{K}^{HJ} (MFIE, PEC) in Figure 5.12.

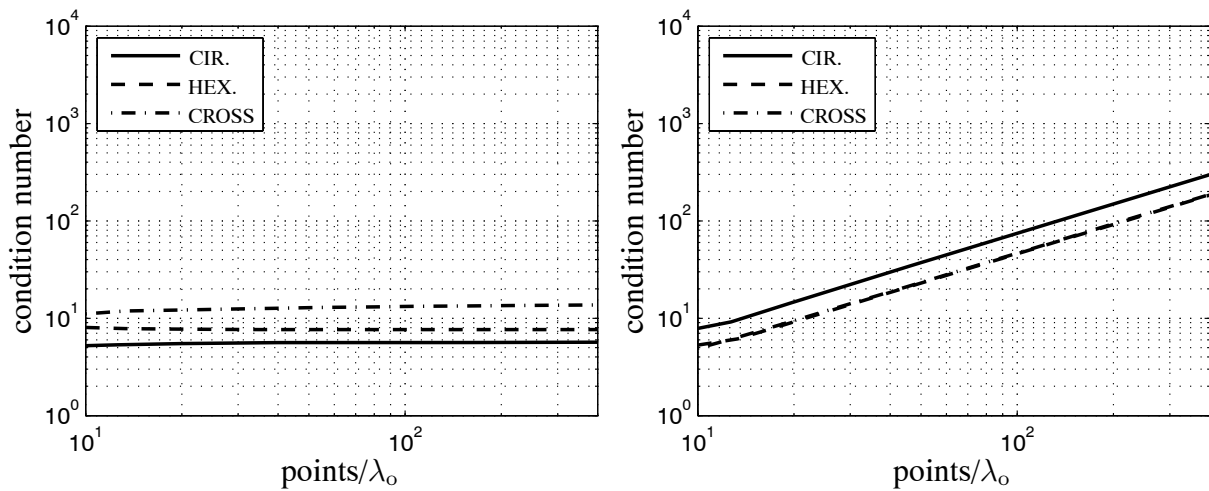


Figure 5.21: The condition number versus the sampling density for a circle, hexagon, and cross. On the left the EFIE (\mathbb{K}^{EM}), and on the right the MFIE (\mathbb{L}^{HM}) results.

5.8 Dielectric objects

General boundary integral equations for the electromagnetic scattering by dielectric objects have been formulated in Section 3.2. This led to two pairs of integral equations, each related to either the interior, or the exterior equivalent state. Both pairs are coupled via boundary conditions. Together the integral equations comprise an overdetermined system of equations. To arrive at a single pair of equations, two possible linear combinations were considered in Section 3.5, viz., the PMCHW and the Müller's formulation. Below, we investigate the solvability and the order of convergence of the discretized version of both formulations. The difference in performance will be elucidated and related to the chosen combination of the two original pairs of integral

equations. Afterwards, an extension is made by means of a different integral formulation with unique mapping properties. Further, the improvement of the solvability of Müller's formulation owing to the proposed additional scaling will be investigated.

In Section 5.3, we briefly stated that the singular behavior associated with the combination of L-operators involving Müller's formulation is less dominant than that of PMCHW. In addition, it was remarked that the low-frequency breakdown is naturally avoided with Müller's formulation. These two properties are inherently related. To elucidate this further, let us recall the definition of the integral operator, L, for the 2D case,

$$\mathbb{L}_v(\boldsymbol{\rho})\mathbf{X} = \gamma_v \int_{\mathcal{C}} \mathbf{X}(\boldsymbol{\rho}') G_v(\boldsymbol{\rho}, \boldsymbol{\rho}') d\ell' - \frac{1}{\gamma_v} \nabla_t \int_{\mathcal{C}} [\nabla_t' \cdot \mathbf{X}(\boldsymbol{\rho}')] G_v(\boldsymbol{\rho}, \boldsymbol{\rho}') d\ell', \quad (5.83)$$

where γ_v being the propagation coefficient and v the medium index. The first term on the right-hand side of Eq. (5.83) denotes the mildly singular vector potential, and the second term the hypersingular scalar potential. The mildly singular behavior may be attributed to the cancellation of the dominant singularities pertaining to the interior and exterior media in the scalar potential. Namely, with the aid of Eq. (5.28), we have

$$\nabla_t [G_1(\boldsymbol{\rho}, \boldsymbol{\rho}') - G_2(\boldsymbol{\rho}, \boldsymbol{\rho}')] = \frac{1}{2\pi} \frac{\boldsymbol{\rho} - \boldsymbol{\rho}'}{|\boldsymbol{\rho} - \boldsymbol{\rho}'|} [\gamma_1 K_1(\gamma_1 |\boldsymbol{\rho} - \boldsymbol{\rho}'|) - \gamma_2 K_1(\gamma_2 |\boldsymbol{\rho} - \boldsymbol{\rho}'|)]. \quad (5.84)$$

In turn, upon considering the small argument behavior of the first-order Bessel function,

$$K_1(z) \sim \frac{1}{z} + \mathcal{O}(z \ln(z)), \quad (5.85)$$

it is clear that the contributions of the singular integrand parts of the interior and exterior medium indeed cancel each other in Eq. (5.28). From the definition of the L-operator, Eq. (5.83), the hypersingular behavior in the scalar potential of the combinations, $\mathbb{L}_1 - \frac{\gamma_2}{\gamma_1} \mathbb{L}_2$, arising in Müller's MoM-matrix, Eq. (5.49), vanishes. Note that this cancellation fully stems from the selected combination of the original two sets of integral equations, irrespective of the applied scaling, which only serves the ease of the numerical implementation.

Taking into account that the propagation coefficient, γ_v , is proportional to the frequency, ω , via Eq. (4.11) and the Laplace transformation, we now consider the low-frequency breakdown. This breakdown originates from the decoupling of the electric and magnetic fields at zero frequency. In a numerical sense, the breakdown is associated with the operator L, i.e., in Eq. (5.83), the frequency dependence of the vector potential is $\mathcal{O}(\omega)$, whereas the scalar potential is $\mathcal{O}(\omega^{-1})$. In addition, from Eq. (3.7b), it readily follows that the operator K is $\mathcal{O}(\omega^0)$. In short, as ω goes to

zero, the vector potential becomes dominant at low frequencies, which results into an unbalanced system of equations, as the contribution from the scalar potential and the operator K are lost. As a consequence the currents cannot be accurately determined from their divergences, and the system becomes numerically unstable, i.e., ill-conditioned. The same phenomenon occurs with subsequent mesh refinements, since the wavelength then also becomes large with respect to the mesh elements. However, since the singular behavior has been removed from Eq. (5.84), it yields $\mathcal{O}(\omega^2)$. Accordingly, in Müller's formulation, the remaining part of the combination of scalar potentials has the same frequency dependence as the combination of vector potentials, i.e., $\mathcal{O}(\omega)$. In this respect, the low-frequency breakdown is naturally avoided in Müller's formulation.

Before we proceed, let us first introduce an additional integral formulation combination which emphasizes different aspects of the mapping properties of L and K . In contrast with the PMCHW formulation, the straightforward subtraction of the electric field equations (3.10a) and (3.11a), and the magnetic field equations (3.10b) and (3.11b), yields the following matrix equation respectively,

$$\begin{bmatrix} \mathbb{L}_1^{EJ} - Y_1 Z_2 \mathbb{L}_2^{EJ} & \mathbb{K}_1^{EM} - \mathbb{K}_2^{EM} + 2\mathbb{I}^{EM} \\ -\mathbb{K}_1^{HJ} + \mathbb{K}_2^{HJ} - 2\mathbb{I}^{HJ} & \mathbb{L}_1^{HM} - Z_1 Y_2 \mathbb{L}_2^{HM} \end{bmatrix} \begin{bmatrix} \mathbb{J} \\ \mathbb{M} \end{bmatrix} = - \begin{bmatrix} Y_1 \mathbf{E}_1^{\text{in}} \\ \mathbf{H}_1^{\text{in}} \end{bmatrix}. \quad (5.86)$$

This alternative Müller formulation, in which the singularity of the operator K instead of that of the operator L vanishes throughout, is henceforth referred to as Mül-K formulation. The original Müller formulation is therefore denoted as Mül-L. Since we apply Galerkin test and expansion in a mixed-order potential formulation, the gradient of the scalar potential is diverted to the test function. Accordingly, in case of an ε -contrast, the kernel of the combined scalar potential of $\mathbb{L}_1^{HM} - Z_1 Y_2 \mathbb{L}_2^{HM}$ in Eq. (5.86) yields $G_1(\boldsymbol{\rho}, \boldsymbol{\rho}') - G_2(\boldsymbol{\rho}, \boldsymbol{\rho}')$. With the small-argument behavior, $K_0(z) \sim \ln(z)$, it is easily deduced that the singular behavior of the scalar potential of \mathbb{L}^{HM} vanishes. In addition, because the scalar potential of \mathbb{L}^{EJ} naturally vanishes for the TM case, the Mül-K formulation has in the absence of an μ -contrast also the singularity cancellation in the scalar potential that is inherent to the Mül-L formulation.

In the following analysis of the boundary integral equations, we consider the same configuration as in the case of the perfect conductor, i.e., the one depicted in Figure 5.6. The contour boundary shapes are also considered for the scattering dielectric object. Because this includes an interior (index 2) and exterior medium (index 1), we set $\lambda_1 = \lambda_0$ to fix the electromagnetic size of the scattering object with respect to the observation contour \mathcal{C}_o . The previously defined error norm, Eq. (5.80), is employed as a measure for the accuracy of the obtained scattered field by means of a normalized error. Since we have a non-vanishing interior field, the interior observation contour

$\mathcal{C}_o^{\text{in}}$ is used as well to incorporate the scattered field inside the scattering object in the evaluation. As such, we have, $\mathcal{C}_o = \mathcal{C}_o^{\text{in}} \cup \mathcal{C}_o^{\text{ex}}$, where the same number of sampling points will be taken on $\mathcal{C}_o^{\text{in}}$ and $\mathcal{C}_o^{\text{ex}}$ (100 points on each side). By including an inner contour, we avoid a one-sided focus on the scattered fields exterior to the scatterers. If only the contribution from the exterior field contribution is accounted for, a possibly complex interior field distribution, e.g., an interior resonance mode, would not be registered. Throughout, the exterior domain is free space, i.e., $\varepsilon_1 = \varepsilon_0$ and $\mu_1 = \mu_0$. Further, the same electric line source as in Section 5.5 that is located at the bottom-right corner of the observation contour $\mathcal{C}_o^{\text{ex}}$ is employed as the impressed source distribution that generates the incident field in the forcing function.

As a measure of solvability, and thus the well-posedness of the problem (Section 3.7), the behavior of the condition number is investigated. Unless mentioned otherwise, the additional scaling in the Mül-L formulation, as proposed in Section 5.3, is applied to minimize the condition number of the MoM-matrix. Because both formulations involve a non-zero scalar potential, expansion by a piecewise-differentiable function is mandatory. Further, we prefer the mixed-order potential formulation. Only piecewise-linear functions in a Galerkin approach are employed, viz., $\wedge\wedge$ test and expansion. Again, to consider the quadrature error separately, adaptive quadrature rules are applied for the test- and/or expansion integrals (with a relative accuracy of 10^{-2}), along with analytical expressions for the corresponding singular integrand parts.

Since the accuracy of the resulting scattered field is also subject to the dielectric contrast, let us first consider the normalized error in the scattered field and the condition number of the corresponding MoM matrix as a function of the medium properties by means of the *refractive index*, n_v , defined as $n_v = c_0\sqrt{\mu_v\varepsilon_v}$ with medium index $v \in \{1, 2\}$. The results for the domain-scaled circle are depicted in Figure 5.22. On the left and right we show the normalized error and the condition number versus the refractive index of the scattering object, n_2 , for the Mül-L (solid) and PMCHW (dashed) formulations, respectively. The exterior medium properties remain unchanged, i.e., $n_1 = 1$. In the top, middle, and bottom figures, we have, $\mu_{r;2} = 1$, $\varepsilon_{r;2} = 1$, and $n_2 = \mu_{r;2} = \varepsilon_{r;2}$, respectively. The number of mesh elements is $N = 96$, which amounts to 34 points/ λ_1 .

In the first place, we observe the spikes arising in the curves of both the condition number and the normalized error. From a careful examination of the figure, it turns out that where the spikes in the condition number of the Mül-L formulation surpass the seemingly smooth magnitude for PMCHW, the condition number for PMCHW also exhibits such a spike of the same magnitude. With reference to the frequency behavior for the scattering of a PEC in Section 5.5, these spikes

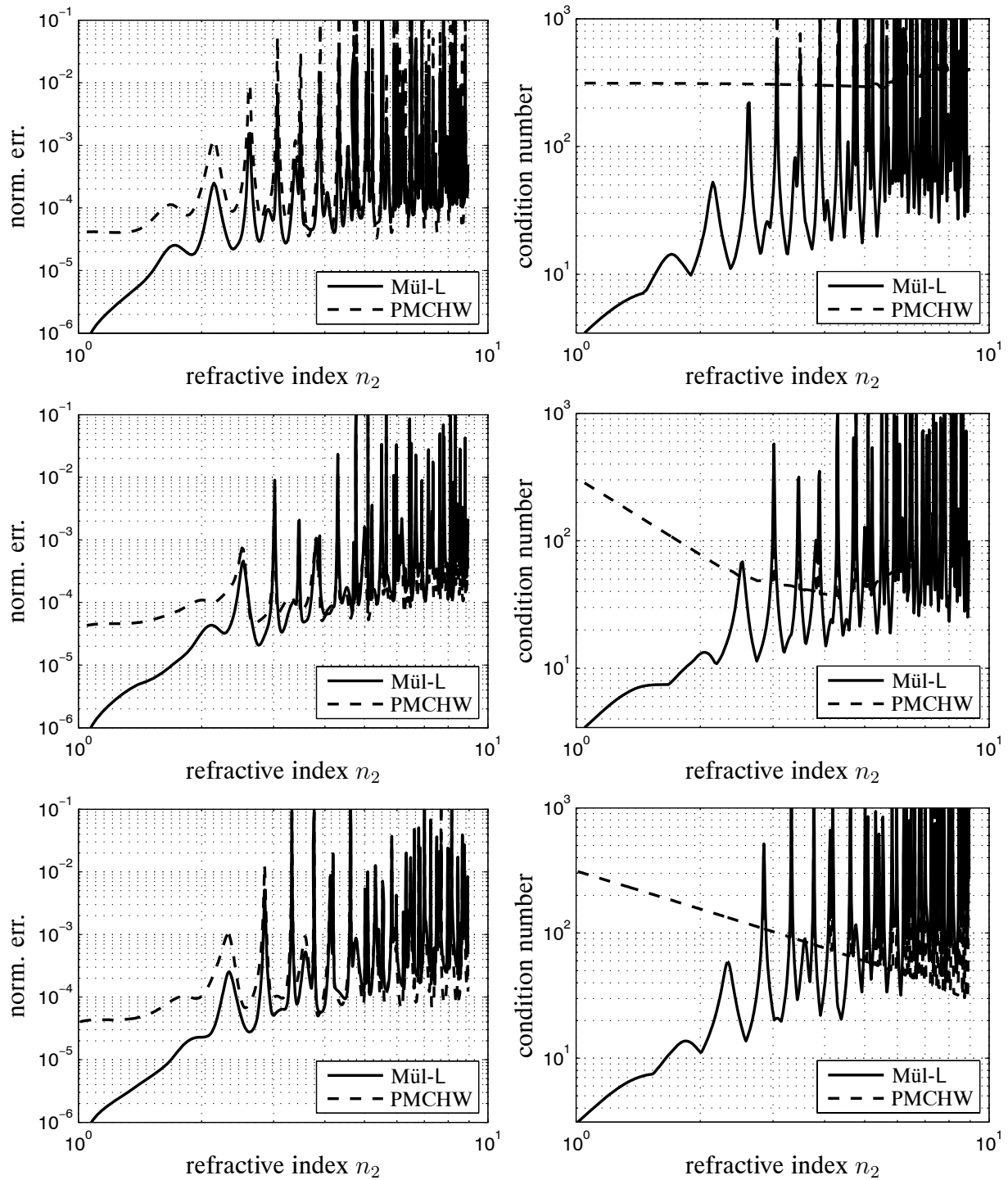


Figure 5.22: Demonstration of the dependence on the refractive index n_2 of a (domain-scaled) circle of the MüL-L and PMCHW formulations, on the left the normalized error in the field, and on the right the condition number. In the top, middle, and bottom figures we have, $\mu_{r;2} = 1$, $\epsilon_{r;2} = 1$, and $n_2 = \mu_{r;2} = \epsilon_{r;2}$, respectively.

also represent interior resonant modes. However, now these interior resonances are physical modes, rather than spurious solutions due to a mathematical non-uniqueness, since the Mül-L and PMCHW formulations are proven to be free of such interior resonances [53]. Because these so-called cavity modes are associated with a pole close to the imaginary axis in the complex plane [Section 2.6.2] [72], the condition number increases considerably. It is clear that the number of cavity modes rises with an increasing contrast as the electromagnetic size of the interior medium becomes larger.

As an example, we compare the field distributions in the presence and absence of a cavity mode. In Figure 5.23 the total electric field is shown on a logarithmic 50 dB scale, where white areas indicate a high field amplitude. We consider an ε -contrast only, with on the left $\varepsilon_{2;r} = 79.1$ for which the condition number is small and on the right $\varepsilon_{2;r} = 77.6$ for which the condition number is large. The observation contours, $\mathcal{C}_o^{\text{in}}$ and $\mathcal{C}_o^{\text{ex}}$, and the impressed electric line source position are highlighted. In the $\varepsilon_{2;r} = 77.6$ case, a cavity mode is excited. In particular, the field pattern comprises a whispering gallery mode as the field propagates along the interior of the circular contour. Note that whispering gallery modes that arise for smaller dielectric contrasts propagate closer to the boundary. Apart from the higher intensity of the interior field, the cavity mode field varies rapidly along the boundary \mathcal{C} of the circle. In turn, because there is a one-to-one correspondence between the tangential field components on \mathcal{C} and the equivalent currents, in a sense, the *effective* number of points per wavelength is larger in case of the non-cavity mode. That is, the fluctuation of the field along the circular contour, and thereby the effective refractive index resembles more the exterior rather than the interior medium properties. Combined, this clarifies the larger error (spikes) in the field for the cavity modes in Figure 5.22. Besides that, this also elucidates the occurring saturation in the magnitude of the error away from cavity modes as the exterior medium properties remain unchanged. On the other hand, as the effective refractive index resembles more the interior medium properties in case of a cavity mode, it is reasonable to expect that the magnitude of the spikes thus increases for larger dielectric contrasts. Despite that the interior domain may involve a cavity mode, the normalized error evaluated at the separate interior and exterior observation contours has the same order of magnitude. Observe that although weak field variations occur along \mathcal{C} for the non-cavity mode on the left in Figure 5.23, strong field variations do arise inside the circle. In such a case, boundary integral formulations are especially accurate, as the unknown boundary currents show hardly any variation.

In a comparison of the condition numbers of both formulations in Figure 5.22, we notice that with the Mül-L formulation, the behavior of the condition number is strongly related to the behavior of the error in the field. Hence, a change in the condition number of the MoM-matrix

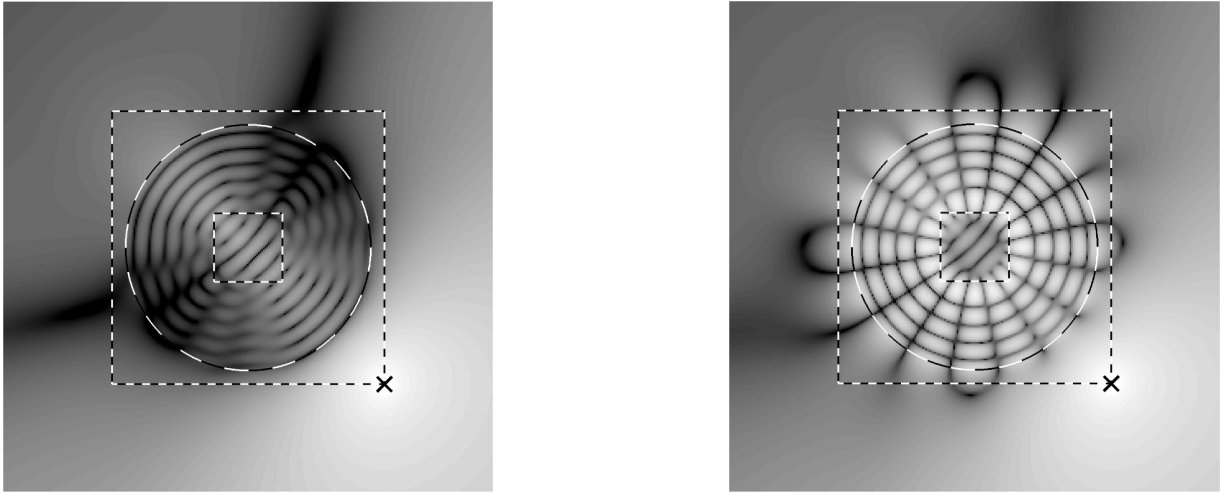


Figure 5.23: The total electric field $|E_z|$ from a circle for $\mu_{2,r} = 1$ on a logarithmic 50 dB scale with on the left $\varepsilon_{2,r} = 79.1$ for a low condition number and on the right $\varepsilon_{2,r} = 77.6$ for a high condition number. The cross indicates the location of the radiating electric line source. The dashed lines are the circle and observation contours. White areas indicate a high field amplitude.

of the Mül-L formulation implies a similar change in the resulting accuracy of the field. Since the singular parts of the scalar potential related to the interior and exterior media cancel each other, the condition number with the Mül-L formulation is primarily determined by the operator K . The condition number of the PMCHW MoM-matrix is initially inversely proportional to μ_2 . This property stems from the mapping properties of the L operators, i.e., for a small contrast, the (fixed) mesh is relatively more dense, in which case L plays a more dominant role with respect to K . The dependence on μ only is raised by the asymmetry in the 2D integral equations, i.e., the vanishing scalar potential in \mathbb{L}^{EJ} . With an increasing contrast, and thus a decreasing mesh density, the contribution of the K operators becomes dominant, and the condition number eventually stabilizes just as is the case of the Mül-L formulation, albeit at a different magnitude due to the different linear combinations of K_1 and K_2 . Recall that in Section 5.5 the resonance spikes in the frequency behavior of the mapping properties involving K and L appear to be much broader for K (MFIE) than L (EFIE), as observed in Figure 5.16 for the PEC. This distinction is also encountered here, as either the properties of K or L dominate the condition number. When the dielectric contrast vanishes, the condition number of the MoM-matrix for the Mül-L formulation diminishes significantly. In that case the Mül-L formulation yields the trivial solution, i.e., the definition of the equivalent currents, Eq. (2.62), as only the contribution of the identity operator remains. This observation is not obvious for PMCHW, as the operators \mathbb{L}^{EJ} and \mathbb{L}^{HM} are not diagonal [53]. For the hexagon and cross shapes, similar curves are obtained for the condition

number, albeit that the magnitude where the error saturates deviates, i.e., it depends on the non-smoothness of the boundary, as has been observed for the individual \mathbb{K}^{HJ} and \mathbb{K}^{EM} matrices in Figure 5.12 and 5.21, respectively.

As regards the error in the resulting scattered field, for a refractive index, $n_2 < 4$, the accuracy obtained with the Mül-L formulation exceeds that obtained with PMCHW, i.e., unlike PMCHW, the overall error with Mül-L decays with a decreasing contrast. For larger values of n_2 , the performance of both integral formulations is comparable. However, for the unscaled circle, the (not shown) normalized error obtained with PMCHW is commensurable with that of Mül-L over the entire range, while the overall error curve is also two orders of magnitude higher. This is consistent with the case of the perfect conductor, where the error for the unscaled circle is primarily determined by the geometrical error, i.e., the approximate boundary.

For the scattering from a dielectric object involving a non-smooth boundary, in particular the hexagon and cross shape depicted in Figure 5.6, the equivalent current may exhibit a discontinuous, and even a singular behavior at the corners. This abrupt current behavior may affect the order of convergence of the equivalent current and thereby also that of the corresponding scattered field. Let us first study the behavior of the equivalent currents. In Figure 5.24, the amplitude of the equivalent electric, $|J_z|$ (left), and magnetic, $|M_\tau|$ (right), current along the contour of the dielectric object are depicted for the cross (solid) and circle (dashed), with in the top and bottom figures an ε and μ -contrast, respectively. For compactness, the currents of the circle and cross are shown in the same figures. The direction of the source position, ρ_S , with respect to the center of the scattering object, ϕ_S , is indicated. The vertical lines indicate the positions of the outward (dotted) and inward (dash-dotted) oriented corners of the cross, respectively. As observed for the perfect conductors, both the electric and magnetic currents exhibit a smooth behavior for the circle, so that \wedge -expansion provides a convenient approximation of the currents.

With regard to the hexagon and cross, the field behavior near a dielectric wedge is somewhat more complex than that of a perfect conductor a detailed description is outside the scope of this thesis. Nonetheless, we will treat the effect of a non-smoothness arising in the boundary due to the presence of corners up to a certain extent, i.e., in relation to the order of convergence of the resulting equivalent current and the scattered field. For a more thorough insight into the field behavior near dielectric wedges, we refer to [80, 81]. Field components normal to a dielectric wedge may become infinite, whereas parallel components remain finite. From the definition of the equivalent currents, Eq. (5.7), it immediately follows that M_τ remains continuous across corners as it is related to E_z , while J_z may exhibit a discontinuous and/or a singular behavior

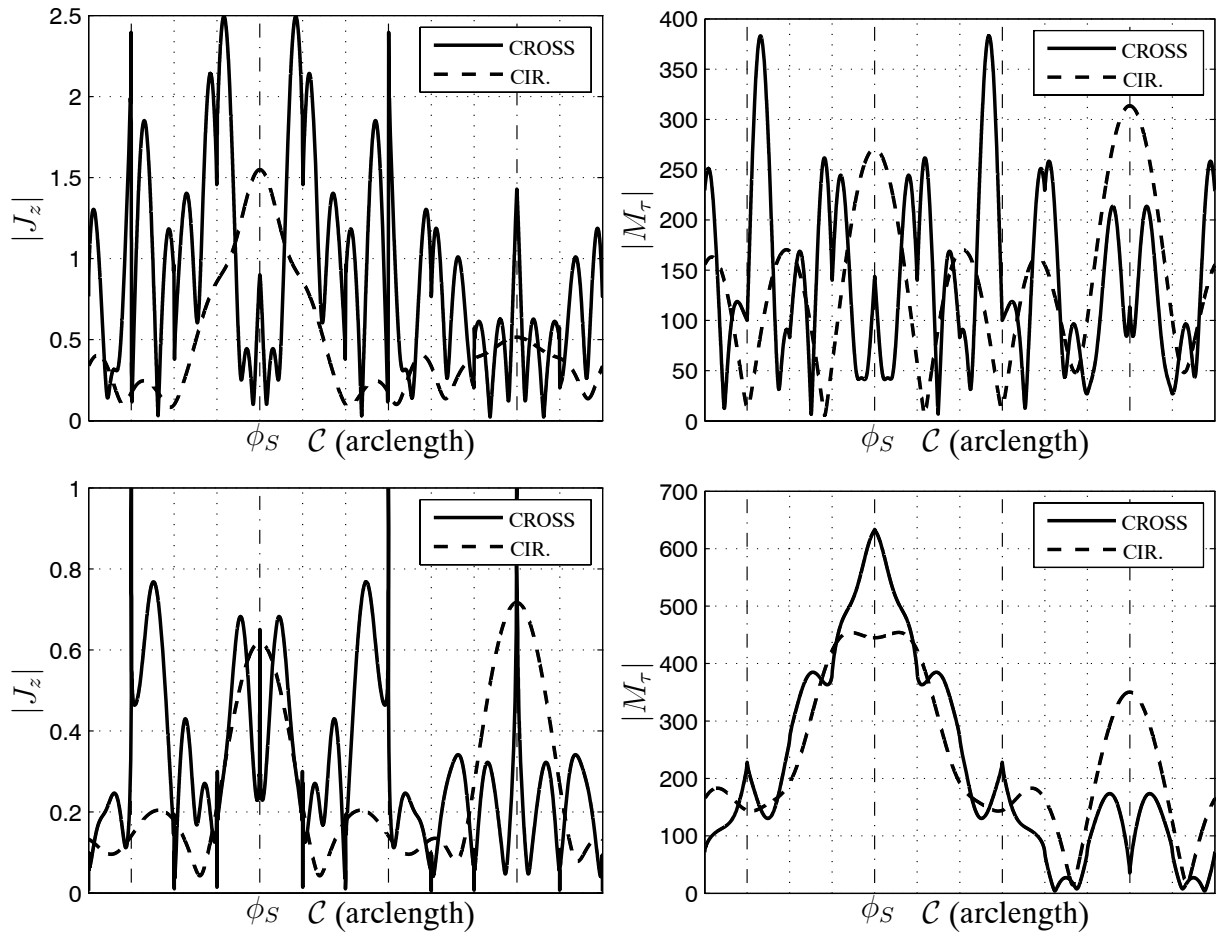


Figure 5.24: On the left and right, respectively, the amplitudes of the equivalent current, $|J_z|$, and $|M_\tau|$ along the boundary \mathcal{C} for the circle and cross. In the top and bottom figures, $\epsilon_{r;2} = 16$ and $\mu_{r;2} = 1$, and $\epsilon_{r;2} = 1$ and $\mu_{r;2} = 16$, respectively. The position that corresponds with the direction of the line source, ϕ_S , is indicated. The vertical lines indicate the location of the outward (dotted) and inward (dash-dotted) corners.

at a corner. More specifically, in the absence of a μ -contrast, the transverse magnetic field is continuous, and the field components normal to the contour remain finite. Accordingly, J_z has no singular behavior, but may become discontinuous at the corners. On the other hand, in the case of a μ -contrast, J_z may also become singular at the corners. However, this is entirely subject to the angle of the corner and the dielectric contrast [81]. The above properties are also encountered in Figure 5.24, viz., at the corners of the cross, M_τ remains continuous, while J_z becomes discontinuous and involves a singular behavior at the inward corners in the case of a μ -contrast.

The applied piecewise linear function, \wedge , which is continuous across adjoining edges, provides a poor approximation for the discontinuities that arise in the electric equivalent current. As a consequence, the approximate electric current exhibits an oscillating behavior near the discontinuous and singular behavior of $|J_z|$ in terms of small ripples that decay exponentially away from the discontinuity. This effect is strongly related to Gibbs' phenomenon. Since the equivalent currents in Figure 5.24 are obtained using more than 200 points per wavelength, these ripples have become narrow (up- and downward) spikes at the corners.

Next, let us investigate the impact of a non-smooth boundary on the convergence of the equivalent current. Since there are no analytical solutions available for the cross and hexagon shape, a well-converged solution is applied as a reference solution. However, the reference solution itself poses a poor approximation of J_z at the corners as J_z becomes discontinuous and singular. As such, application of the error norm, Eq. (5.80), will lead to improper results for J_z . Therefore, only the convergence rate of M_τ is considered. In Figure 5.25 the order of convergence of M_τ is shown for the (domain) scaled circle (solid), hexagon (dashed) and cross (dash-dotted) contour shapes. On the left, an ε -contrast with $\varepsilon_{r;2} = 16$, and on the right an μ -contrast with $\mu_{r;2} = 16$. These results are generated with the PMCHW formulation. Those of the Mül-L formulation are virtually the same.

For the circle, M_τ converges quadratically. This is also the case for J_z . The indicated range is chosen such that upon expressing the mesh density in terms of the exterior medium, $\lambda_1 = \lambda_o$, the range corresponds with that of the results for the perfect conductors. This allows for a direct comparison. The error for the circle is virtually the same as the one obtained for the perfect conductors, depicted in Figure 5.7 and 5.20 for the PEC and PMC, respectively. Since the operating frequency is away from cavity modes for the selected dielectric contrasts, this similarity confirms the statement that the relative mesh density is more related to the exterior medium properties for non-cavity modes. Just as was the case for the perfect conductors, the

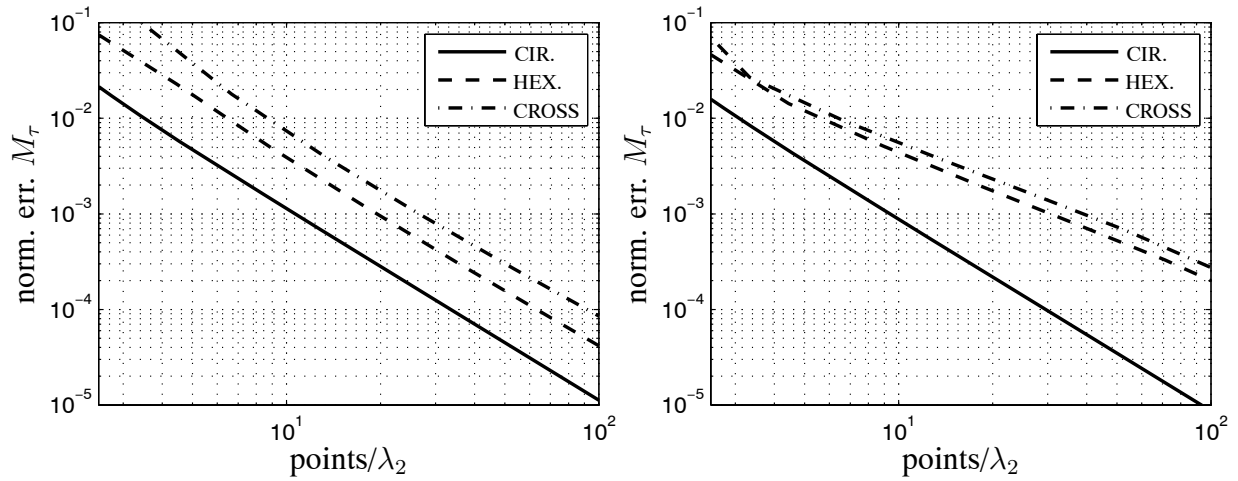


Figure 5.25: The normalized error in M_τ versus the number of unknowns, points/λ_2 for the PM-CHW formulation involving the scaled circle (solid), hexagon (dashed) and cross (dash-dotted). On the left, $\varepsilon_{r;2} = 16$ and $\mu_{r;2} = 1$, and on the right, $\varepsilon_{r;2} = 1$ and $\mu_{r;2} = 16$.

domain scaling of the circle leads to an improvement in the magnitude only, as the order of convergence is bounded by the smoothness of the expansion function. Recall that the gain in accuracy of the equivalent current seems to be negligible for the perfect conductors. For the dielectric object, however, a more substantial improvement of about one order of magnitude is obtained.

For the hexagon and cross shapes involving an ε -contrast, M_τ converges quadratically as well. In contrast with the results for the PMC in Section 5.7, the non-smoothness in the boundary results in a shift in magnitude only. Apparently, the discontinuous behavior of J_z does not affect the convergence of M_τ . On the other hand, the error convergence rates for both the hexagon and cross reduce to $\mathcal{O}(N^{-1.3})$ for a μ -contrast. Although J_z may now also become singular across corners, this may seem strange at first glance, as M_τ remains, like for the ε -contrast, continuous across corners. However, the derivative of J_z , in terms of the surface divergence of M_τ , may become singular, i.e., upon considering the boundary conditions for the normal field components, Eq. (2.18), the singular behavior of J_z , associated with the normal magnetic field component, reappears in the scalar potential with M_τ via its surface divergence. Up to 5 points/λ_2 , M_τ still converges quadratically. In this region, the overall error is not yet governed by the contribution from the singular current behavior at the corners. Regarding the cross, quadratic convergence is even exceeded at first as the mesh density is critically too coarse with respect to the interior medium and the boundary geometry.

Now, we consider the order of convergence of the scattered field on the observation contour, \mathcal{C}_o , obtained with the Mül-L, the PMCHW, and the Mül-K formulations. Accordingly, in Figure 5.26 the normalized error of the scattered field as a function of the number of unknowns, points/ λ_2 , due to the scattering from the hexagon (left) and the cross (right). In the top, middle, and bottom figures, we have $\varepsilon_{r;2} = 16$ with $\mu_{r;2} = 1$, $\mu_{r;2} = 16$ with $\varepsilon_{r;2} = 1$, and $\mu_{r;2} = \varepsilon_{r;2} = 4$, respectively. The results for the unscaled circle have been omitted as the pertaining error is primarily determined by the geometrical error of the approximate boundary rather than the mapping properties of the integral formulation itself. More specifically, considering fields instead of currents only leads to a minor improvement. The extension to the domain-scaled circle will be treated later on. The obtained convergence rates for the cross and hexagon are not as steady as the ones observed with the perfect conductors, because of the various combinations of integral operators that are dominant at different mesh densities. In general, the results for the hexagon shape are better than those for the cross. This may be attributed to the more severe non-smoothness of the cross, but also partly to the fact that the operating frequency is closer to a cavity mode. Since the order of convergence appeared to be independent of the object shape for the separate integral operators involving the perfect conductors, the variations in the convergence may solely be accounted to the mapping properties of the integral operators and the specific combinations of integral operators. For the PMCHW formulation, the convergence eventually becomes quadratic with further mesh refinement, irrespective of the object shape and dielectric contrast. The PMCHW formulation is then dominated by the contribution from the L operators, as observed in the investigation of the dependence on the refractive index in Figure 5.22.

For the ε -contrast (top row), the convergence for all three formulations is initially cubic, albeit that after a certain mesh density the convergence declines for further mesh refinements for the Mül-L and PMCHW formulation, eventually deteriorating to quadratic convergence. Only the Mül-K formulation retains cubic convergence. This improved convergence may be elucidated by considering the results for the equivalent current J_z . The corresponding surface divergence of M_τ is discontinuous across corners, while M_τ remains continuous. Accordingly, only with the Mül-K formulation, the singularities of the interior and exterior integral operator parts that produce these discontinuities cancel each other. In particular, this is the case for \mathbb{K}^{HJ} , the vector potential of \mathbb{L}^{EJ} , and the scalar potential of \mathbb{L}^{HM} . Together, these cancellations supply the improvement of one order in the convergence with the Mül-K formulation. The kernels of the integral operators containing the discontinuity of J_z are more smooth due to the cancellation of their singular parts. This improved smoothness allows for a less strict differentiability of the currents, and thus increases the solution space, which leads to the increased convergence rate. With regard to the Mül-L formulation, the singularities of the vector potential of \mathbb{L}^{EJ} do not

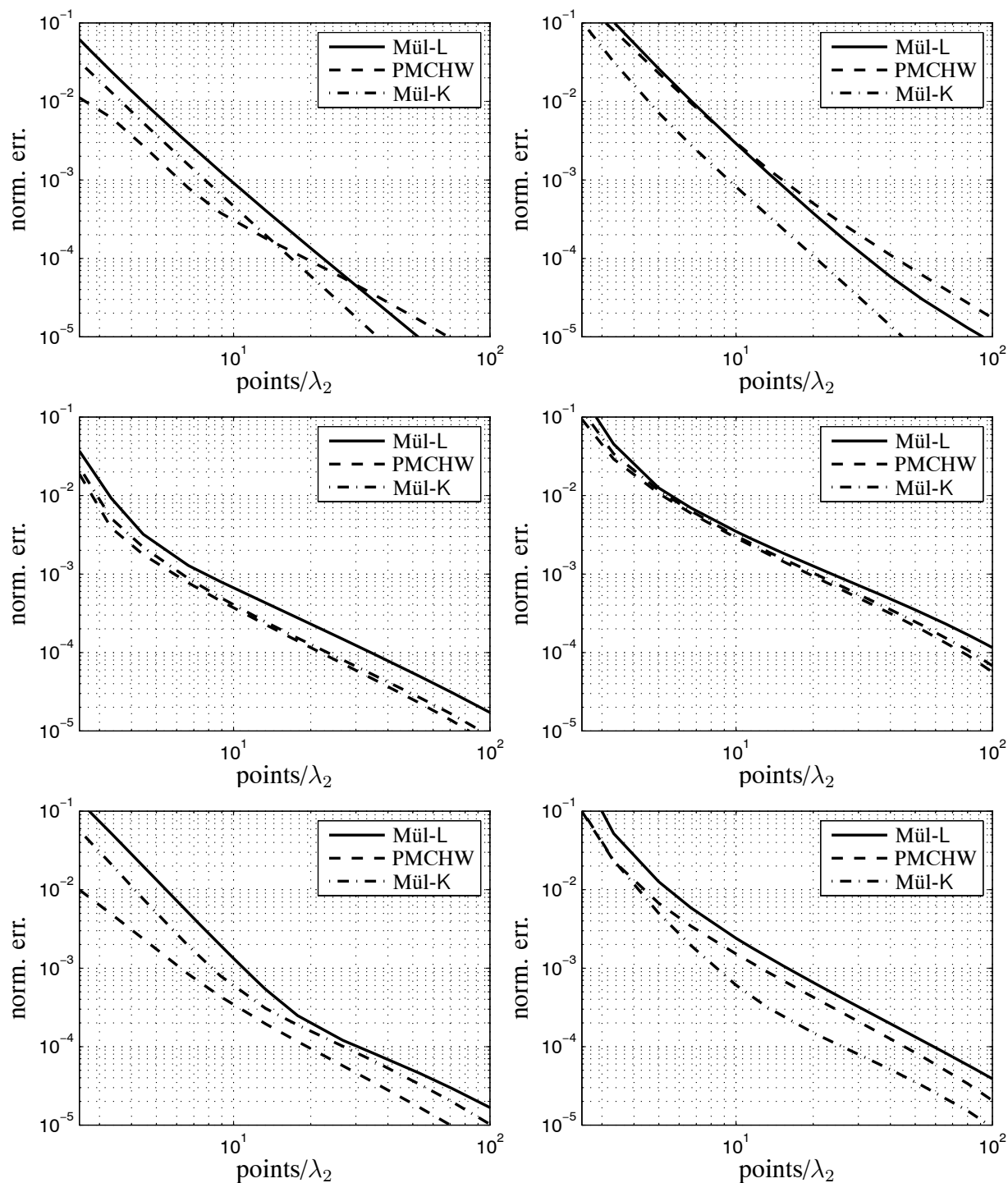


Figure 5.26: The normalized error versus the number of unknowns, points/λ_2 , for the hexagon (left) and cross (right) shape. In the top, middle, and bottom figures, we have $\varepsilon_{r;2} = 16$ with $\mu_{r;2} = 1$, $\mu_{r;2} = 16$ with $\varepsilon_{r;2} = 1$, and $\mu_{r;2} = \varepsilon_{r;2} = 4$, respectively.

cancel each other, which gives rise to the observed drop in the convergence rate. Since none of these cancellations occur in the PMCHW formulation, its convergence is affected even stronger. Yet, the initial cubic convergence with PMCHW may be attributed to the fact that the overall error in the equivalent currents is not yet dominated by the contribution from the discontinuities at the corners. Since the K operators appear to control the behavior of the PMCHW formulation, the initial cubic convergence may also be attributed to a less prominent role of the singularity cancellation in the kernel of K^{HJ} , since otherwise the convergence would remain quadratic.

With respect to the μ -contrast shown in the second row of Figure 5.26, both the order of convergence and the magnitude of the error in the scattered field obtained with the three formulations is comparable. Apart from a shift in magnitude, the results obtained with the hexagon and cross shapes are clearly similar. Now that J_z and the surface divergence of M_τ may also become singular across corners, the error convergence rate even drops to $\mathcal{O}(N^{-1.6})$. Nevertheless, like the PMCHW formulation, the Mül-L and the Mül-K eventually yield quadratic convergence for further mesh refinement. Note that the Mül-K formulation is more closely related to the PMCHW formulation as there is no cancellation of the singularity associated with the scalar potential of \mathbb{L}^{HM} for a μ -contrast. Since the required operator combination differs for a cancellation of the singularities involving K^{HJ} and the scalar potential of \mathbb{L}^{HM} , it is unfortunately not possible to construct an integral formulation for a μ -contrast that has the same singularity cancellations as the Mül-K formulation for the ε -contrast. Again, a strong convergence (quartic) is observed for a coarse discretization, where the overall error is then not yet determined by the contributions from the corners. Note that similar plots are expected for the TE case, since the results of the ε and μ -contrast are interchangeable.

Finally, for a combined ε - and μ -contrast, treated in the bottom row of Figure 5.26, the integral formulations involve the composite properties of the separate ε and μ -contrasts. For instance, the Mül-K formulation yields cubic error convergence up to about 10 points/ λ_2 , which is associated with the properties of an ε -contrast. With more sampling points per wavelength, the order of convergence is bounded by the behavior of the inferior performance involving the μ -contrast.

To demonstrate the impact of domain scaling of the dielectric circle on the order of convergence of the scattered field, we consider the normalized error of the scattered field for an ε -contrast in Figure 5.27. Similar to a perfect conductor, both the PMCHW and the original Mül-L formulation improve by one order, which yields cubic convergence. The proposed Mül-K formulation even yields quartic convergence, viz., one order is gained by the domain scaling, and one order by the cancellation of the singularities involving the operator parts with a discontinuous kernel

associated with a J_z discontinuity at corners. In this case, we refer to the corners created by the application of a flat-facetted, rather than a curved mesh.

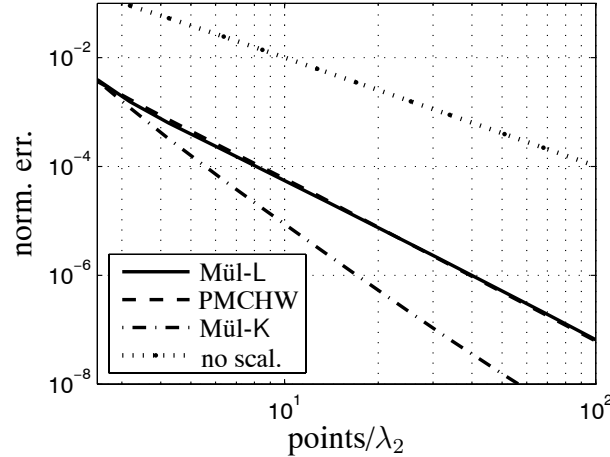


Figure 5.27: The normalized error of the field versus the number of unknowns in points/ λ_2 for the circle with and without domain scaling for $\varepsilon_{r;2} = 16$ and $\mu_{r;2} = 1$.

Next, let us consider the solvability of the integral formulations in terms of the condition number of the MoM-matrix subject to the mesh density. On that account, in Figure 5.28 the condition number for the MüL-L (left) and PMCHW (right) formulations is shown for the circle, hexagon and cross shapes with $\varepsilon_{r;2} = \mu_{r;2} = 4$. The solvability of the MüL-L formulation appears to be independent of the applied mesh density, which makes it ideal for the use of iterative solvers involving dense meshes. This observation also corroborates that the low-frequency breakdown is indeed naturally avoided with the MüL-L formulation. Moreover, the magnitude of the condition number, determined by the K operators, increases with an increasing non-smoothness of the boundary.

With regard to the PMCHW formulation, the condition number is virtually the same for all three boundary shapes and increases quadratically once the mesh density exceeds 10 points/ λ_2 ; this behavior may be attributed to the L operators. Note that this is one order larger than for the MoM-matrices based on a single L operator involving the scattering from perfect conductors. Since the condition number for the PMCHW formulation is inversely proportional to μ , the condition number for an ε or μ -contrast only, are four times larger or smaller for the same refractive index, respectively. In the range where the condition numbers for the object shapes are different, the condition number is determined by the K operators, and is more or less insensitive to the applied mesh density. Again, the magnitude thus depends on the non-smoothness of the boundary shape at hand. With reference to the dependence of the condition number on the medium properties

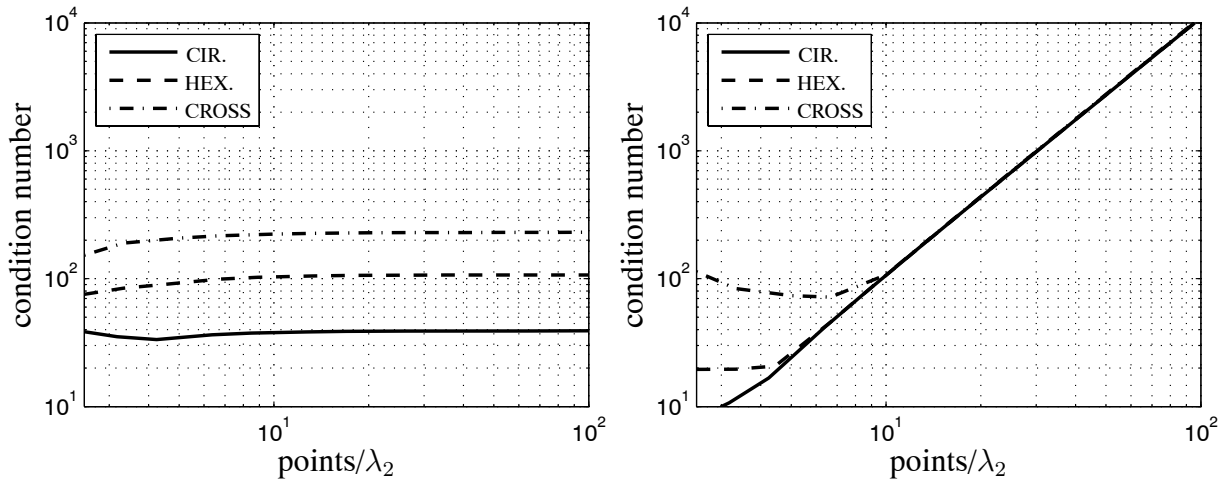


Figure 5.28: The condition number as a function of the number of unknowns in points/ λ_2 for the scattering from the circle, hexagon and cross with $\varepsilon_{r;2} = \mu_{r;2} = 4$. On the left and right the Mül-L and PMCHW formulations.

of the scatterer object, depicted in Figure 5.22, we observed that the condition number resulting from a K operator depends on the interior field distribution. Spikes in the condition number occurred at cavity modes. In conclusion, the point where L start to determine the condition number depends primarily on the smoothness of the boundary, and the presence of cavity modes. In case of a cavity mode, or a less smooth boundary, L becomes dominant at more points per wavelength.

The condition number for the Mül-K formulation is independent of the applied mesh density for objects with an ε -contrast only. The condition number is then of the same order of magnitude as with Mül-L. With regard to objects with a μ -contrast only, the condition number of Mül-K yields a behaves similarly as that of PMCHW. In relation with the results above, we may infer that the choice of the combination of integral operators has a negligible influence on the equivalent currents, but it may improve the solvability of the resulting integral formulation and/or the order of convergence of the corresponding scattered fields.

Up to this point, for the presented condition numbers for Müller's formulation (Mül-L) we have applied the additional scaling suggested in Section 5.3. To determine the improvement gained over conventional scaling, we consider the condition numbers of the MoM-matrix in Tab. 5.1 for the three object shapes involving conventional, Eq. (5.49), and additional scaling, Eq. (5.52). A sufficiently dense mesh has been applied such that the shown values represent a converged (stable) condition number with respect to further mesh refinements. In case the impedances of the

interior and exterior medium match, there is no improvement in the condition number as the additional scaling vanishes, because both scalars, ς_ε and ς_μ defined in Eq. (5.50) then have the same magnitude, and the additionally scaled matrix elements involve a multiplication by $\varsigma_\varepsilon/\varsigma_\mu$ or $\varsigma_\mu/\varsigma_\varepsilon$ only. In that case, the MoM-matrix is already optimally scaled with conventional scaling. In case of only an ε or μ contrast, the improvement varies between a factor of three to four. Moreover, as the dielectric contrast increases, a stronger reduction is observed in the condition number with additional scaling, while for a vanishing contrast the effect of this scaling diminishes naturally. In particular, if we omit the additional scaling and reconsider the dependence of the condition number on the dielectric contrast in Figure 5.22, this leads to an increase of the condition number by one order, i.e., proportional to μ_2 and ε_2 for a μ - and ε -contrast, respectively. The observed saturation of the condition number for large dielectric contrasts is then lost. If the reduced condition number remains relatively large, this may indicate the presence of a cavity mode. As it happens, the operating frequency is near such a cavity-mode frequency for the cross shape for all three cases. Otherwise, the presented condition numbers would have been closer to those of the hexagon.

medium par.	circle		hexagon		cross	
	conv.	add.	conv.	add.	conv.	add.
$\varepsilon_{r;2} = 16, \mu_{r;2} = 1$	111	27	106	30	698	215
$\varepsilon_{r;2} = 1, \mu_{r;2} = 16$	52	18	72	21	328	144
$\varepsilon_{r;2} = \mu_{r;2} = 4$	39	39	107	107	229	229

Table 5.1: The (stable) condition number of the Mül-L MoM-matrix involving conventional (conv.) and additional (add.) scaling for different object shapes and medium parameters.

In our examination of Figure 5.22, we investigated the dependence on the refractive index n_2 of the scattered field from the domain scaled circle. Because the Mül-L formulation approaches the trivial solution for a vanishing dielectric contrast, it produced better results for small contrasts than the PMCHW formulation. However, it is uncertain whether a better performance can also be achieved for objects involving non-smooth boundaries. Consequently, we consider the normalized error in the scattered field from a cross, depicted in Figure 5.29 for the Mül-L, PMCHW and Mül-K formulations, with an ε -contrast on the left and a μ -contrast on the right. The applied number of mesh elements is $N = 96$, which amounts to 26 points/ λ_1 . At each sample point we used a mesh which is four times more dense as a reference solution. In comparison with the results for the circle as depicted in Figure 5.22, we observe a similar trend, albeit that for the cross shape the overall magnitude is larger and the improvement of Mül-L over PMCHW for

small contrasts seems less pronounced. Both effects may be attributed to the non-smoothness of the boundary. Hence, the advantage of the Mül-L formulation for small contrasts is more distinct for the scattering from objects with a smooth boundary. Observe that the reduced gain in performance may also be partly attributed to a more dense mesh, i.e., although we also have taken $N = 96$ for the circle, which amounted to $34 \text{ points}/\lambda_1$, the effect of doubling the mesh density is that the difference between the Mül-L and PMCHW formulation increases with approximately a factor of two. Notice also that the Mül-K and Mül-L results match for small contrasts. This is not strange as the Mül-K formulation also converges towards the trivial solution for a vanishing contrast.

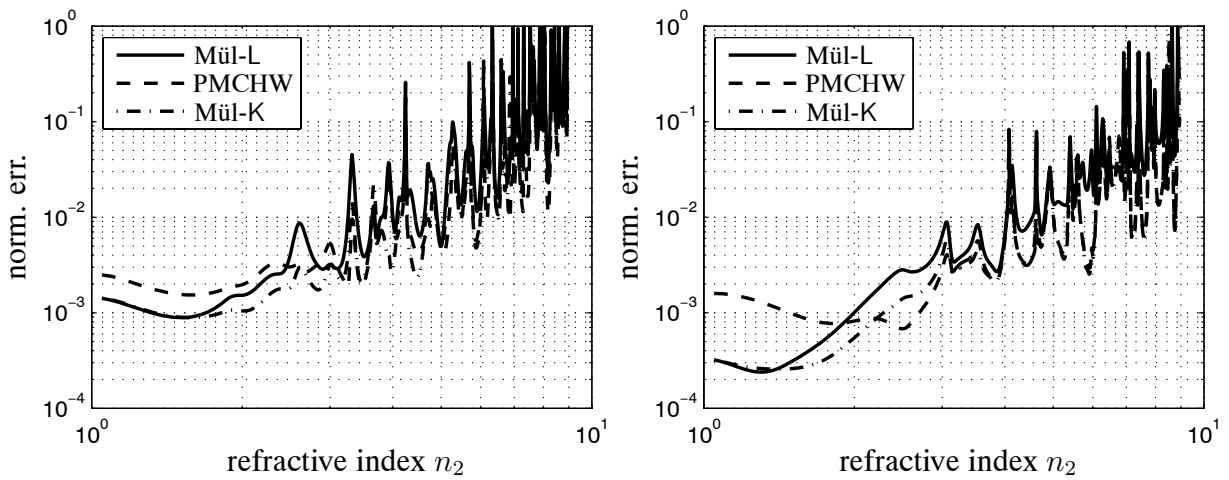


Figure 5.29: The normalized error in the field as a function of the refractive index n_2 of a cross with the Mül-L, the PMCHW, and the the Mül-K formulation. On the left and right, $\mu_{r;2} = 1$ and $\epsilon_{r;2} = 1$, respectively.

Next, we would like to obtain a lower bound for the convergence rate and an estimation of the minimum mesh density required to guarantee a certain accuracy of the scattered field irrespective of the chosen integral formulation, the presence of cavity modes, and the type of dielectric contrast. In Figure 5.30, the order of convergence is shown for the Mül-L, the PMCHW, and the the Mül-K formulation involving the cross shape. On the left we have shown an ϵ -contrast ($\epsilon_{r;2} = 18$) and on the right a μ -contrast ($\mu_{r;2} = 16.6$). For these medium parameters and operating frequency, the cross has a cavity mode. In accordance with Figure 5.29, the presence of a cavity mode adversely affects the convergence and hence provides a lower bound for the overall performance. Most importantly we note that for successive mesh refinements the Mül-L and PMCHW formulations yield a comparable performance, dropping to quadratic convergence for both the ϵ - and μ -contrasts. This is also the case with Mül-K involving the μ -contrast. However,

irrespective of the influence of the cavity mode, the convergence remains cubic for the ε -contrast due to the cancellation of *all* operator terms. The difference of one order in the convergence rate between Mül-K and Mül-L may solely be attributed to the singularity cancellation of the vector potential of L^{EJ} in Mül-K. Hence, if the singular terms of not all of the integral operators involving a discontinuous kernel cancel, the cancellation of those singularities only leads to a partial improvement, as the convergence is eventually dominated by the presence of the remaining one(s).

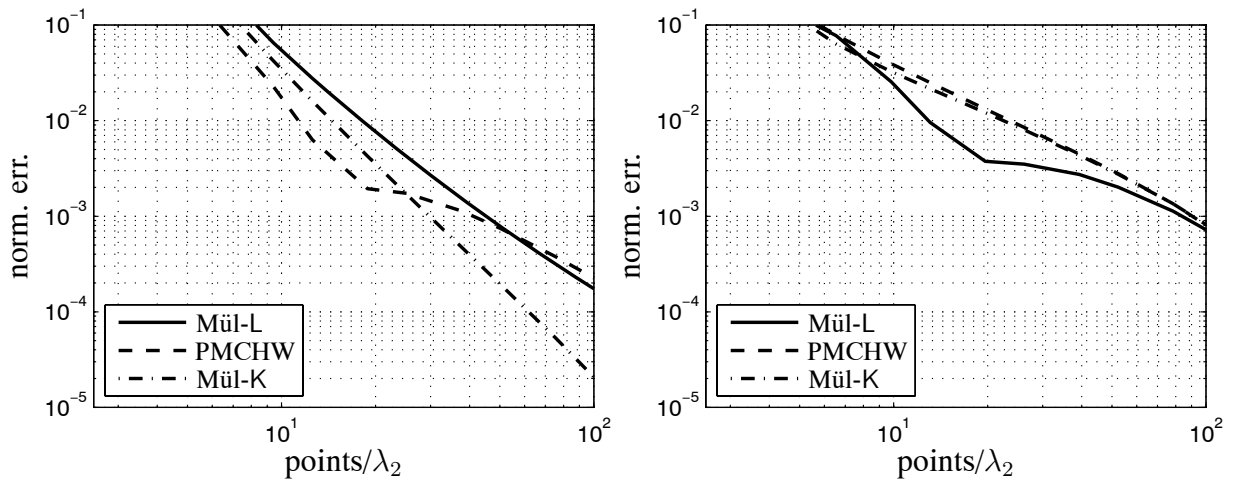


Figure 5.30: The normalized error in the field as a function of the number of unknowns in points/λ_2 for the Mül-L, the PMCHW, and the the Mül-K formulation for the cross involving a cavity mode. On the left, $\mu_{r;2} = 1$, and $\varepsilon_{r;2} = 18$, and on the right, $\mu_{r;2} = 16.6$, and $\varepsilon_{r;2} = 1$.

The sudden strong decline in the convergence of the PMCHW formulation for the ε -contrast corresponds to the point where the L operators start to determine the condition number as displayed in Figure 5.28. Before that point, quartic convergence is observed. Since the field fluctuations along the boundary are stronger in case of a cavity mode, the error contribution from the discontinuity of the current at the corners becomes dominant at a relatively denser mesh size, which prolongs the range of quartic convergence. Because a μ -contrast implies a discontinuous as well as a singular current behavior at the corners, quartic convergence is never attained. For the μ -contrast, the Mül-L formulation produces better results than the other two formulations across a definite range. This may be attributed to the cancellation of the singularity involving the scalar potential of L^{HM} , as this only occurs with the traditional Mül-L formulation for the μ -contrast. Nevertheless, at least $20 \text{ points}/\lambda_2$ are required to guarantee 1% accuracy for the scattered field, while the *overall* convergence is quadratic. Note that in relation to Figure 5.26, the required mesh density may be less stringent for objects involving smoother boundaries.

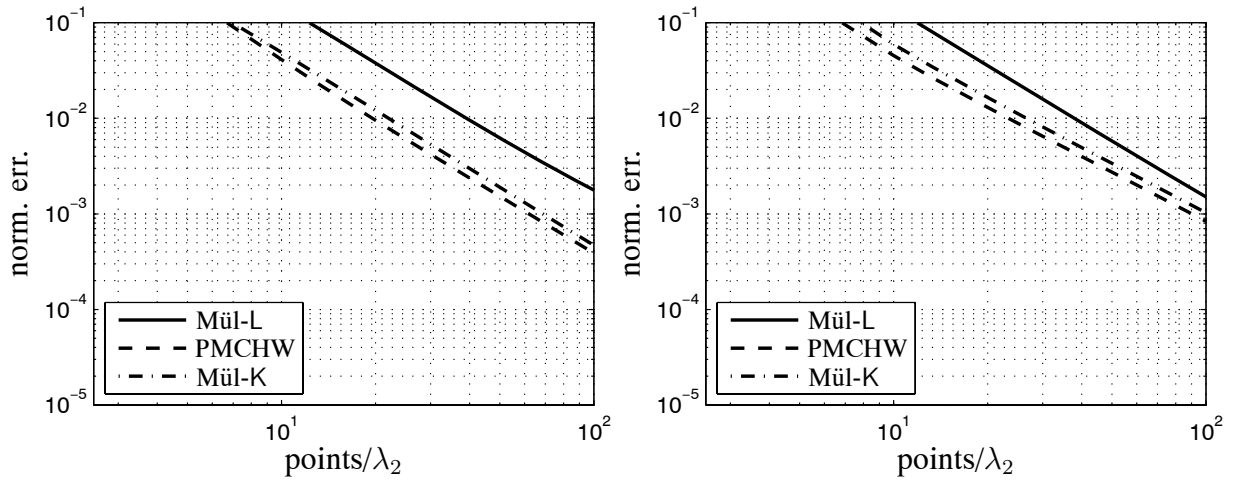


Figure 5.31: The normalized error in the field as a function of the number of unknowns in points/λ_2 for the MüL-L, the PMCHW, and the MüL-K formulation for the cross with the midpoint rule applied to the test and expansion integrals. On the left, $\mu_{r;2} = 1$, and $\varepsilon_{r;2} = 16$, and on the right, $\mu_{r;2} = 16$, and $\varepsilon_{r;2} = 1$.

To investigate the impact of the quadrature error on the integral formulations, we employ the coarse midpoint rule for the test and expansion integral involving the MoM-matrix and the excitation vector. Analytical solutions remain being used for the singular-kernel parts, as well as the self term. The integral representation that produces the scattered field from the resulting equivalent current is still determined by means of adaptive integrals. In Figure 5.31, the midpoint rule is applied to the MüL-L, the PMCHW, and the MüL-K formulations for the scattering from the cross. All three formulations yield quadratic convergence, since the quadrature error is the limiting factor. The same reduction in the convergence is observed for the domain-scaled circle. To allow a comparison with previous results, the same axes as in Figure 5.26 have been used. Consequently, instead of 6 points/λ_2 for 1% accuracy with adaptive quadrature rules, we need at least 40 points/λ_2 with the midpoint rule to obtain the same accuracy. Because the singular operator parts, for which analytical solutions are used, play a dominant role in the PMCHW, that formulation produces slightly better results.

Chapter 6

Demonstration of LEGO with EBG structures

The principle of linear embedding via Green's operators (LEGO) has been introduced in terms of a transparent operator formalism in Chapter 4. The general definition of the pertaining operators applies to both Schelkunoff's and Love's equivalence principles (SEP and LEP). We have extended the LEGO approach to optimize large structures efficiently. After the discretization of the operators, we have provided an efficient numerical scheme of LEGO specialized to either SEP or LEP and have compared the computational costs with direct solvers. At this stage, a practical demonstration of the LEGO approach remains. We shall concentrate on the validation, the possible applications and the accuracy of the method.

In this chapter, we apply the LEGO approach to model electromagnetic bandgap (EBG) structures [82]. The strong field interactions that occur between the unit cells of EBG structures render such applications ideal to validate and demonstrate the potential of the LEGO approach. In addition, for EBG structures the elementary blocks are often reusable, which makes LEGO very efficient as a modeling technique. The results are of interest for further research on application of EBG structures.

6.1 Introduction

The first numerical validation of the LEGO concept is presented in Section 6.2, where two elementary building blocks with a common boundary part are combined via a straightforward low-order discretization. Next, the wide applicability of LEGO as a design tool for large finite structures is demonstrated in Section 6.3. In particular, we consider the normalized radiation pattern of sources placed above large finite EBG structures of various sizes. We also consider an EBG waveguide example. We will point out the implicit advantages of a scattering operator in combination with the modular approach of LEGO. Further, in LEGO we comment on the computational costs and the efficiency by which interior fields can be reproduced. To illustrate local structure optimization features of LEGO, the method is applied to two EBG examples in Section 6.4. In particular, the optimization is employed for local tuning of the transmission properties at the Y-junction of a power splitter and a mode splitter in EBG waveguide technology.

In Section 6.5, the accuracy of the scattered field that can be attained with the LEGO approach is quantified in terms of the mesh density on the boundary of a composite scattering domain. In particular, we compare SEP with LEP and evaluate the different discretization approaches, but also the use of an inverse propagator versus an inverse Gram matrix. The consequences of the direct transfer of equivalent currents for transfer operators with common boundary parts is considered. More general aspects are treated as well, e.g., the dependence on the building sequence, the choice of domain shape and the loss of accuracy due to the accumulation of errors associated with a sequence of embedding steps. Further, we investigate whether the CFIE sufficiently suppresses the interior resonance effect that affects SEP for LEGO. Where possible, results are compared with the results from integral equations for 2D perfectly conducting or dielectric objects in Chapter 5.

Often 2D EBG materials consist of circular cylinders. So far, we have employed analytic solutions for the scattering of a single cylinder required for the construction of the elementary scattering operators. In Section 6.6, the scattering object that is enclosed by the elementary scattering domain is not a canonical one. There, a boundary integral equation will be applied. In addition, we will consider scattering objects that are continuous across domain boundaries. In Section 6.7, we use LEGO to determine the band structure of EBG materials. For the solution of the associated eigenvalue problem, two alternative algorithms, with unique advantages over existing methods, will be introduced.

In Section 4.2 we have illustrated that a scattering object, but also the enclosing domain, may be of arbitrary shape. To establish a framework for the analysis of LEGO for 2D EBG structures, the shape of an elementary scattering domain is restricted to the three shown in Figure 6.1, viz., a hexagonal, a rectangular or a rhombic shape. Further, the coordinate system depicted on the right in Figure 6.1 is employed throughout. The z -axis points in the longitudinal direction.

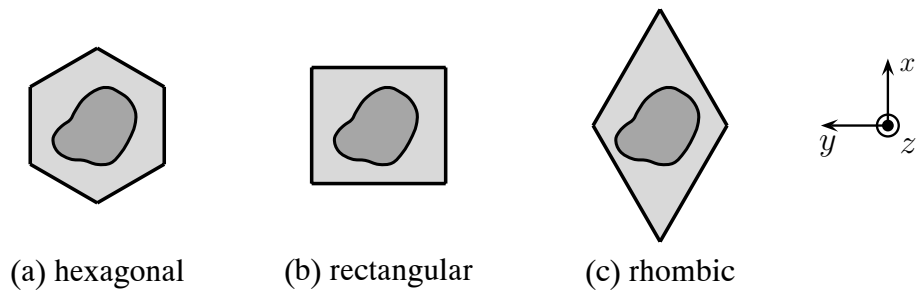


Figure 6.1: Three different shapes for the elementary scattering domains that are chosen to demonstrate the LEGO approach in the field of 2D EBG structures. On the right-hand side the coordinate system is depicted that will be used throughout this chapter.

6.2 Numerical validation

To test the numerical behavior of the embedding approach, let us consider two hexagonal unit cells of a 2D triangular EBG with periodicity a , consisting of circular air cylinders inside a dielectric background with relative permittivity $\varepsilon_r = 11.4$. To let an EBG structure consisting of such cylinders operate within the full bandgap for both polarizations, the frequency is normalized such that $fa/c = 0.48$, and the radius of the cylinders is set to $r/a = 0.475$. For reference, we employ the PMCHW boundary integral equation with 1250 unknowns on each cylinder boundary for both the equivalent electric and magnetic surface currents ($\wedge\wedge$ -discretization cf. Section 5.3). The corresponding total electric-field strength is shown on the left in Figure 6.2. An electric line source (TM polarization), marked by a small dot, generates the incident field.

We first consider embedding based on Schelkunoff's equivalence principle (SEP). The domain shapes of the two scattering domains have been chosen to be hexagonal, as illustrated in Figure 6.1a. For EBG structures with cylinders closely packed in a triangular array, the cylinders can not be contained in periodic rectangular or rhombic scattering domains as depicted in Figure 6.1, and hence hexagonal contour shapes are appropriate. To distinguish between the performance

of the LEGO and the numerical approach for the evaluation of the scattered fields inside the domains, we have employed analytical solutions for the fields scattered by a single cylinder, as described in Appendix B.1. In this way, additional errors that originate from the construction of the initial scattering operator of the individual scattering domains are avoided. Upon completing the embedding scheme, the total field in the entire configuration follows from Eq. (4.40), i.e., the composite scattering operator directly accounts for the exterior scattered field, while the interior field operators transform the field response of a single cylinder into the complete interior field of each hexagonal subdomain. A delta test function and a piecewise constant expansion function are used to illustrate that a straightforward low-order $\uparrow \square$ -discretization already provides good results. Moreover, the regular part of the expansion integrals is evaluated using the lowest-order quadrature rule, i.e., the midpoint rule.

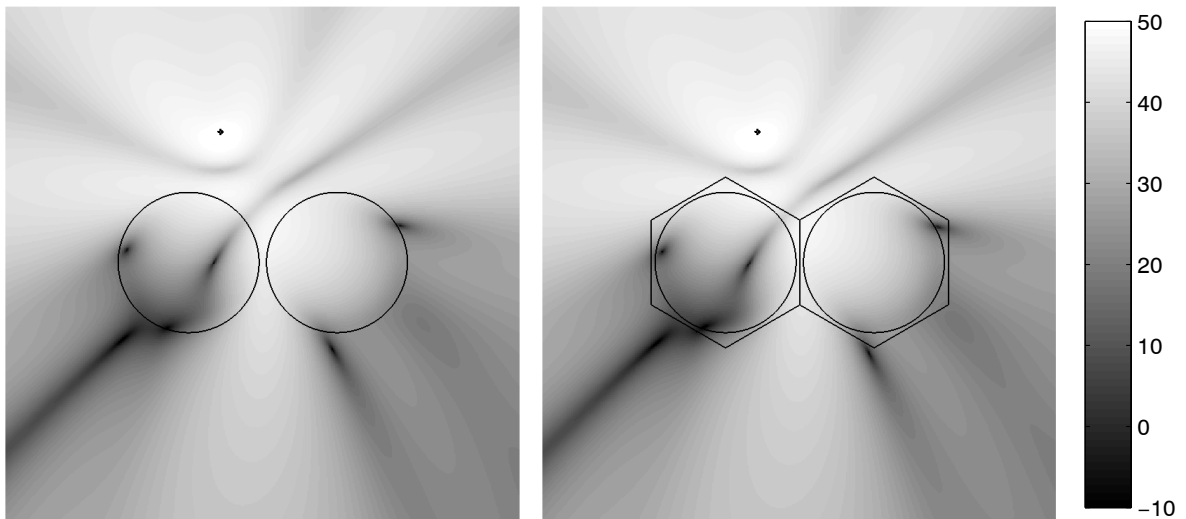


Figure 6.2: The magnitude of the electric field on a logarithmic scale (dB) for the scattering from two circular cylinders with the PMCHW method (left) versus the embedding approach (right). The dot marks the position of the electric line source.

On the right in Figure 6.2 we have shown the electric field computed with the LEGO approach. The hexagonal domain contours are shown. The equivalent electric current distributions on the boundaries of the scattering domains are discretized using 40 points per wavelength. The common boundary has been removed in the combined scattering operator of the composite structure. Both plots are scaled in dB to capture possible deviations at different amplitude scales. There is hardly any visual difference between the field plots, which indicates that the LEGO approach performs well. In particular, the field across the domain boundaries remains continuous. For a quantification of the error in the field, we refer to Section 6.5.

6.3 The construction of large scattering operators

Below we illustrate the wide applicability of the embedding approach as a design tool for large *finite* EBG structures. Each EBG structure that is considered follows from one elementary domain through successive combinations and duplications along properly chosen translation vectors. Common boundaries are removed in this process. In only a few steps, structures are obtained that are already large, i.e., after n embedding steps the composite structure may consist of up to 2^n elementary domains.

In this section we restrict ourselves to unit cells containing circular cylinders. A single unit cell of an EBG structure is chosen as the elementary scattering domain. Again, the scattering operator of the elementary domain is computed analytically, avoiding computational errors. Once the scattering operator of the combined domains and the interior field operator of the subdomains of interest are determined through successive embedding steps, the field response of the composite structure may be investigated in its dependence on the excitation, since the incident field may be arbitrary. To demonstrate the use of LEGO for antenna applications, we have placed electric line sources above finite 2D EBG structures of various widths to characterize the effect of the EBG size and the source location on the radiation patterns. Here, EBG structures act as a support structure for the antenna and enhance its radiation pattern.

We define the normalized radiation pattern, $\wp(\phi)$, as the power radiated per unit angle ϕ by an electric line source in the presence of a scatterer, normalized to the power radiated per unit angle by that electric line source in the absence of the scatterer. In Appendix C.2, the normalized radiation pattern resulting from LEGO with SEP is presented in closed form. An EBG with a triangular arrangement of dielectric cylinders ($\varepsilon_r = 11.4$) in air is employed as a basis. The cylinders are circular with radius $r = 0.15a$ and periodicity a . This corresponding EBG meta-material exhibits a large TM gap around $fa/c = 0.45$. The line source position is varied only along the y -direction in between the two cylinders in the middle of the EBG structure (see Figure 6.5). Here, the rhombic computational domains illustrated in Figure 6.1c are used. We use \square discretization, with 12 unknown current amplitudes along each edge, which amounts to 27 points per wavelength.

Since EBG structures are constructed that are relatively large in terms of the wavelength, a combined field integral equation (CFIE) is applied to suppress unwanted interior resonances. For now, the midpoint rule is used to evaluate the regular parts of the test and expansion integrals. In

Section 5.5 it is established that for $\square\square$ test and expansion functions, the EFIE is superior to the MFIE as regards the accuracy of the pertaining scattered field. Hence, the EFIE should only be supplemented with the MFIE to suppress unwanted interior resonances. Accordingly, the combination constant α in the CFIE formulation (Eq. (3.20)) is set to $\alpha = 0.99$ to favor the EFIE. For $\alpha = 0.2$, the condition number of the MoM matrix would be much better. For $\alpha = 0.99$, the condition number is still sufficiently low for the use of the LU-factorization for the inverse propagators. A robust way of avoiding interior resonances problems in the LEGO approach with SEP is investigated in Section 6.5.2.

Simulations have indicated no further improvement in the forward direction of the normalized radiation pattern, $\varphi(0)$, for EBG layers of more than four periods thick. Hence, a thickness of four periods is maintained throughout and only the width of the EBG structure is varied. The locations of the line source above the EBG structure, at which $\varphi(0)$ has a maximum or a minimum, turn out to be independent of the width. Therefore, we may select a set of fixed locations where the local maxima occur, and consider the envelope of these maxima.

On the left in Figure 6.3, we show the $\varphi(0)$ with its envelope for an EBG structure of 16 periods wide. The dotted and dash-dotted vertical lines represent the locations where the forward direction has a maximum and minimum, respectively. The first maximum appears at 0.22λ and reoccurs every $\lambda/2$. The minima are offset by $\lambda/4$ with respect to the maxima. On the right in Figure 6.3, we have shown the envelope of $\varphi(0)$ versus the position of the line source above the top of the structure. The variations in the envelope of $\varphi(0)$ increase for higher source positions and smaller EBG structures, i.e., the source ‘sees’ more the edges for smaller structures. Hence, the variations in the envelope may be attributed to the edge effect at the sides of the EBG structure. For increasing width and fixed height, $\varphi(0)$ appears to converge to about 6 dB, except very close to the EBG due to near-field effects. Accordingly, the EBG structure almost acts as a perfectly conducting reflector.

In Figure 6.4, $\varphi(\phi)$ is depicted for the local maximum and minimum in the forward direction for the source positions that are closest to the EBG structure with 8 and 32 periods width. At the minimum the beam is split in two. The back- and sideward radiation does not substantially differ between a maximum and minimum. Increasing the width of the EBG structure reduces both the backward and sideward radiation. It should be pointed out that the plots are not symmetric due to the asymmetric nature of the finite size EBG structures under consideration (see also Figure 6.5 and Figure 6.6). For the 32 periods width, this edge effect virtually vanishes.

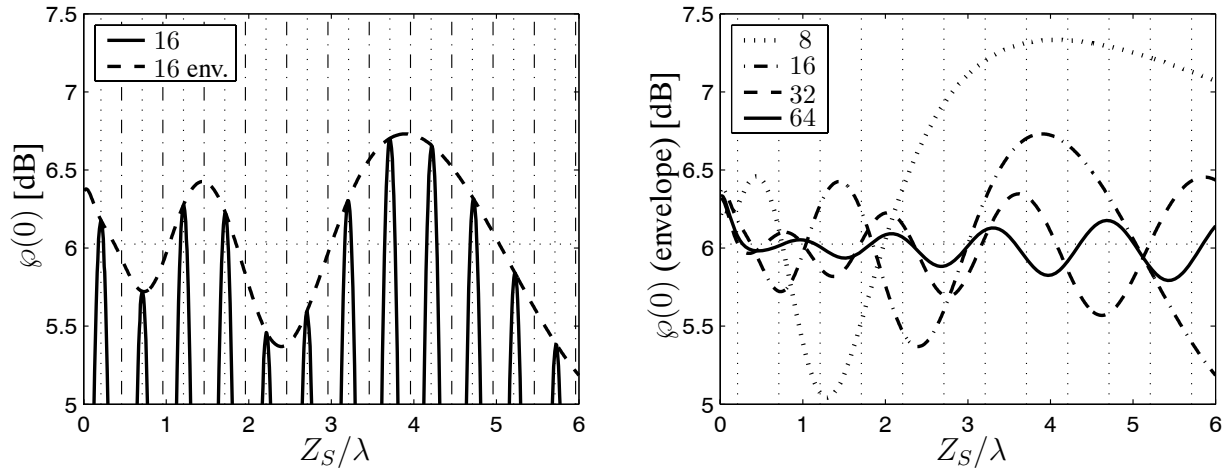


Figure 6.3: The forward normalized radiation pattern, $\varphi(0)$, versus the normalized distance Z_S/λ of an electric line source above an EBG structure similar to the one in Figure 6.5 (four periods thick). On the left, $\varphi(0)$ and its envelope are shown for an EBG structure that is 16 periods wide. The dotted and dashed vertical lines indicate line source positions with local maxima and minima in $\varphi(0)$, respectively. On the right, the envelope of $\varphi(0)$ for several EBG widths.

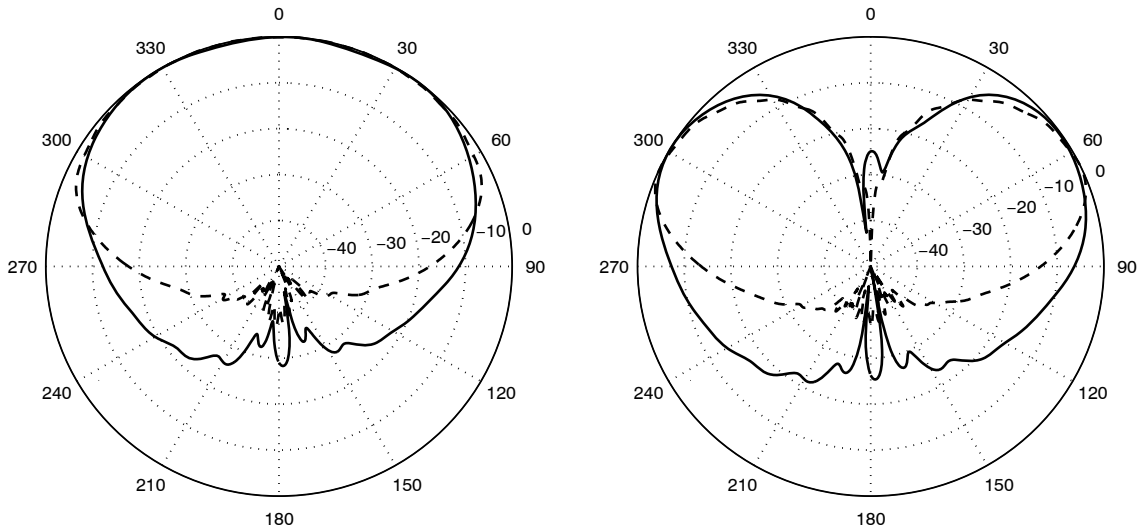


Figure 6.4: The normalized radiation pattern, $\varphi(\phi)$, with a maximum (left) and minimum (right) in the forward direction as a function of ϕ for a line source above an EBG structure of 8 (dashed), respectively 32 (solid) periods wide and 4 periods thick.

In Figure 6.5 the total electric field is shown for the first line-source position above an EBG structure (32×4) that produces a local minimum in $\varphi(0)$. Since the radius of the circular cylinders is considerably here smaller than in Section 6.2, the rhombic shape is used for the elementary scattering domain. For the figure at the top, we have used the midpoint quadrature rule. The dotted lines in the composite scattering domain indicate the common contours that have been removed in the embedding sequence. Accordingly, the combined scattering operator is defined only on the outer (solid) contour. At the bottom the field plot is produced using adaptive quadrature rules for the regular integral parts, with a relative accuracy set to 10^{-2} . The location of the source position above the EBG has been marked. Both plots are scaled in dB to facilitate a continuity check of the field across the domain contours.

We observe that for strong field amplitudes above the EBG, there is hardly any visual difference between the two figures. On the other hand, at the back of the EBG structure, both field plots clearly differ. These deviations may be attributed to the low-order midpoint quadrature rule used for the figure at the top. The relative poor midpoint accuracy leads to field discontinuities across the domain boundaries at the back of the EBG. However, it should be noted that the corresponding field amplitudes are at least 40dB lower than in the main beam. The increasing loss of symmetry upon approaching the left or right sides of the EBG structure is due to the local asymmetry of the EBG structure. With the adaptive quadrature rules at the bottom, the asymmetries are more confined to the corners of the EBG structure. This observation may indicate that the additional asymmetry in the upper figure stems from the asymmetric building sequence in the embedding scheme. The impact of the choice of building sequence and the accumulation of errors will be further investigated in Section 6.5.3.

To validate the results, the simulations have been repeated using the rectangular elementary scattering domain illustrated in Figure 6.1b. The results agree very well. The maximum deviation of $\varphi(0)$ is 0.1 dB, which amounts to a mere deviation of 1%. This maximum deviation occurs for the largest structure (256 cylinders), probably due to the accumulation of errors accumulated in the successive embedding steps.

In Figure 6.6 the magnitude of the electric field is depicted for the first maximum in $\varphi(0)$, simulated using rectangular elementary cells in Figure 6.1b. Adaptive quadratures have been used in the LEGO approach to generate this plot. Refining the mesh density or changing the domain shapes hardly results in any visible improvement in the logarithmic field plot, which may serve as an endorsement for using adaptive quadrature rules. We observe that the field distributions for maximum and minimum of $\varphi(0)$ are fairly similar at the back of the EBG structure. Some small

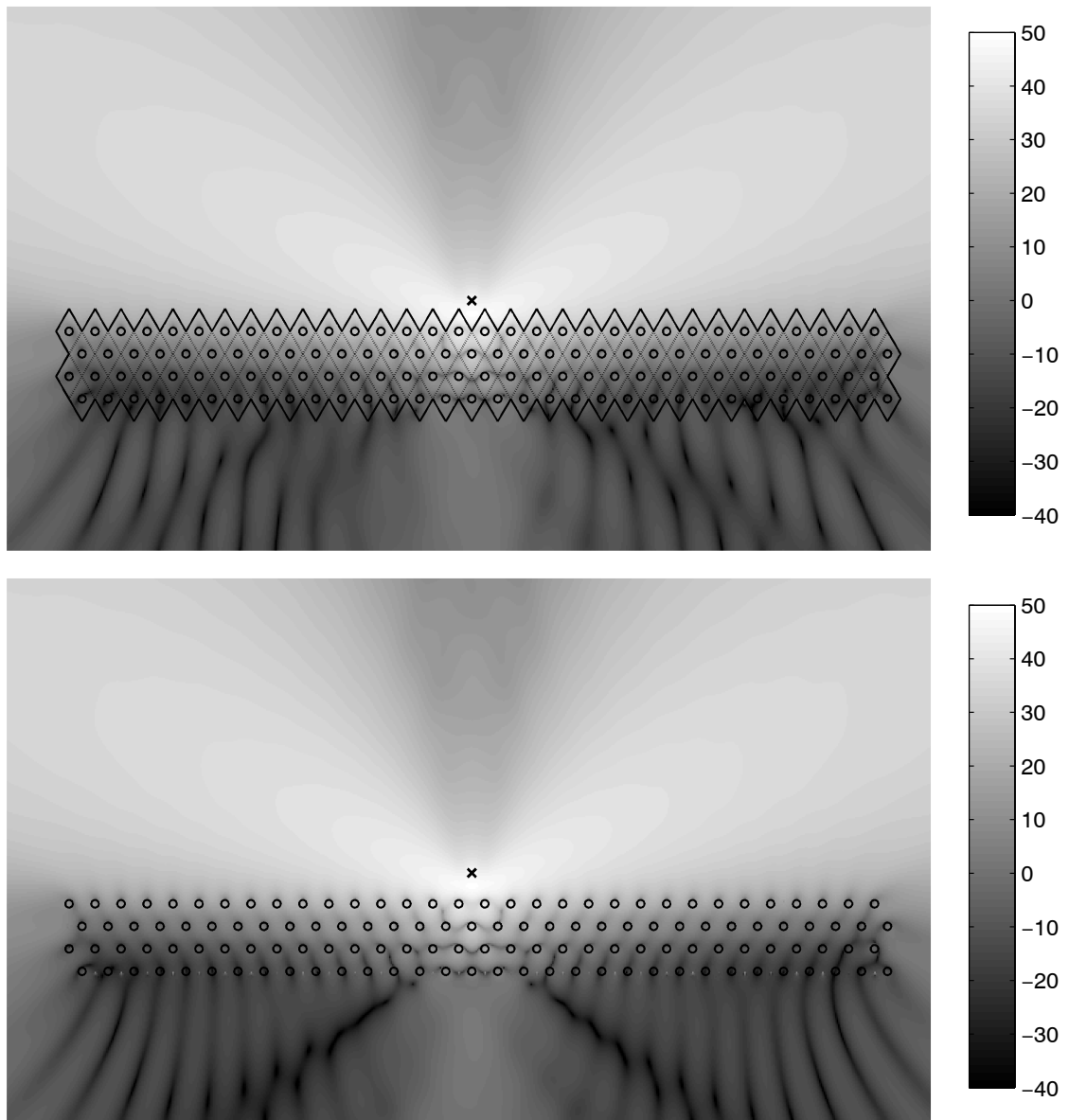


Figure 6.5: The magnitude of the electric field on a logarithmic scale (dB) generated by an electric line source above an EBG (32×4 periods). The position of the line source is such that a local minimum is produced in $\varphi(0)$. Rhombic scattering domains have been used. The dotted lines indicate removed common boundaries. For the top and the bottom, the midpoint rule and an adaptive quadrature rule have been used, respectively.

field discontinuities remain at the left and right edges of the EBG structure, especially at the inward corners of the outer boundary. Similar discontinuities remained at the inward corners of the rhombic domain shape at the bottom in Figure 6.5. This may be due to the sharp edges in the domain boundary, although these discontinuities may also be attributed to the interior resonance effect inherent to SEP (see Section 6.5.2).

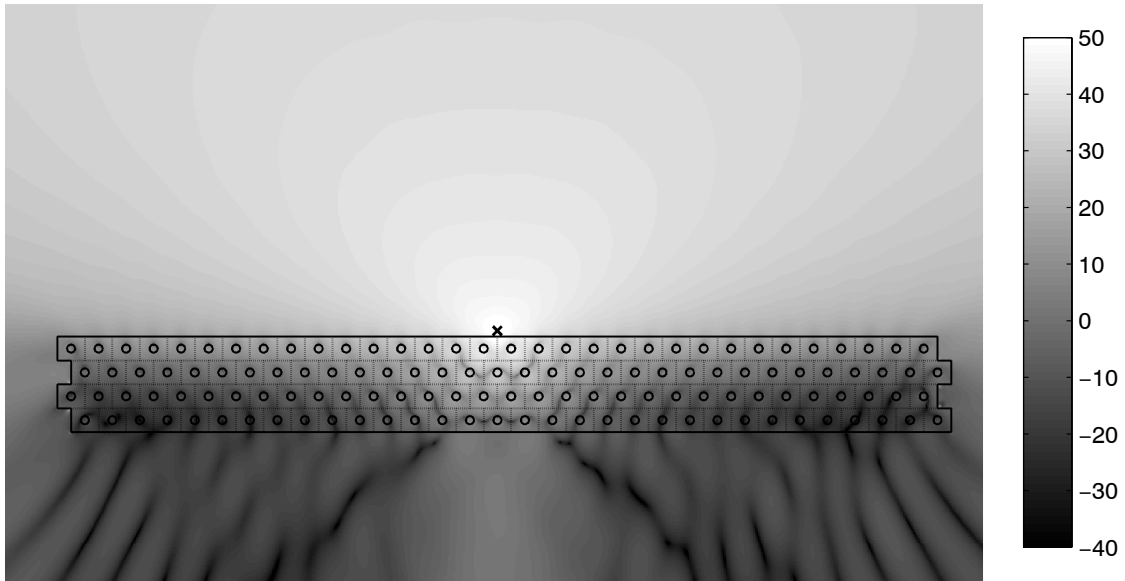


Figure 6.6: The magnitude of the electric field on a logarithmic scale (dB) generated by an electric line source above an EBG (32×4 periods). The position of the line source is such that a local maximum is produced for $\varphi(0)$. Rectangular scattering domains have been used. The dotted lines indicate removed common boundaries.

The low computational advantages of the LEGO approach have been explained in Section 4.8. However, the amount of computational improvement over a direct solver may vary subject to the choice of domain shape. For instance, throughout the sequence of embedding steps, the size of the outer boundary is significantly larger for the rhombic domain shape than for the rectangular domain shape.

Furthermore, we would like to comment on the efficiency of the LEGO approach for the generation of the field plots in comparison with conventional direct solvers. With a boundary integral equation as a direct solver, the field from the current distributions at the boundary interfaces of all circular cylinders is computed for each point where the field is required. In case a high resolution is desired, this step may become rather time-consuming. In contrast, in the LEGO approach, the field within the composite structure is obtained instantly. More specifically, from the interior

field operators Q_{i3} , where C_3 denotes the outer contour, we obtain an equivalent current Q_i^{cp} for each individual subdomain \mathcal{D}_i . These currents transform the known scattered field of the single circular cylinder inside a subdomain into the proper complete field. The fast computation of the interior field originates from the negligible computation time of the scattered field from a circular cylinder (analytically) inside such a small subdomain in combination with the reusability of that field in all subdomains. Despite that the field exterior to the composite structure is computed in the same way as with the boundary integral, the ratio of the length of the outer contour of the combined scattering domain and the circumferences of all circular cylinders may be considerably smaller than one. In this particular example with small cylinders, the pertaining ratio already is about 0.6, implying that in comparison, the exterior field is obtained 1.667 times faster via the LEGO approach.

As an additional example we consider the EBG waveguide shown in Figure 6.7. Because the propagation and field confinement within an EBG waveguide primarily relies on strong field interactions between nearby scatterers, this is another good example to demonstrate the LEGO concept. Again, we consider a triangular array of dielectric circular cylinders with $r/a = 0.15$ and $\varepsilon_r = 11.4$, embedded in air with $f a/c = 0.45$. Also, SEP($\square\square$)-discretization is used, with a CFIE combination constant $\alpha = 0.99$. A mere seven embedding steps were required to obtain the field in the EBG structure depicted in Figure 6.7. The field in the EBG waveguide is excited by an electric line source at a position (marked) that is aligned with the waveguide axis. The waveguide mode is nearly symmetric with respect to the waveguide axis and has an almost constant peak amplitude, which indicates that the complex field interactions are properly accounted for by the LEGO approach.

In the absence of proper tapers, there are strong impedance mismatches at the transitions between the waveguide ends and the surrounding free-space. Further, the EBG structure seems to bend the field around the structure. To improve the mode confinement even further, we could simply reuse the obtained structure and add a row of unit cells on the top and bottom of the EBG structure. For more complicated configurations, however, repeated optimization steps of the structure may be required in a design process. This can already be achieved directly through successive embedding of small domains with the large scattering operator. However, with an additional step in the LEGO scheme, optimization processes can become significantly faster. This will be demonstrated in Section 6.4.1.

Finally, we wish to point out that a certain building sequence produced strong field deviations. With a slight shift in the operating frequency or a change in building sequence this problem

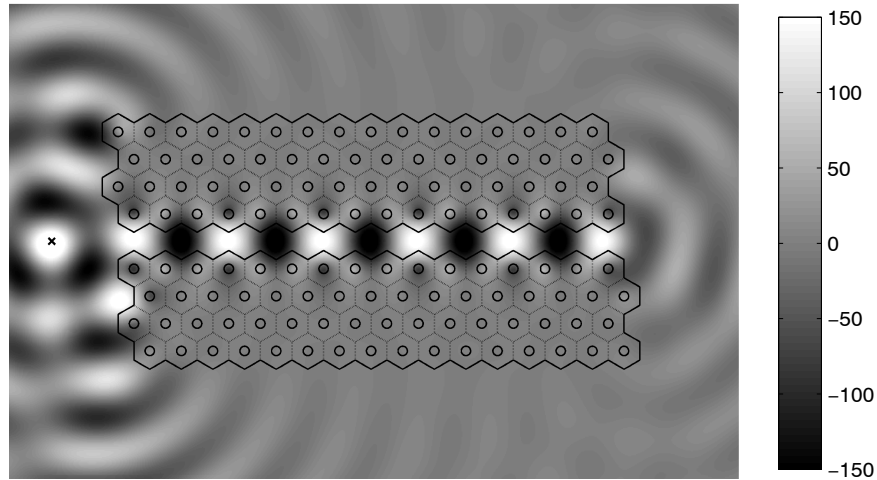


Figure 6.7: The real part of the electric field in an EBG-waveguide with circular dielectric cylinders in air. The position of the generating electric line source is marked by a cross. A hexagonal shape is chosen for the elementary scattering domain. The dotted lines indicate common boundaries that have been removed in the embedding process.

can be solved. This seems to indicate an interior-resonance problem, even though a CFIE was employed. This matter will be discussed further in Section 6.5.2. For Figure 6.7, a building sequence has been selected by which this particular problem is avoided.

6.4 Local structure optimization

In Section 6.3, the composition of large scattering domains through successive embedding steps and the convenient use of the pertaining scattering and interior field operators have been demonstrated for two possible EBG applications. Because the field operators encompass all possible excitations, the computation time and the required storage demand will grow considerably for large structures, especially when the interior field operators of all subdomains are stored. However, both computation time and storage demands can be reduced significantly if the embedding of subsequent domains is restricted to a designated domain of interest. This so-called optimization stage has been described in Section 4.7 and is considered to be ideal to tune/optimize large structures locally for design purposes. In addition, with the hybrid variety of LEGO introduced in Section 4.9, the optimization stage may be integrated into existing design packages as an additional tool. To demonstrate this optimization stage of LEGO, we present two design examples

below. First, the scattering operator of the large composite scattering domain of interest is determined via a sequence of embedding steps. Subsequently, critical design parameters are tuned in the optimization stage of LEGO.

6.4.1 EBG power splitter

First, we apply the embedding approach by considering a power splitter for a single-mode linear-defect waveguide inside a large, finite EBG structure. The actual structure is superimposed on the field plots in Figure 6.8 and Figure 6.9. A triangular arrangement of dielectric circular cylinders ($\epsilon_r = 11.56$) in air is employed here as a basis. The corresponding periodic EBG structure exhibits a large TM (with respect to \hat{z}) bandgap about $fa/c = 0.407$ for $r/a = 0.175$. Within the rectangular supporting structure of 17 by 17 cylinders, three linear defect waveguides are created by omitting rows of cylinders. The waveguides are joined at a Y-junction through a cavity consisting of a cylinder of arbitrary radius and permittivity surrounded by regular EBG cylinders. In our example, the cavity is tuned to attain high transmission across the junction, as suggested in [83] for bends.

Due to the relatively small cylinder radius, in comparison with the ones in Figure 6.2, the shape of the computational domain is not restricted to a hexagonal one. To test the influence of the chosen computational domain, we employ the rhombic shape illustrated in Figure 6.1 aligned with the x -direction, as indicated in Figure 6.8. Schelkunoff's equivalence principle is employed in the embedding approach with $\square\square$ -discretization and 18 unknowns on each edge of the rhombic domain. The EBG structure itself is symmetric with respect to the yz -plane. However, the computational domains are not symmetric, and hence, all asymmetries which occur in the results for a symmetric excitation can be attributed to the embedding approach.

In contrast with popular simulation packages, by which the optimum operating frequency can be determined for a given structure, we are able to optimize the structure for a given operating frequency. In particular, we apply embedding to analyze the effect of different cavity configurations at the Y-junction of the power splitter.

The first stage towards structure optimization is the composition of the scattering operator, S_{LL} , of the large domain \mathcal{D}_L through repeated application of embedding for reusable scattering domains, starting from a single scattering cylinder. The final outer contour \mathcal{C}_L for which S_{LL} is defined is indicated by solid lines in Figure 6.8. The dotted lines in \mathcal{D}_L indicate common contour

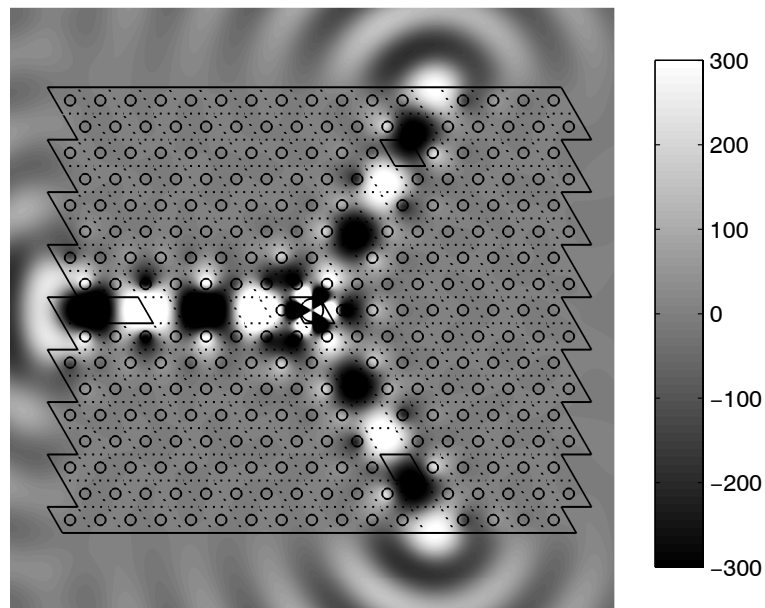


Figure 6.8: The real part of the electric field of the hexapole mode with high transmission at $\varepsilon_r = 28$ and $r/a = 0.3767$. The contour \mathcal{C}_L of the large domain \mathcal{D}_L has been highlighted, where the dotted lines indicate removed common contour parts.

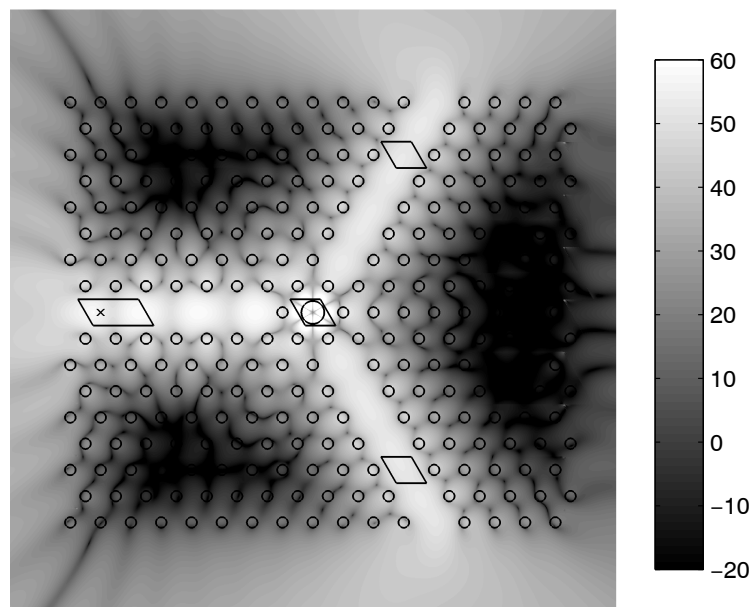


Figure 6.9: The magnitude of the electric field in Figure 6.8 on a logarithmic scale (dB). The contour \mathcal{C}_D of the designated domain \mathcal{D}_D has been highlighted, and the location of the radiating electric line source has been marked by a cross.

parts that have been removed at preceding embedding stages in the composition of \mathcal{D}_L . Because \mathcal{D}_L is constructed from single unit cells containing circular cylinders, the initial scattering operator may still be computed analytically. Although the first stage is very time-consuming, in the order of hours, it is performed only once. This, in contrast with the repeated full recomputations of the entire structure for each set of parameter values that is common to direct solution methods.

In the initial step of the optimization stage, we assign a relatively small designated domain \mathcal{D}_D , which contains the source and the region where the structure may be varied, as well as the domains where the field values are to be optimized. In the current configuration, this includes the cells containing the defect cylinder inside the cavity, the source in the left waveguide branch, and cells in each of the two branches where the transmitted power is monitored. The corresponding contour \mathcal{C}_D is indicated by solid lines in Figure 6.9. On \mathcal{C}_D , the reduced scattering operator, S_{DD} , which describes the scattering response of the large environment of the small domain \mathcal{D}_D , is obtained from S_{LL} through Eq. (4.57).

The subsequent optimization stage involves the repeated application of embedding for a variable r/a and ε_r of the defect cylinder with the large domain \mathcal{D}_L . Here, the unit cell that contains the defect cylinder inside the cavity is taken as the embedding domain \mathcal{D}_E . Because each embedding step involves the scattering operator S_{DD} , instead of S_{LL} , such an embedding step takes relatively little time, in the order of seconds.

In Figure 6.10, the resonant modes of the cavity are shown as a function of the filling ratio r/a and the relative permittivity ε_r of the defect cylinder. These modes represent local maxima and minima in the power transmitted through the cavity, indicated by solid and dashed lines, respectively. An electric line source that produces the incident field is positioned in the left waveguide branch in the horizontal symmetry plane of the power splitter. Hence, only even cavity modes are excited with respect to the symmetry plane. The first monopole mode is not shown, because it occurs for a (nearly) unloaded cavity. The application of scattering operators also allows us to vary the source position for each cavity configuration in Figure 6.10 without additional costs. Since the optimum remains fairly stable throughout, we have chosen to fix the source position.

In Figure 6.11, we have presented a measure of the transmission in terms of the normal component Poynting vector at the center of the upper waveguide branch at $\varepsilon_r = 28$. With the exception of the first monopole, the local maxima and minima transmission regions appear to be very narrow. The corresponding electric field distributions of the resonant states inside the cavity are

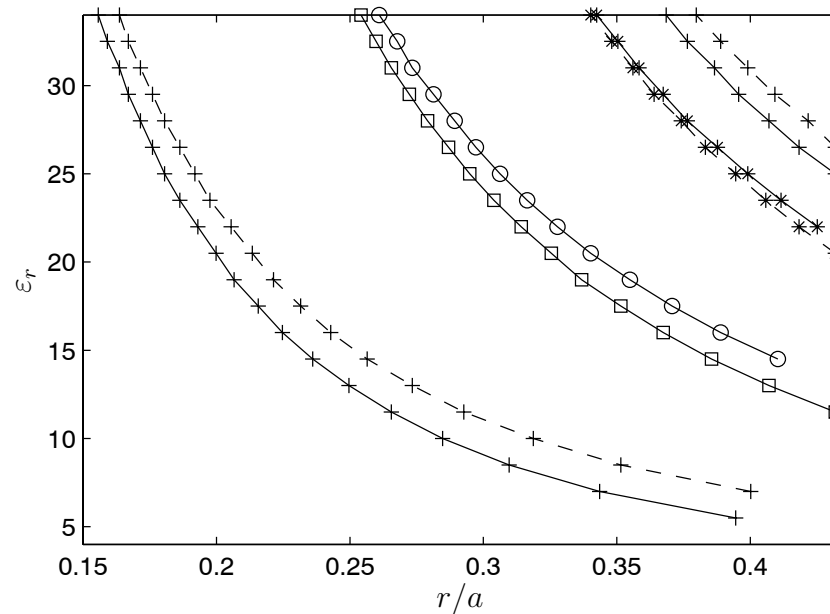


Figure 6.10: The resonant cavity modes as a function of ϵ_r and the radius of the defect cylinder. Solid and dashed lines denote local maxima and minima in the transmitted power, respectively. o : monopole, + : dipole, \square : quadrupole, and * : hexapole.

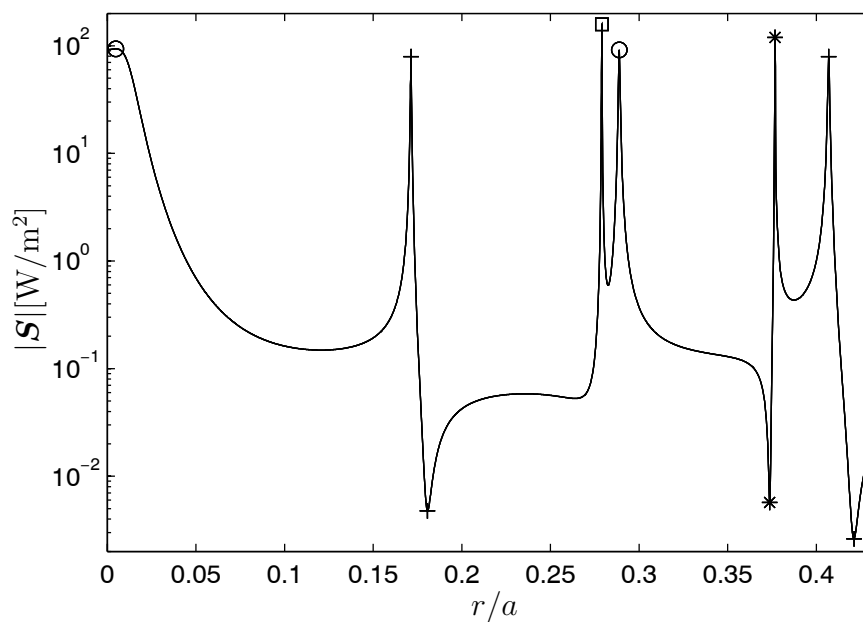


Figure 6.11: The Poynting vector normal to the cross section of the upper waveguide branch as a function of the defect cylinder radius r/a for $\epsilon_r = 28$ excited by an electric line source of 1A. The markers indicate the cavity modes of Figure 6.10.

shown in Figure 6.12. Each maximum, at a dipole or hexapole mode, appears to have an asymmetric counterpart nearby that produces a minimum. This is caused by the asymmetry of the cavity with waveguide branches in the vertical plane (the xz -plane in Figure 6.1 with respect to the center of the cavity) due to the attached waveguide branches. This phenomenon would not be observed if the cavity was placed in an otherwise perfect crystal, which is a common assumption in the analysis of these structures. As a consequence, the vertical asymmetric modes reoccur at nearly the same cavity configuration.

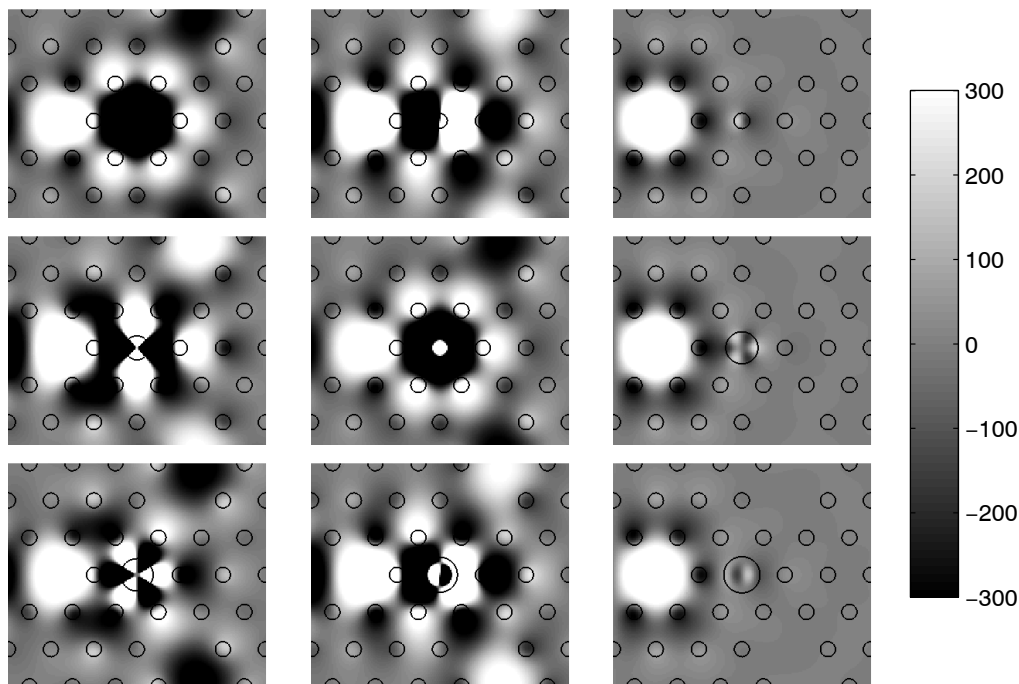


Figure 6.12: From left to right and top to bottom the real part of the electric field of each of the resonant cavity modes indicated in Figure 6.11, at $\epsilon_r = 28$ for increasing r/a with the connected waveguide branches included.

The total electric field in the entire structure for the hexapole mode with a local maximum is depicted in Figure 6.8. Despite the vertical asymmetry of the chosen computational domains and building sequence, the obtained field distribution turns out to be completely symmetric. To capture possible deviations at different amplitudes, the same field distribution is shown in Figure 6.9 on a logarithmic 90-dB scale. The symmetry of the field at lower amplitudes deeper within the supporting EBG remains intact. At the right-hand side of the structure some minor anomalies are just visible, but given the amplitude scale and the modest discretization, the results may be considered very accurate.

6.4.2 EBG mode splitter

Now that we have demonstrated the optimization stage of large scattering domains on the basis of an EBG power splitter, let us consider a more complicated example with potentially interesting applications. In particular, we employ the LEGO approach to construct and tune an EBG mode splitter. As the point of departure, we will consider the simple design of the power splitter in Section 6.4.1. A straightforward extension towards a mode splitter is readily achieved if the input waveguide supports both polarizations and the output waveguides supports either the TE or TM polarization. The optimization stage of the LEGO approach is ideally suited to tune the transition at the waveguide junction with respect to maximum transmission. This will be demonstrated below.

To design a mode splitter, the basic EBG structure should support a full bandgap, i.e., an overlapping bandgap for both polarizations. Therefore, we employ a triangular arrangement of air holes in a dielectric material with relative permittivity $\varepsilon_r = 11.4$ and filling ratio $r/a = 0.45$ with radius r and periodicity a . The corresponding EBG structure exhibits a full bandgap for normalized frequencies of about $0.41 \leq fa/c \leq 0.45$. Similar to the design of the power splitter in Section 6.4.1, we consider three EBG waveguides that are joined at a Y-junction. The actual structure is superimposed on the field plots in Figure 6.13. Each linear defect waveguide is created by changing the radii of a row of cylinders. The modes that the waveguide can support depend on the defect radius that is selected. In particular, for a defect radius $r/a = 0.33$, the input waveguide supports modes of both polarizations in the bandgap. Within the frequency region of about $0.430 \leq fa/c \leq 0.434$, one output waveguide with a defect radius $r/a = 0.2365$ supports only TE modes (with respect to \hat{z}). For a defect radius of $r/a = 0.1925$, the other output waveguide supports only TM modes (with respect to \hat{z}) in this frequency region. Consequently, the normalized frequency is set to $fa/c = 0.432$. These parameters have been taken from [84].

To tune the transmission at the Y-junction, we apply embedding based on SEP($\square\square$). The singular part of the test and expansion integrals is computed analytically, whereas the midpoint quadrature rule is used for the regular part. Further, to construct the elementary scattering domains, analytic expressions are employed to describe the scattering by a single circular cylinder. Due to the large filling ratio of the unit cell of the basis EBG structure, only the hexagonal domain shown in Figure 6.1a can be used. The mesh density is 18 points per edge, which amounts to 21 points per wavelength. Note that the implementation of LEGO based on either SEP or LEP for the TE-case readily follows by duality. In fact, this can be achieved by starting from a configuration in which ε_r and μ_r are interchanged.

The first stage towards structure optimization is the composition of the scattering operator, S_{LL} , of the large domain \mathcal{D}_L through repeated application of embedding for reusable scattering domains, starting from a single scattering cylinder. This step is time-consuming, but it is performed only once. The final outer contour \mathcal{C}_L for which S_{LL} is determined is indicated by solid lines in the lower figure of Figure 6.13. Common boundary parts have been removed at preceding embedding stages in the composition of \mathcal{D}_L .

In the initial step of the optimization stage, we assign a relatively small designated domain \mathcal{D}_D , which contains the source and the region where the structure may be varied, as well as the domains where the field values are to be optimized. In the current configuration, this includes the cells containing the defect cylinder at the Y-junction, the line source in the lower waveguide branch, and a cell at each end of the other two branches where the transmitted power is monitored. The corresponding contour \mathcal{C}_D is indicated by solid lines in the upper figure of Figure 6.13. On \mathcal{C}_D , the reduced scattering operator, S_{DD} , which describes the scattering response of the large environment of the small domain \mathcal{D}_D , is obtained from S_{LL} through Eq. (4.57).

The subsequent optimization stage involves the repeated application of embedding for a variable filling ratio r/a of the defect cylinder with the large domain \mathcal{D}_L . Here, the unit cell that contains the defect cylinder inside at the Y-junction is taken as the embedding domain \mathcal{D}_E . Because each embedding step involves the scattering operator S_{DD} , instead of S_{LL} , such an embedding step takes very little time. More specifically, the filling ratio is varied for $0 \leq r/a < 0.5$ in 500 steps. Because the maximum transmission for each radius may require a different excitation, the transmission is evaluated for 150 source positions for each radius. The computation time associated with each radius is in the order of a few seconds. Since the introduction of a cavity at the waveguide junctions to improve the transmission for the power splitter in Section 6.4.1 has shown that frequency bands of operation are narrow, the cavity is omitted here to investigate whether the transmission band broadens.

The results of the optimization stage are shown in Figure 6.14. The transmitted power in the left (TM) and right (TE) waveguide branches is plotted as a function of the defect cylinder radius r/a in terms of the Poynting vector at the center of and normal to the cross section of the waveguides. On the left an electric line source of strength 1 A is used to generate a TM wave and on the right a notional magnetic line source of 1 V is used to generate a TE wave. For each value of r/a , the source position is chosen such that maximum depolarization occurs. This causes the discontinuities in the curves. The strongest mode depolarization occurs for $r/a = 0$. Around $r/a = 0.22$ there is also a local optimum for both polarizations, however, with significantly less

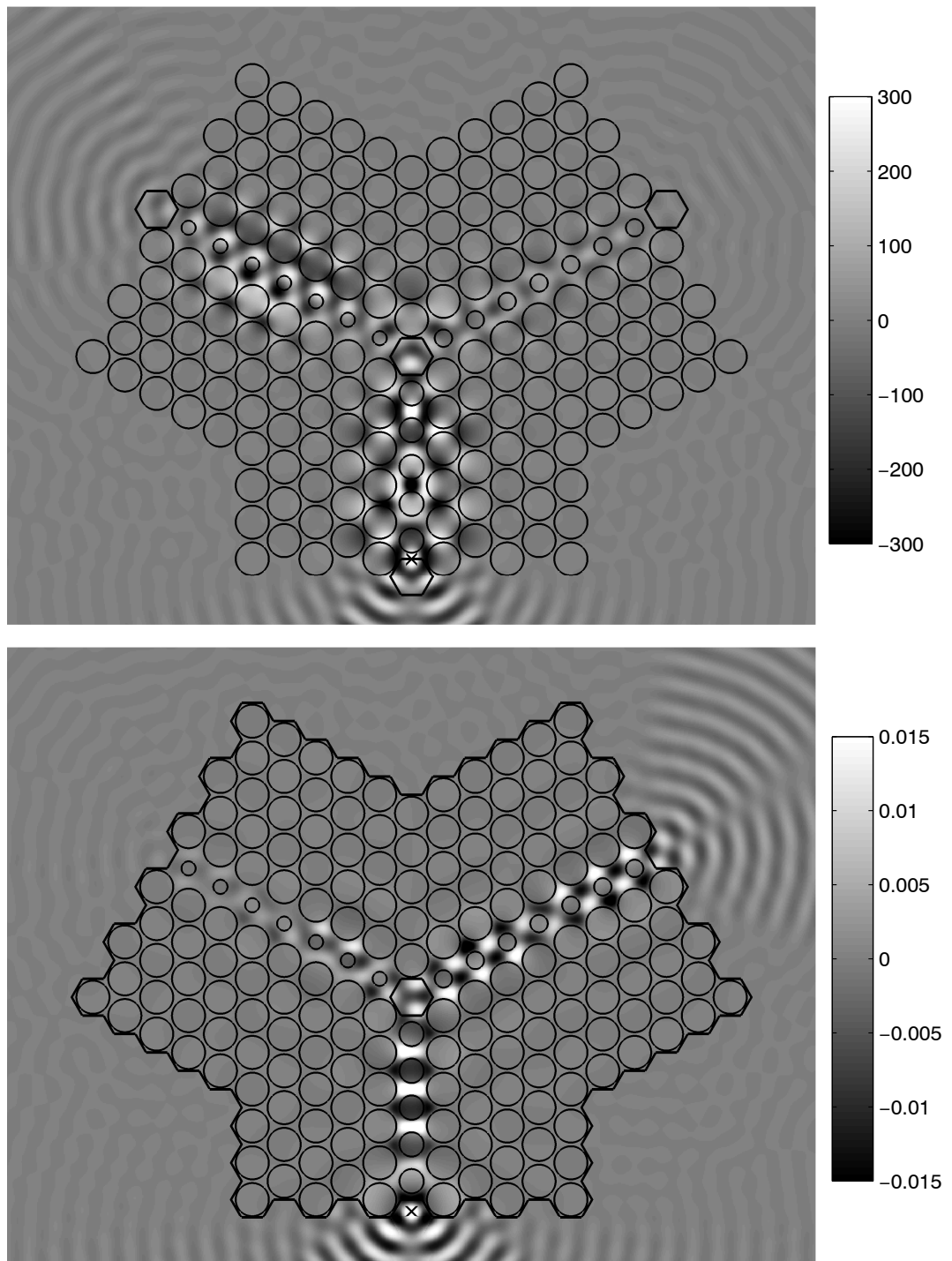


Figure 6.13: On the top, the TM-case with the electric field E_z generated by an electric line source. The boundary of the designated domain is indicated. In the bottom figure, the TE-case with the magnetic field H_z generated by a magnetic line source. The boundary of the large scattering domain is indicated. The position of the line sources has been marked. The left and right branch are associated with only a TM- and TE-mode, respectively. At the junction, $r/a = 0$.

transmitted power. For these cases, the introduction of a resonance cavity might have facilitated in a better mode transition at the Y-junction with respect to the transmission.

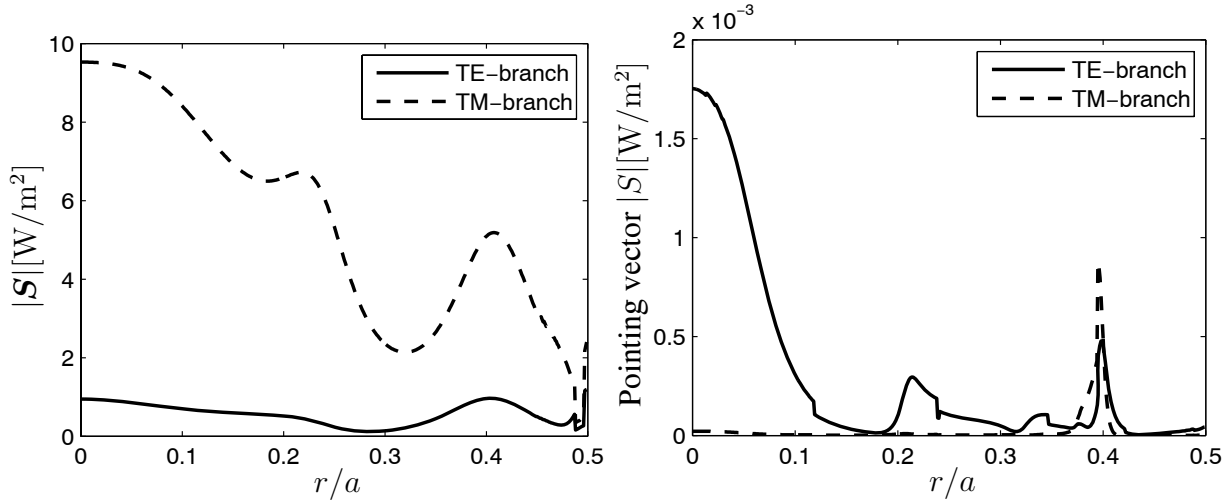


Figure 6.14: The Poynting vector normal to the cross section of the left (TM) and right (TE) waveguide branches as a function of the defect cylinder radius r/a . On the left an electric line source of strength 1 A generates a TM wave, and on the right a notional magnetic line source of strength 1 V generates a TE wave. For each value of r/a , the source position is chosen such that maximum depolarization occurs.

In Figure 6.13, the field plots of the mode splitter are shown for a filling factor $r/a = 0$. On the top, the TM case is presented with an electric field $\mathbf{E} = E_z \hat{z}$ generated by an electric line source. In the bottom figure, the TE-case is depicted with a magnetic field $\mathbf{H} = H_z \hat{z}$ generated by a magnetic line source. The position of the line sources has been marked. The field plots demonstrate the functionality of the EBG mode splitter. The TE-bandgap is much broader than the TM-bandgap [85, p. 125], which results in a stronger confinement for the TE mode. The stronger confinement amounts to a narrower field distribution of the TE mode. In addition, the suppression of TE modes in the TM waveguide and vice versa is weaker than the confinement from the surrounding basis EBG structure. Inspecting the waveguide modes reveals that there is a strong mode mismatch at the transition of each waveguide branch with the background medium similar to the waveguide mode in Figure 6.7. These mode mismatches reduce the performance of the splitter and hampered the optimization of the waveguide-junction. Hence, a first step in the design of integrated technology through EBG-waveguides would be the design of a transition into conventional technologies. The ability to position the feed inside an air cylinder of the input waveguide may be an advantage in this matter.

6.5 Numerical Comparison

Now that the principles underlying the LEGO approach have been explained and demonstrated, let us quantify the accuracy with which the scattered field can be obtained. The accuracy is considered in terms of the mesh density in the discretization of the domain boundaries. In addition to the magnitude of the accuracy, the rate of improvement with subsequent mesh refinement is of interest. The accuracy of the scattered field is investigated for 2D configurations. In particular, the framework of the analysis is relevant to EBG applications. For details concerning the implementation of LEGO for 3D scattering configurations, we refer to Section 7.6.

There are various aspects that may affect the accuracy of the LEGO approach. For instance, there is the choice of equivalence principle, i.e., either Love's or Schelkunoff's equivalence principle. Moreover, LEP can be employed either with inverse propagator or inverse Gram matrices. The choice of the test and expansion functions is evaluated by considering both piecewise constant and piecewise linear functions. If common boundary parts occur in the embedding process, current amplitudes may be transferred directly, for which two methods have been introduced in Section 4.5. More general aspects are considered as well, e.g., the dependence on the building sequence and the choice of domain shape, but also the error accumulation associated with a sequence of embedding steps. Finally, we investigate whether a degradation of the accuracy due to the interior resonance effect, which may occur if a combination of SEP and the EFIE is employed, can be avoided with embedding by application of the CFIE.

6.5.1 Love's versus Schelkunoff's equivalence principle

Below, the application of Love's and Schelkunoff's equivalence principle in the LEGO approach is investigated with respect to the scattered field for 2D EBG applications. For now, we restrict ourselves to the dependence on the choice of discretization, the mesh density and the shape of the scattering domains. Other properties follow in later sections. Further, the use of Gram matrices is compared with conventional inverse propagators. In addition, the direct transfer of current amplitudes is investigated. Finally, we consider the dependence of the various implementations of LEGO on the quadrature error. Where possible, the results are related to those of the integral equations used for the scattering from perfectly conducting and dielectric objects in Sections 5.5 and 5.8, respectively.

Before we proceed with the actual comparison between embedding based on SEP and LEP, let us first elucidate the framework in which the analysis is carried out. In particular we employ the basis configuration depicted in Figure 6.15. Four dielectric circular cylinders in a triangular array with periodicity a are considered. The filling ratio is $r/a = 0.175$ with radius r . The relative permittivity of the circular cylinders is $\varepsilon_r = 11.56$. The operating frequency is set to $fa/c = 0.4$, which corresponds with the center frequency of the bandgap in case of an infinite array. To investigate the dependence on the chosen scattering domain shape, the results from the use of a hexagonal and rhombic shape for the elementary scattering domains will be compared. The composite structures shown in the figure can be constructed in two embedding steps, i.e., after first embedding two elementary scattering domains, the pertaining combined domain is used as the elementary ones in the second embedding step. Wherever appropriate, the building sequence is indicated by the dashed line. In this way, both for the hexagon and rhombic domain shapes, both embedding steps involve common boundaries.

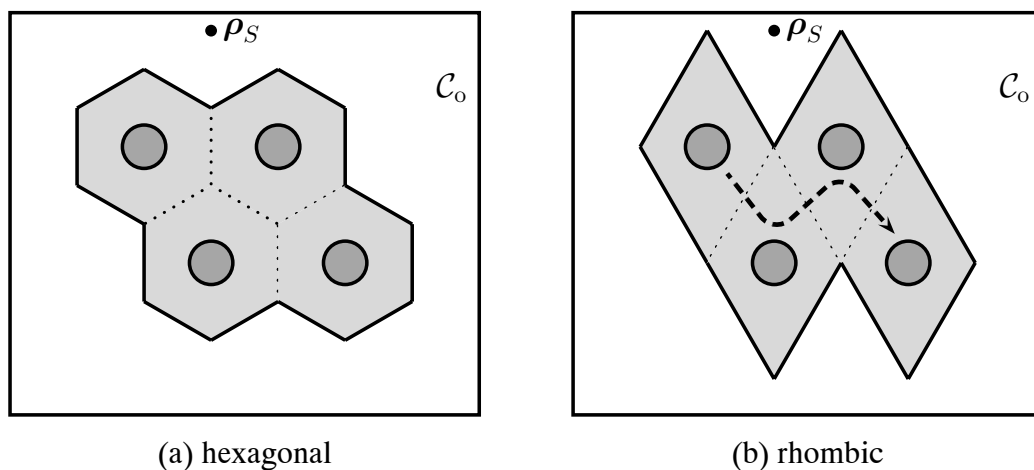


Figure 6.15: The composite scattering configuration used to evaluate the LEGO approach with hexagonal and rhombic elementary scattering domains. Dotted lines represent common boundaries that are removed in the embedding process. An electric line source at ρ_S generates the incident field. The pertaining scattered field is evaluated on the observation contour \mathcal{C}_o . The dashed line indicates the building sequence.

To evaluate the performance of the LEGO approach, analytical solutions are employed for the fields scattered by a single circular cylinder that are used to construct the elementary scattering domains. Further, the scattered fields are evaluated on an observation contour, \mathcal{C}_o , as indicated in Figure 6.15. Each side of the observation contour is positioned one period away from the center of the closest cylinder and has 250 sampling points. An electric line source (TM polarization) at ρ_S in between the top two cylinders generates the incident field. The normalized error least

squares defined by Eq. (5.80) is employed as an error criterion for the scattered field components tangential to \mathcal{C}_o . As a reference solution, the PMCHW integral formulation for multiple dielectric objects is employed, with a total of 8000 unknowns in the expansion of the electric and magnetic equivalent currents. With reference to Figure 5.27, the corresponding mesh density amounts to a normalized error of about 10^{-8} in the range $\mathcal{O}(N^{-8})$.

For LEGO based on SEP with only electric equivalent currents we consider both $\square\square$ - and $\wedge\wedge$ -discretization. A CFIE with combination constant α , as defined in Eq. (3.20), is employed to calculate the field propagators for the transfer operators. Recall that $\alpha = 0$ and $\alpha = 1$ amounts to pure MFIE and EFIE implementations, respectively. With $\square\square$ -discretization, the scattered field obtained using the EFIE proved to be superior to that using the MFIE. By following the same line of argument as in Section 6.3, the combination constant for $\square\square$ -discretization is therefore set to $\alpha = 0.99$. In contrast, the accuracy of the scattered fields obtained using the EFIE and MFIE via $\wedge\wedge$ -discretization were found to be commensurate. Accordingly, we set $\alpha = 0.5$ for $\wedge\wedge$ -discretization. For LEGO based on LEP, we restrict ourselves to $\wedge\wedge$ -discretization for both the electric and magnetic equivalent currents. Unless mentioned otherwise, the regular parts of the test and expansion integrals will be determined via adaptive quadrature rules with a relative error of 10^{-2} .

Let us start by comparing the accuracy of the scattered fields via embedding based on SEP and LEP. In Figure 6.16 the normalized error in the scattered fields versus the mesh density is shown for embedding based on LEP and SEP. The results for hexagonal and rhombic shaped elementary scattering domains are shown on the left and on the right, respectively. For coarse mesh densities we obtain cubic convergence with $\wedge\wedge$ -discretization for both SEP and LEP. Like with the EFIE and MFIE in Section 5.5 for the scattering from perfectly conducting objects, the convergence of the scattered field with SEP for $\square\square$ -discretization, $\text{SEP}(\square\square)$, hardly exceeds quadratic convergence for coarse mesh densities. Further, recall that the convergence rates for perfectly conducting scatterers decrease with an increasing non-smoothness of the boundary. This dependence also seems to occur with embedding based on SEP, since the convergence rate with $\wedge\wedge$ -discretization, $\text{SEP}(\wedge\wedge)$, reduces to $\mathcal{O}(N^{-1.7})$ for dense mesh sizes for both the hexagonal and the rhombic shape. To a lesser extent, this effect also occurs with $\text{SEP}(\square\square)$. Similar to the scattering from dielectric objects in Section 5.8, embedding based on LEP eventually yields quadratic convergence.

Propagator matrices are used with LEP, indicated by $\text{LEP}(\mathcal{P})$. The discretization and computational scheme of $\text{LEP}(\mathcal{P})$ is similar to that of $\text{SEP}(\wedge\wedge)$, albeit that $\text{LEP}(\mathcal{P})$ involves both electric

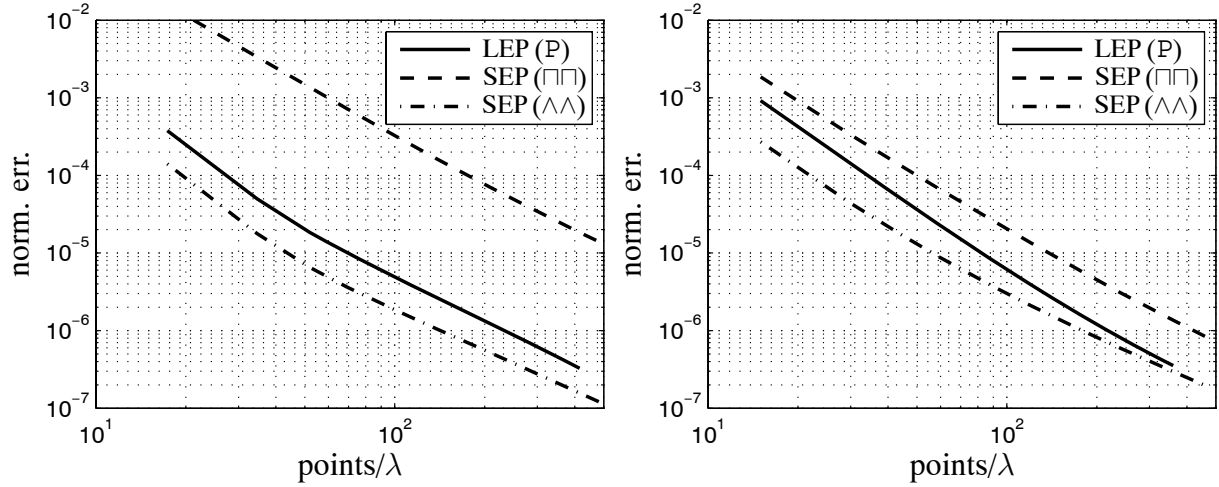


Figure 6.16: The normalized error in the scattered field versus the mesh density for embedding based on LEP and SEP. In case of LEP, propagator matrices are used. The results for hexagonal and rhombic shapes are shown on the left and on the right figure, respectively.

and magnetic equivalent currents. It is not surprising that results of LEP(P) are more accurate than those of SEP($\square\square$), since LEP(P) involves the higher-order $\wedge\wedge$ -discretization. Clearly, for the mesh densities under consideration, embedding based on SEP($\wedge\wedge$) seems superior to LEP(P). Nonetheless, because the convergence of LEP(P) and LEP(G) remains quadratic upon mesh refinement, the accuracy of the scattered field may eventually even exceed that of SEP($\wedge\wedge$) with an estimated $\mathcal{O}(N^{-1.7})$ convergence.

As regards the dependence on the choice of the shape for the elementary scattering domains, the results obtained with the hexagonal and rhombic domain shapes are comparable for LEP(P) and SEP($\wedge\wedge$). The slightly better results for the hexagonal domain shape may be explained from the fact that the line source position, ρ_S , and the observation boundary, \mathcal{C}_o , for a rhombic domain shape are closer to the boundary of the combined scattering operator. In case of a rectangular domain shape, Figure 6.1b, the accuracy of the scattered field obtained with SEP($\square\square$) (not shown) is comparable to that obtained with a rhombic domain shape, which indicates that the significantly larger error for the hexagonal domain shape with SEP($\square\square$) may be attributed to unwanted interior resonances. This matter will be further addressed in Section 6.5.2. Ultimately, we may infer that the accuracy of the scattered field remains largely independent on the choice of the domain boundary in case that boundary is not smooth.

Next, for a more consistent comparison between embedding based on SEP and LEP, we consider LEP with inverse Gram matrices, LEP(G), instead of inverse propagator matrices, LEP(P). In Figure 6.17, the normalized error in the scattered field is shown as a function of the mesh density for LEP(G), with on the left and right-hand side the hexagonal and rhombic domain shape, respectively. For comparison, the results obtained with LEP(P) and SEP($\wedge\wedge$) in Figure 6.16 have been repeated. Clearly, for the mesh densities under consideration, LEP(P) seems superior to LEP(G). However, this observation may be slightly misleading at this point since the current amplitudes are automatically transferred directly with SEP($\wedge\wedge$) and LEP(P), but not with LEP(G). More specifically, the direct transfer of current amplitudes is inherent to the use with inverse propagators, since it follows from the definition of the transfer operator. This is not the case with LEP(G). These properties have been explained in Section 4.5. From a computational point of view, Section 4.6, LEP(G) is preferred over LEP(P) since the computational costs for LEP(G) is at most a factor five times higher than that for SEP($\wedge\wedge$), while for LEP(P) this amounts to a factor eight throughout.

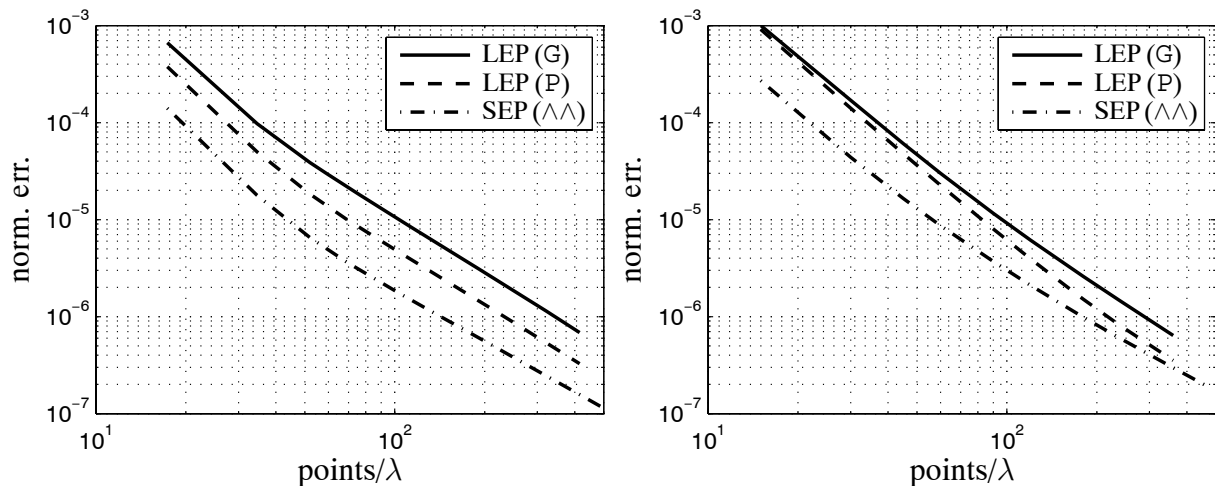


Figure 6.17: The normalized error in the scattered field versus the mesh density for embedding based on LEP through inverse Gram matrices and inverse propagator matrices, LEP(G) and LEP(P), respectively. The results for hexagonal and rhombic shapes are shown on the left and on the right figure, respectively.

In case of embedding based on LEP via inverse Gram matrices, LEP(G), we have a choice regarding the direct transfer of current amplitudes for coinciding source and observation boundary parts in the transfer operators. In Section 4.5, we proposed two methods for the *direct transfer of current amplitudes*. The first method, method I, is based on Huygens principle, i.e., the current part that is not on the shared boundary is transferred. In the second method, method II, the field

part that is not on the shared boundary is reproduced first. Afterwards, the associated current part follows from the definition of the equivalent currents. Both methods yield a considerable reduction in the computational costs, and may also lead to more accurate results. In Figure 6.18, the normalized error in the scattered field versus the mesh density is shown for LEP(G). The implementations with the direct transfer of current amplitudes via method I and II are indicated by LEP(G^I) and LEP(G^{II}), respectively. The results for hexagonal and rhombic shapes are shown on the left and on the right, respectively. For the hexagonal domain shape, the magnitude of the error with both LEP(G^I) and LEP(G^{II}) is smaller than with LEP(G) for coarse mesh densities. However, with further mesh refinement, the order of convergence with both transfer methods becomes linear. The same observation applies to the results for the rhombic scattering domain.

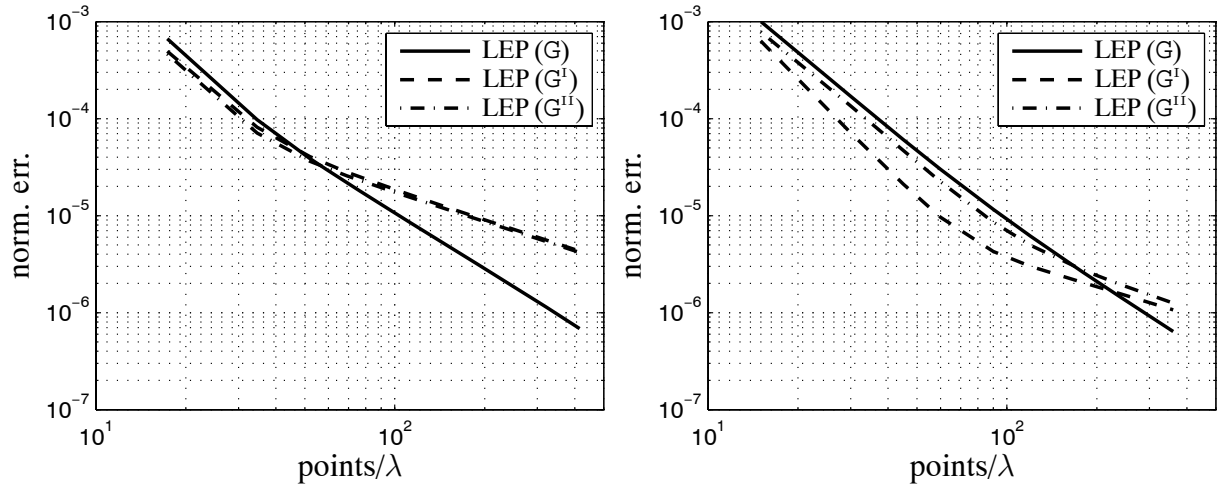


Figure 6.18: The normalized error in the scattered field versus the mesh density for embedding based on LEP with the direct transfer of current amplitudes via method I and II. For the shape of the elementary scattering domains, hexagonal and rhombic ones are employed in the left and right figure, respectively.

To explain the linear convergence observed in Figure 6.18, let us consider the outer boundary of the composite configuration in Figure 6.15a with the hexagonal elementary scattering domains. The reason for the linear convergence is concealed in the definition of the corresponding transfer matrix. For instance, if the outer boundary contour is denoted by $\partial\mathcal{D}_3$, the transfer matrix \mathbb{T}_{33} , with $\partial\mathcal{D}_3$ as both the source and observation boundaries, is defined as $\mathbb{T}_{33} = \mathbb{G}_{33}^{-1}\mathbb{P}_{33}$. Clearly, if instead of the inverse Gram matrix, \mathbb{G}_{33}^{-1} , the inverse propagator matrix, \mathbb{P}_{33}^{-1} , is employed, \mathbb{T}_{33} reduces to an identity matrix, \mathbb{I}_{33} . The direct transfer of current amplitudes in that case explicitly follows from the matrix product. The application of method I merely yields a computational advantage. This applies to embedding based on SEP($\square\square$), SEP($\wedge\wedge$) and LEP(P). With LEP(G),

the transfer matrix T_{33} is not an identity matrix and its use actually requires an additional discretization step. If only a subset of the current amplitudes is transferred directly, these current amplitudes are not affected by the additional discretization step applied to the other ones. This discrepancy gives rise to a reduced convergence.

To test our explanation of the linear convergence numerically, the current amplitude vector, Q_3^{in} , which represents the incident field, is repeatedly multiplied by T_{33} . Each multiplication amounts to an additional discretization step that will lead to a loss of accuracy in the pertaining scattered field. The decrease in accuracy of the scattered field due to subsequent multiplication of T_{33} by Q_3^{in} is shown in Figure 6.19 for several mesh densities. A hexagonal domain shape is employed. In the left figure, none of the current amplitudes are transferred directly if we apply the straightforward multiplication Q_3^{in} by $T_{33} = G_{33}^{-1}P_{33}$. The relative decrease in accuracy due to subsequent multiplications by T_{33} for the mesh densities under consideration is comparable. On the right, the results of transferring the current amplitudes on half of the boundary directly with method I are shown, $\text{LEP}(G^{\text{I}})$. The transition between direct transfer and straightforward propagation has been set at two diametrically opposed junctions with a removed common boundary part (See Figure 6.15). The direct transfer of the current amplitudes on half of the boundary leads to a larger loss of accuracy for denser mesh sizes. Hence, the decrease in accuracy is indeed caused by the imbalance in accuracy created by the indirect transfer of part of current amplitudes.

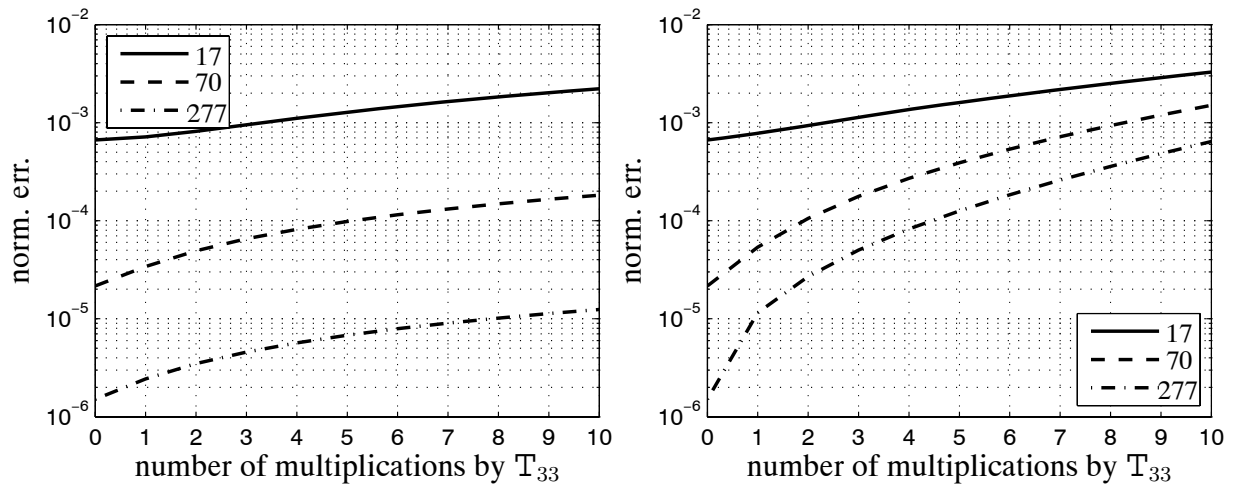


Figure 6.19: The decrease in accuracy due to subsequent multiplication of Q_3^{in} with T_{33} for several mesh densities, points/ λ . A hexagonal domain shape is employed. In the right figure the current amplitudes on half the boundary are directly transferred with method I.

In the LEGO approach, the boundary transition between direct current transfer and straightforward propagation occurs at the junctions with the common boundary parts. Since boundary junctions only occur at corners of the scattering domains, the discontinuities in the local boundary may have an adverse affect on the error from the transition. To investigate this, the transition between direct transfer and propagation of current elements for common boundary parts is shifted away from the junction. As an example, in Figure 6.20 the common boundary part, $\partial\mathcal{D}_1 \cap \partial\mathcal{D}_3$, for the transfer matrix \mathbb{T}_{31} is shown. The black triangles indicate \wedge -expansion functions at the junction elements. The centers of the \wedge -expansion functions to the left of the junction element on the common boundary are numbered increasingly. Expansion function number one is the first one to the left of the junction element, of which the current amplitude can be transferred directly to $\partial\mathcal{D}_3$.

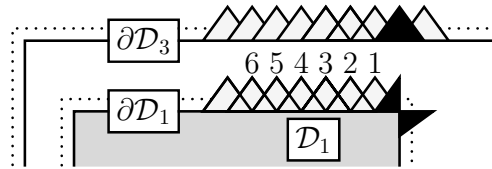


Figure 6.20: The centers of the \wedge -expansion functions to the left of the junction element on the common boundary $\partial\mathcal{D}_1 \cap \partial\mathcal{D}_3$ for the transfer matrix \mathbb{T}_{31} are indicated by increasing numbers away from the junction element.

Next, in Figure 6.21 we have presented the normalized error in the scattered field versus the mesh density for $\text{LEP}(G^{\text{II}})$. The current amplitude associated with the i -th expansion function is the first one that is transferred directly. In this way the transition between direct transfer and propagation of current elements for common boundary parts has been shifted away from the junction. Hexagonal and rhombic shapes are employed for the elementary scattering domains on the left and on the right, respectively. From the figure, we infer that the mesh density at which the convergence becomes linear may be shifted towards denser meshes by simply not employing the direct transfer of the current amplitudes that are near a junction element. Hence, the imbalance in accuracy between directly transferred and propagated current amplitudes is intensified by the singular behavior of the equivalent currents at the corners (and thus the junctions).

By considering the elements of a column vector of the inverse Gram matrix shown in Figure 6.22, it is clear that the inverse of the Gram matrix is also bandlimited. This corroborates that if the first current amplitude, which is transferred directly, is a few elements away from the junction, the influence of the corner elements becomes negligible. Further, when regions of direct transfer and propagation overlap slightly, the effective finite bandwidth of the Gram matrix constitutes a taper

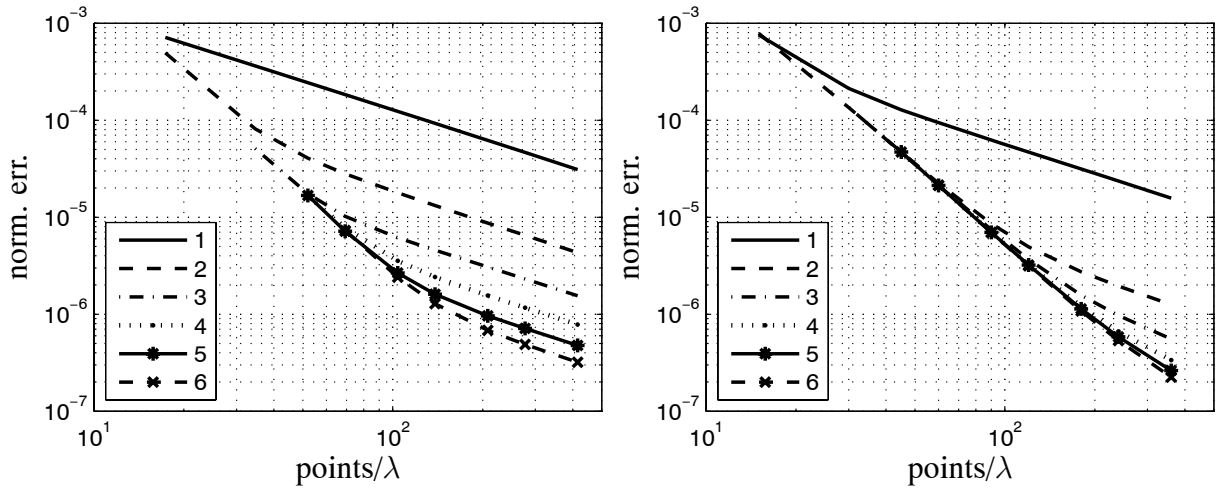


Figure 6.21: The normalized error in the scattered field for embedding based on LEP via Gram matrices. The current amplitudes are transferred directly via method II, LEP(G^{II}), for increasing numbers of expansion elements from the boundary junction. The elementary scattering domains on the left and on the right are hexagonal and rhombic shapes, respectively.

by which the imbalance may be mitigated. Note that in Figure 6.18, the current amplitude of the second expansion function to the left of the junction element is the first one that was transferred directly. The attained order of convergence with LEP(G^I) and LEP(G^{II}) is significantly better than the $O(N^{-1.7})$ convergence for dense mesh densities with SEP($\wedge\wedge$). However, up to 100 points per wavelength, SEP($\wedge\wedge$) remains superior.

$$G_{11}^{-1} = 6 \begin{bmatrix} 4 & 1 & 0 & \dots & 0 & 1 \\ 1 & 4 & 1 & \ddots & & 0 \\ 0 & 1 & \ddots & \ddots & \ddots & \vdots \\ \vdots & \ddots & \ddots & \ddots & 1 & 0 \\ 0 & & \ddots & 1 & 4 & 1 \\ 1 & 0 & \dots & 0 & 1 & 4 \end{bmatrix}^{-1}$$

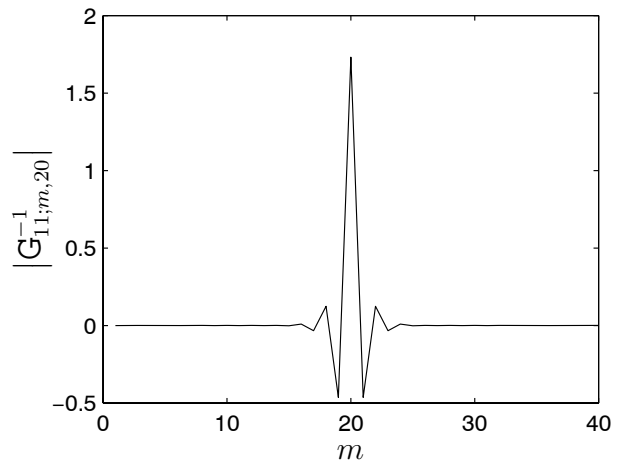


Figure 6.22: On the left, the inverse of the circulant Gram matrix. On the right, the elements of a column vector for forty unknowns.

For the cases considered so far, all test and expansion integrals for the propagator matrix have been determined with adaptive quadrature rules, to a maximum error of one percent in the evaluation of these integrals. Next, let us investigate the loss in accuracy due to more elementary quadrature rules. We aim at obtaining an estimate for the optimum balance between the efficiency of constructing the propagator matrices, versus the obtained accuracy. Accordingly, to assess the worst loss of accuracy, we consider the most simple quadrature, i.e., the midpoint rule, as it involves only a single sampling point per edge. Beware though, that this affects the regular integrand contributions only, i.e., the singular integrand contributions of the various test and expansion integrals are accounted for analytically. Further, the self-contributions (overlapping edges) are still determined accurately.

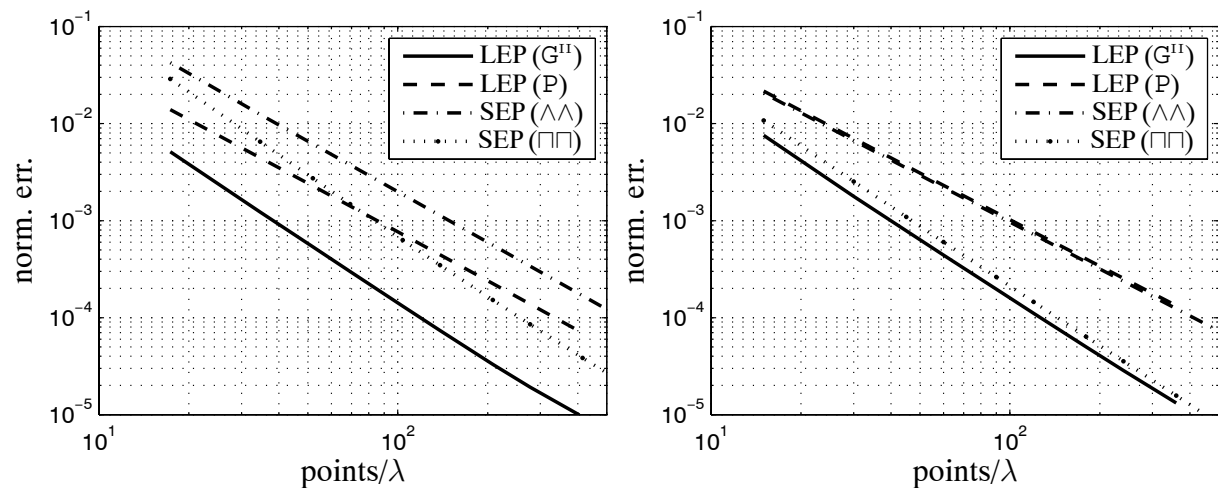


Figure 6.23: The normalized error in the scattered field versus the mesh density for embedding based on LEP and SEP. Instead of adaptive quadrature rules, the midpoint rule is employed to compute the regular part of the test and expansion integrals related to the propagator operators. In case of LEP, Gram matrices are used with the direct transfer of current amplitudes via method II. For the shape of the elementary scattering domains, hexagonal and rhombic ones are employed in the left and right figure, respectively.

In Figure 6.23, the results of the $LEP(G^{II})$, $LEP(P)$, $SEP(\wedge\wedge)$ and $SEP(\square\square)$ are repeated with the midpoint rule. Hexagonal and rhombic shapes are employed for the elementary scattering domains in the left and right figure, respectively. The impact of the quadrature error is the strongest for the implementations involving inverse propagator matrices in combination with $\wedge\wedge$ -discretization, i.e., $LEP(P)$ and $SEP(\wedge\wedge)$. The best accuracy is obtained with $LEP(G^{II})$, which also seems to maintain quadratic convergence for the mesh densities under consideration. This is not surprising since a Gram matrix is determined analytically, whereas the use of a propagator

matrix comes with a quadrature error. Hence, the implementation of LEGO with LEP via Gram matrices is least sensitive to a quadrature error. With reference to the EFIE and MFIE with $\square\square$ -discretization in Section 5.5, we noted that the accuracy of the scattered field determined via the midpoint rule and the adaptive quadrature rule are comparable. However, the magnitude of the error with the midpoint rule applied to $\text{SEP}(\square\square)$ has increased noticeably in comparison with the corresponding adaptive quadrature results in Figure 6.16. The increased error magnitude may be attributed to close source and observation boundaries (connecting domains) in the embedding process.

6.5.2 Interior resonances

In the preceding examples of the LEGO approach based on SEP, it has been assumed that the interior resonance effect associated with the separate EFIE and MFIE is avoided with a CFIE. However, in the construction of the large scattering domains in Section 6.3, we encountered a building sequence that produced strong field deviations for a certain boundary shape. This seemed to indicate an interior resonance, even though a CFIE was applied. For this reason, we will investigate below whether the CFIE can properly suppress interior resonances in LEGO.

As a starting point, the basis configuration presented in Figure 6.15 will be employed here. To ensure that one of the domain boundaries in the sequence of embedding steps is associated with an interior resonance, the frequency of operation is changed such that the outer boundary in case of hexagonal elementary domain shapes gives rise to an EFIE resonance. An estimate for the resonance frequency has been obtained for a particular mesh density with $\square\square$ -discretization by monitoring the condition number of the EFIE MoM-matrix in a frequency sweep. Accordingly, the frequency of operation has been changed to $fa/c = 0.416$. Note that the estimate resonance frequency may depend on the mesh density and the choice of discretization. To ensure that the CFIE has the ability to suppress the EFIE resonance, the combination constant α in the CFIE formulation, Eq. (3.20), is set to $\alpha = 0.5$ for both $\square\square$ and $\wedge\wedge$ discretizations.

To illustrate the impact of an interior resonance on the accuracy of the scattered field, we refer to Figure 6.24. On the right, we have presented the normalized error in the scattered field versus the mesh density for embedding based on $\text{SEP}(\square\square)$, and hexagonal elementary scattering domains. On the left, the results have been presented for a non-resonance case, viz., $fa/c = 0.41$. The poor results obtained with $\text{SEP}(\square\square)$ for resonance conditions clearly indicates that interior resonances are not properly suppressed. Note that the maximum error corresponds to the mesh density

that has been used to determine the resonant conditions. Hence, by a slight variation in the operating frequency, the error peak may shift. Due to the different discretization, SEP($\wedge\wedge$) is not exactly at resonance. In a similar way, the accuracy for SEP($\wedge\wedge$) will deteriorate when the frequency of operation is closer to one of its interior resonances. Nevertheless, up to 100 points per wavelength, the error is at least one order of magnitude larger in comparison with the off-resonance situation, which renders it slightly less accurate than LEP(P) (cf. Figure 6.17). Hence, close to resonance condition, the accuracy of the scattered field decreases significantly. Upon performing the same computations with embedding based on LEP (not shown), the accuracy of the scattered field at resonance proved to be virtually the same as in the non-resonance case.

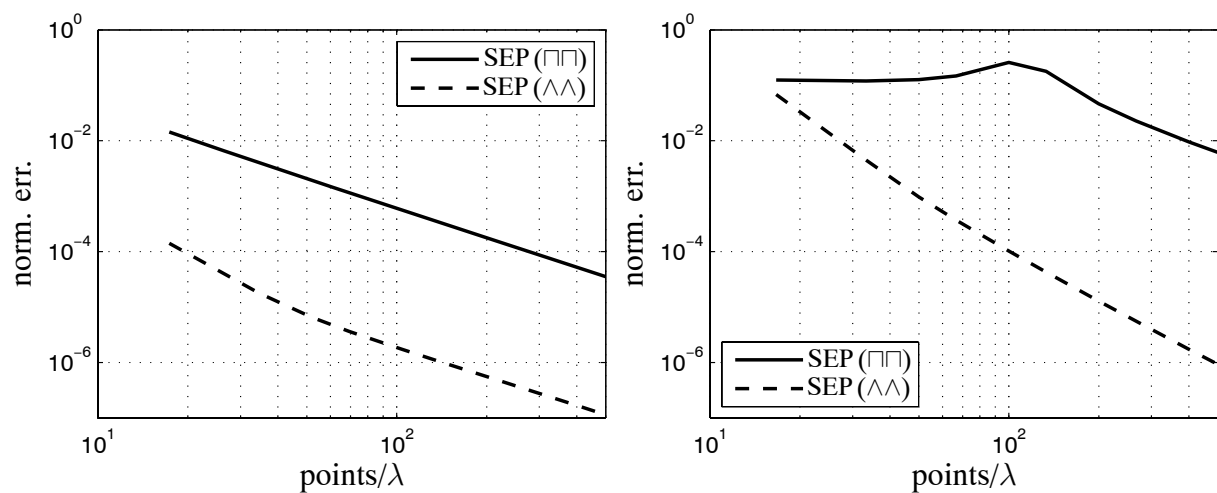


Figure 6.24: The normalized error in the scattered field versus the mesh density with embedding based on SEP. The elementary scattering domains are hexagonal. On the left and right the off-resonance ($fa/c = 0.41$) and resonance ($fa/c = 0.416$) cases, respectively.

To clarify the persistent interior resonance effect associated with the CFIE, let us consider the plots of the pertaining total electric field in Figure 6.25 for the resonance case $fa/c = 0.416$. The fields have been obtained via embedding based on SEP with $\square\square$ -discretization and 100 points per wavelength. The top figure shows the field determined via the rhombic scattering domain shape. In that case, interior resonances occur at different frequencies. For the bottom figure, the computation has been repeated for elementary scattering domains with a hexagonal shape. The outer boundary in the bottom figure is associated with an interior resonance for the EFIE. Apparently, only the exterior field is affected by the interior resonance since the interior field is practically the same as the field shown in the top figure. Observe the significant errors at the corners of the outer contour. In the cases discussed in Figure 6.5 and Figure 6.6, the small errors at the corners of the boundary have probably been caused by interior resonances.

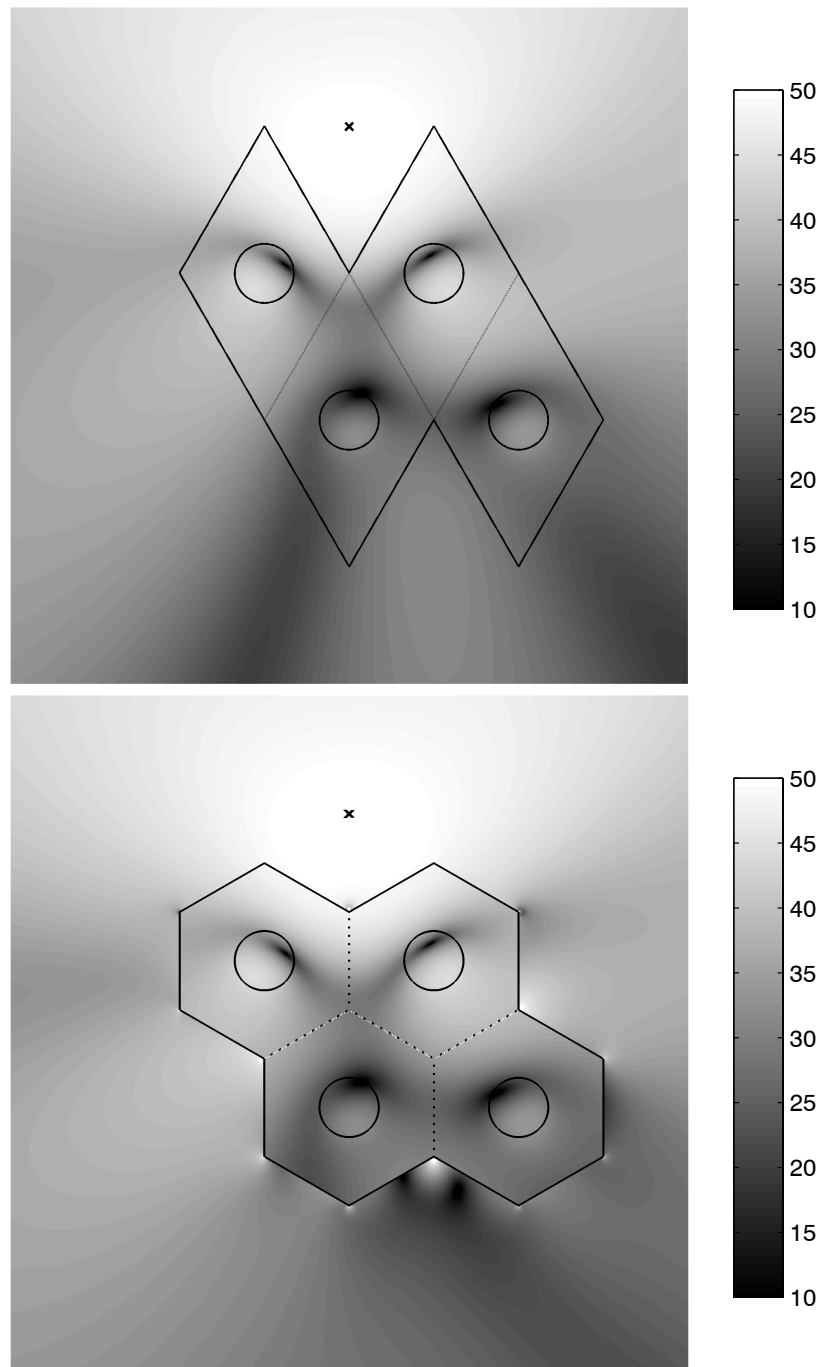


Figure 6.25: The magnitude of the electric field on a logarithmic scale (dB) generated by an electric line source above an EBG (2×2 periods). The dotted lines indicate removed common boundaries and the position of the line source has been marked. In the top and bottom figure, we deployed rhombic and hexagonal scattering domains, respectively, with embedding based on SEP via a CFIE with $\square\square$ -discretization. The outer boundary in the bottom figure allows an interior resonance for the EFIE.

We have observed that the interior field is left intact. Hence, the CFIE used as the inverse propagator that produces the incident current amplitudes on the outer boundary does properly suppress the interior resonances. In other words, an equivalent current that reproduces the interior field generated by an exterior source distribution is free of interior resonances. This corresponds with the usual application of the EFIE, viz., the scattering from a PEC. One of the steps in which the interior resonance problem of the CFIE in the LEGO approach can occur is the final one, in which common boundaries are removed. In the composition of scattering operators in Section 4.5, the removal of common boundaries involves the transfer operators T_{31} and T_{32} . These transfer operators produce equivalent currents that reproduce the exterior field generated by an interior source distribution. In that case, the interior resonance is a physical mode which is not suppressed by a CFIE, as it is a valid part of the solution. Because T_{31} and T_{32} are only used to construct the composite scattering operator, this explains why the interior field is not affected by the interior resonance effect. Clearly, if the combined scattering domain is reused in a following embedding step, also the field inside the previously combined domains will be affected by the interior resonance. Note that interior resonances may also hamper the construction of the elementary scattering domains. If this is not the case, we emphasize that the interior resonance effect can only occur if embedding is applied to scattering domains that have common boundary parts. In the absence of a common boundary, T_{31} and T_{32} are not used according to the corresponding computational scheme in Tab. 4.1.

An interior resonance may for some configurations be cunningly avoided in a sequence of SEP embedding steps by simply changing the building sequence or by modifying the shape of the elementary scattering domains. However, the density of interior resonances increases with the operating frequency and the size of the scattering domain, rendering it increasingly more difficult to avoid interior resonance effects, especially since the effective resonance width associated with the MFIE is broader in frequency than that of the EFIE. For full 3D scattering configuration the chance of operating at or near an interior resonance increases even more.

Finally, we have applied a singular value decomposition (SVD) in an attempt to remove the resonant current parts from the solution. However, this did not solve the problem at hand in the sense that the cavity mode which corresponds with the resonance current may well be part of the physical solution. A different strategy proposed in Section 3.4 may turn out to be a better choice, e.g., via a dual (parallel) boundary or the null-field method. Clearly, the application of LEP is robust and leads to a more rigorous and elegant solution than the application of SEP.

6.5.3 Building sequence and accumulation error

Up to this point, the influence on the scattered field error of the mesh density and the choice of discretization have been investigated. A composite structure may also be constructed in alternative ways by changing the order of the translation vectors used, e.g., by building in the vertical direction first and then in the horizontal direction, or in the opposite order. Below, the analysis is extended by considering the influence of the building sequence. In addition, we investigate the accumulation error due to repeated embedding steps. These properties are considered for various domain shapes. Finally, we will obtain an indication of the dependence of the error on the size of the composite structure under construction.

The building sequence and the accumulation error are investigated by extending the basic configuration illustrated in Figure 6.15 to the one shown in Figure 6.26. We have a triangular array of dielectric circular cylinders in air, with $\varepsilon_r = 11.56$, filling ratio $r/a = 0.175$ and normalized frequency $fa/c = 0.4$. To investigate the accumulation error, the combined domain is constructed by adding only a single subdomain in each embedding step. A total of 15 embedding steps is required in this process. Further, the dependence on the building sequence is investigated by comparing the scattered field obtained with the two different building sequences indicated by the dashed lines. Analogous to Section 6.5.1, we employ an observation boundary contour, \mathcal{C}_o , along which the scattered field has been evaluated in Figure 6.15. Of course, the size of \mathcal{C}_o is adjusted for the larger size of the combined scattering domain in Figure 6.26.

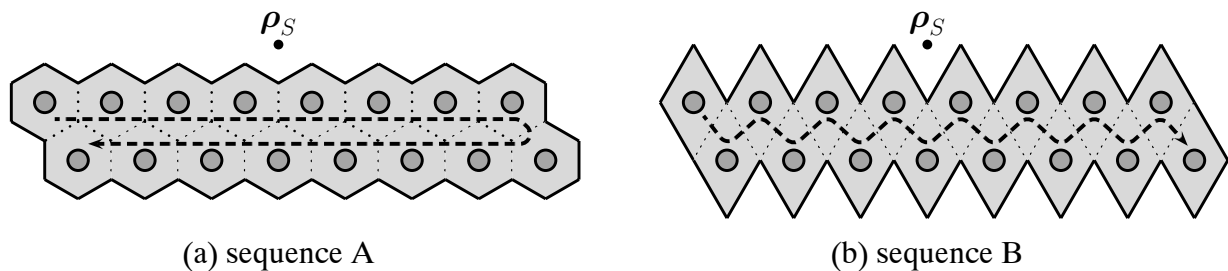


Figure 6.26: The combined scattering domain of an array of circular dielectric cylinders (8×2). Dotted lines represent common boundaries that are removed in consecutive embedding steps. The dashed lines indicate the two building sequences that are considered. An electric line source positioned at ρ_S generates the incident field.

Let us start by investigating the error accumulation and the building sequence for embedding based on LEP via Gram matrices, $\text{LEP}(G)$. Note that there is no direct transfer of current amplitudes associated with $\text{LEP}(G)$. In Figure 6.27 the resulting normalized error in the scattered

field versus the mesh density is presented. The results for hexagonal and rhombic shapes are shown on the left and on the right, respectively. Further, since all subdomains of the composite structure are the same, the combined scattering operator can be constructed in four embedding steps by simply reusing previously combined domains. These results have been included in Figure 6.27 as a comparison with the extensive building sequences A and B (15 steps) to quantify the accumulation error. The different ways of constructing the combined scattering operator has led to a difference in magnitude only, as the order of convergence seems comparable (quadratic). Clearly, there is a severe loss of accuracy for embedding via the building sequences A and B in comparison with the most efficient building sequence (4 steps). Hence, the error accumulation is significant LEP(G). Also the choice of building sequence is important, albeit to a smaller extent than the error accumulation.

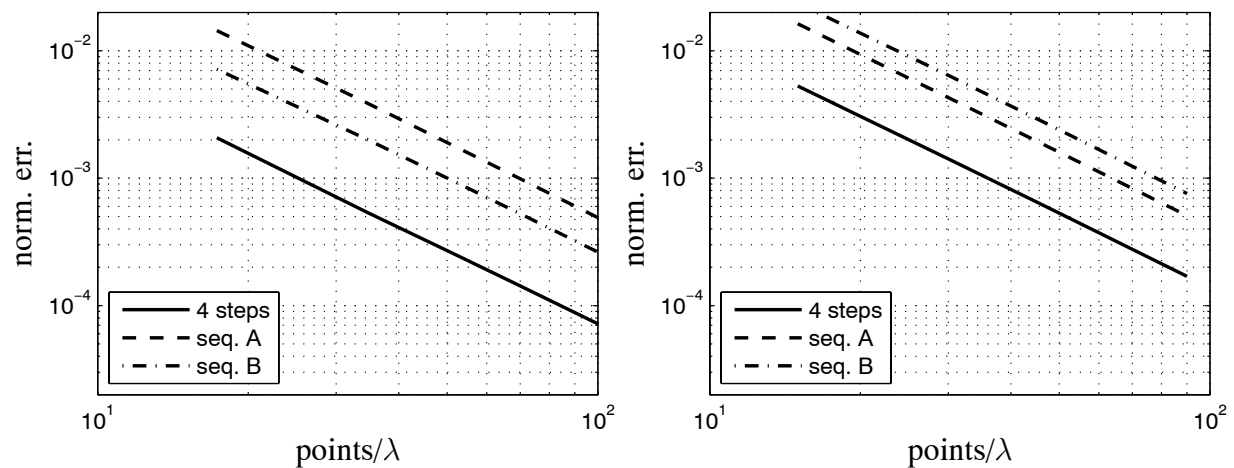


Figure 6.27: The normalized error in the scattered field versus the mesh density for embedding based on LEP via Gram matrices, LEP(G). The extensive building sequences A and B (15 steps) in comparison with the direct one (4 steps). The results for hexagonal and rhombic shapes are shown on the left and on the right figure, respectively.

Since the building sequences A and B amount to 15 embedding steps, currents are repeatedly transferred from one boundary to another. Via the direct transfer of current amplitudes, the loss of accuracy due to the transfer of currents primarily occurs on the source and observation boundary parts that do not coincide. Thus, for the extensive building sequences at hand, this may lead to a considerable improvement. To investigate this, the results obtained with LEP(G) in Figure 6.27 have been recomputed in Figure 6.28, with the direct transfer of current amplitudes via method II, LEP(G^{II}). There is virtually no difference in the accuracy between the building sequences A and B and the 4-step approach, neither for the hexagonal nor for the rhombic boundary shapes.

This indicates that with embedding based on $LEP(G^{II})$, the accumulation error is negligible and the results are largely independent of the building sequence. Hence, the direct transfer of currents is important not only in a long sequence of embedding steps to prevent loss of accuracy due to accumulation, but also for the embedding of large domains. The computational schemes of LEGO for the cases with and without common boundary differ. For the rhombic domain shape, there is a common boundary for the first seven embedding steps via building sequence B, but not for building sequence A. Accordingly, the embedding process is also insensitive to the presence of a common boundary. From the observations so far, we infer that, in the choice of the building sequence and the shape of the elementary domains, one can primarily focus on computational efficiency. Note that with reference to Section 6.5.1 the decrease in the order of convergence for an increasing mesh density is due to the direct transfer of current amplitudes in combination with Gram matrices. If current amplitudes near a junction of a common boundary are not transferred directly, this decrease in convergence rate is avoided.

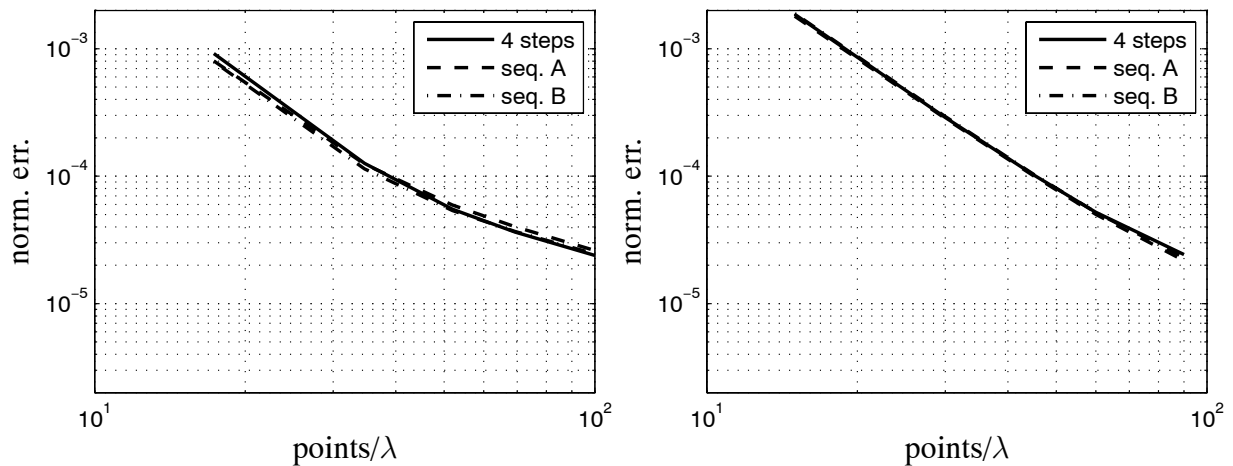


Figure 6.28: The normalized error in the scattered field versus the mesh density for embedding based on LEP via Gram matrices with the direct transfer of current amplitudes via method II, $LEP(G^{II})$. The extensive building sequences A and B (15 steps) in comparison with the direct one (4 steps). The results for hexagonal and rhombic shapes are shown on the left and on the right figure, respectively.

Next, let us consider the accumulation error and dependence on the building sequence for embedding based on $SEP(\wedge\wedge)$. Note that the direct transfer of current amplitudes is inherent to $SEP(\wedge\wedge)$ owing to the use of P^{-1} instead of G^{-1} . The pertaining normalized error in the scattered field versus the mesh density is presented in Figure 6.29. There is virtually no difference in accuracy between the building sequences A and B and the 4-step approach. Hence, also for

embedding based on $\text{SEP}(\wedge\wedge)$, it turns out that the error accumulation is negligible and that the results are largely independent of the building sequence.

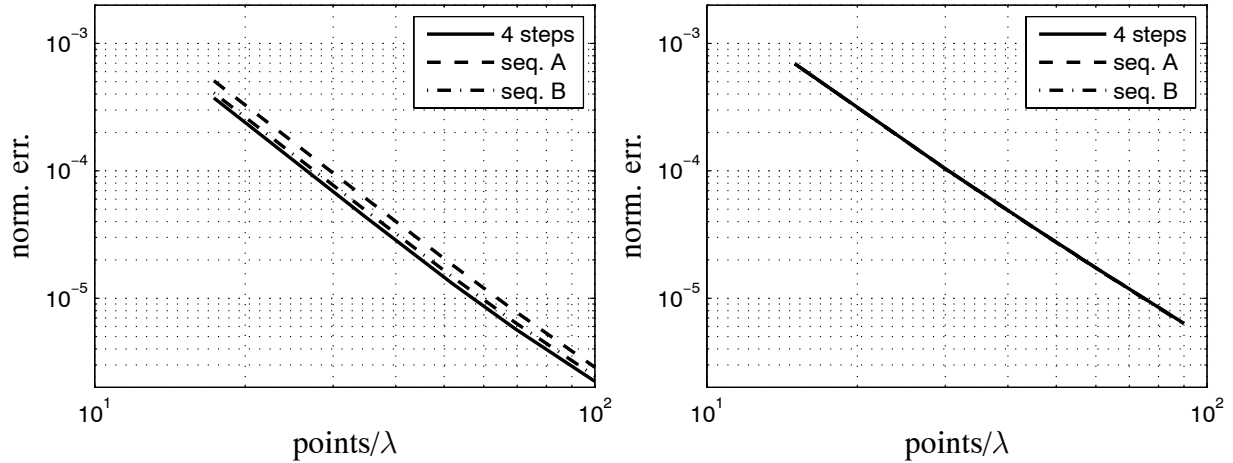


Figure 6.29: The normalized error in the scattered field versus the mesh density for embedding based on SEP with $\wedge\wedge$ -discretization, $\text{SEP}(\wedge\wedge)$. The extensive building sequences A and B (15 steps) in comparison with the direct one (4 steps). The results for hexagonal and rhombic shapes are shown on the left and on the right figure, respectively.

Finally, let us review the results in Figure 6.27 and 6.29 with array size (8×2) , in comparison with those in Section 6.5.1 with array size (2×2) . In case of a dense mesh, the accuracy of the pertaining scattered fields of both mesh sizes is comparable. In contrast, for a course mesh density, a noticeably better accuracy is attained with the smaller array. Hence, the embedding for large composite structures only seems to lead to a reduced accuracy for coarse mesh densities.

6.6 Continuity of objects across adjacent domains

In the results presented so far it was convenient to use circular cylinders as the scattering objects that are enclosed by the elementary building blocks. Below, we demonstrate that the LEGO approach is not restricted to scattering objects that are not canonical. These scattering objects need not even be continuous across the boundary of the elementary scattering domain.

To demonstrate that the boundary, $\partial\mathcal{D}_o$, of a scattering object, \mathcal{D}_o , that is enclosed by a scattering domain may be of arbitrary shape, we consider a cross-shaped dielectric cylinder. The

corresponding elementary scattering domain \mathcal{D}_1 is depicted on the left in Figure 6.30. The relative permittivity of the cross is $\varepsilon_r = 16$. We evaluate the scattered field along an observation contour as illustrated in Figure 6.15. However, instead of a triangular array of circular cylinders, we employ a square array of crosses. The periodicity of the array is a and the arm's length of the dielectric cross is d . The operating frequency is set to $fa/c = 0.4$. To investigate whether the accuracy may be affected by scattering objects that are continuous across domain boundaries, the results for two filling ratios will be compared, viz., $d/a = 0.95$ and $d/a = 1$. In case $d/a = 1$, the four ends of the branches of the cross coincide with the boundary of the enclosing scattering domain. The mesh of the scattering object and the scattering domain are chosen to be uniform, and the respective mesh densities with respect to the background medium are the same throughout. In addition, for $d/a = 1$, both meshes are identical for the mesh segments that constitute $\partial\mathcal{D}_o \cap \partial\mathcal{D}_1$.

In Section 4.2, we have constructed the scattering operator using boundary integral equations. Recall that after the discretization has been performed, we have $S_{11} = T_{1o} X_{oo}^{-1} P_{o1}$ (cf. Eq. (4.30)). Because the scattering object \mathcal{D}_o is dielectric, the PMCHW formulation is chosen for the corresponding MoM-matrix, X_{oo} . We determine X_{oo} in the same way for $d/a = 1$ and $d/a = 0.95$. More specifically, we consider a single cross in a homogeneous background medium for X_{oo} . The propagator matrix, P_{o1} , generates the forcing vector associated with the current amplitudes of the expansion functions on $\partial\mathcal{D}_1$. Also for $d/a = 1$, P_{o1} involves only the background medium properties. For the source and observation boundary parts that coincide, $\partial\mathcal{D}_o \cap \partial\mathcal{D}_1$, the self-contribution case (overlapping edges) is applied. The transfer matrix, T_{1o} , transfers the current amplitudes on $\partial\mathcal{D}_o$, associated with the scattered field from \mathcal{D}_o , to the scattering domain boundary $\partial\mathcal{D}_1$. Again, T_{1o} involves only the background medium. In addition, for the boundary segments, $\partial\mathcal{D}_o \cap \partial\mathcal{D}_1$, the current amplitudes are transferred directly.

As a demonstration of continuity across domain boundaries, we choose LEGO based on LEP with the application of Gram matrices. In addition, current amplitudes on coinciding boundary segments are transferred directly via method II, i.e., we use $LEP(G^{II})$. We emphasize that the LEGO approach has been implemented with locally coinciding boundaries of the cross and enclosing square domains, rather than taking an infinitesimally small gap between both boundaries. On the right in Figure 6.30, the normalized error in the scattered field versus the mesh density is shown for embedding based on $LEP(G^{II})$. The filling ratios are $d/a = 0.95$ and $d/a = 1$. As a reference solution, we have employed a well-converged solution obtained using the PMCHW boundary integral equation for multiple dielectric objects. The accuracy of the scattered fields obtained with both filling ratios is comparable. Hence, there is no loss in accuracy asso-

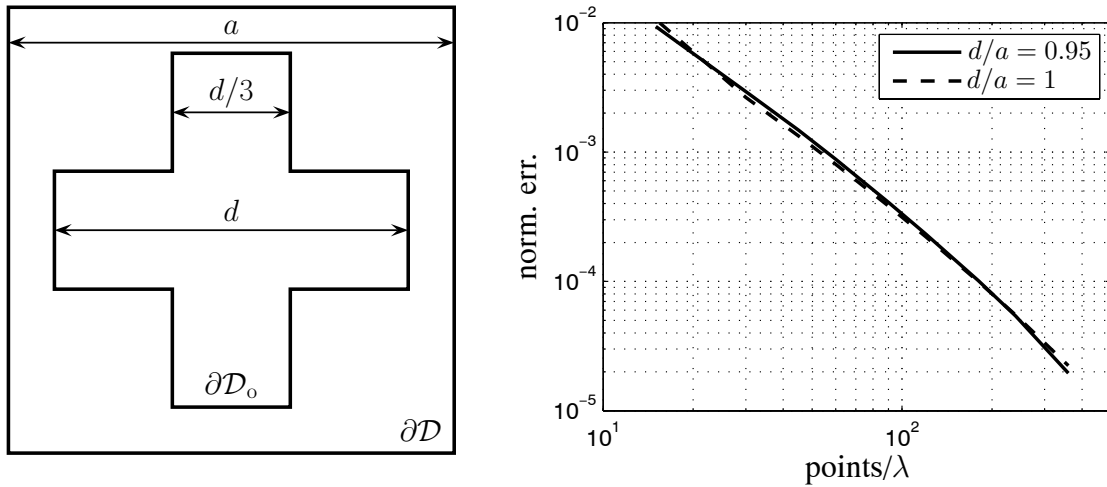


Figure 6.30: On the left the scattering dielectric object with a cross shape boundary, $\partial\mathcal{D}_o$, and size d inside the elementary scattering domain with a square shape boundary $\partial\mathcal{D}$ and size a . On the right, the normalized error in the scattered field versus the mesh density for embedding based on LEP via Gram matrices with the direct transfer of current amplitudes via method II.

ciated with scattering objects that are continuous across adjacent domains. So, with regard to accuracy, there are no restrictions as far as the choice of the embedding domains in scattering configurations is concerned.

As regards the dependence on the scattering object shape, the accuracy attained for the circular-cylinders case in Section 6.5.1 is significantly better than the accuracy attained with for the cross shape in Figure 6.30. On the other hand, the accuracy that is achieved with the direct scattering of a single dielectric cross in Section 5.8 is comparable to the accuracy attained with the embedding of the four crosses. Hence, the accuracy shown on the right in Figure 6.30 is limited by the PMCHW boundary integral equation used to construct the elementary scattering operator. In conclusion, the mesh of the enclosed scattered object should be dense enough to attain sufficient accuracy. The analysis of integral equations in Chapter 5 provides an indication of the required mesh density for various object shapes in combination with the appropriate choice of integral equation. In case the boundaries of the scattering object and the enclosing scattering domain coincide, while aiming for a similar accuracy of the pertaining scattered fields, the application of graded meshes may become expedient.

To investigate whether the continuity of scattering objects across domain boundaries affects the local accuracy near transitions between domain boundaries, let us consider the electric field plot in Figure 6.31. There, the total field is presented for an incident field generated by an electric line

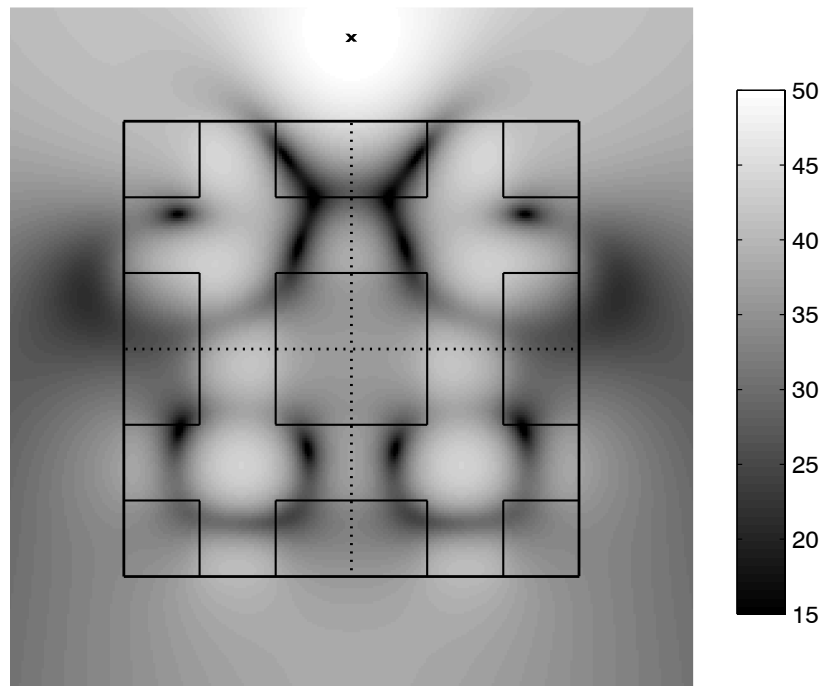


Figure 6.31: The magnitude of the electric field on a logarithmic scale (dB) where the incident field is generated by an electric line source. The position of the line source is marked. The dotted lines indicate common boundary parts that have been removed in the embedding process. The filling ratio is $d/a = 1$. The field response has been determined with embedding based on $LEP(G^{\text{II}})$.

source. The position of the line source has been marked by a cross. The dotted lines indicate the common boundary segments that have been removed in the embedding process. The elementary scattering domain is discretized using 72 unknowns, which amounts to 45 points per wavelength. The plot is scaled in dB to capture possible deviations at different amplitude scales. The field seems free of discontinuities across the various domain boundaries. In addition, there is no visual asymmetry between the left and right-hand side of the field plot although the building sequence has been asymmetric. These observations corroborate our claim that objects that are continuous across domain boundaries can be handled within the LEGO approach without significant loss of error.

6.7 Band-gap diagrams

In the preceding sections, the LEGO approach has been applied to composite structures consisting of identical building blocks in regular, but finite grids. Further, the accuracy of the pertaining scattered fields has been investigated. Electromagnetic band-gap structures are periodic structures that impede wave propagation in any direction in some frequency band. The band structure associated with EBG materials can be computed via the LEGO approach. In this way, we can predict the basic material properties of a large finite EBG structure via a single elementary LEGO block *a priori*. This band structure is determined via the scattering operator in combination with Bloch conditions. A possibly composite scattering domain serves as the periodic unit cell for which the band structure is computed. Since LEGO is a hybrid method, Section 4.9, the medium interior to the scattering domain may be inhomogeneous. In addition, since the scattering operator is a frequency-domain quantity, dispersive media may be considered as well. Below, we present two alternative methods for solving the eigenvalue problem that is associated with the band structure. The theory is explained in terms of the operators introduced in the LEGO approach, Chapter 4. Afterwards, the method is validated through a comparison with the plane-wave method for examples involving two-dimensional arrays. Further, we will demonstrate the diversity of applications by considering unit cells that contain scattering objects which extend across the boundary of the unit cell. Below we mostly follow our description in [86].

Electromagnetic fields in EBG materials are usually studied by determining the Bloch modes of the periodic structure. The associated eigenvalue problem may result in a band structure. Several algorithms have been proposed to compute the band structure of EBGs, such as the transfer matrix method [87], the plane-wave expansion method [88], and the order- N method [89]. Typically, these methods start from Maxwell's differential equations and involve a discretization procedure similar to finite-difference or finite-element techniques. In that respect, the plane-wave expansion method is somewhat different, since the discretization process involves plane-wave projections instead of a (local) polynomial projection. In all of these cases, the entire volume of a unit cell is discretized, which amounts to a relatively large number of unknowns, especially in the 3D case. In addition, the convergence of the plane-wave method decreases for large contrasts between the background medium and the inclusions or scatterers [90]. Although this drawback was avoided with the introduction of a hybrid method [91, 92], the method still requires a discretization of the entire volume of the unit cell.

In case the materials in the periodic structure are homogeneous, the electromagnetic field can be expressed entirely in terms of the fields at the material interfaces via an integral representation. Therefore, a boundary-integral equation seems a logical choice for the reduction of the computational complexity. However, the pertaining periodic Green's function depends both on the Bloch vector in the Brillouin zone and on the radial frequency, which makes the procedure of finding the Bloch modes rather complicated. In addition, the computation of the periodic Green's function itself is almost impossible.

A way out is to employ the scattering operator used for the LEGO approach in Section 4.2. The boundary of the scattering domain, which may be of arbitrary shape, can be identified with the boundary of a unit cell. Via the scattering operator, the electromagnetic field may be expressed in terms of an integral representation that is valid for *any* fundamental solution to Maxwell's equations for the enclosed interior domain. This has been described in Section 4.9. The scattering operator is independent of the Bloch vector. Consequently, we still have to enforce the boundary conditions for the exterior domain. Due to the periodicity, the qualifications interior and exterior have become meaningless. Instead, we formulate the boundary condition on the boundary of this unit cell in terms of Bloch conditions. By itself, this observation is not new as it has been used within the context of absorbers for a three-dimensional setup with two-dimensional periodicity [93]. Here, we extend that observation to the case where all boundaries are periodic and where the Bloch vector is not fixed *a priori*.

Let us start by explaining how the scattering operator used in the LEGO approach can be employed for the computation of the band structure of 2D EBG structures. The Bloch conditions will be enforced at the boundary of the scattering domain. For most EBG structures, it is natural to choose the elementary domain to coincide with a unit cell of the lattice. For simplicity, we restrict ourselves to square unit-cell shapes. The analysis is based on the operator formalism introduced in Chapter 4. If a scattering domain \mathcal{D}_1 is associated with the periodic unit cell, the total electric and magnetic field at the boundary $\partial\mathcal{D}_1$ are represented by $\mathbf{F}_1^{\text{per}}$, where the superscript indicates the periodicity of the field. Further, we consider embedding based on LEP via Gram matrices. Thus, the corresponding equivalent current representation $\mathbf{Q}_1^{\text{per}}$ at $\partial\mathcal{D}_1$ amounts to both electric and magnetic currents. Recall that, after discretization, the elements of the vectors $\mathbf{F}_1^{\text{per}}$ and $\mathbf{Q}_1^{\text{per}}$ are the field amplitudes obtained from testing $\mathbf{F}_1^{\text{per}}$ and the current amplitudes in the expansion of $\mathbf{Q}_1^{\text{per}}$, respectively. As has been described in Section 4.4, the equivalent currents are defined in terms of the field components tangential to the boundary $\partial\mathcal{D}_1$, and the current amplitudes follow from the field amplitudes via the inverse Gram matrix. Accordingly, we have

$$\mathbf{Q}_1^{\text{per}} = \mathbf{G}_{11}^{-1} \mathbf{F}_1^{\text{per}}. \quad (6.1)$$

The current Q_1^{per} can be decomposed according to

$$Q_1^{\text{per}} = Q_1^{\text{in}} + Q_1^{\text{sc}}. \quad (6.2)$$

The equivalent states associated with the currents Q_1^{in} and Q_1^{sc} are different. Both states are depicted in Figure 6.32. On the left, Q_1^{in} produces the field constituent F_1^{in} , incident on \mathcal{D}_1 . Similarly, on the right, Q_1^{sc} produces the field constituent F_1^{sc} , scattered by \mathcal{D}_1 . The superposition of both states gives rise to the field that is produced by Q_1^{per} . The currents Q_1^{in} and Q_1^{sc} are related through the scattering matrix via $Q_1^{\text{sc}} = S_{11}Q_1^{\text{in}}$. Since we apply LEP, Q_1^{in} and Q_1^{sc} yield a zero field in $\bar{\mathcal{D}}$ and \mathcal{D} , respectively. This is a consequence of Oseen's extinction theorem and an important element of the method described here.

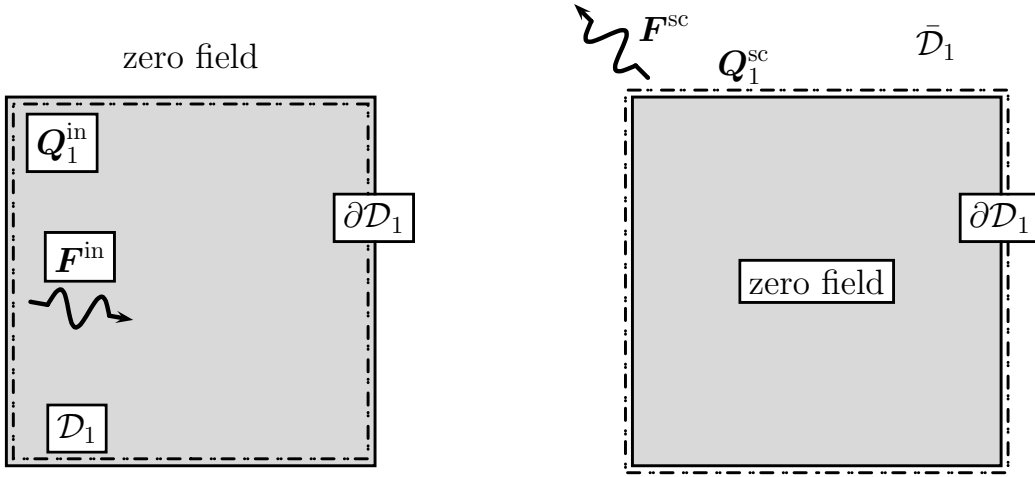


Figure 6.32: The partitioning of the field configuration into two equivalent states via Love's equivalence principle (LEP). Equivalent currents on $\partial\mathcal{D}_1$ reproduce the interior and exterior field in the left and right figure, respectively.

Let us consider Figure 6.33. On the left, Q_1^{sc} is obtained via the scattering matrix S_{11} from the incident field that Q_1^{per} produces in \mathcal{D}_1 . On the right, Q_1^{sc} is obtained via the transfer matrix T_{11} from the scattered field that Q_1^{per} produces in $\bar{\mathcal{D}}_1$. In short, Figure 6.33 describes the relations

$$Q_1^{\text{sc}} = S_{11}Q_1^{\text{per}}, \quad (6.3a)$$

$$Q_1^{\text{sc}} = T_{11}Q_1^{\text{per}}. \quad (6.3b)$$

Note that these relations used here are based on the fact that the equivalent currents Q_1^{sc} and Q_1^{in} produce a zero field in \mathcal{D}_1 and $\bar{\mathcal{D}}$, respectively. This is a unique feature of LEP.

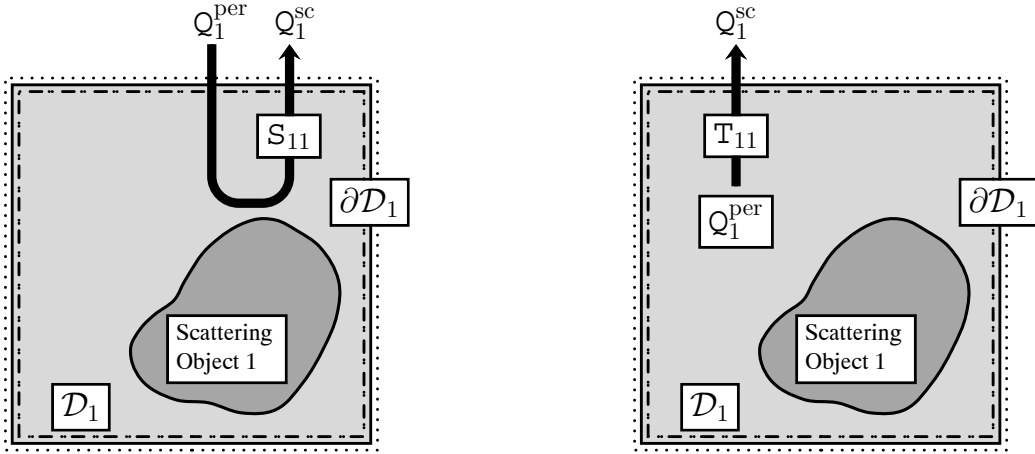


Figure 6.33: On the left-hand side, Q_1^{sc} is obtained via the scattering matrix S_{11} from the incident field that Q_1^{per} produces in \mathcal{D}_1 . On the right hand-side, Q_1^{sc} is obtained via the transfer matrix T_{11} from the scattered field that Q_1^{per} produces in $\bar{\mathcal{D}}_1$.

Subsequently, by subtracting Eq. (6.3b) from Eq. (6.3a), we enforce consistency, which results in

$$[S_{11} - T_{11}] Q_1^{\text{per}} = 0. \quad (6.4)$$

Based on the definition of the transfer and scattering matrices in terms of Gram matrices, multiplication on the left by the Gram matrix G_{11} , leads to

$$[F_{11}^{\text{sc}} - P_{11}] Q_1^{\text{per}} = 0. \quad (6.5)$$

Here, the propagator matrix, P_{11} , is associated with an exterior field representation. Recall that the matrix F_{11}^{sc} describes the scattered field response of the objects in \mathcal{D}_1 in terms of field and current amplitudes for the respective test and expansion functions on $\partial\mathcal{D}_1$. The matrix F_{11}^{sc} can be determined via boundary integral equations and propagator matrices, as in Eq. (4.12), or via other electromagnetic solvers, as described in Section 4.9. The operator form of the matrix equation (6.5) has an infinite-dimensional null space, since all electromagnetic fields that are generated by sources outside \mathcal{D}_1 belong to this null space. However, in the case of a periodic structure, we seek particular elements of the null space, i.e., those that satisfy the Bloch condition on \mathcal{D}_1 . To formulate this condition, we partition the boundary into two sets of partial boundaries.

If the dimension of the periodicity is $N = 1, 2, 3$, then there are N unit vectors \mathbf{u}_i and N corresponding periods p_i , such that $\sum_{i=1}^N m_i p_i \mathbf{u}_i$, $m_i \in \mathbb{Z}$ forms the Bravais lattice with respect to the unit cell \mathcal{D}_1 . This is shown in the inset of Figure 6.34 for a square array. For the elementary domain \mathcal{D}_1 , the first set of the partition of boundaries is denoted by $V_1 = \{\partial\mathcal{D}_{1;1}, \dots, \partial\mathcal{D}_{1;N}\}$ and

the second set is $V_2 = \{\partial\mathcal{D}_{1;N+1}, \dots, \partial\mathcal{D}_{1;2N}\}$. To arrive at a suitable partition of the boundary $\partial\mathcal{D}_1$, we enforce the condition

$$\forall \mathbf{r} \in \partial\mathcal{D}_{1;i}, \quad \mathbf{r} + p_i \mathbf{u}_i \in \partial\mathcal{D}_{1;N+i}, \quad (6.6)$$

for all $i \in \{1, \dots, N\}$. The Bloch condition is then formulated as

$$\forall \mathbf{r} \in \partial\mathcal{D}_{1;i}, \quad \mathbf{F}(\mathbf{r}) = \mathbf{F}(\mathbf{r} + p_i \mathbf{u}_i) \exp(-j\mathbf{k} \cdot p_i \mathbf{u}_i), \quad (6.7)$$

for all $i \in \{1, \dots, N\}$, where \mathbf{k} denotes the Bloch vector in the unit cell of the reciprocal lattice. Note that the Bloch condition amounts to multiplication by a *constant* along the entire boundary $\partial\mathcal{D}_{N+i}$, irrespective of its particular shape. Therefore, curved boundaries due to discontinuities in material properties are readily included. To deal with possible ambiguities on the corners and/or edges of the partitioning, the set V_1 contains only those corners and edges, which connect at least two partial boundaries that are in V_1 . The Bloch condition on all other edges and corners, set V_2 , can then be uniquely related to the corners and edges that belong to V_1 .

To arrive at a numerical scheme, we discretize the Bloch condition in Eq. (6.7) at the boundary of the scattering domain, which results in

$$\mathbf{F}_1^{\text{per}} = \mathbf{B}_{1\bar{1}} \mathbf{F}_1^{\text{per}}. \quad (6.8)$$

The diacritical check on the boundary subscript indicates that the field amplitude vector $\mathbf{F}_1^{\text{per}}$ contains only *independent* field amplitudes. Field amplitudes are considered independent if the support of the pertaining test function is entirely on the boundary parts contained in set V_1 . Further, the matrix $\mathbf{B}_{1\bar{1}}$ enforces the Bloch condition and is a sparse connection matrix that contains the exponential functions (phases) of Eq. (6.7), similar to the one in [93]. More specifically, $\mathbf{B}_{1\bar{1}}$ generates all field amplitudes on $\partial\mathcal{D}_1$ from the independent ones. Since Eq. (6.8) applies to field amplitudes of test functions, the Bloch conditions are enforced point-wise. Apart from 2D corner or 3D edge elements, this approach is exact. To avoid loss of accuracy due to the corner/edge elements, we decrease the size of the support of the corner/edge elements such that their contribution becomes negligible. By substituting Eqs. (6.1) and (6.8) in Eq. (6.5), we obtain

$$[\mathbf{F}_{11}^{\text{sc}} - \mathbf{P}_{11}] \mathbf{G}_{11}^{-1} \mathbf{B}_{1\bar{1}} \mathbf{F}_1^{\text{per}} = 0, \quad (6.9)$$

which enforces both the extinction theorem and the Bloch condition. To obtain the band structure, we have to establish the relation between frequencies and Bloch vectors. By inspection of Eq. (6.9), it may seem more efficient to utilize the periodicity of the current $\mathbf{Q}_1^{\text{per}}$ rather than the field $\mathbf{F}_1^{\text{per}}$. One might think that for $\mathbf{Q}_1^{\text{per}}$, the formulation, $[\mathbf{F}_{11}^{\text{sc}} - \mathbf{P}_{11}] \mathbf{B}_{1\bar{1}} \mathbf{Q}_1^{\text{per}} = 0$, would be

correct. However, this is not the case. With the absence of the inverse Gram matrix, the zero field conditions inherent in LEP in Figure 6.32 are not enforced, which implies that Eq. (6.3) ceases to hold.

Let us comment on the numerical scheme by which Eq. (6.9) may be solved for either various frequencies or for various Bloch vectors. The matrix $[\mathbf{F}_{11}^{\text{sc}} - \mathbf{P}_{11}] \mathbf{G}_{11}^{-1}$ is dense, whereas the Bloch matrix, $\mathbf{B}_{1\bar{1}}$ is sparse. Further, the fundamental solutions, and therefore also the dense matrix, will depend on the radial frequency. Hence, the band structure is most conveniently and efficiently computed by finding Bloch vectors for a fixed radial frequency, i.e., for each fixed frequency we look for tangential electromagnetic fields and Bloch vectors for which both the integral equations on the boundary $\partial\mathcal{D}_1$ and the Bloch conditions are satisfied. The additional advantage is that we can readily refine the boundary mesh for higher frequencies to maintain a fixed level of accuracy. A disadvantage is that it is more difficult to construct the traditional band structure, since it is not *a priori* clear to which particular curve the solution belongs. Also, tracing (almost) horizontal curves is more difficult.

Depending on the size of the scattering and Bloch matrices, it may be worth considering different formulations for solving the problem. If the matrices are small, then it seems most logical to enforce the extinction theorem first, i.e., to determine the null space of the integral-equation matrix, and then to find elements in the null space that satisfy the Bloch condition. The advantage of this approach is that the null space is independent of the Bloch condition and therefore the entire Brillouin zone can be searched efficiently after the null space has been determined. On the other hand, if the matrices are large, the determination of the null space can be prohibitively expensive in terms of computation time and memory. In that case it is more practical to enforce the Bloch condition within the integral equation. The advantage of this approach is that the Bloch condition reduces the number of unknowns by a factor of two. On the other hand, a non-linear search procedure is required to find Bloch vectors for which a singular value or eigenvalue zero is obtained. The repeated computation to find the smallest singular values or eigenvalues for a large and dense linear system is in that case the most expensive part. In the following examples, the second algorithm will be employed. In that case, we have an overdetermined system that may be satisfied for certain Bloch vectors at a fixed frequency. A robust way of solving an overdetermined system $\mathbf{A}\mathbf{x} = 0$, with systems matrix \mathbf{A} and unknown vector \mathbf{x} , is to evaluate the minimum eigenvalue λ of $\mathbf{A}^H \mathbf{A} \mathbf{x} = \lambda \mathbf{x}$ and to impose the condition that $\lambda = 0$. This amounts to the minimization problem

$$\lambda = \min_{\mathbf{x}} \frac{\mathbf{x}^H \mathbf{A}^H \mathbf{A} \mathbf{x}}{\mathbf{x}^H \mathbf{x}}, \quad (6.10)$$

and imposing that that minimum vanishes.

As a validation of the concept, we have computed the band structures for a two-dimensional square array of circular dielectric cylinders with $\varepsilon_r = 8.9$ and filling ratio $r/a = 0.2$, where a denotes the period of the array and r the radius of the cylinder. The EBG setups and the paths in the Brillouin zone are identical to the one in [94, p. 56, Figure 2]. The currents are expanded with 96 unknowns equally distributed over the four edges of the square boundary. Further, the fundamental solutions for a circular cylinder embedded in free space were computed analytically in Appendix B.1. The resulting band structures are shown in Figure 6.34. For comparison, the results obtained by a plane-wave method have been included. In the expansion, 127×127 plane waves have been used. The results are found to be in good agreement.

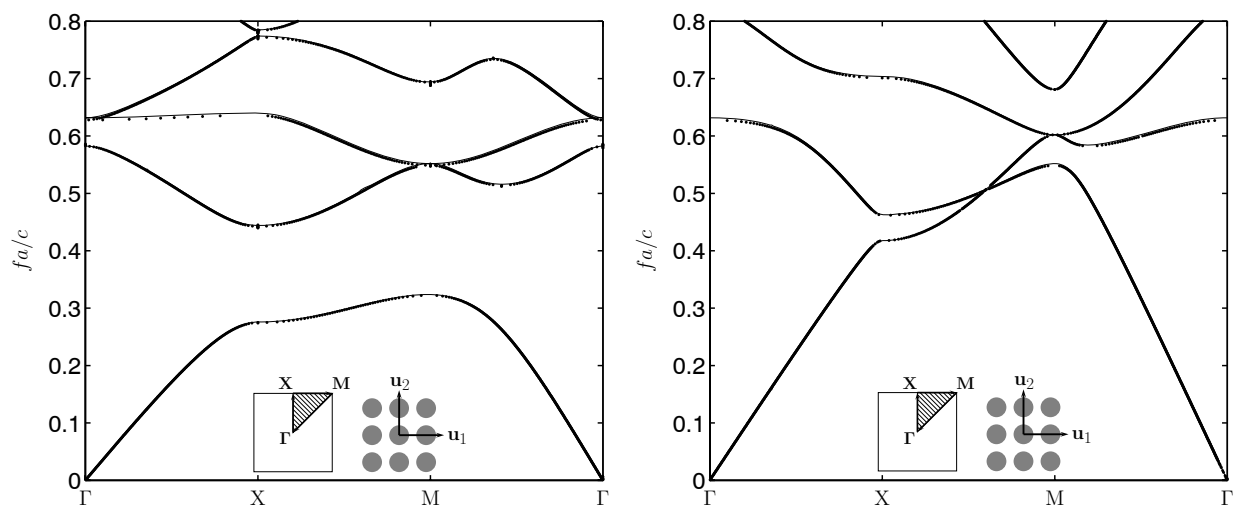


Figure 6.34: The band structures for a square array of circular dielectric cylinders with filling ratio $r/a = 0.2$ and $\varepsilon_r = 8.9$ embedded in air. On the left and right the respective TM and TE bands are shown. The solid lines are the results obtained with the plane-wave method (127×127), and the dots are the results obtained with the LEGO approach.

In Section 6.6, we have demonstrated that the scattering objects enclosed by the scattering domain may be continuous across domain boundaries. As a result, there are no restrictions on the choice of domain shape as regards the distribution of matter. Consequently, we consider the continuity of objects across domains in the computation of band structures. As an example, we have computed the band structure of a square array of dielectric veins in air with $\varepsilon_r = 8.9$. The filling ratio is $d/a = 0.16$ where d is the width of the veins. The configuration is illustrated in the inset of Figure 6.35. The usual approach to determine the band structure is to consider square holes inside a dielectricum [95]. In that case the medium properties along the boundary of the

unit cell are constant. In contrast, here a unit cell is selected such that the dielectric veins cross the boundary of the cell, similar to the scattering domain shown in Figure 6.30. The fundamental solution for the scattering of the cross-shaped dielectric object in the unit cell has been computed with the PMCHW approach, as explained in Section 6.6.

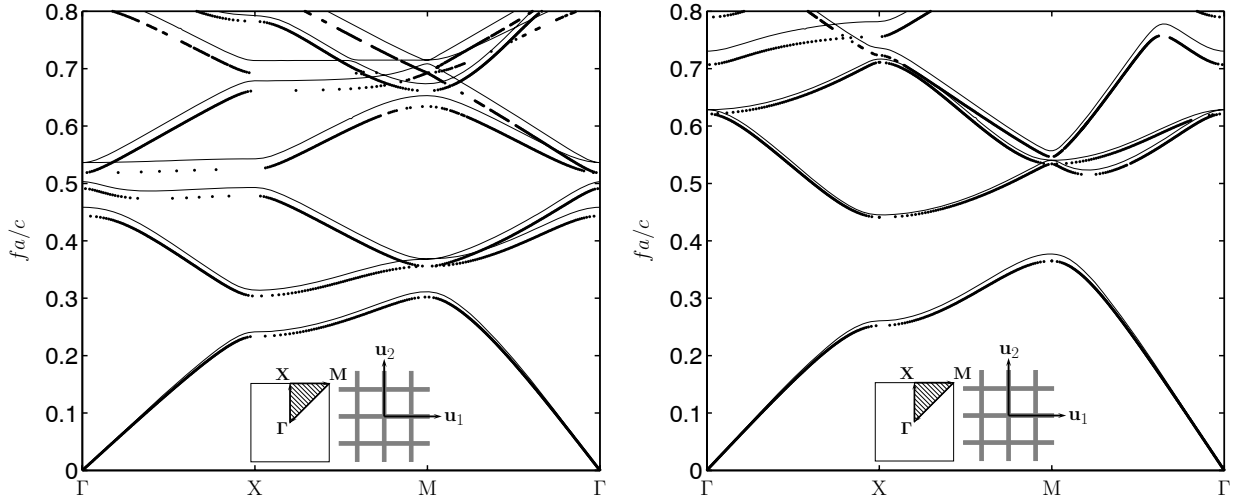


Figure 6.35: The band structure for a square array of dielectric veins embedded in air with $\varepsilon_r = 8.9$ and filling ratio $d/a = 0.16$ where d is the width of the veins. On the left and right-hand side the TM and TE bands, respectively. The solid lines are the results obtained with the plane-wave method (31×31), and the dots are the results obtained with the LEGO approach.

The resulting band structure is presented in Figure 6.35. For comparison, the results obtained by a plane-wave method are included. In the expansion, 31×31 plane waves have been used. The results of the plane-wave method are generally higher in frequency than those of the LEGO approach. Because the minimization in a plane-wave method applies to a space that is spanned by a truncated plane-wave expansion, the minimum and thus the frequency will be higher than the exact one. Clearly, this effect becomes stronger for higher frequencies. Upon increasing the number of plane waves, the results converge towards the ones obtained with the LEGO approach (cf. Figure 6.34). Further, observe that some gaps occur in the diagram with the LEGO approach for large values of fa/c . To avoid this, further fine-tuning is required regarding the parameters associated with the minimization algorithm that ensues from Eq. 6.10, as these turned out to dependent on the mesh density.

Finally, let us demonstrate the application to periodic structures involving perfectly conducting materials. A square array of circular PEC cylinders is considered with filling ratio $r/a = 0.187$ embedded in air, where a denotes the period of the array and r the radius of the cylinder. The

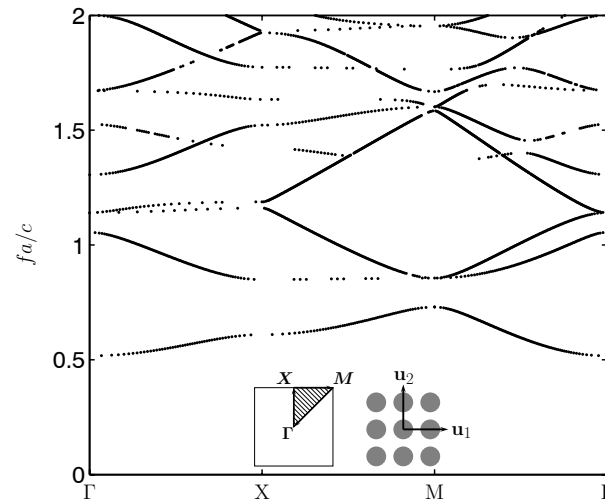


Figure 6.36: The TM band structure for a square array of PEC cylinders with filling ratio $r/a = 0.187$ embedded in air computed with the LEGO approach.

fundamental solutions for a cylinder embedded in free space were computed analytically. The band structures for the PEC cylinders is shown in Figure 6.36. The results are found to be in good agreement with the results from the literature [96].

Chapter 7

3D scattering objects

In this chapter, the integral equations for the scattering from three-dimensional (3D) objects are investigated and the application of LEGO to full 3D scattering problems is demonstrated. In Section 4.4, the fundamental propagator operator of the LEGO approach has been discretized. This was based on the discretized integral operators discussed in detail below. The insight that is gained through the investigation of the integral equations for perfectly conducting and dielectric object has been used in the LEGO approach to attain maximum performance, through an optimal choice of the equivalence principle, the domain shape, the mesh density, the quadrature rule and the test and expansion functions. Furthermore, the integral equations can also be employed to construct the elementary scattering operators in the LEGO approach.

7.1 Introduction

From the mapping properties of the integral operators, the restrictions on the the choice of test and expansion function are determined in Section 7.2. A mesh is generated via a triangulation of the surface of a scattering object. Throughout, Rao-Wilton-Glisson (RWG) functions are used to expand the equivalent currents. The Galerkin approach is employed, albeit that also rotated RWG-functions are considered. To minimize the computational costs of the construction of the MoM matrices, and thus the efficiency of the filling process, we aim at maximum efficiency in the computation of the matrix elements by avoiding redundant integrals and using quadrature rules that are symmetric with respect to the three vertices of a triangle. In addition, the test and ex-

pansion integrals are determined in closed form in those cases where the far-field approximation may be applied. The parts of the test and/or expansion integrals that become singular when the source and observation point coincide are integrated analytically. There are several approaches available in literature for the evaluation of integrals involving RWG-functions. In Section 7.3, we discuss those methods that provide the most efficient and complete expressions.

In Section 7.4, we investigate the influence of the object shape and the mesh density and quality on the solvability of the MoM-matrix equation and the order of convergence of the accuracy of the resulting scattered fields for both the EFIE and MFIE formulations. In particular, we consider plane-wave incidence and point-source excitation. Further, we discuss domain scaling for a sphere and inspect the combination constant α in the CFIE formulation. We investigate the solvability and the order of convergence of the numerical approximation of the PMCHW and Müller formulations for dielectric scattering objects in Section 7.5. The dependence on both the mesh density and the refractive index is examined. For Müller's integral formulation, we consider the use of a specific combination of RWG and rotated RWG functions. Finally, as a proof of principle, LEGO is demonstrated for a full 3D scattering configuration in Section 7.6.

7.2 Discretization

Let us return to the solvability of 3D integral equations based on the operator L by completing the evaluation of its mapping properties discussed in Section 3.7. Similar to the original two-dimensional TE case, the construction of a bounded coercive operator hinges on an appropriate splitting of the function space. This has to do with the null space of the surface divergence operator, which consists of surface curls. The Helmholtz decomposition is a useful tool to split the function space of the surface current density into a subspace that is divergence free and a subspace that is orthogonal to the divergence-free part. Upon considering the part of the operator associated with the scalar potential, a static Green's function can be extracted that acts as the coercive part for the non-divergence-free part of the function space. Likewise, for the vector potential of the operator, a static Green's function can be extracted that acts as the coercive part for the divergence-free part of the function space. The remaining part of the operator is compact. See also [97], for smooth open surfaces. For surfaces that are not smooth, investigations are ongoing [98].

Next, we consider the restrictions on the choice of the test and expansion functions. To a certain extent, there is freedom in the choice for the solution spaces of the electric and magnetic current densities. This freedom originates from the fact that the integral operators can operate on a wide range of functional spaces. Therefore, it is important to make a suitable choice for the solution space of the pertaining current densities. For the results to be physically meaningful, the solutions should correspond to electromagnetic fields with locally finite energy, i.e., the electromagnetic fields should belong to $\mathcal{L}^2(\mathcal{D})$. Furthermore, it is desirable to consider Maxwell's equations on $\mathcal{L}^2(\mathcal{D})$ and therefore both the electromagnetic fields and the curl of the electric and magnetic field should belong to $\mathcal{L}^2(\mathcal{D})$. In the mixed-potential formulation, the surface divergence acts on the current density which gives rise to a surface charge density. Hence, it is natural to demand that both the surface current density and the surface charge density correspond to electromagnetic fields with locally finite energy. This leads to the definition of the function space $H^{-1/2}(\text{div}, \partial\mathcal{D})$ for the surface current density. This space consists of all vectorial functions, that have Cartesian components and surface divergence belonging to $H^{-1/2}(\partial\mathcal{D})$ [99, p. 35], [100].

Since the space $H^{-1/2}(\text{div}, \partial\mathcal{D})$ imposes explicit requirements on the surface divergence of the current densities, the test and expansion functions should have a certain degree of continuity with respect to the surface divergence. Since the surface divergence is not a uniform derivative in all spatial directions, the continuity of the test and expansion functions is also not uniform. A necessary continuity condition for a function \mathbf{f} to belong to $H^{-1/2}(\text{div}, \partial\mathcal{D})$ is the following. Let \mathcal{C} be a regular closed curve on the boundary $\partial\mathcal{D}$ and let $\hat{\nu}$ be a unit vector orthogonal to \mathcal{C} and tangential to the boundary $\partial\mathcal{D}$, then $\mathbf{f} \cdot \hat{\nu}$ should be continuous almost everywhere, i.e., $\mathbf{f} \cdot \hat{\nu}$ can only be discontinuous at a finite number of discrete points on $\partial\mathcal{D}$. Physically, this condition implies that line and point charges do not occur in this function-space setting. In the context of local basis functions, the above requirement implies that the components of the function normal to the boundary of its support has to be zero. Further, we may deduce from the above that the expansion function may have a line discontinuity within its support, albeit that the component normal to that "line" (contour) in $\partial\mathcal{D}$ must remain continuous. Further, the expansion functions should be chosen such that some superposition can approximate the currents reasonably well. Finally, with respect to the implementation, the choice of expansion functions also depends on the ease of evaluation of the matrix elements of the MoM-matrix.

An expansion function that meets all these requirements is the well-known *Rao-Wilton-Glisson* (RWG) function [101]. The RWG-function spans a pair of adjoining planar triangles Γ_n^\pm , which cover the areas A_n^\pm and are connected through the n^{th} common edge with base length ℓ_n , as illustrated in Figure 7.1. The plus and minus sign designation of the triangles is determined

by choosing the positive surface current direction to be from Γ_n^+ to Γ_n^- . Here $\boldsymbol{\rho}^\pm$ are the local position vectors in Γ_n^\pm with respect to the free vertices \mathbf{r}_n^\pm of the RWG-function, i.e., $\boldsymbol{\rho}^\pm = \pm(\mathbf{r} - \mathbf{r}_n^\pm)$ for $\mathbf{r} \in \Gamma_n^\pm$. The RWG-function associated with the n^{th} common edge is defined by

$$\Lambda_n(\mathbf{r}) = \begin{cases} \frac{\ell_n}{2A_n^+} \boldsymbol{\rho}_n^+, & \mathbf{r} \in \Gamma_n^+, \\ \frac{\ell_n}{2A_n^-} \boldsymbol{\rho}_n^-, & \mathbf{r} \in \Gamma_n^-, \\ 0, & \text{otherwise.} \end{cases} \quad (7.1)$$

The factor $\ell_n/(2A_n)$ normalizes Λ_n such that the component normal to the common edge has unit length and is therefore continuous. Further, the component normal to the boundary of its support is zero. Hence, Λ_n is a divergence-conforming basis function that belongs to $H^{-1/2}(\text{div}, \partial\mathcal{D})$. A full description of the RWG-function and further reasons why it is suitable as an expansion function can be found in [101] and [24, Appendix D.1].

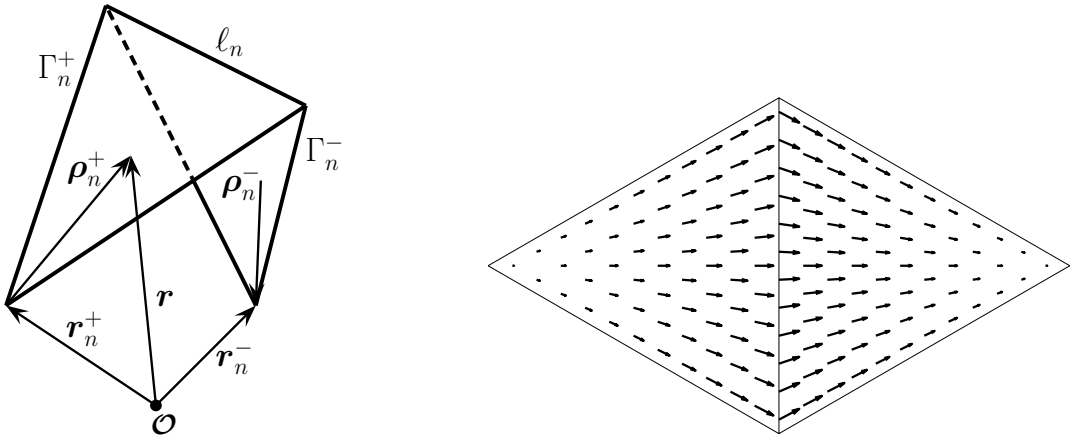


Figure 7.1: On the left the position vectors associated with the RWG-function \mathbf{f}_n for the n^{th} -common edge with edge length ℓ_n . On the right the vectorial current behavior on a RWG-function from Γ^+ to Γ^- .

In [102], two spatially orthogonal sets of basis functions are used to expand the currents. In particular, the electric surface current \mathbf{J}_S was expanded in terms of the RWG-function Λ_n , and the magnetic surface current \mathbf{M}_S in terms of $\hat{\mathbf{n}} \times \Lambda_n$, which obviously is orthogonal to Λ_n . Although it was claimed that this method yields a more stable solution due to the orthogonality of the two sets of basis functions, the expansion of the magnetic current in terms of $\hat{\mathbf{n}} \times \Lambda_n$ is incorrect if a solution is sought in $H^{-1/2}(\text{div}, \partial\mathcal{D})$. The argument is that, since the RWG-function Λ_n is constant and continuous across edges, at the edges of the scattering object, $\hat{\mathbf{n}} \times \Lambda_n$ imposes continuity of \mathbf{M}_S tangential to the boundary $\partial\mathcal{D}$ at the edge. This in turn implies that the electric

field tangential to $\partial\mathcal{D}$, normal to the edge from one patch to another, should be continuous also, because the electric field is related to the magnetic current by Eq.(2.62b). However, this is not true if the two patches are not in the same plane. A similar reasoning is applicable for the expansion of \mathbf{J}_S with $\hat{\mathbf{n}} \times \Lambda_n$. Hence, $\hat{\mathbf{n}} \times \Lambda_n$ is not allowed as a expansion function. This observation was also made in [103], based on physical grounds. Instead, we shall use the RWG-function throughout as the expansion function for both the electric and magnetic surface current densities.

To determine the required properties of the testing functions we have to take into account the solution space for the current densities and the mapping properties of the integral operators. If we choose to find solutions in $H^{-1/2}(\text{div}, \partial\mathcal{D})$, then the integral operators $\hat{\mathbf{n}} \times \mathbf{L}$ and $\hat{\mathbf{n}} \times \mathbf{K}$, and the identity operator \mathbf{I} map $H^{-1/2}(\text{div}, \partial\mathcal{D})$ onto $H^{-1/2}(\text{div}, \partial\mathcal{D})$. As explained before, the testing functions should then belong to the dual space of the range space, $H^{-1/2}(\text{div}, \partial\mathcal{D})$. The dual space of $H^{-1/2}(\text{div}, \partial\mathcal{D})$ may be associated with $H^{-1/2}(\text{curl}, \partial\mathcal{D})$ [99, p. 38] if the $\mathcal{L}^2(\partial\mathcal{D})$ inner product is used to define the duality product. The space $H^{-1/2}(\text{curl}, \partial\mathcal{D})$ can be characterized in terms of $H^{-1/2}(\text{div}, \partial\mathcal{D})$, by observing that $\hat{\mathbf{n}} \times \mathbf{I}$ is an invertible mapping from $H^{-1/2}(\text{curl}, \partial\mathcal{D})$ to $H^{-1/2}(\text{div}, \partial\mathcal{D})$ and vice versa. Therefore, any function $\mathbf{g} \in H^{-1/2}(\text{curl}, \partial\mathcal{D})$ can be associated with a function $\mathbf{f} \in H^{-1/2}(\text{div}, \partial\mathcal{D})$ through $\mathbf{g} = \hat{\mathbf{n}} \times \mathbf{f}$. Hence, $\mathbf{n} \times \mathbf{g}$ has to satisfy the condition that $\hat{\boldsymbol{\nu}} \cdot (\hat{\mathbf{n}} \times \mathbf{g}) = \mathbf{g} \cdot (\hat{\boldsymbol{\nu}} \times \hat{\mathbf{n}}) = \mathbf{g} \cdot \hat{\boldsymbol{\tau}}$ is continuous almost everywhere, where $\hat{\boldsymbol{\nu}}$ is the vector orthogonal to a regular closed curve \mathcal{C} on $\partial\mathcal{D}$ and tangential to $\partial\mathcal{D}$ and $\hat{\boldsymbol{\tau}}$ a vector tangential to \mathcal{C} . As such, in terms of RWG-functions, the integral operator $\hat{\mathbf{n}} \times \mathbf{L}$ is properly tested with $\hat{\mathbf{n}} \times \Lambda_n$. Recall that there are no continuity restrictions in any direction for the test and expansion functions applied to the integral operator $\hat{\mathbf{n}} \times \mathbf{K} + \mathbf{I}$, as argued in Section 3.7.

As a final remark concerning the solvability of the integral equations we emphasize that a further impediment for a stable numerical approximation of the current density is the circumstance that the coercive parts of the two terms in the operator \mathbf{L} , for the non-divergence-free and divergence-free part of the function space, have opposite signs. As a consequence, any set of basis and testing functions that does not take into account the splitting of the function spaces will mix the two coercive parts and thereby will ultimately destroy the stability of the numerical approximation. In that case, the condition number of the linear system will blow up for decreasing mesh sizes, which is known as the low-frequency breakdown effect (Section 5.8). For rooftop and RWG-functions, the splitting is not accounted for automatically. However by combining sets of these basis functions into loop-star and loop-tree constructions [54, 55, 104], the stability may be resolved.

Now that suitable test and expansion functions have been chosen, we proceed with the discretization of the integral operators. The first step in the discretization process of the surface of an arbitrarily shaped object is the generation of a mesh. For the RWG-function, this implies a triangulation of the surface. Because triangles are capable of describing any geometrical surface accurately, they are well suited to approximate the surface of an arbitrarily shaped object. The resulting triangles are preferably as equilateral and uniform in size as possible, since the relative mesh density is determined by the largest edge length. Moreover, such uniformity properties may also improve the solvability of the resulting integral equations [105]. The preferred uniform size and shape of the triangles make it difficult to construct a mesh generator that can handle an arbitrary surface shape while providing a good mesh quality. Since the design of a general mesh generator lies beyond the scope of this thesis, we assume that a (reasonably) good mesh is available a priori and focus below on the corresponding discretization of the integral equations.

The most commonly supplied mesh format starts with an array containing all vertices of the mesh, $Vertex(v, k)$, where $k \in [1, 3]$ are the indices for the three coordinate components associated with vertex v . The mesh is complemented with an array of triangles, $Triangle(q, j)$, where the index $j \in [1, 3]$ assigns three vertices v to triangle Γ^q with area A^q . The orientation of the normal, \hat{n} , to triangle Γ^q is determined by ordering the vertices in a counter-clockwise fashion with respect to \hat{n} . A graphical representation is presented in Figure 7.2 for triangle Γ^q with the position vectors \mathbf{r}_j^q associated with the three vertices $j \in [1, 3]$ and the outward normal \hat{n} . Further, ℓ_j represents the length of edge j opposite to vertex j of Γ^q .

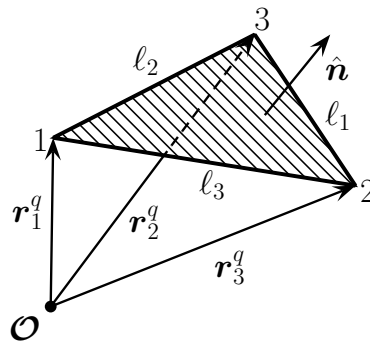


Figure 7.2: A spatial view of triangle Γ^q with the normal \hat{n} and the position vectors of the three vertices.

The next step concerns the initialization process for the filling of the MoM-matrix, i.e., the assignment of each edge and the associated two connecting triangles to a specific RWG function together with the reference direction of the current normal to that edge. The construction of one array that relates the edges to the triangles is sufficient to complete the filling process of

the MoM-matrix, and provides in our view also the most appropriate and efficient approach. An important topological property of closed surfaces is the Euler-Poincaré characteristic, which interrelates the number of edges E , vertices V and triangles T , according to

$$E = V + T - 2 + 2g, \quad (7.2)$$

where g is the genus of the surface, which may be interpreted as the number of handles attached to the surface. For the torus, for example, we have $g = 1$. Further, T is related to E by $3T = 2E$.

Since for closed surfaces each triangle is associated with three RWG-functions, it is obvious that some of the integrals required to determine a matrix element can be reused for other matrix elements. In fact, each combination of test and expansion integrals associated with a certain test and expansion triangle pair can be used up to nine times (3×3). Accordingly, if one focusses on pairs of triangles rather than edges, this may lead to a nine-fold increase in efficiency for the filling of the MoM-matrix, since each combination of triangles is considered only once.

To determine the surface integrals related to the test and expansion function it is convenient to use a local coordinate system for each individual triangle [106]. Accordingly, we introduce a new set of normalized area coordinates. The position of a point on the triangle Γ^q is given by

$$\mathbf{r} = \sum_{i=1}^3 \xi_i \mathbf{r}_i^q, \quad \text{where } 0 \leq \xi_i \leq 1 \text{ with } \sum_{i=1}^3 \xi_i = 1, \quad \text{for } \mathbf{r} \in \Gamma^q. \quad (7.3)$$

Accordingly, only two coordinates are actually independent. The triangle Γ^q is subdivided into three subtriangles at $\mathbf{r} \in \Gamma^q$. The normalized area coordinates are related to the areas of the subtriangles via

$$\xi_i = \frac{A_i^q}{A^q}. \quad (7.4)$$

A geometric interpretation can be found in Figure 7.3. Clearly, $\xi_i = 0$ at edge i , while $\xi_i = 1$ at vertex i . The surface integral of a function $g(\mathbf{r}')$ across a triangle Γ^q becomes

$$\int_{\Gamma^q} g(\mathbf{r}') dA' = 2A^q \int_{\xi_2=0}^1 \int_{\xi_1=0}^{1-\xi_2} g(\xi_1 \mathbf{r}_1^q + \xi_2 \mathbf{r}_2^q + \xi_3 \mathbf{r}_3^q) d\xi_1 d\xi_2, \quad (7.5)$$

with $\xi_3 = 1 - \xi_1 - \xi_2$. The factor $2A^q$ represents the Jacobian.

Next, we express an RWG-function in terms of normalized area coordinates. Unlike in the 2D discretization process in Section 5.3, there is no one-to-one relation between the triangular mesh

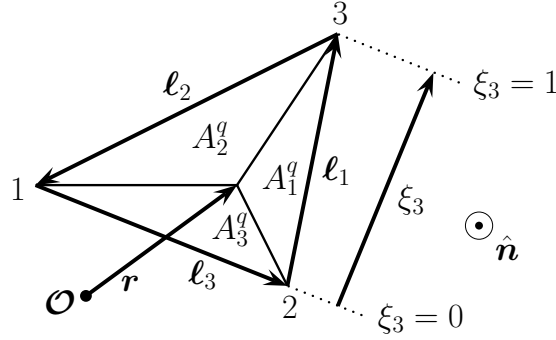


Figure 7.3: The subdivision of triangle Γ^q into subtriangles for the definition of the normalized area coordinates for the local coordinate system relevant to Γ^q .

elements and the reference direction of the normal component of the RWG-function at a particular edge. Accordingly, we fix the orientation of the RWG-function on each triangle with respect to its free vertex, and include the corresponding reference direction of the normal component separately. Accordingly, we apply the following transformation of the RWG-function to the local coordinate system

$$\Lambda_n(\mathbf{r}') = \sigma_j^q \Lambda_j^q, \quad \text{for } \mathbf{r}' \in \Gamma^q, \quad (7.6)$$

where σ_j^q is the sign accounting for the reference direction of the current component normal to the n^{th} -common edge (towards or away). A positive sign is selected if $\Gamma_n^+ = \Gamma^q$, and a negative sign if $\Gamma_n^- = \Gamma^q$. The position vector $\boldsymbol{\rho}_j$ of the local basis of the RWG-function, Λ_j^q , is expressed in terms of the three edge vectors, $\boldsymbol{\ell}_j$ of Γ^q , shown in Figure 7.3. The edge vectors of Γ^q are defined as

$$\boldsymbol{\ell}_j = \mathbf{r}_{j-1}^q - \mathbf{r}_{j+1}^q, \quad (7.7)$$

where the subscripts progress modulo 3, i.e., cyclically around the three vertices of a triangular element. Further we introduce $\ell_j = |\boldsymbol{\ell}_j|$. Accordingly, Λ_j^q reads

$$\Lambda_j^q = \frac{\ell_j}{2A^q} \boldsymbol{\rho}_j, \quad \text{where } \boldsymbol{\rho}_j = \mathbf{r}' - \mathbf{r}_j^q = \xi_{j+1} \boldsymbol{\ell}_{j-1} - \xi_{j-1} \boldsymbol{\ell}_{j+1}, \quad (7.8)$$

for $\mathbf{r}' \in \Gamma^q$. As Λ_j^q is expressed in terms of constant vectors only, the test and expansion integrals can be reduced to a sum of scalar integrals. The testing function Λ_m involving \mathbf{r} is expressed in a similar local coordinate system. However, to distinguish between the local coordinate systems associated with the test and expansion functions, the area coordinate ξ and the indices $\{q, j\}$ are replaced by the area coordinate η and the indices $\{p, i\}$ in Eqs. (7.6-7.8) for the definition of the test function.

Since the formulation of the integral equations for the scattering from perfectly conducting scatterers as well as from dielectric ones is the same for the 3D and the 2D case, the matrix equations in Section 5.3 are also relevant for the 3D case upon redefining the discretized integral operators, \mathbf{L} , \mathbf{K} and \mathbf{I} . However, the 3D case is fully vectorial, i.e., the two polarizations are coupled. Therefore, there is no distinction between the integral operators associated with the electric and magnetic equivalent currents. On that account, the corresponding discretized integral operators may differ only due to dissimilarities with respect to the test and expansion functions that are applied. However, as the electric and magnetic surface currents are both expanded by RWG-functions throughout, only the difference in the test functions is of importance. In contrast with the superscript for the discretized integral operators, \mathbf{L} , \mathbf{K} and \mathbf{I} in the 2D case, where it indicates that the operator is used in an electric or magnetic field integral equation with an electric or magnetic current, the superscript in the 3D-case henceforth indicates the chosen test function. For instance, \mathbf{L}^{EJ} changes into \mathbf{L}^{\wedge} if tested with the RWG-function, \wedge_m .

Because the integral formulations for dielectric and perfectly conducting objects involve $\hat{\mathbf{n}} \times \mathbf{L}$, the test functions $\hat{\mathbf{n}} \times \mathbf{f}_m$ with $\mathbf{f}_m = \wedge_m$ are appropriate in the context of the mapping properties of \mathbf{L} . Accordingly, testing \mathbf{L} with \wedge_m , and expanding the associated surface currents with \wedge_n , yields

$$\begin{aligned} \mathbf{L}_{v;mn}^{\wedge} = & \gamma_v \int_{\Gamma_m^{\pm}} \int_{\Gamma_n^{\pm}} \wedge_m(\mathbf{r}) \cdot \wedge_n(\mathbf{r}') G_v(\mathbf{r}, \mathbf{r}') dA' dA \\ & - \frac{1}{\gamma_v} \int_{\Gamma_m^{\pm}} \wedge_m(\mathbf{r}) \cdot \nabla_S \int_{\Gamma_n^{\pm}} [\nabla'_S \cdot \wedge_n(\mathbf{r}')] G_v(\mathbf{r}, \mathbf{r}') dA' dA. \end{aligned} \quad (7.9)$$

Since \wedge_m has only components tangential to $\partial\mathcal{D}$, the volume gradient of the scalar potential has been reduced to a surface gradient, which can be diverted to the test function via integration by parts with respect to the test integral. More specifically, for a scalar function $\Phi(\mathbf{r})$, we have

$$\int_{\Gamma_m^{\pm}} \wedge_m(\mathbf{r}) \cdot \nabla_S \Phi(\mathbf{r}) dA = \oint_{\mathcal{C}_m} \hat{\nu} \cdot [\wedge_m(\mathbf{r}) \Phi(\mathbf{r})] d\ell - \int_{\Gamma_m^{\pm}} [\nabla_S \cdot \wedge_m(\mathbf{r})] \Phi(\mathbf{r}) dA. \quad (7.10)$$

where Gauss' theorem, Eq. (2.14), has been applied to arrive at the first term on the right-hand side. Further, $\hat{\nu}$ is the outward unit vector normal to the outer contour \mathcal{C}_m of Γ^{\pm} and tangential to Γ_m^{\pm} . Because \wedge_m has no component normal to the boundary of its support, only the last term on the right-hand side of Eq. (7.10) remains. Thus, with the surface divergence of \wedge_n in local coordinates,

$$\nabla_S \cdot \wedge_j^q = \frac{\ell_j}{A^q}, \quad (7.11)$$

Eq. (7.9) may be written in local coordinates as

$$\mathbb{L}_{v;ij}^{\wedge;pq} = \sigma_i^p \sigma_j^q \left[\gamma_v \int_{\Gamma^p} \int_{\Gamma^q} \wedge_i^p \cdot \wedge_j^q G_v(\mathbf{r}, \mathbf{r}') dA' dA + \frac{\ell_i \ell_j}{\gamma_v A_i A_j} \int_{\Gamma^p} \int_{\Gamma^q} G_v(\mathbf{r}, \mathbf{r}') dA' dA \right]. \quad (7.12)$$

Note that $\mathbb{L}_{v;ij}^{\wedge;pq}$ provides a contribution to the matrix element \mathbb{L}_{mn}^{\wedge} with test and expansion common edges that correspond with edges i and j of Γ^p and Γ^q , respectively. The used superscript indicates that the integral operator \mathbb{L} is tested with \wedge_m . By substituting the expressions for \wedge_i^p and \wedge_j^q in Eq. (7.12), the integrals associated with the vector potential, are conveniently written as

$$\int_{\Gamma^p} \int_{\Gamma^q} \wedge_i^p \cdot \wedge_j^q G_v(\mathbf{r}, \mathbf{r}') dA' dA = \sum_{k=1}^2 \sum_{\ell=1}^2 \ell_{i-k}^p \cdot \ell_{j-\ell}^q \Psi_{v;i+k,j+\ell}^{pq}. \quad (7.13)$$

The introduced potential constituent $\Psi_{v;ij}^{pq}$ is given by

$$\Psi_{v;ij}^{pq} = \int_{\eta_2=0}^1 \int_{\eta_1=0}^{1-\eta_2} \int_{\xi_2=0}^1 \int_{\xi_1=0}^{1-\xi_2} \eta_i \xi_j \frac{e^{-\gamma_v R}}{4\pi R} d\xi_1 d\xi_2 d\eta_1 d\eta_2, \quad (7.14)$$

with the distance given by

$$R = |\hat{\mathbf{R}}| = |\mathbf{r} - \mathbf{r}'| = |\eta_1 \mathbf{r}_1^p + \eta_2 \mathbf{r}_2^p + \eta_3 \mathbf{r}_3^p - \xi_1 \mathbf{r}_1^q - \xi_2 \mathbf{r}_2^q - \xi_3 \mathbf{r}_3^q|. \quad (7.15)$$

Upon recalling that the sum of the three area coordinates of ξ and η is unity, Eq. (7.3), the integrals associated with the scalar potential in Eq. (7.12) become

$$\int_{\Gamma^p} \int_{\Gamma^q} G_v(\mathbf{r}, \mathbf{r}') dA' dA = 4 \sum_{k=1}^3 \sum_{\ell=1}^3 \Psi_{v;k\ell}^{pq}. \quad (7.16)$$

The applied combination of test and expansion function satisfies the mixed-order potential formulation. The MoM-matrix, and therefore the potential constituent $\Psi_{v;ij}^{pq}$, is symmetric, i.e.,

$$\Psi_{v;ij}^{pq} = \Psi_{v;ji}^{qp}. \quad (7.17)$$

For each triangle pair, Ψ_{ij}^{pq} involves nine integrals. If these integrals are determined separately, the focus on triangles rather than on edges does not provide computational advantage. However, the time required to evaluate each integrand is dominated by the determination of the complex exponentials. Accordingly, to approach an acceleration by a factor of nine, the corresponding integrals are computed simultaneously. Hence, it is essential that the same sample points are used for the explicit edges belonging to a triangle pair. For that reason we employ a specific type

of Gaussian quadrature rules that are fully symmetric with respect to the three vertices of the triangle as introduced in [107]

$$2A \int_{\xi_2=0}^1 \int_{\xi_1=0}^{1-\xi_2} f(\xi_1, \xi_2) d\xi_1 d\xi_2 \approx A \sum_{n=1}^N w_n f(\xi_1^{(n)}, \xi_2^{(n)}), \quad (7.18)$$

where $\xi_1^{(n)}$ and $\xi_2^{(n)}$ are the area coordinates of the n^{th} -sampling point and w_n is the corresponding weight. A table of N -points Gaussian quadrature formulae for the symmetrically placed integration points is provided in [108]. Note that the quadrature order required for sufficient accuracy generally depends on the relative distance between source and observation points.

The rotated RWG-functions used as test functions are defined through

$$\mathbb{V}_m(\mathbf{r}) = \hat{\mathbf{n}} \times \mathbb{\Lambda}_m(\mathbf{r}). \quad (7.19)$$

Note that $\mathbb{\Lambda}_m$ and \mathbb{V}_m are point-wise orthogonal in a triangle. Although \mathbb{V}_m is not a suitable testing function for the integral operator L , it is required in the implementation of the 3D LEGO concept and the discretization of the 3D Müller formulation.

In the construction of the MoM-matrix elements $\mathbb{L}_{v;ij}^{pq;\mathbb{V}}$, the derivation of the contribution from the vector potential is performed in a similar manner as for $\mathbb{L}_{v;ij}^{pq;\mathbb{\Lambda}}$ and therefore is left out. However, the \mathbb{V}_m -counterpart of the scalar potential is somewhat different as \mathbb{V}_m contains, unlike $\mathbb{\Lambda}_m$, components normal to the boundary of its support. There are two ways of treating the scalar potential. The most common approach involves integration by parts and the application of Gauss' theorem [109, 110], as performed in Eq. (7.10). In contrast with $\mathbb{\Lambda}_m$ -testing, the contour integral of \mathbb{C}_m does not vanish. On the other hand, by basic vector analysis, we have

$$\nabla_S \cdot (\hat{\mathbf{n}} \times \mathbb{\Lambda}_m) = (\nabla_S \times \hat{\mathbf{n}}) \cdot \mathbb{\Lambda}_m - \hat{\mathbf{n}} \cdot (\nabla_S \times \mathbb{\Lambda}_m) = 0, \quad (7.20)$$

as the surface curl of $\hat{\mathbf{n}}$ and $\mathbb{\Lambda}_m$ both vanish, i.e., the surface curl of $\boldsymbol{\rho}_i$ is zero. Therefore, the last term on the right-hand side of the counterpart of Eq. (7.10) involving \mathbb{V}_m now vanishes. Hence, with \mathbb{V}_m -testing, the scalar potential in Eq. (7.9) may be written in local coordinates as

$$\sigma_i^p \sigma_j^q \frac{\ell_j}{\gamma_v A_j} \int_{\mathcal{C}^p} \hat{\boldsymbol{\tau}} \cdot \mathbb{\Lambda}_i^p \int_{\Gamma^q} G_v(\mathbf{r}, \mathbf{r}') dA' d\ell, \quad (7.21)$$

with $\hat{\boldsymbol{\tau}}$ being the unit vector tangential to \mathcal{C}^p oriented in a counterclockwise fashion with respect to $\hat{\mathbf{n}}$. The line integrals are to be taken over the entire triangle, as the contributions from the

common edge of Γ_m^+ and Γ_m^- do not cancel out, because the tangential component of Λ_m is discontinuous across most of the common edge. A disadvantage associated with the transformation to a contour integral is that additional integrals are required, i.e., the shared sample points used in the evaluation of the double surface integrals cannot be used for the computation of Eq. (7.21). Hence, the introduction of a second set of sample points comprises a computational overhead regarding the filling process of the MoM-matrix.

Alternatively, if the gradient is diverted to the Green's function [111], the use of a second set of sample points may be avoided, which is more efficient. However, the singular behavior of the integrand of the test integral becomes more pronounced, which would normally increase the quadrature error. Fortunately, analytic solutions for the associated singular integral parts can be used instead, leaving regular integrals only (see Section 7.3). In this approach the overall quadrature error remains small, thus retaining the efficiency of using a single set of sampling points.

Next, let us consider the weak form of the integral operator K using RWG-functions,

$$\mathbb{K}_{v;mn}^\wedge = \int_{\Gamma_m^\pm} \Lambda_m(\mathbf{r}) \cdot \int_{\Gamma_n^\pm} \Lambda_n(\mathbf{r}') \times \nabla' G_v(\mathbf{r}, \mathbf{r}') dA' dA, \quad (7.22)$$

where the gradient of Green's function is given by

$$\nabla' G_v(\mathbf{r}, \mathbf{r}') = (\mathbf{r} - \mathbf{r}') [1 + \gamma_v R] \frac{e^{-\gamma_v R}}{4\pi R^3}. \quad (7.23)$$

Since $\Lambda_i^p = \mathbf{r} - \mathbf{r}_i^p$ and $\Lambda_j^q = \mathbf{r}' - \mathbf{r}_j^q$, we may replace Λ_j^q by $(\mathbf{r}' - \mathbf{r}) + (\mathbf{r} - \mathbf{r}_i^p) + (\mathbf{r}_i^p - \mathbf{r}_j^q)$ and rewrite Eq. (7.22) in local coordinates as

$$\mathbb{K}_{v;ij}^{pq;\wedge} = \int_{\Gamma^p} \Lambda_i^p \cdot \left[(\mathbf{r}_i^p - \mathbf{r}_j^q) \times \int_{\Gamma^q} \nabla' G_v(\mathbf{r}, \mathbf{r}') dA' \right] dA. \quad (7.24)$$

By substituting the gradient of Green's function into Eq. (7.24), it is clear that $\mathbb{K}_{v;ij}^{pq;\wedge}$ is zero in case triangles Γ^p and Γ^q are located in the same plane, or if the free vertices of the test and expansion functions coincide. Likewise, by testing the integral operator K with \vee_m , Λ_j^q would be replaced by $(\mathbf{r}' - \mathbf{r}) + (\mathbf{r} - \mathbf{r}_j^q)$. Hence, $\mathbb{K}_{v;ij}^{pq;\vee}$ follows from Eq. (7.24) upon replacing $\{\vee, \mathbf{r}\}$ by $\{\wedge, \mathbf{r}_i^p\}$. When Λ_n is used as an expansion function, the support of the identity operator is $\mathbf{r} \notin \Gamma_n^\pm$. Subsequent testing with Λ_m or \vee_m leads to $\mathbb{I}_{ij}^{pq} = 0$, for $\Gamma^p \neq \Gamma^q$. For coinciding test and expansion triangles, Λ_i^p and Λ_j^q , we have

$$\Lambda_j^q = \Lambda_i^p + (\mathbf{r}_i^p - \mathbf{r}_j^q), \quad \text{for } \Gamma^p = \Gamma^q. \quad (7.25)$$

The integrals are computed analytically and the result for Λ_m -testing is given by [24, Appendix F.1]

$$\mathbb{I}_{ij}^{\wedge;pq} = \frac{\sigma_i^p \sigma_j^q}{2} \int_{\Gamma^p} \Lambda_i^p \cdot \Lambda_j^q dA = \delta_{p,q} \sigma_i^p \sigma_j^q \frac{\ell_i \ell_j}{8A} \left[\frac{|r_1|^2 + |r_2|^2 + |r_3|^2}{12} + \frac{3}{4} |\mathbf{r}^c| - (\mathbf{r}_i + \mathbf{r}_j) \cdot \mathbf{r}^c + \mathbf{r}_i \cdot \mathbf{r}_j \right], \quad (7.26)$$

where we have omitted the superscripts $\{p, q\}$ in the resulting expression, since $\Gamma^p = \Gamma^q$. Further, \mathbf{r}^c denotes the centroid of the triangle. Likewise, for \vee_m -testing, we obtain

$$\mathbb{I}_{ij}^{\vee;pq} = \frac{\sigma_i^p \sigma_j^q}{2} \int_{\Gamma^p} (\hat{\mathbf{n}} \times \Lambda_i^p) \cdot \Lambda_j^q dA = \delta_{p,q} \sigma_i^p \sigma_j^q \frac{\ell_i \ell_j}{24A} \hat{\mathbf{n}} \cdot (\boldsymbol{\ell}_i \times \boldsymbol{\ell}_j). \quad (7.27)$$

For diagonal elements, $m = n$, Eq. (7.27) implies that $\mathbb{I}_{mn}^{\vee} = 0$, since then $i = j$, and thus $\boldsymbol{\ell}_i \times \boldsymbol{\ell}_j = \mathbf{0}$. This means that the testing of the identity operator with \vee_m functions leads to an ill-conditioned MoM-matrix. Further, the test functions associated with the integral operator \mathbb{K} and the identity operator \mathbb{I} are always orthogonal as a direct consequence of the integral formulation, i.e., as we have $\mathbb{K} + \hat{\mathbf{n}} \times \mathbb{I}$, testing with Λ_m yields $\mathbb{K}^{\wedge} + \mathbb{I}^{\wedge}$.

In case \mathbb{L} and \mathbb{K} are tested with Λ_m functions, the forcing vector for the electric field is given by

$$\mathbf{E}_{v;m}^{\text{in};\wedge} = \int_{\Gamma_m^{\pm}} \Lambda_m(\mathbf{r}) \cdot \mathbf{E}_v^{\text{in}}(\mathbf{r}) dA. \quad (7.28)$$

A similar expression is obtained for the incident magnetic field or when testing is performed with \vee_m functions. Let us consider incident plane waves, represented in spherical coordinates by

$$\mathbf{E}_v^{\text{in}} = \left[E_{\theta}^{\text{in}} \hat{\boldsymbol{\theta}}_a + E_{\phi}^{\text{in}} \hat{\boldsymbol{\phi}}_a \right] e^{\gamma_v(\hat{\mathbf{r}}_a \cdot \mathbf{r})}. \quad (7.29)$$

The introduced unit-amplitude vectors represent the usual spherical coordinates, where the corresponding coordinates (θ_a, ϕ_a) indicate the angle of propagation of the plane wave, and $\hat{\mathbf{r}}_a$ represents the direction of propagation of that wave. The associated magnetic field \mathbf{H}_v^{in} readily follows from Eq. (2.22). The test integral in Eq. (7.28) can be computed analytically for plane-wave incidence, i.e., upon substitution of Eq. (7.29), the elements of the forcing vector in local coordinates read

$$\mathbf{E}_{v;i}^{\text{in};p;\wedge} = \sigma_i^p \left[E_{\theta}^{\text{in}} \hat{\boldsymbol{\theta}}_a + E_{\phi}^{\text{in}} \hat{\boldsymbol{\phi}}_a \right] \cdot \int_{\Gamma^p} \Lambda_i^p e^{\gamma_v(\hat{\mathbf{r}}_a \cdot \mathbf{r})} dA. \quad (7.30)$$

The expressions for the remaining integral are presented in Appendix C.1. If the incident field is generated by some superposition of electric and magnetic point sources, $\mathbf{E}_k^{\text{in}}(\mathbf{r})$ and $\mathbf{H}_k^{\text{in}}(\mathbf{r})$ are obtained from Eq. (2.43).

Since there are no continuity constraints on the test function for $\mathbf{K} + \hat{\mathbf{n}} \times \mathbf{I}$, testing with \mathbb{V}_m functions is preferred, since using \mathbb{I}_{mn}^\vee would lead to an ill-conditioned MoM-matrix. However, proper testing of \mathbf{L} requires Galerkin testing and expansion with \mathbb{A}_n functions. Thus, the appropriate testing functions for the EFIE and MFIE are orthogonal. The corresponding matrix equations read

$$- [Z_1 \mathbb{L}_1^\wedge] [\mathcal{J}] = [\mathbf{E}_1^{\text{in};\wedge}], \quad \text{and} \quad [\mathbf{K}_1^\vee + \mathbb{I}^\wedge] [\mathcal{J}] = [\mathbf{H}_1^{\text{in};\vee}]. \quad (7.31)$$

respectively. Accordingly, due to the difference in test functions, the EFIE and MFIE are considered as separate equations in a CFIE-approach, which are combined numerically after discretization. The matrix equations for the PMCHW and the Müller formulation for the 2D-case, Eq. (5.48) and Eq. (5.49), respectively, may also be used in the 3D-case. In particular, for testing with \mathbb{A}_m functions, these equations represent the 3D-case upon replacing the superscripts of the pertaining integral operators, viz., \wedge for \mathbf{L} and \mathbf{K} , and \vee for \mathbb{I} . Likewise, the superscript \wedge is used for the forcing vectors.

Once the current amplitudes J_n and/or M_n are determined, the corresponding electric and magnetic field distribution follow from the integral representations presented in Section 3.2. For instance, the exterior scattered fields for the dielectric object follow from Eqs. (3.5) and (3.6). Substituting the current expansion, Eq. (3.32), back into the integral representations leads to the following representation of the scattered fields

$$\mathbf{E}^{\text{sc}} = \sum_{n=1}^N [J_n \mathbb{L}_1 \wedge_n + M_n \mathbf{K}_1 \wedge_n] Z_1, \quad (7.32a)$$

$$\mathbf{H}^{\text{sc}} = \sum_{n=1}^N [M_n \mathbb{L}_1 \wedge_n - J_n \mathbf{K}_1 \wedge_n], \quad (7.32b)$$

for $\mathbf{r} \in \bar{\mathcal{D}}$. Changing the medium index of \mathbb{L}_v and \mathbf{K}_v into $v = 2$, and including a minus sign as we deal with an interior equivalent state, Eqs. (5.53), produce the total interior fields, $\mathbf{r} \in \mathcal{D}$.

One is often interested to know how the electromagnetic field behaves for an observer far from the scattering object. Let $\mathbf{r} = r\hat{\mathbf{r}}$, where the unit vector $\hat{\mathbf{r}}$ of the spherical coordinate system indicates the direction of observation. Then, we may write

$$|\mathbf{r} - \mathbf{r}'| = \sqrt{r^2 - 2r\hat{\mathbf{r}} \cdot \mathbf{r}' + |\mathbf{r}'|^2} = r - \hat{\mathbf{r}} \cdot \mathbf{r}' + \mathcal{O}\left(\frac{1}{r}\right) \quad (7.33)$$

as $r \rightarrow \infty$. In the far field, the vector potential for a surface current \mathbf{X}_S follows from

$$\int_{\partial\mathcal{D}} \mathbf{X}_S(\mathbf{r}') G_v(\mathbf{r}, \mathbf{r}') dA' = \frac{e^{-\gamma_v r}}{4\pi r} \int_{\partial\mathcal{D}} \mathbf{X}_S(\mathbf{r}') e^{\gamma_v(\hat{\mathbf{r}} \cdot \mathbf{r}')} dA' = \frac{e^{-\gamma_v r}}{4\pi r} \mathbf{F}_v(\mathbf{r}) \mathbf{X}_S, \quad (7.34)$$

with F_v being the far-field integral operator with medium index v . Upon applying the relation $\nabla' e^{\gamma_v(\hat{\mathbf{r}} \cdot \mathbf{r}')} = \gamma_v \hat{\mathbf{r}} e^{\gamma_v(\hat{\mathbf{r}} \cdot \mathbf{r}')}$ and Eq. (2.40) to the definition of the integral operators L and K in Eq. (3.7), we arrive at their far-field counterparts, resulting in the slant stack transform [112]

$$L_v(\mathbf{r})\mathbf{X}_S \approx -\gamma_v \frac{e^{-\gamma_v r}}{4\pi r} \hat{\mathbf{r}} \times [\hat{\mathbf{r}} \times F_v(\mathbf{r})\mathbf{X}_S], \quad (7.35a)$$

$$K_v(\mathbf{r})\mathbf{X}_S \approx -\gamma_v \frac{e^{-\gamma_v r}}{4\pi r} \hat{\mathbf{r}} \times F_v(\mathbf{r})\mathbf{X}_S. \quad (7.35b)$$

The scattered far field is obtained by substituting these far-field approximations in Eq. (7.32). The far-field properties are used to determine the Radar Cross Section later on. Note that the far-field integral operator F is also identified in the plane-wave incident field, Eq. (7.30). A closed form solution for $F_v\mathbf{X}_S$ in case \mathbf{X}_S is expanded by Λ_n or \mathbb{V}_m functions is presented in Appendix C.1.

7.3 Integration of the singular integrand parts

In the construction of the MoM-matrix equation, the integrand of the test and expansion integrals exhibits a singular behavior when the source and observation point approach each other, due to the singularity entrenched in Greens function. Such singularities are preferably avoided in the numerical evaluation of these integrals. As in the 2D-case in Section 5.4, the integrals that are integrated numerically are preferably reduced to regular integrals. To this end, the singular terms of Green's function are subtracted, i.e.,

$$G(\mathbf{r}, \mathbf{r}') = [G(\mathbf{r}, \mathbf{r}') - G_{\text{sing}}(\mathbf{r}, \mathbf{r}')] + G_{\text{sing}}(\mathbf{r}, \mathbf{r}'). \quad (7.36)$$

Accordingly, the first term on the right-hand side is used in the numerical integration, while analytical solutions are sought for the remaining singular integrals. We employ

$$G_{\text{sing}}(\mathbf{r}, \mathbf{r}') = \frac{1}{4\pi R} + \frac{\gamma^2}{8\pi} R. \quad (7.37)$$

Although only the first term on the right-hand side of Eq. (7.36) is singular, the last term has a discontinuous derivative at $R = 0$ and is therefore not suited for numerical integration by Gaussian quadrature rules either. However, for the integral parts that do not involve spatial derivatives operating on Green's function, subtraction of only the first term suffices if Γ^p and Γ^q have no common vertices.

The analytical integration of the singular integral parts is more complicated for the full-vectorial 3D-case. Only in case of coincident triangles, analytic expressions for the singular term R^{-1} of the vector and scalar potential of the integral operator $\mathbb{L}_{k;ij}^{\wedge;pq}$ are available for the *combined* expansion and test integrals. These were first presented in [113], yet, we prefer the significantly simpler expressions reported in [114]. For the integration of the singular terms of Green's function involving *only* the expansion integral, analytic solutions have been reported in [115] and [116] for the L and K operators, respectively. However, the most elegant and complete expressions in terms of recurrence schemes have recently been presented in [110]. The relevant (singular) integrals are of the form

$$K_1^n = \int_{\Gamma^q} R^n dA', \quad \mathbf{K}_2^n = \int_{\Gamma^q} \wedge_j^q R^n dA', \quad \text{and} \quad \mathbf{K}_3^n = \int_{\Gamma^q} \nabla R^n dA', \quad (7.38)$$

for $n = -1, 1, 3, \dots$. The notation is based on [117]. For conciseness, the reported expressions are not repeated here. The analytical expressions for the integrals in Eq. (7.38) are used in the MoM-matrix. Since we also consider source and observation points close to scattering objects, these expressions are also used in the forcing vector and the integral representations that reproduce the scattered field, Eqs. (3.5) and (3.6), respectively.

The singular behavior of the integral operator K is more complicated due to the gradient of the Green's function in its kernel. In that case, both terms in Eq. (7.37) for $\nabla G_{\text{sing}}(\mathbf{r}, \mathbf{r}')$ lead to singularities in the expansion integral. Although the remaining kernel of the expansion integral is regular, and can be integrated numerically, the gradient of the first term on the right-hand side of Eq. (7.37) poses a problem concerning the test integral. More specifically, in case Γ^p and Γ^q have common points and are not in the same plane, the test integral will be singular. Since K has no self term ($\Gamma^p = \Gamma^q$), this only occurs for edge/vertex singularities in case of connecting edges/vertices of Γ^p and Γ^q . For those cases, the gradient of the singular terms is subdivided into a surface and a normal gradient, and the test integral involving the surface gradient is transformed into a contour integral by means of Gauss' theorem. By integrating both singular parts analytically, the remaining integrand of the contour integral becomes regular again. This is elaborated in [110], for both, \wedge_m - and \vee_m -function testing.

Let us finally comment on the efficiency aspect related to the evaluation of the singular parts. Clearly, as K_1^n and \mathbf{K}_3^n are independent of the expansion function, their evaluation is required only once for every $\mathbf{r} \in \Gamma^p$. Although it may seem that the evaluation of \mathbf{K}_2^n is required for all three expansion functions associated with Γ^q , this is not the case. That is, according to [110], \mathbf{K}_2^n consists of two parts, viz., one part independent of \wedge_j^q , while the other part involves the

scalar K_1^n and a vector projection on Γ^q . Thus, as K_1^n is independent of Λ_j^q , a single evaluation of the singular integrals is sufficient for the contribution to all nine integrals associated with a triangle pair. Hence, the separate treatment of the singular and regular integrand parts will not compromise the gain in efficiency by considering triangles rather than edges.

7.4 Perfect electric conductors

In this section, we consider the individual integral operators, L and $K + \hat{n} \times l$, that occur in the EFIE and MFIE formulations for the electromagnetic scattering from perfect conductors. The solvability of the MoM-matrix equation and the order of convergence of the accuracy of the resulting scattered fields are investigated, subject to the mesh density and quality. In particular, the far and near fields are considered for plane-wave incidence and point-source excitation. Further, the dependence of the condition number and the accuracy of the scattered near field on the combination constant α in the CFIE formulation is inspected. In addition, the effect of a simple matrix equation scaling to improve the condition number of the MoM-matrix in case of non-uniform edge-lengths is investigated. In the LEGO-concept we are primarily interested in fields generated by equivalent currents, and not in the equivalent currents itself. Therefore, we are not concerned with the accuracy of the equivalent currents.

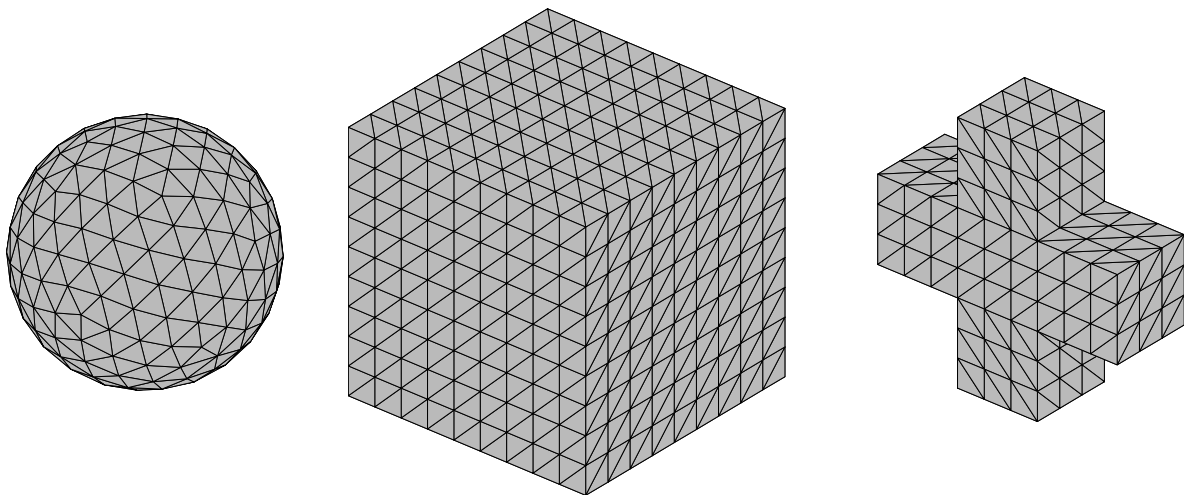


Figure 7.4: The sphere, cube and cross shape of the scattering object in consideration.

Before we proceed with the analysis of the EFIE and MFIE, let us first elucidate the 3D framework in which the analysis is carried out by means of the basis mesh shapes depicted in Figure 7.4. As a point of departure, the dependence on the smoothness of the exact boundary of

the scattering object is investigated by considering three different object shapes, viz., a sphere, a cube and a cross. Their maximum electromagnetic size is set to 0.4λ . For this particular choice, none of the three shapes support interior resonances. To gain a perception of the coarseness of the various object shapes with respect to their electromagnetic size, the illustrated mesh sizes amounts to roughly 20 points/ λ and are shown with corresponding scale.

To analyze the near-field properties of the scattering objects, the scattered field is evaluated at discrete points on an observation surface $\partial\mathcal{D}_o$. This observation surface encloses a cubical shape with edge length 0.5λ , where the evaluation points are distributed at the vertices of a scaled version of the cubical mesh in Figure 7.4. As error criterion for the scattered field, the following *normalized error* is employed,

$$\text{norm. err.} = \sqrt{\frac{\int_{\partial\mathcal{D}_o} |\mathbf{E}^{\text{ref}} - \mathbf{E}^{\text{num}}|^2 + Z_0^2 |\mathbf{H}^{\text{ref}} - \mathbf{H}^{\text{num}}|^2 dA}{\int_{\partial\mathcal{D}_o} |\mathbf{E}^{\text{ref}}|^2 + Z_0^2 |\mathbf{H}^{\text{ref}}|^2 dA}}. \quad (7.39)$$

In all cases, 100 evaluations points are taken on each face of the observation cube. To investigate the near-field properties, the incident field is generated by a unit-amplitude electric point source, positioned at a corner of the observation box. The point source is directed outwards in the radial direction. Since the observation surface and the point of excitation are situated within 0.05λ away from the scattering object, the near field is strong at the sampling points on the observation cube. In case the scattering object is a sphere, analytical solutions are used as the reference solution in Eq. (7.39). The scattered field from a sphere due to a point-source excitation is evaluated in Appendix B.2. For other object shapes, a sufficiently converged solution will be used, bearing in mind that the applied expansion functions are ultimately dense in the solution space of the integro-differential operators. With reference to Section 7.2, $H^{-1/2}(\text{div}, \partial\mathcal{D})$ represents the solution space that is associated with a current expansion using RWG functions.

As with the 2D case, attention is focused on the error generated by the mapping properties of the involved integral operator, the applied discretization, and the smoothness of the exact boundary. To exclude the quadrature error in the following analysis, the numerical integration of the test and expansion integrals associated with the MoM-matrix, the forcing vector, and the scattered field representation, is performed with adaptive quadrature rules, viz., the routine D01PAF of the NAG Mark 20 library [118], which specifically deals with triangular domains and is an implementation of the n -point ($n = 1, 4, 10, 20, 35, \dots$) Gaussian quadrature rule. The involved integral kernels are regular, because the singular integrals are extracted, as discussed in Section 7.3.

We now turn our attention to the order of convergence of the scattered fields generated by the approximate equivalent currents \mathbf{J} via the integral representations Eq. (7.32). In Figure 7.5, the normalized error in the scattered field at the observation surface $\partial\mathcal{D}_o$ is shown as a function of the mesh density for the three object shapes depicted in Figure 7.4, with on the left the EFIE, and on the right the MFIE results. The indicated number of points per wavelength reflects the ratio between the wavelength and the average edge length. It should be pointed out that the number of unknowns N increases quadratically with respect to the relative mesh density.

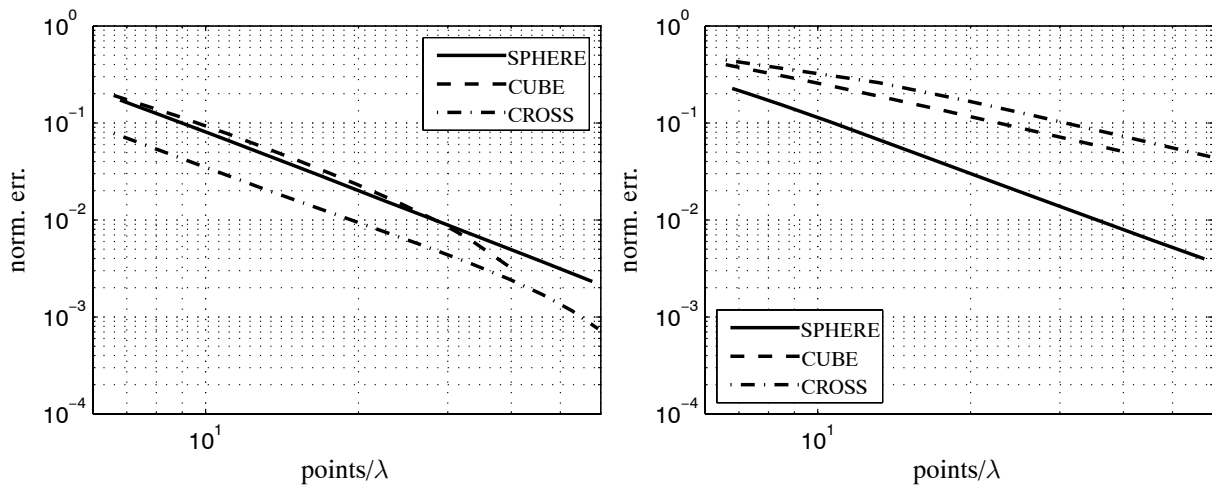


Figure 7.5: The normalized error as a function of the mesh density for the EFIE (left) and MFIE (right) for the sphere, cube, and cross.

In contrast with the 2D version, where the order of convergence reduces with an increasing loss of smoothness in the exact boundary, the EFIE converges quadratically, irrespective of the boundary shape. The stronger non-smoothness of the cross with respect to the cube translates itself into a decrease in magnitude only. On the other hand, the order of convergence of the MFIE remains subject to the smoothness of the boundary. In particular, the MFIE converges as $\mathcal{O}(N^{-1.9})$ for the sphere and $\mathcal{O}(N^{-1.2})$ for the cube and cross. The decrease in convergence is more pronounced than for the 2D case involving $\wedge\wedge$ -discretization (cf., Figure 5.9). The difference may be attributed to the use of dissimilar types of test- and expansion functions. Namely, although the 3D expansion function \wedge_n is linear in one direction, it is constant in the other direction, i.e., the RWG-function is complete to the zeroth order only. According to Cea's lemma, the equivalent current therefore converges linearly, albeit that the linear direction of the expansion function \wedge_n may improve this lower-bound convergence. The testing of the identity operator emphasizes the constant direction of the expansion function \wedge_n . For instance, proper testing of the identity operator involves the duality product, $\langle \wedge_m, \nabla_n \rangle$, where the point-wise orthogonality of \wedge_m and

∇_n for $n = m$ implies that the direction in which ∇_n is constant is the direction in which Λ_m is linear as opposed to the product of both linear directions, as was the case for L. Apart from that, the loss of smoothness of the approximate boundary of the sphere in relation to the circular cylinder may play a role here as well. These reasons may have caused the poor results of the MFIE.

The apparent improved convergence of the EFIE for a dense mesh of the cross and cube is slightly misleading, as the mesh density approaches that of the applied reference solution. This is not the case for the MFIE, as the EFIE results have been as a reference solution, because of its superior performance. Despite the less smooth boundary of the cross, the results with the EFIE are more accurate than those for the cube, albeit only in magnitude. This is probably due to the fact that the cube is positioned closer to the electric point source. Moreover, the distance between the observation cube and the cube itself is 0.05λ , while this is only locally the case for the surface of the cross. Finally, the error decay rate obtained for the sphere is bounded by the geometrical error created by the approximate boundary of the sphere.

Next we consider the solvability of the EFIE and MFIE in terms of the condition number of the MoM-matrix. Accordingly, in Figure 7.6 the condition number as a function of the mesh density is shown for the EFIE and MFIE. The condition number of the EFIE increases quadratically, and appears largely insensitive of the boundary shape. For the the MFIE on the other hand, the condition number is virtually independent of the mesh density, but its magnitude increases with decreasing boundary smoothness.

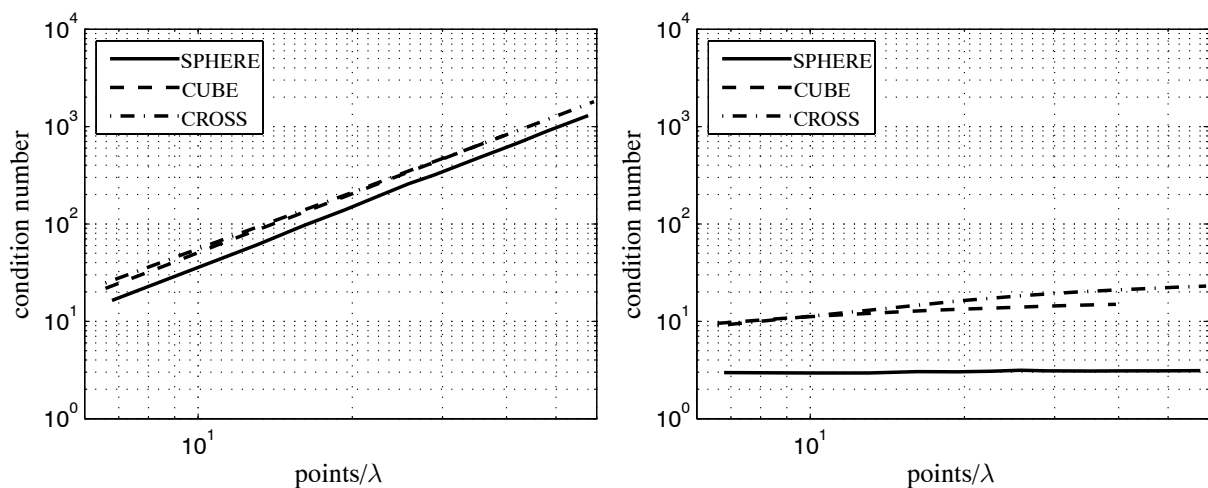


Figure 7.6: The condition number as a function of the mesh density for the EFIE (left) and MFIE (right) for the sphere, cube, and cross.

Next, let us consider the impact of the type of discretization on the condition number of the MoM-matrix and the accuracy of the scattered field, i.e., the size and shape of the triangles. To this end, the results from three different approaches in the construction of a mesh for a sphere are compared. In addition, the improvement of domain scaling is considered (otherwise the attainable accuracy is bounded by the geometrical error of the approximate boundary). In Figure 7.7, a graphical illustration of the three considered types of sphere meshes are shown. The one on the left, denoted as SPHERE1, is obtained by minimizing the sum of squared distances between the vertices and the vertices in their simplicial stars. An alternative, commonly used way to generate a mesh for a sphere is the projection of the mesh of a cube onto the surface of the sphere [24]. The resulting type of mesh, indicated as SPHERE2, is depicted on the middle in Figure 7.7. Finally, one of the earliest and easiest meshes used for a sphere [101] is shown on the right of Figure 7.7, denoted by SPHERE3. This type of mesh readily follows by splitting up the surface via equally sized discrete steps along the $\hat{\theta}$ - and $\hat{\phi}$ -directions.

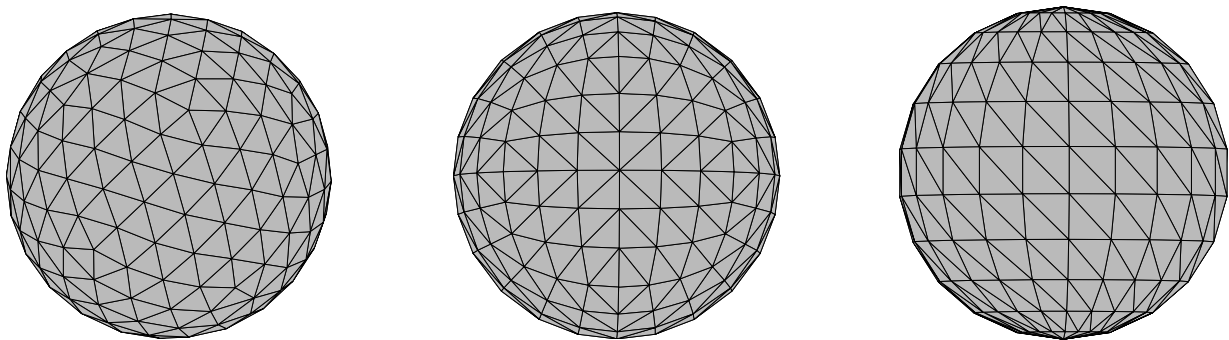


Figure 7.7: Three different types of meshes for a sphere. On the left, the sum of squared distances between the vertices and the vertices in their simplicial stars is minimized. In the middle, the mesh of a cube is projected onto the surface of the sphere. On the right, the straightforward splitting up of the surface via equally sized discrete steps along the $\hat{\theta}$ - and $\hat{\phi}$ -directions.

In Figure 7.8 the normalized error as a function of the mesh density is shown for the three mesh types with the domain scaling proposed in Section 5.5. First of all we observe that, like the 2D case for the circular cylinder, an improvement of the order of convergence from quadratic to cubic order in case of domain scaling for the EFIE. This feature particularly occurs for SPHERE1, and to a lesser extent for SPHERE2. However, observe further that the order of convergence varies and appears to decline with further mesh refinements for SPHERE1 and SPHERE2. This saturation may be completely attributed to the fact that not all triangles are equilateral and equally sized. In particular, as the scaling applies to the average triangle shape and size, the relative improvement of domain scaling diminishes upon increasing the mesh density as the surface irreg-

ularity raised by the dissimilar triangles becomes more important than the change in volume by the (decreasing) scaling factor. Nonetheless, SPHERE1, which contains the nearest to equilateral equally sized triangles outperforms the other mesh types. Note that the difference in scaling factor of the three spheres reflects the superiority of SPHERE1 and the saturation of the improved convergence. More specifically, for a corresponding mesh size, the mesh having the smallest scaling factor provides the best overall approximation of the surface. Likewise, the saturation in convergence corresponds with a saturation in scaling factor.

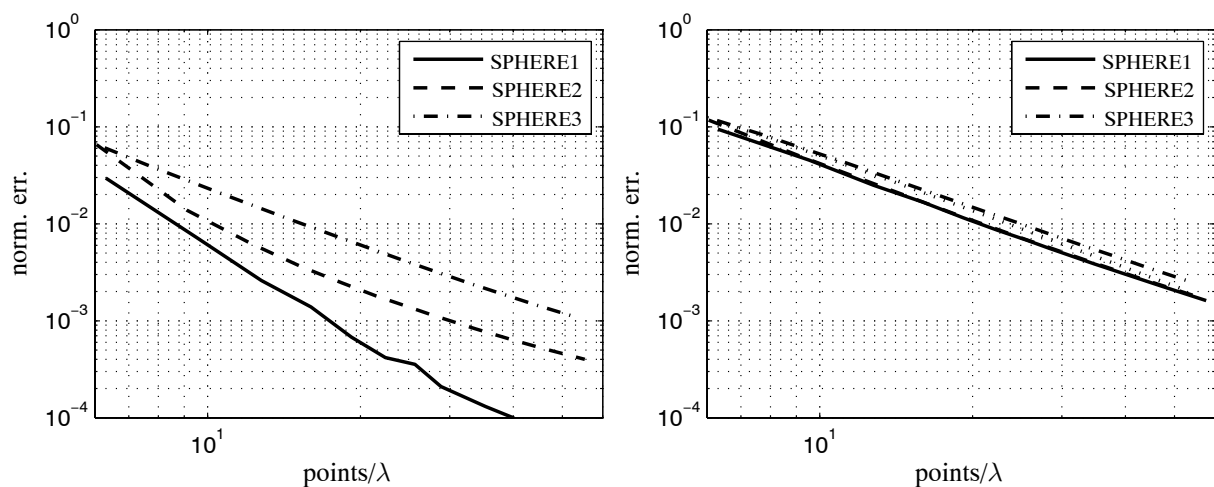


Figure 7.8: The normalized error as a function of the mesh density for the EFIE (left) and MFIE (right) for three different kind of sphere meshes.

However, applying domain scaling has not improved the results for the MFIE. If the radius of the discretized sphere is varied between its inner and outer spherical enclosure, the optimum scaling of the EFIE occurs indeed with domain scaling, whereas the optimum scaling factor for the MFIE occurs at a radius larger than the outer closure of the initial mesh, for which we have no convincing explanation. In comparison with Figure 7.5, domain scaling yields only a minor improvement in magnitude for the MFIE. The impact of the mesh quality is therefore of minor importance for the accuracy of the MFIE.

The dependence of the condition numbers of the MoM-matrices on the mesh density is shown in Figure 7.9. It is clear that the mesh quality also affects the condition number, especially for SPHERE3, for which the condition number increases with two orders of magnitude for both the EFIE and MFIE formulation. This may be attributed to the strong dissimilarity between the triangle shapes and sizes. In particular, comparing the ratio between the largest and smallest edge length of SPHERE3, we remark that this ratio increases quadratically as the mesh is refined. To

reduce the increase in condition number of the MoM-matrix due to the non-uniformity in edge length, we point out a simple additional scaling of the corresponding matrix equation. The scaling amounts to the division of each row m of the matrix equation by the edge length ℓ_m . Applying the proposed scaling to SPHERE3 led to the improved results indicated by SPHERE3* in Figure 7.9. With reference to Figure 7.6, the scaling decreases the magnitude of the condition number for the EFIE, while the curve of the condition number for the MFIE flattens.

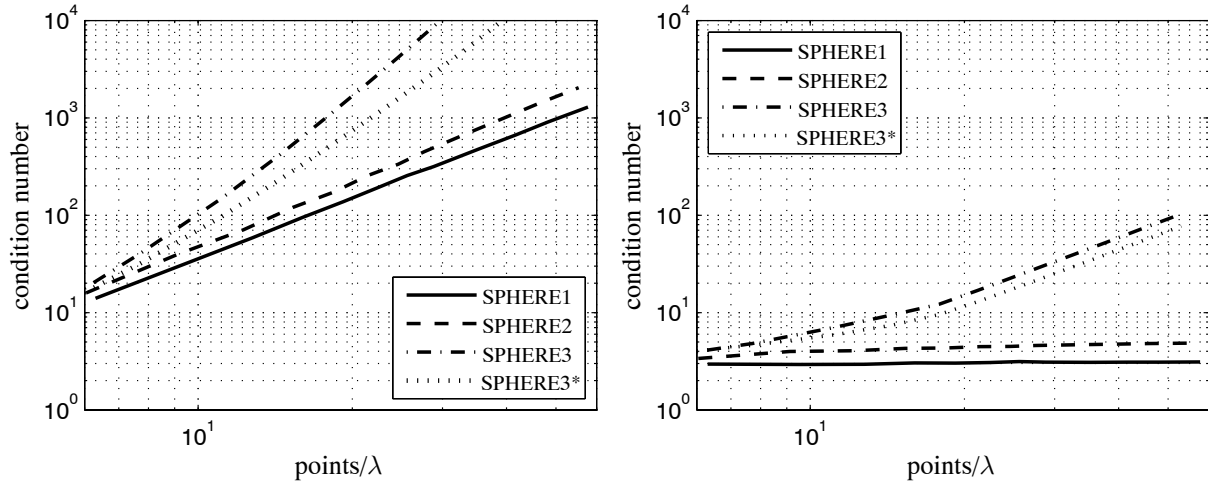


Figure 7.9: The condition number as a function of the mesh density for the EFIE (left) and MFIE (right) involving three different kind of sphere meshes.

Let us further comment on the combination constant α in the CFIE formulation. An α ranging between 0.2 and 0.8 is commonly referred to as an overall good choice to sufficiently suppress the interior resonances of the individual EFIE and MFIE. However, little attention has been given to impact on the accuracy of the scattered field, especially the near field, subject to scatterers involving smooth and non-smooth boundaries. In addition, it is often claimed that the CFIE yields a smaller condition number [119]. In view of the poor results of the MFIE with respect to the EFIE, a similar accuracy as with the EFIE seems improbable with the CFIE. Apart from that, insufficient accuracy of the test and expansion integrals due to low-order quadrature rules or improper handling of the singular integrand parts may have influenced earlier reported findings. For this reason, we determine an optimal choice for the combination constant α of the CFIE. In Figure 7.10 the normalized error (left) and the condition number of the MoM-matrix of the CFIE has been plotted as a function of α for the unscaled sphere, the cube and the cross. Recall that CFIE=MFIE for $\alpha = 0$ and CFIE=EFIE for $\alpha = 1$. Hence, the accuracy of the scattered field produced by the CFIE formulation is clearly inferior to that of the EFIE, irrespective of the value of α . This is not strange as the order of convergence of the EFIE exceeds that of the MFIE for

the cube and cross. The difference only increases for a denser mesh. This would also have been the case if we had applied domain scaling to the sphere. Hence, with respect to performance, the EFIE should only be used in combination with the MFIE in case interior resonances could emerge. Even then, the parameter α should be chosen as large as possible, yet small enough such that the MFIE can still suppress the interior resonances associated with the EFIE.

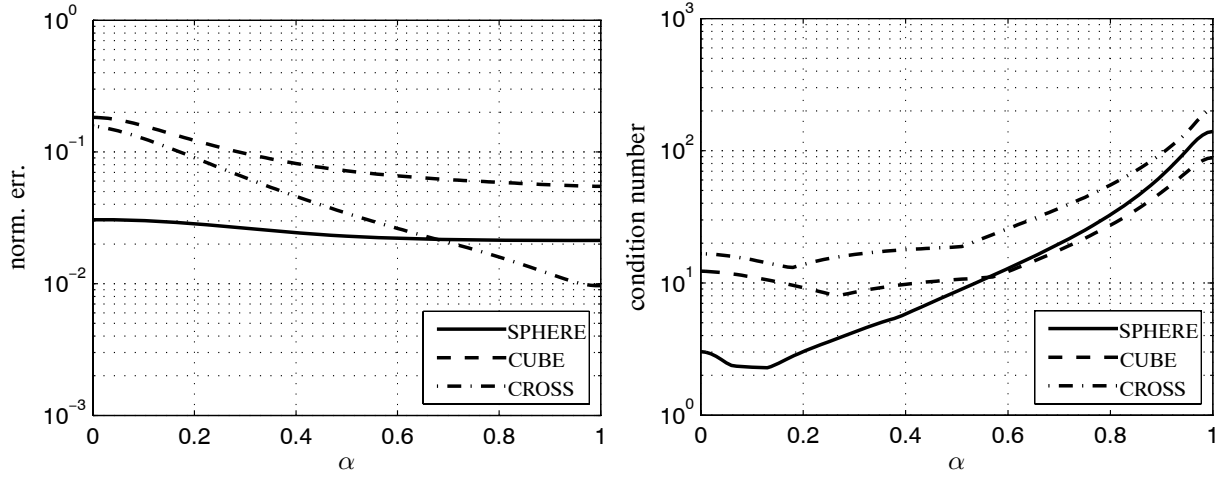


Figure 7.10: The normalized error (left) and condition number (right) of the CFIE as a function of the combination constant α .

Next, let us consider the performance of the integral equations in the far field by determining the *Radar Cross Section*. The Radar cross section is a measure of the strength of radar signals reflected from a target in the direction of the radar receiver. In particular, it is a measure of the ratio of backscatter power per unit solid angle in the direction of the radar (from the target) to the power density that is intercepted by the target. In terms of the scattered and incident field, the RCS, indicated by σ , is defined as

$$\sigma(\hat{\mathbf{r}}, \hat{\mathbf{r}}_a) = 4\pi \lim_{r \rightarrow \infty} r^2 \frac{|\mathbf{E}^{\text{sc}}(\hat{\mathbf{r}}, \hat{\mathbf{r}}_a)|^2}{|\mathbf{E}^{\text{in}}(\hat{\mathbf{r}}_a)|^2}. \quad (7.40)$$

The factor 4π stems from the definition of the solid angle. Note that the definition in Eq. (7.40) refers to the scattered field in the far-field region. The special case $\sigma(\hat{\mathbf{r}}_a, \hat{\mathbf{r}}_a)$ is called the *monostatic* RCS. If the RCS is determined for various directions $\hat{\mathbf{r}}$, while the incident field, and thus $\hat{\mathbf{r}}_a$, remains fixed, this is referred to as the *bistatic* RCS. In case of test and expansion by Λ_m and ∇_n , respectively, the incident and scattered far-field is determined analytically via the expression derived in Appendix C.1. Here, we assume that the incident plane wave propagates in the negative $\hat{\mathbf{z}}$ -direction, i.e., $\hat{\mathbf{r}}_a = \hat{\mathbf{z}}$. The bistatic RCS is normalized with respect to the geometrical cross-section of the scattering object. For a sphere with a radius a , the geometrical cross section is πa^2 .

Further, the RCS is often considered in decibels by the relation $\sigma_{\text{dB}}(\hat{\mathbf{r}}, \hat{\mathbf{r}}_a) = 10 \log_{10} \sigma(\hat{\mathbf{r}}, \hat{\mathbf{r}}_a)$. Due to the symmetry of the scattering objects at hand and the incident field, only two polarizations are of interest, i.e., the planes tangential to the E - and H -plane cross-sections of the incident plane wave.

Since an RCS may contain zeros, an error criterion like Eq. (7.39) is inadequate as the error would blow up at the zero crossings. Therefore, we apply the following average error norm for the bistatic RCS

$$\text{Err}_{\text{RCS}} = \int_{\theta=0}^{\pi} |\sigma_{\text{dB}}^{\text{ref}} - \sigma_{\text{dB}}^{\text{num}}| \, d\theta, \quad (7.41)$$

which returns the average RCS error in dB of both polarizations. As a reference solution for the RCS of a sphere, exact solutions also known as the *Mie series* [120] are available. For the other scatterers, results obtained with a relatively dense mesh are used as a reference solution.

As an example, consider the RCS plots depicted in Figure 7.11. On the left-hand side, the RCS is shown for a sphere with $ka = 7.6$, obtained with the EFIE involving a mere 288 unknowns. The Mie-series exact solution is plotted for comparison. The relative mesh density of the sphere is quite coarse, i.e., with 2.5 points per wavelength, the smallest edge-length just satisfies Nyquist criterion. Nevertheless, the average RCS error is only 0.16dB. Naturally, below the Nyquist criterion the accuracy rapidly decreases, while with 450 unknowns (3.1 points per wavelength), the error already drops to 0.07dB. In [24] the same RCS is depicted in Figure 3.6. However, there the midpoint rule was applied to evaluate the test integral and not all singular integral parts were computed analytically. Despite that this reduces the evaluation time of a matrix element, a similar accuracy as achieved in Figure 7.11 is not nearly achieved for 3042 instead of 288 unknowns. Thus, the computation time gained by an efficient (but less accurate) evaluation of a single matrix element is lost due to the increased matrix size required to obtain an accuracy similar to the one obtained for small quadrature errors. Hence, by proper handling of the singular test and expansion integral parts in conjunction with adequate quadrature rules for the remaining regular parts, the MoM-matrix can be kept relatively small. We emphasize that such a reduction of the required number of unknowns is highly beneficial for the 3D implementation of the LEGO-approach demonstrated in Chapter 6, since the computational cost are then governed by the multiplication of MoM matrices.

On the right of Figure 7.11, the RCS of a cube is shown with $kd = 3$, where d is the edge length of the cube. The average relative mesh density is about 7 points per wavelength with 288 unknowns, which yields an accuracy of less than 0.12dB error. For a comparison, a well-converged reference

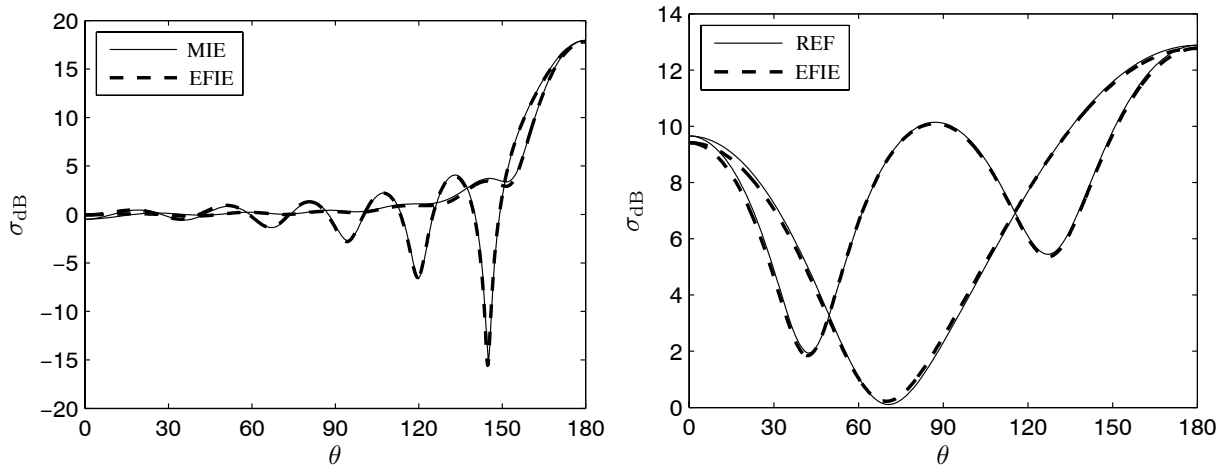


Figure 7.11: The normalized bistatic RCS, σ_{dB} , for the E - and H -plane cross-sections of a sphere with $kr = 7.6$ (left) and a cube with $kd = 3$ (right) involving both 288 unknowns.

solution is shown as well. The non-smoothness of a scattering object also increases the error in the far-field region. A relatively coarse mesh density with the low quadrature error of the adaptive quadrature rules (10^{-2}) already leads to quite reasonable results. Unfortunately, like the near-field, the (not shown) far-field results from the MFIE are inferior to those of the EFIE.

Let us now consider the frequency dependence of the integral equations and the suppression of the interior-resonance modes by means of the CFIE. For the combination constant of the CFIE, we apply the commonly applied choice, $\alpha = 0.2$. The frequency dependence of the sphere is expressed in terms of its electromagnetic size, viz., ka . Accordingly, the average RCS error and the condition number of the MoM matrix in case of a domain-scaled sphere is depicted in Figure 7.12, as a function of ka . Observe that, unlike the 2D case involving a single polarization, the EFIE and MFIE resonances occur at the same discrete frequencies, as argued in Section 3.4. The interior resonances of a sphere occur at the zeros of the spherical bessel functions $j_n(kr)$ and $j'_n(kr)$, for $n \in N$. Despite the coinciding resonance conditions for the EFIE and MFIE, the CFIE remains free of interior resonances, which can be seen upon inspecting the condition number and accuracy. Notice that in the region where the mesh is coarse with respect to the wavelength, around $ka = 8$ and $ka = 9$, the resonant current of the EFIE does produce an error spike in the RCS despite that based on Eq. (3.19) an EFIE resonant current theoretically produces a zero scattered field. For such coarse meshes, the resonant current generates a nonzero field due to the geometrical error of the approximate boundary.

Although the condition number of the CFIE is less than that of the EFIE and MFIE, the accuracy follows that of the (poor) MFIE results. As such, regarding the accuracy, the EFIE is preferred. Hence, like the comments on the near-field behavior, the MFIE should only be used in combination with the EFIE to suppress the interior resonances of the latter as a “regularizer”. Even then, the parameter α should be chosen as large as possible to maintain a reasonable accuracy. However, upon enlarging the electromagnetic size of the scattering object, ka , the density of resonant frequencies increases, so that it becomes increasingly difficult to avoid these interior resonances. Moreover, the exact resonance frequency of the approximate mesh varies slightly for different mesh densities. This comment also applies to the cube and cross shapes, where the exact and approximate boundaries coincide. Hence, the chance of hitting such an interior resonance rapidly increases. Above $ka = 6$, the condition number is no longer inversely proportional to $\mathcal{O}(N^2)$, due to the density of resonances at higher frequencies. For such high frequencies, the application of the CFIE becomes inevitable. Furthermore, the solvability may become an issue in case of iterative solvers, in which case the more robust CFIE should also be chosen. Without domain scaling of the sphere, the EFIE remains superior to the MFIE, though to a smaller extent than shown in Figure 7.12, since the accuracy of the EFIE is in that case bounded by the geometric error of the approximate boundary.

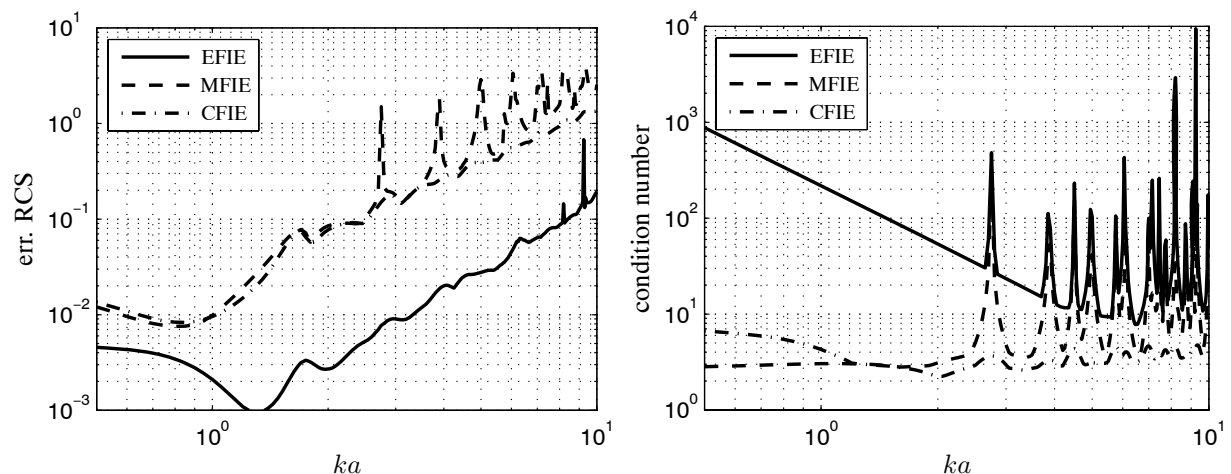


Figure 7.12: The RCS error (left) and condition number (right) as a function of the frequency in terms of ka .

7.5 Dielectric objects

Next, let us investigate the solvability and the order of convergence of the numerical approximation of the 3D PMCHW and Müller formulations. The differences in comparison to their 2D counterparts and the properties of the individual EFIE and MFIE integral operators will be elucidated. In addition, we investigate the use of a specific combination of \wedge_m - and \vee_m -test functions for Müller's integral formulation.

In Section 5.8, it has been demonstrated that by using Müller's formulation the low-frequency breakdown in the PMCHW formulation is avoided, which yields a stable condition number of the associated MoM-matrix with respect to mesh density. This is also the case for the 3D version of Müller's formulation. In particular, the gradient of the series expansion of the exponential function in the Green's function, can be written as

$$\begin{aligned} \nabla [G_1(\mathbf{r}, \mathbf{r}') - G_2(\mathbf{r}, \mathbf{r}')] &= \frac{1}{4\pi} \nabla \left[\sum_{n=0}^{\infty} (-1)^n \frac{R^{n-1}}{n!} (\gamma_1^n - \gamma_2^n) \right] \\ &= \frac{1}{4\pi} \sum_{n=2}^{\infty} (-1)^n (n-1) \frac{R^{n-3}}{n!} (\gamma_1^n - \gamma_2^n) (\mathbf{r} - \mathbf{r}'). \end{aligned} \quad (7.42)$$

The leading term in Eq. (7.42) is constant in space and depends on ω . Hence, in Müller's formulation the singular terms cancel each other. As a consequence, the low-frequency breakdown is thereby naturally avoided, since the scalar potential has the same frequency dependence as the vector potential, viz., they are both $\mathcal{O}(\omega)$. As a consequence, the condition number of the MoM-matrix should be largely insensitive to changes in the mesh density.

In the following analysis of the boundary integral equations, the same framework is applied as in the case of the perfect conductor. In particular, we consider the basis configuration depicted in Figure 7.4. The surface boundary shapes shown in that figure are also considered for the scattering dielectric object. Because we now have an interior (index 2) and exterior medium (index 1), the electromagnetic size of the scattering object is fixed with respect to exterior domain, i.e., the largest dimension of the objects is set to $0.2\lambda_1$. The observation surface is placed $0.05\lambda_1$ away from the scattering objects. Accordingly, the edge length of the observation cube is $0.3\lambda_1$. Along the observation surface, Eq. (7.39), is employed as a measure for the accuracy of the obtained scattered field by means of a normalized error. In Section 5.8 we have observed that an interior cavity mode leads to a similar decrease in accuracy of the interior and exterior scattered field regardless of whether the PMCHW or Müller formulation is used. For simplicity, we restrict ourselves to the exterior observation cube. Throughout, the medium properties of the exterior

domain are those of free-space, i.e., $\varepsilon_1 = \varepsilon_0$ and $\mu_1 = \mu_0$. An electric point source located at a corner of the observation cube and oriented outwards in the radial direction is employed as the source that generates the incident field. Unless mentioned otherwise, the refractive index of the interior medium n_2 is set to $n_2 = 4$. Finally, the additional matrix-equation scaling for Müller's formulation, as proposed in Section 5.3, is used throughout, as the improvement in the condition number has already been demonstrated in Section 5.8.

Since the accuracy of the scattered field also depends on the dielectric contrast, let us first consider the normalized error in the scattered field and the condition number of the corresponding MoM-matrix as a function the refractive index. The results for the domain-scaled sphere are depicted in Figure 7.13. The exterior medium properties remain unchanged, $n_1 = 1$. On the left we have, $\mu_{r;2} = 1$, and on the right we have $\varepsilon_{r;2} = 1$. The applied number of mesh elements is $N = 288$, which implies an average edge length of $0.04\lambda_1$ for the exterior medium. Further, in Figure 7.14, the condition number of the corresponding MoM-matrices is shown as a function of the refractive index n_2 . The condition number of the MoM-matrix for an ε -contrast is the same as for a or μ -contrast, because one follows from the other upon exchanging the diagonal submatrices and the off-diagonal submatrices, some with a change in sign.

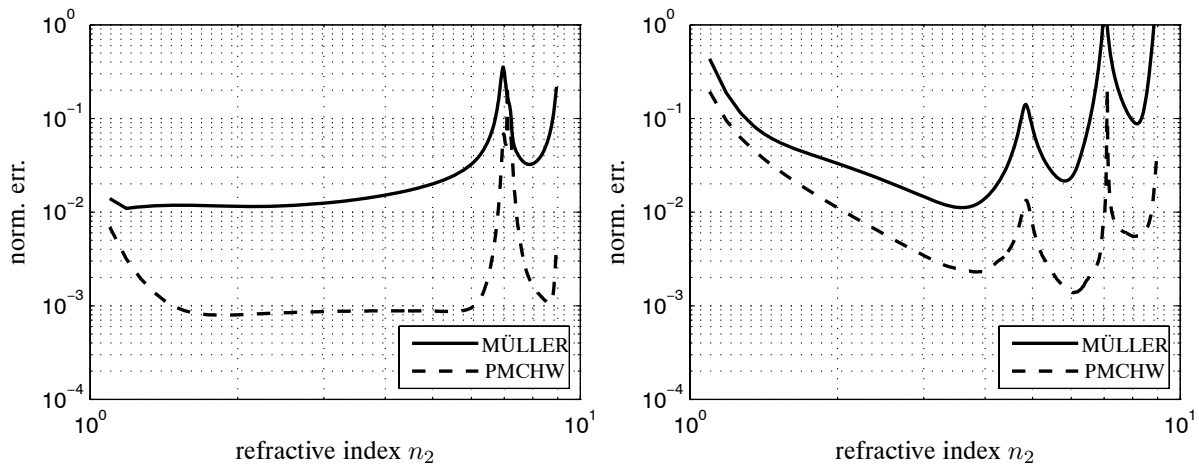


Figure 7.13: The normalized error as a function of the refractive index n_2 of a (scaled) sphere for the Müller and PMCHW formulation with on the left, $\mu_{r;2} = 1$ and on the right, $\varepsilon_{r;2} = 1$.

Like in the 2D-case, cavity resonant modes arise, albeit not as many since the sphere is chosen electromagnetically smaller, ($0.2\lambda_1$), than the 2D circular cylinder, ($0.9\lambda_1$). We have argued that at resonance the interior medium properties (larger refractive index) determine the effective relative mesh density. In the 2D-case, Müller's formulation proved to be superior to the PMCHW formulation with respect to solvability and accuracy for small dielectric contrasts. The poor

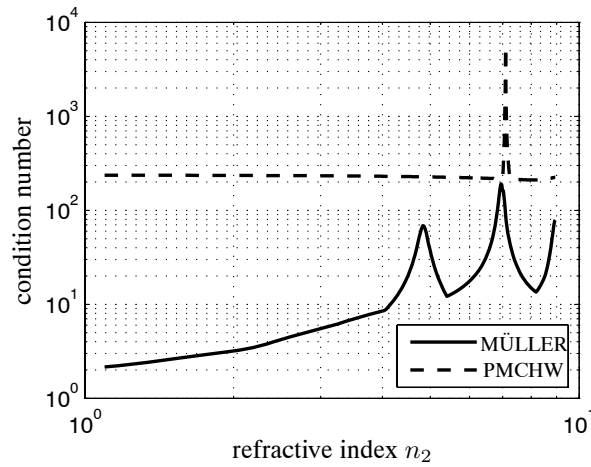


Figure 7.14: The condition number as a function of the refractive index n_2 of a (scaled) sphere for the Müller and PMCHW formulation with $\mu_{r;2} = 1$.

results of Müller's formulation in the 3D case with respect to those of PMCHW's formulation are primarily due to the integral operator $\mathbf{K} + \hat{\mathbf{n}} \times \mathbf{l}$, as has been demonstrated in Section 7.4. Without domain scaling, the accuracy of both formulations is comparable, since in that case the geometric error is the limiting factor. Furthermore, observe that the frequencies at which the resonance modes occur are slightly different depending on which integral equation is used. The difference may be attributed to the dissimilar mapping properties of the formulations in conjunction with the irregularities of the approximate boundary surface.

In Section 5.8, we remarked that the condition number of Müller's MoM-matrix is a measure for the accuracy of the scattered field and the smoothness of the exact boundary. More specifically, due to the cancellation of singular integral parts of the scalar potentials of \mathbf{L}_1 and \mathbf{L}_2 , their combination is, like the \mathbf{K} operator, a compact perturbation of the identity operator. Hence, the condition number of Müller's MoM-matrix is primarily determined by $\mathbf{K}^\wedge + \mathbf{I}^\vee$. However, only one of the two spikes in the condition number reoccurs in the error of the scattered field in case of the ε -contrast. The first spike is absent since the associated cavity mode is apparently not excited by the electric point source oriented along the radial direction. In case of the μ -contrast, both cavity modes are excited. Hence, the behavior of the condition number is only a measure for the accuracy of the scattered field if the incident field excites the corresponding cavity modes. In the LEGO approach, the excitation generally involves superpositions of surface sources, such that a possible cavity mode will probably be excited. Hence, both the condition number of the MoM-matrix and the accuracy of the scattered field may be used to locate resonances.

On the other hand, the condition number of the MoM-matrix associated with the PMCHW formulation is almost constant. Although one intuitively would expect that the condition number decreases as the relative (interior) mesh density decreases for an increasing refractive index, the condition number depends on the denser but fixed relative mesh density of the exterior medium. In the 2D case we have observed an dependence of the condition number of PMCHW's formulation on the medium parameters. This is no longer true in the 3D case because of the presence of a scalar potential for both the electric and magnetic equivalent currents. Recall that Müller and PMCHW are dominated by the respective K and L operators, and that the L-operator contains the scalar potential. This explains the difference in the behavior of the condition number. However, for coarse meshes or non-smooth boundaries both formulations are dominated by the K-operator. Hence, in those cases both formulations show a similar behavior with respect to the condition number.

Next, we compare the scattered field obtained using the Müller and the PMCHW formulations. In Figure 7.15 the normalized error in the scattered field is shown as a function of the number of unknowns due to the scattering from a domain-scaled sphere, a cube, and a cross. On the left and right, we have shown the Müller and the PMCHW formulation, respectively. On the top $\mu_{r;2} = 1$, $\varepsilon_{r;2} = 16$, and on the bottom $\mu_{r;2} = 16$, $\varepsilon_{r;2} = 1$. The PMCHW results are more accurate and have been used as a reference solution. As a result, the improvement in convergence rate for the PMCHW formulation as the mesh for the cube and cross shapes become denser is slightly misleading. Because the integral formulations are symmetric with respect to the type of material contrast (ε versus μ), the resulting difference in convergence and magnitude may solely be attributed to the dissimilar field distributions, whereas the difference in formulations is related to the dissimilar mapping properties of the dominant integral operators.

The domain scaling of the sphere yields no improvement in convergence for Müller's formulation. In Section 7.4, we have observed that the results using the MFIE could not be improved via domain scaling. The same phenomenon applies to Müller's formulation, since it primarily depends on the K-operator. Since the integral operator L is dominant in the PMCHW formulation, the domain scaling leads to an increase in the convergence rate by one order, i.e., from quadratic to cubic. Again, due to the irregularity in shape and size of the triangles of the approximate boundary (mesh quality), this improvement is not preserved when the mesh is refined further.

For the PMCHW formulation, the order of convergence depends on the mesh density. The strong convergence of the scattered field observed with a μ -contrast for the cube, quartic, and cross, cubic, at the coarser end is caused by the fact that the overall error of the equivalent currents

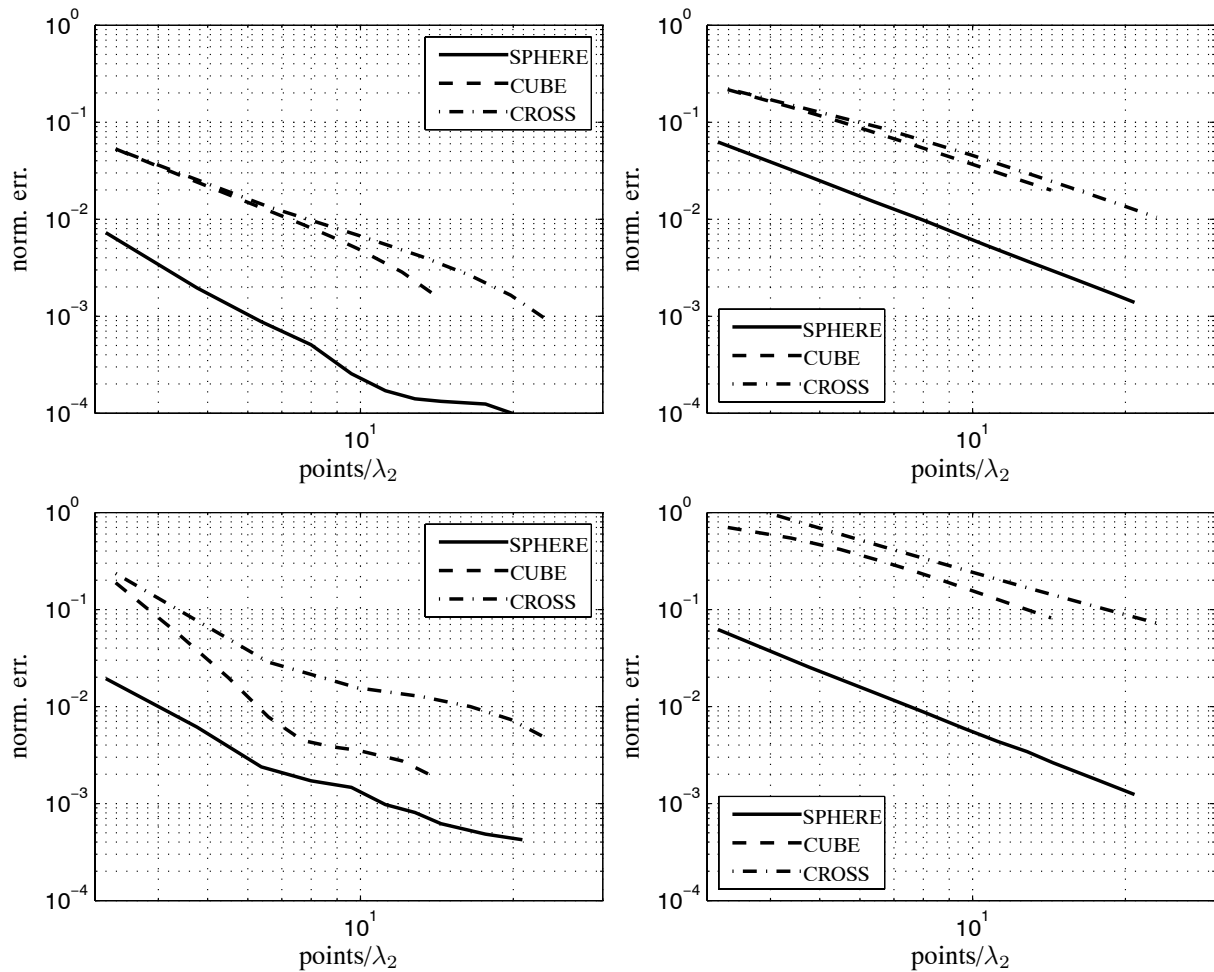


Figure 7.15: The normalized error as a function of the mesh density for the PMCHW (left) and the Müller (right) formulation, with on the top and bottom an ε - and μ -contrast, respectively.

for coarse meshes is not yet dominated by the error generated at the corners where the current may become discontinuous and singular. Beyond eight points per wavelength, the convergence is only linear. Although the convergence rate eventually seems to improve with further mesh refinement, this observation is not obvious as there is also an improvement from the fact that the PMCHW formulation has been used to generate the reference solution. The magnitude of the error with Müller's formulation is significantly larger than with that of PMCHW. On the other hand, the order of convergence with Müller's formulation is less sensitive to the mesh density. In particular, the order of convergence gradually seems to increase towards a quadratic one.

A difference with the 2D case is that the performance of the PMCHW formulation is throughout superior to that of Müller. This discrepancy may be attributed to the difference in behavior of

the individual L and $K + \hat{n} \times I$ operators, as observed for the 3D EFIE and MFIE in Section 7.4, respectively. This is not the case for the 2D-counterpart involving the $\wedge\wedge$ -discretization. So, if the 3D EFIE and MFIE results would presumably have been comparable, the PMCHW and Müller formulations would yield comparable results for the 3D implementation as well. Hence, such an equalization of the two integral operators might be achieved using a different choice for the test and/or expansion function.

Next, we evaluate the condition number of the MoM-matrix associated with the PMCHW and Müller formulations as a function of the mesh density for the sphere, cube, and cross shape. A similar behavior is observed with respect to their 2D counterparts or in relation to the individual integral operators. In particular, the condition number for the PMCHW formulation increases quadratically. Further, it is hardly affected by the non-smoothness of the boundary. The condition number for Müller's formulation is independent of the mesh density. However, it is affected by the non-smoothness of the boundary and possible cavity modes. Observe that because the condition number for the cube exceeds that for the cross, even though the accuracy for the cube is better than for the cross, the frequency of operation must be near a resonance frequency of the cube.

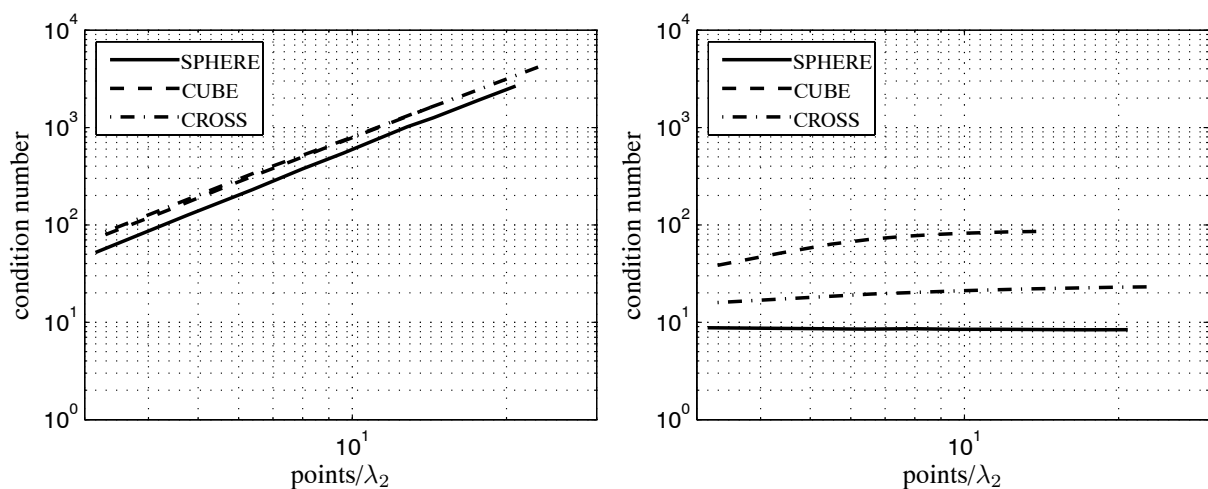


Figure 7.16: The condition number as a function of the mesh density for the PMCHW (left) and the Müller (right) formulation.

In an attempt to bring the accuracy of Müller's formulation up to par with that of the PMCHW formulation, we may try a linear combination of the \wedge_m and \vee_m test functions, as that may prove to be a better choice than \vee_m alone. Namely, since \wedge_m properly tests the integral operator L , whereas \vee_m improves the condition number of the MoM-matrix, mixing these properties may

turn out better. To that end, we evaluate the linear combination $\beta \Lambda_m + (1 - \beta) \nabla_m$, as a test function. The normalized error in the scattered field and the corresponding condition number of the MoM-matrix as a function of the combination factor β is depicted in Figure 7.17 for an ε -contrast. The most striking feature is the increased error and condition number around $\beta = 0.9$. Because this feature occurs for all three object shapes at about the same combination factor, this may indicate a fundamental error in the combined test function, i.e., the vector orientation of the combined test function may be inadequate to properly test the integral operators and/or the incident field. The same feature emerges when both test functions are subtracted instead of added. Despite the poor results around $\beta = 0.9$, the error for all three object shapes is reduced around $\beta = 0.7$ with respect to the original $\beta = 0$ case, while the low condition number of $\beta = 0$ is maintained. Unfortunately, the optimum mixing ratio does depend on the mesh density.

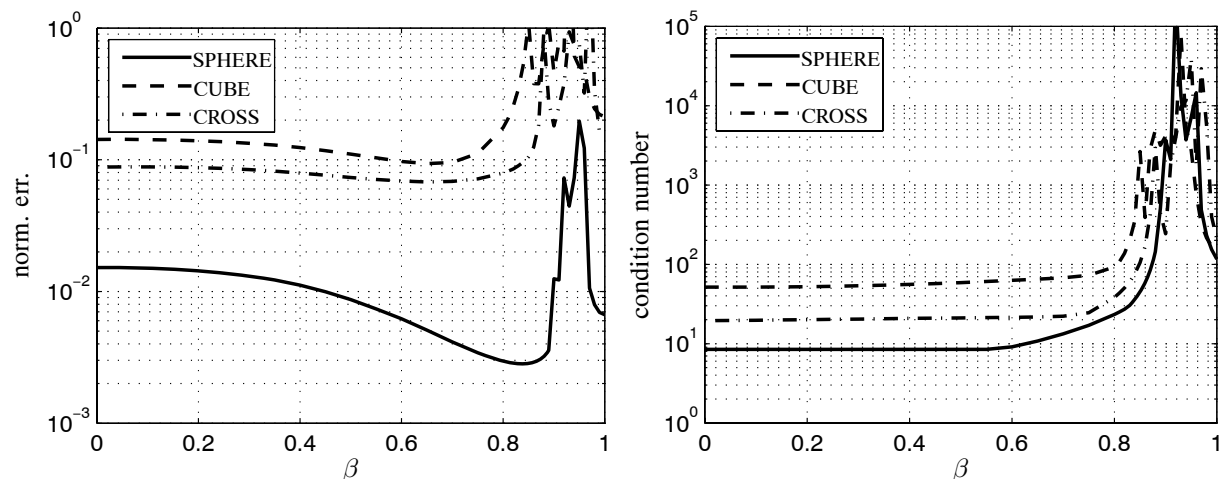


Figure 7.17: The normalized error (left) and the condition number (right) as a function of the combination constant for the applied test function in the Müller formulation.

To investigate the dependence of the optimum mixing ratio on the mesh density, we consider the normalized error in the scattered field from a cube and the condition number of the corresponding MoM-matrix, depicted in Figure 7.18. For an ultimately dense expansion function, the convergence rate represents a minimum based on Cea's Lemma. This poor convergence rate is eventually attained for $\beta = 1$. Finally, in case $\beta = 1$, the identity operator is poorly tested, producing contributions to the off-diagonal elements only. The figure shows that ultimately $\beta = 0$ is the optimum choice. In view of the faster rate of convergence for $\beta = 0$, a linear combination of Λ_m with ∇_m provides no advantages over using ∇_m only.

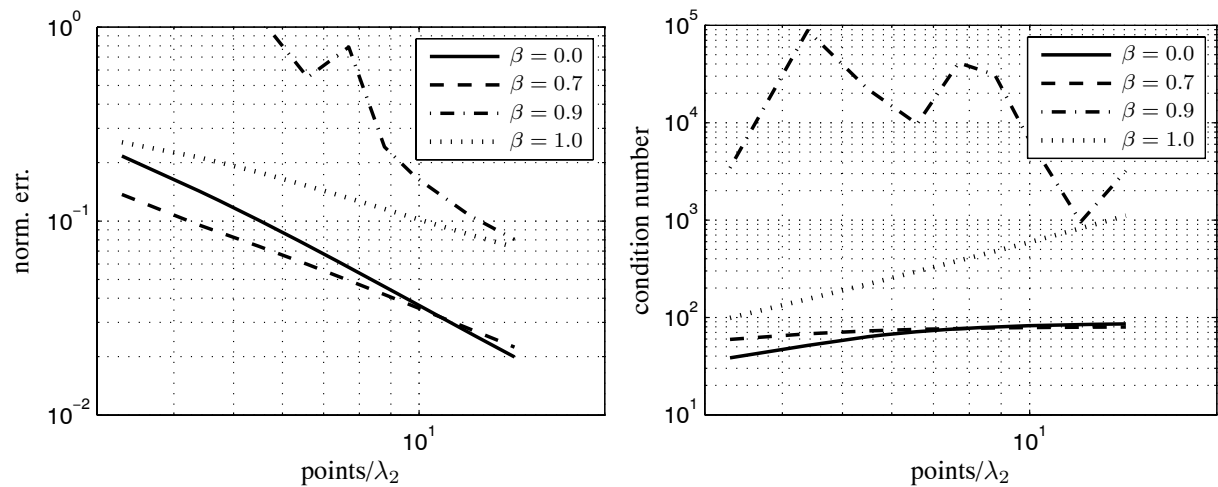


Figure 7.18: The normalized error in the scattered field of the cube (left) and the condition number of the MoM-matrix (right) as a function of the mesh density. The Müller formulation is applied for various combinations of Λ_m - and ∇_m -test functions.

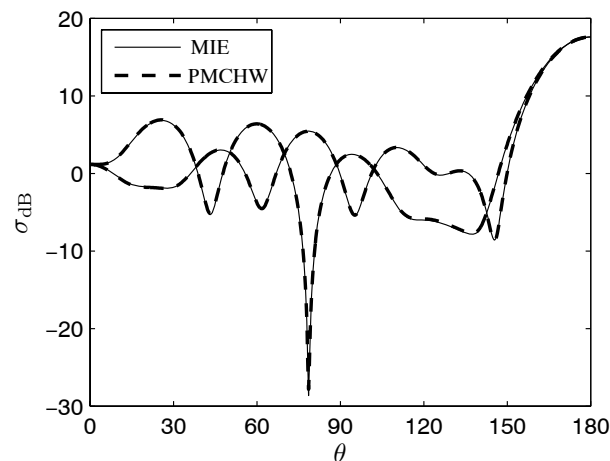


Figure 7.19: The normalized bistatic RCS of a sphere with $k_1 r = 6$, $\varepsilon_{2;r} = 16$ and 2.8 points/ λ_2 .

Finally, let us consider the bistatic RCS of a dielectric scattering object. In Figure 7.19 the bistatic RCS is depicted with $k_1 a = 6$. The results are produced with the PMCHW formulation and compared with the exact solution of the MIE-series. The average RCS error of both polarizations is just about 0.04dB with a modest 2.8 points per wavelength, given the error criterion in Eq. (7.41). In case of an internal resonance as was the case in Figure 7.13, at least eight points per wavelength are required. As with the perfect electric conductors in Section 7.4, an accurate

MoM-matrix element computation error prevents an unnecessarily dense mesh, yielding optimum performance with respect to computational and memory costs. This is an important issue in the 3D LEGO approach. The minimum required mesh density for an accurate rendition of the scattered far-field depends on the smoothness of the scattering surface. Further, the geometric error caused by the fact that the approximate and exact boundaries do not coincide for smooth boundaries influences the accuracy as well, especially in case of electromagnetically small scatterers.

7.6 Embedding of 3D structures

In Chapter 6, the potential applications and the accuracy of the LEGO approach have been investigated for 2D cases. In this section, we demonstrate its application for a full 3D scattering configuration. Further, we consider the degradation of accuracy of the scattered field due to the use of a scattering operator instead of a direct solver. The results presented in this section are intended as a proof of principle. For simplicity we restrict ourselves to far-field scattering.

To validate the LEGO approach for 3D scattering configurations, we consider the two homogeneous dielectric spheres of radius r depicted on the left in Figure 7.20 with relative permittivity $\varepsilon_r = 20$. The spheres are embedded in air with $k_0 r = 1.5$. The dielectric contrast and the frequency of operation are representative for EBG applications. Each sphere is meshed with 192 triangles, which amounts to 288 unknowns. The meshes of the spheres are domain-scaled, which leads to more accurate results (see Section 7.5). In the LEGO approach, we compose the scattering operator of the combined spheres starting from the scattering operators of the individual spheres. Because closed 3D structures are prone to spurious interior resonance modes, we employ LEP-based embedding. Gram matrices are used to construct the transfer matrices.

All electric and magnetic current distributions are expanded in terms of Rao-Wilton-Glisson (RWG) functions, indicated by Λ_n . Further, we restrict ourselves to Galerkin test and expansion. The size of the matrices involved with embedding is a measure of the computational costs, since the pertaining matrix multiplications are the decisive factor. To optimize performance, we want to keep the mesh size as small as possible. Therefore, we aim for maximum accuracy by minimizing the quadrature error. As such, we employ adaptive quadrature rules for the regular test and expansion integral parts and closed-form solutions for the singular integral parts. The relative accuracy of the adaptive quadrature rule is set to 10^{-2} .

Recall that optimum testing of the integral operators L and $K + \hat{n} \times I$, are mutually exclusive, and hence a compromise must be found. In particular, if L which contains the scalar potential is properly tested regarding the mapping properties of the operator, the same test function will lead to an ill-conditioned matrix for $K + \hat{n} \times I$, which may jeopardize the stability of the solution. Despite the application of the inverse Gram matrix, similar conflicting demands occur regarding the choice of an appropriate test function for the 3D implementation of the LEGO approach. In Section 4.4 we have argued that the condition number of the Gram matrix is an indication of the well-posedness of the problem and therefore the stability of the solution. The elements of the Gram matrix are given by the duality product $\langle \mathbf{f}_m, \hat{n} \times \mathbf{f}_n \rangle$, where \mathbf{f}_m and \mathbf{f}_n are the test and expansion functions. In addition, in Section 7.5 we have established that the best accuracy is attained if L is properly tested, i.e., $\mathbf{f}_m = \Lambda_m$. Since $\mathbf{f}_n = \Lambda_n$, optimum testing regarding accuracy amounts to an ill-conditioned Gram matrix, which leads to unstable solutions. As a compromise, we have applied the linear combination, $\beta \Lambda_m + (1 - \beta) \mathcal{V}_m$, where $\mathcal{V}_m = \hat{n} \times \Lambda_m$, as the test function in the LEGO approach. The combination constant β has been set to $\beta = 0.8$, as it turned out to be an overall good choice.

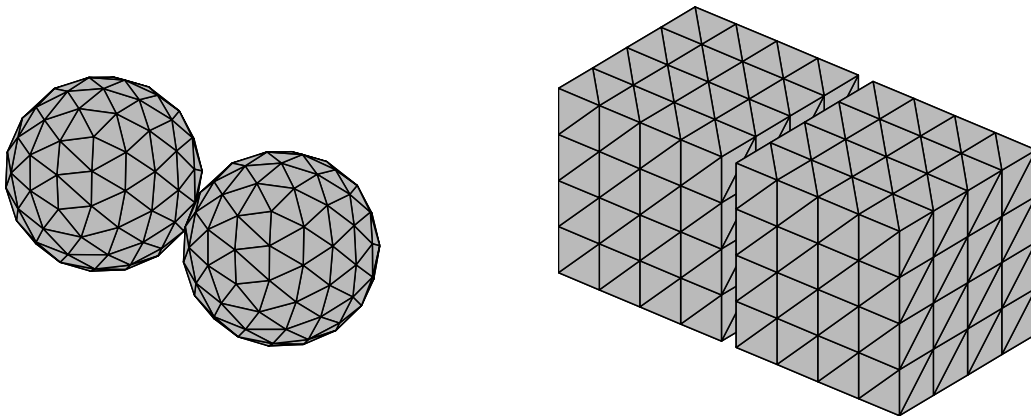


Figure 7.20: On the left, two dielectric spheres with radius r and relative permittivity $\varepsilon_r = 20$. The frequency is such that $k_0 r = 1.5$. Each sphere is meshed with 192 triangles (288 unknowns). On the right, two cubical domains that enclose the two spheres. The cubical domains are meshed with 192 triangles (288 unknowns). The size of the domains is $2.2r$ and the distance between both domains is $0.2r$.

First, we construct the scattering operator of a single sphere inside a single cubical scattering domain illustrated on the right in Figure 7.20 with lattice constant $a = 2.2r$. The minimum distance between the boundary of a sphere and the enclosing cube is thus $0.1r$. The average triangle edge length of the mesh of the dielectric sphere correspond to 2.4 and 11 points per wavelength in the interior and exterior media, respectively. For the cubical scattering domain, we take a mere 192 triangles, which amounts to an average mesh density of 6.7 points per wavelength

for the cube. In Section 7.5, we have established that despite such coarse mesh densities, good accuracy can already be attained for the scattered far-field of dielectric 3D objects.

For the near-field scattering from a single sphere, the analytic expressions determined in Appendix B.2 may be applied. However, to investigate the loss of accuracy associated with the construction of the elementary scattering domains for a more general case, we apply the approach that accounts for an arbitrarily shaped scattering object. Therefore, we employ the PMCHW integral equation for the scattering properties of the sphere. The elementary scattering operator is thus constructed via Eq. (4.30). In short, the incident field is propagated from the cube to the sphere. The equivalent currents that follow from the PMCHW integral equation are transferred back to the cube. Note that the PMCHW integral equation is tested with Λ_m -functions only.

The scattered far field is evaluated in terms of the bistatic RCS as defined in Eq. (7.40). In Figure 7.21, the bistatic radar cross-section (RCS), σ_{dB} , of a single sphere is shown for the E - and H -plane. The RCS has been determined via the direct PMCHW approach on the surface of the sphere (solid) and via the scattering operator on the surface of the cube (dashed). To quantify the RCS error we have applied the average error norm defined in Eq. (7.41). Via the direct PMCHW approach, the corresponding average error in the RCS is 0.03dB in comparison with the exact solution via the *Mie series* (not shown). To investigate the degradation of the accuracy of the scattered field due to the cubical scattering domain we compare the RCS plot of the elementary scattering operator with the PMCHW results, which yields an error of 0.11dB. Hence, the additional RCS error by considering the scattering operator instead of the direct PMCHW approach seems small. In view of the coarseness of the mesh, the non-smoothness of the cubical boundary and the small distance between the boundaries of the cube and sphere, the accuracy attained with the scattering operator may be regarded as excellent.

Second, the scattering operator of a single sphere is combined with itself in the embedding procedure to arrive at the scattering operator of the two spheres. The computational scheme as presented in Table 4.2 has been applied for the embedding procedure. The direct transfer of current amplitudes is not applicable in this example, as there are no common boundary parts. The composite configuration is shown in Figure 7.20 with the original spheres (left) and the pertaining scattering domains (right). To illustrate the coarseness of the applied mesh sizes, the actual meshes are shown to scale. The distance between the two cells is $0.2r$, which is about half the average edge length of a triangle. The high refractive index of the spheres in combination with the small distance between them guarantee strong field interactions between the scattering domains, for which the LEGO approach is well suited.

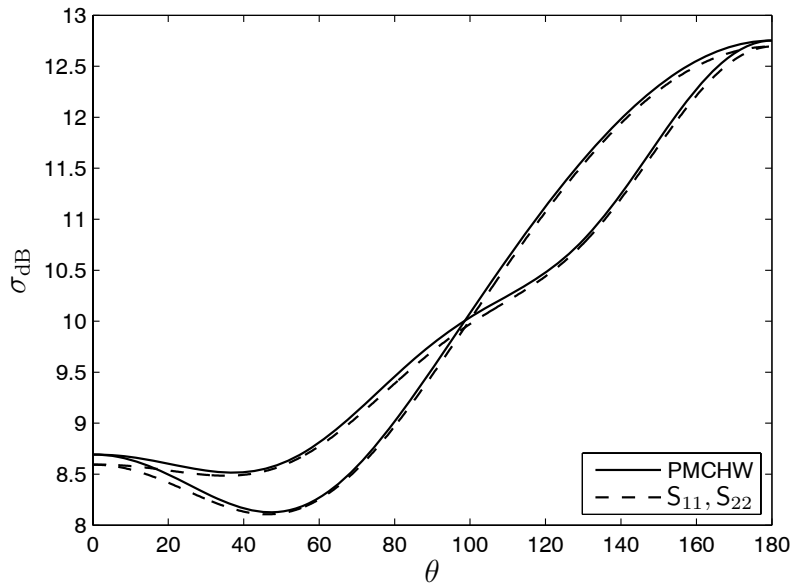


Figure 7.21: The bistatic RCS, σ_{dB} , for the E - and H -plane cross-sections of a single dielectric sphere on the left in Figure 7.20. The solid and dashed lines are the results computed with the PMCHW integral equation, and with the scattering operator S_{11} of the sphere inside a single cubical scattering domain on the right in Figure 7.20.

In Figure 7.22, the bistatic RCS of the two spheres is shown. With reference to Figure 7.20, the plane wave is incident from above with the E -plane aligned with the direction of translation of the spheres. The result of applying the direct PMCHW approach are included as a reference. The results of the combined scattering operator that follows from the embedding procedure agree very well with the reference solution. More specifically, the average error in the bistatic RCS of the embedded spheres via combined scattering operator is 0.25dB in comparison with the PMCHW results. This is remarkable regarding the coarseness of the discretization. Further, it is possible that the deviations should partly be attributed to the PMCHW formulation.

Finally, let us comment on the computational costs associated with 3D scattering configurations. The application of scattering matrices in combination with all matrix multiplications involved with LEGO may seem significantly more computationally expensive than the use of a regular direct solver. On the contrary, in case of a closely packed structure (large common boundary parts) and a high reusability of previously combined domains, LEGO is quite competitive, especially for those cases where the response from multiple different excitations are examined. In particular, at best, the computational cost of LEGO may only increase as $\mathcal{O}(N^2)$ with N a measure of the domain size. This has been demonstrated in Section 4.8.

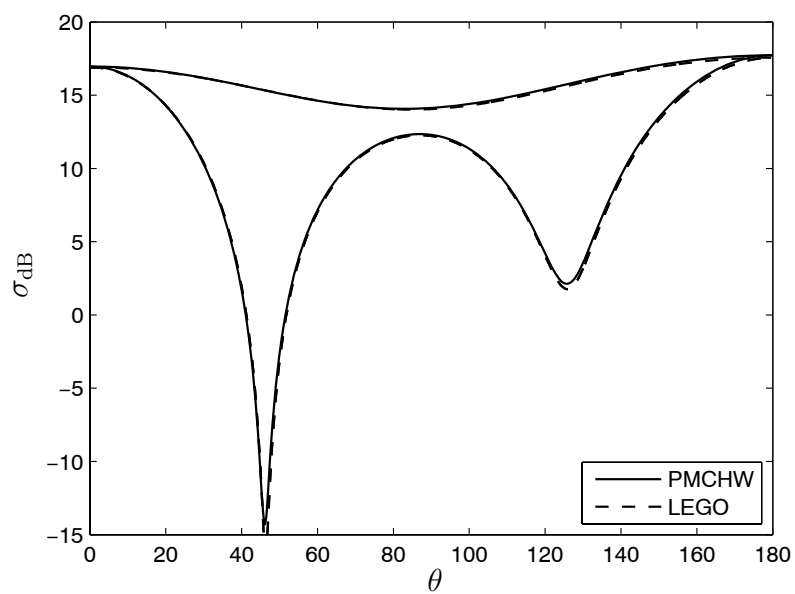


Figure 7.22: The bistatic RCS, σ_{dB} , for the E - and H -plane cross-sections of the two dielectric spheres depicted on the left in Figure 7.20, computed with the PMCHW integral equation (solid lines) and with the scattering operator of the combined spheres obtained with the LEGO procedure (dashed lines).

Chapter 8

Conclusions and recommendations

The fierce competition that businesses are facing calls for ongoing reductions in product development time. Owing to the speed of modern computers, it has recently become possible to use numerical methods to predict the behavior of the final product. Thus, the slow construction and measurement cycle may be shortened. The initial product design draft is normally arrived at via a systematic top-down approach, in which the product is regarded as a tree of interacting product constituents, the building blocks, each with their own specific (sub)system's response. Conversely, in device design one often follows a bottom-up approach, in which the building blocks are designed separately to set specifications before assembly. In electromagnetic design, the optimization and sensitivity analysis often involves straightforward but time-consuming parameter sweeps that require a full recomputation of the entire device. Such brute force approaches are not in line with the desired systematic design approach. Although recently "marching on in anything" [9] has been introduced to accelerate parameter sweeps, these techniques are not available in present commercial software packages.

We have proposed a modular modeling procedure that describes the electromagnetic interaction between large finite structures, called linear embedding via Green's operators (LEGO). We have started by constructing the linear Green's operators via Huygens' principle with equivalent boundary current sources that electromagnetically characterize the interaction of a specific building block with its environment, as a continuous multi-port system. Such a Green's operator is a scattering operator. In its most elementary form, we have generalized an embedding procedure introduced in inverse scattering to describe multiple scattering between adjacent blocks, by considering one of the blocks as the environment of the other and vice versa. Subsequently, scat-

tering operators have been merged to compose a combined block and common boundaries have been removed. We have validated the principle of LEGO for both 2D and 3D configurations.

A cascade of embedding steps can be employed to form scattering operators that fully characterize various types of larger complex composite blocks. We have demonstrated this principle via the construction of large finite electromagnetic bandgap (EBG) structures. In addition, we have shown that in a sequence of LEGO steps it remains possible to describe the complete interior field within previously combined subdomains. In fact, with each subsequent LEGO step one may choose for which of the subdomains the interior fields are preserved and updated for the presence of additional domains. By building large databases, previously combined blocks may be reused at will. Owing to its modular approach, LEGO is in line with the preferred systematic approach of a design process. Further, LEGO is suitable for parallel or distributed processing.

Device design often involves tuning local medium properties in a compact designated domain within a large environment. We have shown that, through an additional embedding step, the equivalent sources on the boundary of the large environment can be transferred to the boundary of the designated domain, so that subsequent design steps can be carried out with great efficiency. This two-stage optimization process has been applied in the local tuning of the transmission properties at the Y-junction of a power splitter, and in the local tuning of a mode splitter in EBG waveguide technology.

We have implemented LEGO using boundary integral equations for the evaluation of the equivalent sources on the subdomain boundaries, as well as for the fields scattered by the homogeneous or perfectly conducting objects of arbitrary shape inside those subdomains. We have explained that various electromagnetic solution methods may be used instead, e.g., to allow for inhomogeneous objects. On the other hand, LEGO may be integrated within existing software packages. Further, we have demonstrated that scattering objects may also be continuous beyond domain boundaries. Moreover, since the frequency is kept fixed, LEGO automatically applies to dispersive and lossy media. We have a large freedom of choice regarding the shape of a scattering domain. For instance, in contrast with plane-wave methods, we may consider closely packed objects for which a rectangular mesh no longer suffices. In case of canonical scatterers, we may conveniently choose the building blocks to contain a single cell only. Further, the shape may be selected so as to achieve minimum outer boundary size and thus optimum efficiency in a sequence of embedding steps. Moreover, the flexibility in selecting the domain shape allows for a strategic choice as far as the reusability of the building blocks is concerned. In view of the above, LEGO may be regarded as a versatile general-purpose method.

Further, we have shown that the scattering operator of LEGO may be applied to compute the band diagram of EBG structures. Two alternative methods have been proposed to solve the pertaining eigenvalue problem.

We have quantified the accuracy of the LEGO method for both Schelkunoff's and Love's equivalence principle (SEP and LEP). The convergence of the scattered field as a function of the mesh density obtained with LEGO is of the same order as that obtained with an integral equation for the scattering from dielectric or perfectly conducting objects. For similar test and expansion functions, the LEGO approach leads to more accurate fields with SEP than with LEP. However, if a coarse quadrature rule is used for the test and expansion integrals, e.g., the midpoint rule, LEP in combination with Gram matrices is superior. Further, we have demonstrated that the construction of the elementary building blocks and the removal of common boundaries may lead to interior resonances for LEGO based on SEP. These resonances can not be suppressed with a combined-field integral equation or a singular value decomposition, since these resonances are physical modal solutions. On the contrary, LEGO based on LEP is free of interior resonances, which makes it more robust than SEP. In general, the dependence on the shape of the elementary scattering domains, the accumulation of errors due to long LEGO sequences, and the choice of building sequence have turned out to be negligible for both SEP and LEP.

At various stages in the LEGO approach we define separate source and observation boundaries, and a source transfer operation from one to the other. For coinciding source and observation boundary parts, this transfer operation can be made more efficient via a direct transfer of the corresponding current parts. For the remaining boundary parts, currents are transferred via either Huygens' principle or Oseen's extinction theorem. We have indicated that some care has to be taken in the direct transfer of current amplitudes with the Gram matrix.

The matrix multiplications that occur in the computational scheme of the LEGO method have proved to be the leading factor in the overall computational costs. Further, LEGO based on LEP is a factor of three to five less efficient than LEGO based on SEP. To attain optimum performance with LEGO, the matrix sizes, and thus the number of unknowns, should be kept as small as possible. Hence, the test and expansion integrals have been determined very accurately throughout to ensure maximum accuracy of the scattered field for the mesh size at hand.

We have illustrated that the most efficient application of LEGO involves a closely-packed configuration of identical elements. In particular, with respect to the number of array elements, the complexity of a sequence of LEGO steps increases as $\mathcal{O}(N^{1.5})$ and $\mathcal{O}(N^2)$ for 2D and 3D con-

figurations, respectively. Although direct solution methods may be more efficient for a single excitation via a multi-level fast-multipole algorithm, LEGO provides a reusable scattering matrix that encompasses the scattered field for all possible excitations. For nearby scattering objects with a large refractive index in comparison with the background medium, the LEGO approach offers additional advantages since, due to a finite distance between the object and the domain boundary, a coarse mesh may be chosen on that boundary without loss of accuracy.

We have investigated integral equations for the scattering from perfectly conducting and dielectric objects to ensure an optimal choice of the discretization for flat-faceted meshes. Further, we have employed piecewise-constant or continuous piecewise-linear functions for 2D and scattering configurations, and Rao-Wilton-Glisson (RWG) functions for 3D ones. For the accuracy of the PMCHW and Müller integral equation in the 2D case, we have illustrated that the difference in formulation only matters for coarse mesh densities, i.e., the non-vanishing singular integral parts eventually limit the convergence to becoming quadratic. We have formulated an alternative integral equation where all dominant singular integral parts vanish for 2D dielectric scatterers (TM case). This leads to cubic convergence, irrespective of the mesh density and object shape. Like the MFIE and Müller's integral equation, the corresponding condition number is independent of the mesh density. Spikes appear in the condition number for the PMCHW and Müller formulations in case of interior cavity modes. In addition to the well-known impedance scaling of the integral equations and the currents, we have proposed additional scaling for Müller's formulation that has led to a further reduction of the condition number. For 2D perfect conductors, the order of convergence varies with the smoothness of the boundary, and is the same for piecewise-constant and linear test and expansion functions, albeit that the magnitude of the error is significantly smaller in the case of the piecewise-linear functions.

Domain scaling of a flat-faceted mesh improves the convergence for scattering objects with a smooth boundary by one order. For the 2D MFIE, this is only the case for piecewise-linear functions. For the 3D MFIE, domain scaling does not improve the convergence rate. For object shapes involving edges or corners, an EFIE leads to more accurate results than its MFIE counterpart. Accordingly, a 3D CFIE or a 2D CFIE with piecewise-constant functions causes a decrease in accuracy in comparison with a pure EFIE. We have used a similar line of reasoning to clarify the inferior results of the 3D Müller formulation in comparison with those of PMCHW. To investigate why domain scaling did not lead to better convergence for piecewise-constant functions, we have regularized the identity operator of the 2D MFIE. This resulted in the same convergence behavior as that of piecewise-linear functions. Further, application of the midpoint rule to the test and expansion integrals in the 2D case has resulted in an increase in magnitude of the error

of the field for piecewise-linear functions. Further, any improvement in the order of convergence owing to domain scaling or singularity cancellations is lost.

8.1 Recommendations

To conclude this thesis, we would like to discuss a few possible applications and extensions of the LEGO approach for future research. Acceleration techniques applied in available boundary integral equations may be used to increase the efficiency of LEGO, e.g., the multi-level fast-multipole algorithm (MLFMA) [121, 122]. Further, for SEP, iterative solvers may be utilized to accelerate the construction of the transfer matrices via a “marching on in anything” scheme [9] in a predictor-corrector scheme. For both SEP and LEP, these techniques may also lead to a reduction of the computational costs of the boundary integral equations that are employed to compose the scattering operator of the elementary building blocks. Finally, since the elementary LEGO blocks and the actual scattering configuration are largely independent, the use of only a few standard domain shapes may suffice for most design applications. Accordingly, by employing entire-domain basis functions for these predefined domain shapes, LEGO may become even more competitive [26, 27].

An interesting extension of LEGO would be de-embedding. For instance, to perform local structure optimization, the designated domain presently has to be identified in advance, i.e., before the surrounding scattering operator is constructed. Otherwise, if part of the designated domain overlaps with the scattering domain, a recomposition of the large scattering domain is inevitable to exclude the subdomains that overlap with the designated domain. With the ability to perform de-embedding this would no longer be necessary, since parts of the large scattering operator could simply be removed. Moreover, the construction of large scattering operators would become more efficient by using only simple large blocks, since local imperfections can be introduced at a later stage. Although the principle of de-embedding is a relatively straightforward reverse embedding process in the absence of common boundaries, de-embedding in case common boundaries have been removed is far more complicated.

The LEGO approach should be considered as a design tool for a range of different applications, e.g., the design of frequency selective surfaces (FSS), large finite antenna integrated arrays or configurations with a few nonlinearly reacting building blocks. A $2\frac{1}{2}$ D extension of 2D LEGO may be a powerful tool for the design of waveguides and cavities embedded in EBG membranes.

Further, by enforcing periodicity in one or two directions, EBG chains and layers may be constructed which in turn may be combined with other structures with the same periodicity. Possible applications may be sources above EBG structures of finite thickness, or, in combination with the optimization stage of LEGO, the computation of band diagrams of linear-defect EBG waveguides using supercells.

The fast optimization stage of LEGO has been demonstrated by means of straightforward parameter sweeps. Existing optimization strategies may be incorporated to attain further acceleration, e.g., gradient-based or genetic algorithms [123, 124]. Although LEGO via SEP lacks the robustness of LEGO via LEP as regards the suppression of interior resonances, it is more efficient and accurate than LEGO via LEP. Therefore, it may still be worthwhile to properly suppress these resonances for LEGO via SEP. Further research is required to determine the most efficient and effective method for LEGO. Only one of the two proposed methods to compute the band diagrams of EBG structures has been implemented. The other method may be more efficient for small systems. A comparison of both methods is recommended. Only scattering operators that are based on LEP can be used with the approach that we have followed. The efficiency of the method may be improved through an extension that applies to SEP as well.

For closely packed configurations, we have shown that LEGO is especially well suited if neighboring blocks are fully concatenated, i.e., if common boundaries are removed. For this, the use of scattering domains with non-smooth boundaries becomes inevitable. From the analysis of boundary integral equations, we have determined that these irregularities in the boundary are decisive for the accuracy of the resulting scattered field. In the LEGO approach we have so far restricted ourselves to uniform meshes. The introduction of graded meshes to create a relatively more dense mesh near the irregularities in the boundary could therefore improve the performance of LEGO.

Since the superiority of the PMCHW over the Müller formulation for 3D scattering configurations is caused by the poor testing of the MFIE part with RWG functions, a systematic search for other test functions may be fruitful. Further, for circular cylinders and spheres we have illustrated that the domain scaling of a flat-faceted mesh increases the convergence rate by one order. It may be worthwhile to investigate whether a simple scheme can be formulated such that domain scaling may also lead to an improvement for smooth scattering objects of a more general shape.

Appendix A

Analytical parts of 2D integrals

In the discretization of the 2D integral equations by proper test and expansion functions, the integrand is singular for coinciding source and observation points. The singular integrand parts may be integrated analytically. In Section 5.4 we have presented the general approach to cast these singular integral parts in the form of two generic singular double integrals in terms of local coordinates. In Section A.1, we present the solution of the remaining singular double integrals. Since the integrand may involve a logarithm, which is a multiply-valued function, care must be taken that no branch cuts are crossed. In Section A.2, the conditions for such a prohibited branch cut crossing are determined, and a simple remedy is presented, which amounts to a rotation of the branch cut in the complex plane. For (partially) overlapping test and expansion functions, the so-called self term, analytical solutions are provided in Section A.3 for both the regular and singular parts of the double integral by means of a series expansion of a modified Bessel function.

A.1 Evaluation of the singular integrals

In the evaluation of the singular integral parts discussed in Section 5.4, the solutions to the following two singular double integrals are yet to be determined, i.e.,

$$I_a[f] = \int_{-1}^1 \int_{-1}^1 f(\eta, \xi) \frac{1}{\xi - \eta q_1 - q_0} d\xi d\eta, \quad (\text{A.1})$$

and

$$I_b[f] = \int_{-1}^1 \int_{-1}^1 f(\eta, \xi) \ln(d_n [\xi - \eta q_1 - q_0]) \, d\xi \, d\eta, \quad (\text{A.2})$$

with $f(\eta, \xi) \in \{1, \xi, \eta, \eta\xi\}$. All combinations of applied test and expansion function combination can be expressed in terms of I_a and I_b . In this section, we ignore the presence of the branch cut of the logarithm, which is accounted for in Section A.2. The integration of the inner (expansion) integral is straightforward for $I_a[f]$,

$$\int_{-1}^1 f(\eta) \int_{-1}^1 \frac{1}{\xi - \eta q_1 - q_0} \, d\xi \, d\eta = \int_{-1}^1 f(\eta) \ln \left(\frac{1 - \eta q_1 - q_0}{-1 - \eta q_1 - q_0} \right) \, d\eta, \quad (\text{A.3})$$

in case $f(\eta, \xi) = f(\eta)$, and

$$\int_{-1}^1 f(\eta) \int_{-1}^1 \frac{\xi}{\xi - \eta q_1 - q_0} \, d\xi \, d\eta = \int_{-1}^1 f(\eta) \left[2 + (q_0 + \eta q_1) \ln \left(\frac{1 - \eta q_1 - q_0}{-1 - \eta q_1 - q_0} \right) \right] \, d\eta, \quad (\text{A.4})$$

in case $f(\eta, \xi) = \xi f(\eta)$. These intermediate results indicate that the integrand of the test integral also has a logarithmic singularity, which implies that proper care must be taken to avoid integration across a branch cut.

Via subsequent application of the standard indefinite integral in [125, Eq. (2.723.1)], solutions may be obtained for I_a and I_b . Upon defining the constants

$$\begin{aligned} A_1 &\equiv 1 - q_1 - q_0, \\ A_2 &\equiv 1 + q_1 - q_0, \\ A_3 &\equiv -1 - q_1 - q_0, \\ A_4 &\equiv -1 + q_1 - q_0, \end{aligned} \quad (\text{A.5})$$

together with,

$$\begin{aligned} B_i &\equiv A_i \ln(A_i), \\ C_i &\equiv A_i B_i, \end{aligned} \quad (\text{A.6})$$

for $i \in [1, 4]$, the solutions to $I_a[f]$ read

$$\begin{aligned}
I_a[1] &= -\frac{1}{q_1} [B_1 - B_2 - B_3 + B_4], \\
I_a[\xi] &= \frac{1}{2q_1} [B_1A_3 - B_2A_4 - B_3A_1 + B_4A_2 + 4q_1], \\
I_a[\eta] &= -\frac{1}{2q_1^2} [B_1A_2 - B_2A_1 - B_3A_4 + B_4A_3 + 4q_1], \\
I_a[\eta\xi] &= \frac{1}{6q_1^2} [B_1(A_3(2q_1 - q_0) - 2) + B_2(A_4(2q_1 + q_0) + 2) \\
&\quad - B_3(A_1(2q_1 - q_0) - 2) - B_4(A_2(2q_1 + q_0) + 2) + 4q_0q_1].
\end{aligned} \tag{A.7}$$

The integral $I_b[f]$ may be expressed in terms of the same constants, i.e.,

$$\begin{aligned}
I_b[1] &= -\frac{1}{2q_1} [C_1 - C_2 - C_3 + C_4] - 6 + 4 \ln(d_n), \\
I_b[\xi] &= \frac{1}{6q_1} [C_1(A_3 - 1) - C_2(A_4 - 1) - C_3(A_1 + 1) + C_4(A_2 + 1) - 8q_0q_1], \\
I_b[\eta] &= -\frac{1}{6q_1^2} [C_1(A_2 + q_1) - C_2(A_1 - q_1) - C_3(A_4 + q_1) + C_4(A_3 - q_1) - 8q_0q_1], \\
I_b[\eta\xi] &= \frac{1}{24q_1^2} [C_1(3A_3A_2 + 2q_0A_1) - C_2(3A_4A_1 + 2q_0A_2) \\
&\quad - C_3(3A_1A_4 + 2q_0A_3) + C_4(3A_2A_3 + 2q_0A_4) - 4q_1(3 + q_0^2 + 3q_1^2)].
\end{aligned} \tag{A.8}$$

In turn, the analytical expressions for the singular double integrals for any of the combinations of test and expansion functions simply follow from a linear combination of $I_a[f]$ and $I_b[f]$.

If the midpoint rule is applied to the test integral, the integral over Γ_m becomes proportional to its value at the edge centroid, $\rho_m = \rho_m^c$. This is equivalent to multiplying $f(\eta, \xi)$ by $\delta(\eta)$ in the original double integrals. For the remaining single integrals, the solutions read

$$\begin{aligned}
I_a[1] &= \ln \left(\frac{1 - q_0}{-1 - q_0} \right), \\
I_a[\xi] &= 2 + q_0 \ln \left(\frac{1 - q_0}{-1 - q_0} \right), \\
I_b[1] &= (1 - q_0) \ln(1 - q_0) - (-1 - q_0) \ln(-1 - q_0) - 2 + 2 \ln(d_n), \\
I_b[\xi] &= -q_0 + \frac{1}{2}(q_0^2 - 1) \ln \left(\frac{1 - q_0}{-1 - q_0} \right).
\end{aligned} \tag{A.9}$$

Note that q_1 no longer appears in the expressions, because the solution is independent of the orientation of the observation edge, and thereby is independent of the angles ψ_m and ϕ .

A.2 The avoidance of branch cuts

Let us consider integrals over a domain of integration defined by $\{\xi, \eta\} \in (-1, 1)$, with integrands that contain a logarithm of the form $\ln(\zeta)$, where the argument

$$\zeta = \xi - \eta q_1 - q_0 \tag{A.10}$$

assumes all values inside a parallelogram centered about q_0 in the complex ζ -plane. The integrals considered here arise from convergent integrals involving test and expansion functions over edges of a discretized boundary, and a logarithmic kernel with an argument that is proportional to the distance between the respective points on the respective edges. The geometric parameters are completely captured by the complex parameters q_0 and q_1 . The parallelogram in the ζ -plane is shown on the left of Figure A.1.

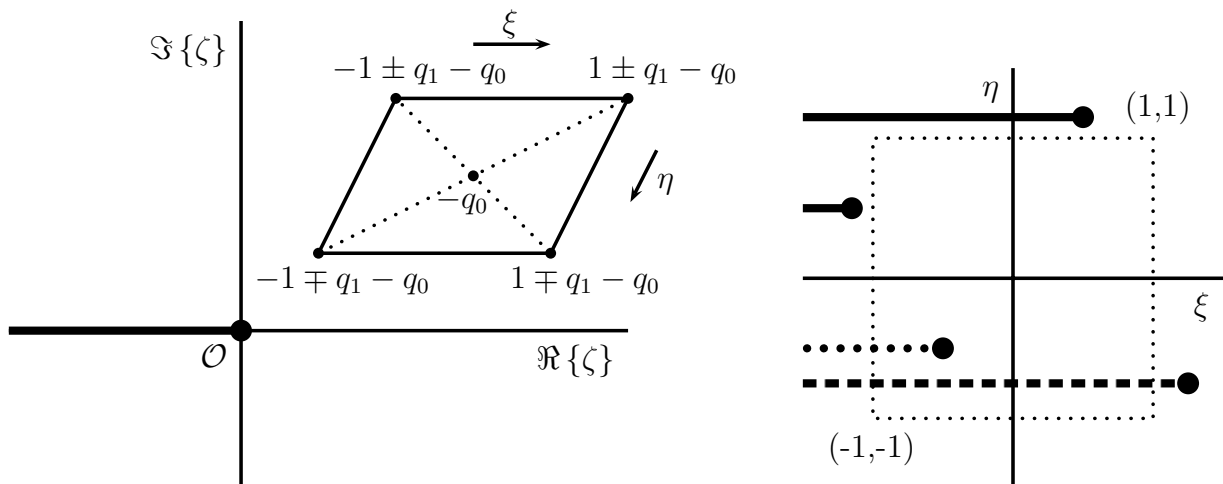


Figure A.1: On the left, the argument of the logarithm is shown as a function of the integration area in the complex plane where the branch cut is indicated. On the right, some possible positions of the branch cut are depicted as a function of ξ and η . The dotted branch cut is implausible since the branch point must lie outside the dotted parallelogram, whereas the dashed branch cut is subject to rotation.

The logarithm is a multiple-valued function, with a branch point at the origin of the complex plane. The principal branch of the logarithm is defined on a Riemann sheet with a branch cut that coincides with the negative real axis, $(-\infty, 0)$. Since the edges do not cross, and the end points of the edges can be excluded from the integration, the branch point must be located outside the domain of integration. However, due to the various algebraic manipulations by which we have

arrived at logarithms of a generic form $\ln(\zeta)$, the branch cuts may have been rotated or even deformed, such that the branch cut may now inadvertently intersect the domain of integration into two parts. This is illustrated on the right of Figure A.1. The remedy is simple, i.e., we may deform the branch cut until it no longer cuts the domain of integration. Since the branch point must lie outside the parallelogram in the complex ζ -plane, a simple rotation of the branch cut over 180 degrees about the origin will suffice. Since the ξ -integral ranges from -1 to 1 , and the logarithm in the integrand is multiplied by a function of either even or odd parity with respect to ξ , the rotation of the branch cut amounts to performing the substitutions $q_0 \rightarrow -q_0$ and $q_1 \rightarrow -q_1$, together with a possible overall change of sign in case of odd parity with respect to ξ .

The branch cut associated with the principal branch in the complex ζ -plane may be parameterized by $\zeta = -p$ with $p \geq 0$. Inversion of Eq. A.10 for ξ, η leads to

$$\begin{bmatrix} \xi \\ \eta \end{bmatrix} = \begin{bmatrix} -p + q_{0\Re} - q_{1\Re}q_{0\Im}/q_{1\Im} \\ -q_{0\Im}/q_{1\Im} \end{bmatrix}. \quad (\text{A.11})$$

Hence, the branch cut (completely) cuts the domain of integration, if and only if

$$|q_{0\Im}/q_{1\Im}| \leq 1 \quad \text{and} \quad q_{1\Re}q_{0\Im}/q_{1\Im} \leq q_{0\Re} - 1. \quad (\text{A.12})$$

If the conditions in Eq. A.12 are met, the substitutions described above should be performed. In the evaluation of these conditions, special care must be taken to avoid that round-off error leads to erroneous decisions. Table A.1 summarizes whether a minus sign should be included in the solution of I_a and I_b after rotating the integration domain around the origin for the various combinations of $f(\eta, \xi)$. Obviously, the opposite results of Table A.1 hold for the product $q_1 I_a[f]$, required for the singular integral in Eq. (5.74).

$f(\eta, \xi)$	$I_a(f)$	$I_b(f)$
1	yes	no
ξ	no	yes
η	yes	no
$\eta\xi$	no	yes

Table A.1: An overview of the integrals $I_a[f]$ and $I_b[f]$, indicating whether a minus sign is to be included after rotation of the integration domain for the terms in $f(\eta, \xi)$.

A.3 Self term

In case the test and expansion function edges under consideration coincide, the most commonly used approach is described in [73]. Below we show that it is possible to derive an analytical expression not only for the singular part of the integral, but also for the regular part up to a desired order of accuracy. Since this avoids the repeated evaluation of Bessel functions, we regard our approach as a more elegant and efficient approach.

With reference to Figure 5.5, the inner product $\hat{\nu} \cdot (\boldsymbol{\rho}_m - \boldsymbol{\rho}_n)$ is zero for $\Gamma_m = \Gamma_n$. In that case, we only need to consider the testing and expansion of the operator L , which involves the modified Bessel function of the second kind of order zero, K_0 , which may be expanded in a convergent series according to [126, Eq. 9.6.54]

$$K_0(2z) = \sum_{k=0}^{\infty} \frac{[\Phi(k) - \ln(z)] z^{2k}}{(k!)^2}. \quad (\text{A.13})$$

Here, $\Phi(k)$ is a harmonic number, which follows from the truncated harmonic series,

$$\Phi(k) = \begin{cases} -\gamma_E + \sum_{n=1}^k \frac{1}{n}, & \text{for } k \neq 0, \\ -\gamma_E, & \text{for } k = 0, \end{cases} \quad (\text{A.14})$$

where γ_E is Euler's constant. Since the test and expansion edges coincide, d_R and the angles ψ_m, ψ_n and ϕ in Figure 5.5 all vanish. As a consequence, Eq. (5.67) reduces to

$$|\boldsymbol{\rho}_m - \boldsymbol{\rho}_n|^2 = d^2 |\xi - \eta|^2, \quad (\text{A.15})$$

where $d = d_m = d_n$.

With Eq. (A.15), the resulting integral for the self term may be written in local area coordinates as

$$I_s(f) = \int_{\hat{c}_m} f_m(\boldsymbol{\rho}) \int_{\hat{c}_n} f_n(\boldsymbol{\rho}') K_0(\gamma |\boldsymbol{\rho} - \boldsymbol{\rho}'|) d\ell' d\ell = d^2 \int_{-1}^1 \int_{-1}^1 f(\eta, \xi) K_0(\gamma d |\xi - \eta|) d\xi d\eta. \quad (\text{A.16})$$

The integral I_s is carried out separately for each term in the series representation of K_0 . With the definition $p = \gamma d$, the solutions to I_s for the various combinations of test and expansion

functions in Eq. (5.69) are given by

$$\begin{aligned}
I_s[\delta(\eta)] &= 2d \sum_{k=0}^{\infty} \frac{1 + (1 + 2k)[\Phi(k) - \ln(p/2)]}{(1 + 2k)^2 (k!)^2} \left(\frac{p}{2}\right)^{2k}, \\
I_s[1] &= 2d^2 \sum_{k=0}^{\infty} \frac{3 + 4k + 2(1 + k)(1 + 2k)[\Phi(k) - \ln(p)]}{(1 + k)^2 (1 + 2k)^2 (k!)^2} p^{2k}, \\
I_s[\eta\xi] &= 2d^2 \sum_{k=0}^{\infty} \frac{2 - k [2(1 + k)(1 + 2k)(2 + k)[\Phi(k) - \ln(p)] + k(7 + 4k)]}{(1 + k)^2 (1 + 2k)^2 (2 + k)^2 (k!)^2} p^{2k}.
\end{aligned} \tag{A.17}$$

The integrals $I_s[\xi]$ and $I_s[\eta]$ are zero because the argument of K_0 in Eq. (A.16) is an even function of $(\xi - \eta)$, whereas the product of the corresponding test and expansion functions $f(\eta, \xi)$, are odd functions of $(\xi - \eta)$. The self term for a certain combination of test and expansion function, follows as a linear superposition of the obtained integral series I_s .

In Eq. (A.15) it is assumed that $\hat{\tau}_m$ and $\hat{\tau}_n$ are oriented in the same direction. This covers the (standard) cases where the MoM approach is applied to determine the scattered field from an object, as in Chapter 3, in the LEGO concept. However, $\hat{\tau}_m$ and $\hat{\tau}_n$ may be oppositely directed for the common contour parts of adjacent domains. If this is the case, either the sign of ξ or η changes in Eq. (A.15), which implies that the sign of $I_s[\eta\xi]$ must be reversed.

The summations in Eq. (A.17) may be truncated. Because the number of terms that is required for sufficient accuracy is inherently related to the maximum value of the argument of K_0 , and hence to the applied discretization via γd , we first determine an upper bound for the argument. For practical applications it is reasonable to assume that the used mesh density satisfies the Nyquist criterion. In that case, the edge length L must be smaller than half a wavelength, i.e., $\lambda > 2L$. With this in mind, an upper bound may be deduced for the argument of K_0 . Because γL is the largest value of the argument of K_0 within the integration range of I_s , we have

$$|\gamma L| = \left| \frac{\omega L}{c} \right| = \frac{2\pi L}{\lambda} < \pi. \tag{A.18}$$

Accordingly, with the substitution of $z = \pi$ in the expression for K_0 we find that truncation after 15 terms guarantees an accuracy of 10^{-16} if the applied mesh density meets the Nyquist criterion. With respect to the numerical implementation, it is computationally efficient to determine the coefficients in the series in a pre-processing stage, as only p may vary. In case of a uniform discretization, p is constant and a single evaluation of I_s suffices.

Appendix B

Scattering from canonical objects

The analytical expressions formulated in this appendix may be used to construct the scattering operator of a domain in case it contains a single circular cylinder or a sphere. After successive embedding steps these analytic solutions are also used to construct the complete interior field within that domain, i.e., the field due to the interaction with other embedded domains. Furthermore, the resulting expressions may also be used as a reference solutions for the assessment of the accuracy of the numerical implementations of the 2D and 3D boundary integral equations. Accordingly, interior and exterior scattered fields are required for both electric and magnetic sources outside a circular cylinder or a sphere. The expressions formulated below are merely included for completeness of the work [38].

B.1 Scattering by circular cylinders

Below, we determine analytical solutions for the field scattered by a dielectric circular cylinder with radius a , due to the action of a line-source positioned at ρ' exterior to the cylinder. The cylinder contains a homogeneous material with $\varepsilon = \varepsilon_2$ and $\mu = \mu_2$, and is centered about the origin. The background medium is homogeneous with $\varepsilon = \varepsilon_1$ and $\mu = \mu_1$. Only the TM-case is treated, as the TE-case readily follows by duality, since both μ and ε contrasts are taken into account.

Before we proceed with the derivation of the Green's function for a circular cylinder, let us first

determine the 2D free-space Green's function in the homogeneous background medium, and express its solution in terms of cylindrical coordinates. The Green's function $G(\boldsymbol{\rho}, \boldsymbol{\rho}')$ is defined as the solution of the scalar Helmholtz equation,

$$[\nabla_t^2 - \gamma_1^2] G(\boldsymbol{\rho}, \boldsymbol{\rho}') = -\delta(\boldsymbol{\rho} - \boldsymbol{\rho}'). \quad (\text{B.1})$$

In terms of cylindrical coordinates, this becomes,

$$\left[\frac{1}{\rho} \partial_\rho \rho \partial_\rho + \frac{1}{\rho^2} \partial_\phi^2 - \gamma_1^2 \right] G(\rho, \phi) = -\frac{\delta(\rho - \rho') \delta_{2\pi}(\phi - \phi')}{\rho}, \quad (\text{B.2})$$

where for convenience the dependence of the Green's function on the source position is omitted. The function $\delta_{2\pi}$ is a 2π -periodic continuation of the delta function. To utilize the invariance of the configuration we apply a Fourier transformation with respect to the angular coordinate ϕ ,

$$G_n(\rho) = \frac{1}{2\pi} \int_0^{2\pi} G(\rho, \phi) e^{-jn\phi} d\phi, \quad (\text{B.3a})$$

$$G(\rho, \phi) = \sum_{n=-\infty}^{\infty} G_n(\rho) e^{jn\phi}. \quad (\text{B.3b})$$

Accordingly, Eq. (B.2) becomes

$$\left[\frac{1}{\rho} \partial_\rho \rho \partial_\rho - \left(\frac{n}{\rho} \right)^2 - \gamma_1^2 \right] G_n(\rho) = -\frac{\delta(\rho - \rho') e^{-jn\phi'}}{2\pi\rho}. \quad (\text{B.4})$$

The corresponding homogeneous solutions are linear combinations of the n^{th} -order modified Bessel functions I_n and K_n of the first and second kind, respectively. In view of Eq. (B.4), $G_n(\rho)$ must be continuous upon crossing $\rho = \rho'$. Demanding that G_n remains regular for $\rho \downarrow 0$ and satisfies the radiation conditions at infinity, the solution may be cast in the general form,

$$G_n(\rho) = C_n I_n(\gamma_1 \rho_{<}) K_n(\gamma_1 \rho_{>}), \quad (\text{B.5})$$

with $\rho_{>} = \max(\rho, \rho')$ and $\rho_{<} = \min(\rho, \rho')$. After multiplication of Eq. (B.4) by ρ and a subsequent integration over ρ , we find that $\partial_\rho G_n(\rho)$ jumps at $\rho = \rho'$. From this jump condition and the Wronskian relation [126, Section 9.6],

$$I'_n(z) K_n(z) - I_n(z) K'_n(z) = \frac{1}{z}, \quad (\text{B.6})$$

the constant C_n may be determined. This leads to

$$G(\rho, \phi) = \frac{1}{2\pi} \sum_{n=-\infty}^{\infty} I_n(\gamma_1 \rho_{<}) K_n(\gamma_1 \rho_{>}) e^{jn(\phi - \phi')}. \quad (\text{B.7})$$

The 2D Green's function may thus be interpreted as the superposition of cylindrical harmonics with a phase difference and amplitude depending on the source and observation positions. If the line source is positioned at the origin instead, we have $\partial_\phi = 0$, such that $n = 0$ in Eq. (B.4). This leads to the general solution

$$G(\rho) = C_1 K_0(\gamma_1 \rho) + C_2 I_0(\gamma_1 \rho), \quad (\text{B.8})$$

where the Green's function depends on ρ only. The constant C_2 is set to zero to comply with the radiation condition. The remaining constant C_1 is determined by integration of Eq. (B.4) over a small circle around ρ with a radius that approaches zero. Accordingly, with the small argument behavior $\partial_z K_0(z) \sim -\frac{1}{z}$ for $|z| \rightarrow 0$, we obtain $C_1 = \frac{1}{2\pi}$. If the line source is not located at the origin, but at ρ' instead, we have without loss of generality

$$G(\boldsymbol{\rho}, \boldsymbol{\rho}_S) = \frac{1}{2\pi} K_0(\gamma_1 |\boldsymbol{\rho} - \boldsymbol{\rho}'|). \quad (\text{B.9})$$

Note that Eqs. (B.7) and (B.9) are solutions to the same problem. Only the “labeling of the map” regarding the Cartesian coordinate system has been changed.

The Green's function, G^{cyl} , associated with the homogeneous circular cylinder also satisfies a Helmholtz equation like Eq. (B.1), albeit that for $\rho \in (0, a)$ we have $\gamma^2 = \gamma_2^2 = -\omega\epsilon_2\mu_2$, while for $\rho \in (a, \infty)$ we have $\gamma^1 = \gamma_1^2 = -\omega\epsilon_1\mu_1$. The Fourier constituents, G_n^{cyl} , may therefore be written as

$$G_n^{\text{cyl}}(\rho, \rho') = \begin{cases} T_n K_n(\gamma_1 \rho') I_n(\gamma_2 \rho), & \rho < a, \\ R_n K_n(\gamma_1 \rho') K_n(\gamma_1 \rho) + I_n(\gamma_1 \rho_{<}) K_n(\gamma_1 \rho_{>}), & \rho > a, \end{cases} \quad (\text{B.10})$$

where the second term on the right-hand side for $\rho > a$ represents the incident field, G_n^{in} . The remaining terms can be attributed to a G_n^{sc} , which represents the reflected scattered field ($\rho > a$) and the scattered interior field ($\rho < a$).

The unknown scattering amplitudes T_n and R_n are determined by enforcing the boundary conditions at the interface $r = a$. Since this is a source-free interface, boundary conditions of the continuity type hold for the tangential field components. Since $E_z = -s\mu G_n$, the appropriate boundary conditions for G_n imply continuity of

$$\hat{\mathbf{n}} \times \mathbf{E} \rightarrow G_n^{\text{cyl}}(\rho, \rho'), \quad (\text{B.11a})$$

$$\hat{\mathbf{n}} \times \mathbf{H} = \frac{1}{s\mu} \hat{\mathbf{n}} \times \nabla \times \mathbf{E} \rightarrow \frac{1}{\mu} \partial_\rho G_n^{\text{cyl}}(\rho, \rho'), \quad (\text{B.11b})$$

where the source-free counterpart of Eq. (2.10b) is used to arrive at the second condition. After applying these conditions to G_n^{cyl} , a set of linear equations is obtained for the unknown coefficients T_n and R_n . The subsequent introduction of the characteristic denominator

$$d_n = [Z_1 K_n(\gamma_1 a) I_n'(\gamma_2 a) - Z_2 K_n'(\gamma_1 a) I_n(\gamma_2 a)] \quad (\text{B.12})$$

yields

$$R_n = [Z_2 I_n'(\gamma_1 a) I_n(\gamma_2 a) - Z_1 I_n(\gamma_1 a) I_n'(\gamma_2 a)] / d_n, \quad (\text{B.13a})$$

$$T_n = \frac{Z_2}{\gamma_1 a d_n}, \quad (\text{B.13b})$$

for $\rho' > a$, where the Wronskian relation Eq. (B.6) has been used for T_n . For the special case of a PEC, the electric conductivity, and thereby the imaginary part of ε_2 , goes to infinity. Accordingly, the scattering amplitude vanishes, i.e., $T_n = 0$, while R_n reduces to

$$R_n = -\frac{I_n(\gamma_1 a)}{K_n(\gamma_1 a)}. \quad (\text{B.14})$$

A similar expression holds for the PMC, with the exception that R_n is expressed in terms of the derivatives of the Bessel functions.

The field response due to an electric or a magnetic line source may be expressed in terms of G_n^{cyl} by means of Lorentz' reciprocity theorem for reciprocal material media. Let state "a" be generated by an electric source, viz., $\mathbf{J}^a = \delta(\boldsymbol{\rho} - \boldsymbol{\rho}_a) \hat{\mathbf{z}}$. Then, the radiated electric field at $\boldsymbol{\rho}_b$ follows from Eq. (2.41), i.e.,

$$E_z^a(\boldsymbol{\rho}_b) = -s\mu_1 G(\boldsymbol{\rho}_b, \boldsymbol{\rho}_a). \quad (\text{B.15})$$

Substitution of Eq. (B.15) into the counterpart of Eq. (2.10b) yields

$$\mathbf{H}_t^a(\boldsymbol{\rho}_b) = -\frac{1}{s\mu_i} \nabla_t^b \times [\hat{\mathbf{z}} E_z^a(\boldsymbol{\rho}_b)] = -\hat{\mathbf{z}} \times \nabla_t^b G(\boldsymbol{\rho}_b, \boldsymbol{\rho}_a). \quad (\text{B.16})$$

Accordingly, for an electric line source $J_z(\rho') \hat{\mathbf{z}}$ in the presence of a circular cylinder with radius $a < \rho'$, Eqs. (B.15) and (B.16) provide the corresponding fields $E_z(\boldsymbol{\rho}) \hat{\mathbf{z}}$ and $\mathbf{H}_t(\boldsymbol{\rho})$, respectively.

To determine the field response in case of a transverse magnetic line source, we select $\mathbf{M}^b = \delta(\boldsymbol{\rho} - \boldsymbol{\rho}_b) \hat{\boldsymbol{\alpha}}$ for state "b" with $\hat{\boldsymbol{\alpha}}$ parallel to the transverse plane. Applying the reaction theorem, Eq. (2.30) to both states yields

$$E_z^b(\boldsymbol{\rho}_a) = -\hat{\boldsymbol{\alpha}} \cdot \mathbf{H}_t^a(\boldsymbol{\rho}_b) = -(\hat{\boldsymbol{\alpha}} \times \hat{\mathbf{z}}) \cdot \nabla_t^b G(\boldsymbol{\rho}_a, \boldsymbol{\rho}_b). \quad (\text{B.17})$$

Note that ρ_a and ρ_b have been interchanged in the Green's function on account of the source reciprocity of the Green's function. Again, the magnetic field follows from E_z^b via the counterpart of Eq. (2.10b), according to

$$\mathbf{H}_t^b(\rho_a) = \frac{1}{s\mu_i} \hat{\mathbf{z}} \times \nabla_t^a E_z^b(\rho_a). \quad (\text{B.18})$$

Accordingly, for a transverse magnetic line source $M_\alpha(\rho')\hat{\boldsymbol{\alpha}}$ in the presence of a circular cylinder with radius $a < \rho'$, Eqs. (B.17) and (B.18) provide the corresponding fields $E_z(\rho)\hat{\mathbf{z}}$ and $\mathbf{H}_t(\rho)$, respectively. Note that the associated equivalent current distributions on $\partial\mathcal{D}$ that would produce the same field via an appropriate integral representation follow from their definitions, Eq. (5.7).

B.2 Scattering by spheres

Below, we determine analytical solutions for the field scattered by a dielectric sphere with radius a , due to the action of a point source positioned at \mathbf{r}' exterior to the sphere with an arbitrary orientation $\hat{\boldsymbol{\alpha}}$. The sphere contains a homogeneous medium with $\varepsilon = \varepsilon_2$ and $\mu = \mu_2$, and is centered about the origin. The background medium is homogeneous with $\varepsilon = \varepsilon_1$ and $\mu = \mu_1$. In a 2D configuration, the fields may be decomposed into two separate polarization states with respect to $\hat{\mathbf{z}}$. A decomposition with respect to polarization is also applicable for spherically layered media, where the configuration is uniform normal to the $\hat{\mathbf{r}}$ -direction in a spherical coordinate system. However, in contrast with the 2D case, $\hat{\mathbf{r}}$ is now the direction with respect to which the two polarizations are labeled. It is convenient to express the fields in terms of uncoupled Debye potentials, Π_e and Π_m , which are scalar functions. In particular, Π_e and Π_m are associated with fields TM and TE with respect to $\hat{\mathbf{r}}$, respectively. For a source-free background medium, we have [38]

$$\mathbf{E} = \nabla \times \mathbf{r}\Pi_m + \frac{1}{s\varepsilon_1} \nabla \times \nabla \times \mathbf{r}\Pi_e, \quad (\text{B.19a})$$

$$\mathbf{H} = \nabla \times \mathbf{r}\Pi_e - \frac{1}{s\mu_1} \nabla \times \nabla \times \mathbf{r}\Pi_m. \quad (\text{B.19b})$$

By substituting these relations into the source-free counterparts of Maxwell's equations, it follows that the Debye potentials satisfy,

$$[\nabla^2 - \gamma_1^2] \begin{Bmatrix} \Pi_e \\ \Pi_m \end{Bmatrix} = 0. \quad (\text{B.20})$$

Next, the \hat{r} -components of the fields are extracted from Eq. (B.19). With the vector identity, $\nabla \times \nabla \times \mathbf{A} = \nabla \nabla \cdot \mathbf{A} - \nabla^2 \mathbf{A}$, and Eq. (B.20), we obtain

$$E_r = \frac{1}{s\varepsilon_1} [\partial_r^2 r \Pi_e - \gamma_1^2 r \Pi_e], \quad (\text{B.21a})$$

$$H_r = -\frac{1}{s\mu_1} [\partial_r^2 r \Pi_m - \gamma_1^2 r \Pi_m]. \quad (\text{B.21b})$$

The expressions for the remaining transverse field components read

$$\begin{bmatrix} E_\theta \\ E_\phi \end{bmatrix} = \begin{bmatrix} \partial_\theta & -\frac{1}{\sin\theta} \partial_\phi \\ \frac{1}{\sin\theta} \partial_\phi & \partial_\theta \end{bmatrix} \begin{bmatrix} \frac{1}{s\varepsilon_1 r} \partial_r r & 0 \\ 0 & -1 \end{bmatrix} \begin{bmatrix} \Pi_e \\ \Pi_m \end{bmatrix}, \quad (\text{B.22a})$$

$$\begin{bmatrix} H_\theta \\ H_\phi \end{bmatrix} = \begin{bmatrix} \partial_\theta & -\frac{1}{\sin\theta} \partial_\phi \\ \frac{1}{\sin\theta} \partial_\phi & \partial_\theta \end{bmatrix} \begin{bmatrix} 0 & -\frac{1}{s\mu_1 r} \partial_r r \\ -1 & 0 \end{bmatrix} \begin{bmatrix} \Pi_e \\ \Pi_m \end{bmatrix}. \quad (\text{B.22b})$$

Before we proceed with the determination of the Debye potentials for a sphere, let us first start with the Debye potentials for a point source. To this end, we express the Green's function in terms of spherical harmonics and Bessel functions. The Green's function $G(\mathbf{r}, \mathbf{r}')$ is the point-source solution of the scalar wave equation (2.36), which may be written in terms of spherical coordinates as,

$$\left[\frac{1}{r^2} \partial_r r^2 \partial_r + \frac{1}{r^2 \sin\theta} \partial_\theta \sin\theta \partial_\theta - \frac{m^2}{\sin^2\theta} - \gamma_1^2 \right] G(r, \theta, \phi) = -\frac{\delta(r-r') \delta(\theta-\theta') \delta(\phi-\phi')}{r^2 \sin\theta}. \quad (\text{B.23})$$

The dependence of the Green's function on \mathbf{r}' has been omitted for convenience. To utilize the invariance of the configuration along the $\hat{\theta}$ and $\hat{\phi}$ directions, we apply the transformation,

$$G_n^m(r) = \frac{2n+1}{4\pi} \frac{(n-m)!}{(n+m)!} \int_0^{2\pi} \int_0^\pi G(r, \theta, \phi) P_n^m(\cos\theta) e^{-jm\phi} \sin\theta \, d\theta \, d\phi, \quad (\text{B.24a})$$

$$G(r, \theta, \phi) = \sum_{n=0}^{\infty} \sum_{m=-n}^n G_n^m(r) P_n^m(\cos\theta) e^{jm\phi}, \quad (\text{B.24b})$$

with P_n^m being the associated Legendre polynomial of integer order m and degree n . By applying the transformation to Eq. (B.23), followed by a separation of variables with separation constant $n(n+1)$, we obtain

$$\left[\frac{1}{r^2} \partial_r r^2 \partial_r - \frac{n(n+1)}{r^2} - \gamma_1^2 \right] G_n^m(r) = -\frac{2n+1}{4\pi} \frac{(n-m)!}{(n+m)!} \frac{\delta(r-r')}{r^2} P_n^m(\cos\theta') e^{-jm\phi'} \quad (\text{B.25})$$

The general solution is expressed in terms of modified spherical Bessel functions of the first and second kind known as $i_n(z)$ and $k_n(z)$, respectively, with order n and argument z . In view of

Eq. (B.25), $G_n^m(r)$ must be continuous across $r = r'$. Accordingly, we may write

$$G_n^m(r) = C_n^m i_n(\gamma_1 r_<) k_n(\gamma_1 r_>), \quad (\text{B.26})$$

with $r_> = \max(r, r')$ and $r_< = \min(r, r')$. Furthermore, Eq. (B.25) implies that $\partial_r G_n^m(r)$ must jump at $r = r'$. Accordingly, from that jump condition and the Wronskian relation

$$i_n'(z) k_n(z) - i_n(z) k_n'(z) = \frac{1}{z^2}, \quad (\text{B.27})$$

the constants C_n^m may be determined. This leads to

$$\begin{aligned} G(r, \theta, \phi) &= \gamma_1 \sum_{n=0}^{\infty} \frac{2n+1}{4\pi} \sum_{m=-n}^n \frac{(n-m)!}{(n+m)!} i_n(\gamma_1 r_<) k_n(\gamma_1 r_>) P_n^m(\cos \theta) P_n^m(\cos \theta') e^{jm(\phi-\phi')} \\ &= \gamma_1 \sum_{n=0}^{\infty} \frac{2n+1}{4\pi} i_n(\gamma_1 r_<) k_n(\gamma_1 r_>) P_n(\cos \Theta), \end{aligned} \quad (\text{B.28})$$

with Θ the scattering angle between the source and observation point. Further, we have used

$$P_n(\cos \Theta) = P_n(\cos \theta) P_n(\cos \theta') + 2 \sum_{m=1}^n \frac{(n-m)!}{(n+m)!} P_n^m(\cos \theta) P_n^m(\cos \theta') \cos(\phi - \phi'), \quad (\text{B.29a})$$

$$\cos \Theta = \cos \theta \cos \theta' + \sin \theta \sin \theta' \cos(\phi - \phi'). \quad (\text{B.29b})$$

Next, we express the field from an electric point source in terms of Green's function. In turn, the corresponding Debye potentials follow from the radial field components. In view of Eq. (2.43), the magnetic field from the electric point source, $\mathbf{J}(\mathbf{r}) = \hat{\boldsymbol{\alpha}} \delta(\mathbf{r} - \mathbf{r}')$, is found to be

$$\mathbf{H} = \nabla \times [\hat{\boldsymbol{\alpha}} G(\mathbf{r}, \mathbf{r}')]. \quad (\text{B.30})$$

The substitution of Eq. (B.30) in the source-free counterpart of the law of Ampère-Maxwell, Eq. (2.11a), yields the electric field outside the source point. By taking the inner product with \mathbf{r} , rE_r is found to be

$$rE_r = \frac{1}{s\varepsilon_1} \mathbf{r} \cdot \nabla \times \nabla \times [\hat{\boldsymbol{\alpha}} G(\mathbf{r}, \mathbf{r}')]. \quad (\text{B.31})$$

Using source reciprocity, (cf. Eq. (2.49)), we have

$$\mathbf{r} \cdot \nabla \times \nabla \times [\hat{\boldsymbol{\alpha}} G(\mathbf{r}, \mathbf{r}')] = \hat{\boldsymbol{\alpha}} \cdot \nabla' \times \nabla' \times [\hat{\mathbf{r}} G(\mathbf{r}, \mathbf{r}')]. \quad (\text{B.32})$$

In view of the identity

$$\nabla' \times [(\mathbf{r} - \mathbf{r}') G(\mathbf{r}, \mathbf{r}')] = \mathbf{0}, \quad (\text{B.33})$$

Eq. (B.31) may be written as

$$rE_r = \frac{1}{s\varepsilon_1} \hat{\boldsymbol{\alpha}} \cdot \nabla' \times \nabla' \times [\mathbf{r}'G(\mathbf{r}, \mathbf{r}')]. \quad (\text{B.34})$$

Via a similar approach for H_r in Eq. (B.30), we obtain

$$rH_r = \hat{\boldsymbol{\alpha}} \cdot \nabla' \times [\mathbf{r}'G(\mathbf{r}, \mathbf{r}')]. \quad (\text{B.35})$$

By subjecting Eq. (B.20) to the transformation in Eq. (B.24), the part within brackets on the left-hand side is the same as that of Eq. (B.25). Consequently, for the n -th harmonic, E_r and H_r in Eq. (B.20) reduce to

$$E_r = -\frac{1}{s\varepsilon_1} \frac{n(n+1)}{r} \Pi_e, \quad (\text{B.36a})$$

$$H_r = \frac{1}{s\mu_1} \frac{n(n+1)}{r} \Pi_m. \quad (\text{B.36b})$$

Hence, the Debye potentials follow from the r -components of the field and the Green's function expressed in terms of spherical harmonics. Combined, we have

$$\Pi_e = -\frac{\gamma_1}{4\pi} \hat{\boldsymbol{\alpha}} \cdot \nabla' \times \nabla' \times \mathbf{r}' \sum_{n=0}^{\infty} \frac{2n+1}{n(n+1)} \Upsilon_n(r, r') P_n(\cos \Theta), \quad (\text{B.37a})$$

$$\Pi_m = s\mu_1 \frac{\gamma_1}{4\pi} \hat{\boldsymbol{\alpha}} \cdot \nabla' \times \mathbf{r}' \sum_{n=0}^{\infty} \frac{2n+1}{n(n+1)} \Upsilon_n(r, r') P_n(\cos \Theta), \quad (\text{B.37b})$$

with,

$$\Upsilon_n(r, r') = i_n(\gamma_1 r_{<}) k_n(\gamma_1 r_{>}). \quad (\text{B.38})$$

Via Eq. (B.19) the electric and magnetic field of an electric point source in a homogeneous medium may be expressed in terms of the Debye potentials. Note that the potentials for a magnetic point source readily follow by duality.

In turn, the potentials associated with the scattering from a dielectric sphere have the same form as they follow from Eq. (B.20) through a similar derivation as performed for the electric point source. In fact, only Υ_n changes, i.e., an interior scattered field for $r < a$, and an exterior scattered field combined with the above incident field for $r > a$. In particular, we may write

$$\Upsilon_n^{\text{cyl}}(r, r') = \begin{cases} R_n^j k_n(\gamma_1 r') k_n(\gamma_1 r) + i_n(\gamma_1 r_{<}) k_n(\gamma_1 r_{>}), & r > a, \\ T_n^j k_n(\gamma_1 r') i_n(\gamma_1 r), & r < a, \end{cases} \quad (\text{B.39})$$

with $j = \text{TM}$ for $\Upsilon_n^{\text{cyl}} = \Pi_e$ and $j = \text{TE}$ for $\Upsilon_n^{\text{cyl}} = \Pi_m$. Here, R_n and T_n represent the as yet unknown reflection and transmission coefficients for the scattered exterior and interior fields,

respectively. The second term for $r > a$ is the electric point source solution, Eq. (B.38). Once the scattering coefficients have been determined, we may account for the presence of the sphere by replacing Υ_n by Υ_n^{cyl} in Eq. (B.37) and considering Π_e and Π_m in the background medium. Notice that all derivatives with respect to θ and ϕ of Π_e and Π_m in Eq. (B.36), only operate on $P_n(\cos \Theta)$. This is also the case for the primed coordinates.

The unknown scattering coefficients follow from the boundary conditions at the interface $r = a$. Since this is a source-free interface, boundary conditions of the continuity type hold for the tangential field components. By inspecting Eq. (B.22), continuity of the individual field components implies that Π_e , Π_m , $\frac{1}{\varepsilon} \partial_r [r \Pi_e]$, and $\frac{1}{\mu} \partial_r [r \Pi_m]$ must remain continuous across $r = a$. We consider the TE-case first. Since the spherical harmonics are linearly independent, the conditions for Π_m lead to the following set of equations,

$$R_n^{\text{TE}} k_n(\gamma_1 a) + i_n(\gamma_1 a) = T_n^{\text{TE}} i_n(\gamma_2 a), \quad (\text{B.40a})$$

$$\mu_2 R_n^{\text{TE}} \partial_a [a k_n(\gamma_1 a)] + \mu_2 \partial_a [a i_n(\gamma_1 a)] = \mu_1 T_n^{\text{TE}} \partial_a [a i_n(\gamma_2 a)], \quad (\text{B.40b})$$

for $r' > a$. Subsequently, with the introduction of the characteristic denominator

$$d_n^{\text{TE}} = \left[Z_1 \check{k}_n(\gamma_1 a) \check{i}'_n(\gamma_2 a) - Z_2 \check{k}'_n(\gamma_1 a) \check{i}_n(\gamma_2 a) \right], \quad (\text{B.41})$$

with $\check{i}_n(z) = z i_n(z)$ and $\check{k}_n(z) = z k_n(z)$, the scattering coefficients are found to be

$$T_n^{\text{TE}} = \mu_2 c_1 / d_n^{\text{TE}}, \quad (\text{B.42a})$$

$$R_n^{\text{TE}} = \left[Z_2 \check{i}'_n(\gamma_1 a) \check{i}_n(\gamma_2 a) - Z_1 \check{i}_n(\gamma_1 a) \check{i}'_n(\gamma_2 a) \right] / d_n^{\text{TE}}, \quad (\text{B.42b})$$

where the Wronskian relation in Eq. (B.27) has been used for T_n^{TE} . The scattering coefficients, T_n^{TM} and R_n^{TM} involving Π_e , follow from Eq. (B.42) by duality. Further, if the sphere comprises a PEC, the electric conductivity, and thereby also the imaginary part of ε_2 becomes infinite. Accordingly, for a PEC the reflection coefficients reduce to

$$R_n^{\text{TE}} = -\frac{\check{i}_n(\gamma_1 a)}{\check{k}_n(\gamma_1 a)}, \quad \text{and} \quad R_n^{\text{TM}} = -\frac{\check{i}'_n(\gamma_1 a)}{\check{k}'_n(\gamma_1 a)}, \quad (\text{B.43})$$

while $T_n = 0$ for both polarizations.

Appendix C

Far field integrals in closed form

In this appendix, we derive analytical expressions for the far-field integrals pertaining to the test and expansion integral for the forcing vector and the scattered field representation, respectively. For the 3D case in Section C.1, this involves the RWG function, \wedge , and the rotated RWG function, \vee . The far-field integral for the 2D case in Section C.2 is used to determine the normalized radiation pattern of a line source near a scattering object. In particular, expressions are provided for the piecewise constant and piecewise linear functions.

C.1 3D far-field integral

The far field due to current distributions, expanded in terms of \wedge - or the \vee -functions, may be determined analytically [127]. A compact derivation for the resulting expressions is presented below. To determine a bistatic RCS, these expressions may be used in the computation of the forcing vector in case of an incident plane wave, Eq. (7.30), but also for the evaluation of the scattered far field, Eq. (7.32).

The far-field integral in question may in case of a \wedge_n -expansion function be cast in the following form (Eq. (7.34)),

$$F_v \wedge_n(\hat{\mathbf{r}}) = \int_{\Gamma_n^\pm} \wedge_n(\mathbf{r}') e^{\gamma_v(\hat{\mathbf{r}} \cdot \mathbf{r}')} dA'. \quad (\text{C.1})$$

It is convenient to evaluate the integral in Eq. C.1 in terms of the local coordinate system intro-

duced in Section 7.2. Upon defining the propagation vector in the radial direction, $\gamma_v \equiv \gamma_v \hat{\mathbf{r}}$, the integral in local coordinates may be rewritten as

$$\int_{\Gamma_n^\pm} \Lambda_n(\mathbf{r}') e^{\gamma_v(\hat{\mathbf{r}} \cdot \mathbf{r}')} dA' = \frac{\ell_j}{2A^q} \int_{\Gamma^q} (\mathbf{r}' - \mathbf{r}_j^q) e^{\gamma_v \cdot \mathbf{r}'} dA' = \frac{\ell_j}{2} e^{\gamma_v \cdot \mathbf{r}_j^q} \nabla_{\gamma_v} \int_{\Gamma^q} e^{\gamma_v \cdot (\mathbf{r}' - \mathbf{r}_j^q)} dA', \quad (\text{C.2})$$

for $\mathbf{r}' \in \Gamma^q$. The remaining integral can be expressed as [128]

$$\int_{\Gamma^q} e^{\gamma_v \cdot (\mathbf{r}' - \mathbf{r}_j^q)} dA' = \frac{X_1(\beta_1) - X_2(\beta_2)}{\beta_1 - \beta_2}, \quad (\text{C.3})$$

where β_1 and β_2 denote the covariant components of the propagation vector in the local basis, Λ_j^q , and are given by

$$\beta_1 = \gamma_v \cdot \boldsymbol{\ell}_{j-1}, \quad (\text{C.4a})$$

$$\beta_2 = -\gamma_v \cdot \boldsymbol{\ell}_{j+1}. \quad (\text{C.4b})$$

The function X_q is given by

$$X_q(\beta) = \beta^{-q} \left[e^\beta - \sum_{\ell=0}^{q-1} \frac{1}{\ell!} \beta^\ell \right]. \quad (\text{C.5})$$

Due to finite-precision arithmetic, the evaluation of $X_q(\beta)$ according to its definition in terms of elementary functions would lead to severe loss of accuracy for small $|\beta|$, especially if q is large. On that account, we apply a Taylor expansion of the exponential functions, such that Eq. (C.5) reduces to

$$X_q(\beta) = \sum_{\ell=q}^{\infty} \frac{1}{\ell!} \beta^{\ell-q} = \sum_{\ell=0}^{\infty} \frac{1}{(\ell+q)!} \beta^\ell. \quad (\text{C.6})$$

If the above expansion is applied for $|\beta| < \pi/2$, truncation after 24 terms is sufficient to obtain an accuracy of 10^{-15} for $q \leq 4$. In turn, the gradient of Eq. (C.3) may be expressed in terms of the edge vectors associated with the local basis Λ_j^q ,

$$\nabla_{\gamma_v} \int_{\Gamma^q} e^{\gamma_v \cdot (\mathbf{r}' - \mathbf{r}_j^q)} dA' = g^1 \boldsymbol{\ell}_{j-1} - g^2 \boldsymbol{\ell}_{j+1}, \quad (\text{C.7})$$

in which the contravariant components of \mathbf{g} in the local basis are given by

$$g^v = \frac{(\beta_v - \beta_{3-v}) [X_1(\beta_v) - X_2(\beta_v)] + X_1(\beta_{3-v}) - X_1(\beta_v)}{(\beta_v - \beta_{3-v})^2}, \quad \text{with } v = 1, 2. \quad (\text{C.8})$$

To avoid loss of accuracy, Eq. (C.8) is evaluated via a truncated Taylor expansion for $\beta_1 \approx \beta_2$, according to

$$g^v = \sum_{n=0}^N \left(\lfloor \frac{n}{2} \rfloor + 1 \right) \left(\frac{\beta_v - \beta_{3-v}}{2} \right)^n \sum_{m=0}^{n+2} \left[\frac{(-1)^m}{(n+2-m)!} X_{m+1} \left(\frac{\beta_1 + \beta_2}{2} \right) \right] + \mathcal{O}([\beta_1 - \beta_2]^{N+1}), \quad (\text{C.9})$$

where the floor function, $\lfloor x \rfloor$, gives the largest integer less than or equal to x . For $|\beta_1 - \beta_2| < 10^{-2}$ we employ Eq. (C.9) with $N = 6$, instead of Eq. (C.8). Because the solution of Eq. (C.7) is expressed in terms of the edge vectors, the solution to Eq. (C.1) with \vee_n instead of \wedge_n follows immediately from the expressions given above.

C.2 2D radiation pattern

Below we determine the radiation pattern normalized to the total power radiated by an electric line source in free space, $\varphi(\phi)$. To determine $\varphi(\phi)$, we require the scattered far field. With embedding based on Schelkunoff's equivalence principle involving only electric equivalent currents, the scattered electric field follows from Eq. (5.54), and is given by

$$E_z^{\text{sc}}(\boldsymbol{\rho}) = \frac{s\mu_v}{2\pi} \int_{\mathcal{C}} J_z(\boldsymbol{\rho}') K_0(\gamma_v |\boldsymbol{\rho} - \boldsymbol{\rho}'|) d\ell', \quad (\text{C.10})$$

where v denotes the medium index and \mathcal{C} represents the outer contour of the composite scattering domain. For large argument z , we may write

$$K_0(z) \approx \sqrt{\frac{\pi}{2z}} e^{-z}. \quad (\text{C.11})$$

Further, in the far field we have, $|\boldsymbol{\rho} - \boldsymbol{\rho}'| = \rho - \hat{\boldsymbol{\rho}} \cdot \boldsymbol{\rho}' + \mathcal{O}\left(\frac{1}{\rho}\right)$, with $\rho = |\boldsymbol{\rho}|$. Accordingly, the far field approximation of Eq. (C.10) is given by

$$E_z^{\text{sc}}(\boldsymbol{\rho}) \approx \frac{s\mu_v}{\sqrt{8\pi}\gamma_v\rho} e^{-\gamma_v\rho} \int_{\mathcal{C}} J_z(\boldsymbol{\rho}') e^{\gamma_v(\hat{\boldsymbol{\rho}} \cdot \boldsymbol{\rho}')} d\ell'. \quad (\text{C.12})$$

The remaining integral is the 2D counterpart of the 3D far-field integral in Eq. (7.34). Likewise, for the far field of an electric line source placed at the origin, we obtain

$$E_z^{\text{in}}(\boldsymbol{\rho}) = -\frac{s\mu_v}{2\pi} K_0(\gamma_v\rho) \approx -\frac{s\mu_v}{\sqrt{8\pi}\gamma_v\rho} e^{-\gamma_v\rho}. \quad (\text{C.13})$$

Upon applying the radiation condition to obtain the magnetic field the Poynting vector is found to be

$$\mathbf{S}(\boldsymbol{\rho}) = \frac{1}{2} \Re \{ \mathbf{E} \times \mathbf{H}^* \} = \frac{Y_v}{2} |E_z(\boldsymbol{\rho})|^2 \hat{\boldsymbol{\rho}}. \quad (\text{C.14})$$

Since the electric field is proportional to $\rho^{-1/2}$, the total power radiated per unit angle is given by

$$P(\phi) = |\rho \mathbf{S}(\boldsymbol{\rho})| = \frac{\rho Y_v}{2} |E_z(\boldsymbol{\rho})|^2, \quad (\text{C.15})$$

with $E_z = E_z^{\text{in}} + E_z^{\text{sc}}$. The total power radiated by the electric line source follows from the integration of the corresponding power density \mathbf{S}^{in} along a circle, which yields

$$P_t = \int_c \rho \mathbf{S}^{\text{in}}(\boldsymbol{\rho}) \cdot \hat{\boldsymbol{\rho}} \, d\ell = \frac{\rho Y_v}{2} \int_0^{2\pi} |E_z^{\text{in}}(\rho)|^2 \, d\phi = \pi \rho Y_v |E_z^{\text{in}}(\rho)|^2. \quad (\text{C.16})$$

Because $P_t/2\pi$ represents the average power radiated per unit ϕ , the normalized radiation pattern follows from

$$\wp(\phi) = \frac{2\pi P(\phi)}{P_t} \approx \left[1 - \int_c J_z(\boldsymbol{\rho}') e^{\gamma_v(\hat{\boldsymbol{\rho}} \cdot \boldsymbol{\rho}')} \, d\ell' \right]^2. \quad (\text{C.17})$$

Similar to the 3D case, the remaining far-field integral may be computed analytically. More specifically, via a transformation to the local coordinate system introduced in Section 5.3, $\boldsymbol{\rho}' = \boldsymbol{\rho}_n^c + d_n \xi \hat{\boldsymbol{\tau}}_n$, the far-field integral may be rewritten as

$$\int_c J_z(\boldsymbol{\rho}') e^{\gamma_v(\hat{\boldsymbol{\rho}} \cdot \boldsymbol{\rho}')} \, d\ell' = d_n e^{\gamma_v(\hat{\boldsymbol{\rho}} \cdot \boldsymbol{\rho}_n^c)} \int_{-1}^1 f(\xi) e^{\xi d_n \gamma_v(\hat{\boldsymbol{\rho}} \cdot \hat{\boldsymbol{\tau}}_n)} \, d\xi, \quad \text{for } \boldsymbol{\rho}' \in \Gamma_n, \quad (\text{C.18})$$

where $f(\xi)$ is a linear combination of the terms $\{1, \xi\}$, which depends on the specific expansion function (\square_n or \wedge_n). The remaining integral may be identified as the standard integral

$$I_{\text{f}}[f] = \frac{1}{2} \int_{-1}^1 f(\xi) e^{\xi a} \, d\xi, \quad (\text{C.19})$$

which solution is expressed in terms of hypergeometric functions

$$\begin{aligned} I_{\text{f}}[1] &= \frac{\sinh(a)}{a}, \\ I_{\text{f}}[\xi] &= \frac{a \cosh(a) - \sinh(a)}{a^2}. \end{aligned} \quad (\text{C.20})$$

For small values of a , a truncated Taylor-expansion is required.

Bibliography

- [1] G. E. Moore, “Cramming more components onto integrated circuits,” *Electronics magazine*, vol. 38, no. 8, pp. 1–4, 1965.
- [2] G. Krohn, “A set of principles to interconnect the solutions of physical systems,” *Journal of Applied Physics*, vol. 24, no. 8, pp. 965–980, 1953.
- [3] A. Neto, S. Maci, G. Vecchi, and M. Sabbadini, “A truncated floquet wave diffraction method for the full-wave analysis of large phased arrays. ii. generalization to 3-d cases,” *IEEE Trans. Antennas Propag.*, vol. 48, pp. 601–611, 2000.
- [4] C. Craeye, A. G. Tijhuis, and D. H. Schaubert, “An efficient mom formulation for finite-by-infinite arrays of two-dimensional antennas arranged in a three-dimensional structure.” *IEEE Trans. Antennas Propag.*, vol. 52, pp. 271–282, 2004.
- [5] P. M. van de Berg and J. T. Fokkema, “Removal of undesired wavefields related to the casing of a microwave scanner,” *IEEE Trans. Microwave Theory Tech.*, vol. 51, pp. 187–192, 2003.
- [6] A. Franchois and A. G. Tijhuis, “A quasi-Newton reconstruction algorithm for a complex microwave imaging scanner environment,” *Radio Sci.*, vol. 38, no. 2, pp. 8011–12, 2003.
- [7] L. Knockaert and D. de Zutter, “Laguerre-svd reduced-order modeling,” *IEEE Trans. Microwave Theory Tech.*, vol. 48, no. 9, pp. 1469–1475, 2000.
- [8] A. G. Tijhuis, K. Belkebir, A. C. S. Litman, and B. P. de Hon, “Theoretical and computational aspects of 2-d inverse profiling,” *IEEE. Trans. Geosci. Remote Sensing*, vol. 39, pp. 1316–1330, 2001.

- [9] A. G. Tijhuis, M. C. v. Beurden, and A. P. M. Zwamborn, "Iterative solution of field problems with a varying physical parameter," *Elektrik (Turk. J. Elec. Engin.)*, vol. 10, pp. 163–183, 2002, special issue for Prof. Leopold B. Felsen's 75th birthday.
- [10] A. M. van de Water, B. P. de Hon, M. C. van Beurden, A. G. Tijhuis, and P. de Maagt, "Linear embedding via green's operators: A modeling technique for finite electromagnetic band-gap structures," *Phys. Rev. E*, vol. 72, p. 056704, 2005.
- [11] C. Huygens, *Traité de la lumière*. Pierre van der Aa, Leiden, The Netherlands, 1690, composed in 1678.
- [12] A. E. H. Love, "The integration of the equations of propagation of electric waves," *Phil. Trans. Roy. Soc. London. Series A*, vol. 197, pp. 1–45, 1901.
- [13] S. Schelkunoff, "Some equivalence theorems of electromagnetics and their applications to radiation problems," *Bell Sys. Tech. J.*, vol. 15, pp. 92–112, 1936.
- [14] C. M. Butler, "Diakoptic theory and the moment method," in *IEEE AP-S Int. Symp. Dig.*, vol. 1, Dallas, TX, 1990, pp. 72–75.
- [15] A. R. Bretones, R. Mittra, and R. G. Martín, "A hybrid technique combining the method of moments in the time domain and fdtd," *IEEE Microwave Guided Wave Lett.*, vol. 8, no. 8, pp. 281–283, 1998.
- [16] S. Ooms and D. de Zutter, "A new iterative diakoptics-based multilevel moments method for planar circuits," *IEEE Trans. Microwave Theory Tech.*, vol. 46, no. 3, pp. 280–291, 1998.
- [17] J. E. Inglesfield, "A method of embedding," *Journal of Physics C*, vol. 14, no. 26, pp. 3795–806, 1981.
- [18] ———, "The embedding method for electromagnetics," *Journal of Physics A: Mathematical and General*, vol. 31, no. 42, pp. 8495–510, 1998.
- [19] A. J. Berkhout and D. J. Verschuur, "Estimation of multiple scattering by iterative inversion, part i: Theoretical considerations," *Geophysics*, vol. 62, no. 5, pp. 1586–1595, 1997.
- [20] R. Kemp and J. E. Inglesfield, "Embedding approach for rapid convergence of plane waves in photonic calculations," *Phys. Rev. B*, vol. 65, no. 11, p. 115103, 2002.

- [21] R. Holtzman and R. Kastner, "The time-domain discrete green's function method (gfm) characterizing the fdtd grid boundary," *IEEE Trans. Antennas Propagat.*, vol. 49, no. 7, pp. 1079–93, 2001.
- [22] R. Holtzman, R. Kastner, E. Heyman, and R.-W. Ziolkowski, "Stability analysis of the green's function method (gfm) used as an abc for arbitrarily shaped boundaries," *IEEE Trans. Antennas Propagat.*, vol. 50, no. 7, pp. 1017–29, 2002.
- [23] A. G. Tijhuis, M. C. van Beurden, and E. Korkmaz, "Modeling electromagnetic fields in large, finite structures using iterative techniques and the equivalence principle," in *2003 ICEAA International Conference on Electromagnetics in Advanced Applications, Torino, Italy, 8-12 September, 2003*, p. 4.
- [24] A. M. van de Water, "Integral equations for scattering by 3d-objects of arbitrary shape," Master's thesis, Eindhoven University of Technology, 2002.
- [25] P. Russer, M. Mongiardo, and L. B. Felsen, "Electromagnetic field representations and computations in complex structures iii: network representations of the connection and subdomain circuits," *International Journal of Numerical Modelling Electronic Networks Devices and Fields*, vol. 15, pp. 127–145, 2002.
- [26] L. Matekovits, G. Vecchi, G. Dassano, and M. Orefice, "Synthetic function analysis of large printed structures: the solution space sampling approach," in *Dig. of 2001 IEEE Antennas and Propagation Society International Symp.*, Boston, Massachusetts, July 2001, pp. 568–571.
- [27] V. V. S. Prakash and R. Mittra, "Characteristic basis function method: a new technique for fast solution of integral equations," *Microwave and Optical Technology Letters*, vol. 36, no. 2, pp. 95–100, 2003.
- [28] M. K. Li and W. C. Chew, "Wave-field interaction with complex structures using equivalence principle algorithm," *IEEE Trans. Antennas Propag.*, vol. 55, no. 1, pp. 130–138, 2007.
- [29] E. Ozbay, A. Abeyta, G. Tuttle, M. Tringides, R. Biswas, C. T. Chan, C. M. Soukoulis, and K. M. Ho, "Measurement of a three-dimensional photonic band gap in a crystal structure made of dielectric rods," *Phys. Rev. B*, vol. 50, no. 3, pp. 1945–1948, 1994.
- [30] T. D. Happ, M. Kamp, and A. Forchel, "Photonic crystal tapers for ultra compact mode conversion," *Opt. Lett.*, vol. 26, no. 14, pp. 1102–1104, 2001.

- [31] A. Mekis and J. D. Joannopoulos, "Tapered couplers for efficient interfacing between dielectric and photonic crystal waveguides," *Lightwave Technol.*, vol. 19, no. 6, pp. 861–865, 2001.
- [32] M. Bayindir, B. Temelkuran, and E. Özbay, "Propagation of photons by hopping: A waveguiding mechanism through localized coupled cavities in three-dimensional photonic crystals," *Phys. Rev. B*, vol. 61, no. 18, pp. R11 855–R11 858, 2000.
- [33] A. T. de Hoop, *Electromagnetic wavefield computation: A structured approach based on reciprocity*. Delft University of Technology, 1996, syllabus.
- [34] E. J. Rothwell and M. J. Cloud, *Electromagnetics*. CRC Press, 2001.
- [35] A. Ishimaru, *Electromagnetic wave propagation, radiation, and scattering*. Prentice-Hall, 1991.
- [36] E. Kuester and D. C. Chang, "Electromagnetic boundary problems," 2000, course notes for ECEN 5144.
- [37] V. H. Rumsey, "Reaction concept in electromagnetic theory," *Phys. Rev.*, vol. 94, pp. 1483–1491, 1954.
- [38] W. C. Chew, *Waves and fields in inhomogeneous media*, D. G. Dudley, Ed. IEEE Press, 1995.
- [39] A. J. Poggio and E. K. Miller, *Integral equation solutions of three-dimensional scattering problems*. Springer-Verlag, 1987, ch. 4, pp. 159–264.
- [40] Oseen, *Ann. Phys.*, vol. 48, no. 1, 1915.
- [41] J. A. Stratton, *Electromagnetic theory*. McGraw-Hill, 1941.
- [42] A. G. Tijhuis, *Iterative techniques for the solution of integral equations in transient electromagnetic scattering*, ser. Pier. Elsevier, 1991, vol. 5, ch. 13.
- [43] J. A. Kong, *Electromagnetic wave Theory*. Wiley, 1986.
- [44] R. E. Collin, *Field theory of guided waves*. IEEE Press, 1990.
- [45] A. D. Yaghjian, "Augmented electric and magnetic-field integral equations," *Radio Science*, vol. 16, pp. 987–1001, 1981.

- [46] A. F. Peterson, "The interior resonance problem associated with surface integral equations of electromagnetics: Numerical consequences and a survey of remedies," *Electromagn.*, vol. 10, pp. 293–312, 1990.
- [47] M. B. Woodworth and A. D. Yaghjian, "Derivation, application and conjugate gradient solution of dual-surface integral equations for three-dimensional, multi-wavelength perfect conductors," in *Progress in electromagnetic research*, T. K. Sarkar, Ed. PIER, 1991, vol. 5, pp. 103–29.
- [48] P. M. van den Berg, E. Korkmaz, and A. A. and, "A constrained conjugate gradient method for solving the magnetic field boundary integral equation," *IEEE Trans. Antennas Propagat.*, vol. 51, no. 6, pp. 1165–1176, 2003.
- [49] P. C. Waterman, "Matrix formulation of electromagnetic scattering," *Proc. IEEE*, vol. 53, pp. 805–812, 1965.
- [50] F. X. Canning, "Protecting efie-based scattering computations from effects of interior resonances," *IEEE Trans. Antennas Propagat.*, vol. 39, pp. 1545–1552, 1991.
- [51] J. R. Mautz and R. F. Harrington, "H-field, e-field, and combined field solutions for conducting bodies of revolution," *Archiv für Elektronik und Übertragungstechnik (AE Ü)*, vol. 32, pp. 466–470, 1978.
- [52] C. Müller, *Foundations of the mathematical theory of electromagnetic waves*. Springer-Verlag Berlin, 1969.
- [53] J. R. Mautz and R. F. Harrington, "Electromagnetic scattering from a homogeneous material body of revolution," *Archiv für Elektronik und Übertragungstechnik (AE Ü)*, vol. 33, pp. 71–80, 1979.
- [54] J. S. Zhao and W. C. Chew, "Integral equation solution of maxwells equations from zero frequency to microwave frequencies," *IEEE Trans. Antennas Propagat.*, vol. 48, pp. 1635–45, 2000.
- [55] S. Y. Chen, W. C. Chew, J. M. Song, and J. S. Zhao, "Analysis of low frequency scattering from penetrable scatterers," *IEEE Trans. Geosci.Remote Sensing*, vol. 39, pp. 726–735, 2001.
- [56] P. Y. Oijala and M. Taskinen, "Well-conditioned mller formulation for electromagnetic scattering by dielectric objects," *IEEE Trans. Antennas Propagat.*, vol. 53, pp. 3316–3323, 2005.

- [57] R. F. Harrington, *Field computation by moment methods*. IEEE Press, 1993.
- [58] R. Kress, *Linear integral equations*, F. John, J. E. Marsden, and L. Sirovich, Eds. Springer-Verlag, 1989.
- [59] A. F. Peterson, S. L. Ray, and R. Mittra, *Computational methods for electromagnetics*, D. G. Dudley, Ed. IEEE Press, 1998.
- [60] A. F. Peterson, D. R. Wilton, and R. E. Jorgenson, "Variational nature of galerkin and non-galerkin moment method solutions," *IEEE Trans. Antennas Propagat.*, vol. 44, pp. 500–503, 1996.
- [61] D. Colton and R. Kress, *Integral equations method in scattering theory*. Wiley, 1983.
- [62] E. Kreyszig, *Introductory functional analysis with applications*. Wiley, 1989.
- [63] C. E. Kenig, "Harmonic analysis technique for second order elliptic boundary value problems," in *Regional conference series in mathematics*. American mathematical society, 1994.
- [64] W. McLean, *Strongly elliptic systems and boundary integral equations*. Cambridge University Press, 2000.
- [65] Z. Q. Peng and A. G. Tijhuis, "Transient scattering by a lossy dielectric cylinder: marching-on-in-frequency approach," *J. Electrom. Waves Applic.*, vol. 7, pp. 739–763, 1993.
- [66] B. de Backer, F. Olyslager, and D. de Zutter, "An integral equation approach to the prediction of indoor wave propagation," *Radio Science*, vol. 32, pp. 1833–1855, 1997.
- [67] G. H. Golub and C. F. Loan, *Matrix computations*, 3rd ed. Johns Hopkins University Press, 1996.
- [68] R. E. Kleinman, G. F. Roach, and P. M. van den Berg, "Convergent born series for large refractive indices," *J. Opt. Sot. Amer.*, vol. 7, no. 5, pp. 890–897, 1990.
- [69] M. Costabel, "Boundary integral operators on lipschitz domains: Elementary results," *SIAM J. Math. Anal.*, vol. 19, pp. 613–626, 1988.
- [70] D. S. Jones, *The theory of electromagnetism*. Oxford, 1964.

- [71] J. Lions and E. Magenes, *Non-homogeneous boundary value problems and applications*. Berlin: Springer, 1972.
- [72] A. G. Tijhuis, “Electromagnetic inverse profiling : theory and numerical implementation,” Ph.D. dissertation, Technische Universiteit Delft, 1987.
- [73] J. Ma, V. Rokhlin, and S. Wandzura, “Generalized gaussian quadrature rules for systems of arbitrary functions,” *SIAM J. Numer. Anal.*, vol. 33, pp. 971–996, 1996.
- [74] G. L. G. Sleijpen and H. A. van der Vorst, “Maintaining convergence properties of BiCGstab methods in finite precision arithmetic.” *Numer. Algorithms*, vol. 10, pp. 203–223, 1995.
- [75] K. F. Warnick and W. C. Chew, “On the spectrum of the electric field integral equation and the convergence of the moment method,” *Int. J. Numer. Meth. Eng.*, vol. 51, pp. 31–56, 2001.
- [76] K. E. Atkinson, *The numerical solution of integral equations of the second kind*. Cambridge, 1997.
- [77] C. P. Davis and K. F. Warnick, “Error analysis of 2d mom for mfie/efie/cfie based on the circular cylinder,” *IEEE Trans. Antennas Propagat.*, vol. 53, pp. 321–331, 2005.
- [78] ———, “High-order convergence with a low-order discretization of the 2-d mfie,” *IEEE Antennas and wireless propagat. letters*, vol. 3, pp. 355–358, 2004.
- [79] K. F. Warnick and W. C. Chew, “Accuracy of the method of moments for scattering by a cylinder,” *IEEE Trans. Micr. Th. Tech.*, vol. 48, pp. 1652–1660, 2000.
- [80] J. B. Anderson and V. V. Solodukhov, “Field behavior near a dielectric wedge,” *IEEE Trans. Antennas Propagat.*, vol. 26, pp. 598–602, 1978.
- [81] J. van Bladel, “Field singularities at metal-dielectric wedges,” *IEEE Trans. Antennas Propagat.*, vol. 33, pp. 450–455, 1985.
- [82] J. D. Joannopoulos, R. D. Meade, and J. N. Winn, *Photonic crystals; Molding the flow of light*. Princeton university press, 1995.
- [83] Y. Naka and H. Ikuno, “Analysis of two-dimensional photonic crystal sharply bent waveguides,” in *2004 URSI International Symposium on Electromagnetic Theory, Pisa, Italy, 23–27 May, 2004*.

- [84] V. Rinnerbauer, J. Schermer, and K. Hingerl, "Polarization splitting based on planar photonic crystals," in *Proceedings of the Seminar at the Vienna University Of Technology*. The Society for Micro- and Nanoelectronics (GMe), 17–18 March 2005, pp. 97–100.
- [85] J. D. Joannopoulos, R. Meade, and J. N. Winn, *Photonic Crystals : Molding the Flow of Light*. Princeton University Press, Princeton, 1995.
- [86] A. M. van de Water, M. C. van Beurden, B. P. de Hon, and A. G. Tijhuis, "Boundary-integral formulation for electromagnetic bandgap calculations," *Institution of Engineering and Technology (IET) Microwaves, Antennas & Propagation*, submitted.
- [87] J. B. Pendry and A. MacKinnon, "Calculation of photon dispersion relations," *Phys. Rev. Lett.*, vol. 69, no. 19, pp. 2772–2775, November 1992.
- [88] K. M. Ho, C. T. Chan, and C. M. Soukoulis, "Existence of a photonic gap in periodic dielectric structures," *Phys. Rev. Lett.*, vol. 65, no. 25, pp. 3152–3155, December 1990.
- [89] C. T. Chan, Q. L. Yu, and K. M. Ho, "Order-N spectral method for electromagnetic waves," *Phys. Rev. B*, vol. 51, no. 23, pp. 16 635–16 642, June 1995.
- [90] H. S. Sözüer, J. W. Haus, and R. Inguva, "Photonic bands: Convergence problems with the plane-wave method," *Phys. Rev. B*, vol. 45, no. 24, pp. 13 962–13 972, June 1992.
- [91] M. G. Silveirinha and C. A. Fernandes, "Efficient calculation of the band structure of artificial materials with cylindrical metallic inclusions," *IEEE Trans. Microwave Theory Tech.*, vol. 51, no. 5, pp. 1460–1466, May 2003.
- [92] —, "A hybrid method for the efficient calculation of the band structure of 3-d metallic crystals," *IEEE Trans. Microwave Theory Tech.*, vol. 52, no. 3, pp. 889–902, March 2004.
- [93] L. C. Trintinalia and H. Ling, "Integral equation modeling of multilayered doubly-periodic lossy structures using periodic boundary condition and a connection scheme," *IEEE Trans. Antennas Propagat.*, vol. 52, no. 9, pp. 2253–2261, September 2004.
- [94] J. D. Joannopoulos, R. D. Meade, and J. N. Winn, *Photonic Crystals : Molding the Flow of Light*. Princeton University Press, 1995.
- [95] R. D. Meade, A. M. Rappe, K. D. Brommer, and J. D. Joannopoulos, "Nature of the photonic band gap: field analysis some insights from a field analysis," *J. Opt. Soc. Am. B*, vol. 10, pp. 328–332, 1993.

- [96] D. R. Smith, S. Schultz, and N. Kroll, "Experimental and theoretical results for a two-dimensional metal photonic band-gap cavity," *Appl. Phys. Lett.*, vol. 65, pp. 645–647, 1994.
- [97] Y. G. Smirnov, "The solvability of vector integro-differential equations for the problem of the diffraction of an electromagnetic field by screens of arbitrary shape," *Computat. Math. Mathem. Phys.*, vol. 33, pp. 1263–1273, 1994.
- [98] A. Buffa, M. Costabel, and C. Schwab, "Boundary element methods for maxwells equations on non-smooth domains," *Numer. Math.*, vol. 92, pp. 679–710, 2002.
- [99] M. Cessenat, *Mathematical methods in electromagnetism*. London : World Scientific, 1996.
- [100] A. Buffa and S. H. Christiansen, "The electric field integral equation on lipschitz screens: definitions and numerical approximation," *Numer. Math.*, vol. 94, pp. 229–267, 2003.
- [101] S. M. Rao, D. R. Wilton, and A. W. Glisson, "Electromagnetic scattering by surfaces of arbitrary shape," *IEEE Trans. Antennas Propagat.*, vol. 30, pp. 409–418, 1982.
- [102] ———, "E-field, h-field and combined field integral field solution for arbitrarily shaped three-dimensional dielectric bodies," *Electromagnetics*, vol. 10, pp. 407–421, 1990.
- [103] X. Q. Sheng, J. M. Jin, J. Song, C. C. Lu, and W. C. Chew, "Solution of combined-field integral equation using multilevel fast multiploe algorithm for scattering by homogeneous bodies," *IEEE Trans. Antennas Propagat.*, vol. 45, pp. 1488–1493, 1997.
- [104] G. Vecchi, "Loop-star decomposition of basis functions in the discretization of the efie," *IEEE Trans. Antennas Propagat.*, vol. 47, no. 2, pp. 339–346, 1999.
- [105] W. C. Thacker, "A brief review of techniques for generating irregular computational grids," *Int. J. Num. Meths. in Eng.*, vol. 15, pp. 1335–1341, 1980.
- [106] P. R. Silvester and R. L. Ferrari, *Finite elements for electrical engineers*. Cambridge University Press, 1983.
- [107] P. C. Hammer, O. J. Marlowe, and A. H. Stroud, "Numerical integration over simplexes and cones," *Math. Tables Aids Comp.*, vol. 10, pp. 130–137, 1956.
- [108] G. R. Cowper, "Gaussian quadrature formulas for triangles," *Int. J. Num. Meth. Eng.*, vol. 7, pp. 405–408, 1973.

- [109] L. N. Medgyesi-Mitschang, J. M. Putnam, and M. B. Gedera, "Generalized method of moments for three-dimensional penetrable scatterers," *J. Opt. Soc. Am. A*, vol. 11, pp. 1383–1389, 1994.
- [110] P. Y. Oijala and M. Taskinen, "Calculation of cfe impedance matrix elements with rwg and $n \times$ rwg functions," *IEEE Trans. Antennas Propagat.*, vol. 51, pp. 1837–1846, 2003.
- [111] B. H. Jung, "A survey of various frequency domain integral equations for the analysis of scattering from three-dimensional dielectric objects," in *Progress in electromagnetic research*, T. K. Sarkar and Y. S. Chung, Eds. PIER, 2002, vol. 36, pp. 193–246.
- [112] G. Beylkin, "Discrete radon transform," *IEEE Trans. acoustics, speech, and signal processing*, vol. 35, no. 2, pp. 162–172, 1987.
- [113] T. F. Eibert and V. Hansen, "On the calculation of potential integrals for linear source distributions on triangular domains," *IEEE Trans. Antennas Propagat.*, vol. 43, pp. 1499–1502, 1995.
- [114] P. Arcioni, M. Bressan, and L. Perregrini, "On the evaluation of the double surface integrals arising in the application of the boundary integral method to 3-d problems," *IEEE Trans. Micr. Th. Tech.*, vol. 45, pp. 436–439, 1997.
- [115] D. R. Wilton, S. M. Rao, A. W. Glisson, D. H. Schaubert, A. M. Al-Bundak, and C. M. Butler, "Potential integrals for uniform and linear source distributions on polygonal and polyhedral domains," *IEEE Trans. Antennas Propagat.*, vol. 32, pp. 276–281, 1984.
- [116] R. E. Hodges and Y. Rahmat-Samii, "The evaluation of mfie integrals with the use of vector triangle basis functions," *Microwave Opt. Technol. Lett.*, vol. 14, pp. 9–14, 1997.
- [117] R. D. Graglia, "On the numerical integration of the linear shape functions times the 3-d green's function or its gradient on a plane triangle," *IEEE Trans. Antennas Propagat.*, vol. 41, pp. 1448–1455, 1993.
- [118] *NAG Library Manual*, Mark 20 ed., Numerical Algorithms Group, Oxford, U.K. : Mayfield House, 2002.
- [119] C. F. Wang, F. Ling, J. Song, and J. Jin, "Adaptive integral solution of combined field integral equation," *Microwave and optical tech. lett.*, vol. 19, pp. 321–328, 1998.
- [120] W. J. Wiscombe, "Improved mie scattering algorithms," *Applied optics*, vol. 19, pp. 1505–1509, 1980.

- [121] R. Coifman, V. Rokhlin, and S. Wandzura, "The fast multipole method for the wave equation: A pedestrian prescription," *IEEE Antennas Propagat. Mag.*, vol. 35, pp. 7–12, 1993.
- [122] J. M. Song, C. C. Lu, and W. C. Chew, "Multilevel fast multipole algorithm for electromagnetic scattering by large complex objects," *IEEE Trans. Antennas Propagat.*, vol. 45, no. 10, pp. 1488–1493, 1997.
- [123] M. H. B. N. Georgieva, S. Glavic and J. W. Bandler, "Feasible adjoint sensitivity technique for em design optimization," *IEEE Trans. Microwave Theory Tech.*, vol. 50, no. 12, pp. 2751–2758, 2002.
- [124] D. Weile and E. Michielssen, "Genetic algorithm optimization applied to electromagnetics: A review," *IEEE Trans. Antennas Propagat.*, vol. 45, pp. 343–353, 1997.
- [125] I. S. Gradshteyn and I. M. Ryzhik, *Table of integrals, series, and products*. Academic Press, 1980.
- [126] M. Abramowitz and I. A. Stegun, Eds., *Handbook of mathematical functions*. Dover, 1965.
- [127] S. W. Lee and R. Mittra, "Fourier transform of a polygonal shape function and its application in electromagnetics," *IEEE Trans. Antennas and Propagation*, vol. 31, pp. 99–103, 1983.
- [128] M. C. van Beurden and B. P. de Hon, "Electromagnetic modelling of antennas mounted on a band-gap slab - discretisation issues and domain and boundary integral equations," in *Proc. of the Int. Conf. on Electromagnetics in Advanced Applications (ICEAA)*, R. D. Graglia, Ed. Politecnico di Torino, Torino, Italy, 8-12 September 2003, pp. 637–640.

Summary

LEGO: Linear Embedding via Green's Operators

Reduction of lead time has long been an important target in product development. Owing to the advance of computer power product optimization has been moved from the production stage to the preceding design stage. In particular, the full electromagnetic behavior of the final product can now be predicted through numerical methods. However, for the tuning of device parameters in the optimization stage, commercial software packages often rely on brute-force parameter sweeps. Further, for each set of parameter values a full recomputation of the entire configuration is usually required. In case of stringent product specifications or large complex structures, the computational burden may become severe. Recently, “marching on in anything” has been introduced to accelerate parameter sweeps. Nevertheless, it remains necessary to further reduce the computational costs of electromagnetic device design. This is the main goal in this thesis.

As an alternative to existing electromagnetic modeling methods, we propose a modular modeling technique called linear embedding via Green's operators (LEGO). It is a so-called diakoptic method based on the Huygens principle, involving equivalent boundary current sources by which simply connected scattering domains of arbitrary shape may fully be characterized. Mathematically this may be achieved using either Love's or Schelkunoff's equivalence principles, LEP or SEP, respectively. LEGO may be considered as the electromagnetic generalization of decomposing an electric circuit into a system of multi-port subsystems. We have captured the pertaining equivalent current distributions in terms of a lucid Green's operator formalism. For instance, our scattering operator expresses the equivalent sources that would produce the scattered field exterior to a scattering domain in terms of the equivalent sources that would produce the incident field inside that domain. The enclosed scattering objects may be of arbitrary shape and composition. The scattering domains together with their scattering operators constitute the LEGO building blocks. We have employed various alternative electromagnetic solution methods to construct the scattering operators. In its most elementary form, LEGO is a generalization of an embedding procedure introduced in inverse scattering to describe multiple scattering be-

tween adjacent blocks, by considering one of the blocks as the environment of the other and vice versa. To establish an interaction between current distributions on disjoint domain boundaries we define a source transfer operator. Through such transfer operators we obtain a closed loop that connects the scattering operators of both domains, which describes the total field including the multiple scattering. Subsequently, a combined scattering block is composed by merging the separate scattering operators via transfer operators, and removing common boundaries.

We have validated the LEGO approach for both 2D and 3D configurations. In the field of electromagnetic bandgap (EBG) structures we have demonstrated that a cascade of embedding steps can be employed to form electromagnetically large complex composite blocks. LEGO is a modular method, in that previously combined blocks may be stored in a database for possible reuse in subsequent LEGO building step. Besides scattering operators that account for the exterior scattered field, we also use interior field operators by which the field may be reproduced within (sub)domains that have been combined at an earlier stage. Only the subdomains of interest are stored and updated to account for the presence of additional domains added in subsequent steps. We have also shown how the scattering operator can be utilized to compute the band diagram of EBG structures. Two alternative methods have been proposed to solve the pertaining eigenvalue problem. We have validated the results via a comparison with results from a plane-wave method for 2D EBG structures. In addition, we have demonstrated that our method also applies to unit cells containing scattering objects that are perfectly conducting or extend across the boundary of the unit cell.

The optimization stage of a design process often involves tuning local medium properties. In LEGO we accommodated for this through a transfer of the equivalent sources on the boundary of a large scattering operator to the boundary of a relatively small designated domain in which local structure variations are to be tested. As a result, subsequent LEGO steps can be carried out with great efficiency. As demonstrators, we have locally tuned the transmission properties at the Y-junction of both a power splitter and a mode splitter in EBG waveguide technology. In these design examples the computational advantageous of the LEGO approach become clearly manifest, as computation times reduce from hours to minutes. This efficient optimization stage of the LEGO method may also be integrated with existing software packages as an additional design tool. In addition to the acceleration of the computations, the reusability of the composite building constitute an important advantage.

The Green's operators are expressed in terms of equivalent boundary currents. These operators have been obtained using integral equations. In the numerical implementation of the LEGO

method we have discretized the operators via the method of moments with a flat-facetted mesh using local test and expansion functions for the fields and currents, respectively. In the 2D case we have investigated the influence of using piecewise constant and piecewise linear functions. For the 3D implementation, we have applied the Rao-Wilton-Glisson (RWG) functions in combination with rotated RWG functions. After discretization, operators and operator compositions are matrices and matrix multiplications, respectively. Since the matrix multiplications in a LEGO step dominate the computational costs, we aim at a maximum accuracy of the field for a minimum mesh density.

For LEGO with SEP, we have determined the unknown currents through inverse field propagators, whereas with LEP, the currents are directly obtained from the tangential field components via inverse Gram matrices. After a careful assessment of the computational costs of the LEGO method, it turns out that owing to the removal of common boundaries and the reusability of scattering domains, the most efficient application of LEGO involves a closely-packed configuration of identical blocks. In terms of the number of array elements, N , the complexity of a sequence of LEGO steps for 2D and 3D applications increases as $\mathcal{O}(N^{1.5})$ and $\mathcal{O}(N^2)$, respectively. We have discussed possible improvements that can be expected from "marching on in anything" or multi-level fast-multipole algorithms. From an evaluation of the resulting scattered field, it turns out that LEGO with SEP is more accurate than with LEP. However, the spurious interior resonance effect common to SEP in the construction of composite building blocks can not simply be avoided through a combined field integral equation. By contrast, LEGO based on LEP is robust. Further, we have demonstrated that additional errors due to the choice of domain shape or building sequence, or the accumulation of errors due to long LEGO sequences are negligible.

Further, we have investigated integral equations for the scattering from 2D and 3D perfectly conducting and dielectric objects. The discretized integral operators directly apply to the LEGO method. For scattering objects that are not canonical, these integral equations are used in the construction of the elementary LEGO blocks. Since we aim at a maximum accuracy of the field for a minimum mesh density, the regular test and expansion integral parts are primarily determined through adaptive quadrature rules, while analytic expressions are used for the singular integral parts. It turns out that the convergence of the scattered field is a direct measure for the accuracy of the scattered field computed with LEGO based on SEP or LEP. As an alternative to the PMCHW and the Müller integral equations, we have proposed a new integral equation formulation, which leads to cubic convergence in the 2D case, irrespective of the mesh density and object shape. In case of scattering object with a regular boundary domain scaling may be used to improve the convergence rate of the scattered field.

Curriculum Vitae

Frank van de Water was born in Wijchen, The Netherlands, on May 14, 1976. After secondary education at the Dukenburg College Nijmegen, he started studying Electrical Engineering at the intermediate technical school in Nijmegen. In 1995 he continued his studies at the polytechnic college in 's-Hertogenbosch. After a half year he obtained his Propaedeutic degree and enrolled as a student in Electrical Engineering at the Eindhoven University of Technology. From September 2000 until Januari 2001 he investigated field distributions within anechoic chambers via ray-tracing models for the National Institute of Standards and Technology (NIST) at the electromagnetics division of the U.S. Department of Commerce, Boulder, Colorado, U.S.A., under the supervision of Dr. Chris Holloway. In December 2001 he graduated with a M.Sc. degree from Eindhoven University of Technology on the numerical modeling of antenna elements via integral equations. This research had been carried out at Thales Nederland in Hengelo. From Januari 2002 until December 2006 he carried out his Ph.D. research on the linear embedding via Green's operators (LEGO) under the joint supervision of Dr. B.P. de Hon and Prof. Dr. A. G. Tijhuis in the electromagnetics group of the COBRA research school at Faculty of Electrical Engineering at the Eindhoven University of Technology. From May 2002 until August 2002 he joined the STARTIGER program of the European Space Agency (ESA) at the Space Science and Technology Department of the CCLRC Rutherford Appleton laboratory, Abingdon, U.K., where he collaborated in an international team of scientists to force a breakthrough in the development of a color submillimetre wave imager. Currently, he is with Thales as engineer antenna development.

Acknowledgements

Now that I have finished this thesis I would like to take the opportunity to express my thanks towards all the people that have contributed to this work and who sincerely earn my gratitude. As a start, I would like to thank Anton Tjihuis for his vision and creative ideas, but also for always expressing such strong confidence and enthusiasm towards my work. I am very grateful for the frequent help and guidance of Bas de Hon throughout the preparations of this thesis. I thank him for being such a good colleague as well as a friend, but also for accompanying me on several interesting and sometimes adventurous conferences. His thorough corrections on the thesis have certainly improved its contents significantly. Further, I appreciate the fruitful discussions I have had with Martijn van Beurden regarding the mapping properties of integral operators. His merits and insights into this topic have made this thesis a more complete one. I would also like to thank Emilia Motoaşcă for implementing an analytic solution for the near-field scattering response of dielectric spheres for me. Thanks is also in order to all the other members of the electromagnetics group at the Eindhoven University of Technology for being truly nice colleagues. Further, I thank Els Kok and Rob van der Heijden for showing me the practical side of electromagnetic bandgap materials at optical frequencies which includes our discussions on their potential applications. In addition, I would like to thank Frans Kanters for designing the cover of my thesis twice.

Further, I thank the European Space Agency for providing me the opportunity to participate in the Startiger programme. Especially the core team members: Dario, Alfred, Alexander, Derek, Jorge, Iñigo, David, James, Luisa, Alec, Geoff, Chris and Peter. Thank you all for your enthusiasm, experience, and great teamwork; it has been a lifetime experience to me.

Also, I owe much gratitude to my family, friends and relatives for their kind assistance and understanding. Especially, I would like to thank my parents for their endless encouraging support throughout the years. Without it, I most certainly wouldn't have been able to come this far. In particular, I would like to thank two of my brothers, Frits and Jeroen, for being my “paranimfen”

during the defense of this thesis. But most of all, my sincere gratitude goes to my girlfriend Karien for her unconditional love, support and believe in me. Especially during the last few months, her pep talks have been most welcome to not give in to the increasing pressure of finishing my thesis in so little time.

Finally, I would like to thank all who have shown interest in my work by reading this thesis. I sincerely hope that the introduction of the LEGO method will encourage new ideas for further research and applications.